NUREG/CP–0133
Vol. 3

Proceedings of the U.S. Nuclear Regulatory Commission

Twenty-First Water Reactor Safety Information Meeting

Volume 3
- Primary System Integrity
- Aging Research, Products & Applications
- Structural & Seismic Engineering
- Seismology & Geology

Held at
Bethesda Marriott Hotel
Bethesda, Maryland
October 25–27, 1993

U.S. Nuclear Regulatory Commission

Office of Nuclear Regulatory Research

Proceedings prepared by
Brookhaven National Laboratory



9405100242 940430
PDR NUREG
CP-0133 R PDR

NOTICE

These proceedings have been authored by a contractor of the United States Government. Neither the United States Government nor any agency thereof, or any of their employees, makes any warranty, expressed or implied, or assumes any legal liability or responsibility for any third party's use, or the results of such use, of any information, apparatus, product or process disclosed in these proceedings, or represents that its use by such third party would not infringe privately owned rights. The views expressed in these proceedings are not necessarily those of the U.S. Nuclear Regulatory Commission.

Available from

Superintendent of Documents
U.S. Government Printing Office
Mail Stop SSOP
Washington, DC 20402-9328

and

National Technical Information Service
Springfield, VA 22161

NUREG/CP-0133
Vol. 3
R1,R2,R3,R4,R5,
RD,RF,RG,RM,RV

Proceedings of the U.S. Nuclear Regulatory Commission

Twenty-First Water Reactor Safety Information Meeting

Volume 3

- Primary System Integrity
- Aging Research, Products & Applications
- Structural & Seismic Engineering
- Seismology & Geology

Held at
Bethesda Marriott Hotel
Bethesda, Maryland
October 25-27, 1993

Manuscript Completed: March 1994
Date Published: April 1994

Compiled by Susan Monteleone

Office of Nuclear Regulatory Research
U.S. Nuclear Regulatory Commission
Washington, DC 20555-0001

Proceedings prepared by
Brookhaven National Laboratory



ABSTRACT

This three-volume report contains 90 papers out of the 102 that were presented at the Twenty-First Water Reactor Safety Information Meeting held at the Bethesda Marriott Hotel, Bethesda, Maryland, during the week of October 25-27, 1993. The papers are printed in the order of their presentation in each session and describe progress and results of programs in nuclear safety research conducted in this country and abroad. Foreign participation in the meeting included papers presented by researchers from France, Germany, Japan, Russia, Switzerland, Taiwan, and United Kingdom. The titles of the papers and the names of the authors have been updated and may differ from those that appeared in the final program of the meeting.

PROCEEDINGS OF THE
21st WATER REACTOR SAFETY INFORMATION MEETING

October 25-27, 1993

Published in Three Volumes

GENERAL INDEX

VOLUME 1

- Plenary Session
- Advanced Reactor Research
- Advanced Instrumentation and Control Hardware
- Advanced Control System Technology
- Human Factors Research
- Probabilistic Risk Assessment Topics
- Thermal Hydraulics
- Thermal Hydraulic Research for Advanced Passive LWRs

VOLUME 2

- Severe Accident Research

VOLUME 3

- Aging Research, Products and Applications
- Primary System Integrity
- Structural and Seismic Engineering
- Seismology and Geology

REGISTERED ATTENDEES (NON-NRC)
21st WATER REACTOR SAFETY INFORMATION MEETING

Y. ABE
NUCLEAR POWER ENGINEERING CORP.
3-17-1,TORANOMON,MINATO-KU
TOKYO, 105
JAPAN

K. ALLARS
HM NUCLEAR INSTALLATIONS
BAYNARDS HOUSE, 1 CHEPSTOW PL.
WESTBOURNE GROVE, LONDON, W24TP
UK

C. ALLISON
INEL-EG&G, IDAHO
PO BOX 1625
IDAHO FALLS, ID 83402
USA

A. AMAEV
KURCHATOV INSTITUTE
123182 KURCHATOV SQ.
MOSCOW,
RUSSIA

B. ARCIERI
SCIENTECH
11821 PARKLAWN. DR.
ROCKVILLE , MD 20852
USA

H. ASCHER
H.E. ASCHER & ASSOCIATES
11916 GOYA DRIVE
POTOMAC, MD 20854
USA

Y. BANG
KOREA INSTITUTE OF NUCLEAR SAFETY
ADVANCED REACTOR DEPT, KINS, PO BOX 6
TAEJON, 305-635
KOREA

M. BARNES
AEA TECHNOLOGY
THOMSON HOUSE, RISLET, WARRINGTON
CHESHIRE, WA36A7
UK

D. BHARGAVA
VIRGINIA POWER
5000 DOMINION BLVD.
GLEN ALLEN, VA 23060
USA

L. BOLSHOV
RUSSIAN ACADEMY OF SCIENCES
52 B. TULSKAYA
MOSCOW,
RUSSIA

M. BOWMAN
BALTIMORE GAS & ELECTRIC
CCNPP BG&E
LUSBY, MD 20657
USA

G. BROWN
AEA TECHNOLOGY
THOMSON HOUSE, RISLEY
WARRINGTON, CHESHIRE 2A3 6AT
UK

S. ADDITON
TENERA/ARSAP
7272 WISCONSIN AVE., SUITE 300
BETHESDA, MD 20814
USA

R. ALLEN
PACIFIC NORTHWEST LABORATORY
BOX 999
RICHLAND, WA 99352
USA

K. ALMENAS
UNIVERSITY OF MARYLAND
MAT. & NUCL. ENG. DEPT.
COLLEGE PARK, MD 20742
USA

H. AMARISOORIYA
SCIENTECH
11821 PARKLAWN DR
ROCKVILLE, MD 20852
USA

N. ARDEY
TECHNICAL UNIVERSITY MUNICH
SENSERSTRASSE 15
81371 MUNICH, 81371
GERMANY

V. ASMOLOV
KURCHATOV INSTITUTE
123182 KURCHATOV SQ.
MOSCOW,
RUSSIA

A. BARATTA
PENN STATE UNIVERSITY
231 SACKETT
UNIVERSITY PARK, PA 16802
USA

V. BARNES
COMPA INDUSTRIES, INC.
270 WALKER DR., STE. 102
STATE COLLEGE PA 16801
USA

W.K BINNER
AUSTRIAN RESEARCH CENTER CONSULTANT
GORGENGASSE 30/3
WIEN, VIENNA A-1190
AUSTRIA

M. BONNER
BROOKHAVEN NATIONAL LABORATORY
BLDG. 197C
UPTON, NY 11973
USA

B. BOYACK
LOS ALAMOS NATIONAL LABORATORY
PO BOX 1663, MS K551
LOS ALAMOS, NM 87545
USA

D. BROWNSON
EG&G IDAHO, INC.
PO BOX 1625
IDAHO FALLS, ID 83415
USA

K. AKHTAR
U.S. DEPT. OF ENERGY
19901 GERMANTOWN RD.
GERMANTOWN, MD 20874
USA

M. ALLEN
SANDIA NATIONAL LABORATORIES
PO BOX 5800
ALBUQUERQUE, NM 87185
USA

A. ALONSO
MADRID POLYTEC. UNIV.
J. GUTIERREZ ABASCAL, 2
MADRID, 28006
SPAIN

L. ANDERMO
SKI
PO BOX 27406
STOCKHOLM, 10252
SWEDEN

H. ASAKA
JAPAN ATOMIC ENERGY RESEARCH INST.
SHIRAKATA
TOKA-MURA, IBARAKI-KEN 319-11
JAPAN

K. BANDYOPADHYAY
BROOKHAVEN NATIONAL LABORATORY
PO BOX 5000, BLDG. 475C
UPTON, NY 11973-5000
USA

R. BARI
BROOKHAVEN NATIONAL LABORATORY
P.O. BOX 5000, BLDG. 197C
UPTON, NY 11973-5000
USA

E. BASSANSKY
KURCHATOV INSTITUTE
123182 KURCHATOV SQ.
MOSCOW,
RUSSIA

T. BLANCHAT
SANDIA NATIONAL LABORATORIES
PO BOX 5800
ALBUQUERQUE, NM 87185
USA

S. BOUGAENKO
R&D INSTITUE OF POWER ENGINEERING
P.O. BOX 788
MOSCOW, 101000
RUSSIA

M. BRECK
NUS
910 CLOPPER ROAD
GAITHERSBURG, MD 20878
USA

I. BRUCE
NUCLEAR INSTALLATIONS INSPECTORATE
ST. PETERS HOUSE, BALLIOL ROAD
BOOTLE, MERSEYSIDE
UK

C. BUCHHOLZ
GE NUCLEAR ENERGY
175 CURTNER AVE MC 754
SAN JOSE, CA 95125
USA

R. CARO-MANSO
CONSEJO SEGURIDAD NUCLEAR
C/JUSTO DORADO
MADRID,
SPAIN

S. CHAE
KOREA ATOMIC ENERGY RESEARCH INSTITUTE
PO BOX 7, DAEDUK-DANJI
TAEJEON, 305-606
KOREA

Y-B CHEN
ATOMIC ENERGY COUNCIL, R.O.C.
67 LANE 144, KEELUNG RD. SEC. 4
TAIPEI, TAIWAN
ROC

T-H CHIEN
ARGONNE NATIONAL LABORATORY
9700 S. CASS AVE.
ARGONNE, IL 60439
USA

T. CHU
SANDIA NATIONAL LABORATORIES
PO BOX 5800
ALBUQUERQUE, NM 87185
USA

D. CHUNG
SCIENTECH
11821 PARKLAWN DR.
ROCKVILLE , MD 20852
USA

A. COMBESCURE
CEA-CENTRE DE SACLAY
DRN/DMT/SEMT-BAT.454
GIF-sur-YVETTE CEDEX, 91191
FRANCE

W. CORWIN
OAK RIDGE NATIONAL LABORATORY
P.O. BOX 2008
OAK RIDGE, TN 37831-6151
USA

H. CURRIN
KNOLLS ATOMIC POWER LAB
RIVER RD.
SCHENECTADY, NY 12309
USA

B. DE BOECK
AIB-VINCOTTE NUCLEAIRE
AVENUE DU ROI 157
BRUSSELS, B-1060
BELGIUM

J. DETERMAN
EG&G IDAHO, INC.
PO BOX 1625
IDAHO FALLS, ID 83415
USA

R. BUDNITZ
FUTURE RESOURCES ASSOCIATES, INC.
2000 CENTER ST., SUITE 418
BERKELEY, CA 94704
USA

D. CASADA
OAK RIDGE NATIONAL LABORATORY
PO BOX 2009
OAK RIDGE, TN 37831-8038
USA

M. CHAIKO
PENNSYLVANIA POWER & LIGHT CO.
2 N. 9TH ST.
ALLENTOWN, PA 18101
USA

C. CHEN
GILBERT/COMMONWEALTH INC.
PO BOX 1498
READING, PA 19603
USA

O. CHOPRA
ARGONNE NATIONAL LABORATORY
9700 S. CASS AVENUE
ARGONNE, IL 60439
USA

C. CHUANG
ATOMIC ENERGY COUNCIL, R.O.C.
67 LANE 144, KEELUNG RD. SEC. 4
TAIPEI, TAIWAN
ROC

H. CHUNG
ARGONNE NATIONAL LABORATORY
9700 S. CASS AVENUE
ARGONNE, IL 60438
USA

S. CONVERSE
NORTH CAROLINA STATE UNIVERSITY
BOX 7801
RALEIGH, NC 27965
USA

K. COZENS
NUMARC
1776 I ST., NW, STE 300
WASHINGTON, DC 20006
USA

R. CURTIS
AECL TECHNOLOGIES
9210 CORPORATE BLVD.
ROCKVILLE, MD 20850
USA

J. DeBOR
SCIENCE & ENGINEERING ASSOCIATES
1700 ROCKVILLE PIKE, ST. 400
ROCKVILLE, MD 20852
USA

H. DEZFULI
SCIENTECH
11821 PARKLAWN DR.
ROCKVILLE, MD 20852
USA

J. BURTT
INEL/EG&G IDAHO INC.
P.O. BOX 1625
IDAHO FALLS, ID 83415-3895
USA

G. CENERINO
INST. DE PROTECTION ET DE SURETE NUCLEAIRE
60-68 AV. DU GENERAL LECLERC
FONTENAY-AUX-ROSES, BP6-92265
FRANCE

O. CHAKH
RRC KURCHATOV INSTITUTE
123182 KURCHATOV SQ.
MOSCOW,
RUSSIA

T. CHIBA
ISHIKAWAJIMA-HARIMA HEAVY INDUST.
1,SHIN-NAKAHARA-CHO, ISOGO-KU
YOKOHAMA, KANAGAWA 235
JAPAN

T-L CHU
BROOKHAVEN NATIONAL LABORATORY
PO BOX 5000, BLDG. 130
UPTON, NY 11973-5000
USA

V. CHUDANOV
NSI RUSSIAN ACADEMY
B. TULSKAYA
MOSCOW, 113191
RUSSIA

M. COLIN
CEA
80-68 AVENUE DU GENERAL LECLERC
FONTENAY AUX ROSES CEDEX, 92365
FRANCE

S. COOPER
SCIENCE APPLICATIONS INTERNATIONAL CORP.
1710 GOODRIDGE DRIVE
MC LEAN, VA
USA

H. CURRIN
MARTIN-MARIETTA
1 RIVER ROAD
NISKAYUNA, NY 12302
USA

F. DAVIS
SANDIA NATIONAL LABORATORIES
PO BOX 5800, DEPT. 6429
ALBUQERQUE, NM 87185
USA

E. DEL ANGEL
CNSNS/MEXICO
DR. BARRAGN #779, COL NARVARTE
MEXICO D.F., 03020
MEXICO

M. DIETRICK
WESTINGHOUSE BETTIS
2895 O'NEILL DR.
BETHEL PARK, PA 15102
USA

M. DIMARZO
UNIVERSITY OF MARYLAND
MECHANICAL ENG. DEPT.
COLLEGE PARK, MD 20742
USA

S. DOCTOR
PACIFIC NORTHWEST LABORATORY
PO BOX 999, MSIN K5-26
RICHLAND, WA 99352
USA

S. DOROFEEV
KURCHATOV INSTITUTE
123182 KURCHATOV SQ.
MOSCOW,
RUSSIA

S. DRUCE
AEA TECHNOLOGY
REACTOR SVCS., B10-28
OXFORDSHIRE, OX11ORA
UK

G. DUPRE
CENTRE NATL. DE LA RECHERCHE SCIENTIFIQUE
1 C AVENUE DE LA RECHERCHE SCIENTIFIQUE
ORLEANS, CEDEX 2 45071
FRANCE

Z. ELAWAR
ARIZONA PUBLIC SERVICE CO.
PO BOX 52034
PHOENIX, AZ 85072
USA

B. EVANS
NUMARC
1776 I ST., NW, STE 300
WASHINGTON, DC 20006
USA

B. FINK
MPR ASSOCIATES, INC.
320 KING ST.
ALEXANDRIA, VA 22314-3238
USA

E. FOX
ORNL, MARTIN MARIETTA ENERGY SYSTEMS
PO BOX 2009
OAK RIDGE, TN 37831
USA

R. GAUNTT
SANDIA NATIONAL LABORATORIES
PO BOX 5800, DEPT. 6423
ALBUQUERQUE, NM 87185
USA

J. GIAMPETRO
WESTINGHOUSE BETTIS
2895 O'NEILL DR.
BETHEL PARK, PA 15102
USA

B. GITNICK
SCIENTECH
11821 PARKLAWN DR.
ROCKVILLE , MD 20852
USA

S. DINGMAN
SANDIA NATIONAL LABORATORIES
DEPT. 6413, PO BOX 5800
ALBUQUERQUE, NM 87185
USA

G. DOMINICI
L'ENERGIA E L'AMBIENTE
VIA MARTIRI DO MONTE SOLE, 4
BOLOGNA, 40129
ITALY

M. DOSTER
NORTH CAROLINA STATE UNIVERSITY
BOX 7909
RALEIGH, NC 27695
USA

R. DUFFEY
BROOKHAVEN NATIONAL LABORATORY
PO BOX 5000
UPTON, NY 11973-5000
USA

R. DURANTE
AECL TECHNOLOGIES
9210 CORPORATE BLVD.
ROCKVILLE, MD 20850
USA

G. EMBLEY
KAPL
BOX 1072
SCHENECTADY, NY 12301
USA

R. FAKORY
S3 TECHNOLOGIES, INC.
8930 STANFORD BLVD.
COLUMBIA, MD 21045
USA

M. FONTANA
OAK RIDGE NATIONAL LABORATORY
PO BOX 2009
OAK RIDGE, TN 37831-8056
USA

P. FULFORD
NUS
910 CLOPPER RD.
GAITHERSBURG, MD 20878
USA

G. GAUTHIER
CEA-IPSN
BP8 60-68 AVE. DU GENERAL LECLERC
FONTENAY AUX ROSES, F92265
FRANCE

R. GILLILAND
OAK RIDGE NATIONAL LABORATORY
PO BOX 2009
OAK RIDGE, TN 37831
USA

F. GIUDICE
AECL-CANDU
2251 SPEAKMAN DR.
MISSISSAUGA, ONTARIO L5K1B2
CANADA

N. DJEBAILI
CENTRE NATL. DE LA RECHERCHE SCIENTIFIQUE
1 C AVENUE DE LA RECHERCHE SCIENTIFIQUE
ORLEANS, CEDEX 2 45071
FRANCE

R. DOREMUS
ADVANCED RESOURCE DEVELOPMENT CORP.
9151 RUMSEY RD.
COLUMBIA, MD 21045
USA

Y. DRAGUNOV
EDO GIDROPRESS
STREET ORDZHONIKIDZE,21
MOSCOW DISTRICT, P 142103
RUSSIA

A. DUMONTET
ELECTRICITE DE FRANCE/SEPTEN
12-14 AVENUE DUTRIEVOZ
VILLEURBANNE, 69628
FRANCE

E. EASON
MODELING & COMPUTING SERVICES
CEDAR BLVD, SUITE 290
NEWARK, CA 94560
USA

H. ESMAILI
ENERGY RESEARCH, INC.
6290 MONTROSE RD.
ROCKVILLE, MD 20847
USA

N. FARUKHI
NUMARC
1776 I ST., NW, STE 300
WASHINGTON, DC 20006
USA

T. FOULT
COMMISSARIAT A L'ENERGIE ATOMIQUE
60-68 AVE. DU GENERAL LECLERC
FONTENAY-AUX-ROSES, 92265
FRANCE

H. GALE
TRW ENVIRONMENTAL SAFETY SYSTEMS, INC.
2650 PARK TOWER DR., STE 800
VIENNA, VA 22180
USA

G. GEISSLER
B&W NUCLEAR TECHNOLOGIES
3315 OLD FOREST RD, PO BOX 10935
LYNCHBURG, VA 24506-0935
USA

T. GINSBERG
BROOKHAVEN NATIONAL LABORATORY
PO BOX 5000, BLDG. 197D
UPTON, NY 11973-5000
USA

M. GOLOVKOV
DIAGNOSTIC COMPLEKS & SYSTEMS
KITAYSKIY PR., 7
MOSCOW, 103073
RUSSIA

M. GOMOLINSKI
INST. DE PROTECTION E DE SURETE NUCLEAIRE
321 RUE DE CHARENTON
PARIS, 75012
FRANCE

R. GREENE
OAK RIDGE NATIONAL LABORATORY
PO BOX 2009
OAK RIDGE, TN 37831-8038
USA

E. HARVEGO
IDAHO NATIONAL ENGINEERING LAB
PO BOX 1625
IDAHO FALLS, ID 83415
USA

M. HASTINGS
OHIO STATE UNIVERSITY
206 W. 18TH AVE
COLUMBUS, OH 43210-1107
USA

T. HEAMES
SCIENCE APPLICATIONS INTERNATIONAL CORP.
2109 AIR PARK RD.
ALBUQUERQUE, NM 87106
USA

L. HERRANZ
CIEMAT-ITN
AVENIDA COMPLUTENSE, 22
MADRID, 28040
SPAIN

J. HIGHTON
NUCLEAR INSTALLATIONS INSPECTORATE
ST. PETERS HOUSE, STANLEY PRECINCT
BOOTLE, MERSYSIDE L20
UK

F. HOFMANN
KfK NUCLEAR RESEARCH CENTER
PO BOX 3640
KARLSRUHE, 76021
GERMANY

Y. HORIKAWA
KANSAI ELECTRIC POWER
1100 17TH ST., NW
WASHINGTON, DC 20036
USA

T. HSU
VIRGINIA POWER
5000 DOMINION BLVD.
GLEN ALLEN, VA 23060
USA

M. ICHIKAWA
JAPAN ATOMIC ENERGY RESEARCH INST.
SHIRAKATA
TOKAI-MURA, IK 319-11
JAPAN

H. ISBIN
NSRRC
2815 MONTEREY PKWY.
ST. LOUIS PARK, MN 55416
USA

W. GRANT
AECB-CANADA
280 SLATER
OTTAWA, ONTARIO K1P 5S9
CANADA

P. GRIFFIN
OAK RIDGE NATIONAL LABORATORY
P.O. BOX 2009, M.S. 8057
OAK RIDGE, TN 37831-8057
USA

R. HARVEY
YANKEE ATOMIC ELECTRIC CO.
580 MAIN ST.
BOLTON, MA 01740
USA

J. HAWTHORNE
MATERIALS ENGINEERING ASSOCIATES, INC.
9700-B M.L. KING, JR. HWY.
LANHAM, MD 20706-1837
USA

M. HEITSCH
Gesellschaft fur Anlagen und Reaktorsicherheit
SCHWERTNERGASSE 1
KOLN 1, 50667
GERMANY

M. HESSHEIMER
SANDIA NATIONAL LABORATORIES
DEPT. 6449
ALBUQUERQUE, NM 87185
USA

H. HIRSCHMANN
PAUL SCHERRER INSTITUTE
CH-5232 VILLIGEN PSI

SWITZERLAND

C. HOFMAYER
BROOKHAVEN NATIONAL LABORATORY
BLDG. 475C
UPTON, NY 11973
USA

P. HOSEMANN
PAUL SCHERRER INSTITUT
WURENLINGEN UND VILLIGEN
VILLIGEN, CH-5232
SWITZERLAND

E. HUBNER
STONE & WEBSTER ENGINEERING
3 EXECUTIVE CAMPUS, PO BOX 5200
CHERRY HILL, NJ 08034
USA

K. IKONEN
VTT TECH. RESEARCH CENTRE OF FINLAND
PO BOX 208
ESPOO, 02151
FINLAND

M. ISHII
PURDUE UNIVERSITY
NUCLEAR ENGINEERING
WEST LAFAYETTE, IND 47907
USA

W. GRANT
MPR ASSOCIATES
320 KING ST.
ALEXANDRIA, VA 22314-3238
USA

C. HALIEMUN
ABACUS TECHNOLOGY CORP.
5454 WISCONSIN AVENUE, SUITE 1100
CHEVY CHASE, MD 20815
USA

H. HASHEMIAN
ANALYSIS & MEASUREMENT SERVICES CORP.
9111 CROSS PARK DR.
KNOXVILLE, TN 37923-4599
USA

P. HAYES
MPR ASSOCIATES
320 KING ST.
ALEXANDRIA, VA 22314-3238
USA

K. HENRIKSEN
CAE-LINK CORPORATION
5111 LEESBURG PIKE
FALLS CHURCH, VA 22041
USA

J. HIGGINS
BROOKHAVEN NATIONAL LABORATORY
BLDG. 130
UPTON, NY 11973
USA

S. HODGE
OAK RIDGE NATIONAL LABORATORY
P.O. BOX 2009, M.S. 8057
OAK RIDGE, TN 37831-8057
USA

D. HOLCOMB
ORNL, MARTIN MARIETTA ENERGY SYSTEMS
PO BOX 2008
OAK RIDGE, TN 37831-6010
USA

M-T HSU
ATOMIC ENERGY COUNCIL, R.O.C.
67 LANE 144, KEELUNG RD. SEC. 4
TAIPEI, TAIWAN
ROC

R. HUDDLESTON
OAK RIDGE NATIONAL LABORATORY
PO BOX 2009
OAK RIDGE, TN 37831-8056
USA

M. INAGAKI
NUCLEAR POWER ENGINEERING CORP.
3-17-1 #7 FL., TORANOMON, MINATO-KU
TOKYO, 105
JAPAN

S. ISKANDER
OAK RIDGE NATIONAL LABORATORY
4500S MS6151/P.O. BOX 2008
OAK RIDGE, TN 37921
USA

N. ITO
MITSUBISHI HEAVY INDUSTRIES, LTD.
2-4-1,SHIBAKOEN, MINATO-KU
TOKYO, 105
JAPAN

J. JANSKY
BTB-JANSKY GmbH
GERLINGER STR. 152
725 LEONBERG,
GERMANY

G. JOHNSEN
IDAHO NATIONAL ENGINEERING LABS
PO BOX 1625
IDAHO FALLS, ID 83415
USA

C. JONES
SCIENTECH
11821 PARKLAWN DR.
ROCKVILLE, MD 20852
USA

J. JUDD
IDAHO NATIONAL ENGINEERING LABS
PO BOX 1625-3890
IDAHO FALLS, ID 83415
USA

H. KARWAT
TECHNICAL UNIV. MUNICH
PORSCHUNOSGELANDE
GARCHING, 85748
GERMANY

M. KATO
TOSHIBA CORP.
8 SHINSUGITA-CHO, ISOGO-KU
YOKOHAMA, KANAGAWA 235
JAPAN

D. KELLY
GILBERT/COMMONWEALTH, INC.
PO BOX 1498
READING, PA 19603
USA

H. KIM
KOREA ATOMIC ENERGY RESEARCH INST.
PO BOX 7, DAEDUK-DANJI
TAEJEON, 305-606
KOREA

M. KINOSHITA
BROOKHAVEN NATIONAL LABORATORY
PO BOX 5000, BLDG. 197D
UPTON, NY 11973-5000
USA

D. KNUDSON
EG&G IDAHO, INC.
PO BOX 1625
IDAHO FALLS, ID 83415
USA

C. KOT
ARGONNE NATIONAL LABORATORY
9700 S. CASS AVE, BLDG. 331
ARGONNE, IL 60439
USA

K. IWAMOTO
NUCLEAR POWER ENGINEERING CORP.
3-17-1,TORANOMON,MINATO-KU
TOKYO, 105
JAPAN

I. JANSSON
ABB ATOM AKTIEBOLAG

VASTERAS, S72163
SWEDEN

AB JOHNSON
PACIFIC NORTHWEST LABORATORY
BATTELE, N.W., P8-10
RICHLAND, WA 99352
USA

F. JOPPEN
STRALINGSKONTROLE, KEURING & VEILIGHEID
BOERETANG 200
2400 MOL
BELGIUM

F. KAM
OAK RIDGE NATIONAL LABORATORY
PO BOX 2009
OAK RIDGE, TN 37831-8056
USA

G. KARZOV
CENT. RES. INST.-STRUCTURAL ANALYSIS
193167 NABEREZHNAYA REKY MONASTYRKY 1
ST. PETERSBURG,
RUSSIA

K. KAWANISKI
MITSUBISHI HEAVY INDUSTRIES
2-1-1 SHINNAMA ARAI-CHO
TAKASAGO, HYOGO 676
JAPAN

D. KELLY
IDAHO NATIONAL ENGINEERING LABS
11426 ROCKVILLE PIKE, STE. 300
ROCKVILLE, MD 20852
USA

I. KIM
BROOKHAVEN NATIONAL LABORATORY
PO BOX 5000, BLDG. 130
UPTON, NY 11973-5000
USA

P. KLOEG
KEMA
POST BOX 9035
ARNHEM, 6800ET
THE NETHERLANDS

K. KORSAH
OAK RIDGE NATIONAL LABORATORY
PO BOX 2008
OAK RIDGE, TN 37831-6010
USA

V. KOVYRSHIN
SCNRS

KIEV,
UKRAINE

A. IWANAGA
NUCLEAR POWER ENGINEERING CORP.
3-17-1 #7 FL, TORANOMON, MINATO-KU
TOKYO, 105
JAPAN

Y. JIN
KOREA ATOMIC ENERGY RESEARCH INST.
P.O. BOX 7, DAEDUK-DANJI
TAEGON,
KOREA

E. JONES
U.C. LAWRENCE LIVERMORE NAT'L LAB
PO BOX 808, L-190
LIVERMORE, CA 94550
USA

J. JOYCE
USNA, DEPT. OF MECHANICAL ENGINEERING

ANNAPOLIS, MD 21402
USA

H. KARASAWA
HITACHI LTD
5-2-2,OMIKA-CHO
HITACHI, IRARAKI 319-12
JAPAN

D. KATAYANAGI
HITACHI ENGINEERING CO., LTD.
3-1, SAIWAI-CHO 3-CHOME
HITACHI-SHI, IBARAKI-KEN 317
JAPAN

K. KELKAR
INNOVATIVE RESEARCH, INC.
2300 UNIVERSITY AVENUE SE
MINNEAPOLIS, MN 55414
USA

M. KHATIB-RAHBAR
ENERGY RESEARCH, INC.
6290 MONTROSE RD.
ROCKVILLE, MD 20852
USA

S. KINNERSLY
AEA TECHNOLOGY
LINFRITH TECHNOLOGY CENTRE
DORCHESTER, DORSET DT28DH
UK

L. KMETYK
SANDIA NATIONAL LABORATORIES
PO BOX 5800
ALBUQUERQUE, NM 87185-5800
USA

G. KORTH
EG&G IDAHO, INC.
PO BOX 1625
IDAHO FALLS, ID 83415-2218
USA

A. KRAEV
R&D INSTITUTE OF POWER ENGINEERING
P.O. BOX 788
MOSCOW, 101000
RUSSIA

C. KRAMER
GILBERT/COMMONWEALTH, INC.
PO BOX 1498
READING, PA 19603
USA

C. KUKIELKA
PENNSYLVANIA POWER & LIGHT CO.
2 N. 9TH ST.
ALLENTOWN, PA 18101
USA

J. LAKE
EG&G IDAHO, INC.
PO BOX 1625, MS 3880
IDAHO FALLS, ID 83415
USA

L. LAMBERT
SANDIA NATIONAL LABORATORIES
DEPT. 6449
ALBUQUERQUE, NM 87185
USA

R. LAW
VIRGINIA TECH
GEOLOGICAL SCIENCES
BLACKSBURG, VA 24061
USA

J. LEHNER
BROOKHAVEN NATIONAL LABORATORY
BLDG. 130, PO BOX 5000
UPTON, NY 11973-5000
USA

S. LEVINSON
B&W NUCLEAR TECHNOLOGIES
3315 OLD FOREST RD
LYNCHBURG, VA 24501
USA

A. LING
ATOMIC ENERGY CONTROL BOARD
C/O ONTARIO HYDRO, PO BOX 160
PICKERING, ONTARIO L1V 2R5
CANADA

R. LOFARO
BROOKHAVEN NATIONAL LABORATORY
BLDG. 130
UPTON, NY 11973
USA

F. LOSS
MATERIALS ENGINEERING ASSOCIATES, INC.
9700-B M.L. KING, JR. HWY.
LANHAM, MD 20706-1837
USA

J. LYLE
NIST
TECHNOLOGY BLDG B266
GAITHERSBURG, MD 20850
USA

A. MACHIELS
ELECTRIC POWER RESEARCH INSTITUTE
3412 HILLVIEW, PO BOX 10412
PALO ALTO, CA 94303
USA

A. KRYUKOV
KURCHATOV INSTITUTE
123182 KURCHATOV SQ.
MOSCOW,
RUSSIA

Y. KURAKOV
USSR MINISTRY OF NUCLEAR POWER & INDUSTRY
STAROMONETNY 26
MOSCOW, 109180
RUSSIA

A. LAKNER
VIKING SYSTEMS INTERNATIONAL
101 CHESTNUT ST.
GAITHERSBURG, MD 20877
USA

L. LARSON
WESTINGHOUSE BETTIS
2895 O'NEILL DR.
BETHEL PARK, PA 15102
USA

C. LECOMTE
INST. DE PROTECTION ET DE SURETE NUCLEAIRE
60-68 AV. DU GENERAL LECLERC
FONTENAY-AUX-ROSES, SP6-92265
FRANCE

C. LENGLADE
IDAHO NATIONAL ENGINEERING LAB
PO BOX 1625
IDAHO FALLS, ID 83415-3880
USA

V. LEVIT
KURCHATOV INSTITUTE
123182 KURCHATOV SQ.
MOSCOW,
RUSSIA

R. LINK
U.S. NAVY
CDNSWC 614
ANNAPOLIS, MD 21402
USA

P. LOPEZ
CNSNS/MEXICO
DR. BARRAGN 8779 COL NARVAR
MEXICO D.F., 03020
MEXICO

A. LOWE, JR.
LOWE ASSOCIATES
P.O. BOX 11964
LYNCHBURG, VA 24506-1964
USA

P. MAC DONALD
EG&G IDAHO, INC
PO BOX 1625
IDAHO FALLS, ID 83415-3860
USA

T. MADDEN
STONE & WEBSTER ENGINEERING
3 EXECUTIVE CAMPUS, PO BOX 5200
CHERRY HILL, NJ 08034
USA

J. KUJAL
NUCLEAR RESEARCH INSTITUTE REZ PLC
NUCL RES. INST./REZ NEAR PRAGUE

CZECH REP.

K. KUSSMAUL
MPA STUTTGART
PFAFFENWALDRING 32
STUTTGART, BADEN-WURTTEMBERG 70569
GERMANY

K. LAM
LOS ALAMOS NATIONAL LABORATORY
PO BOX 1663, MS K575
LOS ALAMOS, NM 87545
USA

K. LAUGHERY
MICRO ANALYSIS AND DESIGN
4900 PEARL EAST CIRCLE
BOULDER, CO 80301
USA

M. LEE
NATIONAL TSING HUA UNIVERSITY
NATION TSING HUS UNIV, DEPT. N.E.
HSINCHU,
TAIWAN

A. LERIDON
COMMISSARIAT A L'ENERGIE ATOMIQUE
C.E. CADARACHE DEC/SECA
ST. PAUL LES DURANCE, 13108
FRANCE

D. LIDBURY
AEA TECHNOLOGY
RISLEY, WARRINGTON
CHESHIRE, WA36AT
UK

M. LIVOLANT
INST. DE PROTECTION E DE SURETE NUCLEAIRE
CE/FONTENAY AUX ROSES
CEDEX, 92265
FRANCE

R. LORENZ
OAK RIDGE NATIONAL LABORATORY
P.O. BOX 2008-6221
OAK RIDGE, TN 37831
USA

W. LUCKAS
BROOKHAVEN NATIONAL LABORATORY
BLDG. 130, PO BOX 5000
UPTON, NY 11973-5000
USA

H. MACHIBA
TOSHIBA CORP.
8 SHINSUGITA-CHO, ISOGO-KU
YOKOHAMA, KANAGAWA 235
JAPAN

I. MADNI
BROOKHAVEN NATIONAL LABORATORY
BLDG. 130, PO BOX 5000
UPTON, NY 11973-5000
USA

D. MAGALLON
CED, JRC, ISPRA
HRC-EURATOM - ISPRA
ISPRA, 21020
ITALY

J. MARTINEZ
CSN SPAIN
C/JUSTO DORADO 11
MADRID, 28040
SPAIN

B. MAVKO
INSTITUTE J. STEFAN
JAMOVA 39, PO BOX 100
LJUBLJANA, 61111
SLOVENIA

N. McMILLAN
AEA TECHNOLOGY
THOMSON HOUSE, RISLEY
WARRINGTON, CHESHIRE 2A3 6AT
UK

E. MENARD
KNOLLS ATOMIC POWER LAB/MARTIN MARIETTA
P.O. BOX 1072
SCHENECTADY, NY 12301-1072
USA

M. MILLER
DUKE POWER CO.
OCONEE DIV., PO BOX 219
SENECA, SC 29679
USA

M. MODRO
EG&G IDAHO, INC.
P.O. BOX 1625, MS 3895
IDAHO FALLS, ID 83515
USA

S. MOROZOV
JCCCNRS-WG12

RUSSIA

R. MUMAW
WESTINGHOUSE STC
13100 BEULAH RD.
PITTSBURGH, PA 15235
USA

D. NAUS
OAK RIDGE NATIONAL LABORATORY
PO BOX 2009, MS-8056
OAK RIDGE, TN 37831-8056
USA

G. NIEDERAUER
LOS ALAMOS NATIONAL LABORATORY
MS K 575
LOS ALAMOS, NM 87554
USA

A. NONAKA
NUCLEAR POWER ENGINEERING CORP.
3-17-1,TORANOMON,MINATO-KU
TOKYO, 105
JAPAN

C. MALLON
NEWMAN & HOLTZINGER, PC
1615 L. SR. N.W.
WASHINGTON, DC 20036
USA

Y. MARUYAMA
JAPAN ATOMIC ENERGY RESEARCH INST.
TOKAI-MURA, NAKA-GUN
IBARAKI-KEN, 319-11
JAPAN

W. McAFEE
MARTIN MARIETTA ENERGY SYSTEMS
P.O. BOX 2009
OAK RIDGE, TN 37831-8047
USA

C. MEDICH
SOCIETA INFORMAZIONE ESPERIENZE TERMOIDRA
VIA NINO BIXIO, 27
PIACENZA, 29100
ITALY

M. MERILO
ELECTRIC POWER RESEARCH INST.
3412 HILLVIEW AVE.
PALO ALTO, CA 94304
USA

N. MIYAZAKI
KYUSYU UNIVERSITY
6-10-1, HAKOSAKI,HIGASHI-KU
FUKUOKA, FUKUOKA 812
JAPAN

D. MONHARDT
FRAMATOME S.A.
1 PLACE DE LA COUPOLE TOUR FIAT
PARIS-LA-DEFENSE, CEDEX 16-92084
FRANCE

L MOSEVITSKI
RRC KURCHATOV INSTITUTE
123182 KURCHATOV SQ.
MOSCOW,
RUSSIA

K. NAMATAME
JAPAN ATOMIC ENERGY RESEARCH INST.
SHIRAKATA
TOKAI-MURA, IK 319-11
JAPAN

C. NEGIN
GROVE ENGINEERING
15215 SHADY GROVE RD., STE. 200
ROCKVILLE, MD 20850
USA

V. NIKOLAEV
CENT. RES. INST.-STRUCTURAL ANALYSIS
193167 NABEREZHNAYA REKY MONASTY. 1
ST. PETERSBURG,
RUSSIA

D. O'CONNOR
OAK RIDGE NATIONAL LABORATORY

OAK RIDGE, TN 37831-8063
USA

R. MARTINELLI
ENEA, ENERGY DEPT.
CRE CASACCIA, 301 V. ANGUILLARESE
ROME, 00060
ITALY

M. MASSOUD
BALTIMORE GAS & ELECTRIC
CALVERT CLIFFS NPP
LUSBY, MD 20657
USA

R. McCARDELL
EG&G IDAHO, INC.
167 N. 4200 E
RIGBY, ID 83442
USA

J. MEINCKE
CONSUMERS POWER CO.
1156 OAK HAMPTON RD.
HOLLAND, MI 49424
USA

A. MEYER-HEINE
INST. DE PROTECTION ET DE SURETE NUCLEAIRE
CEN CADARACHE DRS/SENAR
ST. PAUL LEZ DURANCE, 13108
FRANCE

D. MODEEN
NUMARC
1776 I ST., NW, STE 300
WASHINGTON, DC 20006
USA

S. MONTELEONE
BROOKHAVEN NATIONAL LABORATORY
BLDG. 130, PO BOX 5000
UPTON, NY 11973-5000
USA

PROF. MULLER
KERNFORSCHUNGSZENTRUM
POSTFACH 3640
KARLSRUHE, D-76021
GERMANY

R. NANSTAD
OAK RIDGE NATIONAL LABORATORY
4500S MS6151/P.O. BOX 2008
OAK RIDGE, TN 37831
USA

D. NEWLAND
ATOMIC ENERGY CONTROL BOARD
280 SLATER STREET
OTTOWA, ONTARIO K1P5S9
CANADA

L. NILSSON
STUDSVIK BCO & SAFETY
S-611 82 NYKOPING

SWEDEN

J. OGATA
MITSUBISHI HEAVY INDUSTRIES, LTD.
2-4-1,SHIBAKOEN, MINATO-KU
TOKYO, 105
JAPAN

C. OLAND
OAK RIDGE NATIONAL LABORATORY
PO BOX 2009
OAK RIDGE, TN 37831-8056
USA

M. ORTIZ
IDAHO NATIONAL ENGINEERING LABS
P.O. BOX 1625
IDAHO FALLS, ID 83415-3895
USA

L. OTT
OAK RIDGE NATIONAL LABORATORY
BLDG. 9104-1, PO BOX 2009
OAK RIDGE, TN 37831-8057
USA

F. PAZDERA
NUCLEAR RESEARCH INSTITUTE REZ PLC
NUC. RES. INST./REZ NEAR PRAGUE

CZECH REPUBLIC

W. PERSONS
LAWRENCE LIVERMORE NAT'L LAB
PO BOX 808, L-632
LIVERMORE, CA 94550
USA

W. PRATT
BROOKHAVEN NATIONAL LABORATORY
BLDG. 130, PO BOX 5000
UPTON, NY 11973-5000
USA

J. PTACEK
ERI
P.O. BOX 2034
ROCKVILLE, MD 20847
USA

E. PURVIS
CONSULTANT
10105 CLEAR SPRING RD.
DAMASCUS, MD 20872
USA

K. REIL
SANDIA NATIONAL LABORATORIES
PO BOX 5800, DEPT. 6423
ALBUQUERQUE, NM 87185
USA

W. RETTIG
U.S. DEPARTMENT OF ENERGY
765 DOE PLACE
IDAHO FALLS, ID 83402
USA

M. RILEY
WESTINGHOUSE BETTIS
2895 O'NEILL DR.
BETHEL PARK, PA 15102
USA

Z. ROSZTOCZY
ZEETECH INC.
10131 WEATHERWOOD CT.
ROCKVILLE, MD 20854
USA

I. ORLOV
NSI RUSSIAN ACADEMY
B. TULSKAYA 52
MOSCOW,
RUSSIA

D. OSETEK
LOS ALAMOS TECHNICAL ASSOCIATES
2400 LOUISIANA NE, BLDG. 1, STE 400
ALBUQUERQUE, NM 87110
USA

J. PAPIN
INST. DE PROTECTION ET DE SURETE NUCLEAIRE
CEN CADARACHE DRS/SENAR
ST. PAUL LEZ DURANCE, 13108
FRANCE

B. PEARSON
ATOMIC ENERGY CONTROL BOARD
280 SLATER STREET
OTTAWA, K1P5S9
CANADA

R. PEKUL
MITRE CORP.
7525 COLSHIRE DR.
MC LEAN, VA 22102
USA

D. PRELEWICZ
SCIENTECH
11821 PARKLAWN DR.
ROCKVILLE, MD 20852
USA

J. PUGA
UNESA
FRANCISCO GERVAS 3
MADRID, 28020
SPAIN

F. QUINN
SCIENTECH
11821 PARKLAWN DR.
ROCKVILLE, MD 20852
USA

J. REMPE
EG&G IDAHO, INC.
PO BOX 1625, MS 3840
IDAHO FALLS, ID 83415
USA

P. REVEL
FRAMATOME USA, INC.
1925 N. LYNN ST., STE. 1100
ROSSLYN, VA 22209
USA

G. ROBINSON
PENN STATE UNIVERSITY

UNIVERSITY PARK, PA 16802
USA

J. ROYEN
OECD NUCLEAR ENERGY AGENCY
12 BOULEVARD DES ILES
ISSY-LES-MOULINEAUX, F-92130
FRANCE

N. ORTIZ
SANDIA NATIONAL LABORATORIES
PO BOX 5800
ALBUQUERQUE, NM 87185-5800
USA

V. OSTREJKOVSKY
OBNINSK INST. OF NUCLEAR POWER ENGINEERING
STUDENT CAMPUS
OBNINSK, KOIUGA 249020
RUSSIA

M. PARKS
SANDIA NATIONAL LABORATORIES
PO BOX 5800, DEPT. 6429
ALBUQERQUE, NM 87185
USA

W. PENNELL
OAK RIDGE NATIONAL LABORATORY
PO BOX 2009
OAK RIDGE, TN 37831-8056
USA

M. PILCH
SANDIA NATIONAL LABORATORIES
PO BOX 5800
ALBUQUERQUE, NM 87185
USA

V. PROKLOV
RUSSIAN RESEARCH CTR KURCHOTOV INST
ROGOVA STREET, 7, AP 32
MOSKOW,
RUSSIA

C. PUGH
OAK RIDGE NATIONAL LABORATORY
P.O. BOX 2009
OAK RIDGE, TN 37831
USA

M. QUINN
PACIFIC SCIENCE & ENG.
6310 GREENWICH DRIVE
SAN DIEGO, CA 92122
USA

M. REOCREUX
INST. DE PROTECTION ET DE SURETE NUCLEAIRE
CEN CADARACHE DRS/SENAR
ST. PAUL LEZ DURANCE, 13108
FRANCE

L. RIB
AECL TECHNOLOGIES
9210 CORPORATE BLVD.
ROCKVILLE, MD 20850
USA

U. ROHATGI
BROOKHAVEN NATIONAL LABORATORY
BLDG. 475B
UPTON, NY 11973
USA

G. RUDY
NUS
910 CLOPPER ROAD
GAITHERSBURG, MD 20878
USA

K. RUSSELL
EG&G IDAHO, INC.
P.O. BOX 1625
IDAHO FALLS, ID 83415-3895
USA

P. SAMANTA
BROOKHAVEN NATIONAL LABORATORY
PO BOX 5000, BLDG. 130
UPTON, NY 11973-5000
USA

G. SAPONARO
ENEA
VIA V. BRANCATI 48
ROMA, 00144
ITALY

R. SCHMIDT
SANDIA NATIONAL LABORATORIES
PO BOX 5800, DEPT. 6423
ALBUQUERQUE, NM 87185
USA

F. SCIACCA
SCIENCE & ENGINEERING ASSOCIATES
1700 ROCKVILLE PIKE, ST. 400
ROCKVILLE, MD 20852
USA

W. SHA
ARGONNE NATIONAL LABORATORY
9700 S. CASS AVE.
ARGONNE, IL 60439
USA

H. SHIBATA
YOKOHAMA NATIONAL UNIVERSITY
156 TOKIWADAI, HODOGAYA-KU
YOKOHAMA,
JAPAN

F. SIMONEN
PACIFIC NORTHWEST LABORATORY
P.O. BOX 999
RICHLAND, WA 99352
USA

I. SMITH
AEA TECHNOLOGY
LINPRITH TECHNOLOGY CENTRE
DORCHESTER, DORSET DT28DH
UK

M. SOKOLOV
OAK RIDGE NATIONAL LABORATORY
P.O. BOX 2008
OAK RIDGE, TN 37831
USA

D. STARCK
MPR ASSOCIATES
320 KING ST.
ALEXANDRIA, VA 22314-3238
USA

V. STREZHOV
NSI RUSSIAN ACADEMY
B. TULSKAYA
MOSCOW, 113191
RUSSIA

Y. SAITO
NUCLEAR POWER ENGINEERING CORP.
8F FUJITA KANKO TORANOMON BLDG.
MINATO-KU, 3-17-1
JAPAN

R. SANDERS
OAK RIDGE NATIONAL LABORATORY
P.O. BOX 2009, M.S. 8057
OAK RIDGE, TN 37831-8057
USA

C. SAVAGE
JUPITER CORP.
2730 UNIVERSITY BLVD. W
WHEATON, MD 20902
USA

R. SCHNEIDER
ABB-COMBUSTION ENGINEERING
1000 PROSPECT HILL RD.
WINDSOR, CT 06095
USA

B. SEHGAL
ROYAL INST. TECHNOLOGY, STOCKHOLM
DEPT. NUCLEAR POWER SAFETY
STOCKHOLM, 10044
SWEDEN

W. SHACK
ARGONNE NATIONAL LABORATORY
BLDG. 212
ARGONNE, IL 60439
USA

Y. SHIRAHIGE
NUCLEAR POWER ENGINEERING CORP.
3-17-1,TORANOMON,MINATO-KU
TOKYO, 105
JAPAN

B. SINGH
JUPITER CORP.
STE. 900, WHEATON PLAZA NO., 2730 UNIV. BLVD.
WHEATON, MD 20902
USA

L. SMITH
LOS ALAMOS NATIONAL LABORATORY
PO BOX 1663, MS E561
LOS ALAMOS, NM 87545
USA

C. SORRELL
VIRGINIA POWER
5000 DOMINION BLVD.
GLEN ALLEN, VA 23060
USA

N. STARFELT
SKI
ORNBOGATAN 41
BROMMA, 16139
SWEDEN

E. STUBBE
TRACTEBEL INGENIERIE
AVENUE ARIANE, 7 BTE 1
BRUXELLES, B-1200
BELGIUM

T. SAITO
UNIVERSITY OF TOKYO
7-3-1 HONGO, BUNKYO-KU
TOKYO, 113
JAPAN

G. SANTAROSSA
ENEA
S.P. 101 CRE CASACCIA
ROMA,
ITALY

P. SCHEINERT
WESTINGHOUSE BETTIS
2895 O'NEILL DR.
BETHEL PARK, PA 15102
USA

G. SCHUECKTANZ
SIEMENS AG
PO BOX 32 20
ERLANGEN, 91058
GERMANY

S. SETH
MITRE CORP.
7525 COLSHIRE DR.
MC LEAN, VA 22102
USA

V. SHAH
IDAHO NATIONAL ENGINEERING LABS
PO BOX 1625
IDAHO FALLS, ID 83415-3870
USA

E. SILVER
OAK RIDGE NATIONAL LABORATORY
PO BOX 2009, MS8065
OAK RIDGE, TN 37831
USA

G. SLAUGHTER
OAK RIDGE NATIONAL LABORATORY
PO BOX 2000
OAK RIDGE, TN 37831-6152
USA

V. SNELL
AECL TECHNOLOGIES
9210 CORPORATE BLVD.
ROCKVILLE, MD 20850
USA

B. SPENCER
ARGONNE NATIONAL LABORATORY
9700 S. CASS AVENUE
ARGONNE, IL 60439
USA

M. STRAND
SCIENTECH
11821 PARKLAWN DR.
ROCKVILLE, MD 20852
USA

D. STURM
STAATL.MAT.I RUFUNGSANSTALT U. STUTTGART
PFAFFENWALDRING 32
STUTTGART, BW 70569
GERMANY

R. SUMMERS
SANDIA NATIONAL LABORATORIES
PO BOX 5800
ALBUQUERQUE, NM 87185-5800
USA

M. SUZUKI
JAPAN ATOMIC ENERGY RESEARCH INST.
SHIRAKATA
TOKAI-MURA, IK 319-11
JAPAN

K. TAKUMI
NUCLEAR POWER ENGINEERING CORP.
3-17-1,TORANOMON,MINATO-KU
TOKYO, 105
JAPAN

B. TEDESCO
SCIENTECH
11821 PARKLAWN DR.
ROCKVILLE , MD 20852
USA

S. THOMPSON
SANDIA NATIONAL LABORATORIES
PO BOX 5800
ALBUQUERQUE, NM 87185-5800
USA

A. TUTNOV
KURCHATOV INSTITUTE
123182 KURCHATOV SQ.
MOSCOW,
RUSSIA

K. VALTONEN
FINNISH CENTRE FOR RAD. & NUCL.SAFETY
PO BOX 268
HELSINKI, SF-00101
FINLAND

R. VIJAYKUMAR
ERI
6290 MONTROSE ROAD
ROCKVILLE, MD 20852
USA

J. WALKER
AECL RESEARCH
CHALK RIVER LABORATORIES
CHALK RIVER, ONTARIO K0J1J0
CANADA

J. WARE
IDAHO NATIONAL ENGINEERING LABS
PO BOX 1625
IDAHO FALLS, ID 83415-3750
USA

F. WHITE
KNOLLS ATOMIC POWER LAB/MARTIN MARIETTA
P.O. BOX 1072
SCHENECTADY, NY 12301-1072
USA

G. WILKOWSKI
BATTELLE-COLUMBUS
505 KING AVE.
COLUMBUS, OH 43201
USA

J. SUN
ARGONNE NATIONAL LABORATORY
9700 S. CASS AVE.
ARGONNE, IL 60439
USA

H. SUZUKI
HITACHI LTD.
5-2-2,OMIKA-CHO
HITACHI, 319-12
JAPAN

N. TANAKA
NUCLEAR POWER ENGINEERING CORP.
4-3-13 TORANOMON, MINATO-KU
TOKYO, 105
JAPAN

H. TEZEL
ATOMIC ENERGY CONTROL BOARD
280 SLATER STREET
OTTOWA, ONTARIO K1P5S9
CANADA

H. THORNBURG
ABB ATOM
901 S. WARFIELD DR.
MT. AIRY, MD 21771
USA

M. TUTTLE
LAMONT-DOHERGY EARTH OBS.

PALISADES, NY 10965
USA

A. VASILE
COMMISSARIAT A L'ENERGIE ATOMIQUE
C.E. CADARACHE DEC/SECA
ST. PAUL LEZ DURANCE, 13108
FRANCE

R. VOGEL
RICHARD C. VOGEL CONSULTANT
3432 STONERIDGE CT.
CALABASAS, CA 91302
USA

D. WALLACE
NIST
BLDG. 225, RM B266
GAITHERSBURG, MD 20899
USA

K. WASHINGTON
SANDIA NATIONAL LABORATORIES
PO BOX 5800, DEPT. 6429
ALBUQUERQUE, NM 87185
USA

B. WHITESEL
NUMARC
1776 I ST., NW, STE 300
WASHINGTON, DC 20006
USA

V. WILLEMS
GILBERT/COMMONWEALTH, INC.
PO BOX 1498
READING, PA 19603
USA

A. SUSLOV
RUSSIAN RESEARCH CTR KUROHOTOV INST.
KURCHATOV SQUARE, 8
MOSKOW,
RUSSIA

T. TAIRA
NUCLEAR POWER ENGINEERING CORP.
4-3-13 TORANOMON, MINATO-KU
TOKYO, 105
JAPAN

J. TAYLOR
BROOKHAVEN NATIONAL LABORATORY
BLDG. 130, PO BOX 5000
UPTON, NY 11973-5000
USA

G. THOMAS
LAWRENCE LIVERMORE NATIONAL LAB
7000 EAST AVE
LIVERMORE, CA 94550
USA

J. TILLS
JACK TILLS & ASSOCIATES, INC.
PO BOX 549
SANDIA PARK, NM 87047
USA

R. VALENTIN
ARGONNE NATIONAL LABORATORY
9700 S. CASS AVE., BLDG. 308
ARGONNE, IL 60439
USA

W. VESELY
SCIENCE APPLICATIONS INTERNATIONAL CORP.
655 METRO PLACE SOUTH
DUBLIN, OH 43017
USA

W. VON RIESEMANN
SANDIA NATIONAL LABORATORIES
ORG. 6403
ALBUQUERQUE, NM 87185
USA

W. WANG
STONE & WEBSTER ENGINEERING
3 EXECUTIVE CAMPUS, PO BOX 5200
CHERRY HILL, NJ 08034
USA

J. WEISSMAN
ABACUS TECHNOLOGY CORP.
5454 WISCONSIN AVENUE, SUITE 1100
CHEVY CHASE, MD 20815
USA

K. WHITT
SOUTHERN NUCLEAR
3117 RENFRO RD
VESTAVIA HILLS, AL 35216
USA

K. WINEGARDNER
PACIFIC NORTHWEST LABORATORY
PO BOX 999
RICHLAND, WA 99352
USA

S. WINGATE
NUS
910 CLOPPER ROAD
GAITHERSBURG, MD 20878
USA

J. WOLF
IDAHO NATIONAL ENGINEERING LABS
PO BOX 1915
IDAHO FALLS, ID 83404
USA

R. YOUNGBLOOD
BROOKHAVEN NATIONAL LABORATORY
BLDG. 130, PO BOX 5000
UPTON, NY 11973-5000
USA

R. WITT
UNIV. OF WISCONSIN-MADISON
147 ERB, 1500 JOHNSON DR.
MADISON, WI 53706
USA

A. WRIGHT
OAK RIDGE NATIONAL LABORATORY
PO BOX 2009
OAK RIDGE, TN 37831-8088
USA

P. ZMOLA
C&P ENGINEERING
5409 NEWINGTON RD.
BETHESDA, MD 20816
USA

L. WOLF
BATTELLE INGENIEURTECHNIK GMBH
AM ROMERHOF 35
FRANKFURT AM MAIN, 60486
GERMANY

H. YASUI
TOKYO ELECTRIC POWER COMPANY
1901 L. STREE, N.W., SUITE 720
WASHINGTON, DC 20036
USA

R. ZOGRAN
MPR ASSOCIATES
320 KING ST.
ALEXANDRIA, VA 22314-3238
USA

PROCEEDINGS OF THE
TWENTY-FIRST WATER REACTOR SAFETY INFORMATION MEETING
October 25-27, 1993

CONTENTS - VOLUME 3

	Page
ABSTRACT	iii
GENERAL INDEX	v
REGISTERED ATTENDEES	vii

PRIMARY SYSTEM INTEGRITY I
Chairperson: C.Z. Serpan, Jr.

Materials Engineering Branch Activities in 1993 C.Z. Serpan, Jr. (NRC)	1
Biaxial Loading and Shallow-Flaw Effects on Crack-Tip Constraint and Fracture-Toughness W. Pennell et al. (ORNL)	3
Heavy-Section Steel Irradiation Program Progress--Recent Results from Midland Low Upper-Shelf Weld Studies W. Corwin, et al. (ORNL)	27
Modeling of Irradiation Embrittlement and Annealing Data E. Eason, J. Wright, E. Nelson (M&CS)	81

PRIMARY SYSTEM INTEGRITY II
Chairperson: C.Z. Serpan, Jr.

VVER-440 Dosimetry and Neutron Spectrum Benchmark E. Sajo (LSU), F. Kam (ORNL)	95
Current Results for the NRC's Short Cracks in Piping and Piping Welds Research Program G. Wilkowski et al. (Battelle)	111
Irradiation-Assisted Stress Corrosion Cracking of Materials from Commercial BWRs: Role of Grain Boundary Microchemistry H. Chung et al. (ANL)	135
Fatigue of Carbon and Low-Alloy Steels in LWR Environments O. Chopra, W. Michaud, W. Shack (ANL)	153

CONTENTS - VOLUME 3 (Cont'd)

Page

Reliability of NDE - Cast Stainless Steel, SAFT-UT Performance, PISC-III Program Status, and Evaluation of Computer-Based UT/ISI Systems 177
S. Doctor et al. (PNL)

Progress on Risk-Based Inspection Guidelines: Application of Surry-1 Pilot Study to Improved Inservice Inspection Plans 197
F. Simonen et al. (PNL)

AGING RESEARCH, PRODUCTS & APPLICATIONS
Chairperson: G. Weidenhamer

Detection and Effects of Pump Low-Flow Operation 225
D. Casada, R. Greene (ORNL)

Understanding Aging in Containment Cooling Systems 237
R. Lofaro (BNL)

Phase I Aging Assessment of Nuclear Air-Treatment System HEPA Filters and Adsorbers 257
W. Winegardner (PNL)

Prioritization of Motor Operated Valves Based on Risk Importances 269
W. Vesely (SAIC), G. Weidenhamer (NRC)

Aging Management of Light Water Reactor Concrete Containments 283
V. Shah (INEL), C. Hookham (Consultant)

STRUCTURAL & SEISMIC ENGINEERING
Chairperson: J. Costello

Probabilistic-Based Evaluation of Design Rules for Components Affected by Intersystem LOCAs 307
A. Ware (INEL)

Structural Aging Program Approach to Providing an Improved Basis for Aging Management of Safety-Related Concrete Structures 331
D. Naus and C. Oland (ORNL), B. Ellingwood (Johns Hopkins U.)

Experiments to Evaluate Behavior of Containment Piping Bellows Under Severe Accident Conditions 357
L. Lambert, M. Parks (SNL)

Page

Guidelines for Seismic Qualification by Experience in ALWRs 381
K. Bandyopadhyay (BNL)

Large-Scale Seismic Test Program at Hualien, Taiwan 387
H. Tang, B. Fong (EPRI), H. Graves (NRC), Y. Liao (Taiwan Power)

Integral Testing of Relays and Circuit Breakers 401
K. Bandyopadhyay (BNL)

Development of an Improved Methodology for Probabilistic
Seismic Hazard Analysis 413
R. Budnitz (Future Resources Assoc.)

SEISMOLOGY & GEOLOGY
Chairperson: R. McMullen

Geologically Recent Near-Surface Faulting and Folding in Giles County,
Southwest Virginia: New Exposures of Extensional and Apparent
Reverse Faults in Alluvial Sediments between Pembroke and Pearisburg 415
R. Law et al. (Virginia Tech)

Materials Engineering Branch Activities in 1993

Charles Z. Serpan, Jr.
U. S. Nuclear Regulatory Commission, Washington D.C. 20555

The Materials Engineering Branch, Division of Engineering, Office of Nuclear Regulatory Research, has had an exceptionally busy year of work, encompassing the traditional research program, regulatory codes and standards development, and direct technical assistance to NRR. The research work is detailed in the following papers of this volume, and is highlighted in this summary; the regulatory codes and standards work and the direct technical assistance to NRR however, are not described elsewhere and so are included in more detail in this summary.

The research program continues to have a strong focus on fracture mechanics issues related to pressurized thermal shock (PTS). The Heavy Section Steel Technology (HSST) program at Oak Ridge has emphasized a number of technical issues within the area of crack-tip constraint, including biaxial loading conditions and shallow-surface crack effects. Accurate understanding and representation of these potentially competing effects is necessary to assess the degree of conservatism and margins in present fracture methodologies. The degradation of pressure vessel steel mechanical properties caused by neutron radiation embrittlement continues to be a critical issue. Irradiation is currently underway on a typical production submerged-arc low upper shelf weldment made with Linde 80 flux; and good progress has been made on developing models to predict transition temperature increase, drop in upper-shelf energy, and the response of both to post-irradiation annealing. Direct neutron flux spectrum measurements are being made on a VVER-440 mockup experiment at the Czech Nuclear Research Institute in a cooperative program; the Czech results are providing important verification of the neutron flux spectrum calculations done in the U.S. using transport codes. In addition to the work underway in the IPIRG (International Piping Integrity Research Group)-2 program on dynamic and seismic effects in piping components, a multi-disciplined effort has continued at Battelle Columbus Laboratories on "Short Cracks" to assess the applicability of current ASME Code rules for long cracks. Environmentally assisted cracking and corrosion continues at Argonne National Lab, wherein studies now show that previous theories on irradiation assisted stress corrosion cracking cannot be substantiated. Additional studies are underway to strengthen the data base on environmental effects on fatigue life particularly for carbon and low alloy steels. A wide range of activities is underway at Battelle-Pacific Northwest Laboratories on non-destructive examination. Progress has been made in the difficult area of ultrasonic (UT) inspection of cast stainless steel, and in evaluation of commercial UT systems so that NRC Regional staff can better interpret inservice inspection results from periodic plant inspections. Lastly, good progress is reported by Battelle PNL on improving the detailed plans for inservive inspection of power plant components, on the basis of risk posed by those components; this work is being done in cooperation with the ASME Research Task Force, and a Section XI working group.

Activities undertaken this year by the MEB staff in the preparation of a series of rule changes and Regulatory Guides, are as follows:

Proposed Revisions to Rules

- 10CFR50.61 "Pressurized Thermal Shock"
- 10CFR50 App. G "Fracture Toughness Rules"
- 10CFR50 App. H "Reactor Vessel Material Surveillance Requirements"

Proposed Rule

- 10CFR50.66 "Thermal Annealing Requirements"

Draft Regulatory Guides

- DG 1-027 "Format and Content of Application for Approval of Thermal Annealing of RPV"
- DG 1-025 "Calculational and Dosimetry Methods for Determining Pressure Vessel Neutron Fluence"
- DG 1-023 "Evaluation of Reactor Pressure Vessels with Charpy Upper Shelf Energy Less than 50 ft-lb."

The rule changes correct a number of inconsistencies, clarify NRC's intent, and respond to Commission guidance on a number of issues. The proposed rule and Reg. Guide on thermal annealing for example, sets forth NRC's requirements for licensees that might be considering annealing in the future. The Reg. Guide on neutron dosimetry has been in preparation for several years, and is very complementary to the vessel integrity and annealing guidance; it integrates and "codifies" the best of current practice today for this technology. Finally, the Reg. Guide on low Charpy upper shelf energy was completed this year. The MEB staff used this methodology to perform generic bounding calculations to determine allowable upper shelf energies in support of the NRR staff's evaluation of Generic Letter 92-01 "Reactor Vessel Structural Integrity. This very critical guide shows a method acceptable to the staff to demonstrate that the margins of safety against fracture are equivalent to those required by Appendix G of the ASME Code, if the Charpy upper-shelf energy of reactor pressure vessel beltline materials fall below 50 ft-lbs during the plant operating lifetime. A final, intense effort this year involved preparation of a report "Evaluation of Steam Generator Tube Leak Rate Under MSLB Conditions,"[1] in support of NRR's reevaluation of interim plugging criteria for steam generator tubes. The evaluation provided a "best estimate" of the primary-to-secondary leak rate that would be expected due to a main steam line break (MSLB) and the resulting leakage from steam generator tubes at the Trojan nuclear power plant. MEB staff were also members of the task group which prepared the draft NUREG-1477 "Voltage-Based Interim Plugging Criteria for Steam Generator Tubes," and will continue to be involved in steam generator activities in the future.

The Materials Engineering Branch will continue strong efforts in both the traditional management of research, and in regulatory code and standards development activities, providing input to both sides through its very close ties to NRR, the Regions, the U.S industrial community, and codes and standards groups, and through contacts and exchange with colleagues in foreign countries.

[1] E. S. Beckjord to T.E. Murley, January 15, 1993.

Biaxial Loading and Shallow-Flaw Effects on Crack-Tip Constraint and Fracture-Toughness*

W. E. Pennell,† B. R. Bass,** J. W. Bryson,† W. J. McAfee,†
T. J. Theiss,† and M. C. Rao‡

Oak Ridge National Laboratory

Abstract

Uniaxial tests of single-edged notched bend (SENB) specimens with both deep- and shallow-flaws have shown elevated fracture-toughness for the shallow flaws. The elevation in fracture-toughness for shallow flaws has been shown to be the result of reduced constraint at the crack-tip. Biaxial loading has the potential to increase constraint at the crack-tip and thereby reduce some of the shallow-flaw, fracture-toughness elevation. Biaxial fracture-toughness tests have shown that the shallow-flaw, fracture-toughness elevation is reduced but not eliminated by biaxial loading. Dual-parameter, fracture-toughness correlations have been proposed to reflect the effect of crack-tip constraint on fracture-toughness. Test results from the uniaxial and biaxial tests were analyzed using the dual-parameter technology. Discrepancies between analysis results and cleavage initiation site data from fractographic examinations indicate that the analysis models are in need of further refinement. Addition of a precleavage, ductile-tearing element to the analysis model has the potential to resolve the noted discrepancies.

Introduction

Fracture mechanics technology is used to assess the structural integrity of irradiation-embrittled reactor pressure vessels (RPV's) containing flaws. The fracture mechanics technology currently in use is based upon analysis methods and fracture-toughness data appropriate for cracks with a high degree of crack-tip constraint. This approach has the advantage that it produces very conservative estimates of allowable RPV operating conditions, and therefore assures high levels of safety. There is a concern, however, that the level of conservatism inherent in the limiting crack-tip constraint approach to RPV safety assessment may have economically unacceptable consequences when applied to configurations and loading conditions where upper-bound levels of crack-tip constraint do not exist.

In part, the current approach to the structural integrity assessment of irradiation-embrittled RPV's stems from limitations of the nondestructive examination (NDE) technology available at the time the fracture mechanics technology was developed. Substantial advances in NDE technology have been made since that time. Detection and accurate sizing of relatively small flaws is now possible. Conceptually it is now possible to define requirements for the fracture analysis of RPVs in terms of the flaws detected and sized during in-service NDE examinations. For this approach to become a practical reality, however, fracture mechanics technology appropriate to these new conditions must be developed and validated.

---

*Research sponsored by Division of Engineering, Office of Nuclear Regulatory Research, U.S. Nuclear Regulatory Commission under Interagency Agreement 1886-8011-9B with the U.S. Department of Energy under contract DE-AC05-84OR21400 with Martin Marietta Energy Systems, Inc.

†Engineering Technology Division.

**Computing Applications Division.

‡Consultant to the Metals and Ceramics Division.

Features of the flaws of interest in an NDE based RPV safety assessment are that they are relatively shallow and located in a biaxial stress field. Fracture technology advances required to address these conditions include the development of a fracture-toughness data base for shallow flaws and determination of the effect of biaxial stress fields on the shallow-flaw, fracture-toughness. Shallow-flaw, fracture-toughness would be expected to be higher than the deep-flaw fracture toughness currently in use because of the proximity of the vessel inner surface to the crack-tip and the consequent decrease in crack-tip constraint. Biaxial loading would act to restore some of the crack-tip constraint and reduce, but not eliminate, some of the fracture-toughness elevation associated with shallow flaws.

Development of analysis techniques which adequately reflect the effects of crack-tip constraint on fracture-toughness is clearly essential to the implementation of an advanced fracture analysis technology. Development of fast and economical high-volume computing capabilities has made possible the detailed analysis of the elastic-plastic stress fields at the crack-tip. Crack-tip constraint can, therefore, be characterized in terms of its effect on the crack-tip stress fields. Dual-parameter, fracture-toughness correlations and corrections have been proposed for this purpose. Refining and validating these dual-parameter fracture analysis methods is an important element of an advanced fracture technology development program.

The above discussion of the use for an advanced fracture mechanics technology has been in terms of its application to the evaluation of flaws discovered and characterized during an in-service NDE examination. It should be noted, however, that other important RPV safety assessment applications exist. These include (a) the probabilistic fracture mechanics analysis of reactor pressure vessel integrity under postulated pressurized thermal shock (PTS) transient loading, and (b) transfer of data from future miniature fracture mechanics RPV surveillance specimens for application to RPV safety assessments.

The Nuclear Regulatory Commission (NRC) sponsored Heavy-Section Steel Technology (HSST) Program at Oak Ridge National Laboratory (ORNL) is conducting research to generate the fracture-toughness data to develop and validate the analysis methods required for the application of an advanced fracture mechanics technology to RPV safety assessments. This paper provides an interim report of results from that research.

Constraint Effects In Fracture

Fracture occurs when the opening mode tensile stresses at the tip of a crack in a brittle material exceed a critical value over a finite length (1). Local yielding of the material at the crack-tip limits the buildup of opening-mode stresses and thereby directly influences fracture-toughness.

Crack-tip stress fields can be divided into hydrostatic and shear components. Yielding of the material is governed by the shear component of the stress field. Tensile hydrostatic stresses contribute directly to the crack-tip opening mode tensile stresses but do not influence yielding. It follows, therefore, that fracture-toughness will be directly influenced when the hydrostatic component of the crack-tip stress field increases.

Crack-tip constraint is the term used to describe conditions which influence the hydrostatic component of the crack-tip stress field. Low constraint reduces the hydrostatic stress contribution to the opening mode stress and thereby increases the fracture-toughness relative to that obtained in a high-constraint configuration.

Plane strain constraint of a crack embedded in a large elastic body represents what may be a practical upper limit to crack-tip constraint. In such a condition the crack-tip plastic zone is very small when compared with the test specimen dimensions. Irwin (2) demonstrated that fracture-toughness of a material for conditions of linear elastic plane-strain (LEPS) constraint of the crack-tip

plastic zone can be adequately characterized by a single parameter, the stress-intensity factor K_{Ic}. Hutchinson (3), Rice, and Rosengren (4) showed that crack-tip stresses can be uniquely defined for these conditions for a power-law hardening material. The singular crack-tip stress distribution associated with LEPS constraint is designated the HRR stress distribution.

The LEPS crack-tip constraint condition is attractive for fracture-toughness testing because it can be readily reproduced in any testing laboratory. Fracture-toughness testing standards such as the American Society for Testing and Materials (ASTM) Standard E399 (5), therefore, requires that LEPS crack-tip constraint be present in a test specimen for the fracture-toughness test data to be considered valid. Assurance that the required LEPS constraint condition was achieved during a test is obtained by requiring that the test specimen size be not less than a minimum acceptable size governed by the material yield stress and the measured fracture-toughness. The requirements of ASTM E399 have the practical effect of limiting the size of the crack-tip plastic zone radius at fracture to approximately 2% of both the crack-depth and the test specimen thickness.

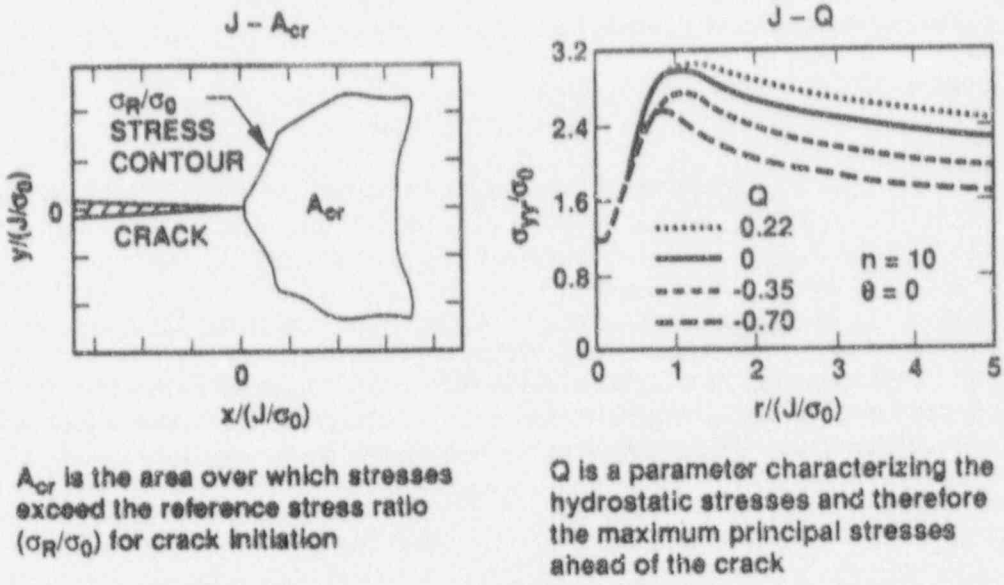
Fracture-toughness data produced using test specimens with LEPS crack-tip constraint represent what is probably a lower bound fracture-toughness for a material. Test specimen dimensions required for the maintenance of LEPS crack-tip constraint conditions can be very large. Fracture-toughness tests of A533B material conducted at temperatures in the transition range of the fracture-toughness curve required the use of 10T and 12T compact tension (CT) test specimens (6). These test specimens incorporate crack depths of 254 mm (10 in) and 304.8 mm (12 in.), respectively.

Departure from conditions of LEPS crack-tip constraint results in a crack-tip stress distribution which is no longer singular. It differs from the HRR stress distribution in a manner dictated by the crack-tip constraint. This difference directly influences the fracture-toughness associated with a particular material and crack-geometry combination. The fracture-toughness now becomes constraint-dependent. It follows, therefore, that a second parameter must be added to the fracture-toughness characterization to account for the influence of departures from LEPS crack-tip constraint.

Dual-Parameter, Fracture-Toughness Corrections and Correlations

Dual-parameter, fracture-toughness corrections and correlations have been proposed to provide a quantitative assessment of effect of reduction of crack-tip constraint on fracture-toughness. Principal features of the J-Acr fracture-toughness correction proposed by Dodds–Anderson (7), and the J-Q dual-parameter, fracture-toughness correlation proposed by O'Dowd and Shih (8, 9) are illustrated in Fig. 1.

The Dodds–Anderson J-Acr correction factor approach provides a quantitative adjustment for fracture-toughness data when the LEPS constraint conditions associated with valid K_{Ic} data have not been maintained. Formulation of the J-Acr correction factor approach is based upon the following principles and assumptions: (a) initiation of cleavage fracture is governed by a stress-based criterion which remains constant for a range of crack-tip constraint conditions; (b) cleavage initiation occurs in a region of the crack-tip stress field where stresses can be adequately defined using small-scale yielding (SSY) continuum mechanics-based, finite-element analysis models; (c) fracture occurs in two specimens with differing levels of crack-tip constraint when stresses at specific locations on the crack plane ahead of the crack tip reach a common reference value. The reference stress value does not have to be rigorously defined if the crack-tip stress fields are self-similar since the same value will be used in each of the constraint conditions being compared; (d) the specific location (r) along the crack plane selected for assuring equivalence of opening mode stresses is not critical, provided that the location selected is within the zone where SSY continuum mechanics-based analysis models can adequately define the stress field. A value of $r = 4*CTOD$ has been used (7); (e) in a simplified form, the Dodds–Anderson fracture-toughness correction



A_{cr} is the area over which stresses exceed the reference stress ratio (σ_R/σ_0) for crack initiation

Q is a parameter characterizing the hydrostatic stresses and therefore the maximum principal stresses ahead of the crack

Fig. 1 Dual-parameter corrections and correlations have been proposed as means for adjusting fracture-toughness data for the effects of crack-tip constraint.

factors can be defined in terms of the constraint-dependent ratio of the applied J-values required to generate the reference opening mode stress value at the selected distance ahead of the crack tip (r); (f) extension of the concept of a reference stress at a specific radius to a reference stress acting over the volume defined by the area contained within a reference stress contour (Acr) in a unit thickness-plate provides a means of reflecting the statistical nature of cleavage initiation in the fracture-toughness process. In practice results obtained using this extension of the concept compare closely with those predicted using the reference stress radius approach (7).

Use of the simplified form of the Dodds–Anderson correction factor approach is illustrated in Fig. 2. Note that the value of "*r*" in the expression $r\sigma_0/J$ remains constant. The critical J-value for

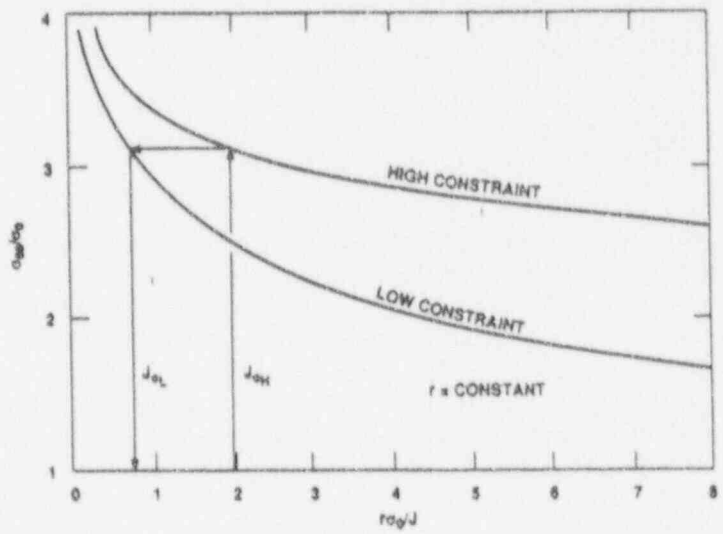


Fig. 2 A simplified form of the Dodds–Anderson correction factor can be used with opening mode stress plots from crack-tip analyses to make J_c predictions for modified constraint configurations.

a low constraint configuration (J_{cl}) can, therefore, be estimated if the critical J for a high constraint configuration (J_{ch}) is known and the crack-tip, opening-mode stress plots are available for both configurations.

The two-parameter (J-Q), fracture-toughness correlation proposed by O'Dowd and Shih characterizes the effects of stress triaxiality on the crack-tip stress field. The HRR crack-tip stress field is used as the basis of comparison for crack-tip stress fields with differing levels of crack-tip stress triaxiality.

In the J-Q fracture-toughness correlation, Q defines the departure of the stress-state dependent opening mode stress distribution on the crack plane from the HRR opening mode stress distribution. Extensive SSY finite-element analysis performed by O'Dowd and Shih indicates that Q remains relatively constant over the region ahead of the crack-tip in which cleavage initiation is postulated to occur. Q can, therefore, be expressed as follows.

$$Q \equiv \frac{\sigma_{yy} - (\sigma_{yy})HRR}{\sigma_O} \qquad (1)$$

Where σ_{yy} is the crack-tip opening mode stress distribution for a specific constraint condition, $(\sigma_{yy})HRR$ is the corresponding stress distribution for the HRR constraint condition, and σ_o is the material yield stress. Q is postulated to remain constant over the crack-tip process zone and is conventionally evaluated at $r = 2J/\sigma_o$.

In physical terms, Q is the difference between the hydrostatic stress associated with the reference HRR crack-tip stress distribution and the crack-tip hydrostatic stress associated with a specific constraint condition. Q is conventionally expressed in a normalized form by dividing the hydrostatic stress increment by the material yield strength. A reduction in constraint relative to the reference HRR constraint condition produces a negative Q-value.

Rice's J-integral (10) sets the size of the zone over which large crack-tip stresses act. Fig. 1(b) shows the crack-tip opening mode stress distribution for a range of constraint conditions characterized by Q. The distance "r" ahead of the crack tip is normalized by dividing by the parameter (J/σ_o). In non-normalized form any one of the curves shown in Fig. 1(b) would appear as a family of curves with the peak on the curve moving further from the crack-tip as J increases.

A fracture prevention margin calculated using a single parameter characterization of fracture-toughness would be expressed as the ratio of the material fracture-toughness to the crack driving force (K_{Ic}/K_I or J_c/J). The equivalent process using the J-Q characterization of fracture-toughness is illustrated in Fig. 3. The single-parameter characterization of fracture-toughness at a particular value of RT_{NDT} is replaced with a J-Q fracture-toughness locus. Given the data scatter inherent to the fracture process, the J-Q locus takes the form of a J-Q data scatter band with upper and lower bounds. Fracture-toughness tests on specimens with varying levels of crack-tip constraint, such as those described later in this paper, are used to generate the data required to define the J-Q locus scatter band.

Elastic-plastic, finite-element analysis of the crack-tip region defines J and Q for each step in the loading sequence. Intersection of the locus of these points with the lower bound of the J-Q fracture-toughness scatter band defines the minimum J and the associated Q for fracture initiation. This value of J can then be compared with J produced by the maximum component loading to determine the fracture prevention margin for the component. Characterization of the J-Q fracture-toughness scatter band in statistical terms permits extension of the concept for use in probabilistic fracture mechanics analyses.

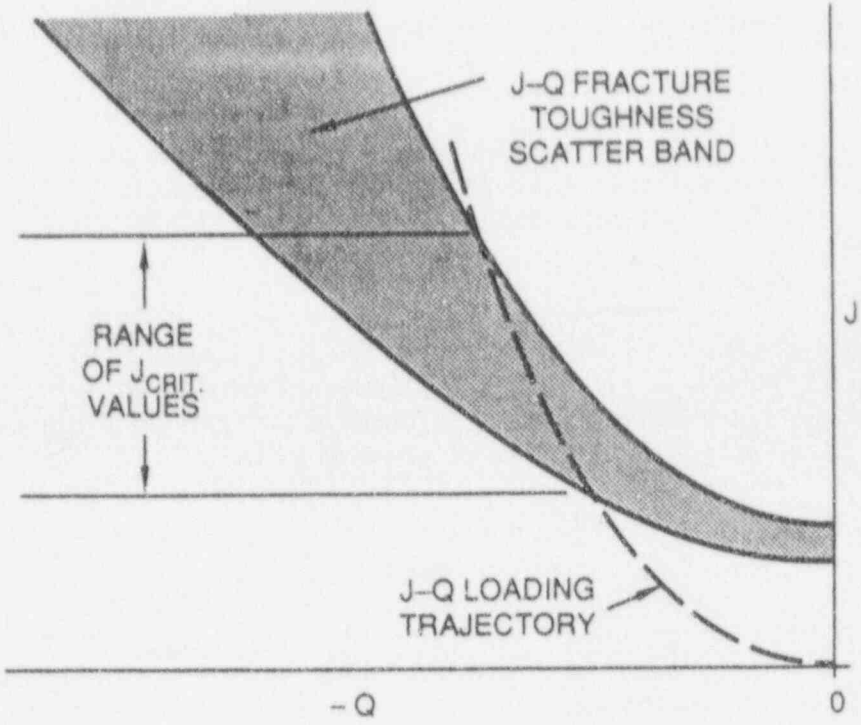


Fig. 3 Intersection of the J-Q loading trajectory for a specific configuration and loading condition with the material J-Q fracture-toughness scatter band defines the range of critical J values

It will be evident from the above discussion of the J-Acr and J-Q dual-parameter concepts that they have much in common. Principles (a) and (b) described above for the J-Acr correction factor concept are equally applicable to the J-Q dual-parameter, fracture-toughness correlation concept. The J-Q concept assumes that Q will remain relatively constant over the process zone and, therefore, does not require that a specific location be selected for a comparison of Q values. It has, however, become customary to use the location defined by $r = 2J/\sigma_0$ for this purpose.

Shallow-Flaw Fracture-Toughness Tests

Fracture-toughness tests have been performed on single-edge, notch-bending (SENB) test specimens using both deep- (a/W = 0.5) and shallow- (a/W = 0.1) flaws (Ref. 11). Beam specimens used in these tests are shown in Fig. 4. The beams were fabricated from A533B material and were nominally 100 mm (4 in.) deep. Use of beams with this depth permitted testing of shallow flaws with depths in the range identified as the critical depth range for PTS analysis. Use of prototypical flaw depths reduced somewhat the uncertainties associated with extrapolation of shallow-flaw, fracture-toughness data for application to full-scale structures (12).

Details of these tests have been extensively reported elsewhere (11, 13, 14), and will not be repeated here. Data from the tests are important to both the ongoing development of dual-parameter, fracture-toughness correlations and the investigation of biaxial loading effects on crack-tip constraint and fracture-toughness. The deep-flaw and shallow-flaw fracture-toughness data generated in these tests were produced using a single material and closely controlled test conditions. Differences between the deep-flaw and shallow-flaw fracture-toughness data obtained can, therefore, be reliably attributed to differences in crack-tip-constraint for the deep and shallow flaws. This attribute permits the data to be used, together with a J-Q analysis of the test specimens and loading conditions, to generate preliminary definitions of the J-Q failure locus scatter band for temperatures (T-RT_{NDT}) investigated in the tests. The shallow-flaw portion of the data base also

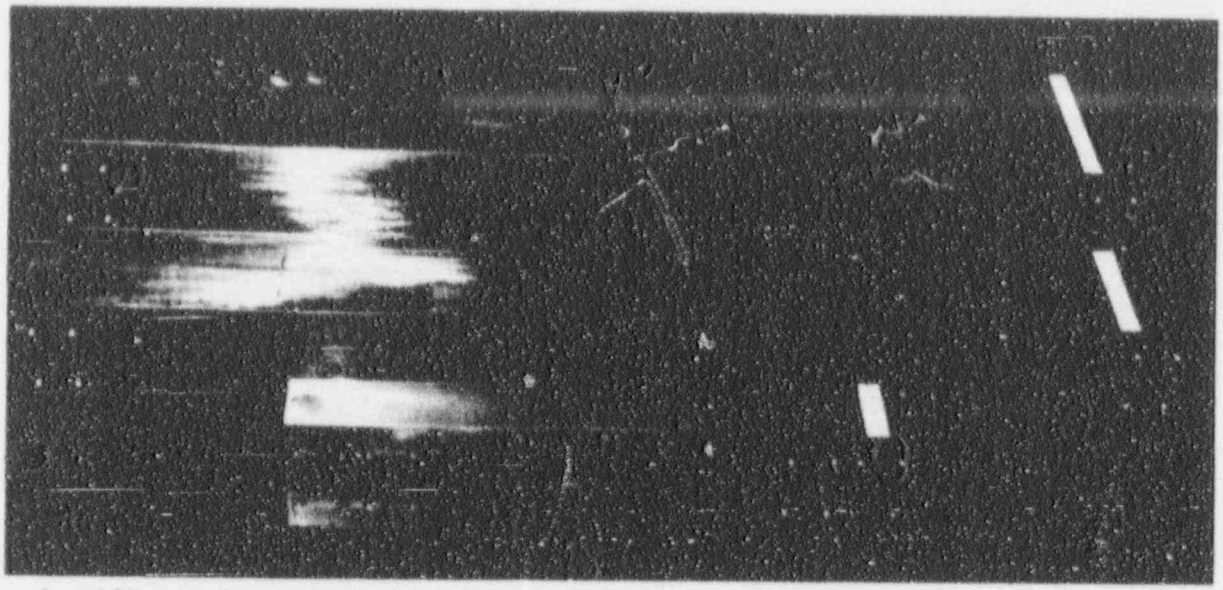


Fig. 4 100 mm deep beams were used in the shallow-flaw test program to permit full-scale testing of surface flaws having depths in the range which PTS analysis has shown to be the controlling range for crack initiation

provides a basis for assessing the effect of biaxial loading on the shallow-flaw, fracture-toughness of A533B material.

Shallow-flaw and deep-flaw fracture-toughness data generated in these tests are plotted in Fig. 5. The data are seen to be grouped into two separate families corresponding to the shallow and deep

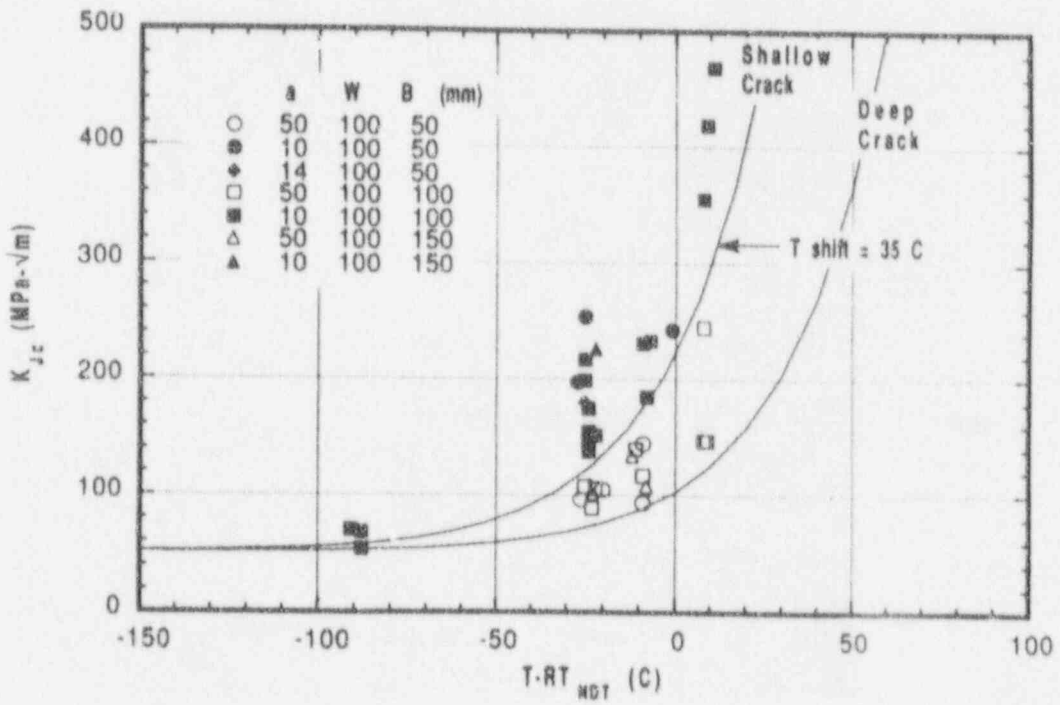


Fig. 5 Data from the shallow-flaw, fracture-toughness testing program show that the shallow-flaw effect produces a substantial increase in toughness at temperatures in the transition region of the fracture-toughness curve.

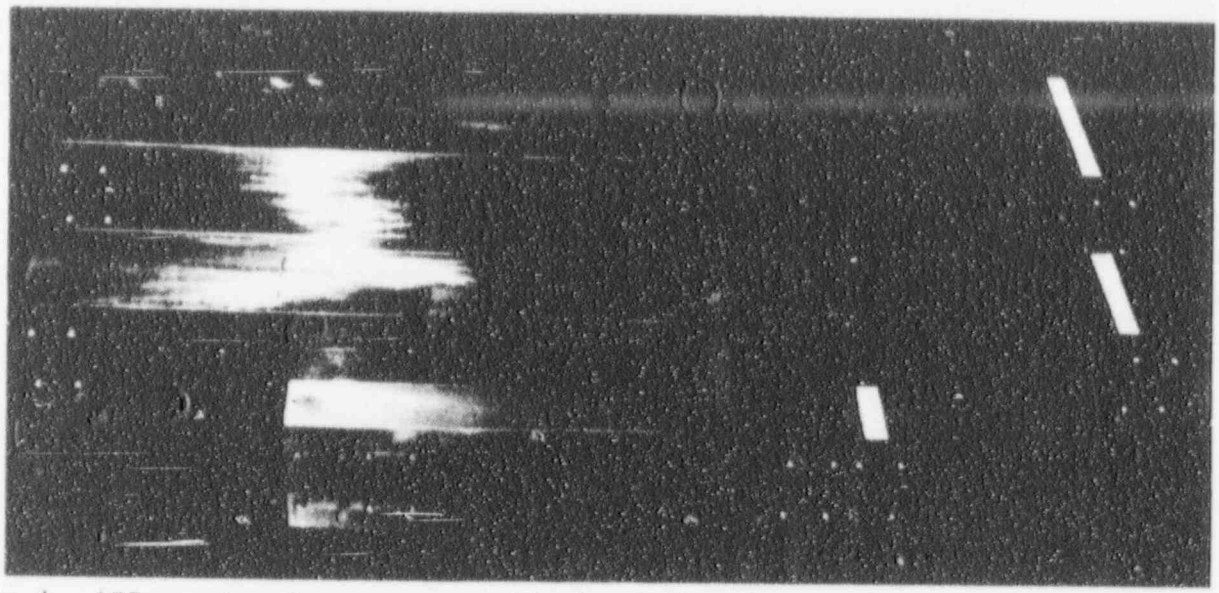


Fig. 4 100 mm deep beams were used in the shallow-flaw test program to permit full-scale testing of surface flaws having depths in the range which PTS analysis has shown to be the controlling range for crack initiation

provides a basis for assessing the effect of biaxial loading on the shallow-flaw, fracture-toughness of A533B material.

Shallow-flaw and deep-flaw fracture-toughness data generated in these tests are plotted in Fig. 5. The data are seen to be grouped into two separate families corresponding to the shallow and deep

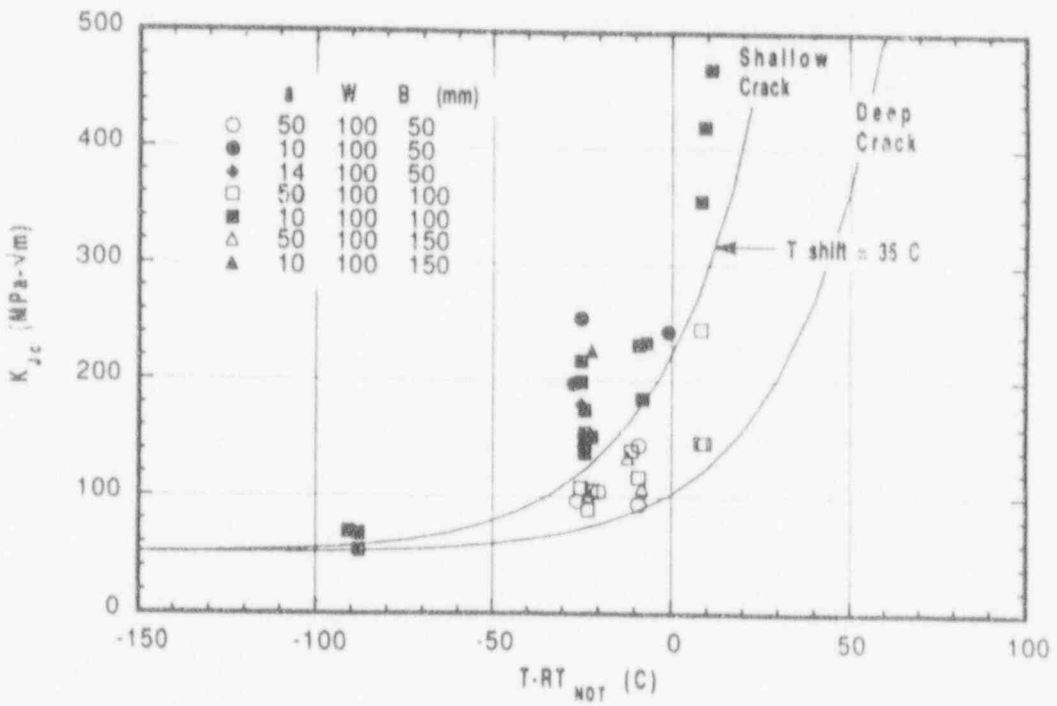


Fig. 5 Data from the shallow-flaw, fracture-toughness testing program show that the shallow-flaw effect produces a substantial increase in toughness at temperatures in the transition region of the fracture-toughness curve.

flaws respectively. Lower bound curves fitted to the data show a 35°C shift in RT_{NDT} between the two data sets. It is appropriate to note that most of the shallow-flaw, fracture-toughness data plotted in Fig. 5 are for a flaw depth of 10 mm (0.4 in.). The shallow-flaw, fracture-toughness would be expected to be flaw-depth dependent, with larger shifts in the RT_{NDT} anticipated as the flaw depth decreases.

Note that the shallow-flaw effect on fracture-toughness is significant in the lower transition range of the fracture-toughness curve, which is the area of the curve important to PTS analysis, but is not significant on the lower-shelf portion of the curve. The transition region of the fracture-toughness curve is a region in which plastic flow at the crack-tip produces crack-tip blunting in advance of cleavage fracture. This result is, therefore, consistent with the concept of reduced crack-tip constraint for shallow flaws producing an associated decrease in hydrostatic stress and increased plastic flow (blunting) prior to cleavage fracture.

Ultimate resolution of the role of the absolute crack-depth "a" and the crack-depth ratio "a/W" in controlling the shallow-flaw, fracture-toughness enhancement effect will require test validation. The HSST Program has initiated the required tests using full-thickness test specimens cut from the wall of a reactor vessel from a canceled nuclear plant. One of the full-thickness test specimens is shown in Fig. 6. These specimens are currently being tested in the 27.10^6 N (6.10^6 lb) test machine at the National Institute of Science and Technology (NIST) under an HSST Program subcontract.

Biaxial Fracture-Toughness Testing Of Shallow Flaws

Biaxial stress fields are produced in a reactor pressure vessel wall by both pressure loading and through-wall temperature gradients. A typical biaxial stress field is shown in Fig. 7, together with a constant depth shallow-surface flaw. One of the principal stresses is seen to be aligned parallel to



Fig. 6 Full thickness shallow- and deep-flaw SENB specimens currently being tested in the 27,000,000 MN (12,000,000 lb) test machine at the National Institute of Standards and Technology.

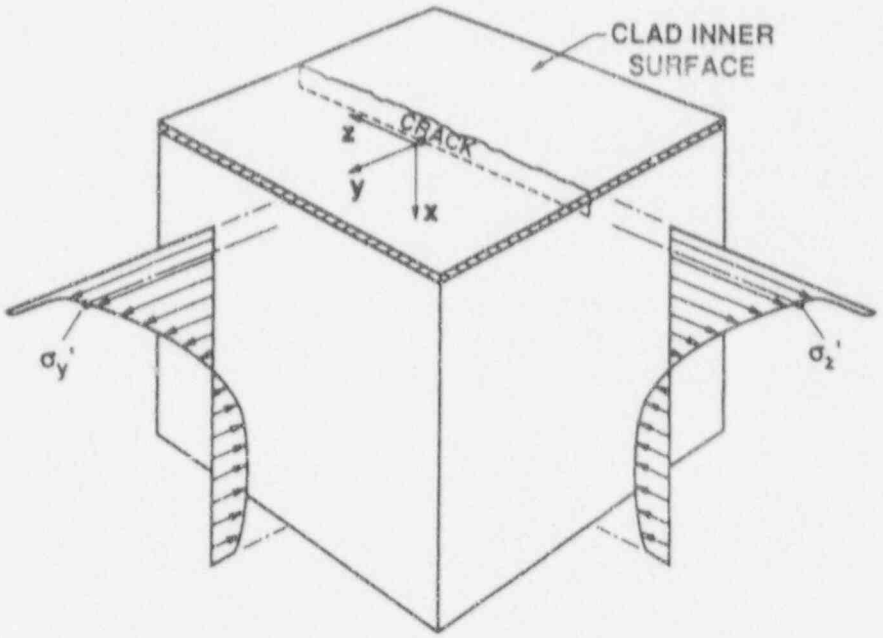


Fig. 7 PTS loading produces biaxial stresses in a reactor vessel wall with one of the principal stresses aligned parallel with the tip of a constant depth shallow-surface flaw.

the crack front. There is no counterpart of this far-field, out-of-plane stress in the shallow-flaw, fracture-toughness tests previously described. The far-field, out-of-plane stress has the potential to increase stress triaxiality (constraint) at the crack-tip and thereby reduce some of the fracture-toughness elevation associated with shallow flaws. The HSST biaxial test Program was instituted to investigate this effect.

Test Specimen Functional Requirements

A number of researchers have investigated the effects of biaxial loading on fracture-toughness (15, 16, 17, 18, 19). These investigations have produced clear indications of a biaxial effect on both cleavage fracture-toughness and on ductile-tearing toughness. They also served to identify some of the difficulties unavoidably associated with biaxial fracture-toughness testing. The specimen size requirement for a meaningful investigation of biaxial loading effects in fracture has emerged as one of the most difficult functional requirements to accommodate. If the specimen size relative to the crack-depth is not adequate, gross plastic deformation can occur in the remaining ligament prior to the initiation of cleavage fracture, making interpretation of the test results difficult.

Increasing the test specimen size will overcome the difficulty outlined above, but at the same time sharply increase the cost of both the test specimen and the test. Increases in the test-specimen size can, therefore, result in testing costs which severely restrict the scope of a testing program. Costs must be tightly controlled in order to permit an adequate investigation of fracture-toughness data scatter under biaxial loading conditions. It follows, therefore, that basic functional requirements for the biaxial fracture-toughness test specimen are (a) low cost, and (b) a configuration, which will minimize departure from elastic behavior in the unbroken ligament up to the instant of fracture.

An equally important functional requirement for the test specimen is that it permits any biaxial effect on shallow-flaw, fracture-toughness to be clearly identified. The test specimen must, therefore, be capable of being loaded in either a uniaxial or a biaxial configuration, with all other test parameters remaining unchanged.

An infinitely long (constant depth) geometry is assumed for all shallow flaws in conformance with the PTS analysis guidelines provided in U.S. NRC Regulatory Guide 1.154 (Ref. 20). Evaluation of flaws discovered during an in-service inspection, and possible future developments of PTS analysis technology, creates a need for data on the fracture-toughness of finite-length shallow surface flaws. A further basic functional requirement for the test specimen design is, therefore, that it be capable of accommodating both of these flaw geometries.

Test Specimen Design

A number of potential test specimen configurations were considered prior to selection of the cruciform design. Several specimen designs were identified which could satisfy the technical elements of the functional requirements. Test specimen cost was a major factor influencing the final selection.

Conceptual features of the cruciform biaxial fracture-toughness test specimen are illustrated in Fig. 8. The specimen design is capable of reproducing a linear approximation of the nonlinear biaxial stress distribution shown in Fig. 7. The cruciform design, coupled with a statically determinate load reaction system, permits the specimen to be loaded in either uniaxial (4 point

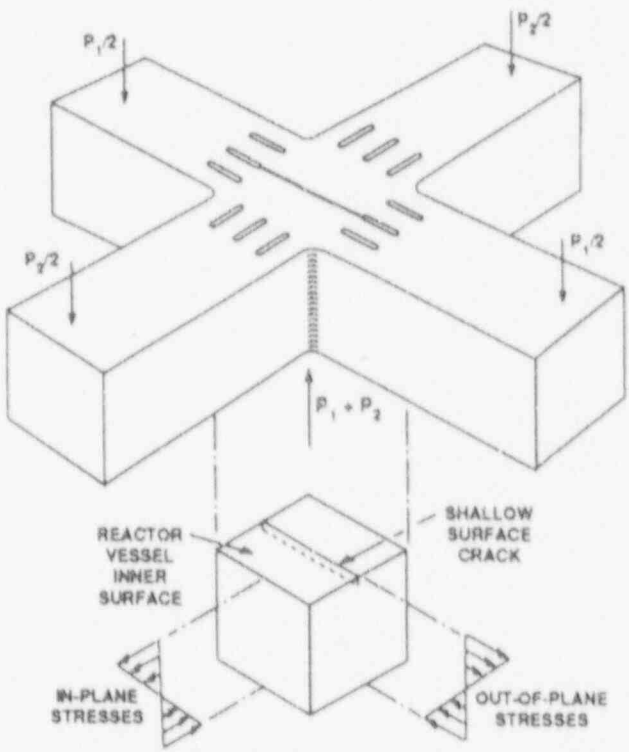


Fig. 8 Conceptual features of the cruciform shallow-flaw, biaxial fracture-toughness test specimen

bending) or biaxial (8 point bending) configurations. Tests of nominally identical specimens can thus be performed with the level of stress biaxiality as the only test variable. Details of the statically determinate load reaction system are given in Fig. 9.

Load diffusion control slots permit the maintenance of a reasonably uniform biaxial stress field within the test section of the specimen. The uniform depth shallow-flaw terminates at the central

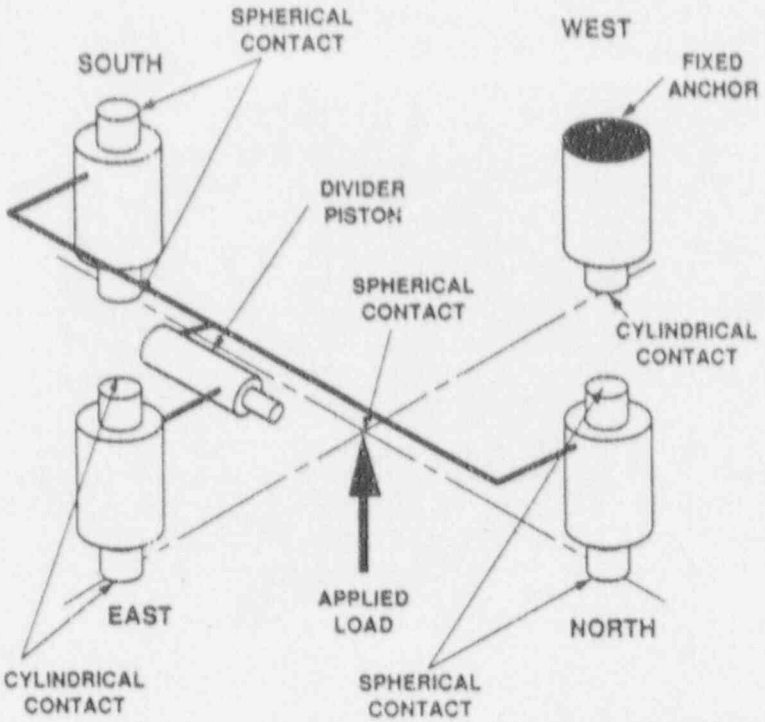


Fig. 9 Hydraulically coupled passive load-reaction jacks assure that the test specimen loading is statically determinate. A divider piston in the hydraulic coupling line provides control of the beam loading ratio.

load diffusion control slots, thereby simulating an infinitely long flaw. Control of the differential length of the central load diffusion control slots relative to the lengths of the outer slots is used to eliminate unacceptable stress concentrations at the ends of the crack.

The central block of the cruciform specimen is the only portion fabricated from fully characterized test material. The load diffusion control slots are machined in both the test block and the reusable arms using a numerically controlled electro-discharge machining (EDM) process. The crack starter slot is machined at the same time. A completed central block is shown in Fig. 10.

Longitudinal arms are attached using a low-heat input electron beam (EB) welding procedure prior to fatigue precracking the specimen in four point uniaxial bending. A mechanical machining operation is used to remove any EDM embrittled material and any fatigue-crack growth irregularities from the central load diffusion control slots at the ends of the crack. Attachment of the transverse load arms by EB welding completes the fabrication process. The resulting test specimen, which is shown in Fig. 11, meets all of the functional requirements and is considerably lower in cost and material requirements than any of the alternate designs evaluated.

Test Specimen Analysis

A three-dimensional, finite-element model of cruciform specimen, incorporating a highly refined representation of the crack-tip region, was used for this analysis. Essential features of the model are shown in Fig. 12. The model has 3890 isoparametric brick elements. For the crack-tip field analysis, the crack-tip region is modeled using collapsed prism elements arranged in a fan configuration. The analyses were run using the ABAQUS (Ref. 21) computer program and a piecewise representation of the material elastic-plastic, stress-strain properties. Further details of the analysis procedure can be found in Ref. 22.

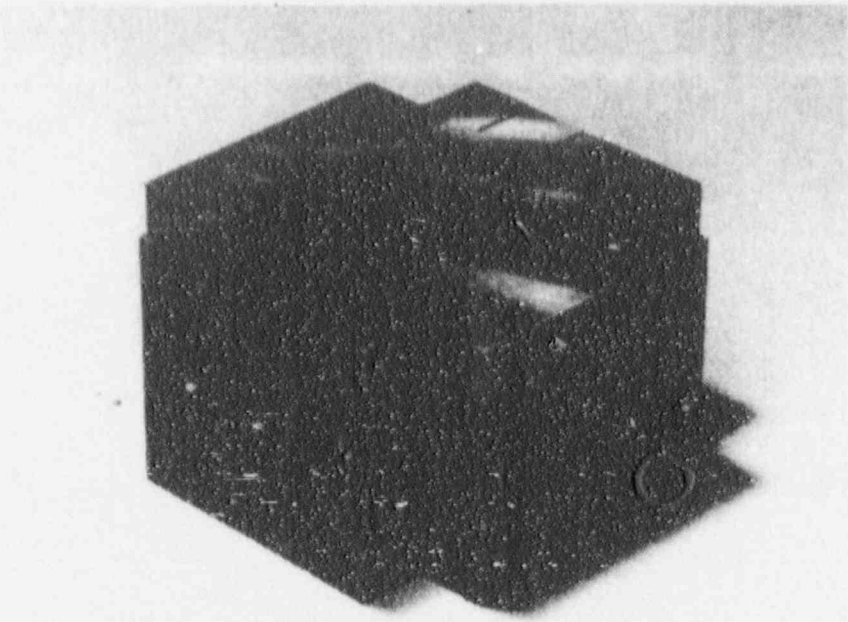


Fig. 10 The differential load-diffusion control slot lengths used to control stress concentrations at the slot-crack interface can be seen in the completed central block.



Fig. 11 Loading arms are electron-beam welded to the central block to complete the cruciform test specimen.

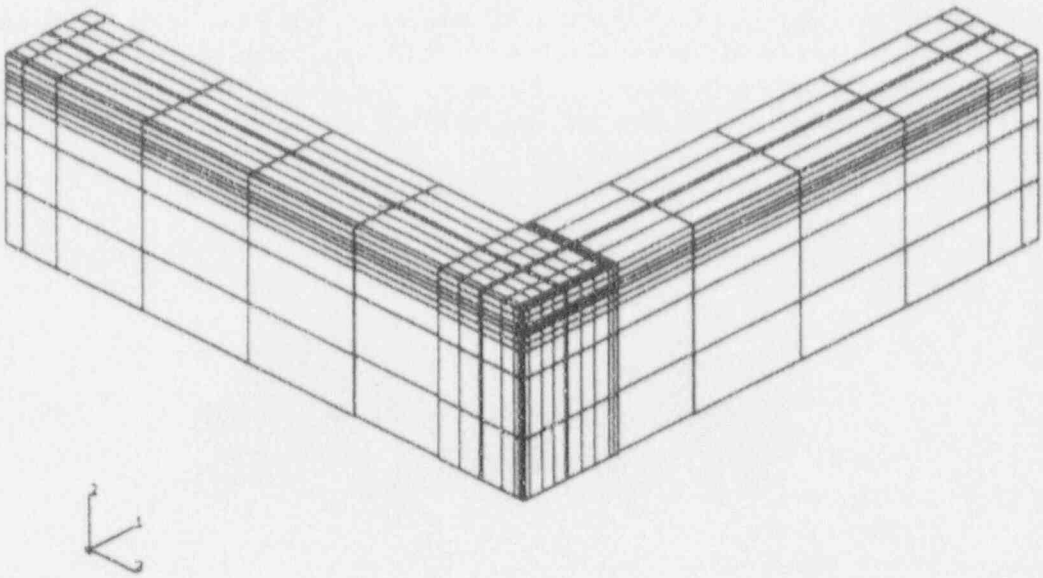


Fig. 12 A cruciform model incorporating a highly refined crack-tip region was used for the local crack-tip field analysis.

Validation checks were performed on the analysis model before it was used to interpret the test data. Results from one of the most stringent of those checks are shown in Fig. 13. Load vs crack-mouth-opening displacement (CMOD) predictions from the analysis were required to match test values for this parameter set over the full range of test values. Iterative adjustments were made to the material stress-strain representation to achieve the close match between analytical predictions and test results shown in Fig. 13.

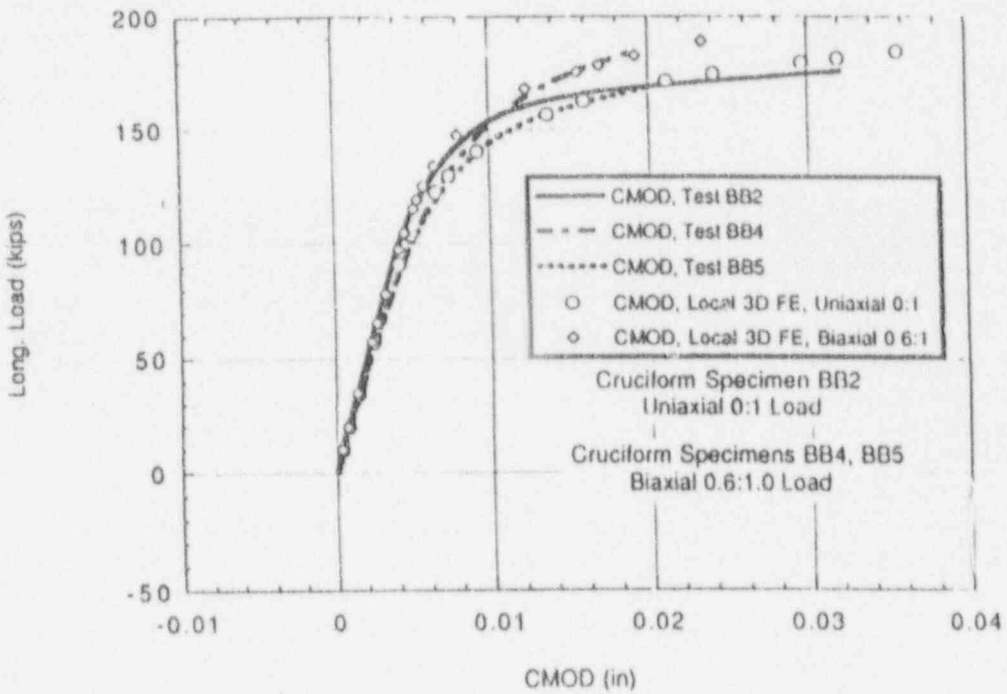


Fig. 13 Analysis model predictions match closely the load vs CMOD results obtained in the uniaxial and biaxial tests.

Two schemes for estimating J_c from the biaxial test results were evaluated by Theiss et al. in Ref. 23. The methods are based on estimating the energy deposited in the crack-tip material using (a) the area under the load vs load-line displacement curve, and (b) the area under the load vs CMOD curve. The latter scheme was considered the more accurate of the two because the CMOD measurement is made close to the crack tip. The load vs CMOD curve provides, therefore, a more sensitive measure of the energy deposited in the crack-tip material.

The applied J integral at fracture (J_c) is expressed in terms of elastic and plastic elements of the load vs CMOD curve in equation 2.

$$J_c = J_{el} + J_{pl} \qquad (2)$$

Where

J_{el} = elastic contribution to $J_c = K_c^2(1 - \nu^2)/E$
K_c = applied stress intensity factor
ν = Poisson's ratio
E = Young's modulus
J_{pl} = plastic contribution to $J_c = \eta_{pl}^c U_{pl}^c B(W - a)]$
η_{pl}^c = dimensionless factor determined by analysis and relating the plastic area under the load vs CMOD curve to J_{pl}. Note that η_{pl}^c is stress-state dependent.
U_{pl}^c = plastic portion of the area under the load vs CMOD curve
a = crack depth
W = test specimen width (depth)
B = test specimen thickness

Output from the analysis also included a definition of the applied crack-tip J for all points along the crack-front. One set of these results is shown in Fig. 14 in terms of the more familiar K_J. Biaxial loading is seen to produce a nonuniform distribution of K_J along the crack-front, with the departure from linearity increasing as specimen is loaded further into the regime of nonlinear behavior. This trend makes consideration of the crack initiation site necessary to an accurate interpretation of the test data.

Plots of the Von Mises equivalent stress distribution over the test specimen ligament are shown in Fig. 15 for uniaxial and biaxial loading conditions. Both plots represent conditions at failure as determined in the tests. Note that the Von Mises equivalent stress exceeds the material yield stress by a small amount over much of the ligament in the uniaxial loading case. Biaxial loading, in contrast, results in the ligament remaining elastic. This result could have been anticipated by imposing an out-of-plane stress on the published stress distributions for notched bars (Ref. 24). One consequence of biaxial loading is, therefore, to increase crack-tip constraint by suppressing large-scale plastic deformation of material in the immediate vicinity of the crack.

Results from the crack-tip field portion of the analysis are shown in Fig. 16. The curves in Fig. 16 show the opening mode stress distribution ahead of the crack for both uniaxial and biaxial loading, together with the reference (high constraint) opening mode stress distribution. It is evident from these curves that Q does not remain constant with distance ahead of the crack tip for the case of uniaxial loading. Biaxial loading, in contrast, results in relatively constant values of Q for $r > 2J/\sigma_0$. This observed trend for uniaxial loading is incompatible with one of the postulates upon which the J-Q fracture-toughness correlation is based, indicating a need for some further development of that correlation. The Dodds–Anderson correction factor approach is not

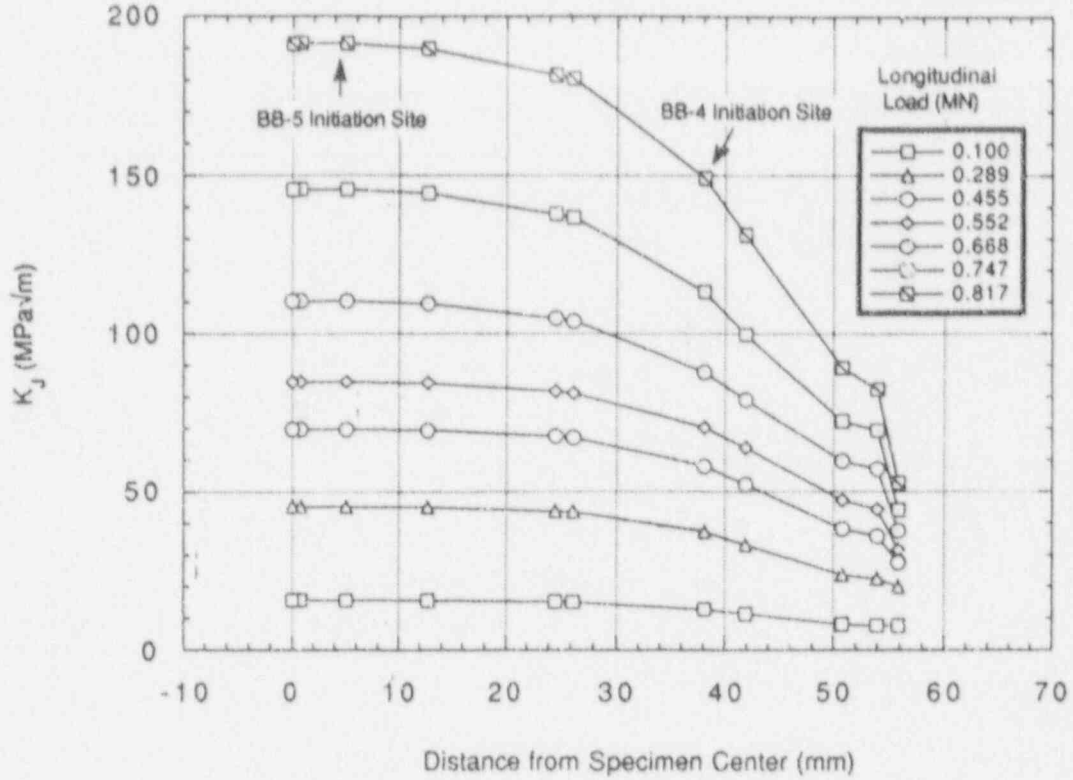


Fig. 14 Variation of K_J along the crack front for a 0.6:1.0 biaxial loading condition.

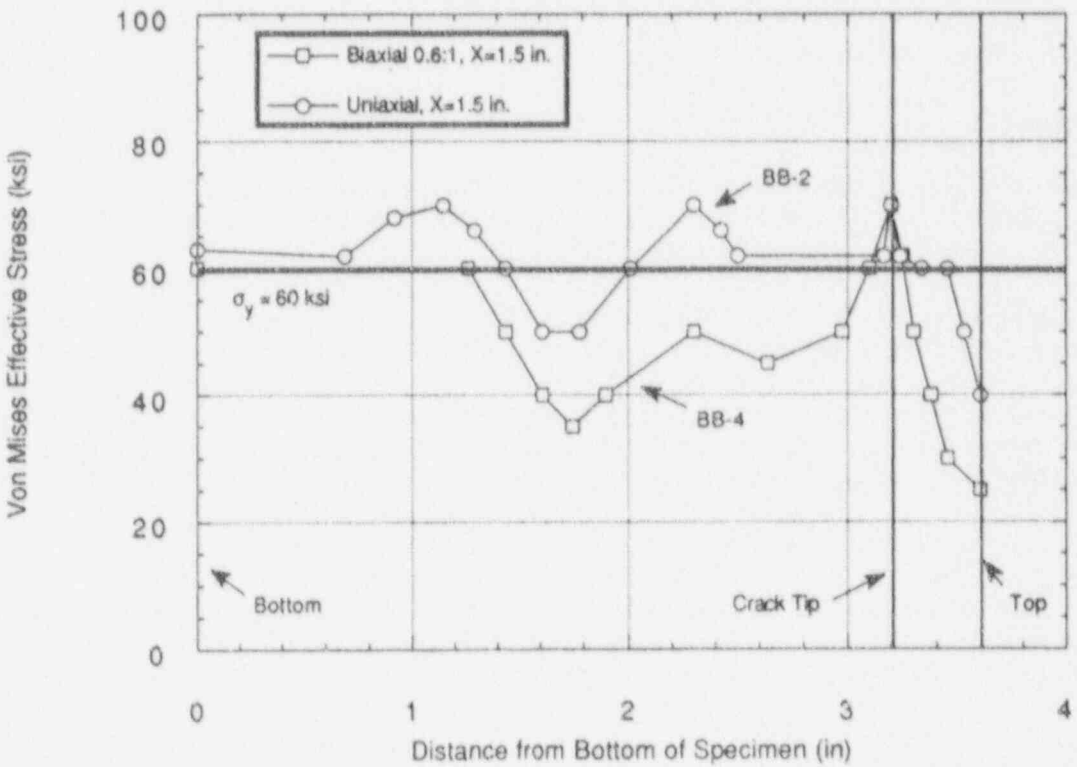


Fig. 15 Ligament stresses at fracture exceed the yield stress under uniaxial loading but remain elastic under biaxial loading.

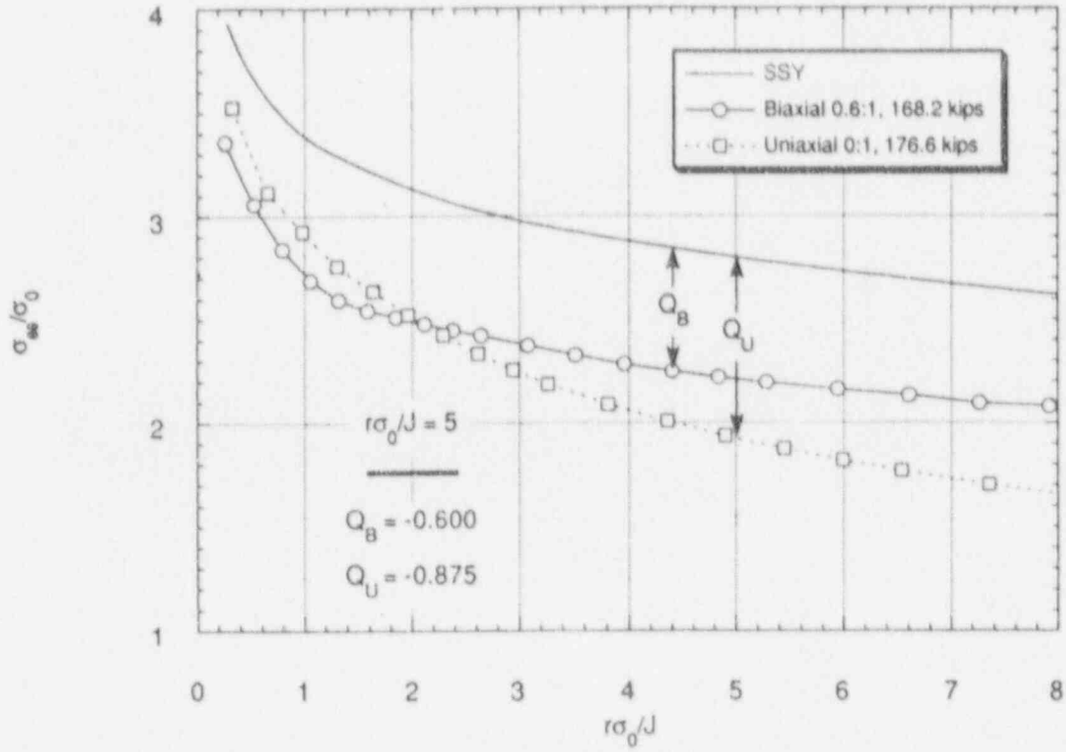


Fig. 16 Stress biaxiality improves the uniformity of the Q-stress field relative to the Q-field obtained with uniaxial loading.

compromised by the results illustrated in Fig. 16 because it is not based upon the assumption of a uniform Q-stress field ahead of the crack tip.

Test Results

The first requirement for the test program was to demonstrate that the configuration of the crack and the load-diffusion control (LDC) slots would produce crack initiation remote from the intersection of these two features. Satisfaction of this requirement was essential to assure that the measured test results were a true reflection of the influence of the test parameters on shallow-flaw, fracture-toughness and were not influenced by stress concentration effects at the ends of the LDC slots. The requirement was found easier to satisfy under uniaxial loading than biaxial loading. The configuration of the crack-geometry and LDC slot geometry finally selected was capable of assuring crack initiation away from the intersection under both uniaxial and biaxial loading. Figure 17 shows a fracture surface from one of the biaxial tests. The river patterns in Fig 17 show the fracture to have initiated close to the mid point of the crack.

Extensive calibration of the test fixture was undertaken prior to the initiation of testing. A dummy cruciform specimen fitted with multiple strain gauges was used in this phase of the program. Results demonstrated that the statically determinate load reaction system was working as planned. Pretest preparations culminated in a test readiness review, in which an independent body of fracture mechanics experts found the test program ready for implementation.

Clip gauges and displacement transducers were used to measure CMOD and load-line displacement (LLD), respectively, as a function of the applied load. Test temperatures were selected to be in the lower transition region of the shallow-flaw, fracture-toughness curve. This is the area of the fracture-toughness curve of particular interest in determining the effect of biaxial loading on ΔRT_{NDT}.

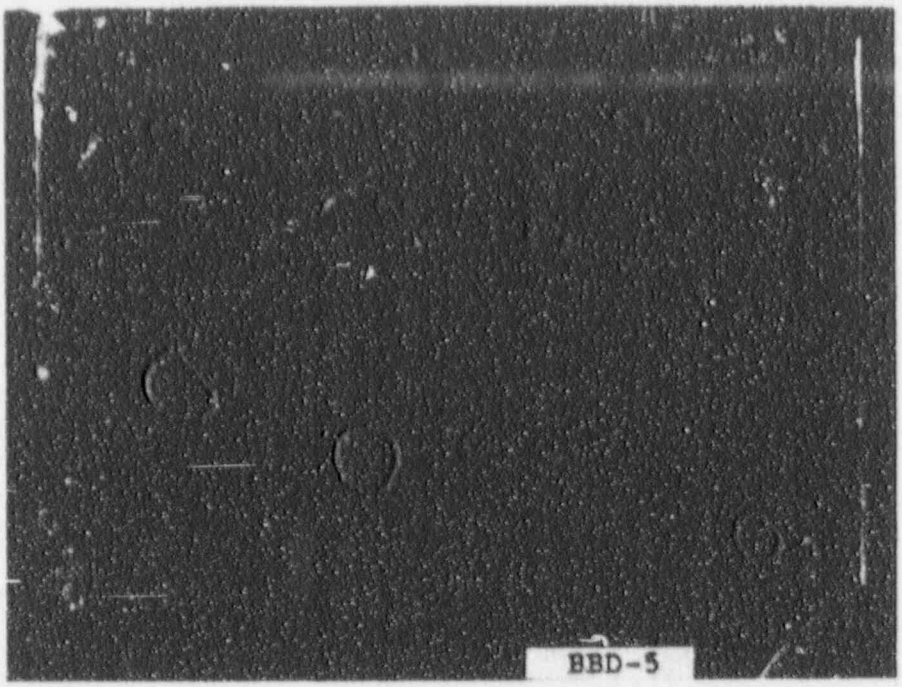


Fig. 17 Cleavage fracture initiated in the mid-thickness of the biaxial test specimen, remote from any structural discontinuities.

Load vs CMOD curves generated in three of the four valid tests completed to date were shown in Fig. 13. Note that the measured CMOD at failure is remarkably similar for the two biaxial tests. Biaxial loading substantially reduces the CMOD at failure when compared with the uniaxial loading result.

Test values for K_{Jc} are shown in Fig 18, superimposed on data from the shallow-flaw and deep-flaw SENB tests. The cruciform beam data plotted in Fig 18 corresponds with the point on the crack front at which post-test examination showed the crack to have initiated. The cruciform specimen tested under uniaxial loading produced a fracture-toughness close to the lower bound of the fracture-toughness scatter band from the shallow-flaw SENB tests. Biaxial loading of the cruciform specimen produced two results below the lower bound of results from the shallow-flaw SENB data set. The two data points from biaxial loading tests on the cruciform specimen are seen to be closely matched.

Test data generated to date are consistent with expectations for the biaxial tests. Biaxial loading appears to reduce K_{Jc} below the values associated with shallow flaws, but not down to the lower bound values associated with highly constrained deep flaws. There are also indications that biaxial loading may reduce the scatter of shallow-flaw, fracture-toughness data. The biaxial testing program is, however, in its infancy, and the amount of data currently available from the program is not sufficient to support an assessment of biaxial loading effects on shallow-flaw, fracture-toughness at this time.

Test Data Interpretation

The objective in this section is to illustrate the practical application of constraint effects technology to the safety assessment of an irradiation-embrittled reactor pressure vessel. Fracture-toughness data reflecting the effect of varying levels of crack-tip constraint are essential input to such a safety assessment. At this time the amount of data available from the biaxial testing program is too small to support a safety assessment. This example, therefore, utilizes data from the previously

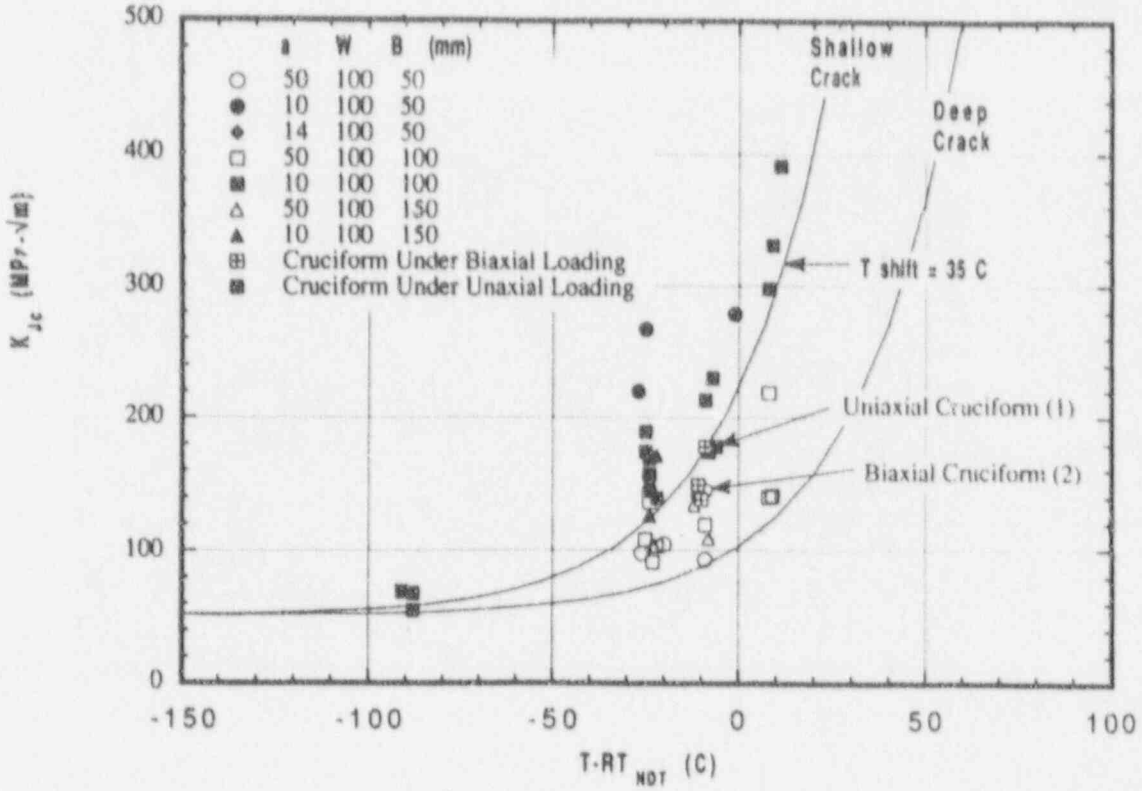


Fig. 18 Biaxial loading resulted in shallow-flaw, fracture-toughness values below the lower bound values obtained under uniaxial loading.

completed HSST shallow-flaw tests on SENB specimens. Data used in this assessment were taken from Ref. 11. The data set of Ref. 11 cover two constraint configurations. These are deep flaws with an a/W of 0.5 and shallow flaws with an a/W ratio of 0.1. Prof. R. Dodds has performed a J-Q analysis of these test specimens under an HSST Program subcontract. J-Q trajectories for both the shallow- and deep-flaw beams are shown in Fig. 19, together with a J-Q loading trajectory from one of the HSST Program wide-plate tests (Ref. 25).

Fracture-toughness data from each of the test series are shown in Fig. 19, superimposed on the appropriate J-Q loading trajectory. Upper and lower bounds to the resulting J-Q scatter band are represented in Fig. 19 by straight lines. This representation reflects the fact that only two constraint-effects data sets are available at this time. A more accurate definition of the bounds of the J-Q failure locus scatter band will be possible when more data become available. The data shown in Fig. 19 were all generated at the same test temperature (–10°C). A similar data set exists for tests performed at –25°C.

The lower bound to the J-Q failure locus scatter band defines the minimum anticipated increase in fracture-toughness over the reference high-constraint toughness as the constraint parameter Q decreases from the reference high constraint value ($Q = 0$). Minimum anticipated fracture-toughness increases due to loss of crack-tip constraint are plotted in Fig. 20(a) for each of the test temperatures. Note that fracture-toughness in Fig. 20(a) has been expressed in terms of K_{Jc} rather than J_c. This was done to permit the final result from this example to be expressed in terms of the fracture-toughness units currently in use in RPV safety assessments.

The plots of Fig. 20(a) can now be used to predict the lower-bound, fracture-toughness curve for a given crack-tip constraint condition. In the example given, a constraint loss characterized by $Q = -0.6$ was used. Predicted fracture-toughness increases for $Q = -0.6$ are 34 MPa$\sqrt{m}$ at T-RT_{NDT} =

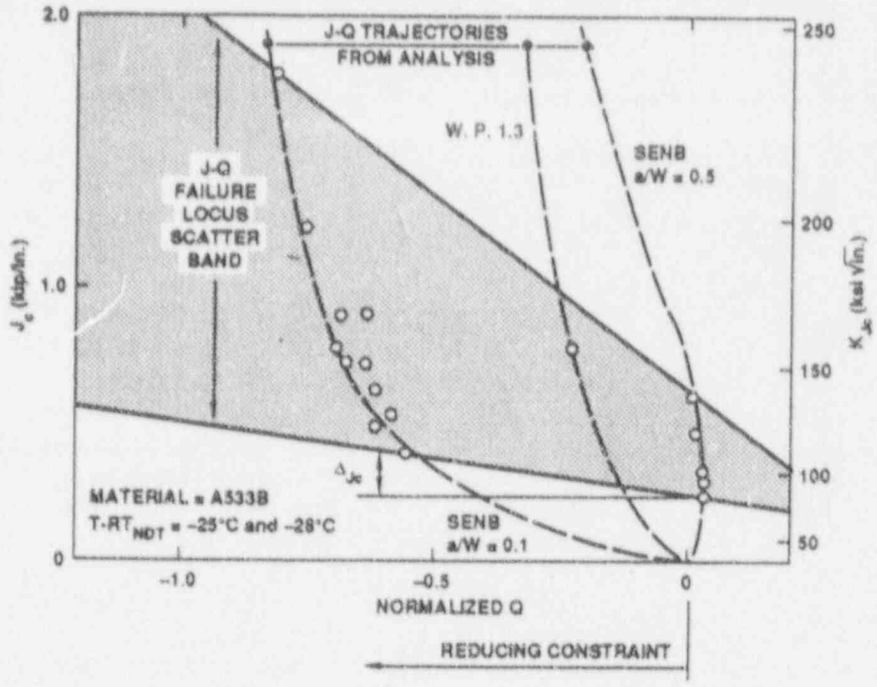


Fig. 19 The J-Q failure locus scatter band shows increased toughness and increased data scatter as the crack-tip constraint decreases (Q becomes more negative).

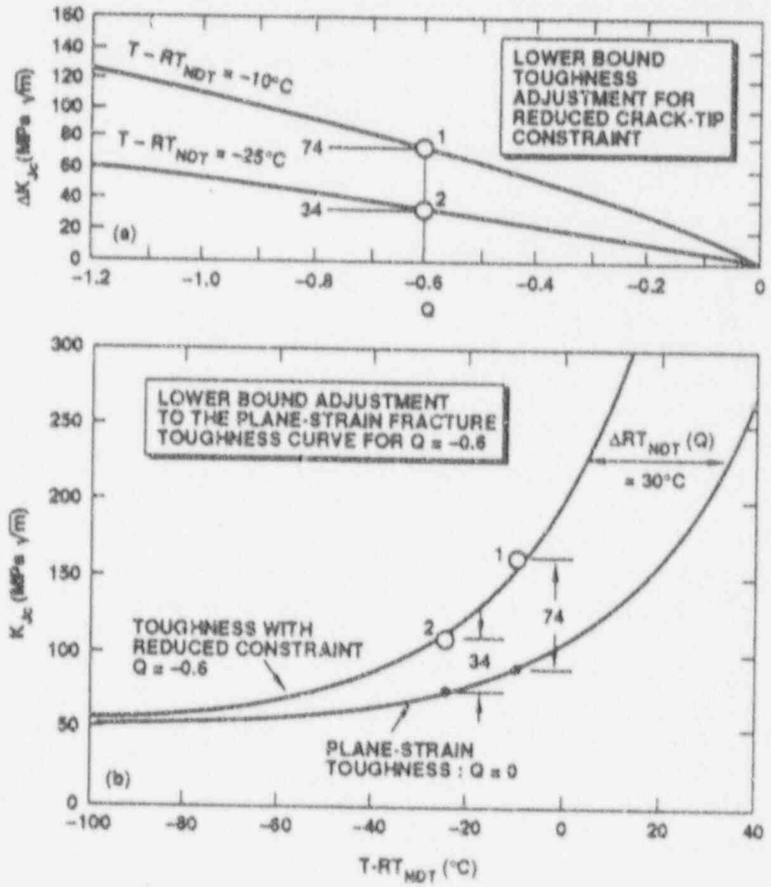


Fig 20. A fracture-toughness curve for a reduced crack-tip constraint condition can be generated using the plane-strain, fracture-toughness curve and the J-Q failure locus envelope.

–25°C and 74 MPa$\sqrt{m}$ at $T\text{-}RT_{NDT}$ = –10°C. These values are now transferred to Fig. 20 (b) where they are shown plotted as increases over the base material fracture-toughness curve. Transition of the base material curve to the left, such that it passes as closely as possible through the two data points, completes the process. The resulting curve represents the lower bound fracture-toughness for a given level of crack-tip constraint, a constraint level characterized by Q = –0.6 in this example.

In a practical application of the J-Q methodology, lower bound fracture-toughness curves could be produced for a range of crack-tip constraint conditions. An analysis of the crack-tip stress fields would, however, be required to determine the constraint condition appropriate for a given geometry and loading condition. It is possible, however, that J-Q analyses for a range of geometry and loading conditions commonly encountered in RPV safety analyses could be performed and the resulting J-Q loading trajectories documented. This approach could eliminate the need for repeated performance of the relatively expensive crack-tip field analysis.

The above example dealt with application of J-Q constraint-effects technology to a deterministic analysis of RPV safety. The technology could also be applied to the probabilistic analysis of RPV safety. The impact of J-Q technology on a probabilistic analysis would be expected to be greater than the impact on a deterministic analysis. This is so because both the mean value of the fracture-toughness scatter band and the width of the scatter band increase more rapidly with loss of crack-tip constraint than does the lower bound fracture-toughness. These trends are evident in the J-Q fracture-toughness scatter band illustrated in Fig. 19.

Verification Checks

Fractographic examination of the broken test specimens provides information on the location of the cleavage initiation sites. Initiation site assumptions are built into the J-Q constraint effects technology. A comparison of the initiation site locations from the test specimens with the initiation site assumptions in the J-Q technology is used as a verification check on the technology.

Opening mode stress plots for the cruciform specimen in both uniaxial and biaxial loading are shown, together with the opening mode stress plot for a high constraint configuration, in Fig. 21(a). These plots were produced in a finite-strain (large-strain) analysis and, therefore, show a downward trend near the crack tip because of the loss of stress triaxiality in material adjacent to the free surface of the blunted crack tip. Cleavage initiation site data from the fractographic examination of SENB and biaxial specimens tested at a range of temperatures are shown in Fig. 21(b). Many of the cleavage initiation site locations are located to the left of the peak on the opening mode stress plots. Locations to the left of the peak of the opening mode stress plots experience a falling opening mode stress as the applied J increases. Experience with warm prestressing indicates that cleavage fracture is unlikely to initiate under conditions of decreasing opening mode stresses. At first sight the analysis results and data of Fig. 21 would appear to call into question the basic assumptions inherent to the J-Q technology. On closer examination, however, the basic question appears to lay with the adequacy of the analytical model used to generate the opening mode stress plots.

The analytical model represents a stationary crack. With such a model, crack-tip blunting increases continuously as the applied J increases. In reality, however, tearing would initiate at some point in the loading cycle for tests conducted at temperatures in the transition range. The primary effect of tearing would be to resharpen the previously blunted crack tip. Resharpening of the crack tip would have the effect of moving the peaks of the opening mode stress plots further to the left. Conceptually, this adjustment could eliminate the incompatibility shown in Fig. 21 between analysis and test results.

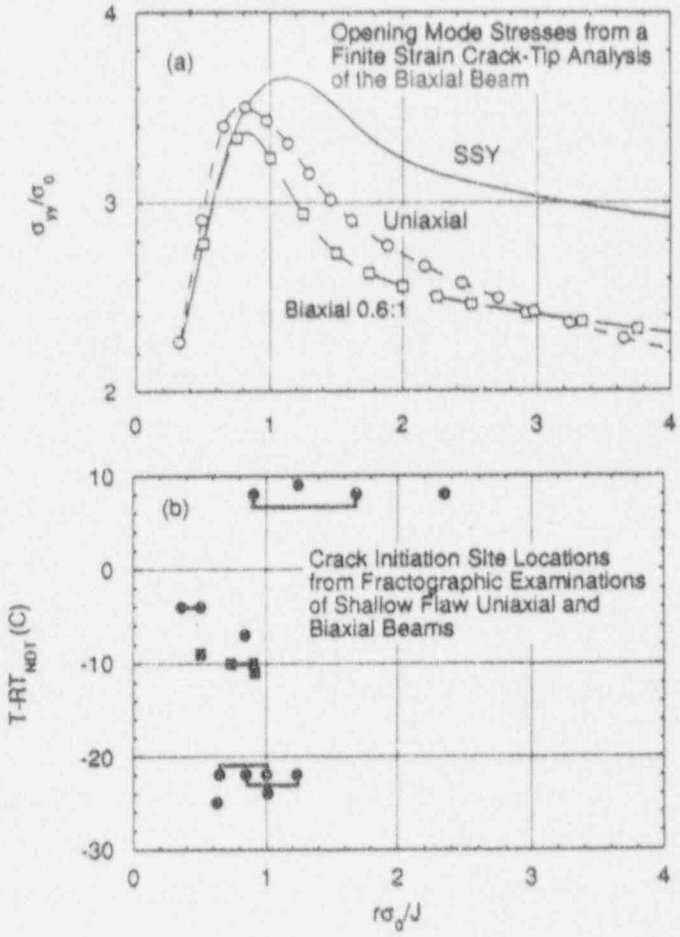


Fig 21. Additional refinement to the crack-tip stress field analysis model appears to be required to reconcile analysis predictions with fractography results.

The analysis model refinement required is one which permits the representation of precleavage tearing. A number of fracture research centers in Europe have had success in developing precleavage tearing models using the critical stress for void formation as defined by the Beremin group and either the Rousselier or Gurson yield models (26, 27, 28). The yield functions take into account the fact that only biaxial stresses can exist at the surface of internal voids. Because of this, application of a hydrostatic stress can result in a plastic volume change. A recent application of this technology by Dr. Dietmar Klingbeil of Bundesanstalt für Materialforschhung und Prufung (BAM), Berlin, Germany, demonstrated that (a) the crack-tip stress field becomes stationary after a relatively small amount of ductile tearing, and (b) the effect of tearing is to "resharpen" the previously blunted crack tip (Ref. 29).

The curves of Fig. 21(a) make it clear that Q cannot be treated as a spatially invariant parameter when, as in the uniaxial loading curve, the overall section and crack-tip plastic stress fields interact. A further question on the selection of the appropriate value for Q derives from the work of Heerens and Read (Ref. 30). They showed, for a low alloy steel tested at –60°C, that the cleavage initiation sites were at the maximum opening mode stress location. A case can, therefore, be made for defining Q as the normalized difference in peak stresses from opening mode stress plots for the reference high constraint configuration and a lower constraint application. It can be seen from the plots of Fig. 21(a) that the value of Q derived using this definition would be considerably smaller than that derived from the "uniform Q-field" definition.

Interim Conclusions

Crack-tip constraint effects of shallow flaws and biaxial loading influence both fracture-toughness and the width of the fracture-toughness scatter band. This influence can have a significant impact on the outcome of an RPV safety analysis.

Dual-parameter (J-Q and J-Acr) fracture-toughness correlations and corrections show promise as a practical means for introducing the effects of crack-tip constraint into reactor pressure vessel safety assessments. Additional refinement of the analysis models used to define crack-tip stress fields appears to be necessary in order to resolve discrepancies between analytical predictions and fractographic data on cleavage initiation sites. Inclusion of precleavage tearing effects into the analysis model appears to have the potential to resolve the observed discrepancies.

Development and validation of technology for the quantitative assessment of crack-tip constraint effects on fracture-toughness is essential to the future utilization of miniature fracture-toughness surveillance specimens.

References

1. R. O. Ritchie, J. F. Knott, and J. R. Rice, "On the Relationship Between Critical Tensile Stress and Fracture Toughness in Mild Steel," *J. Mech. Phys. Solids* 21, 395–410 (1973).

2. G. R. Irwin, "Analysis of Stresses and Strains Near the End of a Crack Traversing a Plate," *American Society of Mechanical Engineers*, Journal of Applied Mechanics, September 1957, pp. 361–364.

3. J. Hutchinson, "Singular Behavior at the End of a Tensile Crack in a Hardening Material," *J. Mech. Phys. Solids* 16, 13–31 (1968).

4. J. R. Rice and G. F. Rosengren, "Plane-Strain Deformation Near a Crack Tip in a Power-Law Hardening Material," *J. Mech. Phys. Solids* 16, 1–12 (1968).

5. *American Society for Testing and Materials Standard No. E399–90*, "Standard Test Method for Plane-Strain Fracture Toughness of Metallic Materials" (1990).

6. T. R. Mager, Westinghouse Electric Corp., "Heavy-Section Steel Technology Program Technical Report No. 10: Fracture Toughness Characterization Study of A533, Grade B, Class 1 Steel," WCAP-7578, October 1970.

7. R. H. Dodds, Jr., T. L. Anderson, and M. T. Kirk, "A Framework to Correlate a/W Ratio Effects on Elastic-Plastic Fracture Toughness (J_c)," *International Journal of Fracture* 48: 1–22, (1991).

8. N. P. O'Dowd and C. F. Shih, "Family of Crack-Tip Fields Characterized by a Triaxiality Parameter: Part I—Structure of Fields," *J. Mech. Phys. Solids* 39, 989–1015 (1991).

9. N. P. O'Dowd and C. F. Shih, *Two-Parameter Fracture Mechanics: Theory and Applications*, USNRC Report NUREG/CR-5958 (CDNSWC/SME–CR–16–92), Oak Ridge National Lab., Oak Ridge, TN, February 1993.

10. J. R. Rice, "A Path Independent Integral and the Approximate Analysis of Strain Concentrations by Notches and Cracks," *Journal of Applied Mechanics*, Vol. 35, pp. 379–386.

11. T. J. Theiss and D. K. M. Shum, *Experimental and Analytical Investigation of the Shallow-Flaw Effect in Reactor Pressure Vessels*, USNRC Report NUREG/CR-5886 (ORNL/TM-12115), Oak Ridge National Lab., Oak Ridge, TN, July 1992.

12. M. T. Kirk, K. C. Koppenhoefer, and C. F. Shih, "Effect of Constraint on Specimen Dimensions Needed to Obtain Structurally Relevant Toughness Measures," *Constraint Effects in Fracture, ASTM STP 1171*, pp. 79–103, March 1993.

13. T. J. Theiss, W. J. McAfee, B. R. Bass, J. W. Bryson, and M. C. Rao, "Preliminary Results from Biaxial Shallow-Flaw Fracture Toughness Tests on Reactor Pressure Vessel Steel," *ASME PVP*, Vol. 250, pp. 271–281, July 1993.

14. B. R. Bass, J. W. Bryson, W. E. Pennell, and T. J. Theiss, "Determination of Out-of-Plane Biaxial Stress Effects on Fracture Toughness for Shallow Surface Cracks in Reactor Pressure Vessel Steels," *ASME PVP*, Vol. 250, pp. 257–269, July 1993.

15. D. Aurich, R. Helms, P. Schmidt, H. Veith, J. Ziebs, "The Influence of the Stress State on K_{Ic}," *Transactions of the Fourth International Conference on Structural Mechanics in Reactor Technology*, Vol. G, August 1977.

16. D. Aurich, W. Brocks, R. Jordan, J. Olschewski, H. Veith, and J. Ziebs, "The Influence of Multiaxial Stress States on Characteristic Parameters for Cleavage Fracture in the Elastic-Plastic Range," *Proceedings of the International Applied Fracture Mechanics to Materials and Structures*, 1984.

17. D. Aurich and E. Sommer, "The Effect of Constraint on Elastic-Plastic Fracture," *Metalle und Metallkonstruktionen*, Steel Research 59, No. 8, pp. 358–367, 1988.

18. H. Clausmeyer, K. Kussmaul, and E. Roos, "Influence of Stress State on the Failure Behavior of Cracked Components Made of Steel," *Applied Mechanics Rev*, Vol. 44, No. 2, February 1991.

19. S. J. Garwood, "The Significance of Biaxial Loading on the Fracture Performance of a Pressure Vessel Steel," *Pressure Vessel Integrity*, PVP-Vol. 213, MPC-Vol. 32, June 23–27, 1991.

20. Office of U.S. Nuclear Regulatory Research, U.S. Nuclear Regulatory Commission Regulatory Guide 1.154 (Task SI 502-4), Format and Content of Plant-Specific Pressurized Thermal Shock Safety Analysis Reports for Pressurized Water Reactors, January 1987.

21. ABAQUS Theory Manual, Version 4–8, Hibbitt, Karlson, and Sorensen, Inc., Providence, R. I., 1989.

22. B. R. Bass, J. W. Bryson, T. J. Theiss, and M. C. Rao, *Biaxial Loading and Shallow-Flaw Effects on Crack-Tip Constraint and Fracture Toughness*, USNRC Report NUREG/CR-6132 (ORNL/TM-12498), to be published in November 1993.

23. J. A. Hendrickson, D. S. Wood, and D. S. Clark, "The Initiation of Brittle Fracture in Mild Steel," Trans., ASM (50), 1958, pp. 656.

24. T. J. Theiss, B. R. Bass, J. W. Bryson, W. J. McAfee, R. K. Nanstad, W. E. Pennell, and M. C. Rao, *Initial Results of the Influence of Biaxial Loading on Fracture Toughness*, USNRC Report NUREG/CR-6036 (ORNL/TM-12349), Oak Ridge National Lab., Oak Ridge, TN, June 1993.

25. D. J. Naus, B. R. Bass, C. E. Pugh, R. K. Nanstad, J. G. Merkle, W. R. Corwin, G. C. Robinson, *Crack-Arrest Behavior in SEN Wide Plates of Quenched and Tempered A533 Grade B Steel Tested Under Nonisothermal Conditions*, USNRC Report NUREG/CR-4930 (ORNL-6388), Oak Ridge National Lab., Oak Ridge, TN, August 1987.

26. K. Kussmaul, M. Seidenfuss, and U. Eisele, "On the Applicability of Damage Models for the Description of the Failure Behavior of Ductile Steels," presented at the International Conference on Fracture, Kiev, Ukraine, June 1993.

27. G. Rousselier, "Ductile Fracture Models and Their Potential in Local Approach of Fracture," Nuclear Engineering and Design 105, North-Holland, Amsterdam, pp. 111, 1987.

28. A. H. Sherry, "Elastic-Plastic, Finite-Element Analysis of Circumferentially Notched Tensile Specimen," AEA Thermal Reactor Services, AEA Technology, January 1991.

29. W. E. Pennell and W. R. Corwin, "ORNL Foreign Trip Report," ORNL/FTR-4673, July 1993.

30. J. Heerens and D. T. Read, "Fracture Behavior of a Pressure Vessel Steel in the Ductile-to-Brittle Transition Region," NISTIR 88-3099, National Institute for Standards and Technology, Boulder, CO, December 1988.

Heavy-Section Steel Irradiation Program Progress—Recent Results from Midland Low Upper-Shelf Weld Studies*

W. R. Corwin, R. K. Nanstad, D. E. McCabe, and S. K. Iskander
Oak Ridge National Laboratory
Oak Ridge, Tennessee 37831

ABSTRACT

Low upper-shelf weld metal removed from two major structural welds in the vessel of the Midland Unit 1 Reactor is being examined to establish its variation in chemistry and fracture properties in the unirradiated condition and to investigate its response to neutron irradiation. Both beltline and nozzle course welds were examined throughout their thickness at a number of different locations. Even though all the weld metal examined carries the identical WF-70 designation, its bulk copper content ranged widely, from 0.21 to 0.46 wt %. Its dropweight nil-ductility transition temperatures ranged from –40 to –60°C (–40 and –76°F). The values of the nil-ductility reference temperature (RT_{NDT}) are all controlled by Charpy impact behavior and varied from –20 to 37°C (–4 to 99°F) while the Charpy upper-shelf energies varied from 77 to 108 J (57 to 80 ft-lb). A newly proposed method for identifying a transition temperature from fracture mechanics-based data established a difference in transition temperatures between nozzle course and beltline weld metal of 27°C (49°F). Crack-arrest toughness values were determined for the beltline weld. The ASME K_{Ic} and K_{Ia} curves were shown to adequately bound all experimental fracture toughness and crack-arrest data, respectively, using the full range of experimentally determined values of RT_{NDT}, but with a relatively large amount of uncertainty in the margin between the data and the toughness curves. The irradiation of the Midland weld is in progress for exposures between 5×10^{18} and 5×10^{19} neutrons/cm^2 to examine fluence effects over this range.

*Research sponsored by the Office of Nuclear Regulatory Research, U.S. Nuclear Regulatory Commission, under Interagency Agreement DOE 1886-8109-8L with the U.S. Department of Energy under contract DE-AC05-84OR21400 with Martin Marietta Energy Systems, Inc.

The submitted manuscript has been authored by a contractor of the U.S. Government under contract DE-AC05-840R21400. Accordingly, the U.S. Government retains a non-exclusive, royalty-free license to publish or reproduce the published form of this contribution, or allow others to do so, for U.S. Government purposes.

INTRODUCTION

The Heavy-Section Steel Irradiation (HSSI) Program at the Oak Ridge National Laboratory (ORNL) includes several activities to examine various aspects of the fracture resistance of materials generally regarded as low upper-shelf (LUS) welds. This class of welds was produced by the submerged-arc welding (SAW) process using a specific type of welding flux (Linde 80). Linde 80 flux was deemed suitable for reactor pressure vessel (RPV) fabrication since it produced a very fine dispersion of inclusions within the weld and a resultant lower number of reportable defects observed by radiography than commonly obtained with other welding fluxes. An unfortunate by-product of this fine dispersion of inclusions was that they provided such a large number of microvoid initiation sites that the macroscopic resistance of these welds to ductile crack extension by the microvoid growth and coalescence process was significantly reduced. This problem was further aggravated by the fact that, at the time these welds were being fabricated, the deleterious effect of impurity copper on the radiation-induced degradation of toughness in pressure vessel materials was not yet generally recognized. Hence, a copper coating on the welding wire, a common practice to minimize corrosion products on ferritic welding wire and enhance electrical contact between the feed rollers and the workpiece, was also used. The combination of the use of Linde 80 welding flux and copper-coated welding wire has resulted in a significant number of pressure vessels in which major fabrication welds have both relatively low resistance to ductile fracture in the unirradiated condition and a high sensitivity to further degradation from neutron exposure.

The principal current activity within the HSSI program to examine LUS welds is the Tenth Irradiation Series, in which the effects of radiation on the fracture toughness of commercially fabricated LUS submerged-arc welds from the RPV of the canceled Midland Unit 1 nuclear plant are being investigated. Additional LUS studies within the Eighth and Ninth Irradiation Series are in their early stages but, in combination, will eventually examine the detailed relationship between the Charpy V-notch (CVN) and fracture toughness degradation for the irradiated, annealed, and reirradiated conditions for a generic LUS weld.

The welds from the Midland plant carry the Babcock and Wilcox Co. (B&W) designation WF-70, a specific combination of weld wire and welding flux that exists in several commercial pressurized-water reactors. The initial part of this study which has been completed involved the determination of variations in chemical composition, reference temperature (RT_{NDT}), tensile properties, and fracture toughness throughout the welds. Four sections of beltline weld and two similar sections of nozzle course weld have been examined. The remainder of this study will focus on the irradiation response of the WF-70 weld. The irradiation of the

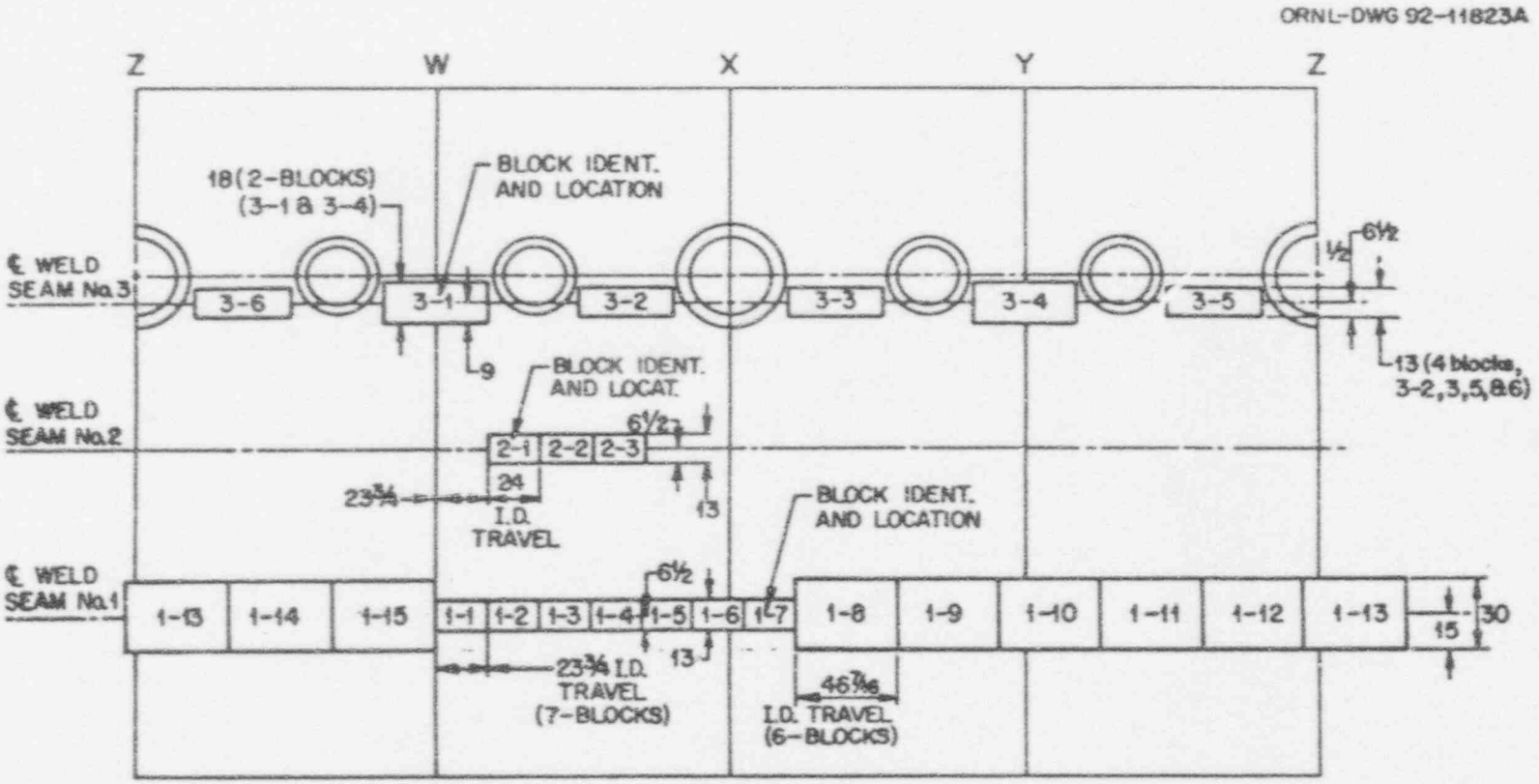
Midland weld is in progress. The exposure of the first of the two large irradiation capsules to the primary target fluence of 1×10^{19} n/cm^2 (> 1 MeV) has been completed and the second begun. Small fracture toughness and CVN specimens are also being exposed in low- and high-fluence scoping capsules to 5×10^{18} and 5×10^{19} neutrons/cm^2, respectively.

A topical report has been published that describes the detailed investigations of unirradiated chemical and RT_{NDT} properties of the Midland welds.[1] A second topical report (D. E. McCabe, R. K. Nanstad, S. K. Iskander, and R. L. Swain, Martin Marietta Energy Systems, Inc., Oak Ridge Natl. Lab., *Unirradiated Material Properties of Midland Weld WF-70*, USNRC Report in preparation) will also provide results of their detailed unirradiated tensile and fracture toughness investigations. This paper combines and summarizes the information presented in the individual topical reports.

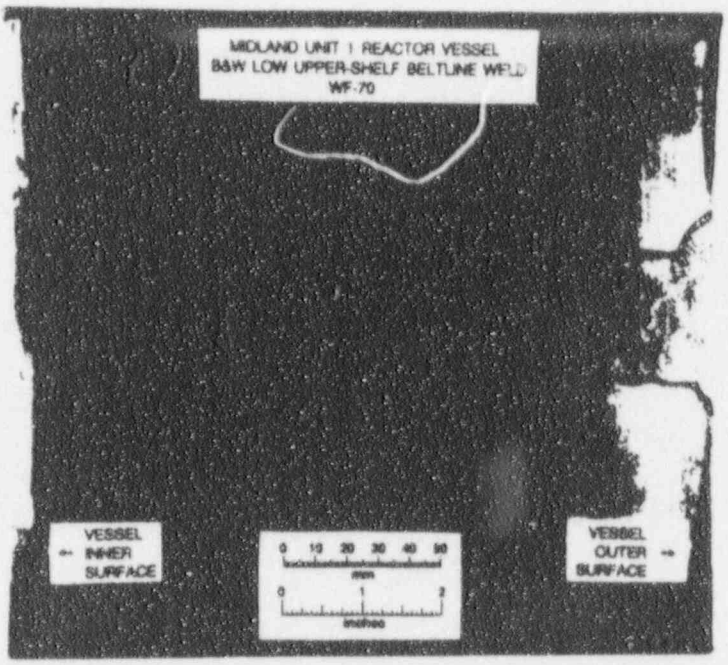
DESCRIPTION OF WELDMENTS

Four beltline sections of weldment that had been removed by B&W, each approximately 1.17 m long (46 in.), were received at ORNL. The sections were those designated 1-9, 1-11, 1-13, and 1-15 in the section removal plan described by B&W in BAW-2070 (ref. 2). Figure 1 is a schematic diagram from that document showing the sectioning plan for the vessel. Figure 2 shows a macrograph through the thickness of beltline section 1-13 of the submerged-arc weld WF-70 with regions designated 1 through 4 from which specimens were removed for optical microscopy, chemical analysis, Charpy impact tests, and drop-weight tests. The thickness of the beltline weld is about 216 mm (8.5 in.). The microstructure of the weld metal was determined to be largely acicular ferrite but with highly decorated grain boundaries and a high inclusion content.

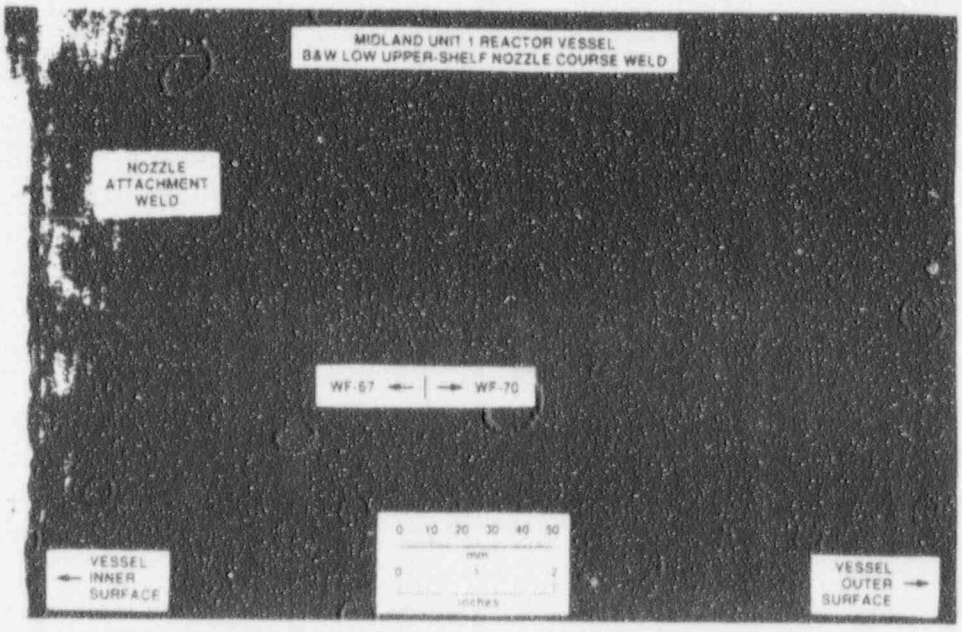
Nozzle course weld sections 3-1 and 3-4 were also received and examined. The thickness of the nozzle course is about 305 mm (12 in.). Figure 3 is a macrograph from section 3-1 and shows that weld WF-70 comprises that portion of the weld from approximately midthickness to the outer surface of the vessel; B&W weld WF-67 comprises approximately the other half of the weld thickness. The remaining sections of weld described in BAW-2070 not received at ORNL were sent by B&W to other recipients. The report BAW-2070 states that the Midland beltline weld received 22 h and 36 min at 1125 ± 25°F (607 ± 14°C) as a postweld heat treatment (PWHT) while the nozzle course weld received 25 h and 31 min at the same temperature. That report also provides the B&W "Record of Filler Wire Qualification Test," which shows the qualification weld was postweld heat treated at 1100 to 1150°F (593 to 621°C) for 48 h. The room-temperature tensile test results of the qualification weld give room-temperature yield strength as 69.0 ksi (475 MPa) and ultimate strength as 85.5 ksi (589 MPa).



1. Sampling layout for Midland beltline sections 1-8 through 1-15 and nozzle course sections 3-1 through 3-5.



2. Macrograph showing locations through the thickness of Midland weld section 1-13 from which Charpy impact and drop-weight specimens were machined.



3. Macrograph of Midland nozzle course weld section 3-1; weld WF-67 comprises approximately the inner half of the weld thickness while WF-70 comprises approximately the outer half.

TENSILE PROPERTIES

Tensile property determinations were made at temperatures ranging from –100 to 288°C (–150 to 550°F). The trend of reduced strength with increased test temperature is clearly evident in Table 1. It also appears that the strength of the nozzle weld is significantly higher than that of the beltline weld. This appeared to have developed despite nominally identical chemistries and the fact that both were given about the same PWHT. Increased strength is usually accompanied by reduced fracture toughness but, as will be shown below, this was not detected in the CVN upper-shelf energies nor in the nil-ductility (NDT) or RT_{NDT} transition temperatures. To compare with the measured tensile values, an automated ball indentation (ABI) test was performed on blocks of the two weld metals.[3] These blocks were appropriately prepared for the ABI test by surface grinding parallel surfaces. These results are also reported in Table 1 at room temperature. The ABI tests of the beltline and nozzle course welds produced reasonably good agreement with the conventionally determined yield strength values.

DROP-WEIGHT TESTS

Figure 2 shows the locations through the thickness of beltline section 1-13 where material was removed for machining of Charpy and drop-weight specimens. The intent was that one set of drop-weight specimens would be used for RT_{NDT} determinations for locations 1 and 2 (about 1/4t) while the second set would apply to locations 3 and 4 (about 3/4t). Similar removal plans were used for the other three beltline sections and the WF-70 portion of the nozzle course weld. Type P-3 drop-weight specimens were fabricated using a single weld pass and tested according to American Society for Testing and Materials (ASTM) E 208-87, "Standard Test Method for Conducting Drop-Weight Test to Determine Nil-Ductility Transition Temperature of Ferritic Steels."[4] The NDT temperatures range from –60 to –45°C (–76 to –49°F) in the beltline weld and from –55 to –40°C (–67 to –40°F) in the nozzle course weld. No clear pattern is evident correlating NDT temperatures with position in the weld thickness.

CVN IMPACT TESTS

CVN impact tests were conducted at various temperatures to obtain a full curve of absorbed energy and lateral expansion versus test temperature. Tests were conducted in general accordance with ASTM E 23-91, "Standard Test Method for Notched Bar Impact Testing of Metallic Materials," and ASTM E 184-79, "Standard Practice for Effects of High-Energy Neutron Irradiation on the Mechanical Properties of Metallic Materials, E 706 (IB)."[5,6] The primary emphases were on determination of the RT_{NDT} and the upper-shelf energy. Additionally, fracture appearance was determined for all specimens. All specimens were machined in the TL orientation

Table 1. Tensile properties of Midland WF-70 weld metal

Temperature (°C) (°F)	Strength (MPa) (ksi)	
	Yield	Ultimate tensile
Nozzle		
−100 (−148)	648 (94)	820 (119)
−75 (−103)	620 (90)	765 (111)
−50 (−58)	579 (84)	717 (104)
23 (73)	545 (79)	655 (95)
23 (73)	538 (78)[a]	
160 (320)	483 (70)	586 (85)
288 (550)	483 (70)	586 (85)
Beltline		
−100 (−148)	548 (80)	758 (110)
−75 (−103)	483 (70)	710 (103)
−50 (−58)	465 (67)	682 (99)
23 (73)	407 (59)	586 (85)
	441 (64)[a]	
288 (550)	427 (62)	558 (81)

[a]Automated ball indentation method.

(specimen major axis across the weld and crack propagation in the direction of welding). Initial CVN tests were conducted after the NDT temperatures had been determined according to E 208-87 so that tests could be performed at NDT + 60°F (33°C) as required by the American Society of Mechanical Engineers (ASME) Code Sect. III (ref. 7) for determination of the RT_{NDT}. In all cases examined, tests at NDT + 60°F (33°C) did not meet the minimum requirements for the RT_{NDT} to equal the NDT. Thus, the RT_{NDT} is higher than the NDT in every case and, for this material, is controlled by the CVN behavior.

CVN Test Results

The absorbed energy versus test temperature was determined as a function of position through the wall for each of the sections of beltline weld obtained. Section 1-13 was examined first. Within region 2 of section 1-13, it was apparent from the data that specimens from the two layers of that region gave consistently different results; thus, the data were examined as a combined set for region 2 as well as for the two layers designated D and E. Using mean hyperbolic tangent curve fits, various transition temperatures and upper-shelf energies were determined for each region. Table 2 provides a summary example of transition temperatures and upper-shelf energies as well as RT_{NDT}s obtained for section 1-13. Similar results were obtained for all other sections of beltline and nozzle weld sections at nominally the same through-thickness locations as well as the 7/8t position. The upper-shelf energies vary from 90 to 108 J (66-80 ft-lb). In paragraph NB-2331, Section III, the ASME Code states:

> "When a C_V test has not been performed at T_{NDT} + 60°F, or when the C_V test at T_{NDT} + 60°F does not exhibit a minimum of 50 ft-lb and 35 mils lateral expansion, a temperature representing a minimum of 50 ft-lb and 35 mils lateral expansion may be obtained from a full C_V impact curve developed from the minimum data points of all the C_V tests performed."

In every case, the 50-ft-lb (68-J) temperature was higher than the 0.035-in. (0.89-mm) lateral expansion temperature; thus, the 50-ft-lb (68-J) temperature controlled the determination of the RT_{NDT}. The precise procedure intended by the ASME Code is vague since it does not define the details of the curve-fitting procedure. The paragraph does not say to develop a curve which bounds all the data obtained, but it does say to develop a full C_V impact curve, presumably meaning one from brittle-to-ductile fracture. This will be discussed in more detail later. For this study, a procedure was adopted in which values of RT_{NDT} were determined by identifying the data points with the lowest energy value at each test temperature and fitting a hyperbolic tangent curve to those minimum data. The 50-ft-lb (68-J) temperature was determined from that curve, and the RT_{NDT} was then calculated by subtracting 60°F (33°C) from the 50-ft-lb (68-J) temperature. For comparison, RT_M values

Table 2. Summary of Charpy impact results for Midland reactor beltline weld section 1-13

Location	Charpy transition temperature °C (°F)						Upper-Shelf Energy	RT_M,[a]	RT_{NDT},[b]	RT_{LB},[c]
	Energy, J (ft-lb)			Expansion mm (in.)		Shear	J (ft-lb)	°C (°F)	°C (°F)	°C (°F)
	27 (20)	41 (30)	68 (50)	.38(.015)	.89(.035)	50%				
1/4 t	-30 (-22)	-11 (12)	-21 (69)	-40 (-39)	2 (36)	-9 (15)	101 (75)	-13 (9)	-10 (15)	-11 (12)
1/2 t	-43 (-45)	-16 (4)	29 (84)	-48 (-54)	7 (45)	12 (54)	104 (77)	-5 (24)	2 (36)	17 (63)
1/2 t"D"	-41 (-42)	-25 (-12)	3 (37)	-45 (-49)	-9 (15)	4 (40)	104 (77)	-31 (-23)	-31 (-23)	-28 (-18)
1/2 t"E"	-23 (-10)	2 (36)	47 (116)	-24 (-11)	24 (75)	19 (66)	98 (72)	13 (55)	20 (68)	15 (59)
5/8 t	-41 (-42)	-22 (-7)	9 (48)	-64 (-83)	-13 (8)	-4 (24)	108 (80)	-25 (-12)	-20 (-3)	-16 (3)
3/4 t	-23 (-10)	-3 (28)	37 (98)	-39 (-37)	9 (48)	2 (36)	90 (66)	3 (38)	6 (43)	12 (54)

NOTE: All temperatures have been rounded to the nearest degree.

[a] Determined from T_{50}-60°F (T_{68}-33°C) using average curve fit, where T_{50} is the temperature corresponding to 50 ft-lb.

[b] Determined from T_{50}-60°F (T_{68}-33°C) using minimum curve fit, where T_{50} is the temperature corresponding to 50 ft-lb.

[c] Determined from T_{50}-60°F (T_{68}-33°C) using lower bound curve fit, where T_{50} is the temperature corresponding to 50 ft-lb.

(similar to RT_{NDT} but not determined from the minimum data curve according to ASME Code) were determined by subtracting 60°F (33°C) from the 50-ft-lb (68-J) temperature defined by the mean hyperbolic tangent curve fits. Also, for comparison, absolute lower-bound curves were manually constructed for each individual data set and "lower-bound" reference temperatures (RT_{LB}) were determined in the same manner used for the RT_{NDT} and RT_M.

Figure 4 shows an example of these procedures applied to the tests of section 1-13 at the 1/2t location (confidence bounds will be discussed later). The reference temperature analysis shows that the RT_{NDT} is about 7°C (12°F) higher than the RT_M. The RT_{LB} is about 15°C (27°F) higher than the RT_{NDT}. For beltline weld section 1-13, the RT_{NDT}s vary from -31°C to 20°C (-24 to 68°F) using the minimum data curve fits [the -31°C value is from the "D" position at the 1/2t location, while the combined curve for the 1/2t location shows an RT_{NDT} value of 2°C (36°F)]. That compares to the drop-weight NDT temperatures of -45 and -60°C (-49 and -67°F). Except for region 2 (combines 2D and 2E) at the 1/2t location, the 41-J (30-ft-lb) temperatures agree with the RT_{NDT}s within 10°C (18°F). As seen in the table, the RT_M values are lower in most cases and range from -31 to 13°C (-24 to 55°F), which is 0 to 7°C (0 to 13°F) lower than the RT_{NDT} values. For comparison, the RT_{LB} values range from about -28 to 17°C (-18 to 63°F). The difference between these values will depend, of course, on the number of tests and the scatter exhibited by each data set, and this will also be discussed later.

Tables 3 and 4 provide overall summaries of the Charpy energy, RT_{NDT}, and RT_M results for the beltline and nozzle course sections, respectively. For all the various locations through the thickness of the beltline weld, the RT_{NDT} values range from -20 to 37°C (-3 to 99°F), while the RT_M values range from -25 to 24°C (-12 to 76°F) and the RT_{LB} values range from -21 to 35°C (-6 to 95°F). For all the individual CVN curves obtained from the nozzle course weld, the RT_{NDT} and RT_M values range from -8 to 18°C (18 to 65°F), while the RT_{LB} values range from -6 to 29°C (21 to 84°F). The maximum difference between RT_M and RT_{NDT} for any one case is 22°C (40°F). A comparison of RT_{NDT} and RT_{LB} values shows that RT_{LB} is 21°C (38°F) greater than RT_{NDT} in one case and 8°C (14°F) less than RT_{NDT} in another case.

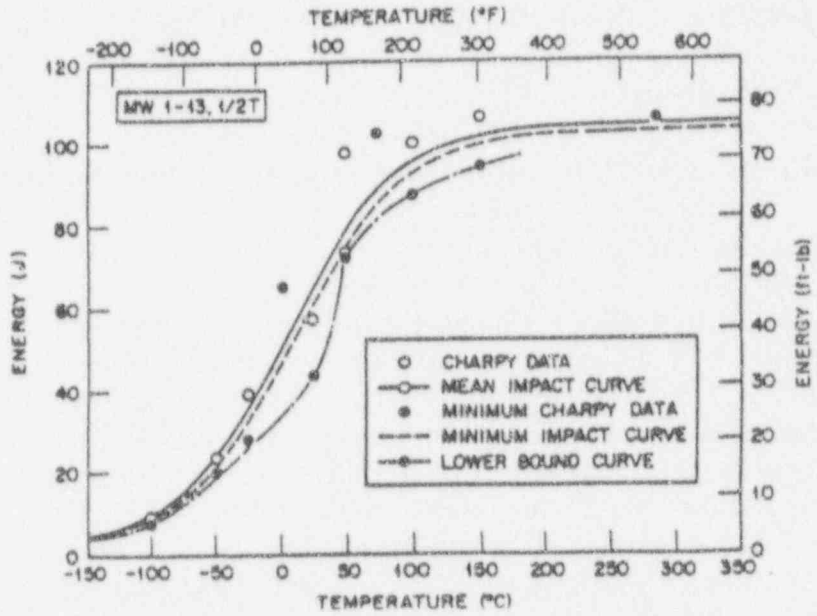
The 41-J temperatures ranged from -22 to 14°C (-7 to 57°F) for the four beltline sections and from -11 to 5°C (13 to 42°F) for the two nozzle course sections. The upper-shelf energies ranged from 77 to 108 J (57 to 80 ft-lb) for the beltline sections and from 85 to 90 J (63 to 66 ft-lb) for the nozzle course sections. Thus, for both the transition temperatures and upper-shelf energies, the nozzle course weld results fall within the scatter bands exhibited by the beltline welds. A mean hyperbolic tangent fit to the entire combined data set reveals 41 and 68-J temperatures of about -8°C (17°F) and 31°C (87°F), respectively. Similarly, the mean 0.89-mm (0.035-in.) lateral

expansion temperature is about 5°C (41°F). The mean lateral expansion at the 68-J (30 ft-lb) temperature is about 1.2 mm (0.043 in.), which supports the earlier observation that the absorbed energy results controlled the RT_{NDT} determinations for this material. At the average NDT temperature of -50°C (-58°F), the mean energy is about 16 J (12 ft-lb), while the mean lateral expansion is about 0.31 mm (0.012 in.).

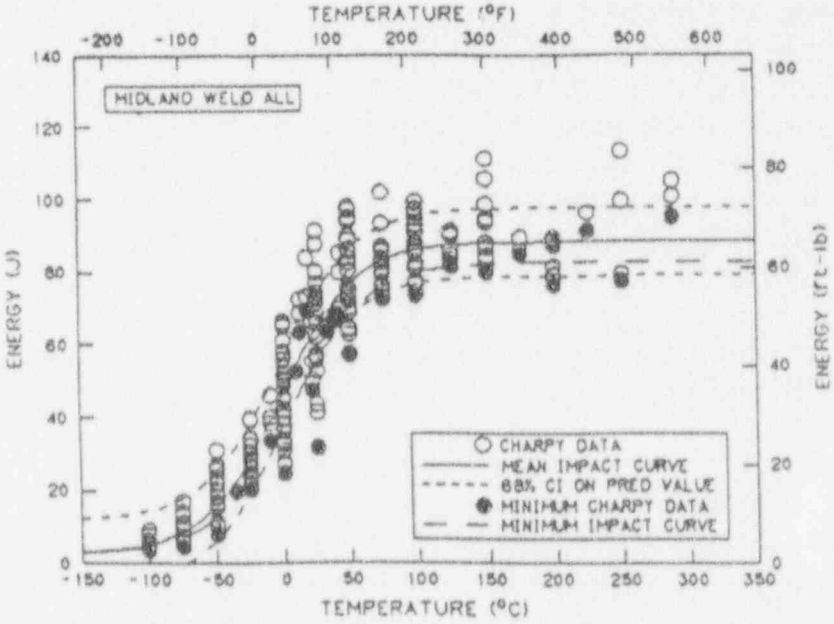
Statistical Analyses of CVN Test Results

The Charpy impact results were also statistically analyzed to determine confidence intervals for the individual data sets and for combined data sets, including each section, each thickness location, all beltline tests, all nozzle course tests, and all tests. The confidence interval on the mean represents the confidence that the true mean value of energy at a given temperature lies between the bounds. The confidence interval on the predicted value represents the confidence that another observation will lie between the bounds. The hyperbolic tangent curve fit and confidence bounds were determined using nonlinear regression analysis. Figures 5 and 6 are plots of Charpy impact energy versus test temperature for all the tests performed (279 individual Charpy impact tests) and show the mean hyperbolic tangent curve fits with 68 and 95% upper and lower confidence bounds on the predicted values, representing approximately 1 and 2 standard deviations on energy, respectively. As shown, the mean 41-J temperature is –8°C (17°F) with 68% confidence bounds from –21 to 4°C (–6 to 39°F) and 95% bounds from –36 to 17°C (–32 to 62°F). On the upper shelf, the overall mean energy is 88 J (65 ft-lb) with variations of about ±9 J (±7 ft-lb) for the 68% level and about ±18 J (±13 ft-lb) for the 95% level. Figure 7 shows a comparison of the 95% confidence bounds on the mean and on the predicted value for the same data set; at the 41-J (30-ft-lb) level, the 95% confidence intervals are about 5°C (9°F) wide on the mean and about 53°C (94°F) wide on the predicted value. Although the scatter is large, the mean value is known with high confidence because the data set is large. On the other hand, Fig. 8 shows a smaller data set. At the 41-J level, the 95% confidence intervals are about 55°C (98°F) wide on the mean and about 130°C (234°F) wide on the predicted value. The confidence intervals for a small data set will, of course, be affected by the goodness of fit to the data as well as by the number of observations. Further reference to confidence bounds will refer to those on the predicted value unless confidence bounds on the mean are specifically noted.

To provide adequate data to establish a lower shelf value for all data sets, five CVN tests were conducted at liquid nitrogen temperature, –196°C (–320°F). The tests resulted in averages of 2.7 J (1.9 ft-lb), 0.061-mm (0.0024-in.) lateral expansion, and 0% ductile fracture. All hyperbolic tangent analyses were performed with the lower-shelf values fixed at the values given above. The upper-shelf value for the percent shear fits was fixed at 100%.



4. Charpy V-notch impact energy vs test temperature for specimens from the 1/2t location in Midland beltline weld section 1-13. The solid curve represents the mean hyperbolic tangent curve fit to all the data while the dashed curve represents a similar fit using the minimum datum at each test temperature. The third curve represents a lower-bound curve to all the data.



5. Charpy V-notch impact energy vs test temperature for all tests of beltline and nozzle course welds of the Midland reactor vessel; the solid curve represents the mean hyperbolic tangent curve fit while the dashed curves represent upper and lower 68% confidence bounds on the predicted value.

Table 3. Summary of Charpy impact results for Midland Unit 1 reactor vessel beltline weld sections

Through-thickness position	Charpy V-notch tests												RT^{a}_{NDT}, °C (°F), at weld section				RT_{NDT},[b] °C (°F), at weld section			
	41-J temperature, °C (°F), at weld section				68-J temperature, °C (°F), at weld section				Upper-shelf energy, J (ft-lb), at weld section											
	1-13	1-9	1-11	1-15	1-13	1-9	1-11	1-15	1-13	1-9	1-11	1-15	1-13	1-9	1-11	1-15	1-13	1-9	1-11	1-15
1/4t	-11 (12)	-6 (21)	-13 (8)	4 (39)	21 (69)	37 (98)	25 (76)	50 (122)	101 (74)	77 (57)	91 (67)	82 (60)	-9 (15)	3 (37)	-9 (16)	16 (61)	-13 (9)	14 (57)	-9 (16)	16 (61)
1/2t	-16 (3)	-11 (13)	-4 (25)	-9 (15)	29 (84)	25 (77)	23 (74)	17 (63)	104 (77)	83 (61)	91 (67)	88 (65)	-5 (24)	-8 (17)	-10 (14)	-16 (3)	2 (36)	-8 (17)	-10 (14)	-15 (5)
5/8t	-22 (-7)	-18 (0)	-10 (13)	3 (37)	9 (48)	18 (64)	17 (63)	49 (121)	108 (80)	88 (65)	90 (66)	85 (62)	-25 (-12)	-16 (3)	-16 (3)	15 (60)	-20 (-3)	-16 (3)	-16 (3)	8 (47)
3/4t	-2 (27)	3 (38)	14 (57)	-6 (21)	37 (98)	53 (128)	58 (136)	28 (82)	90 (66)	81 (60)	84 (62)	89 (66)	3 (37)	20 (68)	24 (76)	-6 (21)	6 (43)	20 (68)	37 (99)	-6 (22)
7/8t		-3 (26)	-13 (8)	-8 (18)		46 (116)	30 (86)	22 (72)		78 (57)	79 (5%)	83 (61)		13 (55)	-4 (25)	-12 (11)		13 (56)	18 (65)	-3 (26)

[a]Determined from T_{50} - 60°F (T_{41} - 33°C) using average curve fit, where T_{50} is the temperature corresponding to 50 ft-lb.

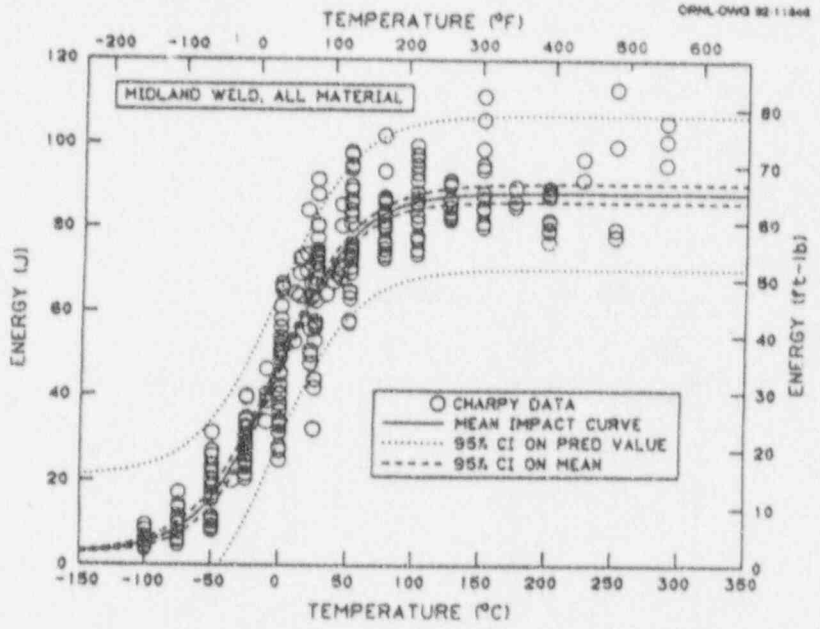
[b]Determined from T_{50} - 60°F (T_{41} - 33°C) using minimum curve fit, where T_{50} is the temperature corresponding to 50 ft-lb.

Table 4. Summary of Charpy impact results for Midland Unit 1 reactor vessel nozzle course weld sections

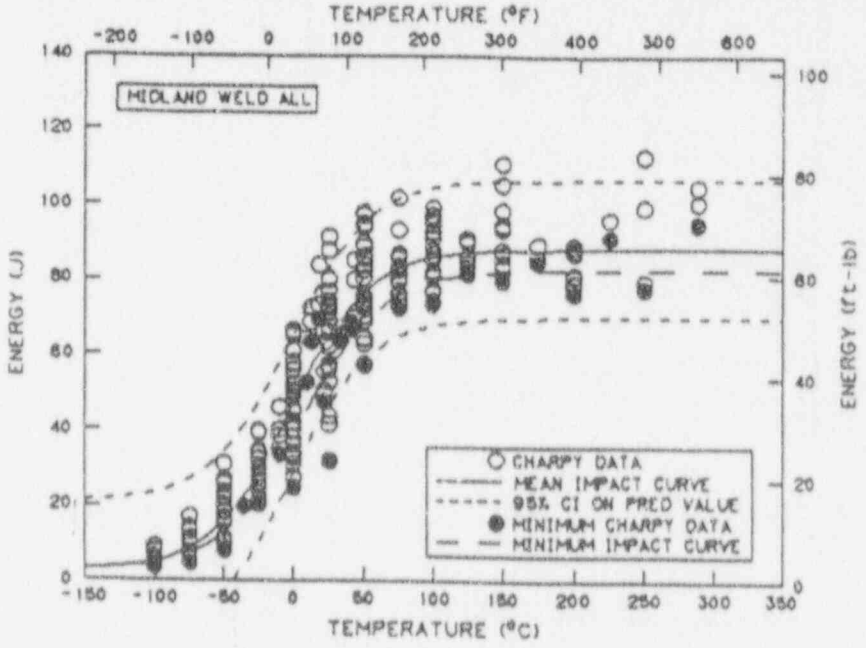
Through-thickness position	Charpy V-notch tests						RT^*_{NDT},[a] °C (°F), at weld section		RT_{NDT},[b] °C (°F), at weld section	
	41-J temperature, °C (°F), at weld section		68-J temperature, °C (°F), at weld section		Upper-shelf energy, J (ft-lb), at weld section					
	3-1	3-4	3-1	3-4	3-1	3-4	3-1	3-4	3-1	3-4
1/2t	5 (42)	-11 (13)	47 (117)	51 (125)	86 (63)	88 (65)	14 (57)	18 (65)	14 (57)	18 (65)
3/4t	2 (35)	-1 (30)	49 (120)	45 (112)	89 (65)	85 (63)	16 (61)	11 (52)	16 (61)	11 (52)
7/8t	-10 (15)	5 (42)	26 (78)	47 (116)	90 (66)	89 (66)	-8 (18)	14 (57)	-8 (18)	14 (57)

[a]Determined from T_{50} - 60°F (T_{68} - 33°C) using average curve fit.

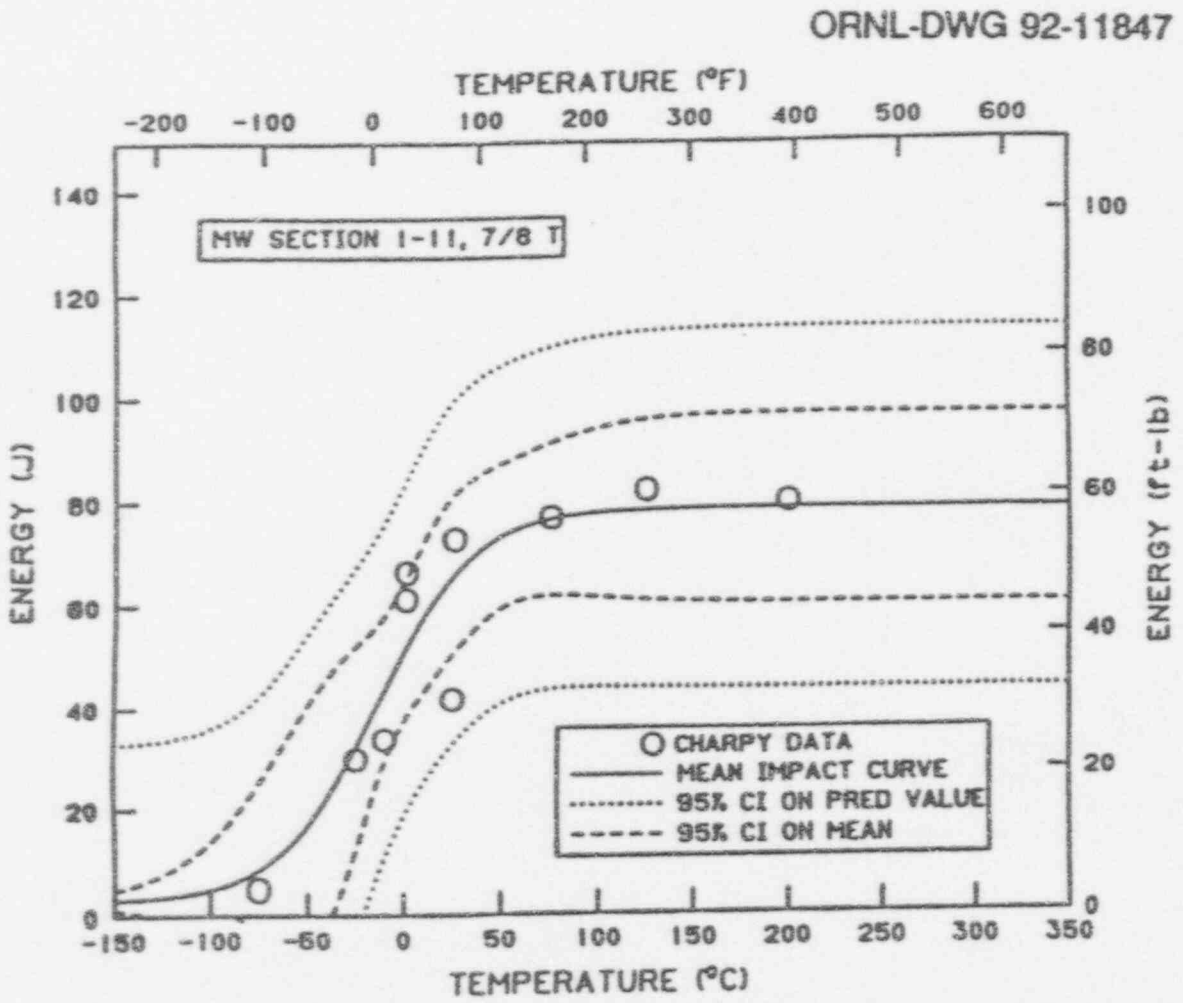
[b]Determined from T_{50} - 60°F (T_{68} - 33°C) using minimum curve fit.



6. Charpy V-notch impact energy vs test temperature for all tests of beltline and nozzle course welds of the Midland reactor vessel; the solid curve represents the mean hyperbolic tangent curve fit while the dashed curves represent upper and lower 95% confidence bounds on the predicted value.



7. Charpy V-notch impact energy vs test temperature for all tests of beltline and nozzle course welds of the Midland reactor vessel. The solid curve represents the mean hyperbolic tangent curve fit while the dashed curves show a comparison of 95% confidence bounds on the mean and on the predicted value.



8. Charpy V-notch impact energy vs test temperature for tests at the 7/8 thickness location in section 1-11 of the Midland reactor vessel beltline weld. The solid curve represents the mean hyperbolic tangent curve fit while the dashed curves show a comparison of the 95% confidence bounds on the mean and on the predicted value.

Table 5 provides a comparison of the various Charpy transition temperatures, upper-shelf energies, RT_M, RT_{NDT}, and RT_{LB} values, with 95% confidence bounds, respectively, from the hyperbolic tangent curve fits of the beltline and nozzle course welds with the total combined data set. Examination of Table 5 shows generally good correspondence between the Charpy results of the beltline and nozzle course welds, with the observation that the nozzle course weld mean curve is somewhat more shallow in the transition region (the temperature interval from 41 to 68 J is greater for the nozzle course weld).

A comparison of confidence intervals, 68, 90, 95, and 99%, for the analyses of the total combined data set is given in Table 6. It is interesting to note that the mean 68-J (50 ft-lb) temperature, 31°C (87°F), is about 39°C (70°F) above the mean 41-J (30 ft-lb) temperature, –8°C (17°F), but that the 95% lower confidence bound 68-J temperature is about 84°C (151°F) above the corresponding 41-J temperature. It is also interesting that the RT_{NDT}, 15°C (59°F), is at a lower temperature than even the 68% lower confidence bound for RT_M, 18°C (64°F), and far lower than the 95% lower confidence bound for RT_M, 67°C (153°F).

The variations shown by the 95% confidence bounds are compared in Table 7 to those from welds 72W and 73W tested in the HSSI Fifth Irradiation Series,[8] two high upper-shelf, submerged-arc welds, made using weld wire specially fabricated with copper in the melt, as compared to typical practice of using a copper-coated wire, to help ensure uniformity of chemistry and properties. The 41-J (30 ft-lb) temperature interval of 53°C (94°F) for the Midland weld compares with intervals of 76 and 54°C (136 and 97°F) for welds 72W and 73W, respectively, while the upper-shelf energy bounds are very similar in terms of percent of mean upper-shelf energy.

Figures 9 (*a*) through (*c*) graphically depict the through-thickness variation of the 41-J (30 ft-lb) temperature, upper-shelf energy, and RT_{NDT}, respectively, for the beltline weld sections, while Figs. 10 (*a*) through (*c*) show the same series for the nozzle course weld sections. There does not appear to be a consistent trend of through-thickness behavior in either case.

CHEMICAL COMPOSITION

Bulk Analyses

To obtain a detailed description of the chemical composition of the weld, fracture surfaces were cut off CVN specimens from the various locations and submitted for chemical analyses to Combustion Engineering, Inc. (CE), Chattanooga, Tennessee, or MQS Inspection, Inc., Woodlawn, Ohio. The first section to be analyzed was beltline weld section 1-13, and the results are shown in Table 8. The carbon contents at 2D

Table 5. Summary of mean hyperbolic tangent curve fits and 95% confidence bounds on predicted value for Charpy energy. RT_{NDT}, and RT_M results for the beltline and nozzle course welds and for the combined data set

Section	Charpy transition temperature °C (°F) for given energy									Upper-shelf energy			RT_M,[a]			RT_{NDT},[b]	RT_{LB},[c]
	27 J (20 ft-lb)			41 J (30 ft-lb)			68 J (50 ft-lb)			J (ft-lb)			°C (°F)			°C (°F)	°C (°F)
	-95%	Model	95%	-95%	Model	95%	-95%	Model	95%	-95%	Model	95%	-95%	Model	95%	Min	Low
Beltline	-77	-29	-3	-37	-9	15	1	28	100	70	89	108	-33	-6	67	15	35
	(-107)	(-20)	(27)	(-35)	(15)	(60)	(33)	(82)	(213)	(51)	(66)	(80)	(-27)	(21)	(153)	(58)	(95)
Nozzle	-53	-25	-4	-21	-1	18	22	44	81	75	88	100	-11	11	47	25	29
	(-64)	(-12)	(24)	(-6)	(30)	(64)	(71)	(112)	(177)	(55)	(65)	(74)	(12)	(52)	(117)	(76)	(84)
All	-75	-28	-2	-36	-8	17	3	31	101	70	89	107	-30	-3	67	15	35
	(-103)	(-19)	(28)	(-32)	(17)	(62)	(38)	(87)	(213)	(52)	(65)	(79)	(-22)	(27)	(153)	(59)	(95)

NOTE: All temperatures have been rounded to the nearest degree.

[a] Determined from T_{50}-60°F (T_{68}-33°C) using average curve fit, where $T_{5(}$ is the temperature corresponding to 50 ft-lb.

[b] Determined from T_{50}-60°F (T_{68}-33°C) using minimum curve fit, where $T_{5(}$ is the temperature corresponding to 50 ft-lb.

[c] Determined from T_{50}-60°F (T_{68}-33°C) using lower bound curve fit, where $T_{50}$is the temperature corresponding to 50 ft-lb.

Table 6. Summary of mean hyperbolic tangent curve fits and various confidence bounds on predicted value for Charpy energy, RT_{NDT}, and RT_M results for the combined beltline and nozzle course welds

Section	Charpy transition temperature °C (°F) for given energy									Upper-shelf energy			RT_M,[a]			RT_{NDT},[b]	RT_{LB},[c]
	27 J (20 ft-lb)			41 J (30 ft-lb)			68 J (50 ft-lb)			J (ft-lb)			°C (°F)			°C (°F)	°C (°F)
	-95%	Model	95%	-95%	Model	95%	-95%	Model	95%	-95%	Model	95%	-95%	Model	95%	Min	Low
Beltline	-77	-29	-3	-37	-9	15	1	28	100	70	89	108	-33	-6	67	15	35
	(-107)	(-20)	(27)	(-35)	(15)	(60)	(33)	(82)	(213)	(51)	(66)	(80)	(-27)	(21)	(153)	(58)	(95)
Nozzle	-53	-25	-4	-21	-1	18	22	44	81	75	88	100	-11	11	47	25	29
	(-64)	(-12)	(24)	(-6)	(30)	(64)	(71)	(112)	(177)	(55)	(65)	(74)	(11)	(52)	(117)	(76)	(84)
All	-75	-28	-2	-36	-8	17	3	31	101	70	89	107	-30	-3	67	15	35
	(-103)	(-19)	(28)	(-32)	(17)	(62)	(38)	(87)	(213)	(52)	(65)	(79)	(-22)	(27)	(153)	(59)	(95)

NOTE: All temperatures have been rounded to the nearest degree.

[a] Determined from T_{50}-60°F (T_{68}-33°C) using average curve fit, where T_{5t} is the temperature corresponding to 50 ft-lb.

[b] Determined from T_{50}-60°F (T_{68}-33°C) using minimum curve fit, where T_{5t} is the temperature corresponding to 50 ft-lb.

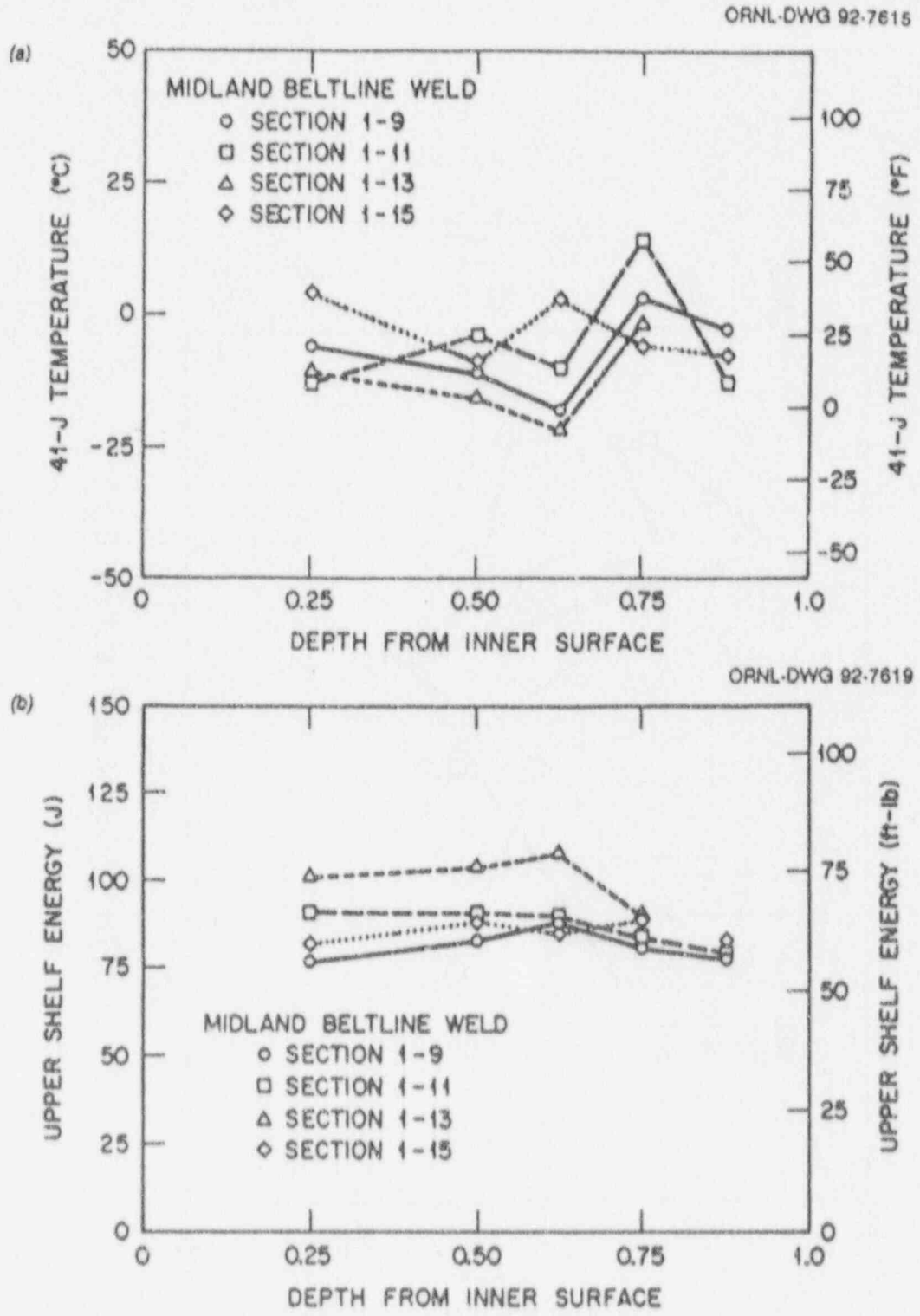
[c] Determined from T_{50}-60°F (T_{68}-33°C) using lower bound curve fit, where T_{50} is the temperature corresponding to 50 ft-lb.

Table 7. Comparison of mean hyperbolic tangent curve fits and 95% confidence bounds on predicted value for combined Midland beltline and nozzle course welds (MW) with welds 72W and 73W from HSSI Fifth Irradiation Series

Section	Charpy transition temperature °C (°F) for given energy									Upper-shelf energy			RT_M,[a]			RT_{NDT},[b]
	27 J (20 ft-lb)			41 J (30 ft-lb)			68 J (50 ft-lb)			J (ft-lb)			°C (°F)			°C (°F)
	-95%	Model	95%	-95%	Model	95%	-95%	Model	95%	-95%	Model	95%	-95%	Model	95%	Min
MW	-75	-28	-2	-36	-8	17	3	31	101	70	89	107	-30	-2	67	15
	(-103)	(-19)	(28)	(-32)	(17)	(62)	(38)	(87)	(213)	(52)	(65)	(79)	(-22)	(28)	(153)	(59)
72W	Undefined	-43	-13	-78	-28	-2	-32	-6	21	105	136	168	-66	-39	-13	-32
	Undefined	(-46)	(8)	(-108)	(-18)	(28)	(-26)	(22)	(69)	(78)	(101)	(124)	(-86)	(-38)	(9)	(-25)
73W	Undefined	-54	-30	-73	-39	-19	-38	-17	3	109	135	160	-71	-51	-30	-48
	Undefined	(-66)	(-21)	(-99)	(-39)	(-2)	(-36)	(1)	(38)	(81)	(99)	(118)	(-96)	(-59)	(-22)	(-54)

[a] Determined from T_{50}-60°F (T_{68}-33°C) using average curve fit, where $T_{5(}$ is the temperature corresponding to 50 ft-lb.

[b] Determined from T_{50}-60°F (T_{68}-33°C) using minimum curve fit, where $T_{5(}$ is the temperature corresponding to 50 ft-lb.



9. Plots of through-thickness Charpy impact results for the Midland beltline weld sections. (a) 41-J temperature. (b) Upper-shelf energy. (c) RT_{NDT}.

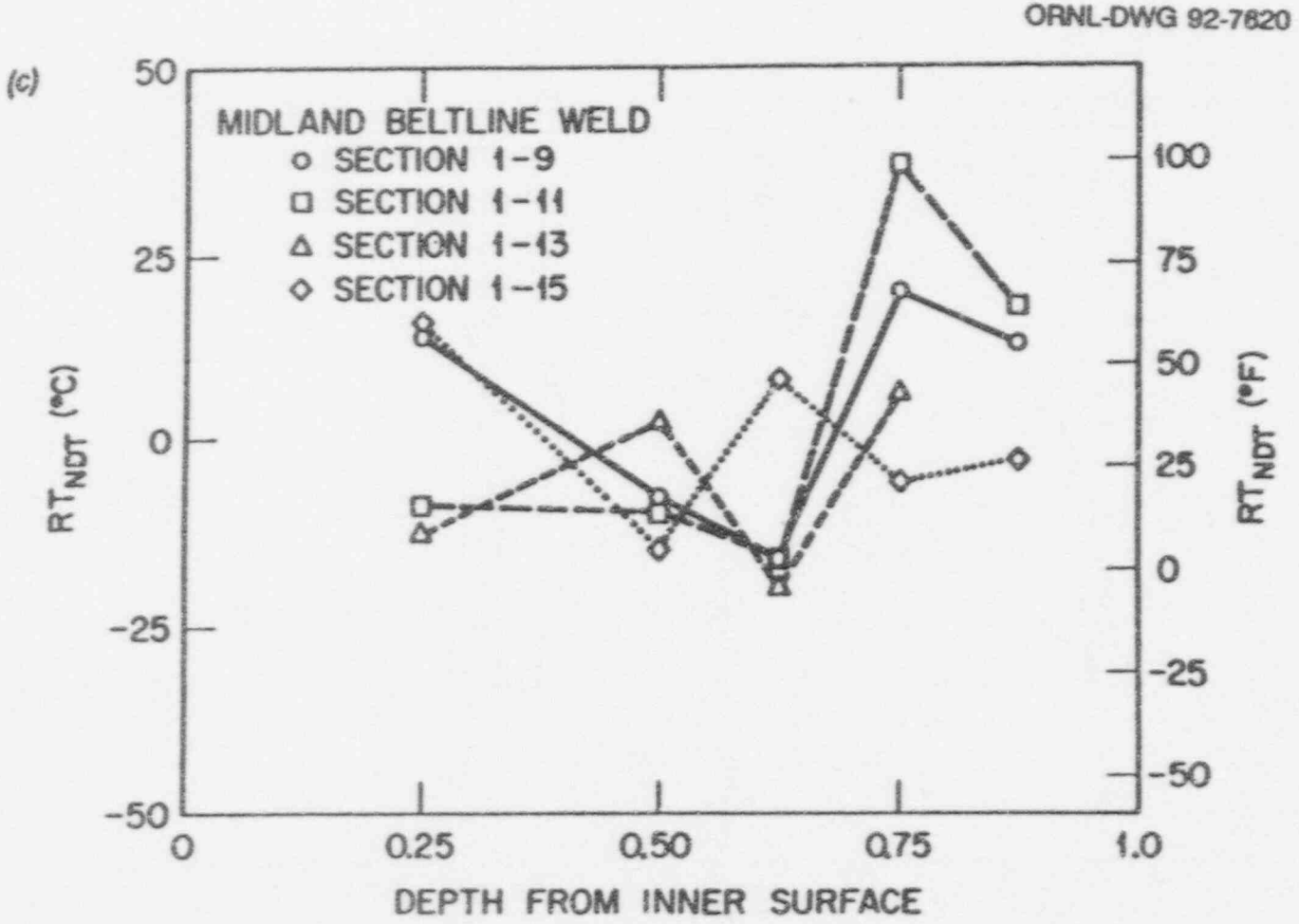
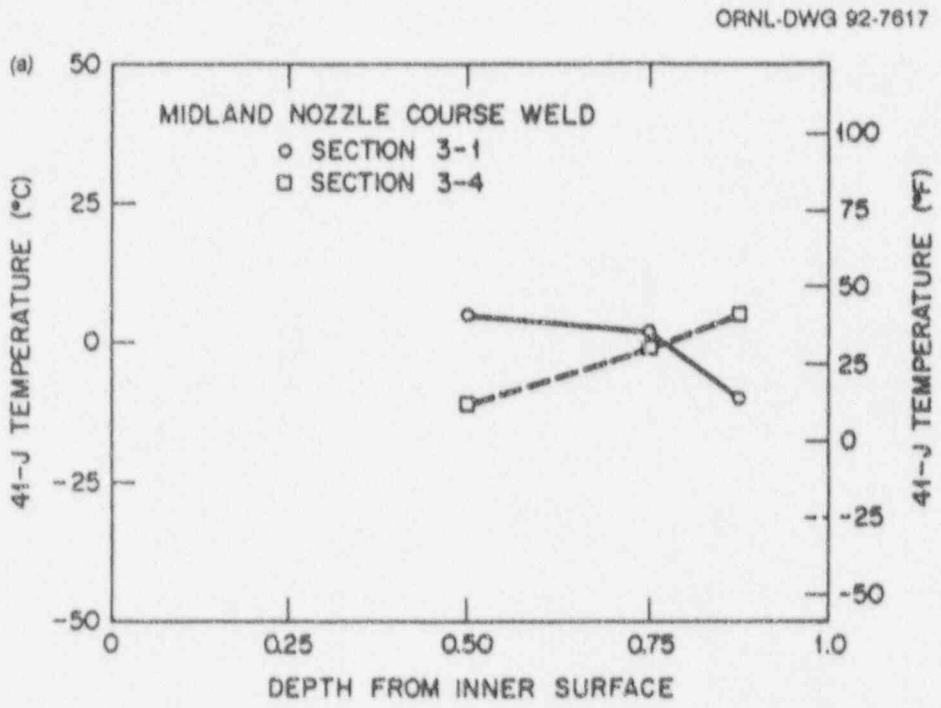
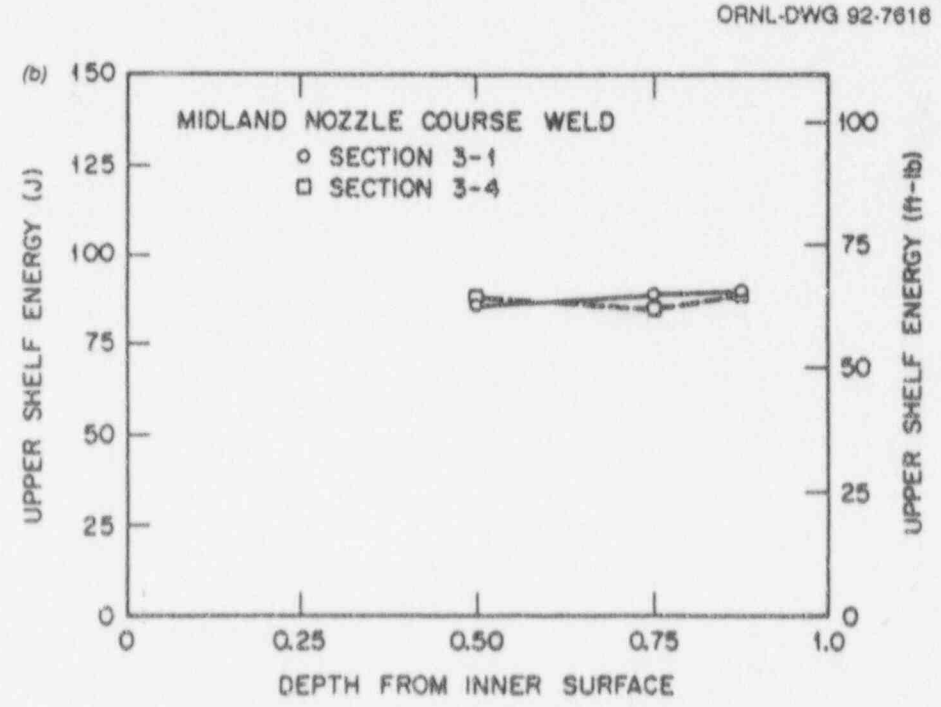


Figure 9 (continued).





10. Plots of through-thickness Charpy impact results for the Midland nozzle course weld sections. (a) 41-J temperature. (b) Upper-shelf energy. (c) RT_{NDT}.

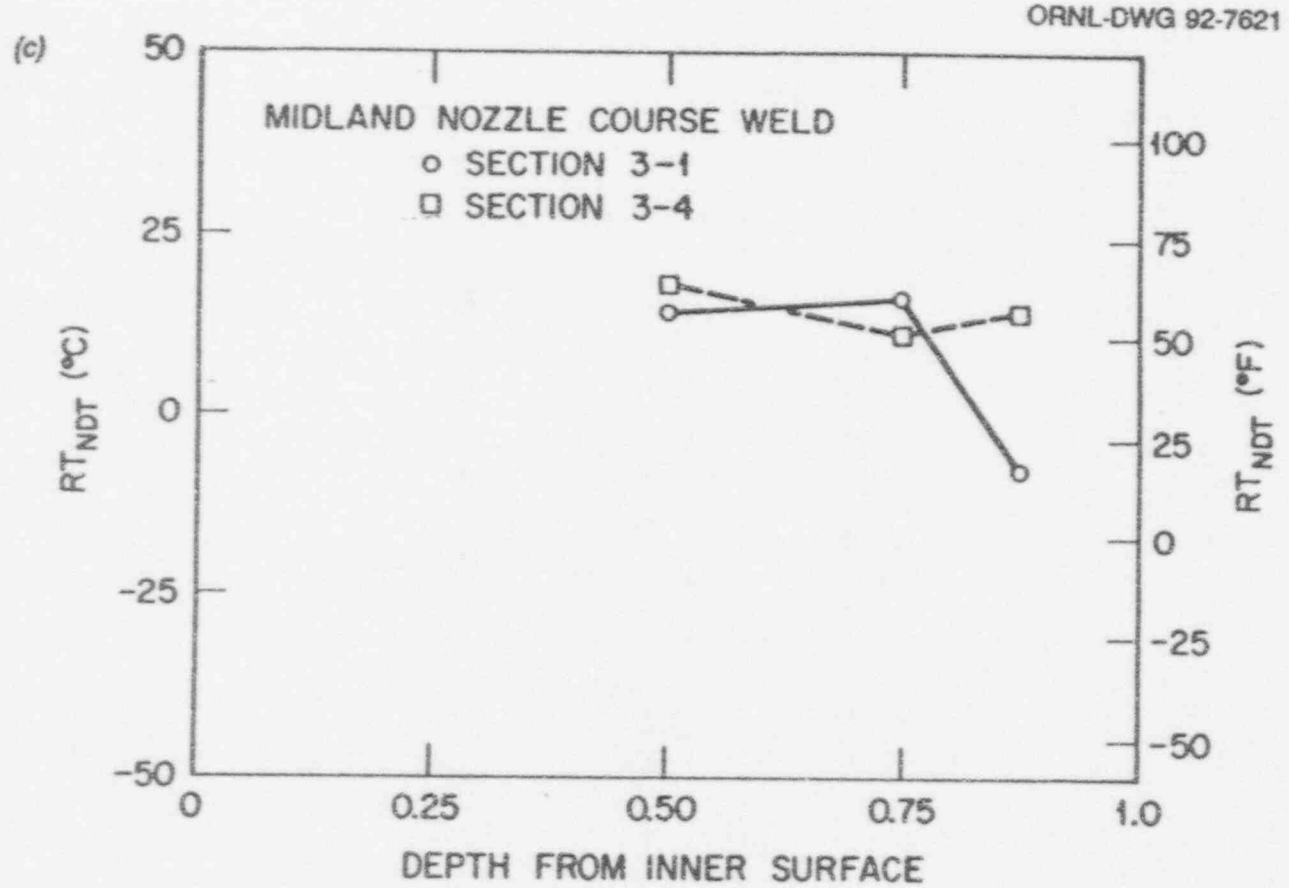


Figure 10 (continued).

Table 8. Chemical composition of Midland reactor weld section 1-13

Set	Chemical composition (wt %)																			
	C	Mn	P	S	Si	Cr	Ni	Mo	Cu	V	Nb	Ti	Co	Al	B	W	Sb	As	Sn	Zr	N
1	0.074	1.60	0.015	0.008	0.58	0.11	0.58	0.40	0.24	0.005	0.002	<0.001	0.015	0.020	<0.001	<0.01	-	0.003	0.003	<0.001	0.017
2D	0.11	1.45	0.018	0.008	0.65	0.14	0.61	0.42	0.21	0.005	0.003	<0.001	0.015	0.008	<0.001	<0.01	-	0.007	0.004	<0.001	0.016
2E	0.11	1.49	0.016	0.008	0.57	0.14	0.63	0.43	0.22	0.005	0.003	<0.001	0.014	0.013	<0.001	<0.01	-	0.007	0.004	<0.001	0.015
3	0.075	1.60	0.018	0.009	0.65	0.11	0.60	0.41	0.25	0.005	0.003	<0.001	0.015	0.017	<0.001	<0.01	-	0.006	0.004	<0.001	0.019
4	0.079	1.51	0.022	0.010	0.67	0.11	0.60	0.41	0.32	0.005	0.003	<0.001	0.016	0.015	<0.001	<0.01	-	0.007	0.004	<0.001	0.018
WQ[a]	0.070	1.60	0.014	0.011	0.48		0.46	0.40	0.27												
BW[b]	0.09	1.63	0.018	0.009	0.54	0.11	0.59	0.40	0.42												

[a]From B&W weld wire qualification report.

[b]From BAW-1799 giving extensive chemical analyses.

and 2E are higher than for the other locations. Those locations are in the root region of the weld where manual metal-arc welding (MMA) was performed prior to grinding and SAW. The MMA electrodes have lower carbon content than the wire used for the SAW welds, and the higher carbon contents at those locations are likely the result of carbon pickup from the higher carbon base metal. The other major alloying elements are present in typical amounts and are fairly consistent through the weld thickness.

The copper contents in section 1-13 range from 0.21 to 0.32 wt % (mean value of 0.25 wt %). Those values are substantially lower than those reported by B&W in BAW-1799 for WF-70 (ref. 9). They are, however, consistent with the copper content reported in the weld wire qualification record, 0.27 wt %. Both of those B&W reported analyses for WF-70 are shown in Table 8 for comparison. Because the copper contents obtained for section 1-13 in this study were relatively low, CE was asked to recheck them. Their recheck procedure incorporated two different measurement techniques, optical emission spectrometry, and X-ray fluorescence, as well as measurements on five different National Institute of Standards and Technology standards. The recheck analyses validated the original copper determinations.

Subsequent analyses of the other three beltline weld sections confirmed the relatively low mean copper contents in the beltline region, while analyses of the two nozzle course sections confirmed the higher copper contents reported by B&W. The B&W analyses were conducted with material removed from nozzle course dropouts, so their analyses represented the nozzle course weld. Table 9 gives a summary of the analyses for the beltline and nozzle welds. Table 9 shows that the copper content ranges from 0.21 to 0.34% in the beltline weld and from 0.37 to 0.46% in the nozzle course weld. The results shown are all in good agreement with those reported by Moore, Heller, and Lowe[10] for a WF-70 nozzle belt drop-out, except that the copper content in the beltline weld is substantially less than their value of 0.42%. Except for section 1-15, Fig. 11(*a*) shows a weak trend of increasing copper content through the thickness of the beltline weld. Figure 11 (*b*) shows the disparity in copper contents between welds WF-67 and WF-70 in the nozzle course weld, but the through-thickness trend in the WF-70 portion is relatively constant in spite of the fairly wide range shown by the individual measurements.

Electron Microprobe Analyses

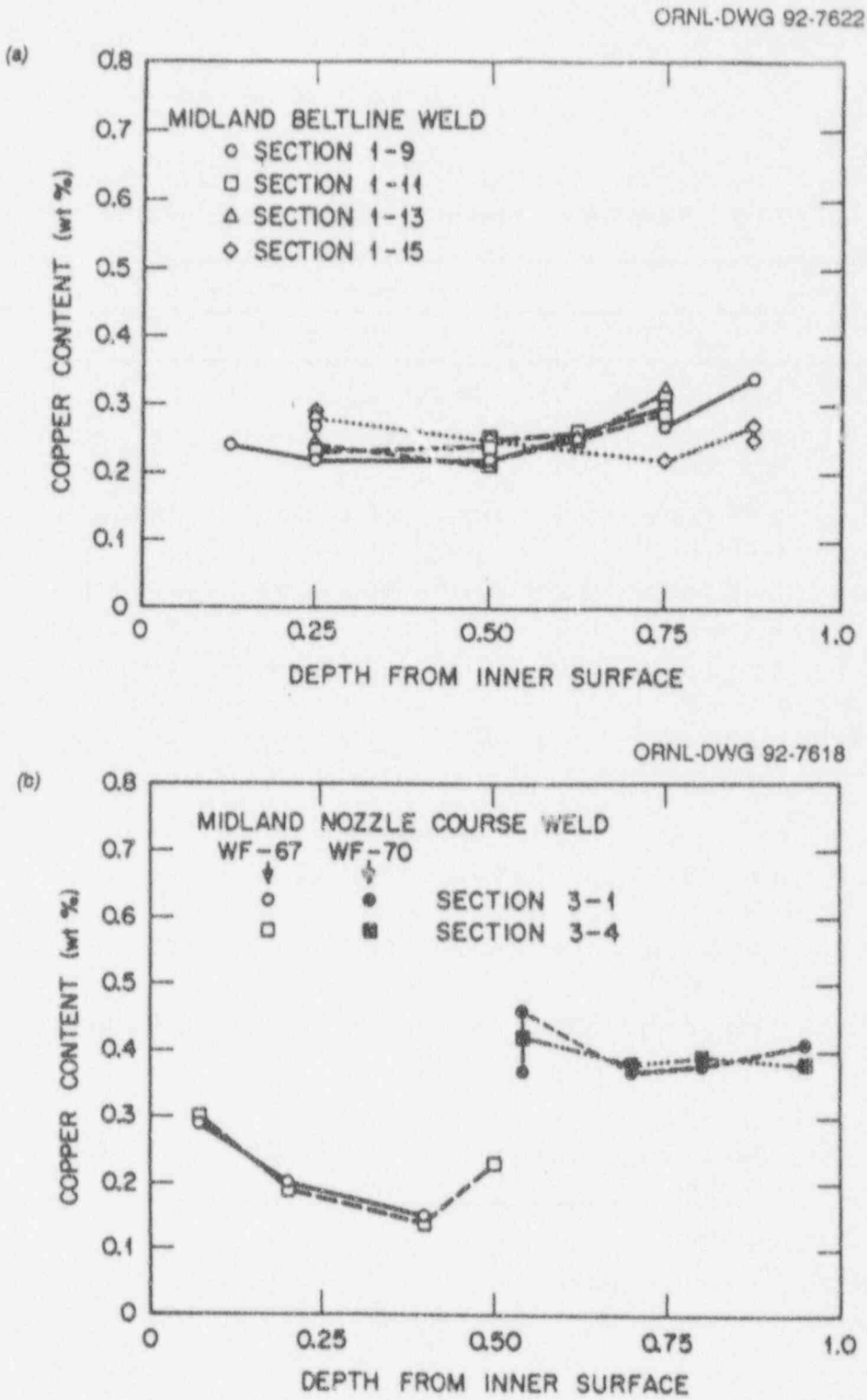
Electron microprobe analyses were conducted to examine elemental variation across the width of the weld. The beltline weld was examined at the 1/4t and 1/2t locations, while the nozzle course weld was examined at the 3/4t location. A 10-μm spot was used at 200-μm intervals across the weld; thus, nearly 100 measurements were made in each case. In the beltline weld, at the 1/4t location, 88 measurements

Table 9. Summary of major radiation sensitive elements for Midland Unit 1 reactor vessel welds

Section number	n[a]	Element, wt % ± 1σ				
		Cu[b]	Ni	P	Mn	Si
			Beltline weld			
1-9	8	0.26 ± 0.041 (0.22-0.34)	0.566 ± 0.031	0.016 ± 0.0013	1.629 ± 0.050	0.605 ± 0.031
1-11	8	0.258 ± 0.027 (0.23-0.31)	0.57 ± 0.007	0.016 ± 0.0014	1.615 ± 0.015	0.62 ± 0.029
1-13	5	0.248 ± 0.039 (0.21-0.32)	0.604 ± 0.016	0.018 ± 0.002	1.55 ± 0.067	0.62 ± 0.041
1-15	7	0.254 ± 0.026 (0.22-0.29)	0.567 ± 0.009	0.018 ± 0.0013	1.614 ± 0.014	0.644 ± 0.016
Average	28	0.256 ± 0.034 (0.21-0.34)	0.574 ± 0.023	0.017 ± 0.0019	1.607 ± 0.049	0.622 ± 0.033
			Nozzle course weld			
3-1	4	0.398 ± 0.034 (0.37-0.46)	0.576 ± 0.021	0.015 ± 0.001	1.59 ± 0.045	0.548 ± 0.051
3-4	5	0.392 ± 0.016 (0.38-0.42)	0.567 ± 0.008	0.015 ± 0.002	1.61 ± 0.018	0.55 ± 0.043
Average	9	0.396 ± 0.028 (0.37-0.46)	0.572 ± 0.017	0.015 ± 0.002	1.59 ± 0.037	0.55 ± 0.048
Total average	37	0.290 ± 0.068 (0.21-0.46)	0.574 ± 0.022	0.016 ± 0.002	1.604 ± 0.046	0.605 ± 0.048

[a]Number of measurements.

[b]Range of copper shown in parentheses.



11. Plots of through-thickness copper content for the Midland reactor WF-70 welds. (a) Beltline weld sections. (b) Nozzle course weld sections.

showed a range of copper from 0.09 to 0.40% with a mean copper content of 0.238% and a standard deviation of 0.061%. Similarly, at the 1/2t depth, the mean copper content was 0.243 with similar standard deviation and range of values. The mean values are in good agreement with the bulk analyses given in Table 9 but do emphasize the variation that exists on the microstructural level. For the nozzle course weld, the mean copper level of 0.340 is somewhat below the 0.396% observed with bulk analyses but does confirm the higher copper in the nozzle course weld. In both welds, the nickel contents are in reasonably good agreement with the bulk analyses. The microprobe analyses of P, Mn, and Si are also in reasonably good agreement with those from the bulk analyses.

Atom-Probe Field-Ion Microscopy Analyses

In addition to the optical microscopy, bulk chemical analyses, and microprobe analyses reported above, atom-probe field-ion microscopy (APFIM) analysis of the beltline weld was performed. The APFIM analyses were conducted to characterize the nature of precipitates or clusters, especially those of copper, in the microstructure and to compare the matrix copper content with the bulk content. Similar APFIM analyses will be conducted with the nozzle course welds and with both welds in the post-irradiated condition. No evidence of darkly imaging copper precipitates or clusters were observed in any of the weld samples. Some ultrafine, brightly imaging refractory carbides were observed that were roughly spherical and approximately 1 nm in diameter. Similar ultrafine carbides have been observed in irradiated A 302 grade B steel[11] and irradiated A 533 grade B class 1 steel.[12]

The average composition of the five beltline weld samples (from the regions of section 1-13 identified in Fig. 2) were determined in the ORNL energy-compensated atom probe. The matrix copper ranges from about 0.07 to 0.13 wt % for positions 1, 2, and 3. The reason for a much higher weight percent (0.25 wt %) for position 4 is not known, but additional analyses will be performed. The results indicate that there was generally a substantial depletion in the copper in the matrix over the bulk chemical analysis (which ranged from 0.21 to 0.32 wt %). This behavior has been observed previously in other reactor steels and is due to copper precipitation at grain boundaries and other microstructural features during the PWHT.[12] The Midland reactor vessel beltline weld was given a PWHT at 607°C (1125°F) for about 22.5 h (ref. 6).

The atom-probe composition data were subjected to statistical analysis to determine whether the copper was in random solid solution in the matrix or if clustering had occurred. The results of the significance of the mean separation of the copper atoms in the atom-probe ion-by-ion data chain were analyzed. In this type of analysis, no significance of greater than 2.0 was observed, indicating that no clustering had occurred. No deviation from a random solid solution was detected. The atom-

probe data were also analyzed in terms of the Johnston and Klotz order parameter, and, again, the results indicated no deviation from a random solid solution. Fine copper precipitation occurred during the PWHT at grain boundaries and other microstructural features, substantially depleting the matrix in copper, but copper clustering within the matrix did not develop.

FRACTURE MECHANICS PROPERTIES

Fracture mechanics toughness data were developed for the Midland weld in the unirradiated condition. These data were then used to evaluate a new fracture mechanics-based transition temperature characterization methodology as well as the Eason et al. multivariable model for estimating J-R curves.[13]

Ductile-to-Brittle Transition Behavior

Beltline WF-70 weld metal was tested in the form of compact specimens in sizes ranging from 1/2T to 4T and at test temperatures ranging from −100 to 0°C (−148 to 32°F). The median K_{Jc} values from multiple tests under each condition in the overall test matrix for the beltline and nozzle course are listed in Table 10. The fewer test conditions applied to the nozzle welds are the result of the limited amount of nozzle material available.

The fracture toughness test practice involved cooling of the specimens to the test temperature using vaporized liquid nitrogen. Each specimen was given sufficient soak time at test temperature to ensure thermal stability prior to running of the test, typically 5 min or more. Most tests terminated in K_{Jc}-type cleavage fracture. However, some of the specimens tested in the mid-transition temperature range did not fail by cleavage but, instead, developed slow-stable crack growth. The unloading compliance method was employed in all cases so that crack growth could be measured and J-R curves could be developed in such cases.

Fracture toughness at the onset of cleavage fracture was calculated in terms of the J-integral (J_c),[14] and then all values were converted to a stress-intensity factor, K_{Jc}, using the following plane-stress expression:

$$K_{Jc} = (J_c \cdot E)^{1/2}, \quad (1)$$

where E is the elastic modulus.

At the beginning of the fracture-toughness testing, a small number of side-grooved specimens, included within the overall test matrix, were tested to evaluate the effects of side grooving on K_{Jc} toughness. The comparison developed is shown in Table 11. Because there is increased constraint with side grooving, one would expect

Table 10. Test matrix of median K_{Jc} for WF-70 weld metal

Size	Test temperature °C (°F)				
	0 (32)	−25 (−13)	−50 (−58)	−75 (−103)	−100 (−148)
			Beltline K_{Jc} MPa√m (ksi√in)		
1/2T		204 (186)	133 (121)		
1T	265 (241)	160 (146)	98 (89)	68 (62)	51 (46)
2T	234 (213)	163 (148)	106 (96)		
4T		109 (99)			
			Nozzle K_{Jc} MPa√m (ksi√in)		
1/2T			92 (84)		
1T	191 (174)	110 (100)	71 (65)		47 (43)

Table 11. Comparison of K_{Jc} for 1T compact specimens with and without side grooves

Test temp. °C (°F)	Beltline MPa√m (ksi√in)		Nozzle MPa√m (ksi√in)	
	With side grooves	Without side grooves	With side grooves	Without side grooves
0 (32)	197 (179)	140 (127)	220 (200)	145 (132)
	274 (249)	256 (233)	229 (208)	168 (153)
	317 (288)	296 (269)		300 (273)
		[a]		
		[a]		
	263 (239)[b]	231 (210)[b]	224 (204)[b]	204 (186)[b]
−25 (−13)	119 (108)	120 (109)	87 (79)	84 (76)
	133 (121)	139 (126)	147 (134)	96 (87)
	193 (176)	139 (126)		97 (88)
	267 (243)	143 (130)		114 (104)
		151 (137)		120 (109)
				121 (110)
	178 (162)[b]	138 (126)[b]	117 (106)[b]	105 (96)[b]

[a] J-R curve.
[b] Average values.

to find either no change or reduced K_{Jc} for specimens that are side grooved. Since the results indicated only a mild reversed effect that could not be reconciled with the physical basis for constraint, it was concluded that there was no evidence of a significant constraint effect on K_{Jc} and, as a consequence, the balance of the testing was performed without side grooving. It is possible that the apparent higher toughness values of the side-grooved specimens could be caused by computational problems associated with the manner in which the effective notched specimen thickness (B_N) is commonly used in the calculation of J_c.

The data from all the beltline weld specimens of all sizes that failed in cleavage are plotted in Fig. 12. Data for the nozzle weld metal are shown in Fig. 13. Almost all of these K_{Jc} values fail to satisfy the validity requirements for plane strain K_{Ic} (ref. 15). Hence, these data would not be considered acceptable according to early concepts for evaluation of transition temperature fracture toughness. Historically, lower-bound fracture toughness has been believed to be achievable only through valid K_{Ic} data. However, recent developments in the technology of ductile-brittle behavior have produced methods that predict specimen size effects and methods by which the transition range behavior can be defined by a different concept of a universal curve.[16] This information is currently being documented for future application in the form of an ASTM standard practice.*

The proposed test practice currently under development is designed to obtain useful fracture mechanics information from small specimens that are of a size suitable for insertion into surveillance capsules. One objective is to model transition toughness data scatter with the three-parameter Weibull data distribution model[17] and to employ a weakest-link statistical theory[18] to adjust fracture toughness for specimen size effects. Then the median trend of fracture toughness, adjusted to a single specimen size, is postulated to fit a universal trend curve, termed a "master curve." Standard deviation of data scatter is a function of the Weibull fitting parameters, and, thus, confidence bounds about the median fracture toughness trend can be calculated. A "reference temperature" is then determined to position the master curve on the temperature coordinate, and affiliated confidence bound curves are then determined as a function of median toughness. The reference temperature (T_o) is the test temperature where the median K_{Jc} for 1T size specimens is expected to be 100 MPa$\sqrt{m}$ (91 ksi$\sqrt{in}$). Additionally, a margin adjustment can be applied to the lower confidence bound curve to cover the uncertainty in reference temperature where only a small number of specimens are used to establish the reference temperature.

---

*Proposed "Test Practice (Method) for Fracture Toughness in the Transition Range," Draft 5, Committee E08 on Fatigue and Fracture, Task Group E08.08.03, American Society for Testing and Materials, Philadelphia, 1993.

If one wishes to test only a small set of replicate specimens to establish T_o, the temperature selection for optimum accuracy (on establishment of T_o) is near to the temperature, T_o. The following crude correlation between the 28-J (21-ft-lb) Charpy energy temperature, T_{28J}, and T_o has been offered as an aid to select a test temperature (in this case assuming 1T-size test specimens):

$$T_o \approx T_{28J} - 18°C, \quad (2)$$

where T_o is in °C. The constant on the right side of Eq. (2) can be adjusted for other specimen sizes. As an example for 1/2T compact specimens, the constant is –28°C (–50°F).

Estimates of temperatures corresponding to the 28-J CVN energy level for beltline and nozzle welds were obtained from data such as that shown in Figs. 12 and 13. Both weld metals indicated –23°C (–9°F), and using Eq. (2) adjusted for 1/2T specimen size, a test temperature of –50°C (–58°F) was indicated to obtain 100-MPa$\sqrt{m}$ median K_{Jc}. As indicated in Table 10, 1/2T compact specimens were tested at –50°C (–58°F), giving median K_{Jc} values of 91.6 MPa$\sqrt{m}$ (83.4 ksi$\sqrt{in}$) for the nozzle weld and 133 MPa$\sqrt{m}$ (121 ksi$\sqrt{in}$) for the beltline weld. These values were converted to 1T equivalents of 80.2 and 115.3 MPa$\sqrt{m}$ (73.0 and 104.9 ksi$\sqrt{in}$), respectively. Then the equivalent values were used to establish reference temperatures, T_o, giving –60°C (–76°F) for the beltline weld and –33°C (–27°F) for the nozzle course weld, a 27°C (49°F) difference in transition temperature. This toughness difference was not detected from the drop-weight NDT tests or the CVN evaluations.

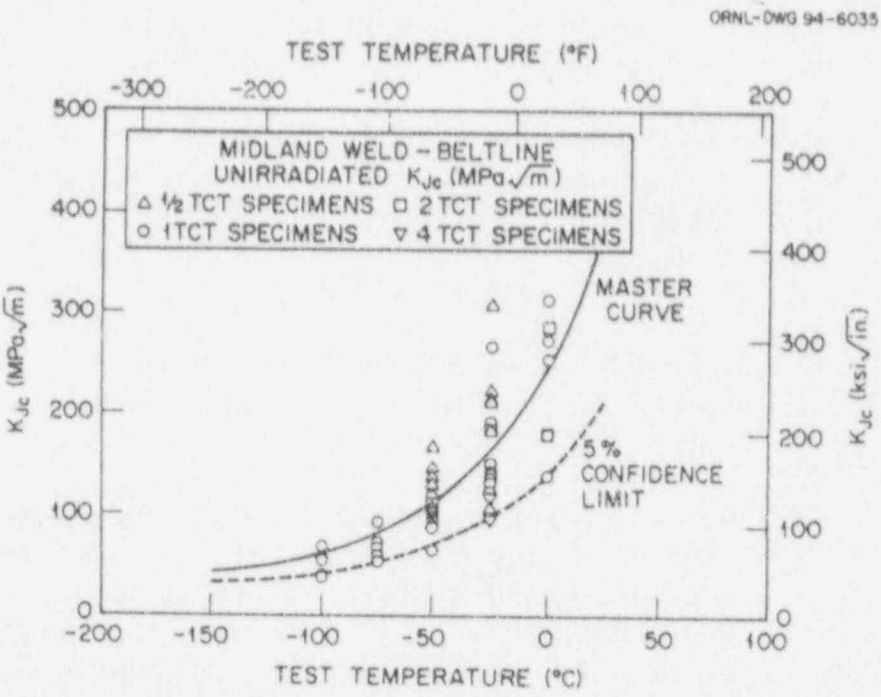
Figures 12 and 13 show the master curves derived from the 1/2T compact specimen data as well as the 5% cumulative probability curves. The data points shown are not specimen size adjusted. Despite this, the 5% confidence bound tends to enclose most of the unadjusted data.

An example margin adjustment to the 5% confidence limit based on the six replicate specimens at the 85% confidence level is shown in Fig. 14. Here, a 10°C (18°F) margin has been calculated and added to T_o.

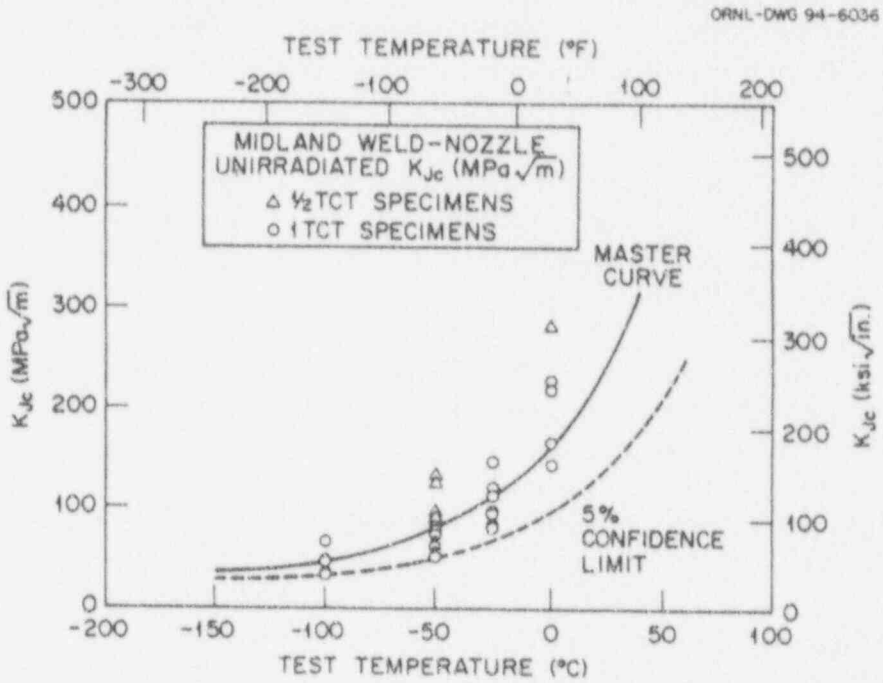
The irradiated specimens will be similarly evaluated to establish the transition temperature shift.

J-R Curve Behavior

Determinations of J-R curve behavior were performed at 21, 150, and 288°C (70, 302, and 550°F). Average values of J_{Ic} are listed in Table 12, showing the levels of



12. Transition temperature data for the Midland WF-70 beltline weld for four compact specimen sizes and a master curve on 1T specimen size.



13. Transition temperature data for the Midland nozzle course weld WF-70 for two compact specimen sizes and a master curve on 1T specimen size.

specimen sizes and test temperatures at which J-R curves were developed in this experiment.

In most cases, duplicate J-R curves were developed, and the data were combined for a least-squares curve fit. The equation (curve) fitted is of the same form as that used by Eason[13] in the multivariable modeling of data bank information:

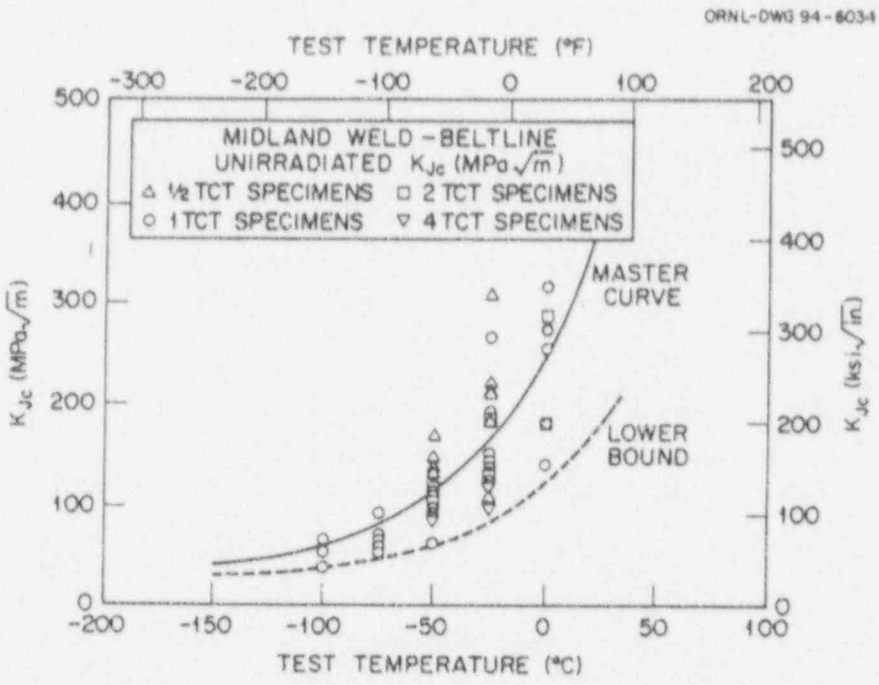
$$J_R = A(\Delta a_p)^B \exp[C/(\Delta a_p)^{1/2}], \quad (3)$$

where

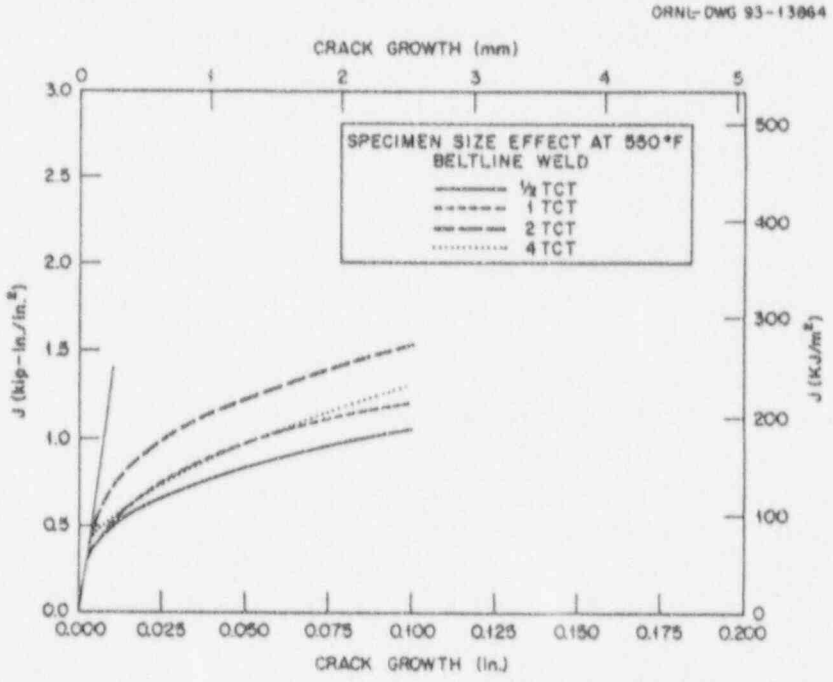
A,B,C	=	curve-fitting constants,
Δa_p	=	physical slow stable crack growth.

Because WF-70 weld metal is an LUS energy material, J-R curve characterization is needed to demonstrate that a reactor vessel can be safely operated with this material. Unfortunately, there are many cases where reactor surveillance capsules do not have fracture mechanics-type specimens that are suitable for J-R curve development. Blunt-notched Charpy V specimens are far more common. For such cases, it is now possible to estimate J-R curve using correlations developed from multivariable modeling of data bank information. The model developed by Eason et al.[13] uses a correlation based principally on upper-shelf CVN energy as well as accounting for other experimental variables that influence J-R curves. Variables such as specimen size, chemistry, test temperature, and irradiation exposure are accounted for in the models. This study presented an opportunity to independently compare the correlation model for Linde 80 weld metals to new experimentally generated data.

Specimen size effect (experimental) was evaluated on beltline weld metal at 288°C (550°F), and the result is shown in Fig. 15. A considerable spread is observed, almost all of which is attributable to the 2T specimens. The 1T and 4T specimens agree reasonably well, and the 1/2T specimens tend to show moderately lower toughness, as might have been expected. Clearly, the lack of a consistent trend from 1/2T to 4T is attributable to the 2T specimens, which behaved like a different material. Unfortunately, an examination of test records and evaluation of physical evidence has turned up no plausible reason for the inconsistency. Both 2T specimens came from the same through-thickness position at 3/4t, and both were from the same cutout (section 1-10) of the weld. Other 2T specimens were made from this segment of the weld, and these were put into an irradiation capsule. The above observation will be kept under consideration when evaluating the postirradiation results.



14. Master curve and 5% confidence limit curve (dashed) adjusted 10°C for uncertainty in reference temperature, T_O.



15. J-R curves of the Midland beltline weld metal with various specimen sizes at 550°F.

Table 12. Average J_{Ic} values from J-R curves

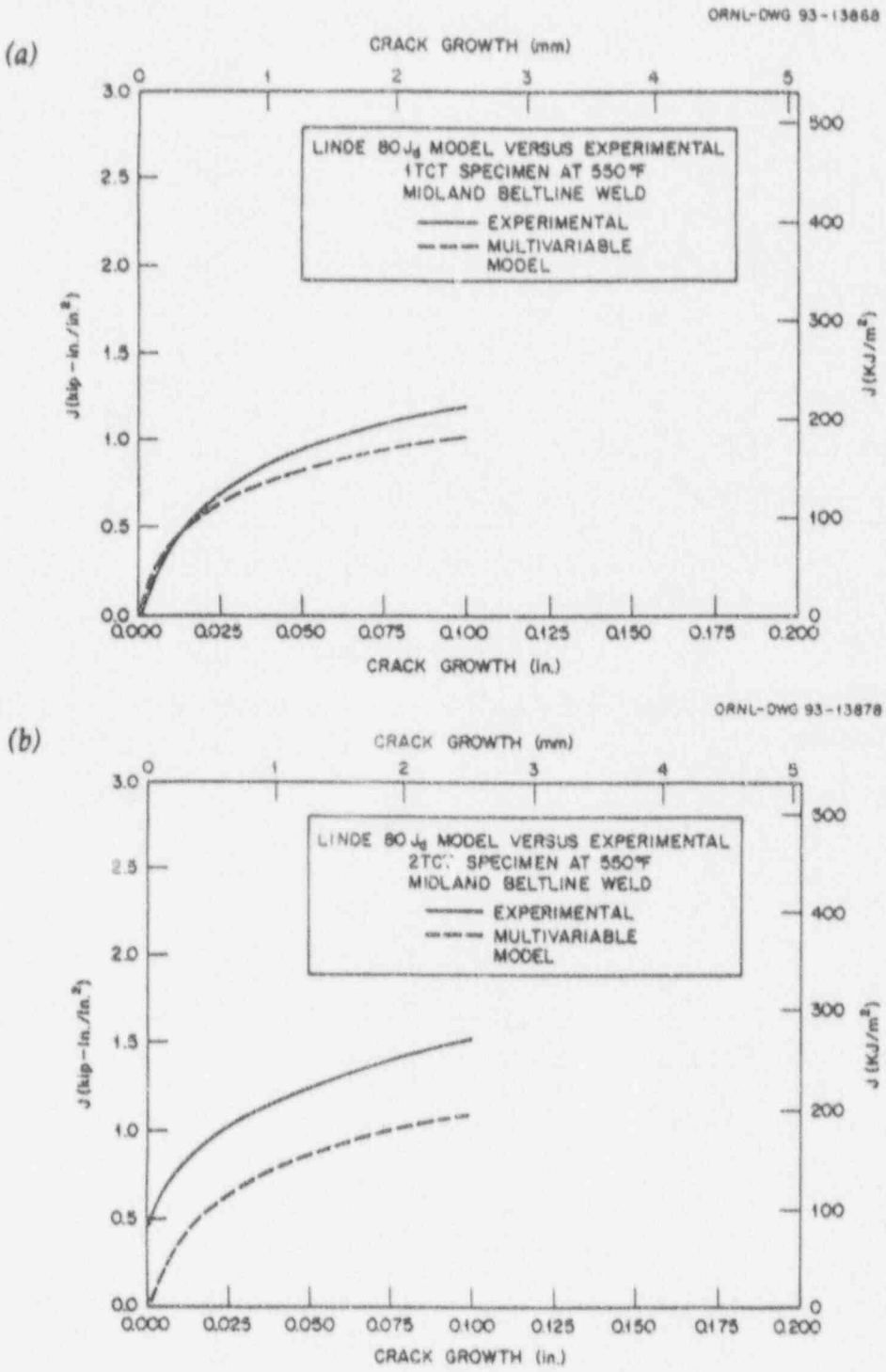
Specimen size	Test temperature °C (°F)			
	0 (32)	21 (70)	150 (302)	288 (550)
Beltline J_{Ic} [in.-lb/in.^{2} (kJ/m)]				
1/2T	920 (160)	740 (130)	670 (115)	495 (85)
1T		750 (130)	685 (120)	435 (75)
2T				850 (150)
Nozzle J_{Ic} [in.-lb/in.^{2} (kJ/m)]				
1/2T	700 (120)	725 (125)	500 (85)	320 (55)
1T				
2T				

A comparison of the WF-70 experimental-to-predicted J-R curves was made using a 65-ft-lb (48-J) upper-shelf energy in the Eason's Linde 80 multivariable model. The predicted curves for 1/2T, 1T, and 4T specimens compare to the experimental curves quite well as illustrated for the 1T specimens in Fig. 16(*a*). The J-R curves for the 2T size specimens do not agree [Fig. 16(*b*)], again seeming to bring into question the legitimacy of the experimental J-R curve result.

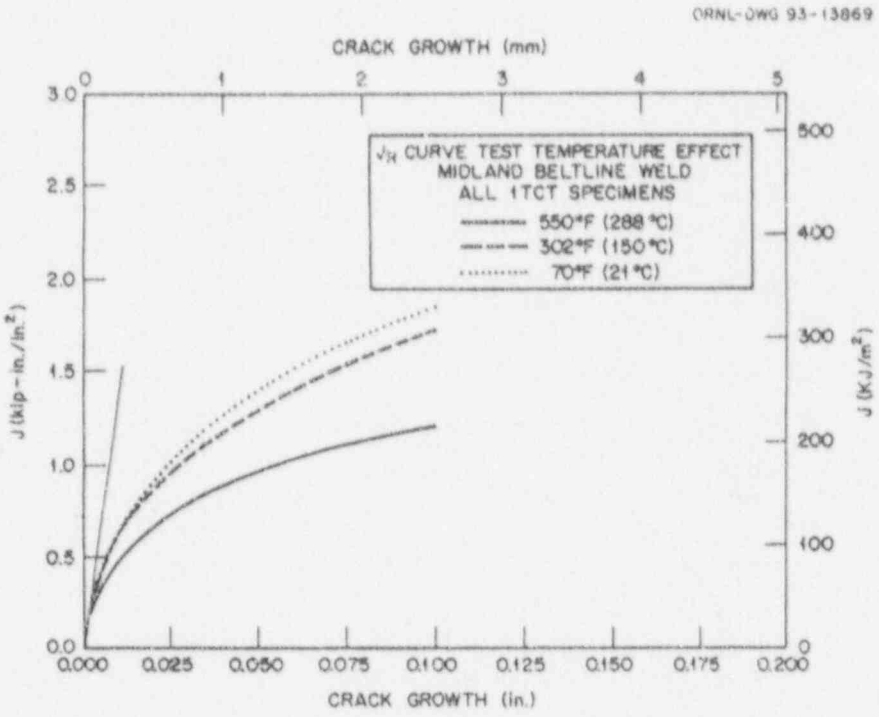
Figure 17 compares experimental J-R curves over three test temperatures for 1T compact specimens. It is clear that slow-stable crack growth resistance diminishes with increased test temperature. Similar behavior was observed for the 1/2T specimens.

Experimentally determined J-R curves that compare the toughness of beltline and nozzle welds were made using one specimen size (1T) at three temperatures, 21, 150, and 288°C (70, 302, and 550°F). There is a common indication that the J-R curve toughness of the nozzle course weld is lower than that of the beltline weld as is illustrated by the 288°C (550°F) J-R curves in Fig. 18. This lower ductile tearing resistance of the nozzle weld was not detected by the upper-shelf CVN energy.

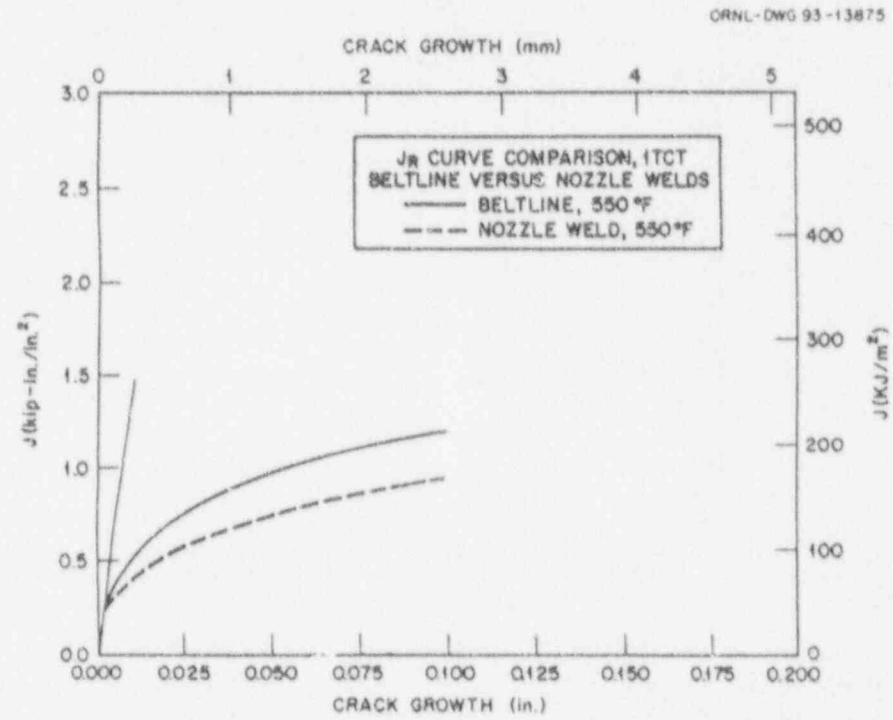
Specimens for J-R curve testing are almost always side grooved to control crack shape, as advised in the ASTM J-R curve test practice.[14] However, side-groove depth, and even the complete absence of side grooves, is not a controlled requirement in the ASTM test standard. Any presumption that J-R curves in LUS weld metal are not significantly affected by side-groove practice would be wrong, as evidenced by Fig. 19. The difference in J-R curve slope between 0 and 20% side groove used here is about a factor of 2. It should be noted, however, that crack growth was measured by compliance in both cases. There almost always is some inaccuracy of crack size determination on thick specimens without side grooves.[19] In this case, there was an approximate 25% lag of Δa_p behind the nine-point heat tint measurement of final crack size. On the other hand, if each compliance-calculated Δa_p is adjusted 25% to compensate for the error, the influence on the dashed line would be relatively minor, and the J-R curve difference still remains highly significant. The disturbing aspect of this is that valid J-R curves developed in conformance with an ASTM standard practice can be radically manipulated through side-groove practice. It is also well known that J-R curve slope is a function of side-groove depth without an asymptotic lower-bound characteristic, at least up to 50% side groove. The potential to manipulate apparent material toughness by side-groove practice should be given attention in analyses that relate to safety issues.



16. Experimental J-R curve and J-R curve calculated from a multivariable model for (*a*) 1T compact specimen and (*b*) 2T compact specimen.



17. Effect of test temperature on J-R curve of WF-70 weld metal for 1T compact specimens.



18. J-R curves that compare the nozzle versus the beltline weld metal ductile tearing resistance at 550°F (288°C).

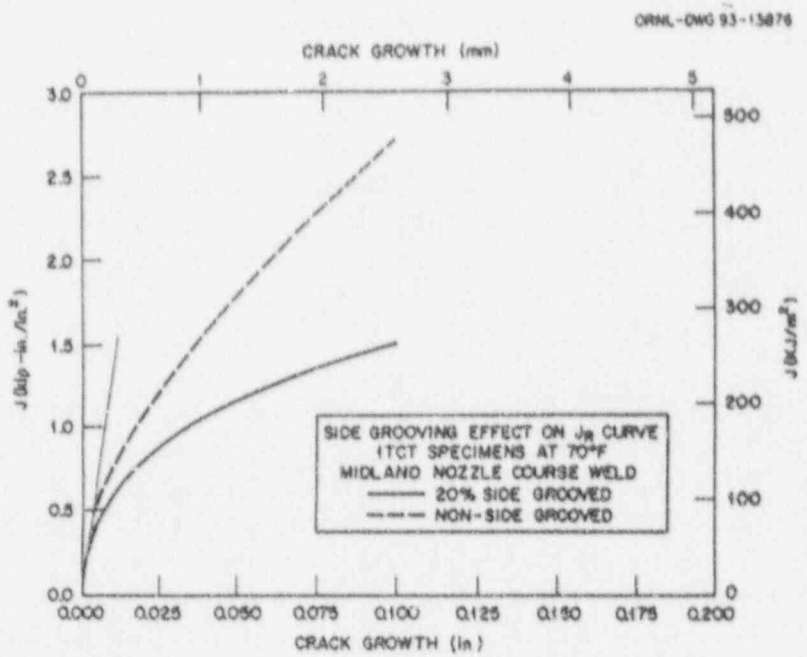
Crack-Arrest Behavior

Crack-arrest fracture toughness was determined for the Midland weld metal using a standard ASTM-type, split-pin, wedge-loaded specimen,[20] but with planform dimensions similar to the basic 2T compact specimen, to facilitate eventual common loading into irradiation capsules. The specimen thickness is not proportional to the conventional 2T design, however, being 25.4 or 33 mm (1 or 1.3 in.) instead of 50.8 mm (2 in.). The notch tips had a brittle weld bead made with McKay DWT stick electrode.

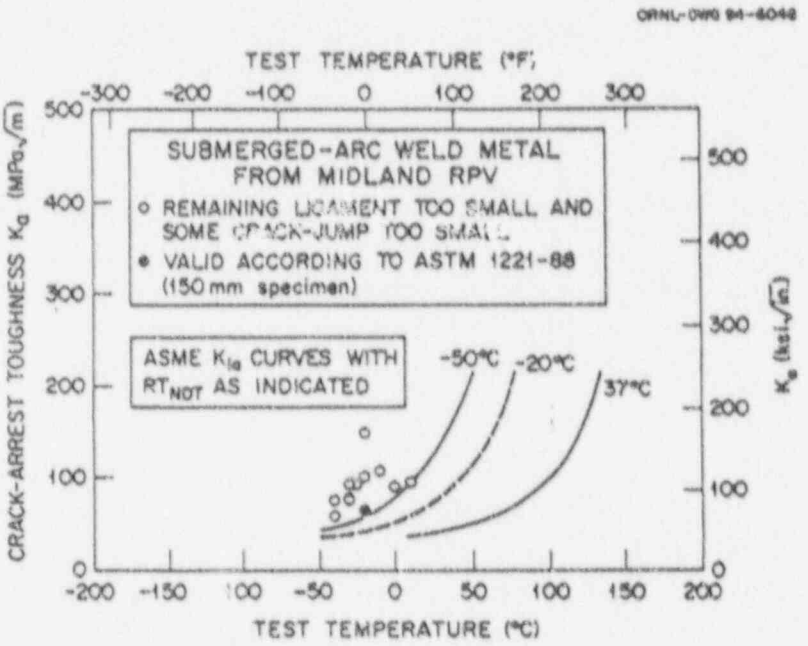
During testing, it was discovered that the running crack introduced by the brittle weld bead would prematurely "pop in" at low loads and then arrest in the heat-affected zone (HAZ) of the weld. With continued wedge loading, cleavage cracks would then initiate from the much tougher HAZ material under high crack-driving forces and oftentimes with some prior slow-stable crack growth. As a result, crack arrest would occur with small remaining ligaments, and the validity conditions of E 1221-88, the ASTM test standard on "Determining Plane-Strain Crack Arrest Fracture Toughness, K_{Ia}, of Ferritic Steels,"[20] were violated. This occurred in all cases except for one specimen made to 3T planform dimensions that produced one valid K_{Ia} datum. Even though the majority of the data is invalid according to the stringent requirements of E 1221-88, there is evidence that the ASTM validity requirements may be overly conservative for pressure vessel steels in general and LUS materials in particular.[22] The validity criteria within E 1221-88 are currently being reviewed by the cognizant committee within ASTM.

The data, while almost entirely invalid, fit well above the ASME K_{Ia} curve when the bounding values determined for the RT_{NDT} of the Midland weld, –20 to 37°C (–3 to 99°F), are used for its indexing (Fig. 20). It is interesting to note that the lower bound of the crack-arrest data coincides exactly with the ASME K_{Ia} curve when –50°C (-58°F) is used as the RT_{NDT} indexing value. While the value of -50°C (-58°F) is in agreement with the average NDT value, it is significantly lower than the established range of RT_{NDT} values which, for the Midland weld, were controlled by its CVN behavior.

While it is desirable to investigate the relationship between RT_{NDT} and crack-arrest toughness in more detail for the Midland weld, the severe constraints imposed by the relatively limited amount of material available for this study have made it difficult to fabricate more large crack-arrest specimens. Additional evaluation is planned using both a limited number of duplex-type crack-arrest specimens and crack-arrest toughness estimation methods based on the conditions at the point of load-drop termination in CVN testing. If additional material can be made available from some of the other recipients of the Midland weld, further large-specimen crack-arrest testing could be performed. In the meantime, the data that should



19. J-R curves comparing the effect of side grooving on the nozzle course weld metal. Both are legitimate by American Society for Testing and Materials standard E 1152-87.



20. Crack-arrest data for Midland beltline weld metal. The data are compared to the American Society of Mechanical Engineers lower-bound K_{Ia} curves established from RT_{NDT} = 37°C (99°F), RT_{NDT} = –20°C (–4°F), and hypothetical RT_{NDT} = –50°C (–58°F).

become available from the crack-arrest specimens currently being irradiated will provide valuable additional information.

DISCUSSION

The B&W "Record of Filler Wire Qualification Test" shows results of CVN testing at 10°F (–12°C) as 35, 39, and 44 ft-lb (47, 53, and 60 J). Those results are somewhat above most of the curves reported here. The qualification record shows the qualification weld was postweld heat treated at 1100 to 1150°F (593 to 621°C) for 48 h. BAW-2070 reports that the Midland beltline weld received 22 h and 36 min at 1125 ± 25°F (607 ± 14°C), while the nozzle course weld received 25 h and 31 min at the same temperature. The slight differences between the Midland weld results obtained in this study and the weld qualification results would likely be mitigated if the Midland weld received a total of 48-h heat treatment. The shorter PWHT given the vessel welds would likely result in somewhat higher strength and higher transition temperature than that reported in the qualification tests (see the earlier section on "Description of Weldments"), and that is borne out by the nozzle course weld, which has a higher yield strength than reported in the weld qualification, but is similar to that reported by Lowe[21] for one WF-70 weld. It is not clear, however, why the beltline weld, which received a PWHT only 3 h less than that of the nozzle course weld, would have a yield strength significantly less than that of the nozzle course weld.

The issue of RT_{NDT} determination is important for steels like the WF-70 weld because the RT_{NDT} is defined by the CVN toughness rather than the drop-weight NDT. The ASME Code paragraph discussed earlier is not perfectly clear as to the procedure to be used for such a determination. It requires the construction of a full Charpy curve from the minimum data points of all the C_V tests conducted. Strictly speaking, because para. NB-2321 in the ASME Code defines a C_V test as three tested specimens, the above paragraph would require one to use the minimum value from each of those groups of three specimens; however, since it only requires C_V tests at NDT + 60°F (33°C) or higher, one could not really develop a full C_V impact curve. On the other hand, the ASME Code allows determination of the RT_{NDT} when a C_V test has not been conducted at NDT + 60°F (33°C). It also is not clear how one should develop a curve from the minimum data points. It could be interpreted to be a best fit or an absolute lower bound. For consistency of RT_{NDT} determination, a clearer procedure needs to be developed and incorporated into relevant regulatory documents.

Even from the analyses of the individual data sets, it is clear that substantial differences in RT_{NDT} can result depending on individual interpretation of the intended procedure. The data from the 7/8t location in beltline weld section 1-11 provide one example of this; Fig. 21 shows the curve fits to all the data, to the

minimum data as discussed previously, and a lower boundary curve. The lower boundary curve is about midway between the lower 68 and 95% confidence bounds. If the ASME Code paragraph is interpreted to mean the construction of a curve which encompasses all the data, the RT_{LB} for the data in Fig. 21 would be about 29°C (84°F). That compares to an RT_{NDT} value of about 18°C (65°F) using the curve fit to the minimum data. The result depends, of course, on the actual construction of the lower boundary curve (e.g., smooth curve or point to point). Since there is no guidance regarding its shape, the 50-ft-lb (68-J) temperature could vary widely. For the individual beltline data sets, the RT_M ranged from 23°C (42°F) lower to 7°C (13°F) higher than the corresponding values of RT_{NDT}. For the individual nozzle course data sets, which generally had even fewer test results in each data set, there were no differences. A comparison of RT_{NDT} and RT_{LB} values shows that RT_{LB} ranged from 21°C (38°F) higher to 8°C (14°F) lower than the corresponding values of RT_{NDT}. Thus, the method used for determination of such an index is also dependent on the number of test results in the data set.

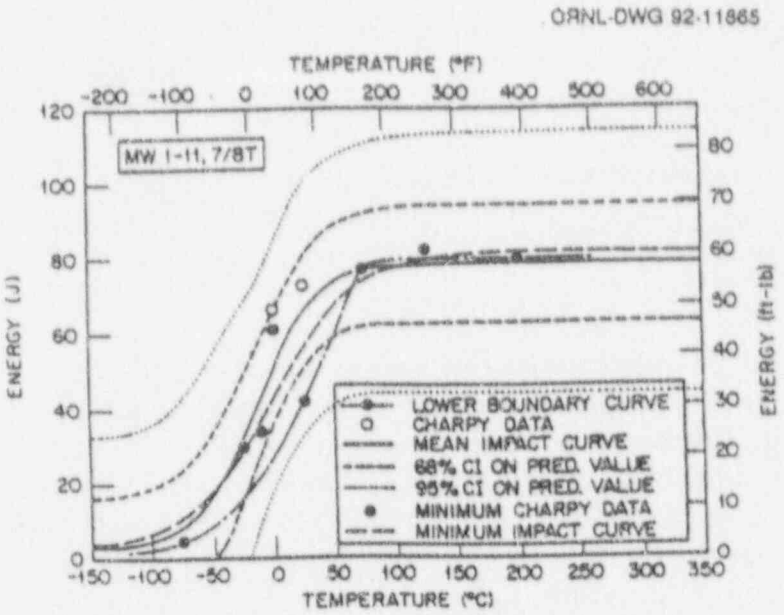
As seen in this study, small data sets for the same weld can result in substantial differences in determination of a transition temperature. The incorporation of statistical methods such as confidence bounds to be applied to the data would require a more well-defined prescription for the selection of test temperatures and number of tests. On the other hand, one could prescribe a value of deviation, based on documented behavior of welds and of base metals, which could be added to the mean value determined from a curve fit to the data. The prescription must be chosen, of course, based on the desired confidence level, such as 95%. There are other potential methods, but they are dependent on various judgments that can result in significantly different results.

The fact that the RT_{NDT} values vary from –20 to 37°C (–3 to 99°F) warrants further consideration relative to both the unirradiated and irradiated test programs. The testing of multiple specimens to allow for statistical analyses is an integral part of the current planned program, as is the testing and irradiation of fairly large specimens. The location in the weld from which specimens are machined will, of course, influence the unirradiated properties; however, because there was not a consistent trend of RT_{NDT}, 41-J temperature, or upper-shelf energy with depth in the welds, one reference RT_{NDT} and 41-J temperature for the beltline weld and one of each for the nozzle weld will be used. It is very interesting that, despite the large scatter in these welds, the 95% confidence interval is similar to the relatively homogenous welds 72W and 73W of the HSSI 5th Irradiation Series, which were fabricated with copper contained in the weld wire and not as a coating as was used for the Midland Welds. The wide variation in copper content, however, will further complicate the analysis of radiation effects. This is particularly true regarding the differences between the beltline and nozzle course welds. Those differences will require the irradiation program to consider the beltline and nozzle

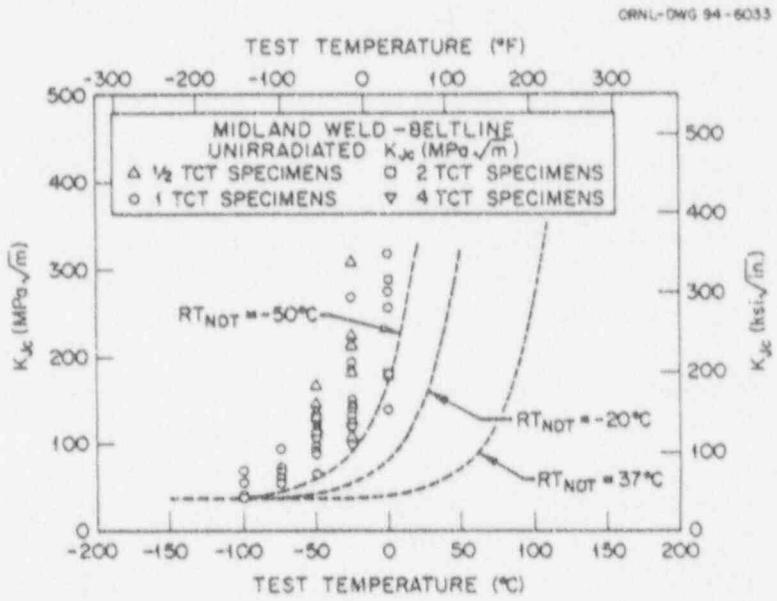
course welds as two different materials. Additionally, for the 4T compact specimens to be used in the program, the mechanical property and copper variations present in the weld will exist in individual specimens. The fact that this weld represents a real reactor vessel was the primary motivation for the study, yet the apparent variation in properties and copper content will only exacerbate the large variations already observed in relatively homogeneous materials. This does not render the study less useful, but it does require a different approach to the conduct of the program and analysis of its results.

The wide range of RT_{NDT} transition temperatures obtained for this material and their rather poor correspondence to the variation observed in fracture toughness testing indicate a need for an improved method to establish a meaningful transition temperature for pressure vessel materials. The 19 sampling positions for beltline Charpy curves produced RT_{NDT} temperatures varying from -20 to 37°C (-3 to 99°F). The application of these 19 RT_{NDT} values to position the ASME lower-bound K_{Ic} curve covers the area bounded by the dashed lines shown in Fig. 22. Furthermore, the fracture toughness are almost bounded by an ASME K_{Ic} curve indexed using the average dropweight NDT value -50°C (-58°F). While these results may be comforting, in that the experimental K_{Ic} data are bounded by the ASME K_{Ic} curves in a manner similar to the bounding of the K_{Ia} data by the ASME K_{Ia} curves, it also shows that an independent sampling of Charpy specimens such as might be applied in a plant-specific analysis could position the lower-bound K_{Ic} curve for design over a relatively wide range. Clearly, the assessment of the material embrittlement would then be a matter of probability, making the decision to license a plant for continued operation dependent on sampling location and chance ordering of the Charpy specimens. A ductile-to-brittle transition temperature (DBTT) procedure that uses fracture mechanics test practices is currently under development in a task group activity within ASTM. This method directly addresses the statistical variability of material toughness as a part of the analysis procedure. Six 1/2T compact specimens of nozzle weld and six 1/2T specimens of beltline weld were used to set up the master curves shown in Figs. 13 and 14 that define the transition toughness and confidence limits on scatter for data obtained from all specimen sizes. This method of material characterization has worked quite well in this case for the unirradiated material and will be used in the analysis of the irradiation-induced shifts in fracture toughness.

J-R curves were developed on beltline and nozzle course weld metals. Both showed loss of ductile tearing resistance with increased test temperature from room temperature to 288°C (550°F). There also was convincing evidence of a difference in J-R curve toughness between beltline and nozzle weld metals. This difference did not show up in the upper-shelf Charpy energy determinations, both indicating about 89-J (66-ft-lb) upper-shelf energy.



21. Comparison of various curve fits to the Charpy impact data from the 7/8 thickness location of Midland beltline weld section 1-11. Shown are the hyperbolic tangent curve fits to all the data and to the minimum data points, and a curve constructed as a lower boundary to all the data, and the 68 and 95% confidence bounds on the predicted value.



22. K_{Jc} data from the beltline weld metal tested in four specimen sizes. The data are compared to the American Society of Mechanical Engineers lower-bound K_{Ic} curves established from RT_{NDT} = 37°C (99°F), RT_{NDT} = -20°C (-4°F), and hypothetical RT_{NDT} = -50°C (-58°F).

The multivariable model of Eason et al. to develop J-R curves from Charpy upper-shelf energy was tested against the experimental J-R curves. The model for Linde 80 welds was used. The comparison of predicted versus experimental J-R curve for beltline weld was quite decent in this case. An unavoidable weakness of the methodology, however, is the use of Charpy upper-shelf energies that tend to lack the sensitivity needed to detect any subtle changes in J-R curve toughness.

Side grooving of compact specimens was evaluated on a relatively small scale within this experiment. It was determined that the choice between side grooving or not for K_{Jc} (transition range) testing was not significant. On the other hand, side grooving is a major variable in J-R curve development. In this experiment, the J-R curve slope was shown to be different by a factor of about 2. Side-grooving recommendations in ASTM Standard E 1152 ("Standard Test Method for Determining J-R Curves") fail to point out or emphasize the significance of such considerations. Side-groove depth has an important impact on J-R curves.

Crack-arrest tests were performed on beltline weld metal with difficulty. Initiation K_o was high and ligament size at arrest was nearly always too small for K_{Ia} validity. As a result, the accuracy of the K_{Ia} values reported here may be questioned. Nonetheless, there is reason to believe that the crack-arrest data may be representative of the material. The one valid result obtained with the larger specimen is seen in Fig. 20 to correspond reasonably well with the remainder of the invalid data, even though it lies toward the lower bound of the data set. The fact that the wide range of RT_{NDT} values determined for the Midland weld bound the crack-arrest data with significantly different amounts of margin raises further questions about the applicability of using an RT_{NDT} based on Charpy properties as the correct indexing parameter for the class of LUS welds. Indeed, the overall question of the most appropriate method to adjust predictions of fracture toughness of pressure vessel materials to account for irradiation-induced embrittlement is being examined within the HSSI program.

OBSERVATIONS AND CONCLUSIONS

The major observations and conclusions from this study are as follows:

1. Drop-weight NDT temperatures from various through-thickness positions in the beltline and nozzle course welds varied from –40 to –60°C (–40 to –76°F).

2. The RT_{NDT} values (determined from a hyperbolic tangent fit to the minimum data in each case) in all 25 individual cases are controlled by the CVN impact energy and vary from –20 to 37°C (–3 to 99°F), with a mean value of about 4°C (39°F) and a standard deviation of 14°C (25°F). From a mean curve fit to the entire data set, the RT_M is -3°C (27°F) with a

temperature interval associated with one standard deviation on energy of about 21°C (37°F). For the same 25 data sets, the RT_{LB} values (determined from the absolute lower bound in each case) vary from -21 to 35°C (-6 to 95°F) with a mean value of about 9°C (47°F) and a standard deviation of 16°C (29°F).

3. Analysis of the combined data from both beltline and nozzle course welds revealed a mean 41-J temperature of -8°C (17°F). Statistical analyses of the combined data (279 tests) show a 95% confidence temperature interval from -36 to 17°C (-32 to 62°F) at the 41-J energy level; that 53°C (94°F) interval width is similar to those observed for welds 72W and 73W in the HSSI Fifth Irradiation Series.

4. Analysis of the combined data set for the beltline and nozzle course welds (279 Charpy impact tests) gives an RT_M [50 ft-lb (68-J) temperature from the mean curve fit less 60°F (33°C)] result of -3°C (27°F) with lower 68 and 95% confidence bounds of 18 and 67°C (64 and 153°F), respectively.

5. The ASME Code procedure for determination of RT_{NDT} is unclear, and different interpretations can result in substantially different results, depending on the nature of the data.

6. Upper-shelf energies for 25 data sets vary from 77 to 108 J (57 to 80 ft-lb) with a mean value of 88 J (65 ft-lb) and a standard deviation of 7.3 J (5.4 ft-lb). Analysis of the combined data from both beltline and nozzle course welds revealed a mean upper-shelf energy of 89 J (65 ft-lb) with 95% confidence bounds from 70 to 107 J (52 to 79 ft-lb).

7. Bulk copper contents range from 0.21 to 0.34% in the beltline weld (average is 0.26%) and from 0.37 to 0.46 wt % in the nozzle course weld (average is 0.40%); the overall average is 0.29% with a standard deviation of ±0.07%.

8. APFIM revealed no evidence of detectable (darkly imaging) copper precipitates or clusters but did indicate substantial depletion of copper in the matrix over the bulk chemical analysis. Thus, fine copper precipitation occurred during the PWHT at grain boundaries and other microstructural features substantially depleting the matrix in copper, but copper clustering within the matrix did not develop.

9. Fracture toughness reference temperatures, T_o, were established as -60°C (-76°F) for the beltline weld and -33°C (-27°F) for the nozzle course weld yielding a 27°C (49°F) difference in transition temperature. This degree of toughness difference was not detected from the drop-weight NDT tests or the CVN evaluations. Using the values of fracture toughness reference

temperature, T_0, it was possible to index the master fracture toughness curve to adequately bound the remainder of the unirradiated fracture toughness data

10. Using the range of values of RT_{NDT} determined for the WF-70 weld metal, it was shown that the ASME K_{Ic} and K_{Ia} curves would adequately bound the experimental fracture toughness and crack-arrest data, respectively. The same data also show the relatively large amount of uncertainty in the margin that would be associated with using a limited data set to establish the RT_{NDT} of the material.

11. Determinations of J-R curve behavior indicated a decrease in crack growth resistance with increases in specimen size from 1/2T to 4T with the exception of the 2T specimens, which are likely exhibiting the effects of material inhomogeneity. J-R curves are also seen to decrease with increasing temperature as expected. The overall ductile crack resistance of the nozzle weld is seen to be somewhat poorer than the beltline weld.

12. The multivariable model for J-R behavior of Eason appears to predict the data for the WF-70 LUS weld reasonably well.

13. Side grooving of fracture specimens was shown to have a significant effect on J-R curve behavior for the LUS weld examined here. Even though wide variation in side grooving is allowed by ASTM standard E 1152-87, caution should be used in evaluating and applying J-R curve data for specimens with variations in specimen side grooving.

PLANS FOR IRRADIATED SPECIMENS

The irradiation of the Midland weld is in progress. The exposure of the first of the two large irradiation capsules (capsule 10.05), containing tensile, CVN, and fracture toughness specimens, to the primary target fluence of 1×10^{19} n/cm^2 (>1 MeV) has been completed and the second (capsule 10.06) begun. Small fracture toughness and CVN specimens are also being exposed in low- and high-fluence scoping capsules to 5×10^{18} and 5×10^{19} neutrons/cm^2 to examine fluence effects over this range.

HSSI capsules 10.05 and 10.06 contain 1/2T, 1T, and 2T compact specimens as well as numerous standard notched and precracked Charpy specimens of beltline and nozzle course material. They also contain 15 crack-arrest specimens of the beltline material.

The overall plan for irradiation evaluations is designed to satisfy the following objectives:

1. Establish a master curve for irradiated beltline and nozzle course welds using a few 1/2T compact specimens of each material, and use it as well as the shifted ASME K_{Ic} curve to assess the most appropriate embrittlement indices and their margins for LUS weld metal.

2. Determine if the master curve of the irradiated materials can also be established from slow-bend precracked Charpy specimens.

3. Establish the data scatter of CVN transition range data. Establish the data scatter on RT_{NDT} and 41-J temperature, and compare this to the fracture mechanics-based results.

4. Determine the postirradiation K_{Ia} lower bound. This evaluation would also include further exploration of crack arrest determined by instrumented Charpy impact tests.

5. Evaluate the effect of irradiation on J-R curves for WF-70 weld metal. Also, compare experimental J-R curves with those predicted by the Eason multivariable model.

REFERENCES

1. R. K. Nanstad, D. E. McCabe, R. L. Swain, and M. K. Miller, Martin Marietta Energy Systems, Inc., Oak Ridge Natl. Lab., *Chemical Composition and RT_{NDT} Determinations for Midland Weld WF-70*, USNRC Report NUREG/CR-5914 (ORNL-6740), December 1992.*

2. *Material Documentation Report for the Weld Material Removed from the Consumers Power (Midland) Reactor Vessel (620-0012-1)*, BAW-2070, Babcock and Wilcox Co., Nuclear Power Division, Lynchburg, Va., January 1989.‡

3. F. M. Haggag, R. K. Nanstad, and D. N. Braski, "Structural Integrity Evaluation Based on an Innovative Field Indentation Microprobe," pp. 101-7 in *Innovative Approaches to Irradiation Damage and Fracture Analysis*, PVP-Vol. 170, ed. D. L. Marriott, T. R. Mager, and W. H. Bamford, American Society of Mechanical Engineers, New York, 1989.†

4. *Standard Test Method for Conducting Drop-Weight Test to Determine Nil-Ductility Transition Temperature of Ferritic Steels*, ASTM E 208-87, American Society for Testing and Materials, Philadelphia, 1990.†

5. *Standard Test Method for Notched Bar Impact Testing of Metallic Materials*, ASTM E 23-91, American Society for Testing and Materials, Philadelphia, 1991.†

6. *Standard Practice for Effects of High-Energy Neutron Irradiation on the Mechanical Properties of Metallic Materials, E 706 (IB)*, ASTM E 184-79, American Society for Testing and Materials, Philadelphia, 1990.†

7. *ASME Boiler and Pressure Vessel Code. An American National Standard*, Sect. III, American Society of Mechanical Engineers, New York, 1989.†

8. R. K. Nanstad et al., Martin Marietta Energy Systems, Inc., Oak Ridge Natl. Lab., *Irradiation Effects on Fracture Toughness of Two High-Copper Submerged Arc Welds, HSSI Series 5*, USNRC Report NUREG/CR-5913 (ORNL/TM-12156), October 1992.*

9. K. E. Moore and A. S. Heller, *B&W 177-FA Reactor Vessel Beltline Weld Chemistry Study*, BAW-1799, Babcock and Wilcox Co., Utility Power Generation Division, Lynchburg, Va., July 1983.‡

10. K. E. Moore, A. S. Heller, and A. L. Lowe, Jr., "Chemical Composition of Nuclear Reactor Vessel Welds," pp. 1046-58 in *Effects of Radiation on Materials: Twelfth International Symposium, ASTM STF 870*, ed. F. A. Garner and J. S. Perrin, American Society for Testing and Materials, Philadelphia, 1985, .†

11. M. K. Miller et al., pp. 523-28 in *Proceedings of the Second International Symposium on Environmental Degradation of Materials in Nuclear Power Systems-Water Reactors, Monterey, 1985*, ed. J. T. A. Robert, J. R. Weeks, and G. Theus, American Nuclear Society, Hinsdale, Ill., 1985.†

12. M. K. Miller and M. G. Burke, "Microstructural Characterization of Irradiated PWR Steels Using the Atom Probe Field-Ion Microscope," pp. 143-49 in *Proceedings of the Third International Symposium on Environmental Degradation of Materials in Nuclear Power Systems - Water Reactors*, ed. G. J. Theus and J. R. Weeks, The Metallurgical Society, Inc., New York, 1987.†

13. E. D. Eason, J. E. Wright, and E. E. Nelson, Modeling and Computing Services, Inc., *Multivariable Modeling of Pressure Vessel and Piping J-R Data*, USNRC Report NUREG/CR-5729 (MCS 910401), May 1991.*

14. *Standard Test Method for Determining J-R Curves*, ASTM E 1152-87, American Society for Testing and Materials, Philadelphia, 1992.†

15. *Standard Test Method for Plane-Strain Fracture Toughness of Metallic Materials*, ASTM E 399-90, Vol. 03.01, American Society for Testing and Materials, Philadelphia, 1992.†

16. K. Wallin, "A Simple Theoretical Charpy V - K_{Ic} Correlation for Irradiation Embrittlement," pp. 93-100 in *Innovative Approaches to Irradiation Damage and Fracture Analysis*, PVP-Vol. 170, ed. D. L. Marriott, T. R. Mager, and W. H. Bamford, American Society of Mechanical Engineers, New York, 1989.†

17. J. D. Landes and D. E. McCabe, "Effect of Section Size on Transition Temperature Behavior of Structural Steels," pp. 378-92 in *Fracture Mechanics: Fifteenth Symposium, ASTM STP 833*, ed. R. J. Sanford, American Society for Testing and Materials, Philadelphia, 1984.†

18. T. L. Anderson, D. Stienstra, and R. H. Dodds, "A Theoretical Framework for Addressing Fracture in the Ductile-Brittle Transition Region," *Reflections in Fracture Mechanics Research, ASTM STP 1207*, American Society for Testing and Materials, Philadelphia, 1994.†

19. T. Hollstein, J. G. Blauel, and B. Voss, "On the Determination of Elastic-Plastic Fracture Material Parameters: A Comparison of Different Test Methods," pp. 104-16 in *Elastic-Plastic Fracture Test Methods: The Users Experience, ASTM STP 856*, American Society for Testing and Materials, Philadelphia, 1983.†

20. *Standard Test Method for Determining Plane-Strain Crack Arrest Fracture Toughness, K_{Ia}, of Ferritic Steels*, ASTM E 1221-88, Vol. 03.01, American Society for Testing and Materials, Philadelphia, 1992.†

21. A. L. Lowe, Jr., "Irradiation Characteristics of Weld Wire Heat Number 72105," pp. 292-308 in *Effects of Radiation on Materials: 15th International Symposium, ASTM STP 1125*, ed. R. E. Stoller, A. S. Kumar, and D. S. Gelles, American Society for Testing and Materials, Philadelphia, 1992.†

22. R. H. Bryan et al., Martin Marietta Energy Systems, Inc., Oak Ridge Natl. Lab., *Pressurized Thermal-Shock Test of 6-in.-Thick Pressure Vessels. PTSE-2 Investigation of Low Tearing Resistance and Warm Prestressing*, USNRC Report NUREG/CR-4888 (ORNL-6377), December 1987.*

---

*Available for purchase from National Technical Information Service, Springfield, VA 22161.

†Available in public technical libraries.

‡Available from B&W Nuclear Technologies, P.O. Box 10935, Lynchburg, VA 24506-0935.

**Available from U.S. Government Printing Office, Washington, DC 20402. ATTN: Regulatory Guide Account.

MODELING OF IRRADIATION EMBRITTLEMENT AND ANNEALING DATA

E. D. Eason
J. E. Wright
E. E. Nelson

Modeling & Computing Services
39675 Cedar Boulevard, Suite 290
Newark, California 94560

ABSTRACT

This project is developing improved irradiation embrittlement equations based on the current understanding of embrittlement mechanisms and the increased amount of embrittlement data that has become available in recent years. The primary sources of data are the Power Reactor Embrittlement Database (PR-EDB) and the Test Reactor Embrittlement Database (TR-EDB) compiled at Oak Ridge National Laboratory. Results from mechanistic studies and advanced statistical techniques, including pattern recognition and transformation analysis, are being used to identify potential modeling variables and their functional forms. An important part of the project is modeling the effectiveness of annealing countermeasures. This paper is focused on the annealing part of the project. Preliminary models for recovery in transition temperature and Charpy upper shelf energy due to annealing are presented.

INTRODUCTION

Modeling & Computing Services (M&CS) is developing improved irradiation embrittlement equations under a project sponsored by the U. S. Nuclear Regulatory Commission (NRC). This project uses advanced data analysis techniques, the results from mechanistic research, and the large body of embrittlement data that has become available in recent years in the Power Reactor Embrittlement Data Base (PR-EDB, Ref. 1) and the Test Reactor Embrittlement Data Base (TR-EDB, Ref. 2) compiled at Oak Ridge National Laboratory (ORNL). An important objective of the embrittlement project is to develop models for predicting the amount of recovery in transition temperature and

Charpy upper shelf energy due to annealing. The preliminary annealing recovery models are the focus of the current paper.

The effects of irradiation embrittlement can be reduced by thermal annealing at temperatures higher than the normal operating conditions. Although such an annealing process has not been applied to any commercial plants in the United States, one U. S. Army reactor (Ref. 3), a commercial plant in Belgium and several plants in the former USSR have been successfully annealed.

A quantitative evaluation of embrittlement recovery due to annealing is required to determine the potential effectiveness of an annealing treatment for aging commercial plants. The objective of this work is to analyze the pertinent data on this issue and develop a quantitative model for estimating the recovery in 41-J (30 ft-lb) Charpy transition temperature and Charpy upper shelf energy due to annealing.

Models for estimating the degree of recovery due to post-irradiation annealing have been previously developed. Powers (Ref. 4) proposed in 1968 that the percentage recovery in the irradiated transition temperature shift could be related to a time-temperature superposition parameter P, where

$$P = T \ln (10^{21} t) \tag{1}$$

In Equation 1, temperature T is in K and time t is in seconds. The parameter P is evaluated both after irradiation and after annealing. The change in P,

$$\Delta P = P_{anneal} - P_{irrad} \tag{2}$$

is approximately proportional to the percentage recovery. This approach works to some extent, but better results are obtained by the method of Macdonald (Ref. 5).

Macdonald refined the approach of Powers by defining an Annealing Effect Parameter,

$$AEP = C\Delta P (\Delta TT_i)^n \tag{3}$$

where C is a constant, ΔP is defined by Equation 2, and ΔTT_i is the shift in transition temperature due to irradiation. The exponent n was found to be approximately -0.5. A reasonable correlation was obtained for estimating the residual transition temperature shift after annealing as a linear function

$$\Delta TT_a = a_1 + a_2 \text{ erf } (AEP) \tag{4}$$

where a_1 and a_2 are empirical fitting constants. Both Powers' and Macdonald's models use the same time-temperature superposition factor, P.

The fitting form used by Macdonald appears to have been determined somewhat arbitrarily. The text of Reference 5 implies that the exponent, n, was chosen by eye, and

the value of the constant, C, was chosen to allow the use of the assumed functional form, erf(AEP). Thus, one potential approach was to determine if the Macdonald model could be improved by applying modern tools for calibrating nonlinear multivariable functions, while preserving the functional form of the AEP parameter as defined in equation (3). A second potential approach was to ignore the AEP parameter and consider completely different model forms and correlating parameters.

In a prior phase of this project, both of the above approaches were successful in improving the fit to available transition temperature recovery data. Improving the model form was more effective than recalibrating the Macdonald model. Based on these encouraging results, the database for annealing studies was expanded, the scope was expanded to include recovery of upper shelf energy, and the work reported here began.

ANNEALING DATABASE

Data were gathered from the TR-EDB and from various annealing reports. Since many of the annealing data were originally generated by R. Hawthorne at Materials Engineering Associates (MEA), Mr. Hawthorne reviewed the data from his experiments and cross checked the computer database with his original laboratory notes as a part of this work. His review resulted in clarifications regarding discrepancies between reports and the TR-EDB, some corrections, a few new data points, and suggestions to omit a few unreliable data points. In addition, it was determined that many of the fluences in the reports and the TR-EDB were fission spectrum fluences; in most cases, Mr. Hawthorne provided calculated spectrum fluence values to replace the older numbers.

The entire database contains 72 data points, although in many cases recovery of only one quantity - transition temperature shift (TTS) or upper shelf drop (ΔC_vUSE) - was available. Several ways of quantifying recovery were investigated for both TTS and ΔC_vUSE, with a different number of available data points depending on the dependent variable used. The generic types of dependent variables considered were:

1) fraction of the irradiated shift or drop recovered by annealing,
2) residual shift or drop after annealing,
3) reduction in shift or drop due to annealing, and
4) final quantity (TT or USE) after irradiation and annealing.

A study was performed to pick the best dependent variable, as described under Results.

The independent variables considered included chemistries, irradiation time and temperature, annealing time and temperature, fluence, flux, preirradiated transition temperature (TT) and upper shelf energy (USE), and shifts in TT and USE due to irradiation. All the independent variables and combinations of variables that were considered are shown in Tables 1 and 2.

Table 1. Independent variables considered in annealing analysis

Variable	Units
Irradiation temperature, T_i	°Rankine
Irradiation time, t_i	hours
Annealing temperature, T_a	°Rankine
Annealing time, t_a	hours
Transition temperature before irradiation, TT_u	°F
Transition temperature after irradiation, TT_i	°F
Shift in transition temperature due to irradiation, dTT_i	°F
Upper shelf energy before irradiation, US_u	ft-lbs
Upper shelf energy after irradiation, US_i	ft-lbs
Drop in upper shelf energy due to irradiation, dUS_i	ft-lbs
Copper content, Cu	weight %
Nickel content, Ni	weight %
Phosphorus content, P	weight %
Sulfur content, S	weight %
Silicon content, Si	weight %
Chromium content, Cr	weight %
Manganese content, Mn	weight %
Molybdenum content, Mo	weight %

ANALYSIS

Advanced statistical techniques were used to identify potentially important variables and their functional forms. Three computer codes - TAC, TACMVS, and CART - were used to determine which variables are most important for prediction of a given dependent variable. Information from other research - e.g., insight into damage mechanisms and

physical models of irradiation embrittlement - was considered to some degree in the choice of combination variables and will be considered further during subsequent iterations of model development.

Table 2. Combinations of variables treated as additional independent variables

$T_a \ln t_a$	$Cu(T_a \ln t_a)$	$Cu*T_i \ln t_i$	Cr/T_a	$Ni*T_a$
$T_i \ln t_i$	Cu*Ni	Ni/T_a	Mn/T_a	$P*T_a$
$Cu*T_a$	Ni/Cu	P/T_a	Mo/T_a	$S*T_a$
Cu/T_a	$Cu*\phi t$	S/T_a	TT_u/T_a	$Mo*T_a$
$Cu(T_a T_i)$	$Cu*dTT_i$	Si/T_a	US_u/T_a	dTT_i*T_a
$Cu/\phi t$,	T_a*T_i	dUS_i*T_a		

The procedure for determining the optimal model form is iterative, as shown in Figure 1. The same analysis procedure has been successful in prior studies, including References 6 and 7. Beginning with various sources of data, the data are put in the form required by the analysis codes. Then pattern recognition and transformation analysis codes are applied to the analysis database, using the available results of mechanistic studies to guide the choice of correlating parameters. The results include identification of key variables and optimal modeling forms as well as improved understanding of any hidden correlations among the supposedly independent variables. Then models are calibrated by conventional or advanced least squares techniques, and the quality of the fit is assessed. Outliers, anomalies, and subdomains where the model equations do not fit well are usually found when assessing the quality of the initial fit. These outliers and anomalies are then researched and the analysis database is refined, then the process iterates. The work reported here is a second iteration to the point of calibrating models. Additional insight from theoretical considerations is expected after the preliminary results reported here are reviewed by mechanisms researchers. Additional improvements in the models and database are expected as the quality of the current models is analyzed in detail. Thus the results presented here should be considered a preliminary result of work in progress.

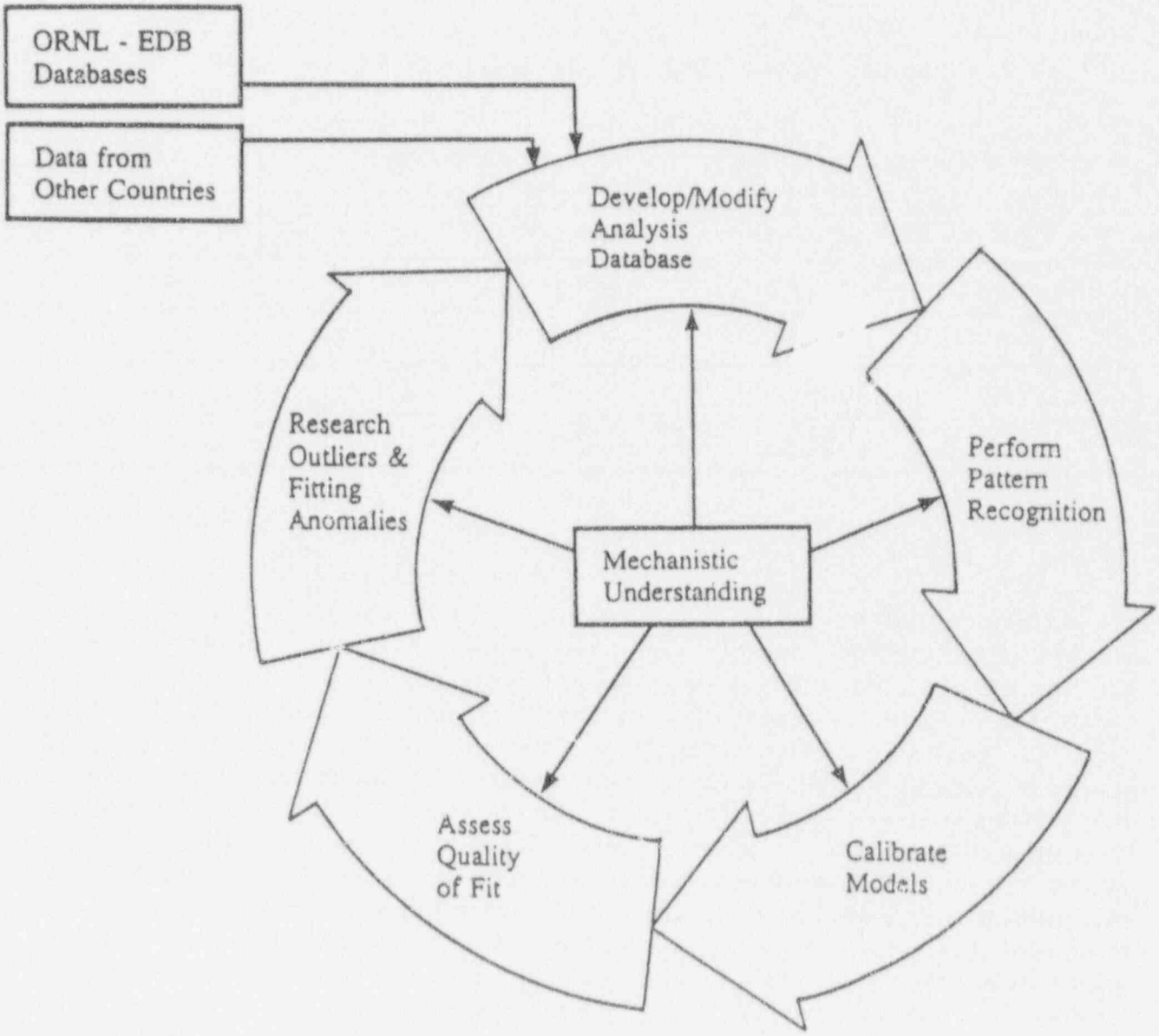


Figure 1. Iterative Analysis Process

RESULTS

The results presented here for transition temperature recovery due to annealing are from the second iteration of analysis, after a significant effort to refine the initial database. The result of the first iteration was a model for the effect of annealing on the transition temperature shift, with the fraction of shift recovered by annealing as the dependent variable.

During the current study, several types of dependent variables were investigated. The candidate dependent variables considered for TT and USE are defined in Table 3. Results of computer codes TACMVS and CART were used to select the dependent variables yielding the best correlations. TACMVS provides cumulative correlation coefficients indicating how well each dependent variable can be predicted as the effects of additional independent variables are considered. CART provides ranking information indicating the relative importance of the independent variables considered. Results of both codes were used to determine which of the dependent variables are predicted best by the five most sensitive independent variables. For both the transition temperature and upper shelf energy, the best type of dependent variable is the value after irradiation and annealing, i.e., TT_{ia} and US_{ia}. For predicting upper shelf energy recovery, the choice of US_{ia} is clear, while for predicting transition temperature recovery, differences among the dependent variable formulations are less significant. Thus, this paper models the effect of annealing on TT_{ia}, the transition temperature after annealing, and US_{ia}, the upper shelf energy after annealing.

The most important independent variables indicated by TACMVS and CART runs were used in TAC runs for TT_{ia} and US_{ia}. TAC provides graphical output, indicating the relative importance of the independent variables as well as their functional forms. For example, Figures 2-4 show TAC results for US_{ia} versus US_i, US_u, and $US_u/T_a ln(5.6E9t_a)$. On these plots, the vertical scale is nondimensionalized in standard deviations of the dependent variable (US_{ia}). Thus, in Figure 2, the value of upper shelf energy after irradiation, US_i, accounts for a three standard deviation range in the raw data, from -1σ to $+2\sigma$. The functional forms of all variables are approximately linear, indicating that the model form should contain linear terms. When potentially important additional independent variables from Tables 1 and 2 were added to the TAC run shown in Figures 2-4, the traces were nearly horizontal. The nearly horizontal traces on TAC plots indicate little effect of additional variables on US_{ia} given that US_u, US_i, and $US_u/T_a ln(5.6E9t_a)$ are in the model.

Table 3. Dependent variable definitions

Dependent Variable	Definition
Fraction TTS recovered by annealing	$T_{rec} = \frac{TT_i - TT_a}{TT_i - TT_u}$
Residual TTS after irradiation and annealing	$dTT_{res} = TT_{ia} - TT_u$
Shift in TT due to annealing	$dTT_a = TT_i - TT_{ia}$
TT after irradiation and annealing	TT_{ia}
Fraction ΔC_vUSE recovered by annealing	$US_{rec} = \frac{US_{ia} - US_i}{US_u - US_i}$
Residual ΔC_vUSE after irradiation and annealing	$dUS_{res} = US_u - US_{ia}$
Increase in USE due to annealing	$dUS_a = US_{ia} - US_i$
USE after irradiation and annealing	US_{ia}

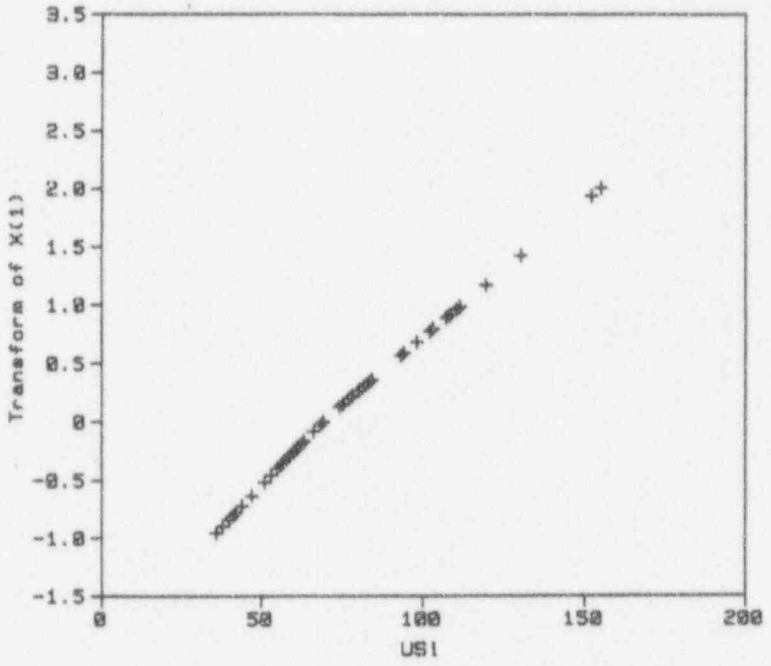


Figure 2. TAC plot of the effect of US_l on US_{la}

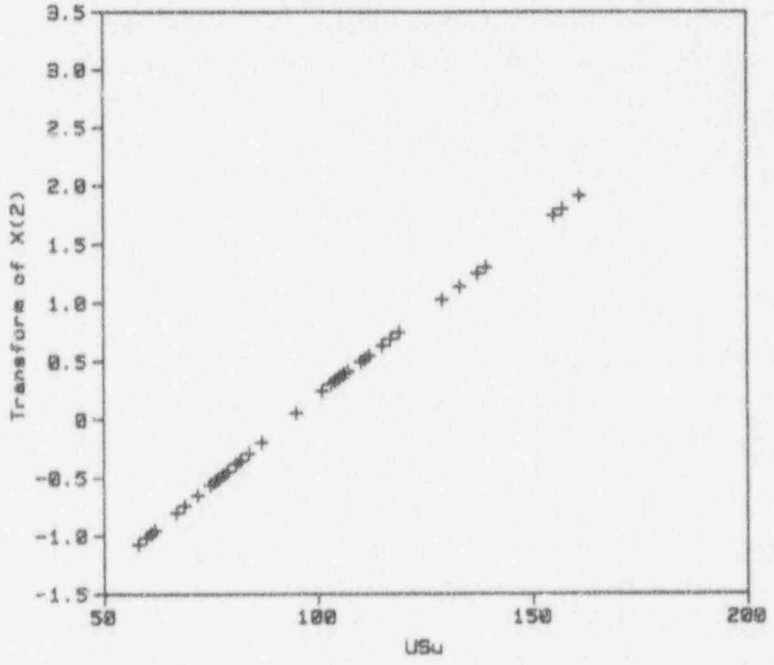


Figure 3. TAC plot of the effect of US_u on US_{la}

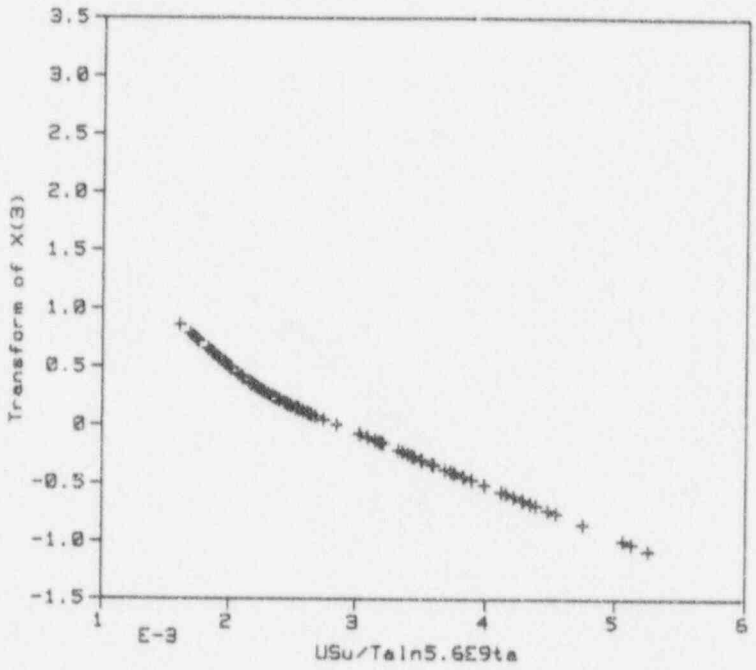


Figure 4. TAC plot of the effect of $US_a/T_a\ln(5.6E9t_a)$ on US_{ia}

Nonlinear surface fitting techniques were used to calibrate preliminary models for US_{ia} and TT_{ia}, based on TAC results. The goodness of fit of the best preliminary upper shelf recovery model is demonstrated in Figure 5. Figure 5 shows the actual US_{ia} versus the predicted US_{ia}, with 95% bounds. The actual TT_{ia} data versus predicted TT_{ia} for the best preliminary transition temperature recovery model are shown in Figure 6. The overall fit appears to be reasonable.

DISCUSSION

The preliminary upper shelf model described by Figure 5 is remarkably effective. The standard error is not substantially different from the level of error expected in repeated Charpy tests at the same conditions. Interestingly, the variables related to annealing process, T_a and t_a are the least sensitive. No significant effect of any chemical composition variable was found. It appears that all of the annealing treatments represented in the available database produced similar recovery of upper shelf energy, such that the upper shelf energy after annealing is more sensitive to the unirradiated and irradiated values of USE than to the annealing treatment. Whatever effect of material composition exists, it is apparently reflected in the unirradiated and irradiated values of USE.

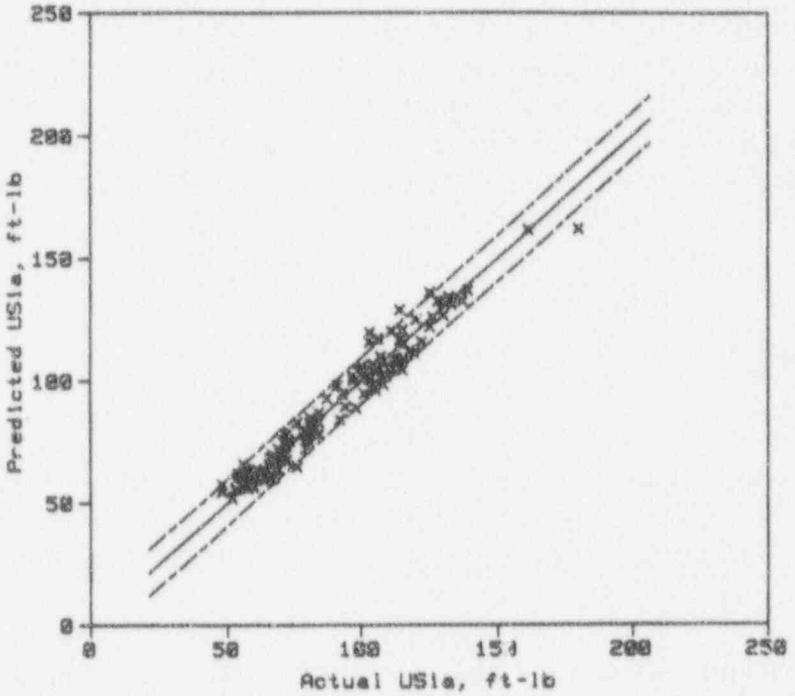


Figure 5. Predicted vs. actual US_{la}, with 95% bounds

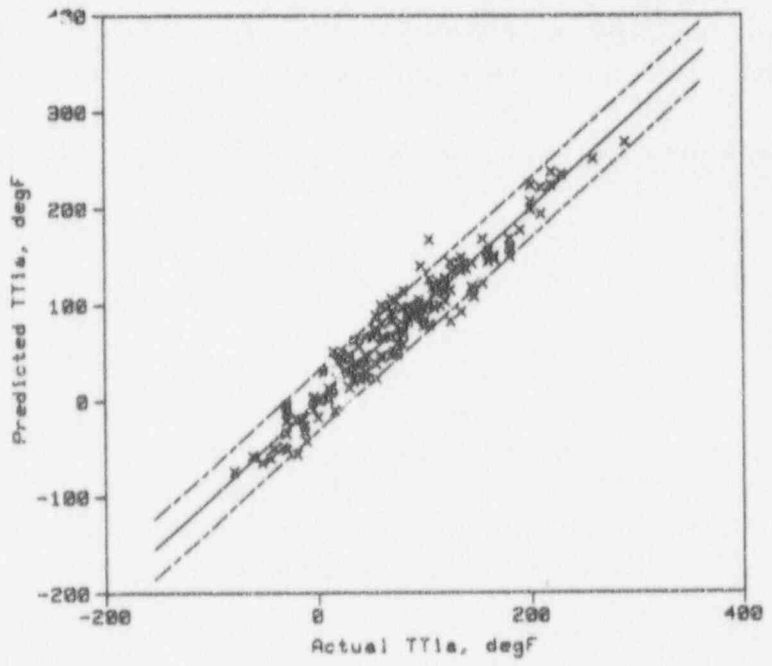


Figure 6. Predicted vs. actual TT_{la}, with 95% bounds

The transition temperature model is also good, as shown by Figur Evaluation of both models is continuing at the time this paper is being written. H..ce, both models given above are preliminary and subject to change. Additional input from mechanisms research may occur after results of the current iteration are reviewed. In addition, all potential outliers (i.e., data points that are outside the 95% bounds in Figures 5 and 6) are being investigated in more detail. The final iteration will reflect both the mechanistic input and any revisions to the database.

CONCLUSIONS

- Several potential measures of annealing recovery were investigated, as shown in Table 3. The best correlations were obtained using the final annealed values of transition temperature and upper shelf energy as the dependent variables.

- Preliminary models have been developed for predicting the final values of Charpy transition temperature (30 ft-lb) and upper shelf energy after irradiation and annealing.

- Potential dependence on material composition was considered for both TT and USE models, with the result that the TT model depends on Cu, while the USE model does not depend on any composition variables.

- The results presented here should be considered preliminary and subject to change.

ACKNOWLEDGMENTS

The authors appreciate the advice and assistance provided by A. Hiser, A. Taboada and M. Mayfield at the NRC, R. Nanstad, B. Corwin, F. Kam and J. Wang at ORNL, R. Hawthorne at MEA, and R. G. Odette at U.C. Santa Barbara. This work is performed under contract NRC-04-92-048, A. Hiser Project Manager.

REFERENCES

1. F. W. Stallman, F. B. K. Kam, B. J. Taylor, "PR-EDB: Power Reactor Embrittlement Data Base, Version 1," NUREG/CR-4816, Revision 1, May 1991.

2. F. W. Stallman, J. A. Wang, F. B. K. Kam, "TR-EDB: Test Reactor Embrittlement Data Base, Version 1," NUREG/CR- , June 1993.

3. U. Potapovs, G. W. Knighton and A. S. Denton, "Critique of In-Place Annealing of SM-1A Nuclear Reactor Vessel," American Society of Mechanical Engineers, Paper 67-WA/ER-3, November 1967; also, Nuclear Engineering and Design, Volume 8, 1968, pp. 39-57.

4. A. E. Powers, "Post-Irradiation and Co-Irradiation Annealing of Iron and Steel," Knolls Atomic Power Lab Report, KAPL 3440, Sept. 1968.

5. B. Macdonald, "Post-Irradiation Annealing Recovery of Commercial Pressure Vessel Steels," Effects of Radiation on Materials: Twelfth International Symposium. ASTM STP 870, F. A. Garner and J. S. Perrin, Eds., American Society for Testing and Materials, Philadelphia, 1985. pp. 972-978.

6. E. D. Eason, J. E. Wright, E. E. Nelson, "Multivariable Modeling of Pressure Vessel and Piping J-R Data," NUREG/CR-5729, May 1991.

7. E. D. Eason, J. E. Wright, E. E. Nelson, "Multivariable Modeling of Reactor Pressure Vessel Weld Fracture Toughness," presented at the 5th International Symposium on Environmental Degradation of Materials in Nuclear Power Systems - Water Reactors, Monterey, California, August 1991.

VVER-440 DOSIMETRY AND NEUTRON SPECTRUM BENCHMARK*

E. Sajo† and F. B. K. Kam

Oak Ridge National Laboratory
†Louisiana State University Nuclear Science Center

ABSTRACT

Light Water Reactor (LWR) benchmark experiments performed in the United States under the Surveillance Dosimetry Improvement Program (SDIP), in general, reported measured reaction rates and not neutron flux spectrum. The VVER-440 benchmark experiments, using a combination of spherical hydrogen-filled proportional counters and a stilbene scintillator detector, were measurements that provided a direct verification of the transport neutron flux spectrum. The original SAILOR cross-section library[1] from ENDF/B-IV were used, except that the iron, hydrogen, and oxygen values from ENDF/B-VI were inserted.

A linear-least-squares analysis showed that the average difference between calculations and measurements below 10 MeV was

a) less than 6% at the surveillance position;
b) less than 5% at the pressure vessel (PV) inner surface;
c) less than 6% at 1/3 thickness into the PV (1/3 T);
d) less than 17% at 2/3 thickness into the PV (2/3 T); and
e) less than 24% at the PV outer surface.

INTRODUCTION

Pressure vessel embrittlement from neutron exposure is a major concern in the operation of commercial nuclear power reactors. The shift in the nil ductility transition temperature has a direct effect on the operational lifetime of a reactor. One of the important parameters, the neutron fluence spectrum, has been investigated extensively in previous U.S. dosimetry benchmarks. However, the transport procedures used to calculate the neutron flux spectrum were, in general, verified in benchmark experiments that measured integral quantities like reaction rates while the present benchmark experiment provides measured neutron spectrum for comparison. The experimental results span the important energy range for embrittlement from about 0.1 to 10.0 MeV. The objective is the comparisons of neutron spectra

*Research sponsored by the Office of Nuclear Regulatory Research, Division of Engineering, U.S. Nuclear Regulatory Commission, under Interagency Agreement 1886804158 with the U.S. Department of Energy under contract DE-AC05-840R21400 with Martin Marietta Energy Systems, Inc.

and of integral flux values in five reactor locations: the surveillance position (R2), the PV inner surface (R3), the 1/3 T position (R4), the 2/3 T position (R5), and the PV outer surface (R6). This benchmark will add to the verification of transport calculational procedures and data bases used in the United States as well as contributing to information exchanges with colleagues who are working in the same area, but on commercial power reactors specifically designed in Russia.

The most recent cross-section evaluations for H, O, and Fe from ENDF/B-VI were used in the 47-group SAILOR library for this evaluation. The complete cross-section libraries derived from ENDF/B-VI data files are being extensively tested in a number of test and power reactor benchmarks,[2-4] but were not available for this study.

2 DESCRIPTION OF THE EXPERIMENT

A multipurpose design[5,6] of the VVER-440 and VVER-1000 assemblies in symmetric or nonsymmetric arrangements with the standard or variable pitch in a triangular-core lattice was constructed in the LR-0 experimental reactor at the Nuclear Research Institute (NRI), Rez, Czech Republic. The experimental and theoretical studies started with a contract between NRI and Skoda Concern, and were later joined by IAE, Moscow. The experimental setup represents a full-scale model in radial direction from the core to the biological shield, including the core periphery and the radial shielding heterogeneities of the VVER-type reactors. The present study focuses on the VVER-440 benchmark experiment.

2.1 Layout of the LV-0/VVER-440

A sixty-degree symmetry sector of the VVER-440 was set up at the LR-0. A 30° part of this layout, symmetrical to the 0° line, is shown in Fig. 1. In the ensuing analysis, the discussion will be restricted to this symmetry segment. The core lattice is hexagonal, and the symmmetry segment shows only 37 assemblies. The fuel composition in the core was chosen so that the radial-azimuthal power distribution in its peripheral region would closely approximate the equilibrium power distribution present in commercial VVER-440 reactors. This is important in that the two outer peripheral assemblies account for the largest contribution to the fast neutron flux incident on the PV. Also, there is a size difference: 147 mm for the peripheral fuel assemblies and 143.5 mm for the internal fuel assemblies. As a result, there is a significant number of water gaps between the internal assemblies that are evenly distributed in the geometric model of the calculations. The water gaps present between the boundary assemblies are modeled by removing one row of fuel rods from the periphery of each adjacent boundary assembly.

The active height of the fuel rods in this experiment is 1250 mm. At the bottom of the core, apart from the supporting steel structure, there is a 120-mm water layer. There is no axial reflector at the top of the core and there are no control rods present. The power of the core is controlled mainly

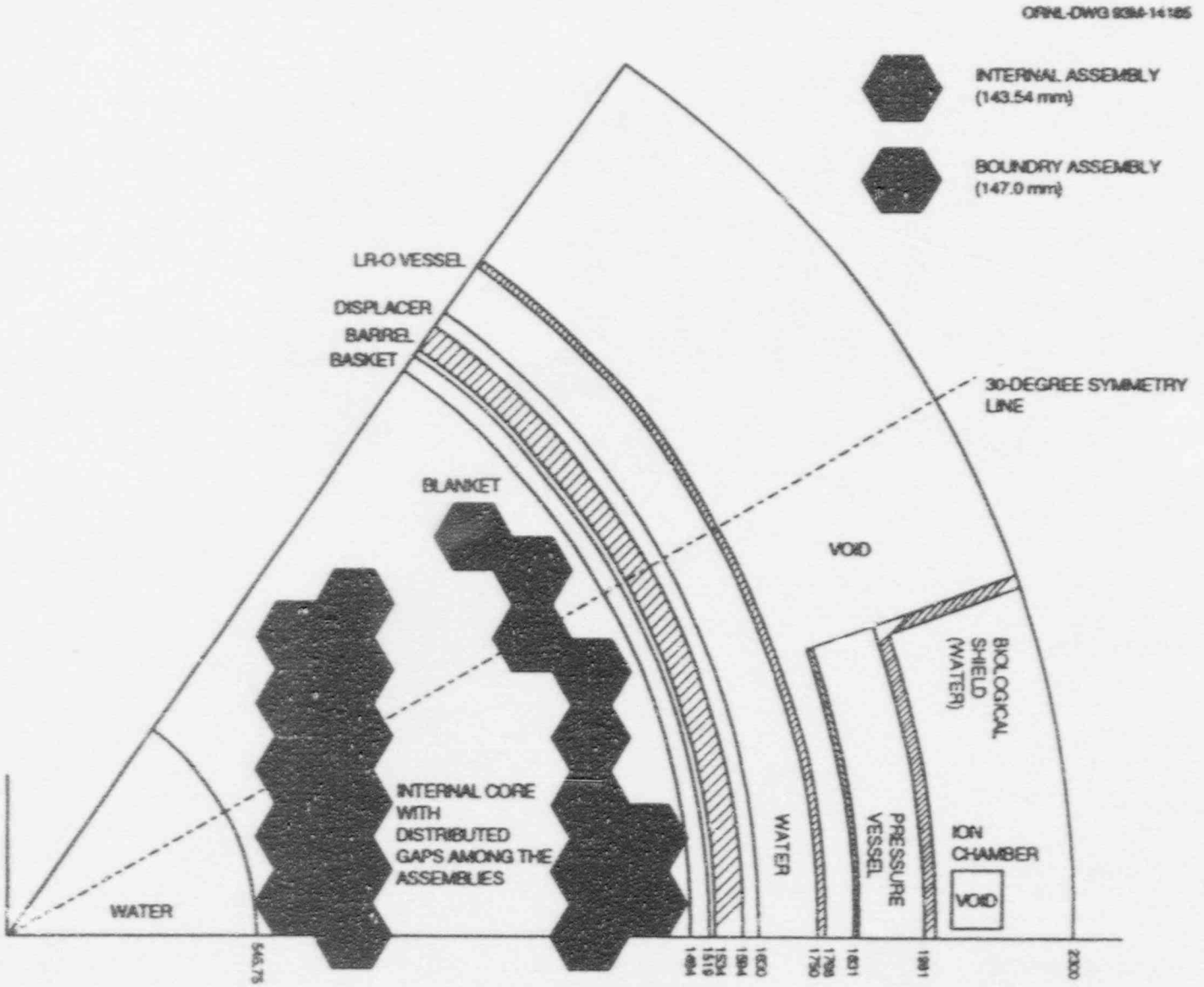


Fig. 1 LR-O/VVER-440 mockup, configuration A (PV at biological shield)

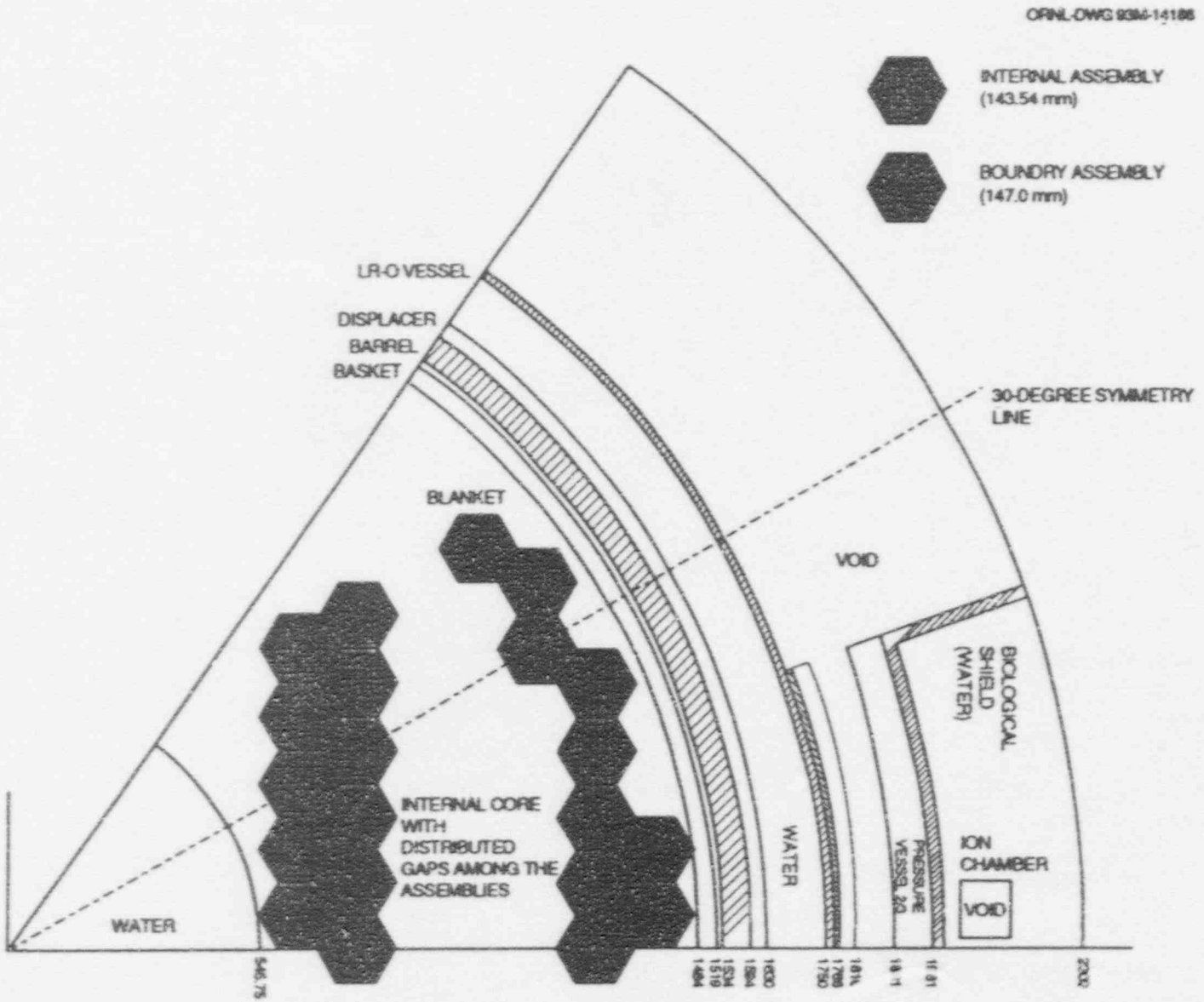


Fig. 2 LR-0/VVER-440 mockup, configuration B (1/3 PV at biological shield)

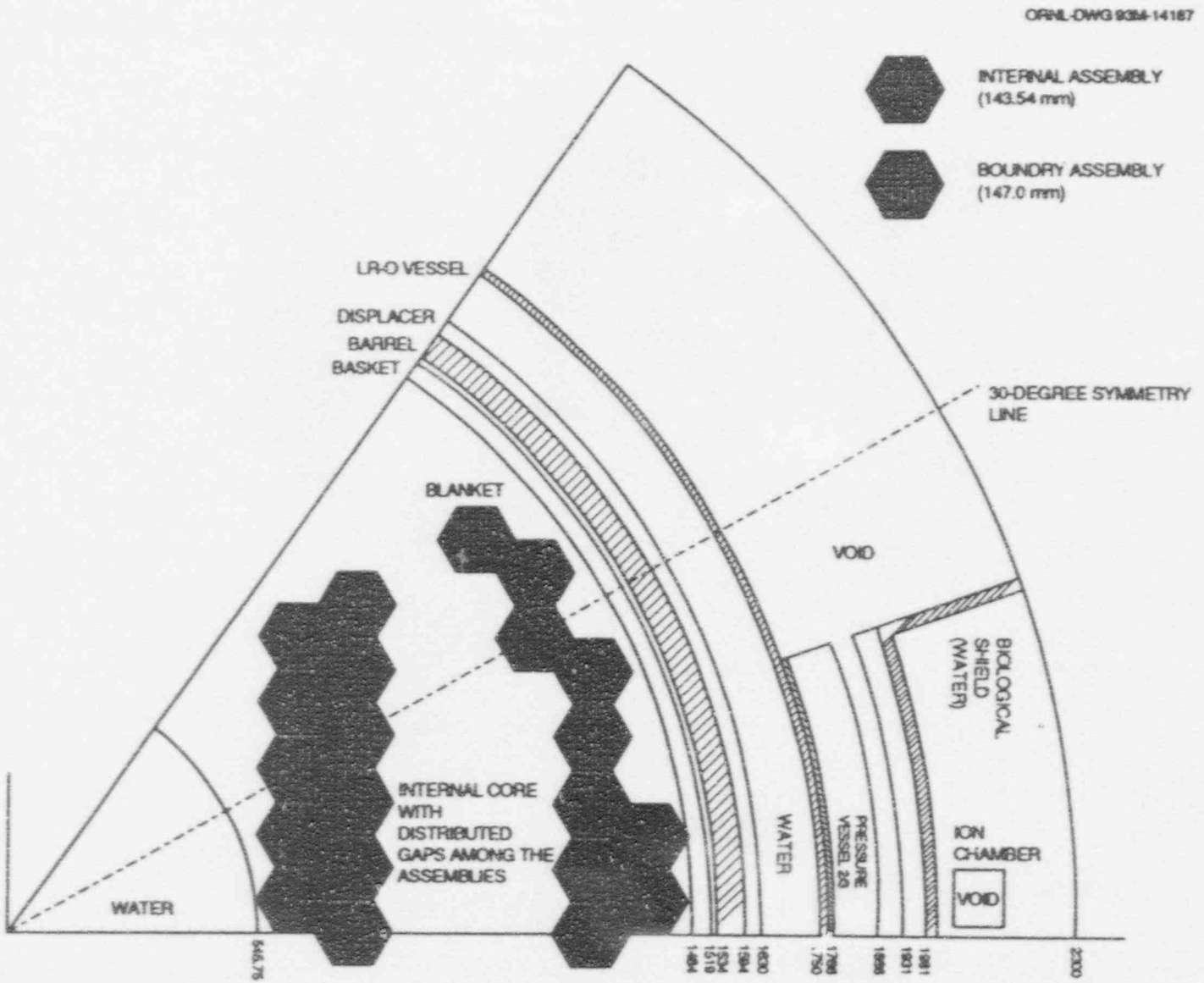


Fig. 3 LR-CWER-440 mockup, configuration C (2/3PV at LR-O Vessel)

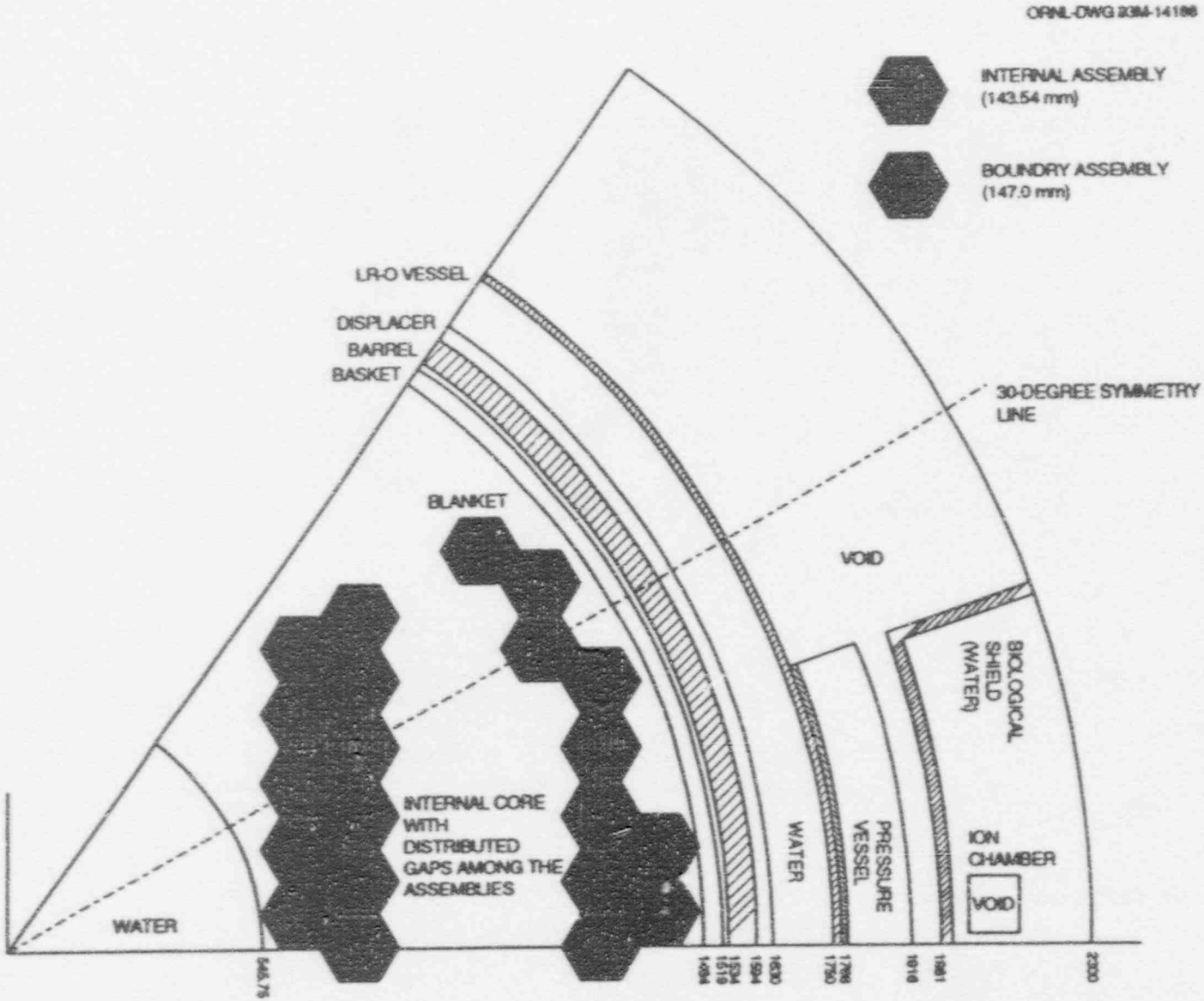


Fig. 4 LR-OVVER-440 mockup, configuration D (PV at LR-O Vessel)

by changing the moderator level. To simulate the operational water temperature and thus the reduced water density in the VVER-440 power reactor, a steel displacer tank (1-mm-thick wall) with a 34-mm void inside is placed in the water gap between the barrel and the LR-0 vessel.

The pressure vessel consists of three 50-mm-thick sections with the innermost section clad with 10-mm austenitic steel. These sections can be shifted radially to form a 65-mm air gap (Figs. 1-4). The biological shield consists of water in a 25-mm-thick-steel tank and a vertical channel to insert an ion chamber. The azimuthal extent of both the PV and the biological shield is approximately half of that of the core.

2.2 Experimental Measurements

The neutron spectra were measured in the energy range of 10.0 keV to 10.0 MeV. The measurements used a 10 mm by 10 mm stilbene scintillation detector for the energy interval 0.5 to 10.0 MeV, and two 40-mm-diameter spherical hydrogen-filled proportional counters with 981 kPa and 392 kPa pressures for energy ranges 0.3 to 1.4 MeV and 0.01 to 1.0 MeV, respectively. The experimental results (50 logarithimically equidistant points per decade) were smoothed using a cubic parabola through 5 to 9 points depending on the statistical spread. The energy boundaries of the spectrum provided to the authors were collapsed to coincide with the 47-group structure of the SAILOR library.

The neutron spectra were obtained at five different positions on the midplane of the reactor corresponding to the 0° azimuth. The five positions are at the surveillance location (R2), at the PV inner surface (R3), at the 1/3 T location into the PV (R4), at the 2/3 T location into the PV (R5), and at the PV outer surface (R6). The sequence of these measurements involved four separate geometrical configurations that are varied by moving the three 50-mm-thick sections of the PV (Figs. 1-4).

3 NEUTRON TRANSPORT METHODOLOGY

Because of the three dimensional (3-D) nature of the source and reactor geometry irregularities, the flux distribution in the PV will also vary in three dimensions. However, since all the measurements were performed at the midplane of the reactor, a 3-D synthesis technique[7] was used. The calculations were performed using the DOT 4.3 discrete-ordinates transport code[8] with an S_8 angular quadrature set and a P_3 cross-section expansion. In the RΘ model, reflected boundaries were placed at 0° and 30°, and vacuum boundaries at R=0 and R-2300 mm. The RZ model corresponds to the reactor geometry at Θ=0. The one-dimensional model in R direction is the 0° mid-plane radial transverse of the RZ model.

The neutron source distribution in the core was determined employing the DOTSOR code,[9] and the flux synthesis was performed using the DOTSYN code.[9] The pin-wise powers of the peripheral assemblies and the assembly-wise average power distribution of the inner bundles were given to the authors on a

diskette. The calculations used the SAILOR library (ENDF/B-IV) supplemented with the recently processed ENDF/B-VI cross sections for Fe, H, and O. To account for the higher temperature and consequently lower density water present in the actual VVER-440 reactors, the LR-0 experiment used an empty tank to displace water between the barrel and the LR-0 vessel.

4 COMPARISON OF CALCULATIONS AND MEASUREMENTS

To compare the calculations with the measurements, all calculated fluxes were normalized to the integral flux above neutron energy of 1.0 MeV (Φ (E > 1.0 MeV)) at location R2. This normalization was done to be consistent with the experimental data procedure adopted by the experimenters. The radial dimension of the detector locations are R2=1621 mm, R3=1771 mm, R4=1821 mm, R5=1871 mm, and R6=1921 mm. The uncertainty of these values was ±2 mm.

The comparison of the spectra between the calculations and measurements at R2 is shown in Figs. 5 and 6. The agreement between 0.3 to 10.0 MeV is very good. Above 10.0 MeV the experimental spectrum was extrapolated using a fission spectrum. A linear-least-squares analysis yields a difference of 5% below MeV, and 8% above MeV. Over the energy range 0.1 to 10.0 MeV the mean of the differences was about 6%.

The agreement at the R3 location is excellent (Figs. 7 and 8). However, it is partially due to the normalization of all data to the flux greater than 1 MeV at this position. A linear-least-squares regression analysis shows that the average relative difference between the calculated and measured values is within 5% below 3.5 MeV and about 7% above 3.5 MeV. In the energy range 0.1 to 10.0 MeV, the mean difference is about 4%.

Since the simulated steel PV consisted of three 5-cm-thick sections, measurements of the neutron fluxes were also performed at the 1/3 and 2/3 thicknesses and at the PV outer surface by shuffling the different sections.

At R4, the calculated flux values underestimated the experimental results by approximately 5% on the average (Figs. 9 and 10). This agreement is very good considering that the experimental uncertainty in the energy interval between 0.1 and 10.0 MeV varies from about 4 to 18%.

At 2/3 thickness into the PV (Figs. 11 and 12) the comparison between the calculations and measurements shows large differences. What was unexpected is the fact that the calculations exceeded the measurements. The linear-least-squares analysis shows a mean relative difference of about 17%.

At the outer surface (Figs. 13 and 14) the calculations exceeded the measurements even more than at R5. The overall mean relative difference was approximately 23% between 0.1 and 10.0 MeV.

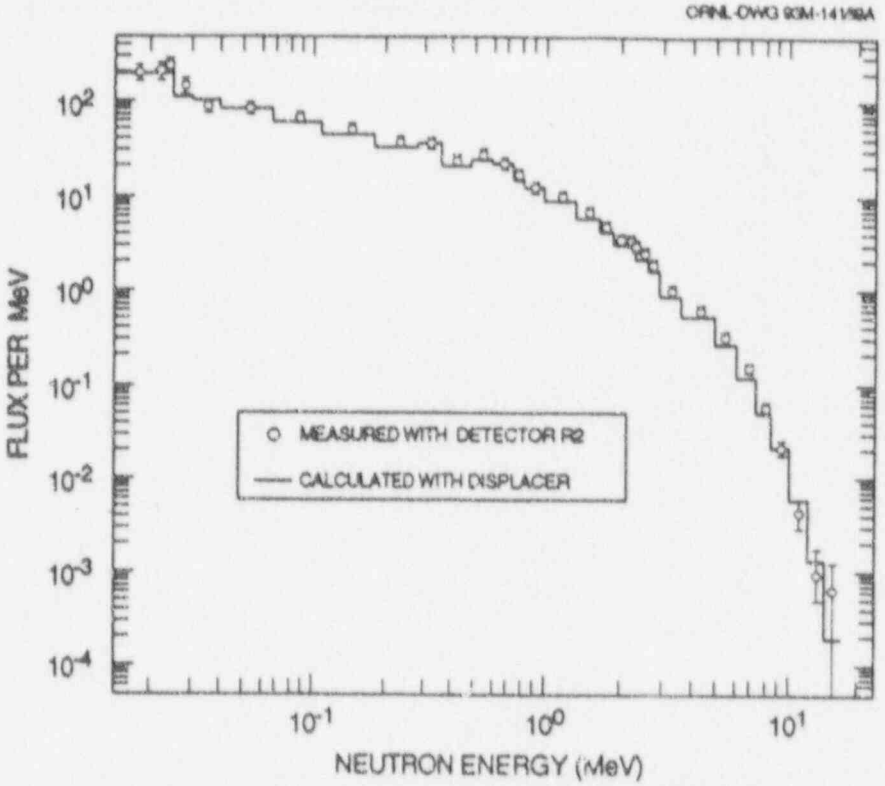


Fig. 5 Spectra at the surveillance position [R2] (configuration A)

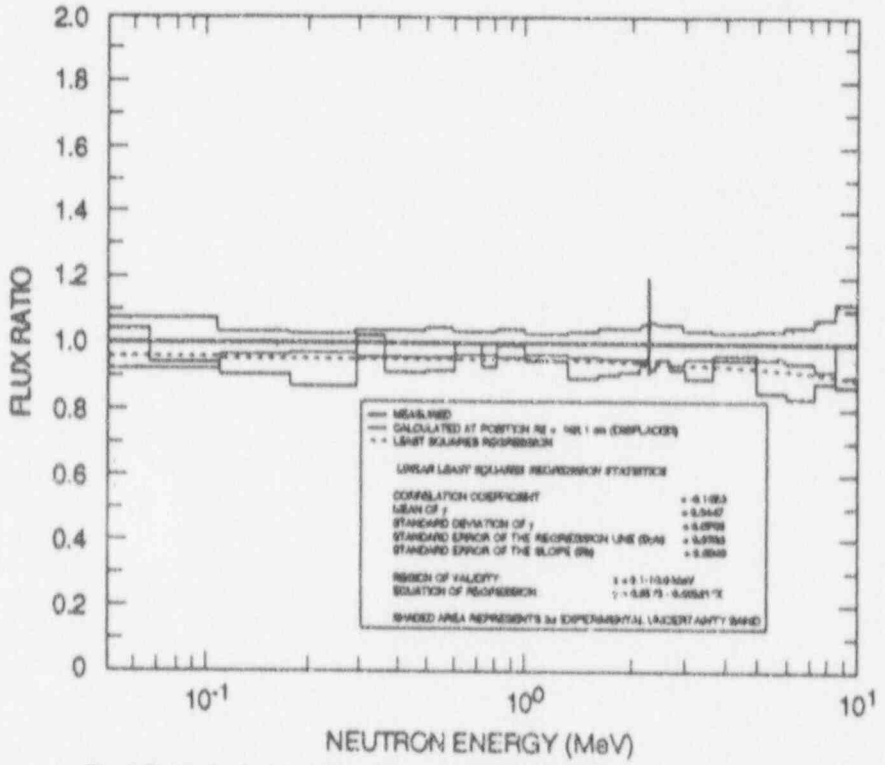


Fig. 6 Ratio of calculated vs. measured spectra, surveillance position (configuration A)

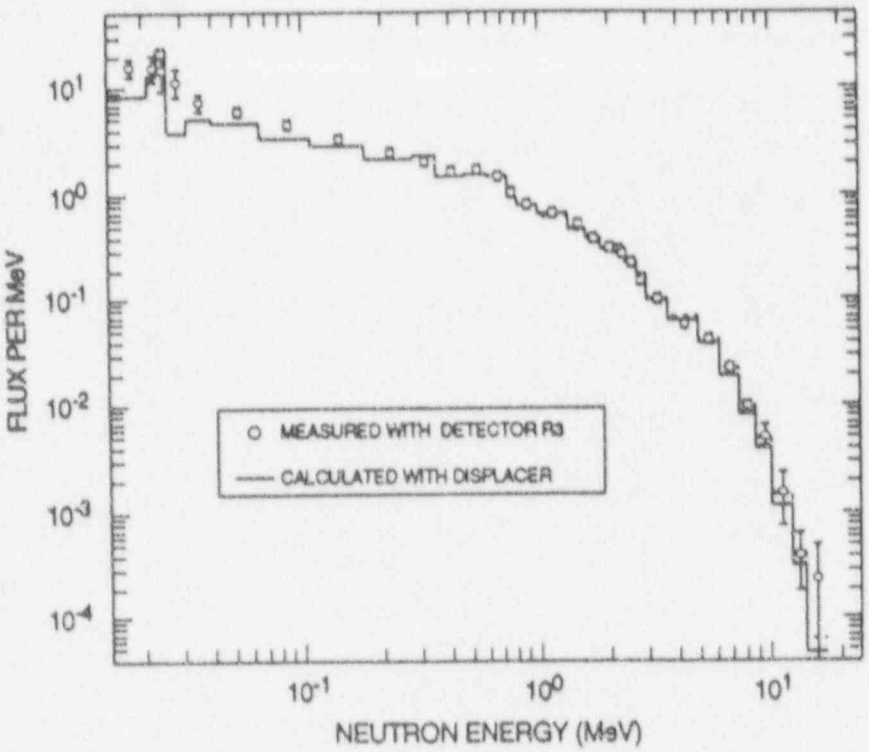


Fig. 7 Spectra at pressure vessel inner surface [R3] (configuration A)

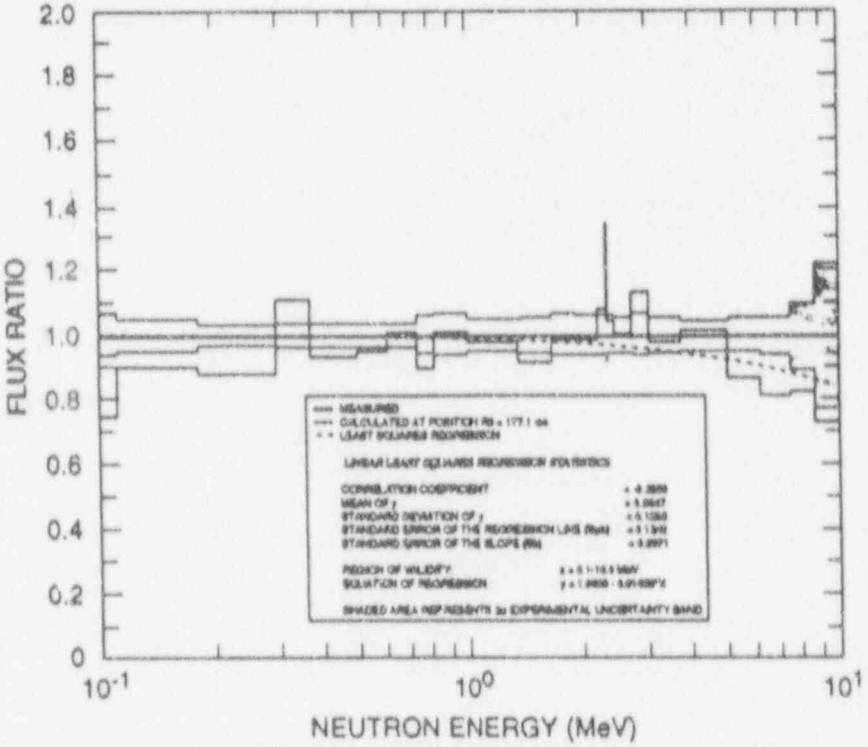
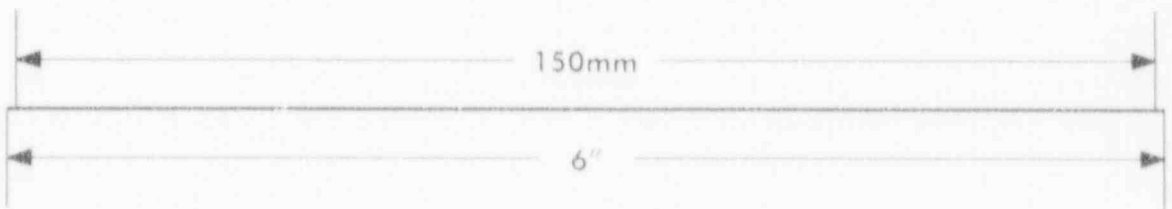


Fig. 8 Ratio of calculated vs. measured spectra, PV inner surface (configuration A)

2

IMAGE EVALUATION TEST TARGET (MT-3)



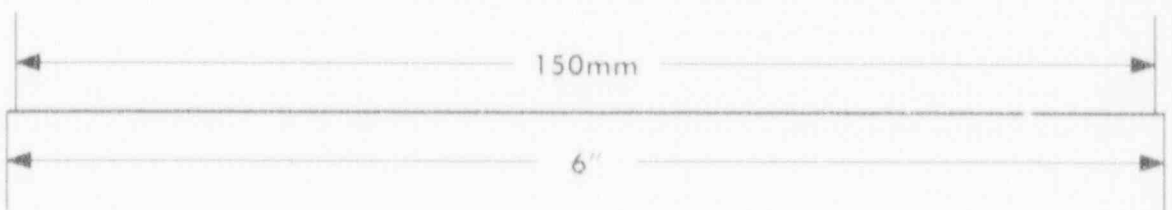


PHOTOGRAPHIC SCIENCES CORPORATION
770 BASKET ROAD
P.O. BOX 338
WEBSTER, NEW YORK 14580
(716) 265-1600

2

IMAGE EVALUATION TEST TARGET (MT-3)



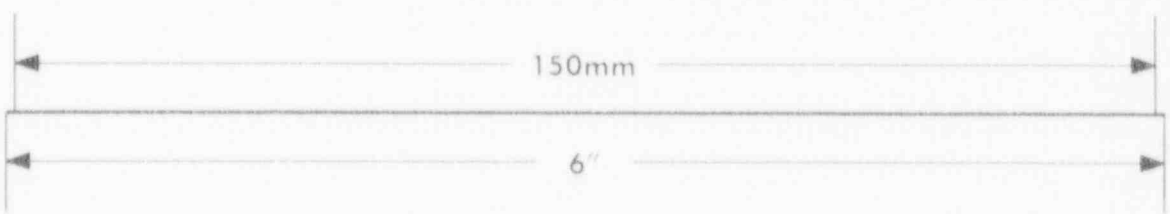


PHOTOGRAPHIC SCIENCES CORPORATION
770 BASKET ROAD
P.O. BOX 338
WEBSTER, NEW YORK 14580
(716) 265-1600

2

IMAGE EVALUATION
TEST TARGET (MT-3)



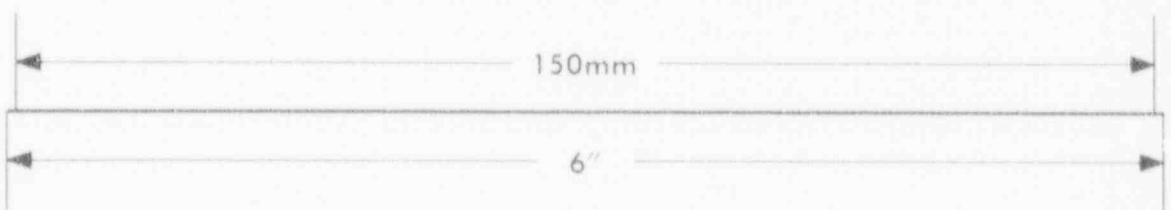


PHOTOGRAPHIC SCIENCES CORPORATION
770 BASKET ROAD
P.O. BOX 338
WEBSTER, NEW YORK 14580
(716) 265-1600

2

IMAGE EVALUATION TEST TARGET (MT-3)



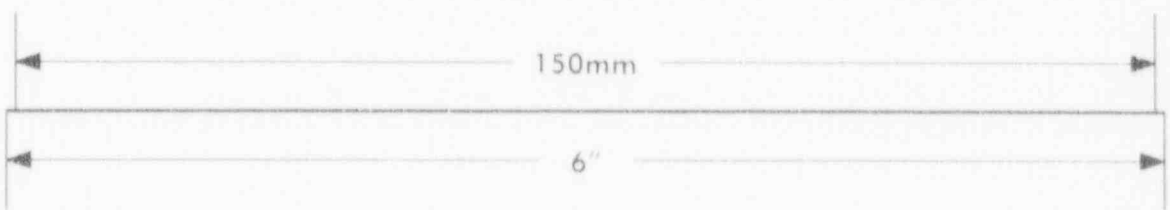


PHOTOGRAPHIC SCIENCES CORPORATION
770 BASKET ROAD
P.O. BOX 338
WEBSTER, NEW YORK 14580
(716) 265-1600

2

IMAGE EVALUATION TEST TARGET (MT-3)
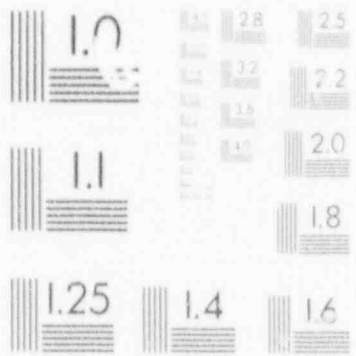


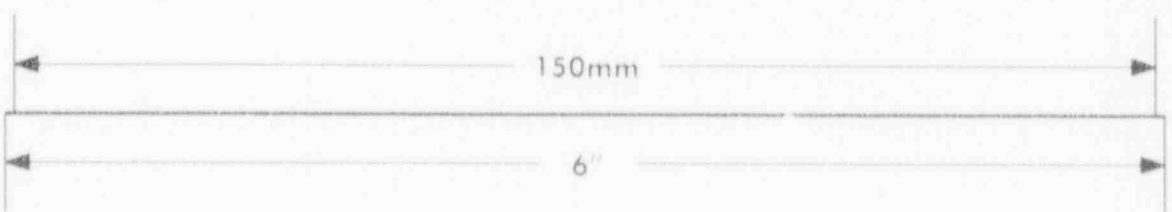


PHOTOGRAPHIC SCIENCES CORPORATION
770 BASKET ROAD
P.O. BOX 338
WEBSTER, NEW YORK 14580
(716) 265-1600

2

IMAGE EVALUATION TEST TARGET (MT-3)





PHOTOGRAPHIC SCIENCES CORPORATION
770 BASKET ROAD
P.O. BOX 338
WEBSTER, NEW YORK 14580
(716) 265-1600

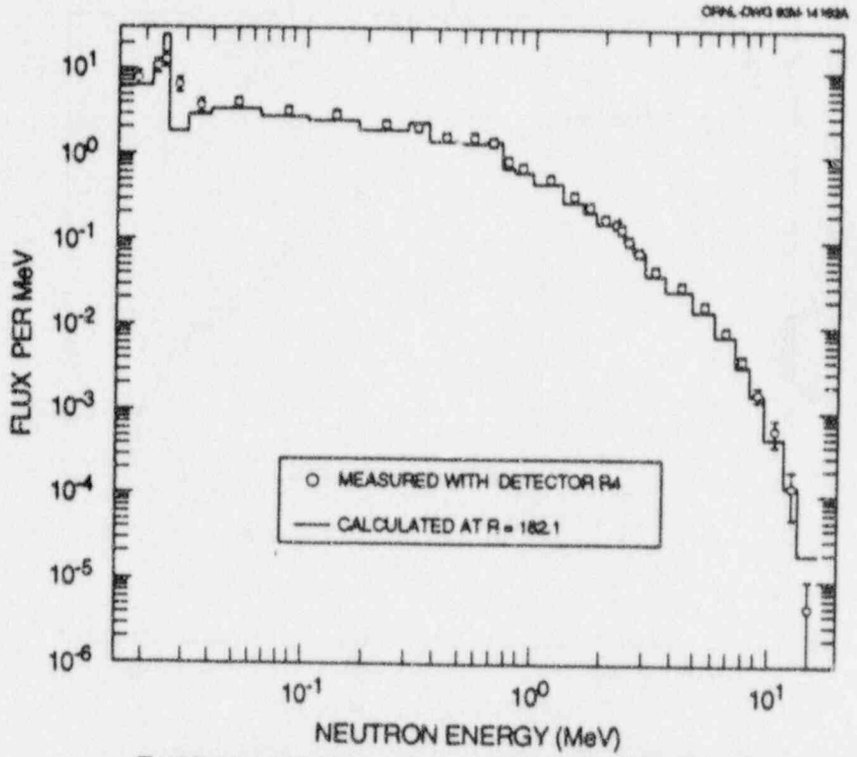


Fig. 9 Spectra at 1/3 thickness of the pressure vessel [R4] (configuration B)

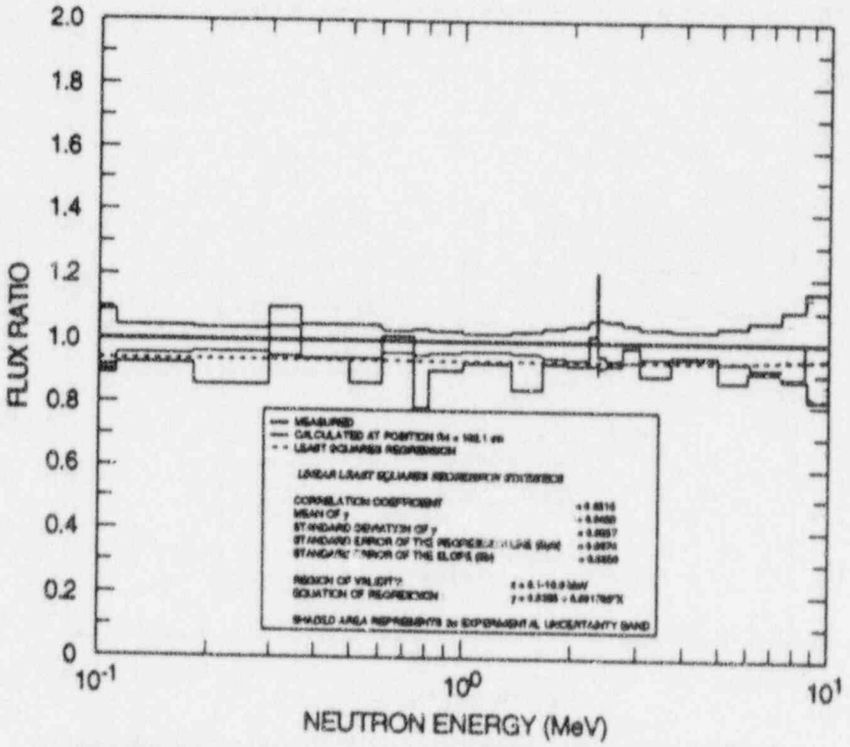


Fig. 10 Ratio of calculated vs. measured spectra at 1/3 thickness of PV (configuration B)

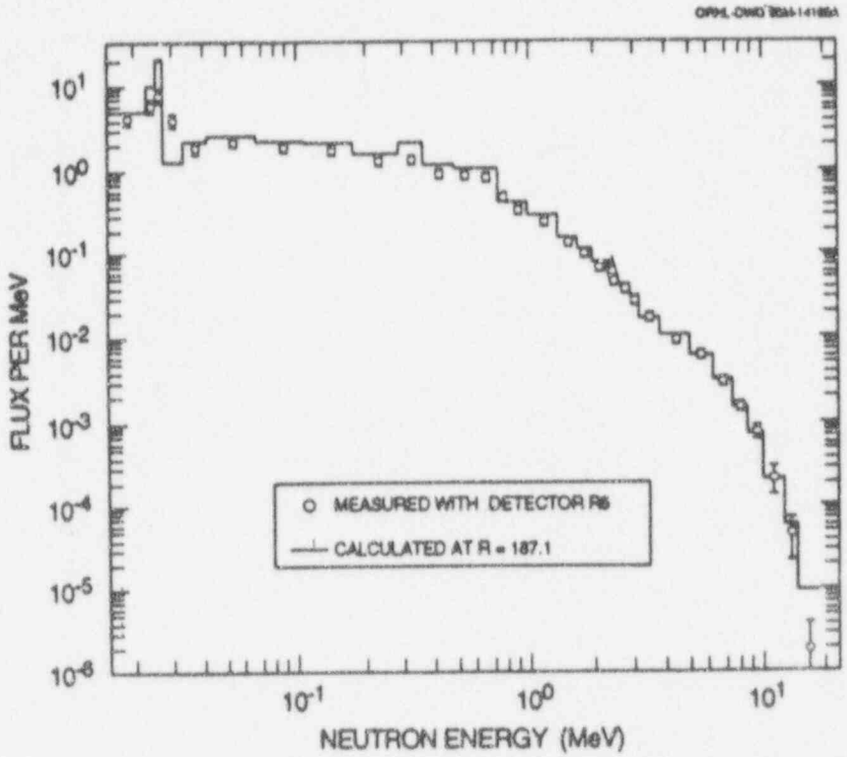


Fig. 11 Spectra at 2/3 thickness of the pressure vessel [R5] (configuration C)

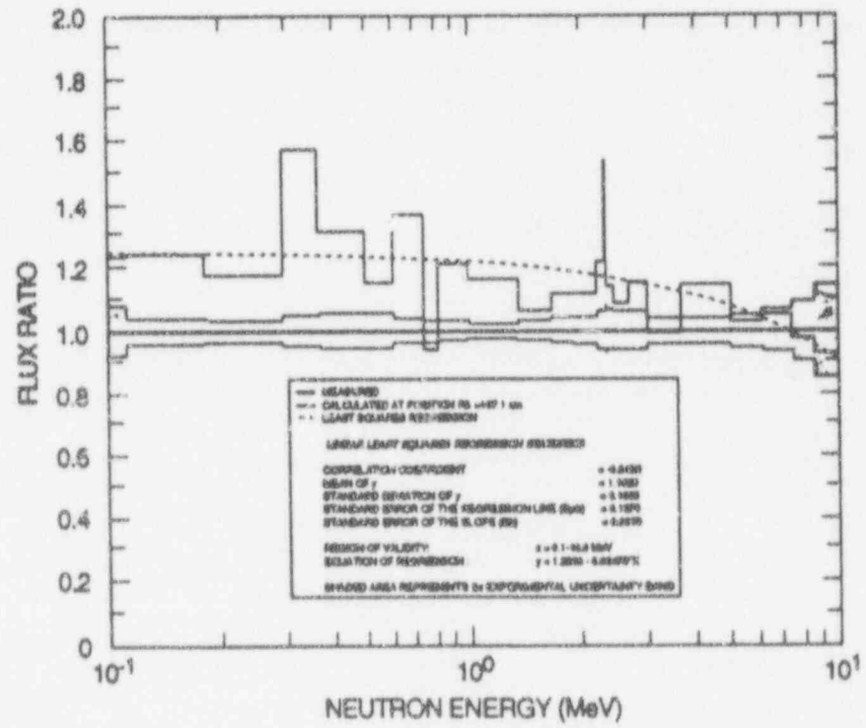


Fig. 12 Ratio of calculated vs. measured spectra at 2/3 thickness of PV (configuration C)

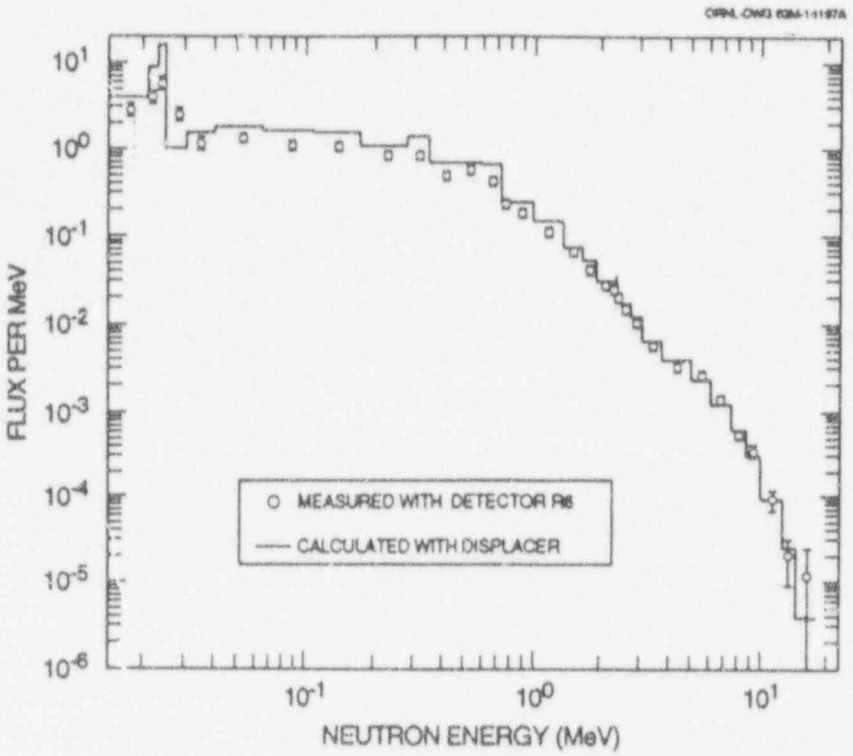


Fig. 13 Spectra at the pressure vessel outer surface [R6] (configuration D)

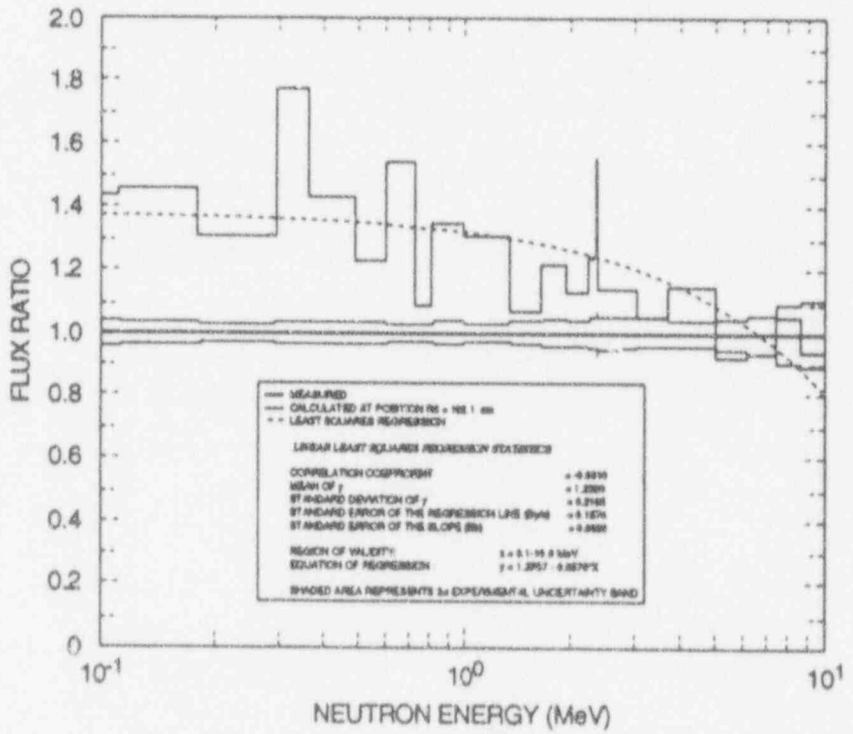


Fig. 14 Ratio of calculated vs. measured spectra, PV outer surface (configuration D)

5 CONCLUSIONS

The transport calculations of the neutron spectra agree very well (less than 6% on the average) relative to the measurements at the surveillance position, at the PV inner surface, and at 1/3 thickness into the PV of the LR-0/VVER-440 benchmark experiment. However, at 2/3 thickness into the PV and at the PV outer surface, the mean relative differences of the ratio between calculations and measurements were high by 17% and 23% respectively. A summary of the calculated-to-measured integral fluxes for the five locations are presented in Table 1. Discussions are under way with our Czech colleagues to review the results.

Table 1 Ratio of calculated to measured integral fluxes*

Detector Position	Φ_C/Φ_E E>0.5 MeV	Φ_C/Φ_E E>1.0 MeV	Φ_C/Φ_E E>2.0 MeV
R2	0.978	0.998	1.049
R3	0.974	1	0.988
R4	0.934	0.936	0.960
R5	1.199	1.144	1.131
R6	1.317	1.217	1.126

*Normalized to their respective Φ(R3, E>1 MeV)

6 REFERENCES

1. G. L. Simmons and R. Roussin, "SAILOR-Coupled, Self-shielded 47 Neutron, 20 Gamma-ray, P_3 Cross-section Library for LWRs," Radiation Shielding Information Center, Oak Ridge, TN 1985.

2. J. E. White et al., *Specifications for the Development of Bugle-93: An ENDF/B-VI Multigroup Cross Section Library for LWR Shielding and Pressure Vessel Dosimetry*, ORNL/TM-12230, November 1992.

3. M. L. Williams et al., "Transport Calculations of Neutron Transmission Through Steel Using ENDF/B-V, Revised ENDF/B-V and ENDF/B-VI Iron Evaluations," *Ann. Nucl. Energy*, Vol. 18, No. 10, pp. 549-565, 1991.

4. E. Sajo et al., "Comparison of Measured and Calculated Neutron Transmission Through Steel for a ^{252}Cf Source," *Ann. Nucl. Energy*, Vol. 20, No. 9, pp. 585-604, 1993.

5. B. Osmera, "Investigations for VVER Reactor Pressure Vessel Neutron Exposure Evaluation in CSFR," Nuclear Research Institute, Rez, Czechoslovakia, June 1992.

6. B. Osmera and M. Holman, "Surveillance Neutron Dosimetry and Cavity Neutron Flux Monitoring at Czechoslovakian VVER-440 Reactors," *Proceedings of the Seventh ASTM-EURATOM Symposium*, August 27-31, 1990.

7. F. B. K. Kam et al., *Pressure Vessel Fluence Analysis and Neutron Dosimetry*, NUREG/CR-5049, December 1987

8. RSIC Computer Code Collection, "DOT-4.3: Two-Dimensional Discrete Ordinates Radiation Transport Code System," Radiation Shielding Information Center, Oak Ridge, TN, 1982.

9. R. E. Maerker, B. L. Broadhead, J. J. Wagschal, and M. L. Williams, "LEPRICON: PWR Pressure Vessel Surveillance Dosimetry Analysis System," RSIC Program PSR-277, Oak Ridge National Laboratory (1990).

CURRENT RESULTS FOR THE NRC'S SHORT CRACKS IN PIPING AND PIPING WELDS RESEARCH PROGRAM

by

G. Wilkowski, P. Krishnaswamy, F. Brust, R. Francini, N. Ghadiali,
T. Kilinski, C. Marschall, S. Rahman, A. Rosenfield, and P. Scott
BATTELLE
COLUMBUS, OHIO 43201

1. INTRODUCTION

The overall objective of the Short Cracks in Piping and Piping Welds Program is to verify and improve engineering analyses to predict the fracture behavior of circumferentially cracked pipe under quasi-static loading with particular attention to crack lengths typically used in LBB or flaw evaluation criteria. The program consists of 8 technical tasks as listed below.

Task 1 Short through-wall-cracked (TWC) pipe evaluations
Task 2 Short surface-cracked pipe evaluations
Task 3 Bi-metallic weld crack evaluations
Task 4 Dynamic strain aging and crack instabilities
Task 5 Fracture evaluations of anisotropic pipe
Task 6 Crack-opening-area evaluations
Task 7 NRCPIPE Code improvements
Task 8 Additional efforts

Since the last WRSM meeting several additional tasks have been initiated in this program. These are discussed in Task 8. Based on results to date, the first seven tasks have also been modified as deemed necessary. A list of the full-scale pipe experiments in this program are given in Table 1. All but one of these tests have been completed. The most significant accomplishments in each of these tasks since the last WRSIM meeting are discussed below. The details of all the results presented here are published in the semiannual reports [Refs. 1-5] from this program.

2. Task 1 - Short Through-Wall-Cracked (TWC) Pipe Evaluations

The five subtasks in this task are:

Subtask 1.1 Material Characterization
Subtask 1.2 TWC Pipe Experiments
Subtask 1.3 Facility Modifications
Subtask 1.4 TWC Pipe Analysis
Subtask 1.5 Topical Report

Material characterization involving tensile and toughness tests on the materials used in the pipe experiments were completed and presented in References 1-3. Subtask 1.3 involving facility modification and upgrading of the pipe test system was completed. Pipe experiments and analysis efforts are discussed below.

2.1 TWC Pipe Experiments

All experiments in Subtask 1.2 have been completed. One large diameter TWC pipe test on A333 Gr6 SAW (Expt. No. 1.1.1.24) was conducted last year. The through-wall flaw for this pipe was 8 percent of the circumference and was in a carbon-high manganese-molybdenum SAW prepared according to the procedure used by Babcock & Wilcox. Figure 1 shows the load versus load-line displacement for this experiment. As shown, the crack initiated at 1.110 MN (249.5 kips). Another experiment on an A515 Gr 60 pipe involved an uncracked pipe (Expt. No. 1.1.1.25) and was conducted to determine the uncracked-moment-rotation curve to be used in developing analysis procedures. Contrary to expectation, the primary buckling took place away from the mid-plane section of the pipe as shown in Figure 2.

2.2 TWC Pipe Analysis

The overall objectives of the TWC pipe analysis efforts are: (1) to improve existing J-estimation analysis procedures, and (2) to compare the predictions of the analyses with pipe experiments from this as well as other past programs to assess the accuracy of them for short cracks. In improving estimation schemes a new method to predict the behavior of TWC in welds has been developed. This is the only J-estimation scheme that incorporates the effect of weld metal strength. This method has already been published as a technical paper, Reference 6, and will not be discussed here.

Also, part of this subtask involved correction and improvement of the GE-EPRI functions presented in the Elastic-Plastic Fracture Handbook [Ref. 7]. Development of these function have been completed. Significant errors were found in the function h_4 used to determine the rotation for the fully plastic case. This error is apparent in Figure 3 which shows a comparison between the original and the modified functions for $R_m/t = 10$ and 20. The error in h_1, the function relating to J was not significant. The complete set of GE-EPRI functions developed in this program are presented in References 3 and 5 and will also be part of the topical report on this task. Analysis of the experiments using available estimation schemes as well as those developed in this program has begun. Figure 4. shows a comparison of these predictions with two experiments. From this figure, three observations can be made.

(1) Short cracks fail closer to the Net-Section-Collapse analysis (limit-load) than long cracks,
(2) There is more scatter in the predictions by the various analyses methods for shorter crack lengths, and
(3) the ASME Section XI Z-factor approach for short cracks, typical of LBB size cracks in larger diameter pipe, is very conservative.

Analysis of other experiments is underway and will be reported in future publications as well as the topical report on this task to be prepared at the end of the program.

3. Task 2 - Short Surface-Cracked Pipe Evaluations

The five subtasks in this task are:

Subtask 2.1 Material Characterization
Subtask 2.2 Small-Diameter Surface-Cracked Pipe Experiments
Subtask 2.3 Large-Diameter Surface-Cracked Pipe Experiments
Subtask 2.4 Surface-Cracked Pipe Analyses
Subtask 2.5 Topical Report.

Key results in material characterization, pipe experiments and the analyses activities are described below.

3.1 Material Characterization

All material characterization efforts involving tensile properties and J-R curves have been completed in this task. One key observation was that the test temperature affected the fracture resistance of the weld DP2-F49W significantly. This weld was made using a C-Mn-Mo weld procedure from Babcock & Wilcox used in their plants. Figure 5 shows a composite J-R curve graph for all the compact tension C(T) specimens tested. The average value of J_i at 288 C (550 F) was approximately sixty percent of the room temperature average. The dJ/da averaged one quarter to one third of the room temperature values depending on the side grooving. Note that the room temperature tests J-R curves terminated with a cleavage fracture.

3.2 Surface-Cracked Pipe Experiments

This task involves conducting smaller diameter pipe experiments with short circumferential surface cracks, to determine the effects of crack size on the Net-Section-Collapse analysis, and large diameter pipe experiments where elastic-plastic fracture may occur.

As seen in Table 1, all but one of the surface-cracked pipe experiments have been completed. Two of these (Expt. No.'s 1.2.3.15 and 1.2.1.20) have been conducted since the last WRSIM meeting. The flaw for Expt. No. 1.2.3.15 was 50 percent of the wall thickness and 25 percent of the circumference. The loading conditions were quasi-static and involved a constant internal pipe pressure of 9.56 MPa (1.39 ksi), the pressurizing medium being subcooled water. Figure 6 shows the load versus load-line displacement curve for this test. As seen the maximum applied load was 1.06 MN (239 kips) corresponding to a maximum bending moment of 2.19 MN-m (19,400 in-kips). The crack broke through at the maximum load.

Experiment 1.2.1.20 also had a flaw of 50 percent of the wall thickness and 25 percent of the circumference and was introduced using the same procedure described above. This pipe was donated by Westinghouse Savannah River Corporation and run at their operating temperature and pressure. The test temperature was 99 C (210 F). The pipe was loaded monotonically in 4-point bending with an internal pressure of 1.55 MPa (225 psi). Figure 7 shows the load versus load-point displacement curve from this experiment. As indicated, the crack initiated at 140 kN with the maximum load being 173 kN (38.9 kips). The crack broke through at maximum load after which the resulting TWC was tested further as indicated in Figure 7. Cooperative finite element analyses with Westinghouse Savannah River Corporation staff on this experiment are underway.

3.3 Surface-Cracked Pipe Analysis

Significant progress was made in the surface-cracked pipe analysis procedures. Figure 8 shows a plot of the ratio of the experimental stress to the predicted stress as a function of pipe radius-to-thickness ratio (R/t) for all data available. As seen, the small diameter pipe experiments showed that the Net-Section-Collapse analysis should have an R/t correction that is independent of the flaw size.

Several activities were undertaken as part of the analyses subtasks. The activity involving the analysis of uncracked pipe was completed. The discrepancy between the finite element (FE) results and experiments observed earlier with 2D and shell element analyses was resolved. A full 3D analysis

showed good agreement with experimental results. In a separate activity, the existing SC.TNP analysis was modified and some improvements made to the estimation schemes, including developing the GE/EPRI h functions for deeply cracked 360-degree surface cracks. Two new activities were initiated. The first investigates the effect of mesh refinement on the FE analysis of surface-cracked pipes while the second evaluates J for surface-cracked pipes so as to verify J-estimation schemes developed in this program. In the mesh refinement study the most important observation made was that line-spring analyses did adequately model surface-cracked pipe. As shown in Figure 9, the load versus load-line displacement for coarse and fine mesh as well as the line-spring method agree very well with experimental observations. Similar conclusions can also be drawn about the values of J with load-line displacement.

Since very few 3D FE analyses exist for surface-cracked pipe in the literature these analyses were undertaken to verify the J-estimation schemes, such as SC.TNP or any others that are developed. The FE analyses are complete. Two new circumferential surface-cracked pipe J-estimation schemes are being developed, SC.NEW which involves slightly different assumptions than SC.TNP which occasionally has problems for growing cracks and SC.ENG which is being developed along the same lines as LBB.ENG2 for TWC pipes. The results from these analyses will be presented in the topical report on this task.

4. Task 3 - Bi-Metallic Weld Crack Evaluations

The objective of this task is to conduct experiments and develop the necessary analytical engineering estimation schemes to assess the behavior of through-wall cracks in bi-metallic welded pipe. There are four subtasks in this task. These are:

Subtask 3.1 Material Characterization
Subtask 3.2 Pipe Experiments
Subtask 3.3 Analysis of Pipe Experiments
Subtask 3.4 Topical Report

This task was initiated late last year. The material characterization efforts are almost complete. These included hardness traverses across the stainless steel to carbon steel in the weld region. A plot of this is shown in Figure 10. As seen the weld metal is 15 to 20 Rockwell B points harder than the carbon steel base metal. Microhardness readings (not shown in figure 10), showed that there was a softer region 0.2 to 1.0 mm (0.008 to 0.04 inch) from the fusion line in the carbon steel. In terms of ultimate strength, the weld metal is approximately 160 to 240 MPa (23 to 35 ksi) stronger than the carbon steel. All C(T) specimens with the crack in the fusion line have also been tested with both fatigue precracked as well as a sharp machine notch. Figure 11 shows a composite plot of the J-R curves from these specimens. In every case, the crack grew out of the weld and into the carbon steel.

The pipe experiment (No. 1.1.3.8 in Table 1) has just been conducted. The data have yet to be reduced and will be presented in the topical report along with the analysis of the experiment. An observation from the pipe test was that the crack also grew in the carbon steel base metal, perhaps in the soft region adjacent to the fusion line.

5. Task 4 - Dynamic Strain Aging and Crack Instabilities

The objective of this task is to predict the effects of crack instabilities, believed to be due to dynamic strain aging (DSA), on the fracture behavior of ferritic pipe. DSA which results in lowering the toughness and can cause unstable crack jumps occurs at certain combination of temperatures and strain rates in ferritic steels and is believed to be due to the interactions between dislocations and free nitrogen and/or carbon atoms during plastic straining. The task has been divided into four subtasks with two optional subtasks. These are:

Subtask 4.1	Establish screening criterion to predict unstable crack jumps
Subtask 4.2	Evaluate procedures for characterizing fracture resistance during crack jumps in laboratory specimens
Subtask 4.3	Assess current procedures for predicting crack jump magnitudes in pipes
Subtask 4.4	Prepare interim and topical reports
Subtask 4.5	Refine procedures for characterizing fracture resistance in laboratory specimens (Optional)
Subtask 4.6	Refine procedures for predicting crack jump magnitudes in pipes (Optional)

Since the last meeting significant progress has been made in the first two subtasks and is discussed below.

5.1 Establish Screening Criterion

A hot hardness test method has been developed as a DSA screening criterion. This criterion was developed by examining 5 different ferritic pipe steel and welds with strength and toughness tests at various temperatures, and comparing the results to high temperature hardness readings. Figure 12 shows a comparison of the hardness readings with the yield and ultimate strength data as a function of temperature. The peak in the ultimate strength curves, indicative of DSA, corresponds to a peak in the hardness readings, but with a shift in temperature. The temperature shift is a result of DSA being sensitive to loading rates also. Standard hardness tests are usually conducted at a higher rate than standard tensile tests.

As part of this effort C(T) specimens from carbon steel weld (DP2-F29W) were recently tested. Previous tensile and hardness tests had indicated that the weld would be susceptible to DSA at high temperature, i.e., temperature greater than 288 C (550 F). The load-displacement curves from these tests is shown in Figure 13. As seen, with increase in the test temperature the crack jumps are larger and less numerous. These findings further support the hypothesis that these crack jumps observed in both laboratory specimens and pipe experiments are due to dynamic strain aging and verify the DSA high-temperature hardness screening criterion.

Also, it was observed that the average crack velocity of a crack jumps was 0.5 meters/second, which is orders of magnitude slower than a cleavage fracture instability, but 40,000 times faster than the stable crack growth in standard C(T) tests. The occurrence of DSA crack instabilities appears to be probabilistic, and the best we can do at this time is to use the hot hardness test to determine if a material is susceptible to DSA at LWR temperatures. Predicting the start of a crack jump does not appear possible.

5.2 Analysis of Laboratory Specimen

The objective of this subtask is to investigate if J-based analysis can be used to assess the effect of unstable crack jumps on the fracture behavior. Therefore, one detailed FE analysis of a C(T) specimen with a distinct crack jump has been conducted to evaluate J during the crack jump process. The experimental crack growth record was used as an input to the FE analysis along with appropriate stress-strain data. A comparison between the experimental and FE load-displacement curves for specimen F26-103 is shown in Figure 14. As seen, this comparison is very good. Values of J from the FE analysis are being evaluated and shall be reported in future publications as well as the topical report on this task.

6. Task 5 - Fracture Evaluations of Anisotropic Pipe

The objective of this task is to assess if anisotropic fracture properties together with having high principal stresses in a helical direction can cause a lower failure stress than when using typical fracture analyses. Typical fracture analyses for circumferential cracked pipe use the toughness in the circumferential orientation and only the longitudinal stresses. The toughness is typically lower in the helical or axial direction than in the circumferential direction for ferritic pipe. There are three subtasks and two optional subtasks. These are:

- Subtask 5.1 Assess effect of toughness anisotropy on pipe fracture under combined loads
- Subtask 5.2 Determine magnitude of toughness anisotropy and establish a screening criterion to predict out-of-plane crack growth.
- Subtask 5.3 Prepare interim and topical reports on anisotropy and mixed-mode studies
- Subtask 5.4 Establish ductile crack growth resistance under mixed-mode loading (Optional)
- Subtask 5.5 Refine J-estimation scheme analyses for pipes (Optional)

Progress has been made in Subtask 5.2 in the last year and is discussed below.

6.1 Determine magnitude of toughness anisotropy and establish a screening criterion to predict out-of-plane crack growth

As discussed in References 3 and 4, considerable effort was made to develop a simple screening criterion to predict the tendency for out-of-plane crack growth based on microstructural examination and Charpy testing. The ratio of the Charpy Energy in the C-L orientation to the L-C orientation was defined as the anisotropy coefficient of the pipe. Microscopic examination of the inclusions revealed that elliptical-type inclusions displayed significantly lower Charpy V-notch toughness values than pipes having stringer-type inclusions. A correlation between the anisotropy coefficient and the out-of-plane crack growth was therefore attempted. Figure 15 shows a plot of the crack growth angle versus the anisotropy coefficient for both TWC and surface-cracked pipes. The scatter in this plot is considerable and it was therefore concluded that such a correlation leading to a simple screening criterion was not feasible at this time.

Based on observations, another possible source of out-of-plane crack growth seemed to be the pipe D/t ratio. Pipe with higher D/t ratios showed less out-of-plane growth. Figure 16 shows that in spite of scatter there is a distinct correlation between crack growth angle and the D/t ratio for the pipe for both TWC and surface-cracked pipe experiments. Therefore it is hypothesized that a combination of

both microstructural features and pipe dimensions determines the crack growth angle. A simple screening criterion based on material property evaluation may therefore not be possible.

FE analysis to determine the driving force and principal stresses for angled cracks in pipe is underway and will be reported in forthcoming publications and also in the topical report in this task.

7. Task 6 - Crack-Opening-Area Evaluations

The objective of this subtask is to make improvements in the crack-opening area predictions for circumferentially cracked pipe, with particular attention to cracks in welds. The crack-opening-area analyses will be incorporated into the NRCPIPE code, and then into the SQUIRT leak-rate code. There are six subtasks:

Subtask 6.1	Create combined loading improvements
Subtask 6.2	Implement short TWC crack-opening improvements
Subtask 6.3	Improve weld crack evaluations
Subtask 6.4	Modify SQUIRT code
Subtask 6.5	Prepare topical report on crack-opening area improvements
Subtask 6.6	Leak-rate quantification.

The major effort undertaken recently has been in Subtask 6.6. A probabilistic LBB analysis specifically to provide a technical basis for the NRC to evaluate their Reg. Guide 1.45 on Leakage Detection Systems was conducted. The probabilistic analysis undertaken provided conditional failure probabilities as a function of leak rate for typical PWR and BWR piping systems. Statistical parameters included the following: strength and toughness data for base and weld metals, locations of cracks in either weld metal or base metal, crack morphology parameters for IGSCC, thermal fatigue, corrosion fatigue cracks, and determination of slightly conservative bounds of the stresses in piping systems. A topical report containing the details of this analysis will be published in the future.

A new version of SQUIRT code was developed with some key modifications and has been released to the NRC. This version of the code allows the calculation of the crack length given the leak rate and the loading on the pipe which was not possible before.

8. Task 7 - NRCPIPE Code Improvements

As part of the Degraded Piping Program- Phase II, a PC computer program NRCPIPE was developed to analyze circumferential TWC pipes under combined pressure and bending using various simplified estimation schemes. The objectives of this task are to improve the existing TWC code based on the results of the above analyses and also to develop a similar code to analyze circumferential surface-cracked pipe. The various subtasks in this effort are:

Subtask 7.1	Improve efficiency of current NRCPIPE code
Subtask 7.2	Incorporate TWC improvements in NRCPIPE
Subtask 7.3	Make surface crack version of the code (NRCPIPES)
Subtask 7.4	Provide new users manuals

To date, a new version of the through-wall-crack version of NRCPIPE Version 1.4g has been issued which incorporates numerous user-friendly changes and a few technical changes. We have also developed a circumferential surface-crack J-estimation scheme code called NRCPIPES which is being beta tested. The new GE/EPRI functions and any new analyses method developed in this program will be incorporated into future versions of these codes.

9. Task 8 - Additional Efforts

To date there are six additional efforts being undertaken. These are:

Subtask 8.1	Validation of J_m Resistance Curves
Subtask 8.2	Evaluation of Fusion Line Toughness of Stainless Steel SAW
Subtask 8.3	Improvements and Addition to the PIFRAC Data Base
Subtask 8.4	Development and Expansion of a Pipe Fracture Data Base
Subtask 8.5	Archiving of Past Degraded Piping Program Pipe Fracture Data
Subtask 8.6	Evaluation of ASME Section III Proposed Allowable Stresses

Subtask 8.1 is being conducted at Brown University by Professor C.F. Shih and is scheduled for completion in the near future and is not reported on in this paper.

9.1 Fusion Line Toughness

The objective of this subtask is to examine the fracture toughness of stainless steel SAW fusion lines. The reason for this is that many of the past pipe experiments on stainless steel SAWs had the crack initially in the center of the low toughness SAW, but the cracks turned and followed the fusion line. This implied that the lowest path of fracture resistance is the fusion line, but there are no fracture toughness data on fusion lines. Additionally, past IGSCCs in thicker wall pipe, have occurred with the IGSCCs following the fusion lines.

Charpy and C(T) specimen tests for J-R curve evaluations are currently in progress. Two different welds are being tested; one with a fusion line normal to a plate surface, and another with a standard single-Vee weld. These results are currently being evaluated, and will be presented in a separate topical report.

9.2 Pipe Fracture Databases

The existing pipe fracture data base PIFRAC originally developed by MEA is now being updated at Battelle. In addition, data from current and past programs from Battelle and data from Westinghouse, GE, B&W, Argonne and Ontario Hydro are also being included in this database.

Another similar effort undertaken is the development of a spreadsheet on PC of all available circumferentially cracked pipe experiments. Table 2 lists the various programs from which this spreadsheet will be developed.

Simultaneously, data from past pipe experiments at Battelle during the Degraded Piping Program - Phase II developed on an HP data acquisition system are being converted to a uniform format PC.

9.3 ASME Section III Allowable Stress Limits

The objective of this effort was to determine the effect of increasing the allowable elastic stress value in the ASME Section III Code from $3S_m$ to $7S_m$ on critical flaw sizes for surface-cracked pipe. For combined bending and pressure loads increasing the allowable stress leads to higher allowable moments resulting in smaller critical flaw sizes.

Since $7S_m$ corresponds to a value that is more than twice the flow stress for most steels a nonlinear correction needs to be made in calculating the applied moment. Several FE analyses have been conducted to determine the actual applied moment corresponding to both $3S_m$ and $7S_m$ allowable stresses. Using the net-section-collapse (limit-load) analysis, allowable flaw sizes were determined for these values of applied moment. Figure 17 shows a plot of the crack aspect ratio (d/t) versus crack length for nominal 16-inch diameter TP304 stainless steel and A106 Grade B pipe with an R/t=10. As shown, the critical flaw sizes for $7S_m$ allowable stress is much lower but still above the ASME workmanship standards assuming all stresses above yield are displacement-controlled.

10. Conclusions

There are over 80 separate technical activities being undertaken in this program to provide basic improvements in the understanding of fracture phenomena and improvements to engineering analyses for piping fracture evaluations. This information provides a technical basis for technology transfer with codes and standards work and technical input to NRC's regulatory decisions.

A significant aspect of this program is the implications of the work to the ASME Section XI pipe flaw evaluation criteria. Data base efforts on pipe fracture experiments and pipe material properties are frequently used to check the proposed criteria and changes to the criteria. We have also developed simplified elastic-plastic fracture mechanics (EPFM) criteria based on Charpy energy for both axial and circumferential flaw evaluations, which eliminate some problems with the current Z-factor criteria. This criteria involves a significant step change from EPFM to limit-load analyses. Figure 18 shows an example of how the circumferential crack Charpy energy based EPFM analysis has a continuously variable Z-factor as a function of the Charpy energy and approaches limit-load conditions where Z = 1.0 as the Charpy energy increases.

11. References

1. Wilkowski, G.M. et al " Short Cracks in Piping and Piping Welds" Semiannual Report, NUREG/CR-4599, BMI-2173, Vol. 1, No. 1, May 1991.

2. Wilkowski, G.M. et al " Short Cracks in Piping and Piping Welds" Semiannual Report, NUREG/CR-4599, BMI-2173, Vol. 1, No. 2, April 1992.

3. Wilkowski, G.M. et al " Short Cracks in Piping and Piping Welds" Semiannual Report, NUREG/CR-4599, BMI-2173, Vol. 2, No. 1, September 1992.

4. Wilkowski, G.M. et al " Short Cracks in Piping and Piping Welds" Semiannual Report, NUREG/CR-4599, BMI-2173, Vol. 2, No. 2, May 1992.

5. Wilkowski, G.M. et al " Short Cracks in Piping and Piping Welds" Semiannual Report, NUREG/CR-4599, BMI-2173, Vol. 3, No. 1, October, 1993.

6. Rahman, S. and Brust, F.W., "Elastic-Plastic Fracture of Circumferential Through-Wall Cracked Pipe Welds Subjected to Bending", J. of Pressure Vessel Technology, Vol. 114, pp 410-416, November, 1992.

7. "An Engineering Approach for Elastic-Plastic Fracture Analysis", EPRI NP-1931, Topical Report July 1981.

Table 1. Restructured test matrix of pipe experiments

Expt. No.	Diameter, in.	Schedule	Material	Temperature	Test Date
Pressurized through-wall-cracked pipe experiments					
1.1.1.21	28	60	A515 Gr60	288C (550F)	10/25/90
1.1.1.23	28	80	TP316L SAW	288C (550F)	5/23/91
1.1.1.24	24	80	A333 Gr6 SAW	288C (550F)	3/13/92
1.1.1.26	4	80	TP316LN	22C (72F)	2/27/91
Unpressurized uncracked pipe experiment					
1.1.1.25	28	60	A515 Gr60	288C (550F)	2/07/92
Bi-metallic weld fusion line experiments - TWC					
1.1.3.8	36	160	A516/SS-SAW	288C (550F)	9/93
Unpressurized surface-cracked pipe experiments					
1.2.1.20	16	30	TP316	99C (210F)	1/15/92
1.2.1.21	6	XXS	TP304	288C (550F)	4/16/91
1.2.1.22	6	40	TP304	288C (550F)	3/15/91
Pressurized surface-cracked pipe experiments					
1.2.3.15	28	60	A515 Gr60	288C (550F)	11/08/91
1.2.3.16	28	80	TP316L SAW	288C (550F)	9/05/91
1.2.3.17	24	100	A106B SAW	288C (550F)	6/93

Table 2. List of programs for which circumferential pipe fracture data will be included

Sponsoring Agency	Laboratory	Program or Report Number	Scope of Experiment
USNRC	Battelle	Degraded Piping	TWC, SC, CC; P&B, P, B; 4"-4-1/2" diameter, QS
USNRC	Battelle	IPIRG-1	TWC and SC; B, P&B; 6", 16", 30" diameter
USNRC	Battelle	Short Cracks	Large diameter, short cracks, TWC and SC
AEC	Battelle	BMI-1908	Carbon steel, pressure tests, SC
EPRI	Battelle	NP-192	Small diameter, stainless steel, TWC
EPRI	Battelle	NP-2347	RT, stainless steel, TW and SC
AGA-NG18	Battelle	Battelle Files	CS, TWC, line pipe pressure
AGA-WSC	Battelle	Battelle Report	Girth weld defects
AGA-WSC	Battelle	Battelle Report	Repair grooves
Offshore Program	Battelle	Battelle Files	4" diameter, bending, carbon steel base metal
EPRI	GE	NP-2472	4" diameter, axial tension, RT
AEC	GE	GEAP-10023	Small diameter, A106, RT
USNRC	DTRC	NUREG/CR-3740	8" A106B
USNRC	DTRC	NUREG/CR-4538	Stainless TIG
USNRC	DTRC	Unpublished	4" Stainless Base
USNRC	DTRC	Unpublished	Carbon steel MIG
STA	JAERI	NED Paper	Stainless steel, 6" and 16" diameter, TWC, SC
STA	JAERI	JAERI Reports	Carbon steel, 6" and 16" diameter, TWC, SC
ENEA	CISE	LBB - Tokyo	Carbon steel, small diameter, TWC
ENEA	CISE	NED paper	Stainless steel, small diameter, TWC
Westinghouse Owner's Group	Westinghouse	ASME PVP-95	Cast stainless steel, small diameter, TWC
CEGB	CEGB	Technical paper	Thin wall, carbon steel tests
KWU	KWU	Technical paper	Carbon steel bend tests
MITI	NUPEC	NED paper	Stainless steel pipe in tension
MITI	NUPEC	NED paper	Carbon steel pipe, pressure and bend
STA	NRCDP	ASME PVP-150	Pipe system tests
BMFT	MPA	Phase I	Pressure to burst, LWR, large diameter
BMFT	MPA	Phase II	Pressure and bend
Hitachi	Hitachi	NED paper	Stainless steel pipe in tension

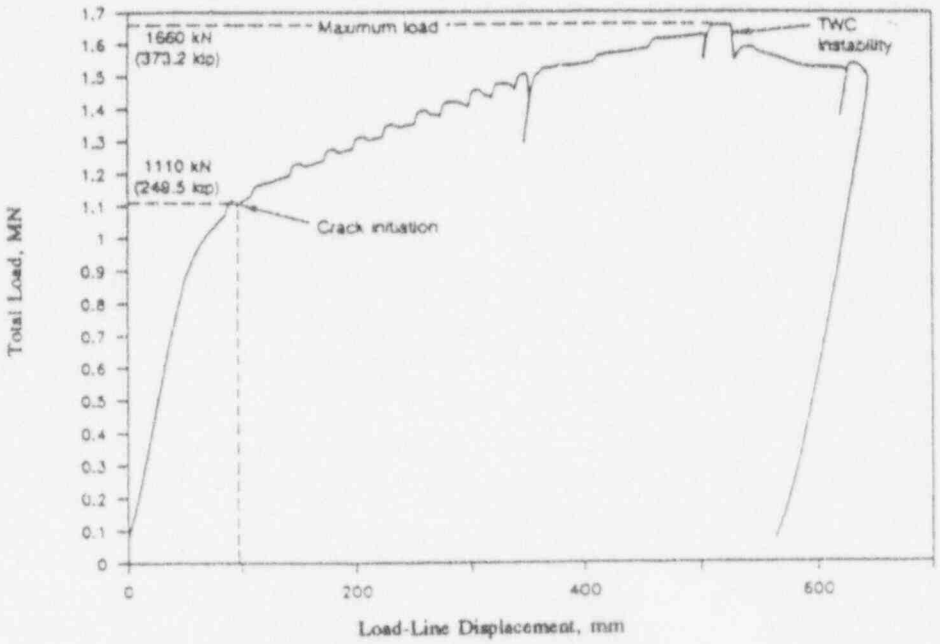


Figure 1. Total applied load versus load-line displacement for Experiment 1.1.1.24

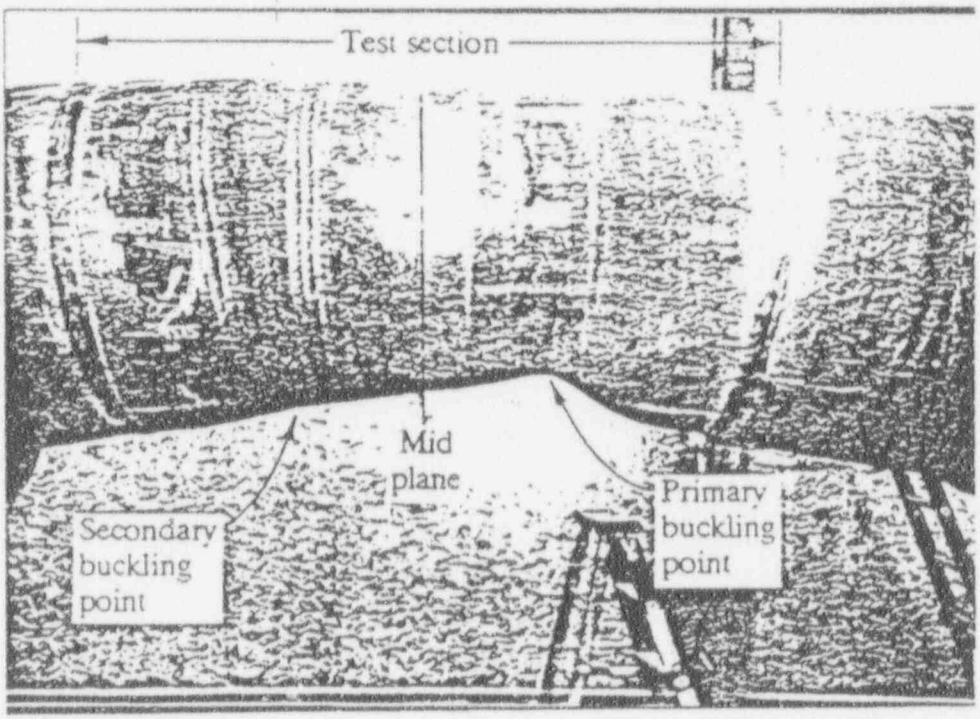
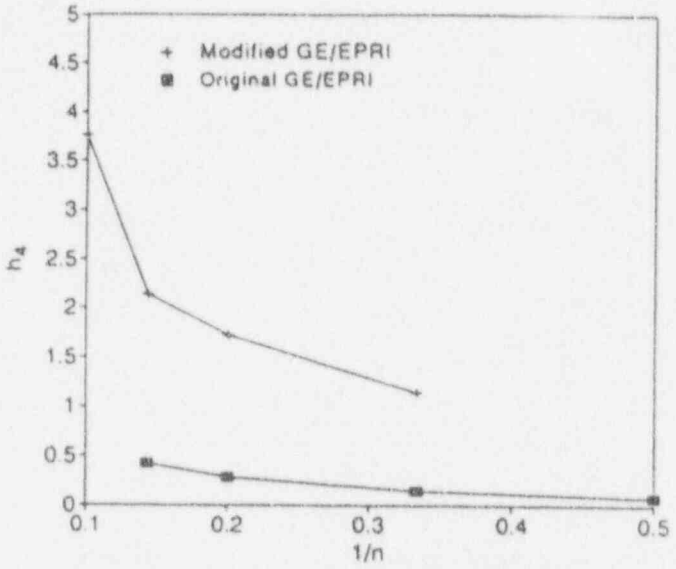
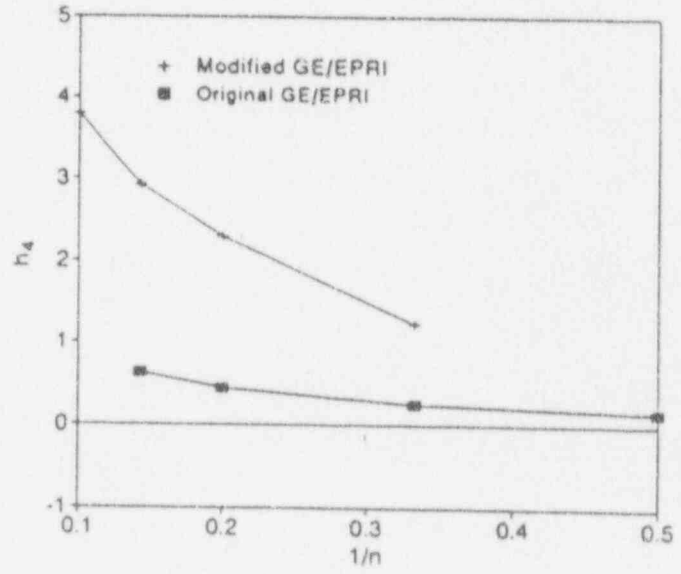


Figure 2. Post-test photo showing buckled section of pipe for Experiment 1.1.25



(c) Comparison of h_4-functions, $R_m/t = 10$, $\theta/\pi = 1/16$ (h_4 relates fully plastic rotation to moment)



(d) Comparison of h_4-functions, $R_m/t = 20$, $\theta/\pi = 1/16$ (h_4 relates fully plastic rotation to moment)

Figure 3. Comparison of ABAQUS FEM results to past GE/EPRI solutions for elastic and fully plastic rotation functions

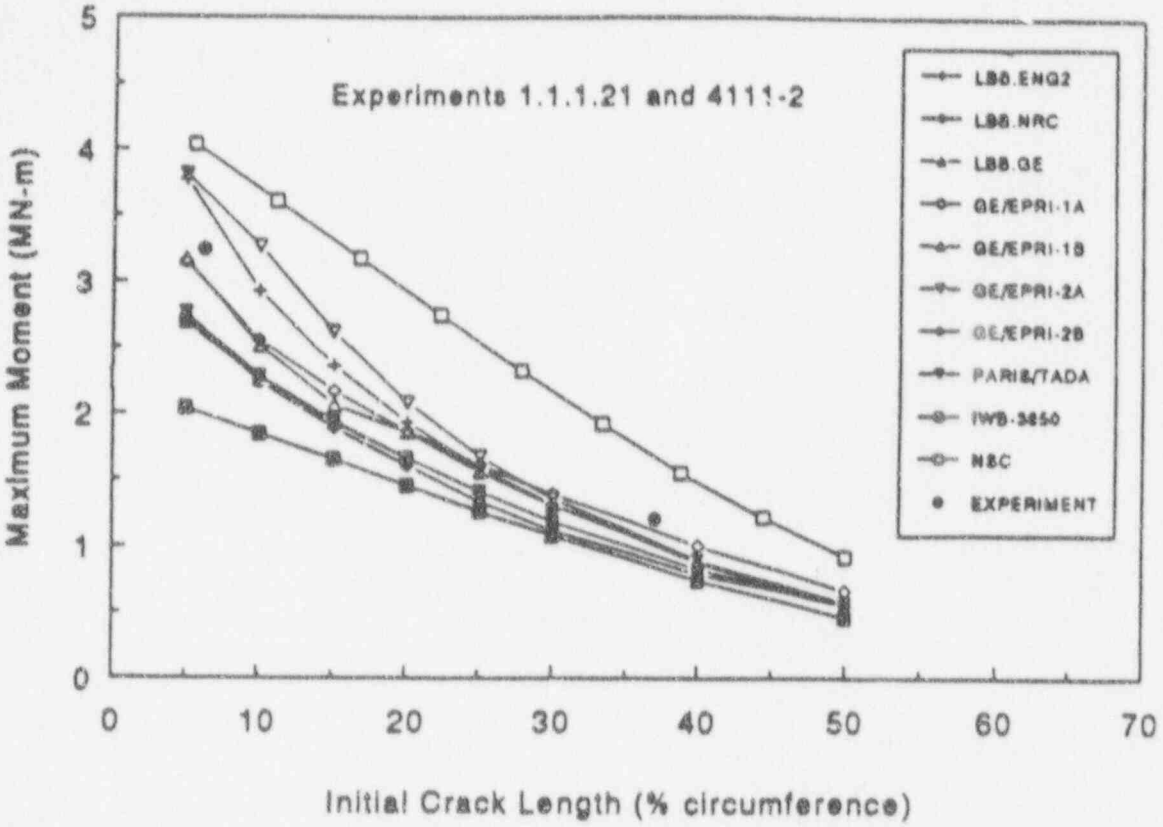


Figure 4. Comparisons of maximum loads from Experiments 1.1.1.21 and 4111-2 on a 28-inch diameter Schedule A515, Grade 60 pipe to predictions by various analyses

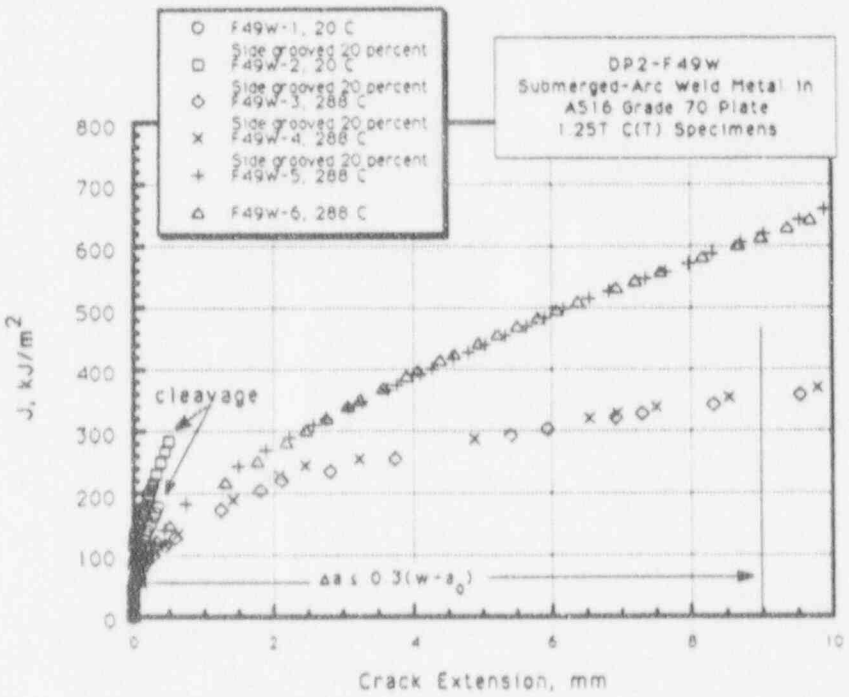


Figure 5. Composite plot of J-resistance curves for Pipe DP2-F49W tests (Data with $\Delta a \leq 0.3\ (w-a_0)$ are believed to be valid)

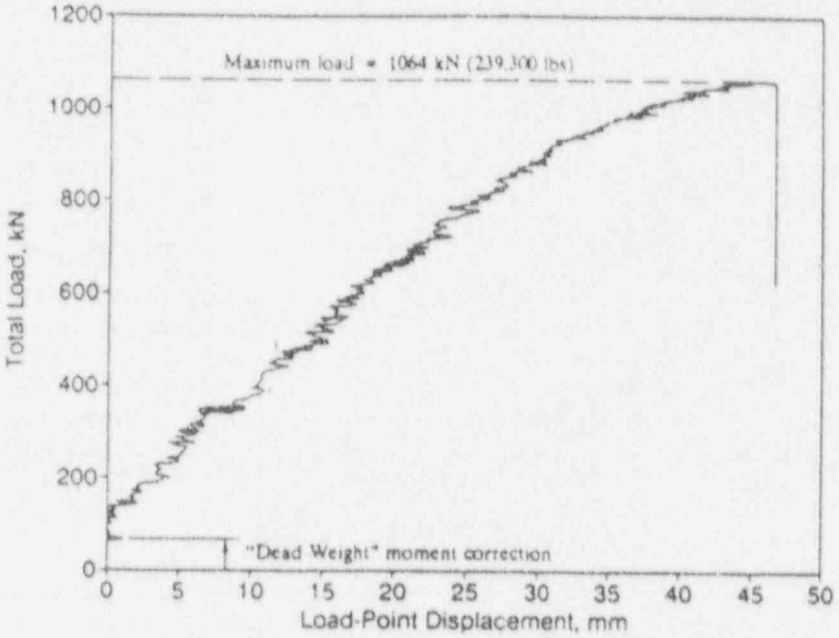


Figure 6. Total applied load versus load-line displacement for Experiment 1.2.3.15

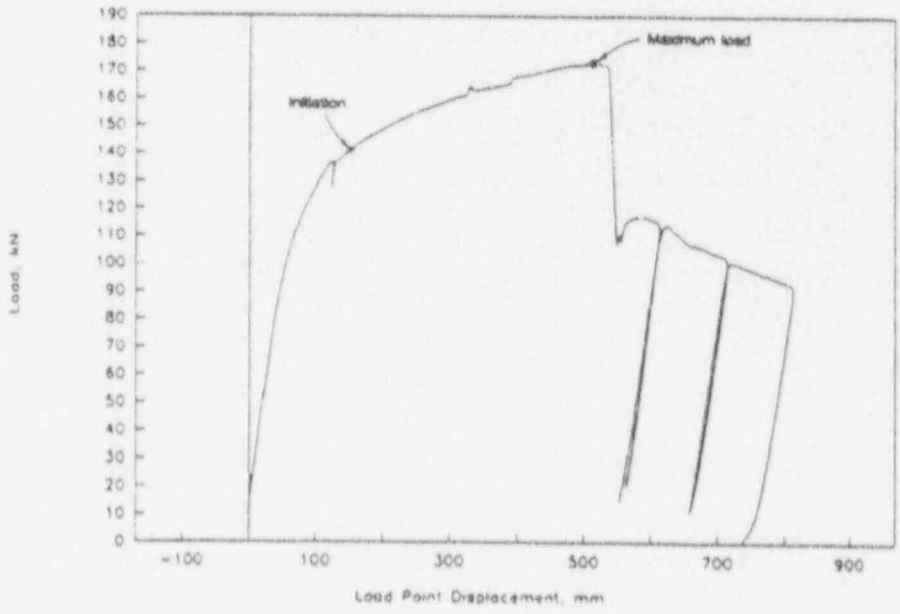


Figure 7. Total load versus load-point displacement for Experiment 1.2.1.20

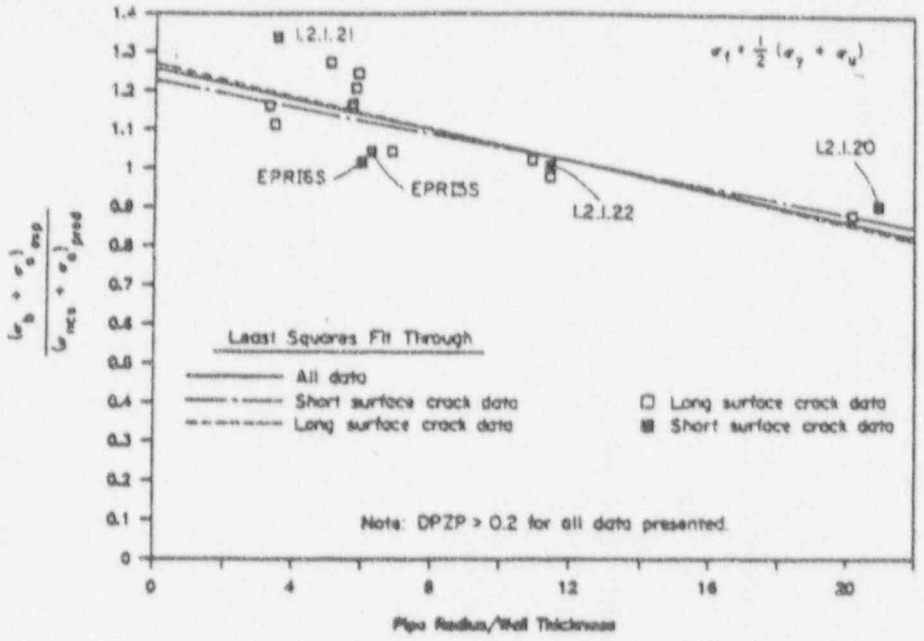


Figure 8. Plot of ratio of experimental stress to predicted stress as a function of pipe radius to thickness ratio (R/t)

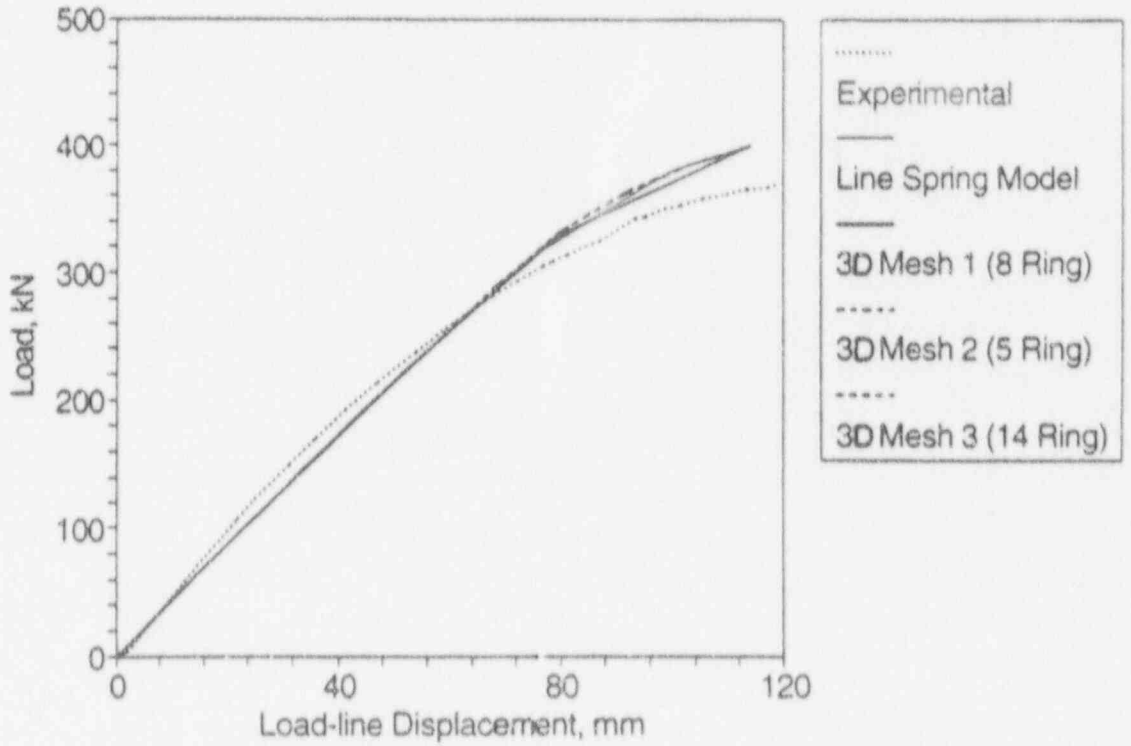


Figure 9. Predicted and experimentally measured variation of load vs load-line displacement of surface-cracked pipe

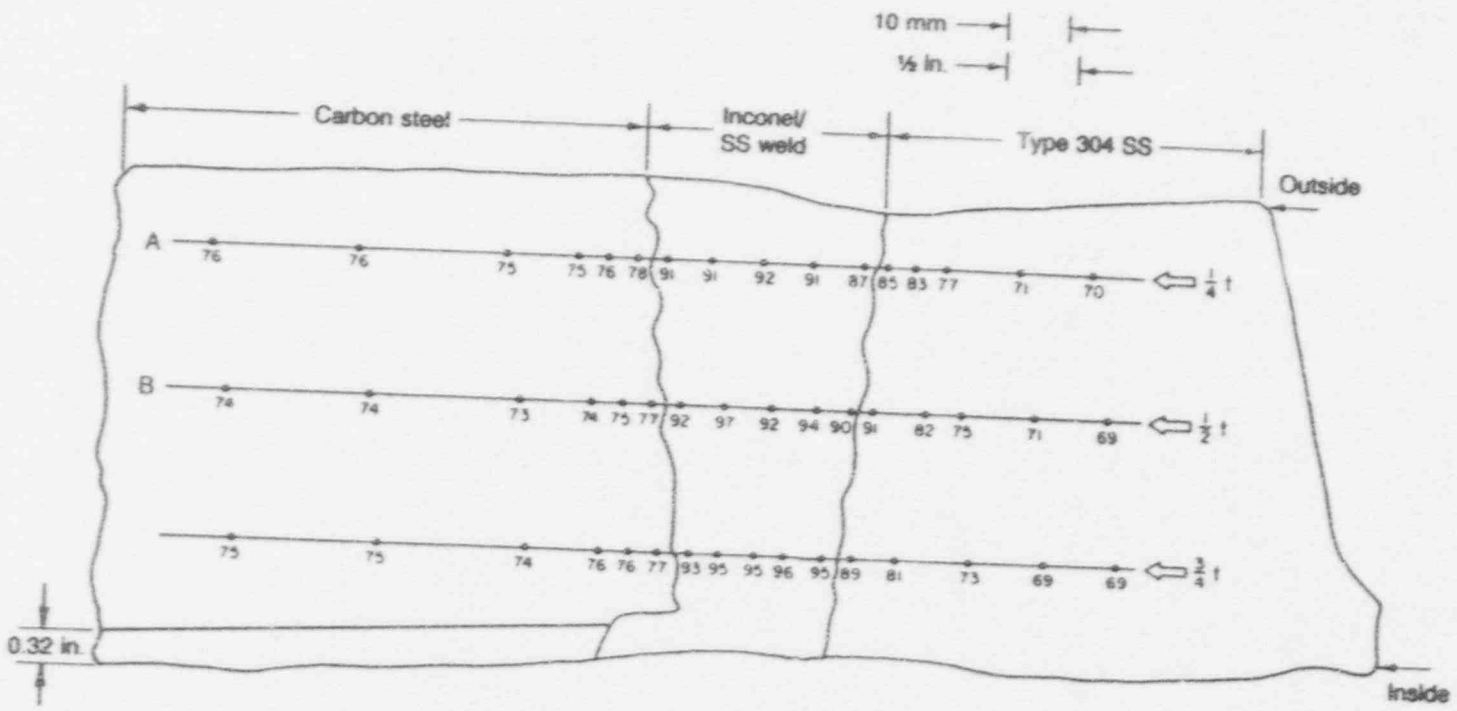


Figure 10. Hardness map of bi-metal weld (Pipe DP2-F33). Hardness values shown are Rockwell B

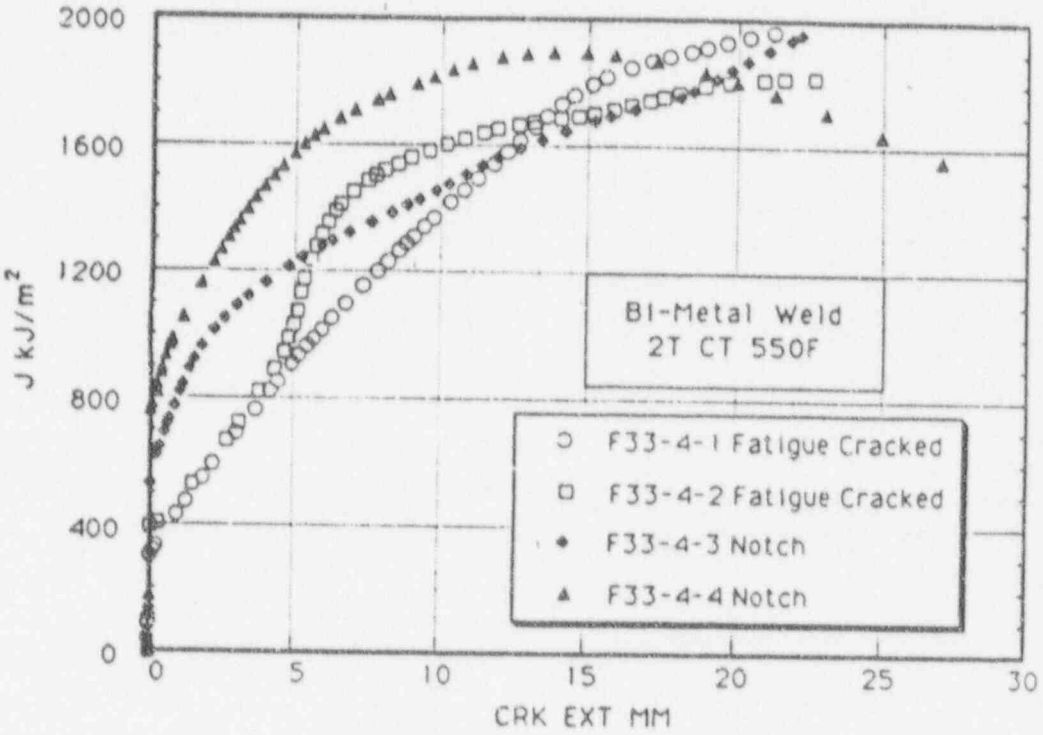


Figure 11. Effect of initial notch acuity on J-resistance curves for a bi-metallic weld

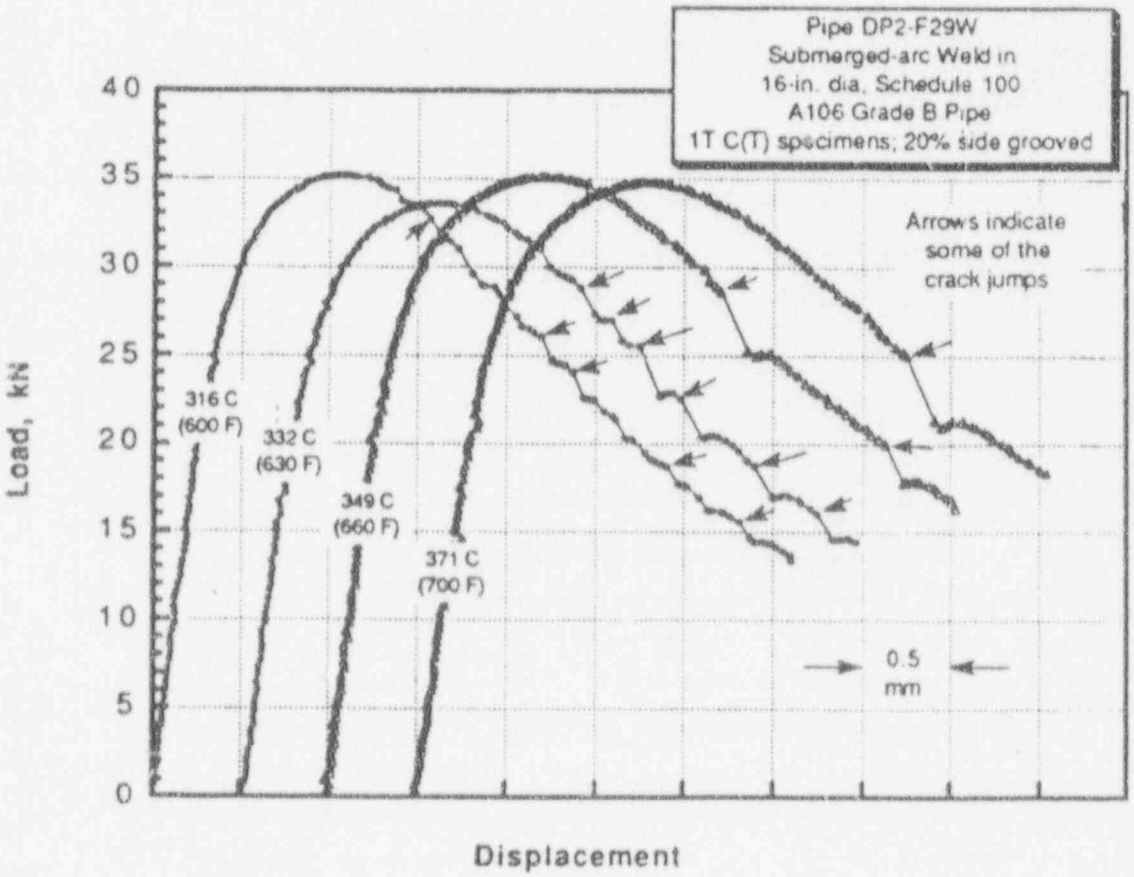


Figure 12. Yield strength, ultimate tensile strength, and Brinell hardness as functions of test temperature for five carbon steels

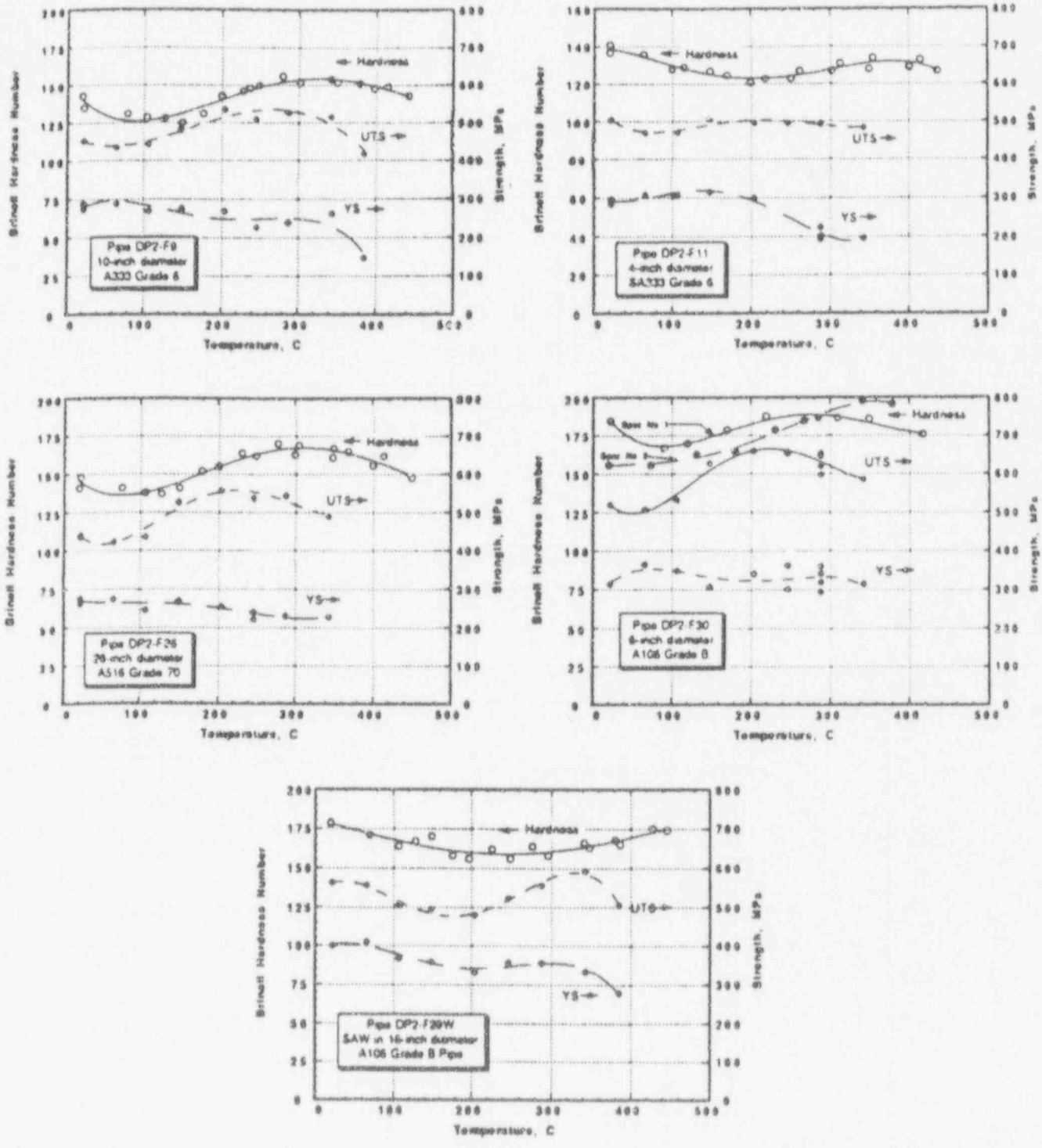


Figure 13. Load-displacement curves for C(T) specimen tests

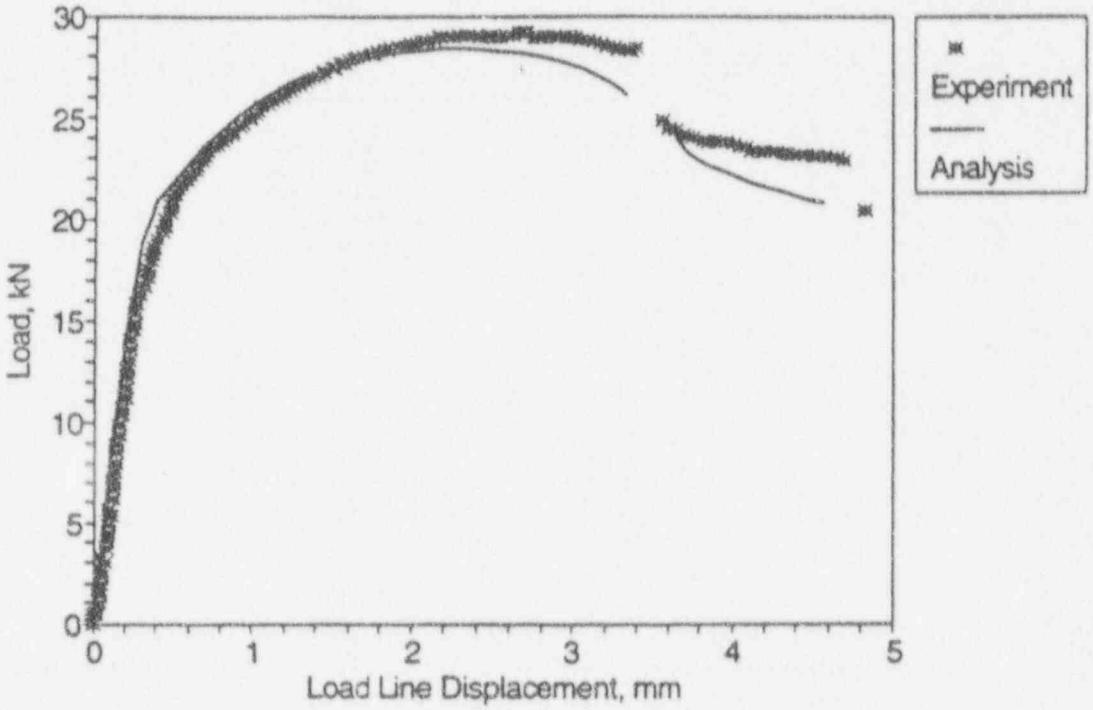


Figure 14. Comparison of experimentally measured load vs load displacement with FEM predictions for C(T) specimens F26-103

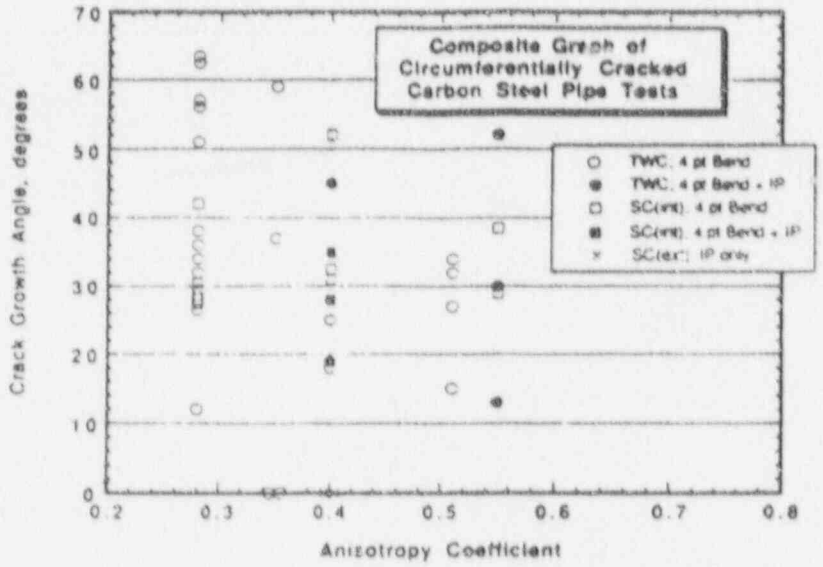


Figure 15. Crack-growth angle versus anisotropy coefficient for circumferentially cracked carbon steel pipes tested at Battelle (TWC = through-wall crack, SC = surface crack, p = internal pressure)

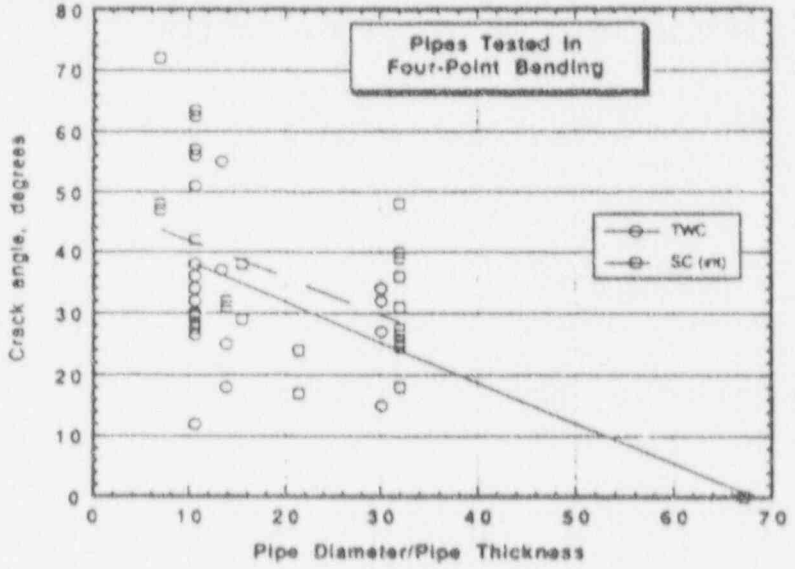


Figure 16. Crack growth angle versus pipe diameter/thickness ratio for carbon steel pipes tested in four-point bending (TWC = through-wall crack, SC = surface crack, p = internal pressure) [Note the data points at pipe diameter/pipe thickness = 67]

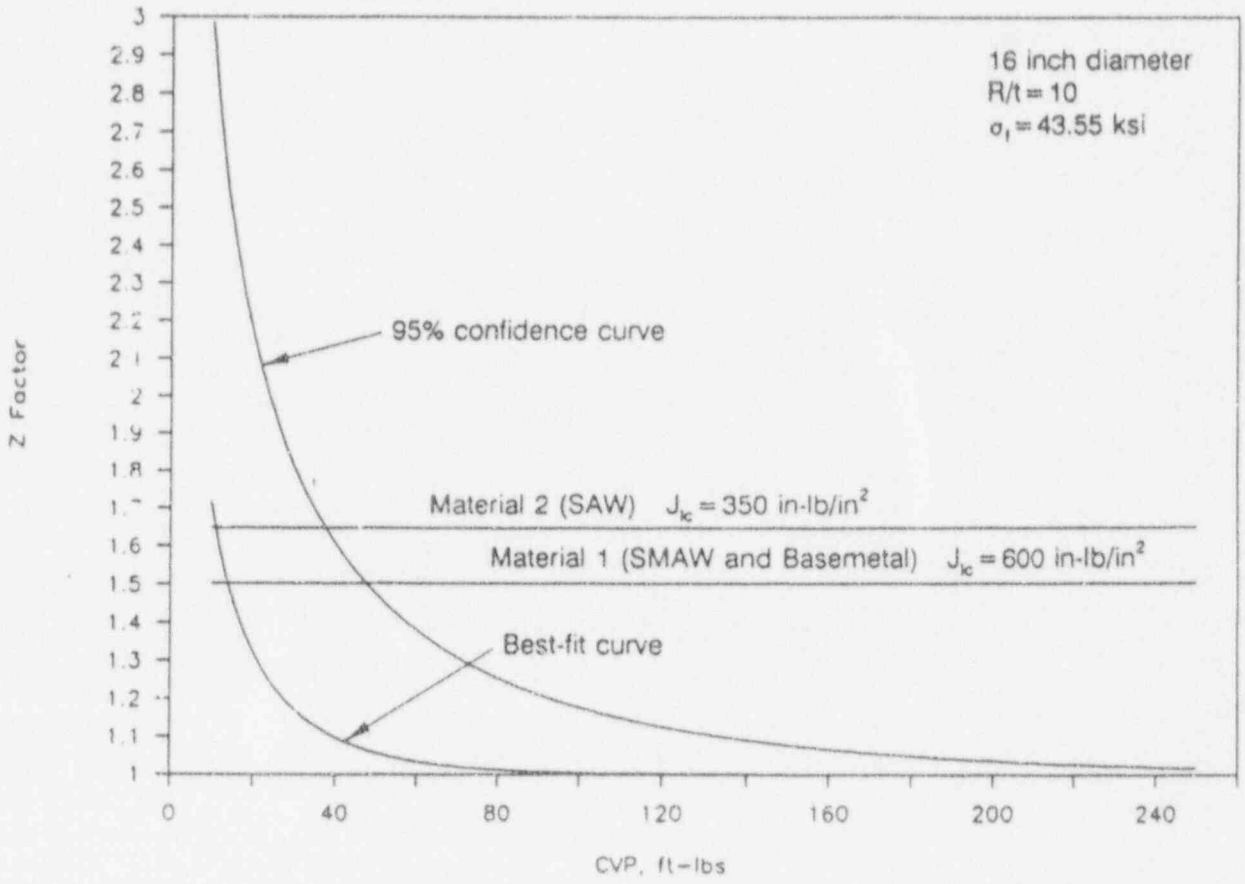
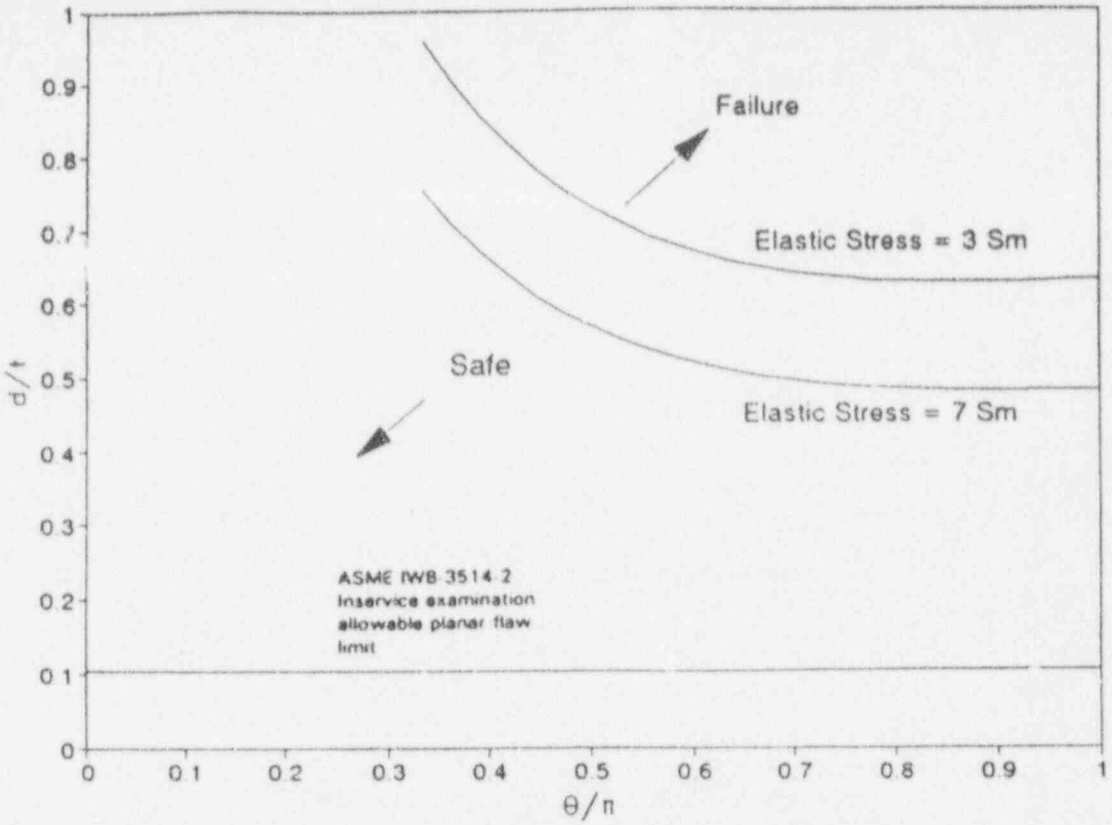
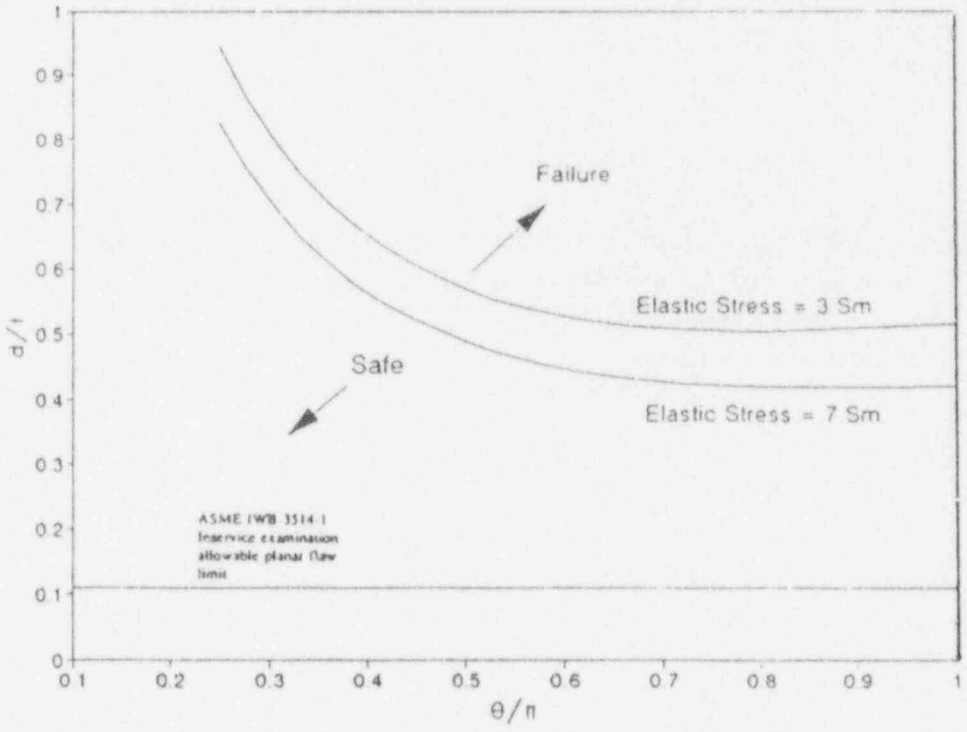


Figure 18. Comparison of ASME IWB-3650 Z factors for circumferentially cracked pipe with Charpy Energy-based EPFM Z factors developed in the Short Cracks program



(a) TP304 Stainless Steel



(b) A106 Grade B

Figure 17. Net-section-collapse analysis calculated surface crack loci for pipes with $3S_m$ and $7S_m$ elastic stresses

IRRADIATION-ASSISTED STRESS CORROSION CRACKING OF MATERIALS FROM COMMERCIAL BWRs: ROLE OF GRAIN-BOUNDARY MICROCHEMISTRY*

H. M. Chung, W. E. Ruther, J. E. Sanecki, A. G. Hins, and T. F. Kassner

Energy Technology Division
Argonne National Laboratory
Argonne, IL 60439

ABSTRACT

Constant-extension-rate tensile tests and grain-boundary analysis by Auger electron spectroscopy were conducted on high- and commercial-purity (HP and CP) Type 304 stainless steel (SS) specimens from irradiated boiling-water reactor (BWR) components to determine susceptibility to irradiation-assisted stress corrosion cracking (IASCC) and to identify the mechanisms of intergranular failure. The susceptibility of HP neutron absorber tubes to intergranular stress corrosion cracking (IGSCC) was higher than that of CP absorber tubes or CP control blade sheath. Contrary to previous beliefs, susceptibility to intergranular fracture could not be correlated with radiation-induced segregation of impurities such as Si, P, C, N, or S, but a correlation was obtained with grain-boundary Cr concentration, indicating a role for Cr depletion that promotes IASCC. Detailed analysis of grain-boundary chemistry was conducted on neutron absorber tubes that were fabricated from two similar heats of HP Type 304 SS of virtually identical bulk chemical composition but exhibiting a significant difference in susceptibility to IGSCC for similar fluence. Grain-boundary concentrations of Cr, Ni, Si, P, S, and C in the crack-resistant and -susceptible HP heats were virtually identical. However, grain boundaries of the cracking-resistant material contained less N and more B and Li (transmutation product from B) than those of the crack-susceptible material, indicating beneficial effects of low N and high B contents.

INTRODUCTION

In recent years, failures of nonsensitized austenitic stainless steel (SS) core internal components in both boiling- and pressurized-water reactors (BWRs and PWRs) have increased after accumulation of relatively high fluence (>5 x 10^{20} n cm^{-2}, E >1 MeV). Although most failed components can be replaced, some safety-significant structural components, such as the BWR top guide, shroud, and core plate, would be very difficult or impractical to replace. Therefore, the structural integrity of these components after accumulation of high fluence has been a subject of concern, and extensive research has been conducted to provide an understanding of this type of degradation, which is commonly known as irradiation-assisted stress corrosion cracking (IASCC).

IASCC failures have been attributed to radiation-induced segregation (RIS) or depletion of impurity and alloying elements at grain boundaries. As early as in the mid-1960s, investigators began to implicate impurities such as Si, P, and S in IASCC failure of fuel cladding fabricated from solution-annealed nonsensitized austenitic stainless steel.[1-5] Since then, it seemed that the concept of superior resistance of high-purity (HP) materials of SSs low in Si, P, S, and C was proved valid after favorable experience with HP Type 348 SS fuel cladding in the La Crosse boiling-water reactor (BWR)[6] and the subsequent demonstration of superior performance of the low-N HP 348 SS heat from swelling-tube tests in a BWR and a pressurized-water reactor (PWR).[7-8] Although data were very limited, results from a laboratory constant-extension-rate tensile (CERT) test[9] also suggest superior performance of the same HP heat of Type 348 SS investigated by the authors of Refs. 6-8. The superior performance seemed to indicate that radiation-induced segregation (RIS) of Si is the predominant process, because RIS of other impurities and Cr depletion in the HP

* Work supported by the U.S. Nuclear Regulatory Commission, Office of Nuclear Regulatory Research.

and commercial-purity (CP) Type 348 SS were either similar or could not be detected by field-emission-gun scanning transmission electron microscopy (FEG-STEM).[9] It has also been reported that Type 316L SS, irradiated in the mixed-spectrum Advanced Test Reactor (ATR), exhibited better resistance to stress corrosion cracking (SCC) than Type 316NG SS,[10] indicating a possible benefit of low N.

On the basis of these experiences with Type 348 and 316 SS, HP materials of Type 304 SS have been suggested as a better alternative to CP Type 304 SS, a material from which the majority of core internal components of operating BWRs and PWRs in U.S. have been fabricated. Recently, Jacobs reported that neutron absorber tubes (QC-AT, Table 1) fabricated from one HP heat (HP304-CD, Table 1) of Type 304 SS performed better than similar counterparts fabricated from CP Type 304 SS in noncreviced positions in the BWR control blade.[11]

However, in direct contradiction of the above experiences, results from CERT tests conducted on other BWR neutron absorber tubes indicated that the resistance of other similar HP heats of Type 304 SS is worse than that of CP materials.[12-13] Results consistent with this have also been reported for Type 304 SS specimens irradiated by either neutrons,[14] ions,[15] or protons.[16] Therefore, the issue of superior performance of HP materials and the mechanisms of IASCC appear to be far from established. Nevertheless, one important point seems to be quite clear: heat-to-heat variation in susceptibility to IASCC can be very large, even among HP materials of virtually identical chemical composition. This seems to pose an important question not only about the role of grain-boundary segregation of other impurities (i.e., impurities other than Si, P, S, and C) but also about the premise that Cr depletion is the primary mechanism of IASCC.

To provide a better answer to this question, CERT tests were conducted on specimens obtained from neutron absorber tubes and a control blade sheath fabricated from several heats of HP- and CP-grade Type 304 SS and irradiated to high fluence during actual service in a BWR. Results from the CERT tests were correlated with results of microstructural analysis by Auger electron spectroscopy (AES) to identify the primary process that controls susceptibility to IGSCC and in-reactor performance of Type 304 SS components.

Among the several materials tested was a unique pair of BWR neutron absorber tubes fabricated from two HP heats of virtually identical chemical composition but exhibiting a significant difference in susceptibility to intergranular stress corrosion cracking (IGSCC) during CERT tests. One of the detailed analyses of grain-boundary microchemistry was conducted on neutron absorber tubes (QC-AT, Table 1), fabricated from the HP Heat HP304-CD, of which superior in-reactor performance has been reported by Jacobs.[11] The other analysis was conducted on neutron absorber tubes (V-AT), which were fabricated from a similar HP heat (HP304-A) of virtually identical chemical composition but one that exhibited a relatively high susceptibility to IGSCC during CERT tests.[12-13] CERT tests independent of those in Refs. 12 and 13 were conducted on both materials, and the result showed that IGSCC susceptibility of the former material (QC-AT) was significantly lower than that of the latter (V-AT) for a similar fluence level.[17] Chemical compositions of the IGSCC-resistant and the -susceptible materials were virtually identical except for N. Therefore, a comparative analysis of grain-boundary microchemistry of the two materials was considered ideal to shed light on the cause of the significant difference in susceptibility to IGSCC.

The objective of this study was twofold: (1) to determine the susceptibility of HP and CP Type 304 SS components to IASCC after actual service in a BWR, and (2) to identify the cause of the strong heat-to-heat variation, thereby providing a better understanding of the primary process of IASCC, which is essential if we are to establish a method to evaulate long-term performance of safety-significant core internal structures.

EXPERIMENTAL PROCEDURES

Specimen preparation, procedures for CERT tests, and a description of the hot-cell CERT apparatus were presented previously.[12,13] Cylindrical tensile specimens were

sectioned from top-, middle-, and bottom-axial positions of neutron-absorber-rod tubes fabricated from several CP and HP heats of Type 304 SS and irradiated in several BWRs. Boron-carbide absorber was removed with high-strength cobalt-steel drills. Sheet tensile specimens, fabricated from BWR control blade sheaths, were also tested. CERT tests were conducted in air and in simulated BWR water at 289°C at a strain rate of 1.65×10^{-7} s^{-1}. The dissolved O concentration and conductivity of the simulated BWR water were ≈0.3 ppm and 0.12 $\mu S \cdot cm^{-1}$, respectively. Analysis of the fracture surfaces of CERT specimens was conducted by scanning electron microscopy (SEM) to determine the types of fracture surface morphology.

The fast neutron fluence and chemical composition of the HP and CP heats of Type 304 SS are given in Table 1. The chemical compositions of the three HP heats are similar except for N. Boron content could not be determined with an accuracy of <0.001 wt.%; however, Heat HP304-CD had a higher B content than did Heats HP304-A or -B.

Grain-boundary microchemistry was analyzed with a JEOL Model JAMP-10 scanning Auger microscope (SAM). Specimens charged with H were fractured at room temperature in the ultrahigh vacuum (≈7 to 20 x 10^{-7} Pa) of the SAM to reveal IG-fracture surfaces. Hydrogen was charged into notched AES specimens for 48 h at 60°C in a solution of 100-mg/l $NaAsO_2$ dissolved in 0.1-N H_2SO_4 at a current density of ≈500 mA/cm^2. Intergranular fracture of the H-charged specimens was observed in bands underneath the free surface of the fractured specimen. Average penetration depth of the more-or-less uniform IG-fracture band was measured in each specimen. A depth profile of Cr was obtained as a function of sputter distance beneath a selected region of IG fracture produced by CERT tests. Details of the procedure have been described elsewhere.[13]

Table 1. Chemical Composition and Fluence of HP and CP Type 304 SS BWR Components.

Heat ID No.	Composition (wt.%)									Source Code	Service Reactor	Fluence (10^{21} $n \cdot cm^{-2}$)
	Cr	Ni	Mn	C	N	B	Si	P	S			
HP304-A	18.50	9.45	1.53	0.013	0.100	<0.001	<0.03	0.005	0.003	V-AT[a]	BWR-B	0.2-1.4
HP304-B	18.30	9.75	1.32	0.015	0.080	<0.001	0.05	0.005	0.005	V-AT[a]	BWR-B	0.2-1.4
HP304-CD	18.58	9.44	1.22	0.017	0.037	0.001	0.02	0.002	0.003	V-AT[a]	BWR-B	0.2-1.4
HP304-CD	18.58	9.44	1.22	0.017	0.037	0.001	0.02	0.002	0.003	QC-AT[a]	BWR-QC	2.0
CP304-A	16.80	8.77	1.65	0.08[b]	0.052	-	1.55	0.045[b]	0.030[b]	BL-AT[c]	BWR-Y	0.2-2.0
CP304-B	18-20	8-10.5	2.00[b]	0.08[b]	-	-	1.00[b]	0.045[b]	0.030[b]	LC-S[d]	BWR-LC	0.5-2.6

[a]High-purity neutron absorber tubes, OD = 4.78 mm, wall thickness = 0.63 mm, composition before irradiation.
[b]Represents maximum value in the specification; actual value not measured.
[c]Commercial-purity absorber tubes, OD = 4.78 mm, wall thickness = 0.79 mm, composition after irradiation.
[d]Commercial-purity control blade sheath, thickness 1.22 mm, actual composition not measured.

RESULTS AND DISCUSSION

Tensile Properties

Results of tensile tests, CERT, and SEM analyses of the specimens from the HP and CP absorber tubes and control blade sheaths are summarized in Table 2. Figures 1 and 2 show the yield strength (YS) and ultimate tensile strength (UTS) versus fast-neutron fluence (E >1 MeV) of the CP and HP neutron absorber tubes and control blade sheath strained to failure in air (from Table 2). The figures contain similar data for CP-grade tensile specimens of Types 304, 304L, 316L, and 316NG SS irradiated in the ATR at 300°C and reported by Jacobs et al.[10] Both the yield and ultimate tensile strengths of the CP-grade

BWR sheath (Heat CP304-B, Table 1) and HP-grade absorber tube (Heat HP304-A) are significantly higher than those of the ATR-irradiated specimens or than those of the CP 304 SS neutron absorber for comparable fluence. It appears that irradiation-induced hardening of the two heats (CP304-B and HP304-A) is more pronounced than that of other materials in Fig. 1 for comparable fluence. The cause of the significant heat-to-heat variation is not understood at present. The irradiation-induced hardening tends to reach saturation at fluence $\geq 2.5 \times 10^{21}$ n cm^{-2} (E > 1 MeV), or ≥3.6 dpa.

Figure 3 shows total elongation versus fast-neutron fluence for the HP and CP 304 SS neutron absorber tubes and control blade sheath. For comparison, similar data from Ref. 10 for CP heats of Type 304, 304L, 316L, and 316NG SS irradiated in the ATR at 300°C are also shown in the figure. The latter data were obtained at a significantly higher strain rate than that used in the present tensile tests, i.e., 4×10^{-4} s^{-1} versus 1.7×10^{-7} s^{-1}. Ductility appears to reach an asymptotic minimum value of ≈5% at fluence levels $>1.5 \times 10^{21}$ n·cm^{-2}. Total elongations of the BWR-irradiated materials are, however, considerably smaller than those of the ATR-irradiated materials at the high fluence level, i.e. 5-10 vs. 8-22%. Therefore, the higher tensile ductility and the lower strength associated with the test-reactor-irradiated specimens should be used with caution.

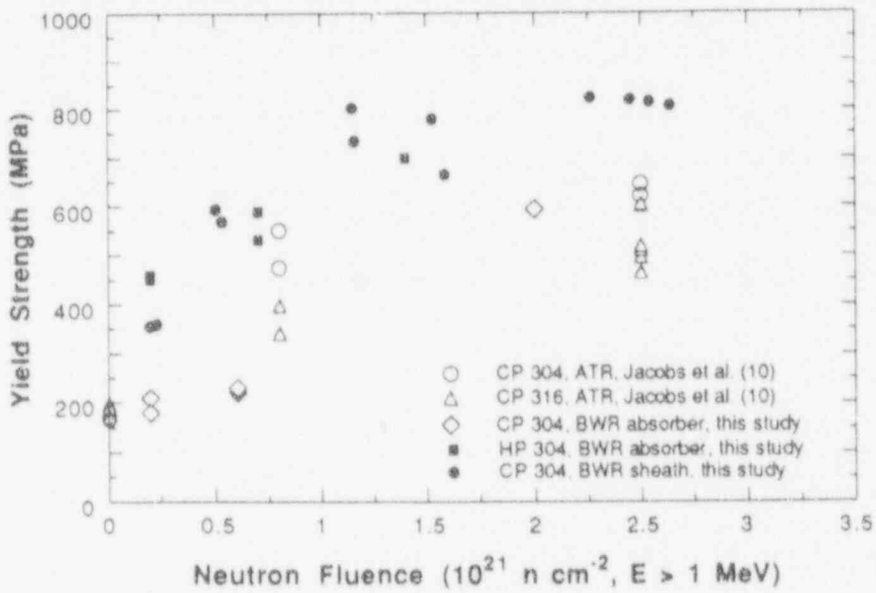


Figure 1. Yield stress vs. fast neutron fluence (E >1 MeV) for solution-annealed CP and HP Type 304 and 316 SS from tensile tests in air at 289°C.

Relative Susceptibilities of HP and CP Materials to IGSCC

The percent IGSCC measured in the BWR specimens has been plotted as a function of fast neutron fluence and yield strength in Figs. 4A and 4B, respectively. Similar results reported by Jacobs et al.[10,18] and Kodama et al.[19] are also shown in the figures. All data in Fig. 4A were obtained from BWR components at a comparable strain rate of $\approx 2 \times 10^{-7}$ s^{-1} in water containing ≈0.3 ppm dissolved O. The figure indicates that the IGSCC susceptibility of the CP control blade sheath is significantly lower than that of the CP neutron absorber

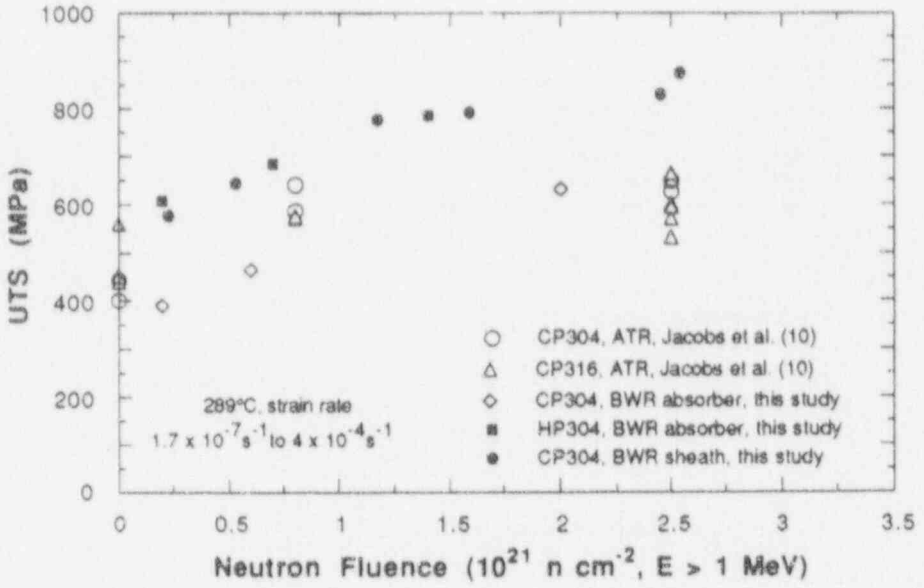


Figure 2. Ultimate tensile stress (UTS) vs. neutron fluence (E >1 MeV) for CP and HP Type 304 and 316 SS from tensile tests in air at 289°C

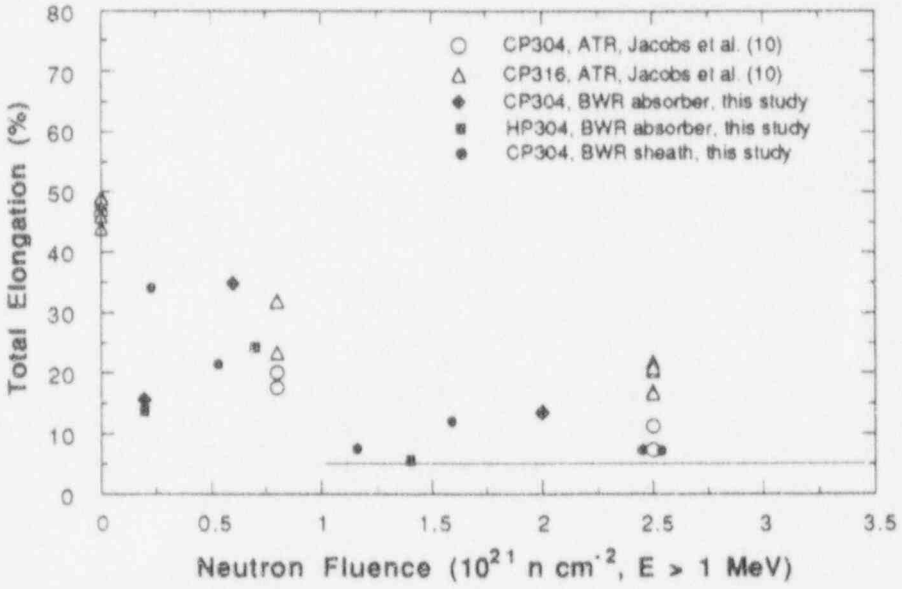
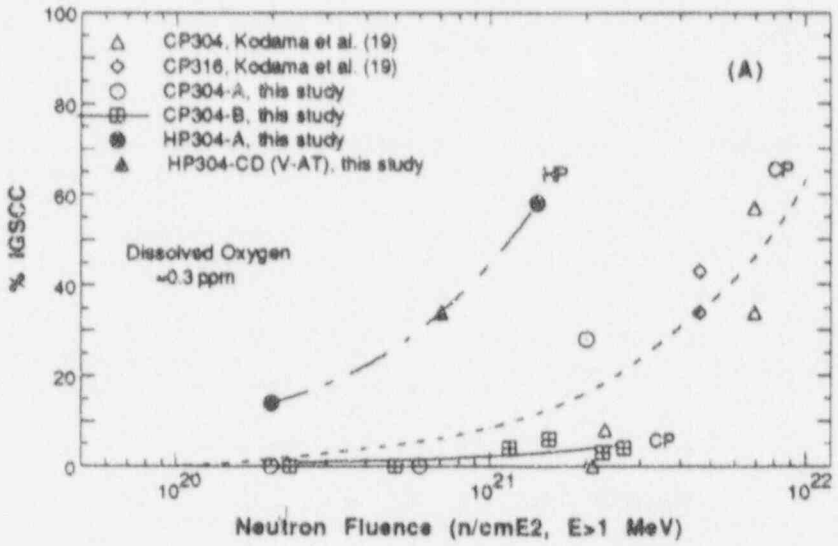


Figure 3. Total elongation vs. neutron fluence (E >1 MeV) for CP and HP Type 304 and 316 SS from tensile tests in air at 289°C

tube or the dry tube of Kodama et al.[19] for a comparable fluence level. The susceptibility of the HP absorber tube is greater than that of any of the CP materials.



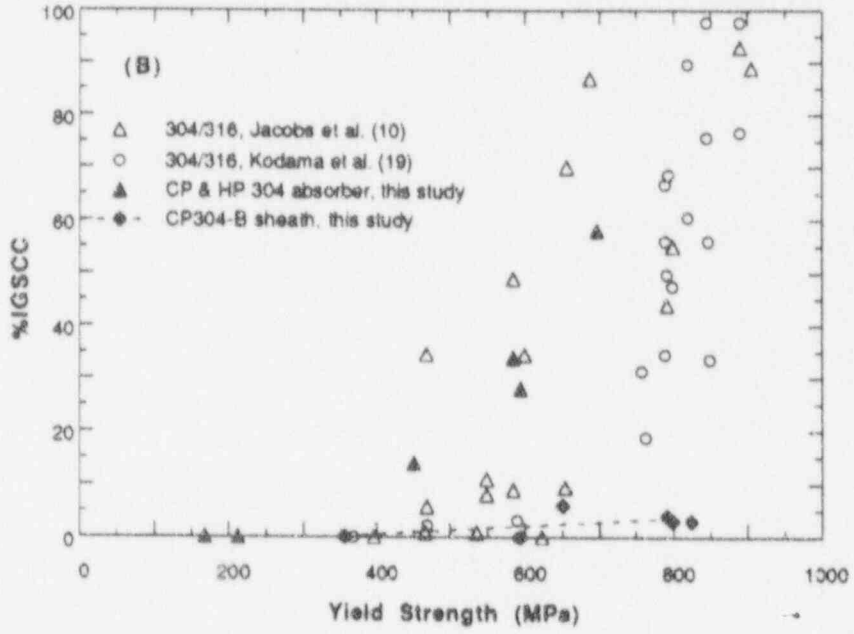


Fig. 4. Percent IGSCC vs. fluence (A) and vs. yield strength (B) for HP and CP Type 304 SS and CP 316 SS BWR components from CERT tests at 289°C in simulated BWR water.

Role of Irradiation Hardening

Figure 4B indicates that, apparently, no good correlation is observed between percent IGSCC and yield strength. For example, CP 304 SS sheath from the BWR-LC exhibited excellent resistance to IG cracking despite more pronounced irradiation-induced hardening for comparable fluence. For a similar yield strength of ≈800 MPa, percent IGSCC could be as high as 100% or as low as ≈3%, depending on composition and structure.

The rationale for implicating yield strength is that IASCC may be controlled primarily by irradiation hardening of grains regardless of a grain-boundary process that promotes stress corrosion. However, results given in Fig. 4B indicate clearly that, although irradiation-induced hardening is one of the necessary conditions of IASCC, which renders plastic deformation within grains more difficult, a certain grain-boundary process is essential to induce IGSCC in the irradiated materials in water.

Effects of Si, P, and S

Auger signals from several spots on ductile and intergranular fracture regions were analyzed, and peak-to-peak amplitudes of the primary peaks of Ni, Si, P, C, N, S, and the unidentified peak at ≈58-59 eV ($X_{59\text{-}eV}$) were measured and normalized with respect to the amplitude of the primary peak of Fe. These basic data from AES analyses were reported elsewhere.[12,13] From the data, degree of grain-boundary segregation of each element was determined. In Figs. 5A-5C, percent IGSCC from CERT tests in water has been plotted as a

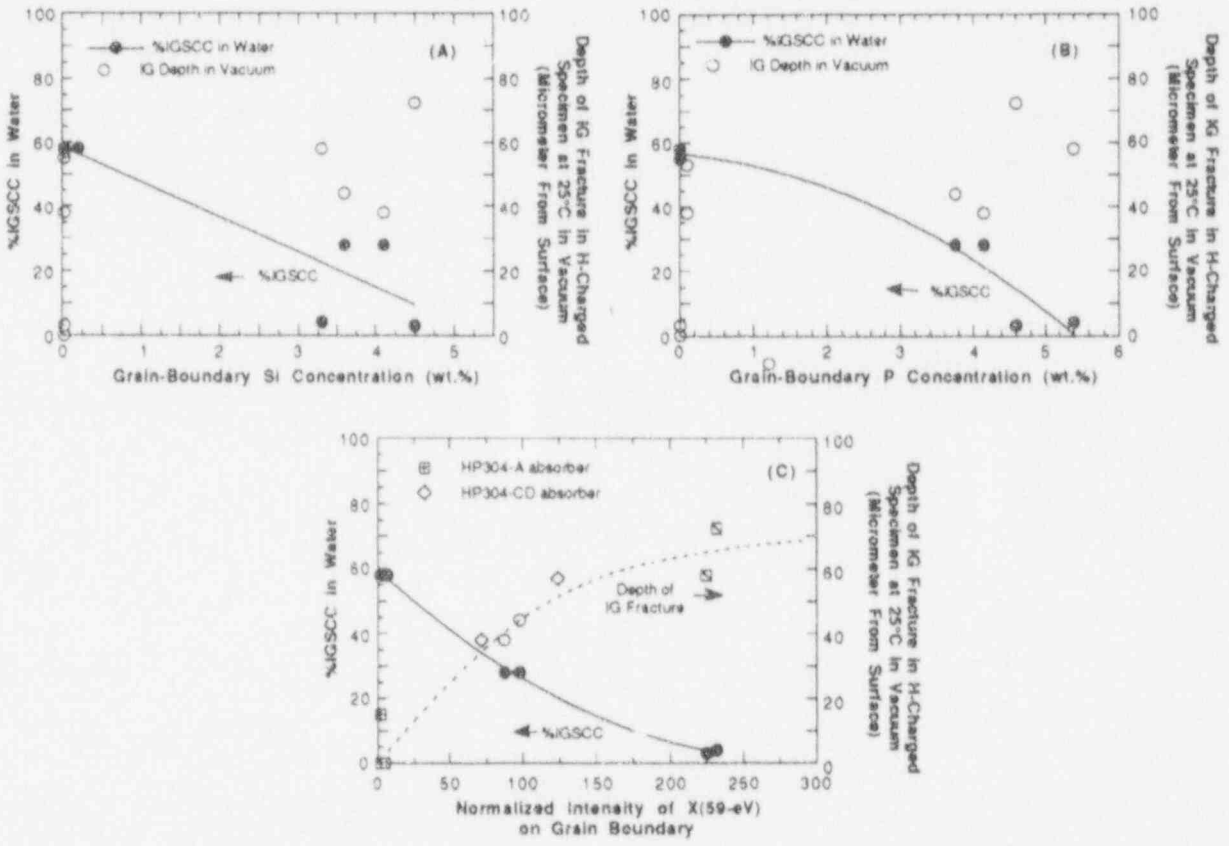


Fig. 5. Percent IGSCC in water and depth of intergranular fracture penetration in hydrogen-charged specimens, fractured at 25°C in vacuo, as a function of grain-boundary segregation of Si (A), P (B), and X (59-eV) (C). Fluence level of the specimens was ≈2 x 10^{21} n/cm^2.

function of the grain-boundary concentration of Si and P. Data for the grain-boundary segregation of Si, P, and other impurities has been reported in Refs. 12 and 13. In Figs. 5A-5C, the depth of IG-fracture penetration, produced in H-charged specimens in vacuo at 25°C, has also been plotted. The X(59-eV) peak shown in Fig. 5C is produced by the secondary Auger electrons of Li and Ni. A more detailed analysis to identify the origin of the peak is given later in this paper. No evidence of segregation of S was observed.[13]

No good correlation was observed between the susceptibility to H-enhanced IG cracking and grain-boundary concentration of Si or P. The percent IGSCC in water decreased monotonically for increased grain-boundary concentrations of Si, P, and X(59-eV). It is difficult, therefore, to explain the significant IGSCC in the HP absorber tube specimens or the negligible SCC susceptibility of the CP sheath specimens on the basis of grain-boundary segregation of Si, P, or S. The present results show convincingly that grain boundary segregation of Si, P, or S is not the mechanism of IASCC of Type 304 SS as has been speculated previously. Furthermore, the results also imply that the low content of Si, P, or S is not the primary factor associated with the better resistance of HP Type 348 SS.[6-9]

Effect of Cr Depletion

Minimum Cr on grain boundaries of the CP and HP absorber tubes and control blade sheath was determined by an AES depth-profile technique[12,13] and was correlated with percent IGSCC in Fig. 6. In the figure, similar results from FEG-STEM[9,20,21] are also plotted for comparison. The latter results were obtained on CERT specimens tested in simulated BWR water containing 8-32 ppm of dissolved O. For a better comparison, percent IGSCC from the present CERT tests conducted with ≈0.3 ppm dissolved O was extrapolated to an O content of 8-32 ppm according to the trend reported by Kodama et al.[19] A comparison similar to that of Fig. 6 has been discussed by Bruemmer et al.[22]

Results obtained by the two techniques appear to be consistent except for HP304-A, in which the Cr depletion profile was extremely narrow and deep according to AES. A more direct comparison of the AES and FEG-STEM data has been given elsewhere.[13] Fig. 6 could be interpreted as suggesting that the FEG-STEM data referred to in Fig. 6 have significant limitations when used to detect Cr content <14 wt.% within ≈1.5 nm of a grain boundary in BWR-irradiated specimens.

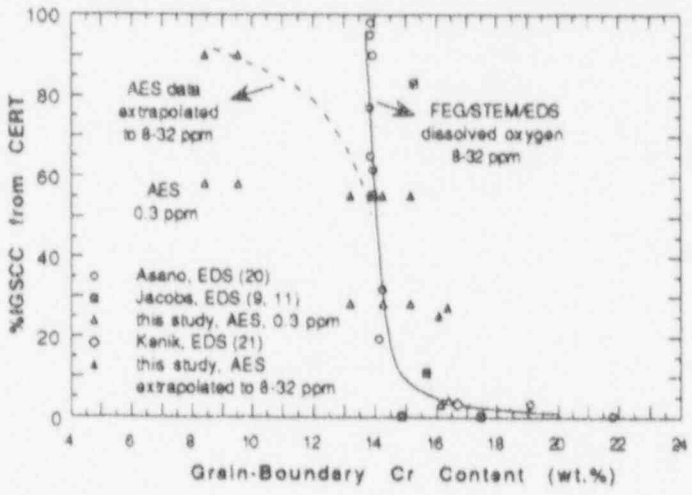


Fig. 6. Percent IGSCC vs. minimum grain-boundary Cr content determined from CERT tests and AES and FEG-STEM analyses of BWR components.

This may be because several limitations are inevitably associated with energy-dispersive spectroscopy (EDS) in the present-generation FEG-STEM. These limitations are the effects of imperfect grain-boundary alignment (e.g., 1-nm uncertainty produced with 1° misalignment in 57-nm-thick film), relatively large beam size, beam broadening,[23,24] effect of a Cr_2O_3 surface layer, and fluoresced Cr X-ray.[9] Because of these limitations, practical resolution in the present-generation FEG-STEM-EDS analysis should be considered close to 3-3.5 nm. This seems to be inadequate to analyze specimens from BWR components in which the Cr-depletion profile is very narrow. The resolution limit can be greatly improved by utilizing the technique of electron energy loss spectroscopy (EELS).[24] Meanwhile, AES data can suffer from the effect of O contamination from the vacuum environment of the microscope.

Without a proper understanding of the limitations of the techniques and uncertainties of measurement, and in the absence of a more convincing database (e.g., data from EELS with a more powerful FEG-STEM), the role of grain-boundary Cr depletion in IASCC (i.e., primary or secondary role) cannot be convincingly determined at the present time. Figure 6, however, indicates that susceptibility is increased significantly by Cr depletion, in particular for percent IGSCC<30% (i.e., lower fluence level). Nevertheless, the large variation in percent IGSCC for a similar grain-boundary Cr content of ≈14-15 wt.% (FEG-STEM data) appears to suggest that an unidentified process other than Cr depletion plays an important role.

Comparative Analysis of Two Similar High-Purity Heats

To provide a clue to the question of whether one or more unidentified processes play an important role in IASCC, a study was conducted with absorber tube specimens that were fabricated from the two virtually identical HP heats, HP304-A (less resistant to IGSCC during CERT tests)[12,17] and HP304-CD (more-resistant to IGSCC during CERT tests[17] and resistant to IASCC failure in reactor[11]). The specimens were irradiated to a similar fluence level of ≈2.0 x 10^{21} n/cm^2. The rationale was that because Si, P, S, C, Ni, Cr, Mn and fluence levels were virtually the same in the two heats, grain-boundary concentrations of these elements and irradiation-induced hardening would also be similar. Therefore, it would be relatively easy to identify other aspects of grain-boundary chemistry, which could be correlated with resistance to IGSCC. The two materials also exhibited a surprisingly large difference in their susceptibility to hydrogen-induced IG fracture in vacuo (see Fig. 5C). In contrast to HP304-CD, it was very difficult to produce IG fracture in vacuum in H-charged specimens of HP304-A, a trend opposite to the susceptibility to IGSCC in water.

Grain-boundary Cr depletion in the two specimens, determined by the AES depth-profiling, is shown in Fig. 7. Not surprisingly, Cr depletion in the specimens was similar.

Grain-boundary segregation behavior of Ni and impurities in the two materials is shown in Fig. 8, where the segregation behavior of Ni, Si, P, C, S, N, X(59-eV), and B can be determined by comparing intensities of the elements on ductile (denoted "D") and intergranular (denoted "I") fracture surfaces. The left- and right-hand columns of Fig. 8 show results measured on HP304-A and HP304-CD, respectively. In Fig. 9, duplicate results obtained from another specimen of HP304-CD are given. In the HP304-A specimen, only Ni segregation was evident. In the HP304-CD specimen, grain-boundary segregation of not only Ni but also of N, X(59-eV), and B was evident. Figures 8H and 9D indicate some extent of segregation of C in the specimens of HP304-CD, although the evidence should be considered less convincing.

Identification of Li on Grain Boundaries

To identify the X(59-eV) peak, Auger spectra were obtained from several types of SS specimens, i.e., irradiated, unirradiated, and Li-corroded specimens. The results are summarized in Fig. 10. The X(59-eV) peak was observed in Auger spectra obtained from irradiated Type 304 SS BWR components (Fig. 10D), unirradiated Type 304 SS specimens

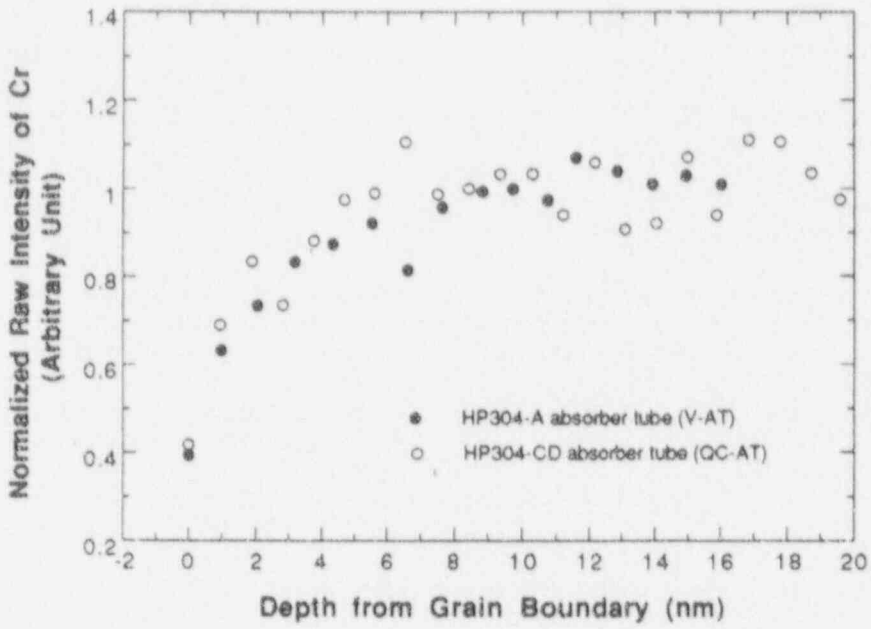


Fig. 7. Grain-boundary Cr-depletion profiles determined by AES analyses of HP304-A and HP304-CD absorber tubes irradiated to 2 x 10^{21} n/cm^2.

that were corroded in liquid Li (at 600°C for 144 h) (Fig. 10B), unirradiated 20 wt.%-Ni Type 310 SS (Fig. 10C), and unirradiated 35 wt.%-Ni Type 330 SS. The characteristic shape of the peak observed in the unirradiated high-Ni 310 SS was somewhat different from those observed in the Li-corroded or irradiated 304 SS specimens. The peak was absent in unirradiated specimens of Types 304, 347, AISI 3340, and martensitic SS, as shown in Fig. 11.

Results from these experiments show that at least some fraction of the intensity of the X(59-eV) peak observed in the specimens of HP304-CD (Figs. 8O and 9G) is due to Li. However, results in Figs. 8A, 8E, and 9A show that the segregation ratios of Ni in HP304-A and HP304-CD are virtually identical. Therefore, grain-boundary concentrations of Ni in the two specimens should be similar, because the bulk concentration of Ni is virtually the same (i.e., 9.45 wt.%; see Table 1). Accordingly, it is difficult to attribute the large difference in the intensities of the X(59-eV) peak between HP304-A (Fig. 8K) and HP304-CD (Fig. 8O) to grain-boundary concentrations of Ni. Segregation behaviors of X(59-eV) (Figs. 8O and 9G) and B (Figs. 8P and 9H) in HP304-CD were also similar. Therefore, we conclude that the X(59-eV) peak observed on the grain boundaries of HP304-CD is, in fact, the secondary peak (≈58 eV) of Li, whereas the primary peak of Li (≈43 eV) was superimposed on the 47-eV peak of Fe.

Li is produced by transmutation of ^{10}B dissolved in specimens by thermal neutrons, i.e., ^{10}B(n, He)^{7}Li. The cross section for this reaction is large, i.e., ≈3840 barn. Natural B dissolved in the absorber tubes is composed of 19.8% ^{10}B and 80.2% ^{11}B. However, it is not clear if one can rule out the possibility that some of the Li atoms detected in the absorber tubes were transported from the side of the B_4C absorber that is enriched in ^{10}B.

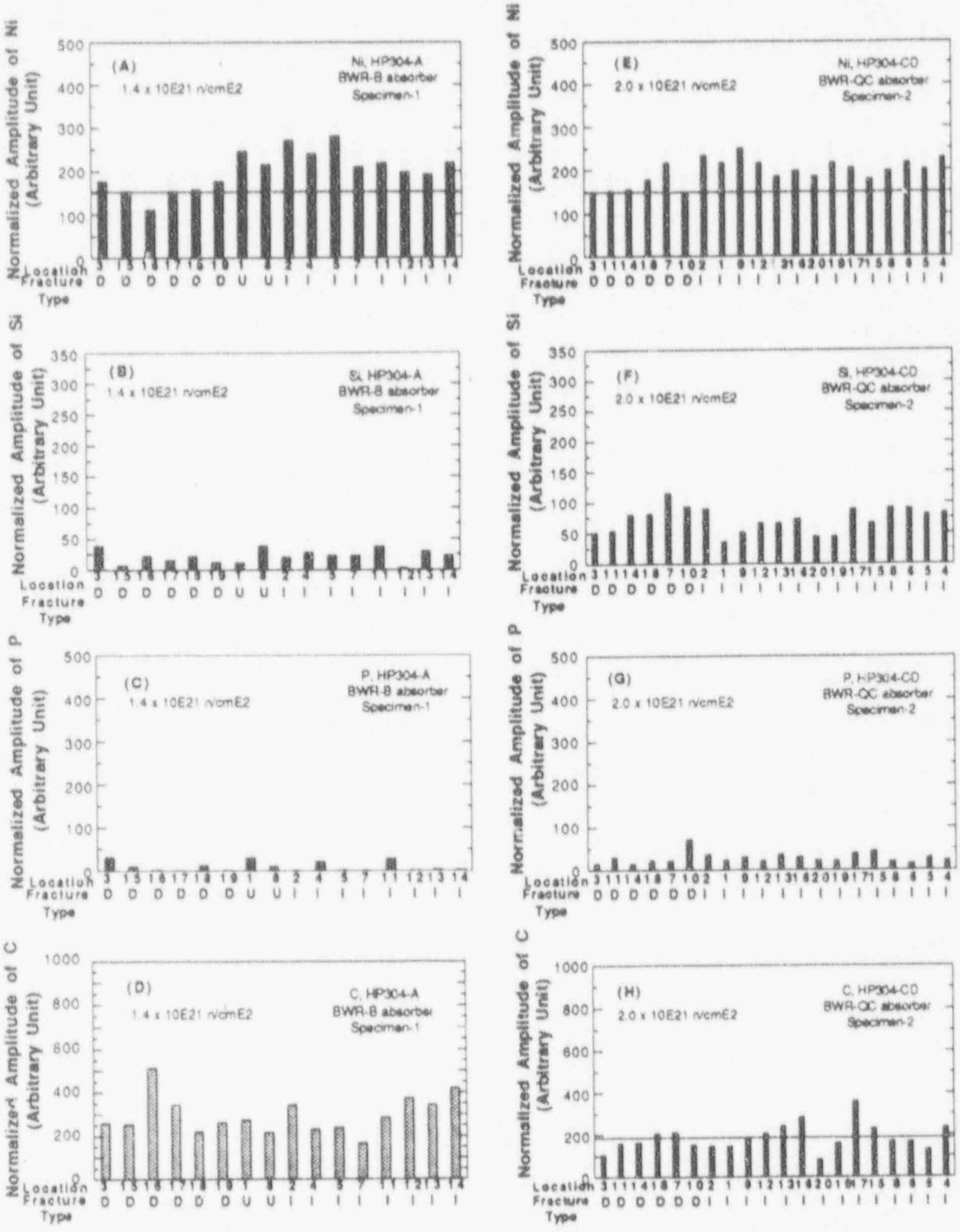


Fig. 8. Intensities of Ni, Si, P, C, S, N, X(59-eV), and B signals from ductile (Denoted by "D"), intergranular ("I"), and faceted ("U") fracture surfaces of the neutron absorber tubes fabricated from HP Heats HP304-A (left columns) and HP304-CD (right columns) and irradiated to ≈2.0 x 10^{21} n/cm^2. When grain-boundary segregation of an element is clear, a horizontal line was drawn to show average intensity of the element away from grain boundaries.

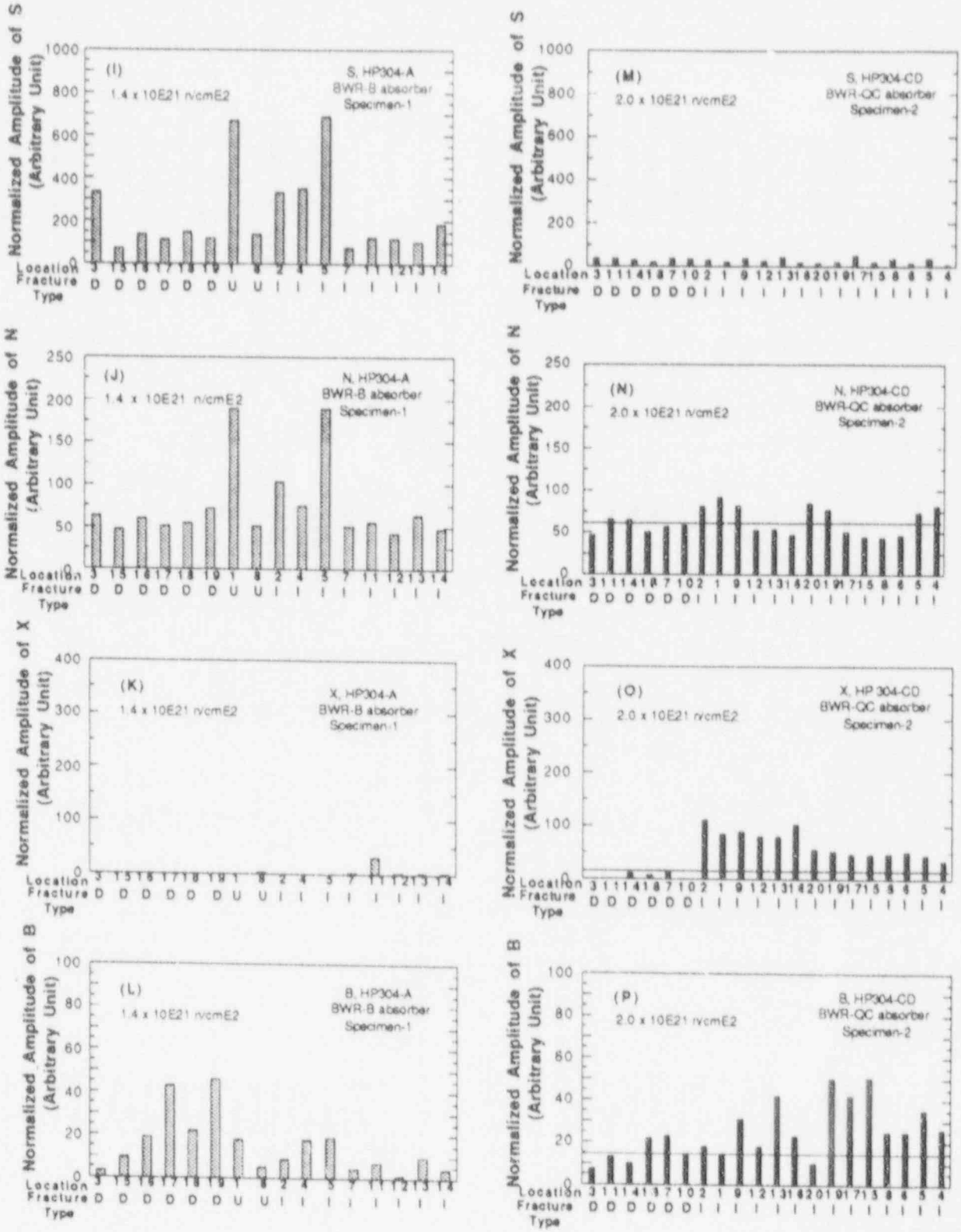

(I)
1.4 x 10E21 n/cmE2
S, HP304-A
BWR-B absorber
Specimen-1
(M)
2.0 x 10E21 n/cmE2
S, HP304-CD
BWR-QC absorber
Specimen-2
(J)
1.4 x 10E21 n/cmE2
N, HP304-A
BWR-B absorber
Specimen-1
(N)
2.0 x 10E21 n/cmE2
N, HP304-CD
BWR-QC absorber
Specimen-2
(K)
1.4 x 10E21 n/cmE2
X, HP304-A
BWR-B absorber
Specimen-1
(O)
2.0 x 10E21 n/cmE2
X, HP304-CD
BWR-QC absorber
Specimen-2
(L)
1.4 x 10E21 n/cmE2
B, HP304-A
BWR-B absorber
Specimen-1
(P)
2.0 x 10E21 n/cmE2
B, HP304-CD
BWR-QC absorber
Specimen-2
Normalized Amplitude of S (Arbitrary Unit)
Normalized Amplitude of N (Arbitrary Unit)
Normalized Amplitude of X (Arbitrary Unit)
Normalized Amplitude of B (Arbitrary Unit)
Location
Fracture Type

Fig. 8. Cont.

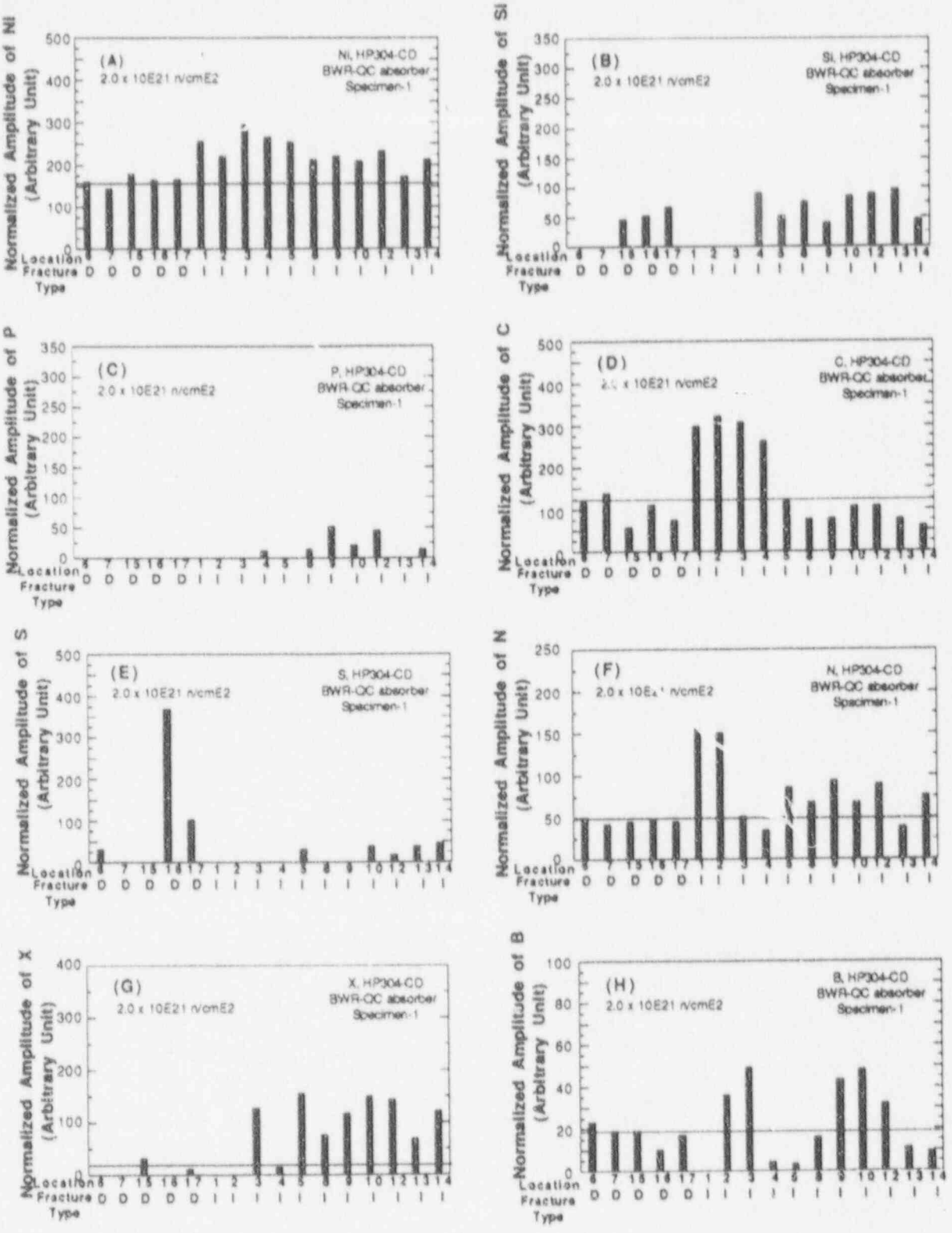


Fig. 9. Intensities of Ni, Si, P, C, S, N, X (59-eV), and B signals (A to H) from ductile (denoted by "D"), intergranular ("I"), and faceted ("U") fracture surfaces of a duplicate specimen from neutron absorber tubes fabricated from HP Heat HP304-CD irradiated to ≈2.0 x 10^{21} n/cm. When grain-boundary segregation of an element is clear, a horizontal line was drawn to show average intensity of the element away from grain boundaries.

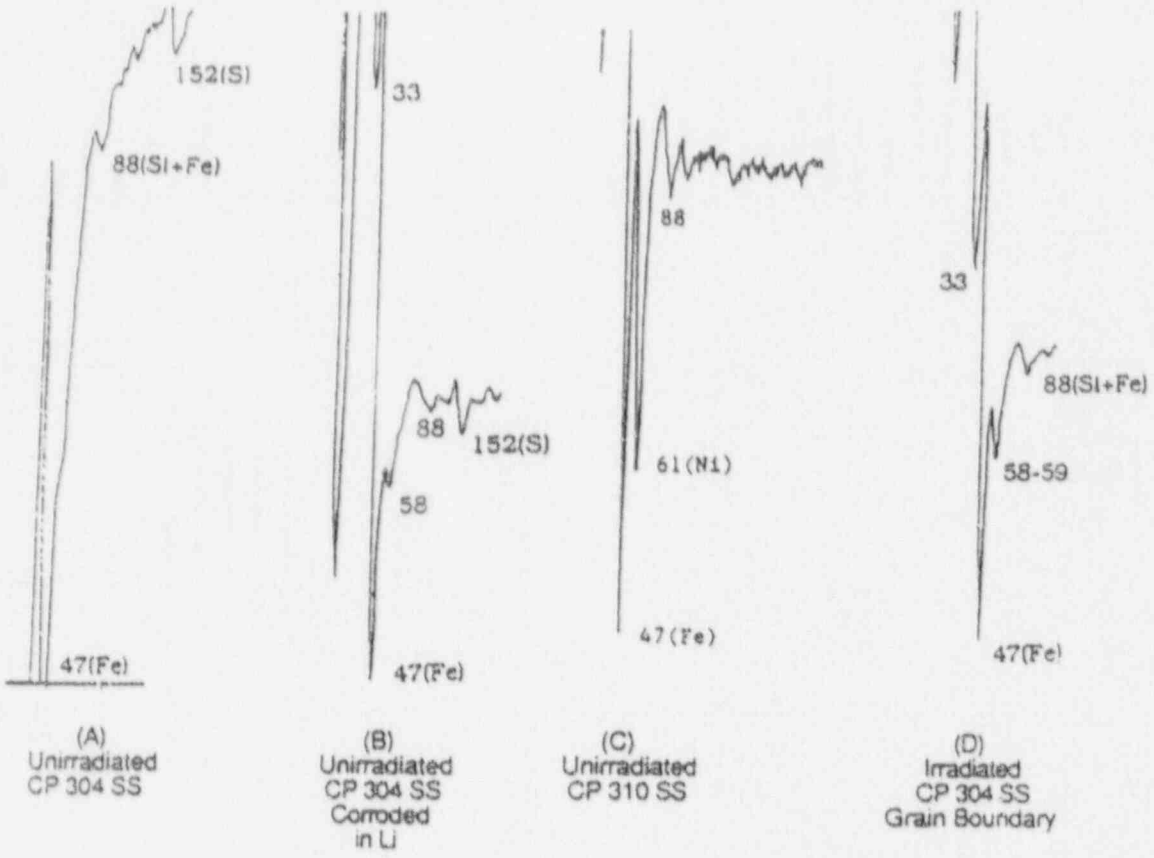


Fig. 10. Characteristic ~59-eV Auger electron peaks obtained from (A) unirradiated CP Type 304; (B) Type 304 unirradiated and corroded in liquid lithium at 600°C for 144 h; (C) unirradiated Type 310 containing ~20 wt.% Ni, and (D) CP Type 304 irradiated to 2 x 10^{21} n/cm^2.

In austenitic steels, B is known to segregate strongly to grain boundaries by a thermal process. Therefore, grain-boundary concentrations of B, and hence Li, could be influenced by the fabrication process in the absorber tubes, even if the tubes were extruded from the same starting material. In a slowly cooled section of a thick component (e.g., BWR top guide), thermal segregation of B is likely to be more pronounced. When segregated, ^{10}B was transmuted to Li and He in the absorber tubes, and Li was scattered away in the vicinity of grain boundaries because of recoil energy from the transmutation. Under these conditions, Li atoms in the HP304-CD specimens seem to have segregated to grain boundaries by the RIS process in significant quantity because the grain-boundary regions were relatively richer in Li. Lithium segregation in HP304-A was negligible, apparently because bulk concentration of B was lower and thermal segregation of B was insignificant during fabrication (Fig. 8L).

Effects of N, B, and Transmutation

Based on grain-boundary segregation behavior (Figs. 7-9) and bulk chemical composition (Table 1), grain-boundary concentrations of alloying and impurity elements in the HP304-A and HP304-CD specimens have been calculated and plotted in Fig. 12. The grain-boundary concentrations were normalized in the plot to facilitate easy comparison of the two materials, with actual numbers given for each element.

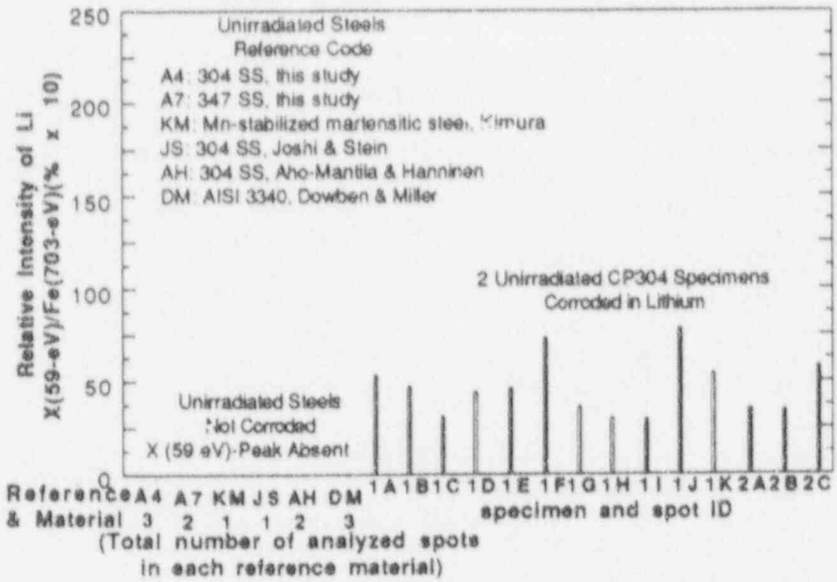


Fig. 11. Intensities of the ≈59-eV Auger electron peaks obtained from several types of unirradiated steels either as-received or corroded in liquid Li at 600°C for 144 h.

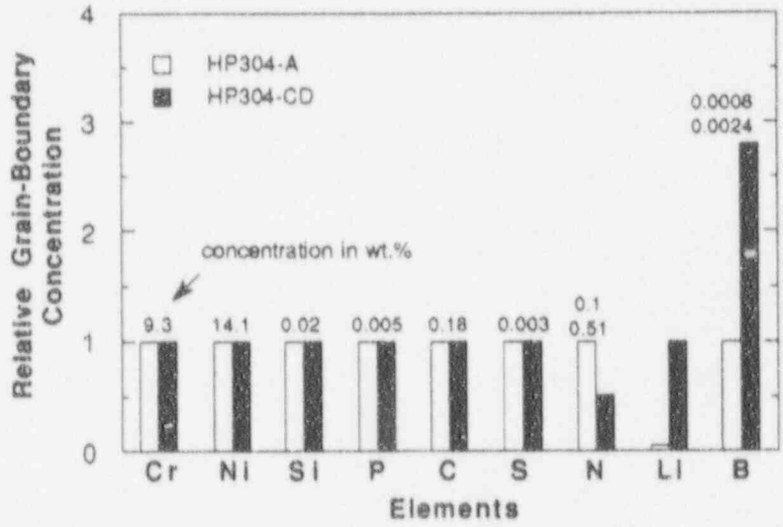


Fig. 12. Relative grain-boundary concentrations of alloying and impurity elements in HP304-A and HP304-CD absorber tube specimens irradiated to ≈2 x 10^{21} n/cm^2.

Figure. 12 shows that grain-boundary concentrations of the two materials are virtually the same, except for N, Li, and B. Grain-boundary concentrations of Cr, Ni, Si, P, C, and S are similar. Therefore, we conclude that higher concentrations of N and lower concentrations of Li and B on grain boundaries are conducive to higher susceptibility to IGSCC.

Higher contents of N and B are known to enhance grain-boundary cohesion in unirradiated steels.[25] However, results of the present investigation indicate an opposite role for N in irradiated steels. The exact mechanism whereby higher N on grain boundaries promotes IGSCC in irradiated materials is not clear. Segregation of N results in a higher concentration of H near grain boundaries because of transmutation of N to H (proton) by thermal neutrons, i.e., $^{14}N(n, p)^{14}C$. The cross section for this reaction is ≈1.83 barn. Although H atoms produced from the reaction recoil from grain boundaries, transmutation of segregated N nevertheless promotes an accumulation of H near a grain-boundary crack tip. The mechanism whereby a greater concentration of Li on grain boundaries is conducive to lower susceptibility to IGSCC is not clear either.

The present study strongly indicates that a synergism between grain-boundary segregation of impurities (N and B) and transmutation by thermal neutrons plays an important role in IASCC. It also suggests that the relative importance of the role of grain-boundary Cr depletion may be not as great as previously believed.

CONCLUSIONS

1. Resistance of in-core components fabricated from high-purity (HP) Type 304 stainless steel to irradiation-assisted stress corrosion cracking (IASCC) is not necessarily superior to that fabricated from commercial-purity (CP) materials. Contrary to previous beliefs, susceptibility to intergranular stress corrosion cracking (IGSCC) could not be correlated with grain-boundary concentrations of Si, P, C, N, or S.

2. Susceptibility to intergranular cracking could be correlated with grain-boundary Cr concentration measured by Auger electron spectroscopy (AES) depth-profiling technique, indicating that Cr depletion influences IASCC. Compounded grain-boundary depletion of Cr by irradiation-induced process and thermal sensitization could aggravate susceptibility of weldments and heat affected zones of in-core components to IGSCC.

3. Grain-boundary concentrations of Cr determined by AES and X-ray energy dispersive spectroscopy (EDS) in currently available field-emission-gun scanning transmission electron microscopes are not sufficiently accurate to clarify the importance of the role of irradiation-induced depletion of grain-boundary Cr (i.e., primary or secondary role).

4. Grain-boundary analysis was conducted on BWR neutron absorber tubes that were fabricated from two HP heats of Type 304 SS of virtually identical chemical composition but differing significantly in susceptibility to IGSCC after irradiation to similar fluence levels. Grain-boundary concentrations of Cr, Ni, Si, P, S, and C of the crack-resistant and -susceptible tubes were virtually identical; however, grain boundaries of the crack-resistant material contained lower concentrations of N and higher concentrations of B and Li than the crack-susceptible material.

5. Boron segregates strongly to grain boundaries by a thermal process in austenitic stainless steels. Therefore, grain-boundary concentrations of B, and hence Li, could be influenced strongly by thermomechanical processes. Even if core-internal components are fabricated from the same starting material, actual grain-boundary concentrations of B and Li could differ significantly during service. In slowly cooled sections of a thicker component (e.g., BWR top guide), segregation of B, and hence Li, is likely to be more pronounced. This is conducive to better resistance to IASCC under otherwise similar conditions. Synergism between grain-boundary segregation (of B or N) and transmutation by neutrons seems to play an important role in IASCC.

ACKNOWLEDGMENTS

The authors are grateful to G. Dragel, D. Donahue, and G. J. Talaber for their experimental contributions. The BWR components were obtained through the kind assistance of Dr. A. J. Jacobs of General Electric Co. and Dr. J. L. Nelson of Electric Power

Research Institute. This work was sponsored by the Office of Nuclear Regulatory Research, U.S. Nuclear Regulatory Commission. The authors are also grateful to Drs. J. Muscara and W. J. Shack for helpful discussions.

REFERENCES

1. J. Low, U. Wolff, and W. Cowden, "Electron Microscopic Examination of Failed Stainless Steel Fuel Cladding - Dresden Advanced Fuel Assemblies PF-1 and PR-4," APED-4242, General Electric Co., May 1963.

2. J. S. Armijo, "Effect of Impurity Additions on the Intergranular Corrosion of High Purity Fe-Cr-Ni Austenitic Alloys," GEAP-5047, General Electric Co., October 1966.

3. J. S. Armijo, "Grain Boundary Studies of Austenitic Stainless Steels," GEAP-5503, General Electric Co., September 1967.

4. J. S. Armijo, "Intergranular Corrosion of Nonsensitized Austenitic Stainless Steels," Corrosion 24 (1968), 24-30.

5. R. Duncan, "Stainless Steel Failure Investigation Program," GEAP-5530, General Electric Co., February 1968.

6. A. Strasser, J. Santucci, K. Lindquist, W. Yario, G. Stern, L. Goldstein, and L. Joseph, "Evaluation of Stainless Steel Cladding in LWRs," EPRI NP-2642, Electric Power Research Institute, Palo Alto, CA, December 1982.

7. F. Garzarolli, D. Alter, and P. Dewes, "Deformability of Austenitic Stainless Steels and Ni-Base Alloys in the Core of a Boiling and Pressurized Water Reactor," Proc. 2nd Int. Symp. Environmental Degradation of Materials in Nuclear Power Systems - Water Reactors, National Association of Corrosion Engineers, Houston, pp. 131-138 (1986).

8. F. Garzarolli, D. Alter, P. Dewes, and J. L. Nelson, "Deformability of Austenitic Stainless Steels and Ni-Base Alloys in the Core of a Boiling and Pressurized Water Reactor," Proc. 3rd Int. Symp. Environmental Degradation of Materials in Nuclear Power Systems - Water Reactors, G. J. Theus and J. R. Weeks, eds., The Metallurgical Society, Warrendale, PA, pp. 657-664 (1988).

9. A. J. Jacobs, R. E. Clausing, M. K. Miller, and C. Shepherd, "Influence of Grain Boundary Composition on the IASCC Susceptibility of Type 348 Stainless Steel," Proc. 4th Int. Symp. Environmental Degradation of Materials in Nuclear Power Systems - Water Reactors, National Association of Corrosion Engineers, Houston, pp. 14-21 to 14-45 (1990).

10. A. J. Jacobs, G. P. Wozadlo, K. Nakata, T. Yoshida, and I. Masaoka, "Radiation Effects on the Stress Corrosion and Other Selected Properties of Type-304 and Type-316 Stainless Steels," Proc. 3rd Int. Symp. Environmental Degradation of Materials in Nuclear Power Systems - Water Reactors, G. J. Theus and J. R. Weeks, eds., The Metallurgical Society, Warrendale, PA, pp. pp. 673-681 (1988).

11. A. J. Jacobs, "The Relationship of Grain Boundary Composition in Irradiated Type 304 SS to Neutron Fluence and IASCC," Effects of Radiation on Materials: 16th Intl. Symp., ASTM STP 1175, A. S. Kumar, D. S. Gelles, R. K. Nanstad, and T. A. Little, eds., American Society for Testing and Materials, Philadelphia (1993).

12. H. M. Chung, W. E. Ruther, J. E. Sanecki, A. G. Hins, and T. F. Kassner, "Stress Corrosion Cracking Susceptibility of Irradiated Type 304 Stainless Steels," Effects of Radiation on Materials: 16th Int. Symp., ASTM STP 1175, A. S. Kumar, D. S. Gelles, R. K. Nanstad, and T. A. Little, eds., American Society for Testing and Materials, Philadelphia (1993).

13. H. M. Chung, W. E. Ruther, J. E. Sanecki, and A. G. Hins, in Environmentally Assisted Cracking in Light Water Reactors: Semiannual Report April-September 1992, NUREG/CR-4667, Vol. 15, ANL-93/2, Argonne National Laboratory, pp. 28-60, June 1993.

14. K. Fukuya, S. Shima, H. Kayano, and M. Narui, "Stress Corrosion Cracking and Intergranular Corrosion of Neutron-Irradiated Austenitic Steels," J. Nucl. Mater., 191-194 (1992), 1007-1011.

15. K. Fukuya, K. Nakata, and A. Horie, "An IASCC Study Using High-Energy Ion Irradiation," Proc. 5th Int. Symp. Environmental Degradation of Materials in Nuclear Power Systems - Water Reactors, American Nuclear Society, La Grange Park, IL, pp. 814-820 (1992).

16. J. M. Cookson, R. D. Carter, D. L. Damcott, M. Atzmon, G. S. Was, and P. L. Andresen, "Stress Corrosion Cracking of High-Energy Proton-Irradiated Stainless Steels," ibid., pp. 806-813.

17. A. J. Jacobs, General Electric Co., San Jose, CA, private communication, 1993.

18. P. L. Andresen, F. P. Ford, S. M. Murphy, and J. M. Perks, "State of Knowledge of Radiation Effects on Environmental Cracking in Light Water Reactor Core Materials," Proc. 4th Int. Symp. Environmental Degradation of Materials in Nuclear Power Systems - Water Reactors, National Association of Corrosion Engineers, Houston, pp. 1-83 to 1-121 (1990).

19. M. Kodama, S. Nishimura, J. Morisawa, S. Shima, S. Suzuki, and M. Yamamoto, "Effects of Fluence and Dissolved Oxygen on IASCC in Austenitic Stainless Steels," Proc. 5th Int. Symp. Environmental Degradation of Materials in Nuclear Power Systems - Water Reactors, American Nuclear Society, La Grange Park, IL, pp. 948-954 (1992).

20. K. Asano, K. Fukuya, K. Nakata, and K. Kodama, "Changes in Grain Boundary Composition by Neutron Irradiation on Austenitic Stainless Steels," ibid. pp. 838-843.

21. E. A. Kenik, "Radiation-Induced Segregation in Irradiated Type 304 Stainless Steels," J. Nucl. Mater. 187 (1992), 239-246.

22. S. M. Bruemmer, B. W. Arey, and L. A. Charlot, "Influence of Chromium Depletion on the Intergranular Stress Corrosion Cracking of 304 Stainless Steel," Corrosion 48 (1992), 42-49.

23. D. I. R. Norris, C. Baker, and J. M. Titchmarsh, "Compositional Profiles at Grain Boundaries in 20%Cr/25%Ni/Nb Stainless Steel," Proc. Symp. on Radiation-Induced Sensitization of Stainless Steels, D. Norris ed., Central Electricity Generating Board, Berkeley, England, pp. 86-98, 1987.

24. J. M. Titchmarsh and I. A. Vatter, "Measurement of Radiation-Induced Segregation Profiles by High Spatial Resolution Electron Microscopy," ibid., pp. 74-85.

25. M. Polak, "Interfacial Segregation in Steel and Steels-Related Alloys," in Surface Segregation Phenomena, P. A. Dowben and A. Miller eds., CRC Press, Boca Raton, FL, pp. 291-325, 1990.

Fatigue of Carbon and Low-Alloy Steels in LWR Environments*

O. K. Chopra, W. F. Michaud, and W. J. Shack
Energy Technology Division
Argonne National Laboratory
Argonne, Illinois 60439

Abstract

Fatigue tests have been conducted on A106-Gr B carbon steel and A533-Gr B low-alloy steel to evaluate the effects of an oxygenated-water environment on the fatigue life of these steels. For both steels, environmental effects are modest in PWR water at all strain rates. Fatigue data in oxygenated water confirm the strong dependence of fatigue life on dissolved oxygen (DO) and strain rate. The effect of strain rate on fatigue life saturates at some low value, e.g., between 0.0004 and 0.001%/s in oxygenated water with ≈0.8 ppm DO. The data suggest that the saturation value of strain rate may vary with DO and sulfur content of the steel. Although the cyclic stress-strain and cyclic-hardening behavior of carbon and low-alloy steels is distinctly different, the degradation of fatigue life of these two steels with comparable sulfur levels is similar. The carbon steel exhibits pronounced dynamic strain aging, whereas strain-aging effects are modest in the low-alloy steel. Environmental effects on nucleation of fatigue crack have also been investigated. The results suggest that the high-temperature oxygenated water has little or no effect on crack nucleation.

1 Introduction

Plain carbon and low-alloy steels are used extensively in PWR and BWR steam supply systems as piping and pressure-vessel materials. The steels of interest in these applications include A106-Gr B and A333-Gr 6 for seamless pipe and A302-Gr B, A508-2, and A533-Gr B plate for pressure vessels. The ASME Code Section III (Division 1, Subsection NB) includes rules for the construction of Class 1 components in nuclear power plants. It recognizes fatigue as a possible mode of failure in pressure vessel steels and piping materials. The current Code design curves, specified in Figure I-90 of Appendix I to Section III, are based primarily on strain-controlled fatigue tests of small polished specimens in air at room temperature.[1] The Code design curves were obtained by decreasing the best-fit curves to the experimental data by a factor of 2 on stress or a factor of 20 on cycles, whichever was more conservative at each point. The factors were intended to account for uncertainties in translating the experimental data of laboratory test specimens to actual reactor components. The factor of 20 on cycles is the product of three subfactors: 2 for scatter of data (minimum to mean), 2.5 for size effects, and 4 for surface finish, atmosphere, etc.[2] "Atmosphere" was intended to reflect the effects of an industrial environment rather than the controlled environment of a laboratory. The effects of the coolant environment are not explicitly addressed in the Code design curves.

*Work supported by the Office of Nuclear Regulatory Research, U.S. Nuclear Regulatory Commission, FIN Nos. A22122 and A22562, Program Manager Dr. J. Muscara.

Recent fatigue strain vs. life (S/N) data from the U.S.[3-10] and Japan[11-13] illustrate potentially significant effects of the LWR environment on the fatigue resistance of carbon and low-alloy steels. Specimen lives in simulated LWR environments can be much shorter than for the corresponding tests in air. In some cases, failures were observed below the ASME Code fatigue design curve for components. These results raise the issue of whether the fatigue design curves in Section III are appropriate for the purposes intended and whether they adequately account for environmental effects on fatigue behavior. The factors of 2 and 20 applied to the mean-data curve may not be as conservative as originally intended.

Several key variables that influence environmental effects can be identified from the available S/N data. The results indicate that environmental effect on fatigue life can be significant when all of the following variables exceed threshold values: (a) sulfur content of the steel is >0.003 wt.%, (b) concentration of dissolved oxygen (DO) in the water is ≥0.1 ppm, and (c) loading rate during the tensile half of the fatigue cycle is ≤0.1 %/s. The actual threshold values for a specific variable may vary with material and environmental conditions. For example, a sulfur content of ≥0.007% may be needed for environmental effects at 0.1 ppm DO, whereas a sulfur content of ≥0.004% may be sufficient at 1 ppm DO. Other factors that also affect fatigue life include alloy composition/structure, temperature, applied strain, loading history, and surface pitting. A threshold value or condition may also exist for these variables, e.g., a minimum plastic strain is required for environmental effects. However, the existing S/N data base is inadequate to establish these thresholds.

At the very low levels of DO characteristic of PWRs or BWRs with hydrogen/water chemistry, environmental effects on fatigue life are modest at all temperatures and strain rates. Fatigue life decreases rapidly as DO increases over a narrow range of ≈0.1-0.3 ppm, but further increases up to 8 ppm cause only a modest decrease in life. In oxygenated water, fatigue life strongly depends on temperature and strain rate. At a given strain rate, fatigue life increases by a factor of 5 or more as the temperature is decreased from 288 to 200°C. For the same environment and strain range, fatigue lives can be decreased by a factor of ≈50 by reducing the strain rate from 0.1 to 0.0001%/s. Based on the existing S/N data, Argonne National Laboratory (ANL) has developed interim fatigue design curves that take into account temperature, DO level in the water, sulfur level in the steel, and strain rate.[14]

The existing S/N data on carbon and low-alloy steels are somewhat limited and do not cover the range of loading conditions found in actual reactor operation. The data do not extend over the range of strain rates normally encountered in service, e.g., some transients may have strain rates as low as 0.00001%/s. Extrapolation of available data to such low values would predict a reduction in fatigue life by a factor of >300. The relatively good service experience of carbon steel piping in BWRs, i.e., 288°C water with 0.2 ppm DO, suggests that the effect of strain rate on fatigue life must saturate at some level, although direct experimental observations of saturation are very limited. Furthermore, environmental effects on crack nucleation have been considered as a possible mechanism for the reduction in fatigue life.[11,12] High-sulfur steels are more susceptible because cracks can initiate at surface micropits that form near manganese sulfide (MnS) inclusions. Effects of crack nucleation are important at low strain ranges, where experimental data are not available. Virtually all data in oxygenated water are at relatively high strain ranges where fatigue life is dominated by crack propagation.

The S/N data from Japan, compiled in the data base JNUFAD* for "Fatigue Strength of Nuclear Plant Component," also indicate that environmental effects on fatigue life are greater for carbon steel than for low-alloy steel.[11] However, most low-alloy steels that have been investigated in JNUFAD are low-sulfur heats (<0.007 wt.%). It is likely that differences between carbon and low-alloy steels are caused by the sulfur content of the steels and that compositional or structural differences have only minor effects on fatigue life.

This paper presents the results from fatigue tests conducted on A106-Gr B carbon steel and A533-Gr B low-alloy steel under conditions where information is lacking in the existing S/N data base. The effect of various material and test variables, e.g., strain rate, DO, strain range, composition, and surface pitting, on fatigue life of carbon and low-alloy steels has been evaluated. One of the major objectives of this year's work was to confirm that high-cycle fatigue life is little affected by LWR environments even at lower strain rates.

2 Experimental

Low-cycle fatigue tests are being conducted on A106-Gr B carbon steel and A533-Gr B low-alloy steel with an MTS closed-loop electrohydraulic machine. The A533-Gr B material was obtained from the lower head of the Midland reactor vessel, which was scrapped before the plant was completed. The A106-Gr B material was obtained from a 508-mm-diameter schedule 140 pipe fabricated by the Cameron Iron Works, Houston, TX. The chemical compositions of the two materials are given in Table 1, and average room-temperature tensile properties are given in Table 2. Microstructures of the steels are shown in Fig. 1; carbon steel has a pearlitic structure, whereas the low-alloy steel consists of tempered bainite. Smooth cylindrical specimens with 9.5-mm diameter and 19-mm gage length were used for the fatigue tests.

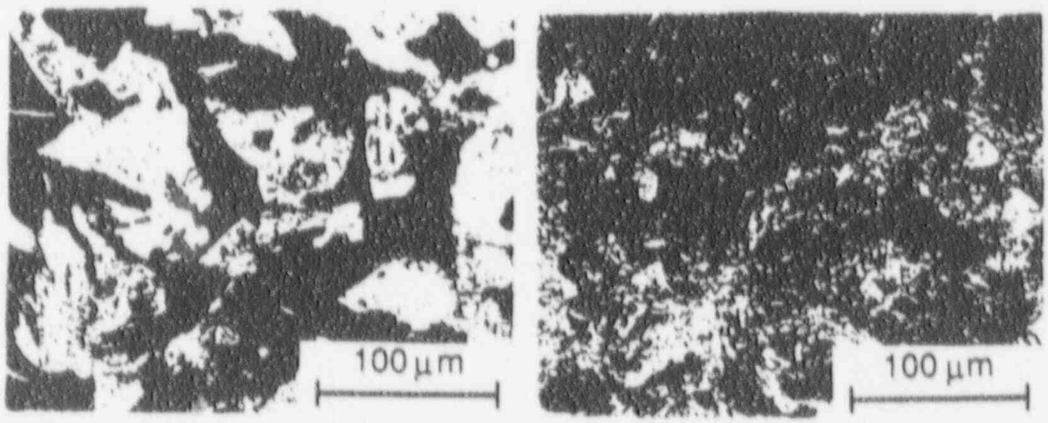


Figure 1. Microstructures of (a) A106-Gr B carbon steel and (b) A533-Gr B low-alloy steel

*Private communication from M. Higuchi, Ishikawajima-Harima Heavy Industries Co., Japan, to M. Prager of the Pressure Vessel Research Council (PVRC), January 1992. The old data base "FADAL" has been revised and renamed "JNUFAD."

Table 1. Chemical composition (wt.%) of ferritic steels used for fatigue tests

Material	Source/ Reference [a]	C	P	S	Si	Fe	Cr	Ni	Mn	Mo
					Carbon Steel					
A106-Gr B [b]	ANL	0.29	0.013	0.015	0.25	Bal	0.19	0.09	0.88	0.05
	Supplier	0.29	0.016	0.015	0.24	Bal	-	-	0.93	-
A106-Gr B	Terrell (7)	0.26	0.008	0.020	0.28	Bal	0.015	0.002	0.92	0.003
A333-Gr 6	Higuchi (11)	0.20	0.020	0.015	0.31	Bal	-	-	0.93	-
					Low-Alloy Steel					
A533-Gr B [c]	ANL	0.22	0.010	0.012	0.19	Bal	0.18	0.51	1.30	0.48
	Supplier	0.20	0.014	0.016	0.17	Bal	0.19	0.50	1.28	0.47
A533-Gr B	JNUFAD	0.19	0.020	0.010	0.27	Bal	0.13	0.60	1.45	0.52

[a] Reference number given within parentheses.
[b] Schedule 140 pipe 508-mm O.D. fabricated by Cameron Iron Works, Heat J-7201. Actual heat treatment not known.
[c] Hot-pressed plate 162 mm thick from Midland reactor lower head. Austenitized at 871-899°C for 5.5 h and brine quenched, then tempered at 649-663°C for 5.5 h and brine quenched. The plate was machined to a final thickness of 127 mm. The I.D. surface was inlaid with 4.8-mm weld cladding and stress relieved at 607°C for 23.8 h.

Table 2. Average room-temperature tensile properties of ferritic steels

Material	Reference[a]	Yield Stress (MPa)	Ultimate Stress (MPa)	Elongation (%)	Reduction in Area (%)
			Carbon Steel		
A106-Gr B	ANL	301	572	23.5	44.0
A106-Gr B	Terrell (7)	300	523	36.6	66.3
A333-Gr 6	Higuchi (10)	302	489	41.0	80.0
			Low-Alloy Steel		
A533-Gr B	ANL	431	602	27.8	66.6
A533-Gr B	JNUFAD	488	630	27.7	65.2

[a] Reference number given within parentheses.

All tests were conducted at 288°C with fully reversed axial loading (i.e., strain ratio $R = -1$) and a triangular or sawtooth wave form. Unless otherwise mentioned, the strain rate for the triangular wave and fast-loading half of the sawtooth wave was 0.4%/s. Tests in water were performed under stroke control where the specimen strain was controlled between two locations outside the autoclave. Tests in air were performed under strain control with an axial extensometer; specimen strain between the two locations used in the water tests was also recorded.

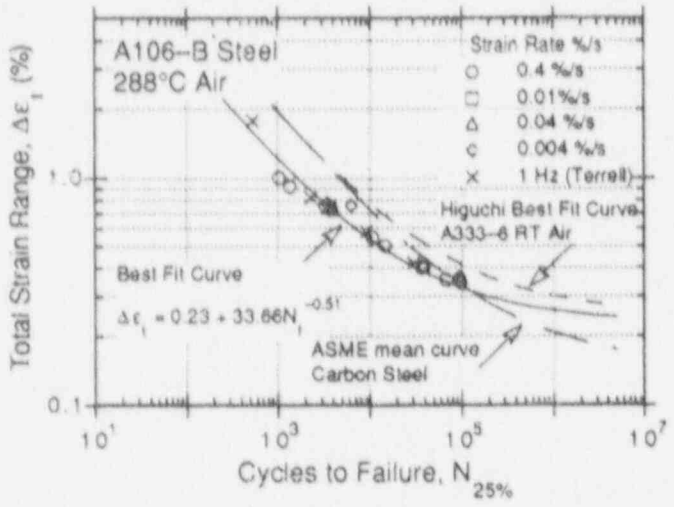


Figure 2.
Total strain range vs. fatigue life data for A106–Gr B steel in air

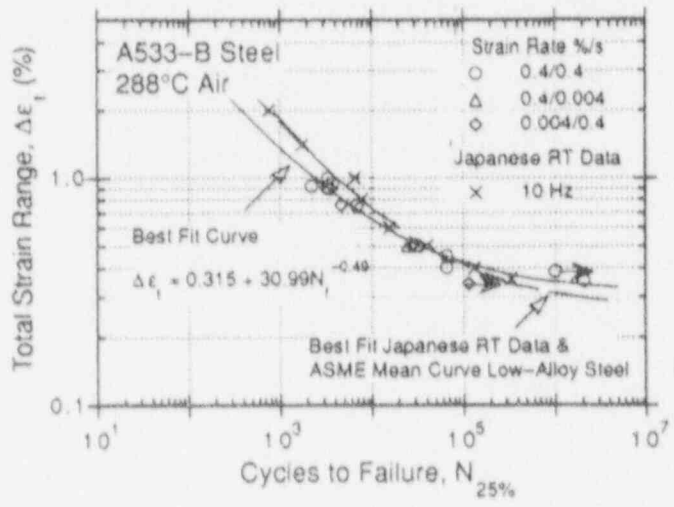


Figure 3.
Total strain range vs. fatigue life data for A533–Gr B steel in air

Information from the air tests was used to determine the stroke required to maintain constant strain in the specimen gage length for tests in water; stroke was gradually increased during the test to maintain constant strain in the specimen. A detailed description of the test facility and procedure have been presented elsewhere.[10]

3 Results

The fatigue results on A106–Gr B and A533–Gr B steels are summarized in Tables 3 and 4, respectively. The total strain range ($\Delta\varepsilon_t$) vs. fatigue life (N_{25}) curves for the carbon and low–alloy steels in air are shown in Figs. 2 and 3, respectively. Fatigue life is defined as the number of cycles required for a 25% decrease in tensile stress amplitude. Results from other investigations[7,11] on similar steels with comparable composition, in particular sulfur content, and the ASME Section III mean–data curves are also included in the figures. The results indicate that

Table 3. Fatigue test results for A106B steel

Test Number	Environment[a]	Dissolved Oxygen (ppb)	pH at RT	Conductivity (μS/cm)	Tensile Rate[b] (%/s)	Comp. Rate[b] (%/s)	Stress Range (MPa)	Strain Range (%)	Life N_{25} (Cycles)	Pre exposure[c]
				Strain Control Tests						
1498	Air	-	-	-	0.4	0.4	1001.4	1.004	1,048	
1553	Air	-	-	-	0.4	0.4	921.1	0.757	3,253	
1615	Air	-	-	-	0.04	0.4	959.8	0.755	3,873	
1609	Air	-	-	-	0.004	0.4	1026.0	0.756	3,721	
1673	Air	-	-	-	0.004	0.4	1003.6	0.759	6,275	
1543	Air	-	-	-	0.4	0.4	818.2	0.502	14,525	
1638	Air	-	-	-	0.4	0.4	803.0	0.440	26,728	1
1636	Air	-	-	-	0.4	0.4	749.6	0.402	34,829	2
1619	Air	-	-	-	0.4	0.4	741.7	0.401	37,142	
1621	Air	-	-	-	0.01	0.4	787.1	0.403	38,128	
1550	Air	-	-	-	0.4	0.4	681.7	0.353	66,768	
1552	Air	-	-	-	0.4	0.4	680.6	0.352	93,322	
1644	Air	-	-	-	0.004	0.4	702.0	0.364	>95,000	
				Stroke Control Tests						
1546	Air	-	-	-	0.4	0.4	975.7	0.916	1,365	
1612	Air	-	-	-	0.004	0.4	1008.2	0.779	3,424	
1554	Air	-	-	-	0.4	0.4	896.8	0.730	3,753	
1548	Air	-	-	-	0.4	0.4	831.9	0.545	10,632	
1555	Air	-	-	-	0.4	0.4	676.3	0.343	98,456	
1547	PWR	8	6.7	23.26	0.4	0.4	1010.9	0.987	692	
1564	PWR	12	6.6	21.74	0.4	0.4	942.0	0.769	1,525	
1549	PWR	8	6.7	25.64	0.4	0.4	827.0	0.533	9,396	
1560	PWR	12	6.6	23.73	0.4	0.4	701.3	0.363	35,190	
1556	PWR	8	6.6	22.73	0.4	0.4	710.9	0.360	38,632	
1632	BWR	800	5.8	0.11	0.4	0.4	913.3	0.740	2,077	
1614	BWR	400	5.9	0.11	0.004	0.4	930.4	0.786	303	
1623	BWR	800	5.9	0.08	0.004	0.004	943.8	0.792	338	
1616	BWR	800	5.8	0.08	0.0004	0.4	912.8	0.799	153	
1620	BWR	900	5.9	0.11	0.00004	0.004	943.1	0.794	161	
1634	BWR	800	5.8	0.16	0.4	0.4	733.2	0.400	19,318	
1624	BWR	800	5.9	0.10	0.004	0.4	775.7	0.456	2,276	
1639	BWR	800	5.9	0.09	0.004	0.4	751.6	0.418	2,951	
1637	BWR	900	5.9	0.11	0.4	0.4	788.0	0.470	16,622	3
1643	BWR	800	6.0	0.11	0.004	0.4	698.5	0.363	>65,000	

[a] Simulated PWR water contains 2 ppm lithium and 1000 ppm boron.

[b] Values for stroke-control tests are approximate. Actual strain rates range between ±5% of the listed value.

[c] Preexposure conditions are as follows:

1. Prior to being tested in air, specimen was fatigued for 570 cycles in oxygenated water with 800 ppb DO at 0.46% strain range with sawtooth wave form, 0.004 and 0.4%/s strain rates in tension and compression.
2. Specimen oxidized in oxygenated water with 600 ppb DO for 100 h at 288°C.
3. Specimen was fatigued for 569 cycles in oxygenated water with 800 ppb DO at 0.46% strain range with sawtooth wave form, 0.004 and 0.4%/s strain rates in tension and compression.

Table 4. Fatigue test results for A533B steel

Test Number	Environment[a]	Dissolved Oxygen (ppb)	pH at RT	Conductivity (μS/cm)	Tensile Rate[b] (%/s)	Comp. Rate[b] (%/s)	Stress Range (MPa)	Strain Range (%)	Life N_{25} (Cycles)	Pre exposure[c]
				Strain Control Tests						
1508	Air	-	-	-	0.4	0.4	910.9	1.002	3,305	
1515	Air	-	-	-	0.4	0.4	866.1	0.752	6,792	
1625	Air	-	-	-	0.004	0.4	887.7	0.757	4,592	
1629	Air	-	-	-	0.4	0.4	782.9	0.503	31,243	1
1505	Air	-	-	-	0.4	0.4	767.6	0.501	31,200	
1576	Air	-	-	-	0.004	0.4	805.8	0.503	28,129	
1590	Air	-	-	-	0.4	0.004	821.1	0.503	24,471	
1640	Air	-	-	-	0.4	0.4	710.9	0.402	65,880	
1517	Air	-	-	-	0.4	0.4	692.5	0.353	2,053,295	
1659	Air	-	-	-	0.004	0.4	656.2	0.343	>114,294	
				Stroke Control Tests						
1521	Air	-	-	-	0.4	0.4	889.4	0.910	3,219	
1523	Air	-	-	-	0.4	0.4	898.6	0.917	2,206	
1522	Air	-	-	-	0.4	0.4	905.4	0.899	3,419	
1524	Air	-	-	-	0.4	0.4	892.3	0.950	3,714	
1525	Air	-	-	-	0.4	0.4	743.6	0.452	65,758	
1538	Air	-	-	-	0.4	0.4	708.0	0.387	>1,000,000	
1526	DI	16	-	-	0.4	0.4	876.4	0.873	3,332	
1527	DI	17	6.0	-	0.4	0.4	752.8	0.493	10,292	
1528	DI	5	5.8	-	0.4	0.4	744.1	0.488	25,815	
1530	PWR	3	6.9	41.67	0.4	0.4	885.5	0.894	1,355	
1545	PWR	8	6.9	22.73	0.4	0.4	889.7	0.886	3,273	
1533	PWR	4	6.9	45.45	0.004	0.4	916.0	0.774	3,416	
1529	PWR	3	6.9	45.45	0.4	0.4	743.4	0.484	31,676	
1588	PWR	6	6.5	23.26	0.004	0.4	828.7	0.514	15,321	
1605	PWR	9	6.5	23.81	0.4	0.004	785.2	0.460	>57,443	
1539	PWR	6	6.8	38.46	0.4	0.4	694.8	0.373	136,570	
1542	PWR	6	6.6	27.03	0.4	0.4	631.8	0.354	>1,154,892	
1645	BWR	800	6.1	0.07	0.4	0.4	831.1	0.721	2,736	
1626	BWR	900	5.9	0.13	0.004	0.4	910.1	0.788	247	
1627	BWR	800	5.9	0.10	0.004	0.4	826.8	0.534	769	
1641	BWR	800	5.9	0.09	0.4	0.4	693.0	0.374	17,367	
1665	BWR	800	6.1	0.08	0.004	0.4	717.0	0.376	3,455	
1666	BWR	750	6.1	0.09	0.0004	0.4	728.4	0.376	>7,000	
1647	BWR	800	6.1	0.09	0.4	0.4	688.0	0.363	26,165	
1660	BWR	750	6.1	0.11	0.004	0.4	689.6	0.360	>83,024	
1649	BWR	700	6.3	0.08	0.4	0.4	673.4	0.352	28,710	
1652	BWR	700	6.1	0.09	0.4	0.4	638.1	0.328	56,923	
1655	BWR	750	6.1	0.10	0.4	0.4	567.6	0.298	>1,673,954	

[a] DI: Deionized water.
Simulated PWR water contains 2 ppm lithium and 1000 ppm boron.
[b] Values for stroke-control tests are approximate. Actual strain rates are ±5% of the listed value.
[c] Preexposure conditions are as follows:
1. Specimen oxidized in oxygenated water with 600 ppb DO for 100 h at 288°C.

for both steels, strain rate has no effect on fatigue life in air. The data for A106-Gr B steel are in excellent agreement with results obtained by Terrell[6,7] on A106-Gr B steel, but are lower by a factor of ≈5 than those obtained by Higuchi and Iida[11] on A333-Gr 6 steel. Also, the data for A106-Gr B steel are below the ASME mean-data curve for carbon steel at room temperature at high strain ranges (by a factor of 3), but are above the ASME mean curve at low strain ranges. The combined data from the present study and those obtained by Terrell for A106-Gr B steel may be expressed by the relationship

$$\Delta\varepsilon_t = 0.230 + 33.66 N_{25}^{-0.51}. \tag{1}$$

The results for A533-Gr B steel show good agreement with the JNUFAD data on A533-Gr B steel and the ASME mean-data curve for low-alloy steel at room temperature. The data for A533-Gr B steel may be expressed by the relationship

$$\Delta\varepsilon_t = 0.315 + 30.99 N_{25}^{-0.49}. \tag{2}$$

3.1 Alloy Composition

The cyclic-hardening behavior of carbon and low-alloy steels is significantly different. Plots of cyclic stress range vs. fatigue cycles for A106-Gr B and A533-Gr B steels tested in air at 288°C and a total strain range of ≈0.75% are shown in Figs. 4 and 5, respectively. Cyclic strain-hardening of the steels is consistent with their microstructure. The A106-Gr B steel, with a pearlitic structure and low yield stress, exhibits rapid hardening during the initial 100 cycles of fatigue life. The extent of hardening increases with applied strain range. In addition, the A106-Gr B carbon steel also exhibits dynamic strain aging, a time-dependent phenomenon caused by interstitial elements dissolved in the ferrite matrix. Consequently, cyclic stress of carbon steel increases significantly with decreasing strain rate, although its fatigue life is not affected (Fig. 4). In contrast, the A533-Gr B low-alloy steel consists of a tempered bainitic structure, has a relatively high yield stress, and shows little or no initial hardening (Fig. 5). At low strain ranges, the A533-Gr B steel shows cyclic softening during the initial 100 cycles of fatigue life (Fig. 6). Because of its tempered bainitic structure, the low-alloy steel exhibits little or no dynamic strain aging.

The cyclic stress vs. strain curves for A106-Gr B and A533-Gr B steels at 288°C are shown in Figs. 7 and 8, respectively; cyclic stress corresponds to the value at half life. The results for A106-Gr B steel show excellent agreement with the data obtained by Terrell.[7] The total strain range $\Delta\varepsilon_t$ (%) can be expressed in terms of the cyclic stress range (MPa) with the equation obtained by Terrell at 288°C:

$$\Delta\varepsilon_t = \frac{\Delta\sigma}{1907.8} + \left(\frac{\Delta\sigma}{1010.4}\right)^{11.55}. \tag{3}$$

The best-fit stress vs. strain curve for A533-Gr B steel is represented by

$$\Delta\varepsilon_t = \frac{\Delta\sigma}{1965.0} + \left(\frac{\Delta\sigma}{956.0}\right)^{11.10}. \tag{4}$$

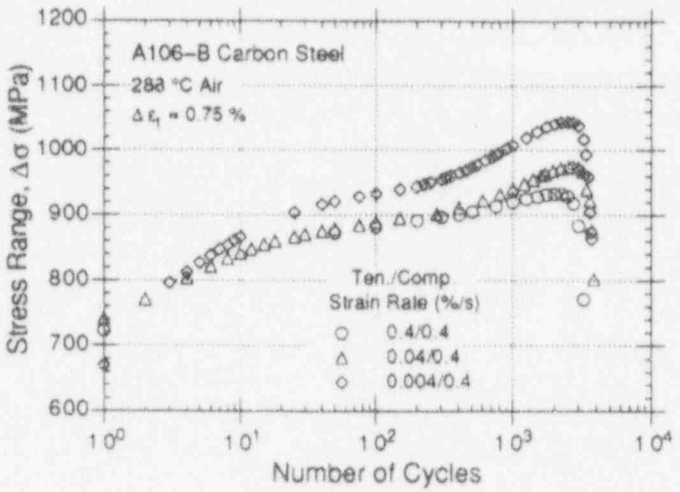


Figure 4.
Effect of strain rate on cyclic strain-hardening behavior of A106–Gr B steel in air at 288°C

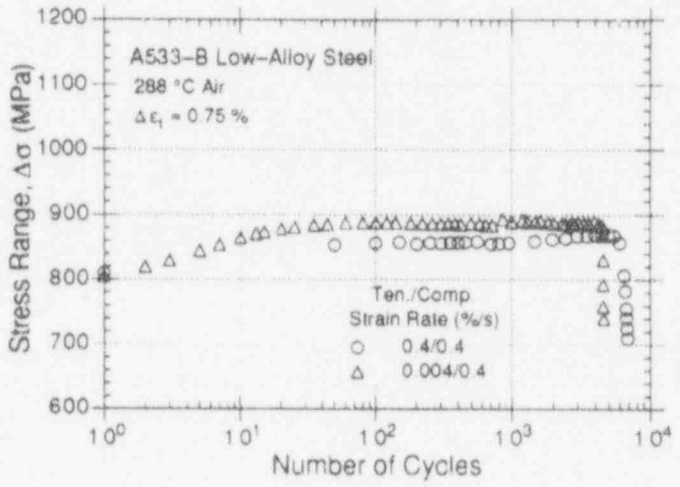


Figure 5.
Effect of strain rate on cyclic strain-hardening behavior of A533–Gr B steel in air at 288°C

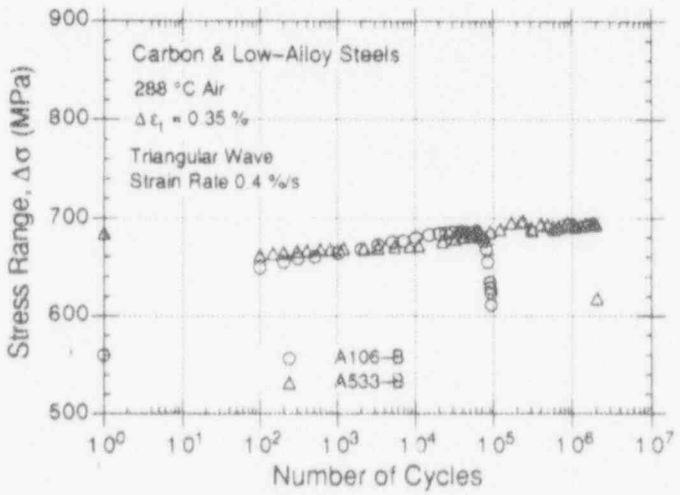


Figure 6.
Cyclic strain-hardening behavior of A106–Gr B and A533–Gr B steels at 0.35% total strain range and 0.4 %/s strain rate in air

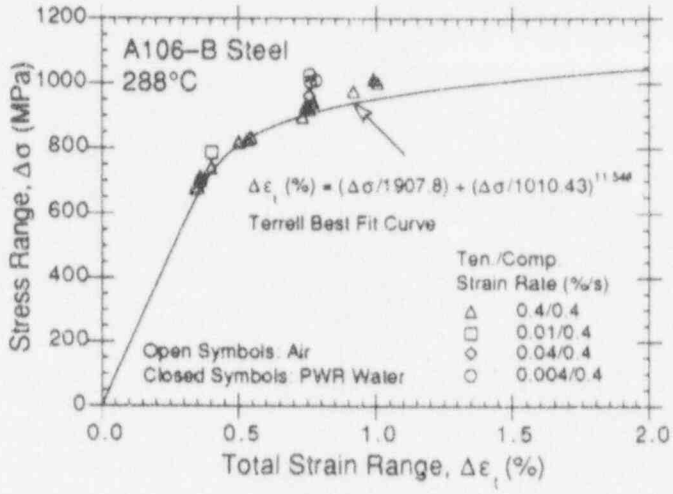


Figure 7.
Cyclic stress–strain curve for A106–Gr B steel at 288°C in air and water environments

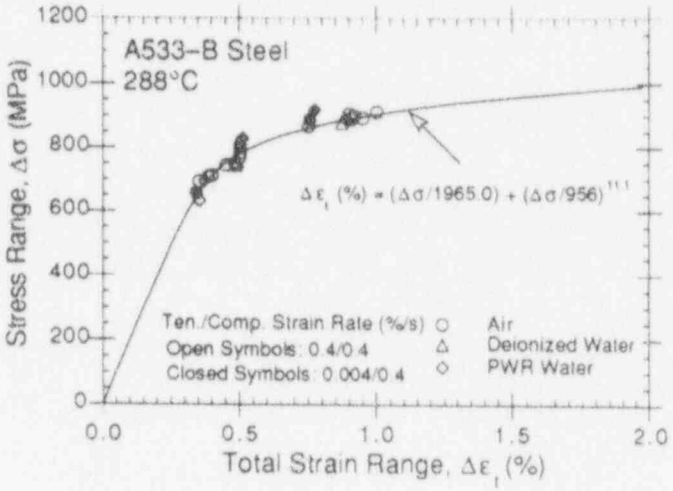


Figure 8.
Cyclic stress–strain curve for A533–Gr B steel at 288°C in air and water environments

The effect of strain rate on the cyclic stress–strain curve is quite pronounced in A106–Gr B carbon steel because of dynamic strain aging of the material, whereas strain rate has only a modest effect on the cyclic stress–strain curve for A533–Gr B low–alloy steel. For both steels, the oxygenated water environment has no effect on the cyclic stress–strain behavior.

Crack propagation behavior is also different for the carbon and low–alloy steels. Micrographs of fatigue cracks along longitudinal sections of the A106–Gr B and A533–Gr B steel specimens are shown in Fig. 9. In the carbon steel, fatigue cracks propagate preferentially along the soft ferrite grains. The low–alloy steel exhibits a typical straight fatigue crack propagating normal to the stress axis.

The surface oxide films that develop on the specimen surfaces tested in air or oxygenated water environments are not significantly different in the carbon or low–alloy steels. Micrographs of the gage surface of the steels tested in air and simulated PWR and BWR water are shown in Fig. 10. In general, the specimens tested in air show slight discoloration, while

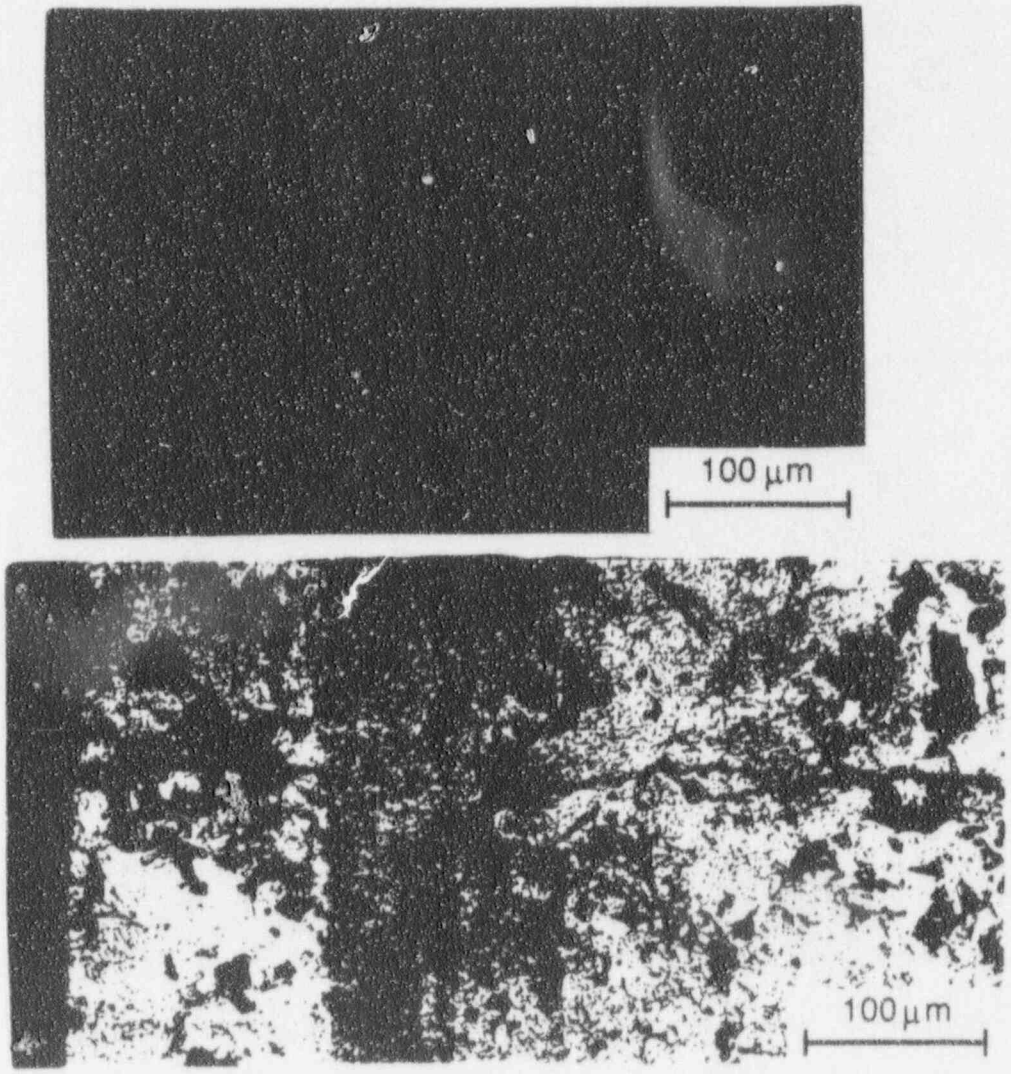


Figure 9. Micrographs of typical fatigue cracks along longitudinal sections of A106-Gr B carbon steel and A533-Gr B low-alloy steel specimens

the specimens tested in oxygenated water develop a gray/black corrosion scale and are covered with surface deposits. The specimens tested at high DO levels (0.8 ppm) also showed patches of loose brown/red deposit. X-ray diffraction analysis of the surfaces indicated that for both steels, the corrosion scale is primarily magnetite (Fe_3O_4) in simulated PWR water but also contains some hematite (Fe_2O_3) after exposure to oxygenated water containing ≈0.8 ppm DO.

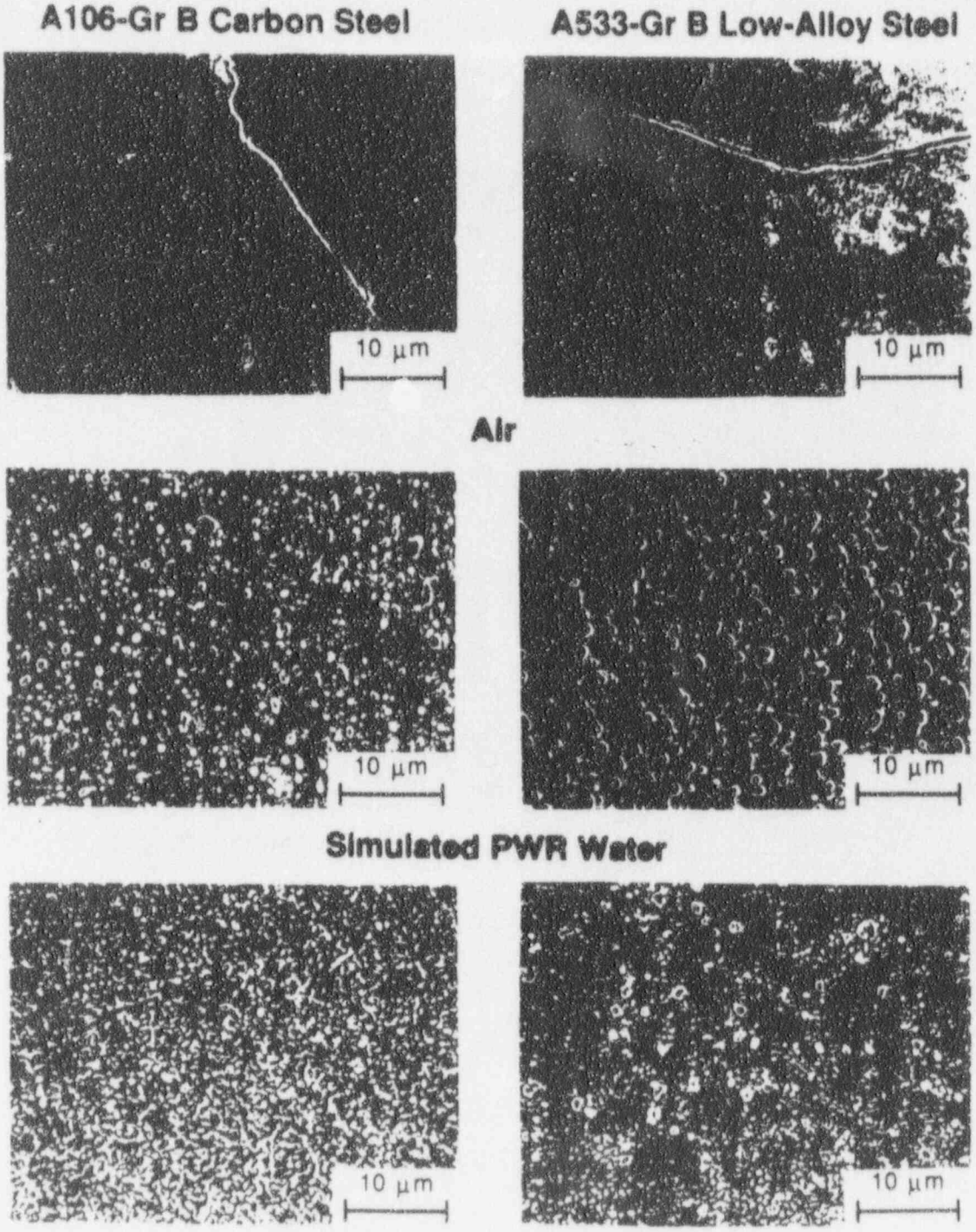


Figure 10. Micrographs of gage surface of A106-Gr B carbon steel and A533-Gr B low-alloy steel tested in different environments at 288°C

3.2 Simulated PWR Environment

The total strain range vs. fatigue life plots for A106–Gr B and A533–Gr B steels in simulated PWR water containing <10 ppb DO, 1000 ppm boron, and 2 ppm lithium are shown in Figs. 11 and 12, respectively. The results indicate a marginal effect of PWR water on fatigue life at high strain ranges. For both steels, fatigue lives in PWR water are lower by a factor of up to 2 than those in air at a strain range >0.5%. Fatigue lives in water and air environments are comparable at a strain range <0.5%. Limited data on A533–Gr B steel indicate that a decrease in the strain rate by two orders of magnitude does not cause an additional decrease in fatigue life. The results for A106–Gr B steel are consistent with the data obtained by Terrell[7] in simulated PWR water where no noticeable effect of strain rate or environment on fatigue life was observed (Fig. 11). The results are also consistent with the data of Iida et al.[12] and Prater and Coffin,[15,16] in which the effects of environment were minimal at DO levels of <100–200 ppb.

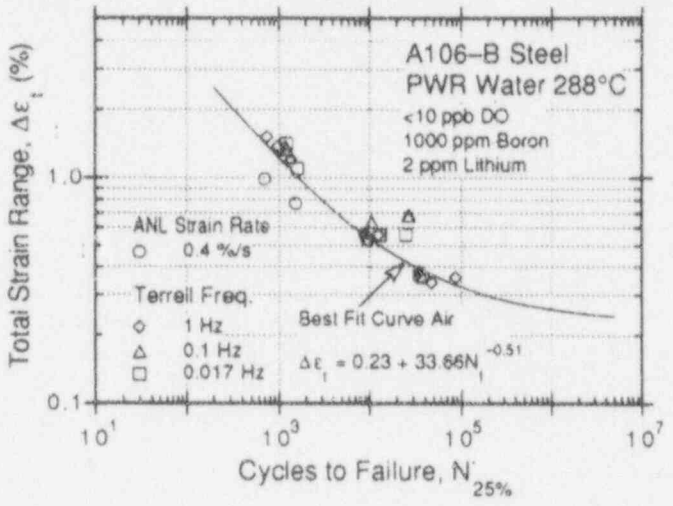


Figure 11.
Total strain range vs. fatigue life data for A106–Gr B steel in PWR water at 288°C

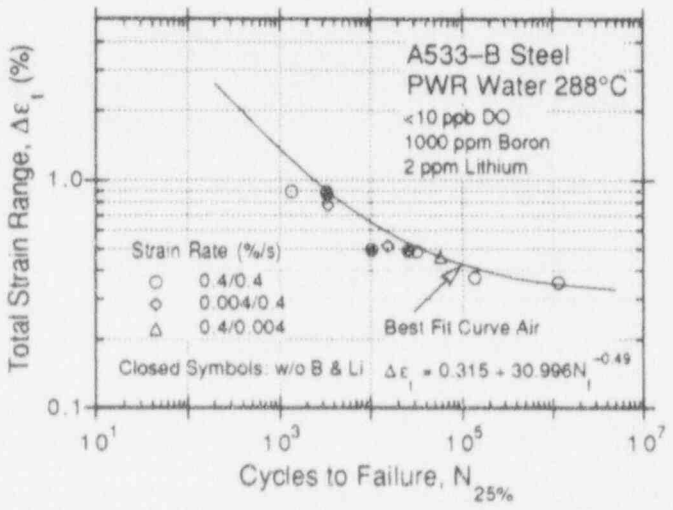


Figure 12.
Total strain range vs. fatigue life data for A533–Gr B steel in PWR water at 288°C

3.3 Oxygenated Water

Environmental effects are significant at high DO levels. The total strain range vs. fatigue life plots for A106–Gr B and A533–Gr B steels in oxygenated water containing ≈0.8 ppm DO are shown in Figs. 13 and 14, respectively. For A106–Gr B steel, fatigue tests were conducted at a total strain range of ≈0.75% with a sawtooth wave form and tensile strain rate between 0.4 and 0.00004%/s; the compressive strain rate for most tests was 0.4%/s. The results indicate that fatigue life decreases rapidly with decreasing strain rate and saturates at a strain rate between 0.001 and 0.0004%/s. Compared with tests in air, fatigue life in oxygenated water is lower by factors of 2, 10, and 20 at strain rates of 0.4, 0.004, and 0.0004%/s, respectively. A further decrease in strain rate to 0.00004%/s does not cause additional decrease in fatigue life. The relative reduction in fatigue life at total strain range of 0.75 or 0.4% are the same. The results also indicate that only the slow tensile-strain cycle is responsible for environmentally assisted reduction in fatigue life. Two fatigue tests on A106-Gr B steel at a strain range of ≈0.75%, one with a sawtooth wave form (i.e., 0.004 and 0.4%/s strain rates, respectively, during the tensile

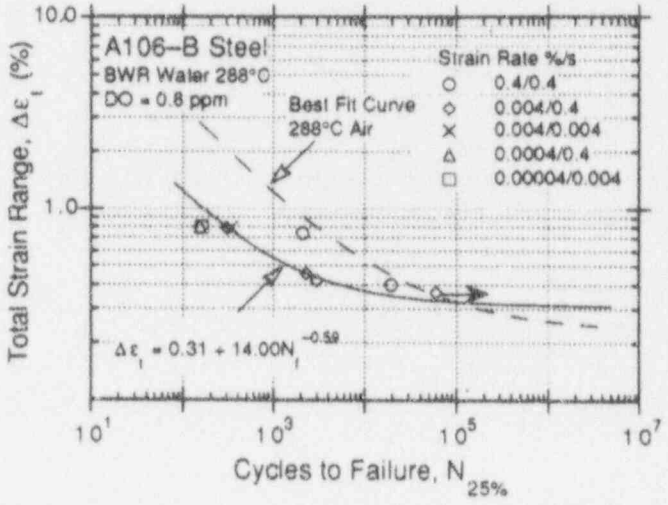


Figure 13.
Total strain range vs. fatigue life data for A106–Gr B steel in high-oxygen water at 288°C

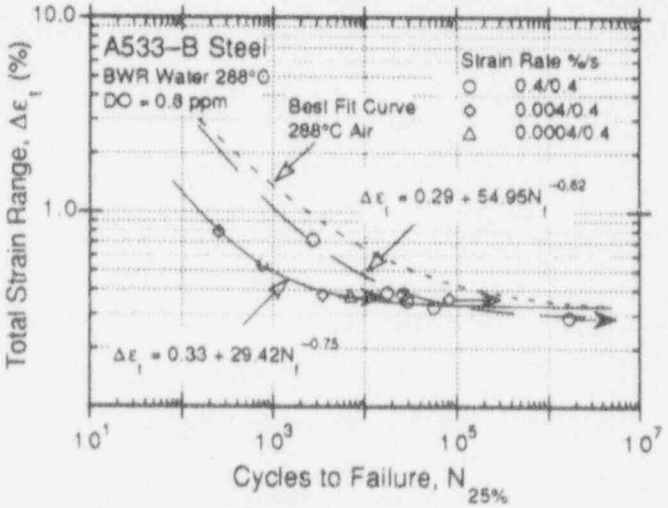


Figure 14.
Total strain range vs. fatigue life data for A533–Gr B steel in high-oxygen water at 288°C

and compressive half of the strain cycle) and the other with a triangle wave form (i.e., 0.004%/s constant strain rate), show identical fatigue lives (Fig. 13).

The low-alloy A533-Gr B steel shows an identical behavior. For similar test conditions, the absolute values of fatigue life for A533-Gr B low-alloy steel are comparable to those for A106-Gr B carbon steel. However, because life in air for A533-Gr B steel is greater than that for A106-Gr B steel, the relative reduction in life for the low-alloy steel is larger than that for carbon steel. This is particularly true at low strain range (0.4%), where even at the high strain rate fatigue life is a factor of 10 lower than in air (Fig 14).

3.4 Strain Rate

Fatigue data in oxygenated water reveal significant reductions in fatigue life and a strong dependence on strain rate. Although the microstructures and cyclic-hardening behaviors of the A106-Gr B carbon steel and A533-Gr B low-alloy steel are significantly different, there is little or no difference in environmental degradation of fatigue life of these steels. The relative fatigue lives of several heats of carbon and low-alloy steels with varying sulfur content are plotted as a function of strain rate in Figs. 15 and 16. Relative fatigue life is the ratio of life in water and life of that specific heat in air.

The results indicate that the reduction in fatigue life depends not only on strain rate but also on DO in the environment and sulfur content in the steel. Environmental effects increase with decreasing strain rates and increasing levels of DO and sulfur. For example, the maximum reduction in fatigue life for the A106-Gr B and A333-Gr 6 carbon steels with similar sulfur content is a factor of 2 at ≤0.05 ppm DO and a factor of 50 or more at 8 ppm DO. Fatigue lives at intermediate values of DO are between these limits.

However, the data obtained on A516 carbon steel (0.033 wt.% sulfur) by General Electric Co. (GE) in a test loop at the Dresden 1 reactor[3] show a different trend. For this steel, the reduction in fatigue lives at 0.2 ppm DO (shown as square data points in Fig. 15) is a factor of ≈2 greater than that for the A106-Gr B steel at 0.8 ppm DO and for A333-Gr 6 steel at 0.2 ppm DO. The difference may be attributed to the higher sulfur content in the A516 steel. Similar effects of DO and sulfur content are observed for the low-alloy steels. The results also indicate that for both steels, the effect of strain rate on fatigue life saturates at a value between 0.001 and 0.0004%/s; actual value may vary with DO and sulfur content.

Another factor that may influence environmental effects is wave shape. Fatigue tests on the A516 steel were conducted with a trapezoidal wave form instead of the sawtooth or triangular wave forms used in the ANL and Japanese studies. The trapezoidal wave form consists of hold periods at peak tensile and compressive strains. It is likely that in addition to the slow tensile strain rate, the tensile hold period also decreases fatigue life. Hold-time fatigue tests are in progress to establish the effects of wave shape.

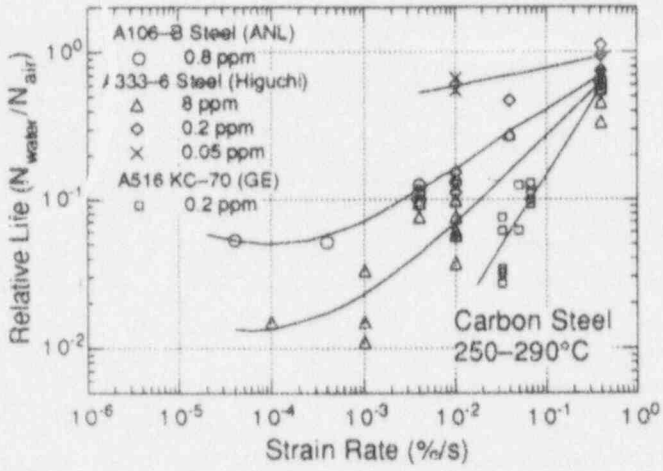


Figure 15.
Relative fatigue life of A106–Gr B carbon steel at different levels of dissolved oxygen and strain rates

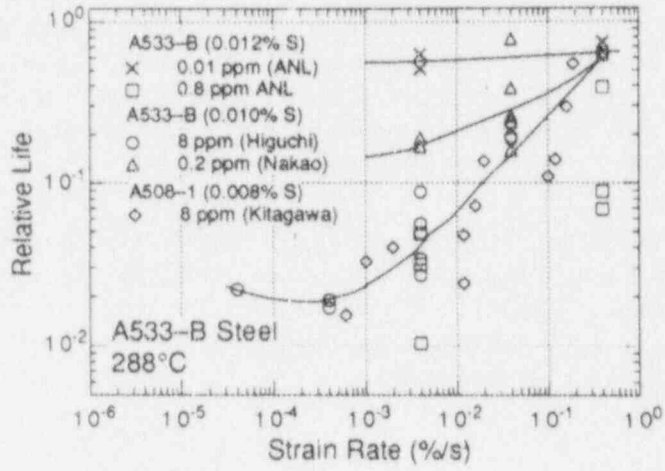


Figure 16.
Relative fatigue life of A533–Gr B low-alloy steel at different levels of dissolved oxygen and strain rates

3.5 Strain Range

The fatigue data in oxygenated water show a distinct threshold for the value of strain range for environmental effects. This threshold for the ANL heats of carbon and low-alloy steels appears to be at 0.36%; fatigue tests on A106–Gr B and A533–Gr B steels at ≈0.36% strain range, ≈0.8 ppm DO, and 0.004%/s tensile strain rate did not fail even after 65,000 and 83,000 cycles, respectively (Figs. 13 and 14). For the carbon steel, the fatigue strain range vs. life curves in air and water environments cross over at low strain ranges, i.e., fatigue life in water is longer than that in air. This apparently different fatigue S/N behavior is not due to the water environment. It is caused by dynamic strain aging of carbon steels and is observed in Fig. 13 because of the difference in strain rate for the tests in air and water environments. The S/N curve in air is based on tests at 0.4%/s strain rate, while the S/N curve in water represents fatigue tests at a slower strain rate of 0.004%/s. For a specific strain range, fatigue tests in water at slower strain rate show greater dynamic strain aging, higher cyclic stress, lower plastic strain range, and longer life.

3.6 Crack Nucleation

The reduction in fatigue life of carbon and low-alloy steels in oxygenated water may be caused by environmental effects on crack propagation and also on crack nucleation. The fatigue crack growth behavior of these steels in high-temperature oxygenated water and the effects of sulfur content and loading rate are well known.[17-24] The dissolution of MnS inclusions changes the water chemistry near the crack tip, making it more aggressive. This results in enhanced crack growth rates because either (a) the dissolved sulfides decrease the repassivation rate, which increases the amount of metal dissolution for a given oxide rupture rate; or (b) the dissolved sulfide poisons the recombination of H atoms liberated by corrosion, which enhances H uptake by the steel at the crack tip.

The water environment may also enhance crack nucleation. For example, corrosion pits or cavities produced by dissolution of MnS inclusions can act as sites for nucleation of fatigue cracks.[25,26] All specimens tested in air or water environments contained several secondary cracks, particularly those tested at high strain ranges. A detailed examination of the gage surfaces of the specimens was conducted to investigate the role of high-temperature oxygenated water on fatigue crack nucleation. The presence of surface deposits often impedes the examination. Consequently, the specimens were descaled with an electrolyte of 2 g hexamethylene tetromine in 1000 cm^3 of 1 N HCl. Micrographs of the gage surface of an A106-Gr B specimen before and after descaling are shown in Fig. 17. The descaled specimens show many details that were hidden by the oxide scale and/or deposits. Also, the descaled specimens show many more cracks that are not visible on the oxidized surface.

All specimens tested in water showed surface micropitting. These pits form either by corrosion of the material in oxygenated water or by selective dissolution of MnS or other inclusions. Typical examples of corrosion pits on A106-Gr B and A533-Gr B steel specimens are shown in

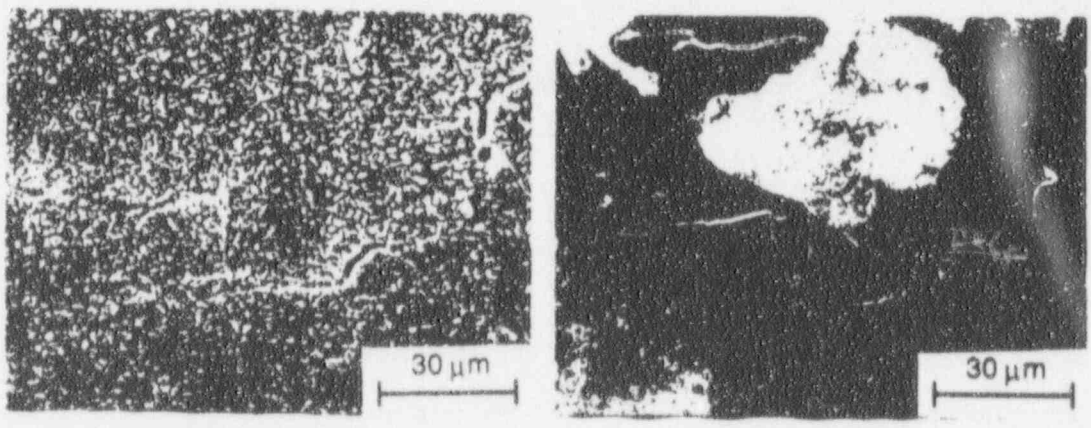


Figure 17. Micrographs of gage surfaces of A106-Gr B carbon steel specimens (a) before and (b) after descaling

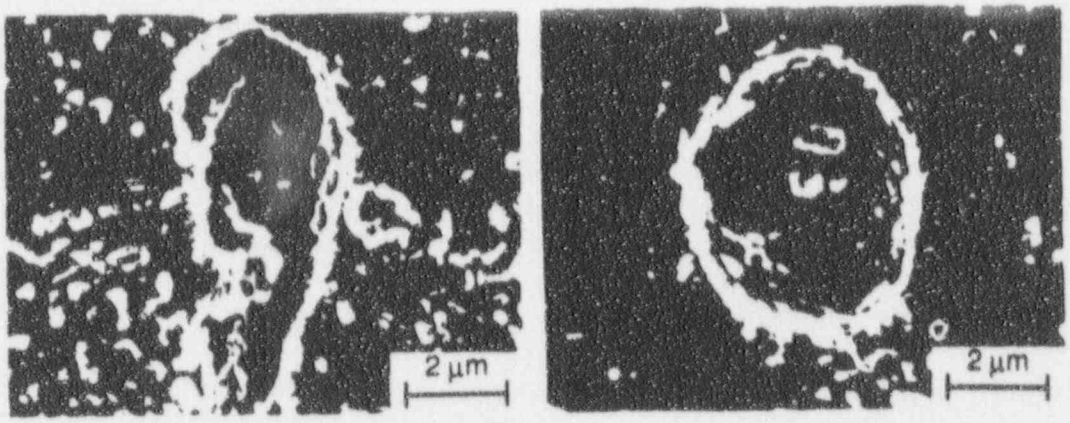


Figure 18. Typical examples of micropits on the surface of (a) A106–Gr B carbon steel and (b) A533–Gr B low–alloy steel specimens tested in oxygenated water at 288°C

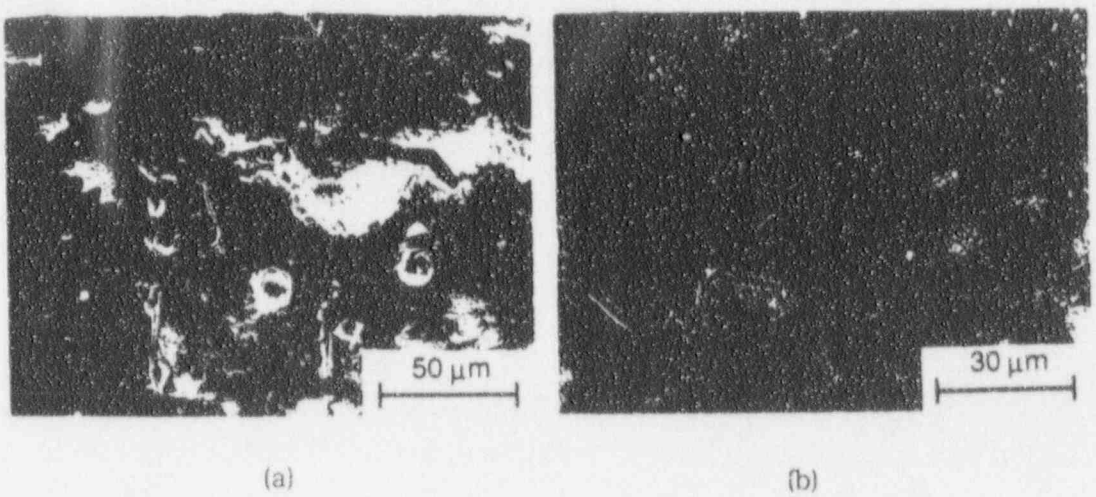


Figure 19. Secondary fatigue cracks on the descaled surface of (a) A106–Gr B carbon steel and (b) A533–Gr B low–alloy steel specimens

Fig. 18. The micropits are often associated with cracks, as seen in Fig. 18; however, these are surface cracks in the oxide scale that do not extend into the material. None of the examined specimens showed any evidence that fatigue cracks nucleate preferentially at the micropits. Typical secondary fatigue cracks on the descaled surfaces of A06–Gr B and A533–Gr B specimens are shown in Fig. 19. Several corrosion pits and cavities created by dissolution of inclusions are visible on the surface and seem to be associated with the crack. However, there is no indication that the crack actually nucleated at any of these sites. The cracks appear to encounter and pass through these corrosion pits or through stringers of inclusions. Examination

of the fatigue specimens indicates that irrespective of environment, cracks in carbon and low-alloy steels nucleate along slip bands, carbide particles, or at the ferrite/pearlite phase boundaries. Examples of such cracks in a carbon steel specimen are shown in Fig. 20.

The metallographic examination was complemented by measuring the cracking frequency for fatigue specimens tested in different environments. Figure 21 shows plots, as a function of strain, of the number of cracks along longitudinal sections of the gage length of A106-Gr B and A533-Gr B specimens tested at two different strain rates in air, simulated PWR, and high-DO water. In all cases, the number of cracks represent the average value along a 7 mm gage length. The results show that with the exception of the low-alloy steel tested in simulated PWR water, environment has no effect on the frequency of cracks. For similar loading conditions, the number of cracks in the specimens tested in air and oxygenated water with 0.8 ppm DO are

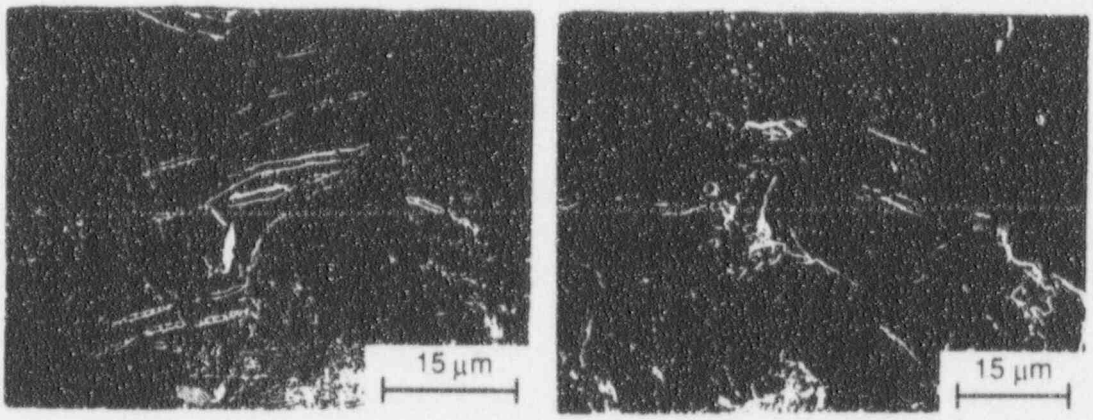


Figure 20. Nucleation of cracks along slip bands, carbide particles, and ferrite/pearlite phase boundaries of the carbon steel fatigue specimen

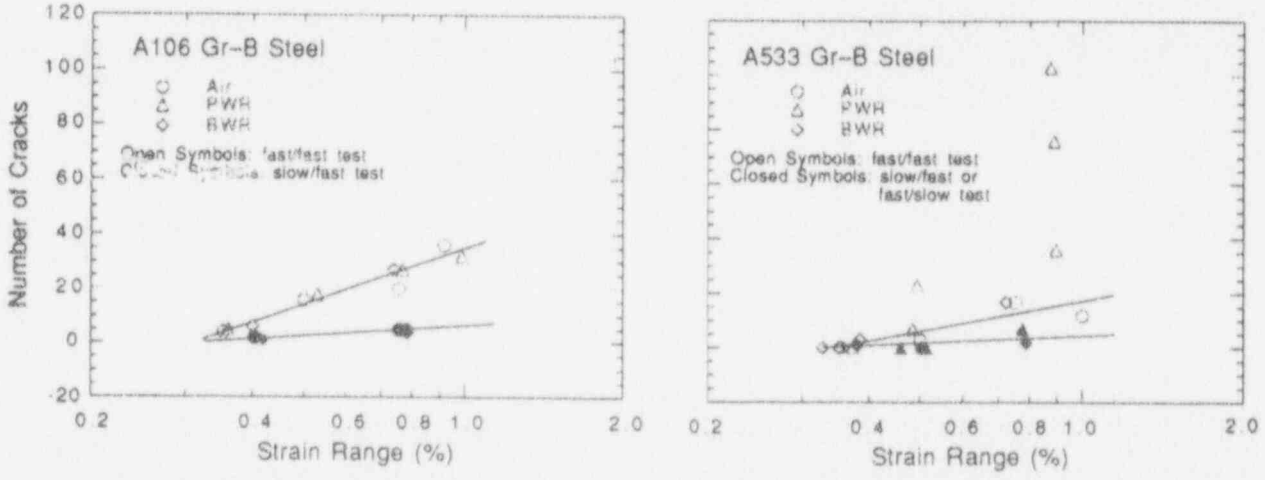


Figure 21. Number of cracks along a longitudinal section of the fatigue specimens tested in different environments

identical, although fatigue life is a factor of ≈8 lower in water. If the reduction in life is caused by enhanced crack nucleation, the specimens tested in high DO water should show more cracks.

The low-alloy steel specimens tested in either simulated PWR water or deionized water with <10 ppb DO show a significantly higher frequency of cracks, although their fatigue life is only marginally lower than that in air. These cracks most likely are caused by hydrogen produced by the corrosion reaction. The frequency of cracks is higher only in the low-alloy steel and not in carbon steel because of structural differences; the low-alloy steel has high tensile strength and consists of tempered bainitic structure.

The contributions of environment to crack nucleation were further evaluated by conducting exploratory tests. Figure 22 shows the fatigue life of A106-Gr B steel in air (dashed line) and in high-DO water at 0.4 and 0.004%/s strain rates (circle and diamond symbols, respectively). A fatigue specimen was preexposed at 288°C for 100 h in water with 0.6 ppm DO and then tested in air at 0.4% total strain range. At this strain range, nearly half the fatigue life may be spent in crack nucleation. Fatigue life should be reduced if surface micropits facilitate crack nucleation; life of this specimen is identical to that of an unoxidized specimen. Similar behavior was observed for a preoxidized A533-Gr B specimen tested at 0.5% strain range. It is possible that the high DO and slow strain rate are also needed to influence crack nucleation. This possibility was checked by first testing a specimen in high-DO water at 0.4% strain range and 0.004%/s strain rate for 570 cycles (≈25% of the life at these loading conditions) and then testing in either air or water environment at 0.4%/s strain rate. Fatigue life of these tests should be reduced if crack nucleation contributes in any way to environmental effects. Once again, no reduction in life is observed. These results suggest that the reduction in fatigue life in oxygenated water is primarily due to environmental effects on fatigue crack propagation. Environment has little or no effect on crack nucleation.

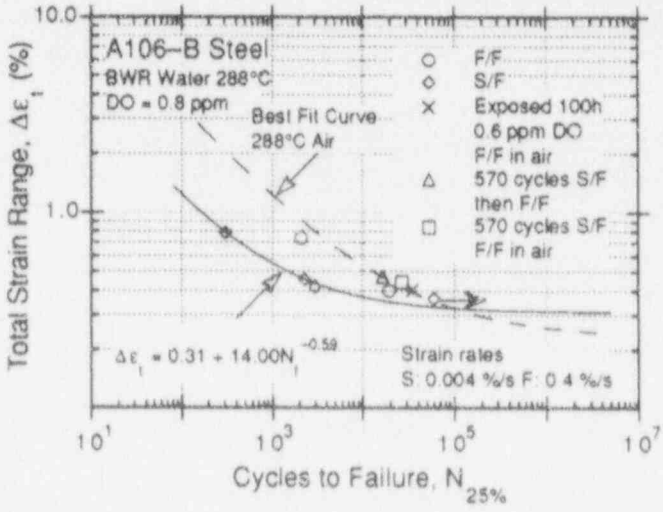


Figure 22.
Environmental effects on nucleation of fatigue crack

4 Conclusions

The fatigue behavior of A106–Gr B carbon steel and A533–Gr B low-alloy steel has been investigated in oxygenated water and in air. The results confirm the significant reduction in fatigue life and strong dependence on strain rate. For both steels, fatigue life in oxygenated water decreases with decreases in strain rate or increases in DO. The effects of strain rate on fatigue life saturate at some low value of strain rate, e.g., between 0.0004 and 0.001%/s in oxygenated water with ≈0.8 ppm DO. The actual value of saturation strain rate may vary with DO and sulfur content of the steel. The results show that although the cyclic stress–strain and cyclic-hardening behavior of carbon and low-alloy steels are distinctly different, there is little or no difference in susceptibility to environmental degradation of fatigue life of these steels, when sulfur levels are comparable. The A106–Gr B carbon steel exhibits pronounced dynamic strain–aging, whereas strain aging effects are modest in the A533–Gr B low-alloy steel.

A detailed examination of the gage surfaces of the specimens was conducted to investigate the role of high-temperature oxygenated water on fatigue crack nucleation. The results suggest that an oxygenated-water environment has no effect on the nucleation of cracks. All specimens tested in water showed surface micropitting, due to either corrosion of the material in oxygenated water or selective dissolution of MnS or other inclusions. However, there is no indication that a fatigue crack nucleated at any of the surface micropits. Examination of the fatigue specimens indicates that irrespective of environment, cracks in carbon and low-alloy steels nucleate along slip bands, carbide particles, or at the ferrite/pearlite phase boundaries.

Acknowledgments

The authors are grateful to W. F. Burke, J. C. Tezak, T. M Galvin, and P. L. Torres for their contributions to the experimental effort in this program. This work was supported by the Office of Nuclear Regulatory Research of the U.S. Nuclear Regulatory Commission, under FIN Number A2212; Program Manager: Dr. J. Muscara.

References

1. *Criteria of Section III of the ASME Boiler and Pressure Vessel Code for Nuclear Vessels*, The American Society of Mechanical Engineers, United Engineering Center, New York, Library of Congress Catalog No. 56-3934 (1989).
2. Tentative Structural Design Basis for Reactor Pressure Vessels and Directly Associated Components (Pressurized, Water Cooled Systems), PB 151987, U.S. Department of Commerce, Office of Technical Service, 1 Dec. 1958 Revision.
3. D. A. Hale, S. A. Wilson, E. Kiss, and A. J. Gianuzzi, Low Cycle Fatigue Evaluation of Primary Piping Materials in a BWR Environment, GEAP-20244, U.S. Nuclear Regulatory Commission (Sept. 1977).
4. D. A. Hale, S. A. Wilson, J. N. Kass, and E. Kiss, "Low Cycle Fatigue Behavior of Commercial Piping Materials in a BWR Environment," *J. Eng. Mater. Technol.* **103**, 15–25 (1981).

5. S. Ranganath, J. N. Kass, and J. D. Heald, "Fatigue Behavior of Carbon Steel Components in High-Temperature Water Environments," in *Low-Cycle Fatigue and Life Prediction*, ASTM STP 770, C. Amzallag, B. N. Leis, and P. Rabbe, eds., American Society for Testing and Materials, Philadelphia, PA, pp. 436–459 (1982).

6. J. B. Terrell, *Fatigue Life Characterization of Smooth and Notched Piping Steel Specimens in 288°C Air Environments*, NUREG/CR-5013, MEA-2232 (May 1988).

7. J. B. Terrell, "Effect of Cyclic Frequency on the Fatigue Life of ASME SA-106-B Piping Steel in PWR Environments," *J. Mater. Eng.* **10**, 193–203 (1988).

8. P. D. Hicks, in *Environmentally Assisted Cracking in Light Water Reactors: Semiannual Report October 1990—March 1991*, NUREG/CR-4667 Vol. 12, ANL-91/24, pp. 3–18 (Aug. 1991).

9. P. D. Hicks and W. J. Shack, Fatigue of Ferritic Steels, in *Environmentally Assisted Cracking in Light Water Reactors, Semiannual Report, April–September 1991*, NUREG/CR-4667 Vol. 13, ANL-92/6, pp. 3–8 (March 1992).

10. O. K. Chopra, W. F. Michaud, and W. J. Shack, "Fatigue of Ferritic Steels," in *Environmentally Assisted Cracking in Light Water Reactors, Semiannual Report, October 1992–March 1993*, NUREG/CR-4667 Vol. 16, ANL-93/27, pp. 3–19 (September 1993).

11. M. Higuchi and K. Iida, "Fatigue Strength Correction Factors for Carbon and Low-Alloy Steels in Oxygen-Containing High-Temperature Water," *Nucl. Eng. Des.* **129**, 293–306 (1991).

12. K. Iida, H. Kobayashi, and M. Higuchi, *Predictive Method of Low Cycle Fatigue Life of Carbon and Low Alloy Steels in High Temperature Water Environments*, NUREG/CP-0067, MEA-2090, Vol. 2 (April 1986).

13. N. Nagata, S. Sato, and Y. Katada, "Low-Cycle Fatigue Behavior of Low-Alloy Steels in High-Temperature Pressurized Water," in *Transactions of the 10th International Conf. on Structural Mechanics in Reactor Technology*, Vol. F, A. H. Hadjian, ed., American Association for Structural Mechanics in Reactor Technology, Anaheim, CA (1989).

14. S. Majumdar, O. K. Chopra, and W. J. Shack, *Interim Fatigue Design Curves for Carbon, Low-Alloy, and Austenitic Stainless Steels in LWR Environments*, NUREG/CR-5999, ANL-93/3 (April 1993).

15. T. A. Prater and L. F. Coffin, "The Use of Notched Compact-Type Specimens for Crack Initiation Design Rules in High-Temperature Water Environments," in *Corrosion Fatigue: Mechanics Metallurgy, Electrochemistry, and Engineering*, ASTM STP 801, T. W. Crooker and B. N. Leis, eds., American Society for Testing and Materials, Philadelphia, pp. 423–444 (1983).

16. T. A. Prater and L. F. Coffin, "Notch Fatigue Crack Initiation in High Temperature Water Environments: Experiments and Life Prediction," *J. of Pressure Vessel Technol.*, Trans. ASME, **109**, 124–134 (1987).

17. M. O. Speidel and R. M. Magdowski, "Stress Corrosion Cracking of Nuclear Reactor Pressure Vessel Steel in Water: Crack Initiation versus Crack Growth," *Corrosion 88*, Paper No. 283, St. Louis, Mo, (March 1988).

18. F. P. Ford and P. L. Andresen, "Stress Corrosion Cracking of Low-Alloy Pressure Vessel Steel in 288°C Water," in *Proc. 3rd Int. Atomic Energy Agency Specialists' Meeting on Subcritical Crack Growth*, NUREG/CP-0112, Vol. 1, pp. 37–56 (August 1990).

19. P. M. Scott and D. R. Tice, "Stress Corrosion in Low-Alloy Steels," *Nucl. Eng. Des.* **119**, 399–413 (1990).

20. W. H. Cullen, "The Effects of Sulfur Chemistry and Load Ratio on Fatigue Crack Growth Rates in LWR Environments," in *Proc. of the 2nd Int. Atomic Energy Agency Specialists' Meeting on Subcritical Crack Growth*, NUREG/CP-0067, MEA-2090, Vol. 2, pp. 339–355 (April 1986).

21. J. D. Atkinson, J. H. Bulloch, and J. E. Forrest, "TA Fractographic Study of Fatigue Cracks Produced in A533B Pressure Vessel Steel Exposed to Simulated PWR Primary Water Environments," in *Proc. of the 2nd Int. Atomic Energy Agency Specialists' Meeting on Subcritical Crack Growth*, NUREG/CP-0067, MEA-2090, Vol. 2, pp. 269–290 (April 1986).

22. W. A. Van Der Sluys and D. S. DeMiglio, "An Investigation of Fatigue Crack Growth in SA508-2 in a 288°C PWR Environment by a Constant ΔK Test Method," in *Proc. Int. Atomic Energy Agency Specialists' Meeting on Subcritical Crack Growth*, NUREG/CP-0044, MEA-2014, Vol. 1, pp. 44–64 (May 1983).

23. J. H. Bulloch, "A Review of the Fatigue Crack Extension Behavior of Ferritic Pressure Vessel Materials in Pressurized Water Reactor Environments," *Res. Mechanica* **26**, 95–172 (1989).

24. T. F. Kassner, W. J. Shack, W. E. Ruther, and J. H. Park, "Environmentally Assisted Cracking of Ferritic Steels," in *Environmentally Assisted Cracking in Light Water Reactors: Semiannual Report, April–September 1990*, NUREG/CR-4667, Vol. 11, ANL-91/9, pp. 2–9 (May 1991).

25. D. D. Macdonald, S. Smialowska, and S. Pednekar, *The General and Localized Corrosion of Carbon and Low-Alloy Steels in Oxygenated High-Temperature Water*, NP-2853 (February 1983).

26. J. Kuniya, H. Anzai, and I. Masaoka, "Effect of MnS Inclusions on Stress Corrosion Cracking in Low-Alloy Steels," *Corrosion*, Vol 48, No. 5, 419–425 (1992)

RELIABILITY OF NDE - CAST STAINLESS STEEL, SAFT-UT PERFORMANCE, PISC III PROGRAM STATUS, AND EVALUATION OF COMPUTER-BASED UT/ISI SYSTEMS[1]

by
S. R. Doctor, L. J. Angel, A. A. Diaz,
R. V. Harris, Jr., F. A. Simonen, and G. J. Schuster
Pacific Northwest Laboratory,
Operated for the U.S. Department of Energy
by Battelle Memorial Institute
Richland, WA 99352

ABSTRACT

This paper describes progress associated with three different NRC-funded programs at the Pacific Northwest Laboratory. The topics, cast stainless steel (CSS) and PISC III program status, are activities being conducted in the program entitled "Evaluation and Improvement in Nondestructive Examination Reliability for Inservice Inspection of Light Water Reactors (LWRs)" - FIN No. B2289, the work on SAFT-UT performance is part of the program entitled "Field Validation, Acceptance, and Training of Advanced NDE Technology" - FIN No. B2913, and the final activity is part of the program entitled "Evaluation of Computer-Based NDE Techniques and Regional Support of Inspection Activities" - FIN No. L1100.

INTRODUCTION

This paper is divided into four sections that will describe the significant work which was performed in each topic area as follows. The first topic is that of cast stainless steel, the second is validation of the SAFT-UT technology, the third is a brief status report on the PISC III program with emphasis on areas where PNL is actively participating in the program, and the fourth is an update on the work to evaluate computer-based UT/ISI systems.

1. CAST STAINLESS STEEL

The purpose of ultrasonic inservice inspection (UT/ISI) of nuclear reactor piping and pressure vessels is the reliable detection and accurate sizing of material defects. Before defects can be sized, they must first be detected. This is typically done by analyzing ultrasonic echo waveforms from material defects. In 1978, a multi-year program entitled "The Evaluation and Improve-

---

[1]Work supported by the U.S. Nuclear Regulatory Commission under DOE Contract DE-AC06-76RLO 1830; A. L. Hiser, Jr., NRC Program Manager, FIN B2289. Dr. J. Muscara, NRC Program Manager, FIN L1100 and B2913.

ment of NDE Reliability for Inservice Inspection of Light Water Reactors" (NDE Reliability) was established at the Pacific Northwest Laboratory (PNL) to determine the reliability of current inservice inspection techniques and to develop recommendations that would ensure a suitably high inspection reliability if fully implemented.

Due to the unreliability of ISI of centrifugally cast stainless steel (CCSS), much work has been performed since 1978. CCSS is an anisotropic and nonhomogeneous material. The manufacturing process can result in the formation of a long columnar grain structure (approximately normal to the surface), with grain growth oriented along the direction of heat dissipation, often several centimeters in length. During the solidification of the material, columnar, equiaxed (randomly speckled macrostructure), or a mixed structure can result, depending on chemical content and control of the cooling process.

The large size of the anisotropic grains, relative to the acoustic pulse wavelength, strongly affects the propagation of ultrasound by causing severe attenuation, changes in velocity, and scattering of ultrasonic energy. Refraction and reflection of the sound beam occur at the grain boundaries, resulting in defects being incorrectly reported (position and/or size), specific volumes of material not being examined, or both. When coherent reflection and scattering of the sound beam occur at grain boundaries, ultrasonic indications are difficult to distinguish from flaw signals. When inspecting pipe sections, where the signal-to-noise ratio is relatively low, ultrasonic examinations can be confusing, unpredictable, and unreliable.

The work described herein was performed in order to provide a firm engineering basis for evaluating and recommending the possible utility of using inherently grain insensitive ultrasonic techniques for the inspection of coarse-grained materials. The concept behind this work is to investigate low frequency ultrasonic techniques inherently insensitive to macrostructural effects and to utilize fracture mechanics evaluations on CCSS in order to establish guidance for the sizes of flaws that need to be detected.

COARSE-GRAINED MATERIAL INSPECTION

The objective of this subtask is to evaluate the effectiveness and reliability of ultrasonic inspection techniques on LWR components containing cast stainless steel material. Work performed in this area was initiated in FY 92 and continued in FY 93.

LOW FREQUENCY INSPECTION OF COARSE GRAINED MATERIALS

Design of the low frequency ultrasonic search unit: The initial thrust of the low frequency inspection work focused on utilizing a simplistic approach to the inspection problem, by examining low frequency probes and conventional hardware readily available to us at the Laboratory. After optimizing the data acquisition electronics for signal transmission and reception, a number of preliminary single A-scans were recorded. Frequencies ranging from 50 kHz to 500 kHz were investigated, and numerous narrowband and broadband large-diameter contact transducers were examined in both pulse-echo and pitch-catch

modes. Results were quite poor, and considerable ringing was evident, which masked backwall echoes and other signal reflections of concern. These transducers were not manufactured for our purposes and were designed with little or no backing material; thus, the low bandwidth and effective "dead zone" of these units was too significant a problem to overcome. Results indicated that an effective ultrasonic inspection of coarse-grained materials using off-the-shelf probes, conventional hardware and a lower frequency was not feasible. This necessitated the design and implementation of a custom-designed search unit and utilization of an arbitrary waveform generator for the purposes of better optimization of the inspection system.

The improved design of a dual element search unit was driven by the criteria established for the low frequency experimentation of coarse-grained materials. Due to the fact that longitudinal wave energy attenuates less than shear wave energy in CCSS, it was decided that this study would examine 30°, 45° and 60° incident longitudinal waves in a pitch-catch configuration. In order to achieve a large bandwidth and optimize the performance of the transmitter and receiver, primary consideration was given to the following parameters:

- Wavelength λ > Average Grain Diameter (Lower Frequency)
- Wave Mode (Longitudinal versus Shear)
- Transducer Type (Bandwidth, Transmit/Receive Materials)
- Pulser/Receiver Characteristics (Electronics)

The functional dependence of ultrasonic attenuation in CCSS is well documented (Jeong 1987). Scattering losses are the predominant factor in ultrasonic attenuation, and by plotting the attenuation of ultrasonic energy as a function of frequency, the most significant decrease in attenuation occurs within the Rayleigh scattering region where the wavelength is greater than the average grain diameter. In order to "desensitize" our inspection to the effects of the grain structure, and since some of the CCSS samples available for testing contain grain diameters on the order of 1/2 inch, a wavelength of 2/3 inch in the material was chosen. This corresponds to a center frequency of approximately 350 kHz. The transmit element was made from a 1 inch by 2 inch K-81 lead metaniobate, piezoelectric crystal with a center frequency of 350 kHz, and a 1 inch by 2 inch PVDF element was used as the receive element. The end product resulted in a dual element, pitch-catch search unit utilizing two rectangular crystals each with dimensions 1 inch by 2 inches. The transmit crystal was fairly broadband with a -6 dB bandwidth of 74%. A set of special wedges (shoes) was designed for each specific angle of incidence. Although much of the initial work investigated flat specimens, the shoes were adapted to conform to the curved inspection condition as well. Due to uneven and curved surfaces of the pipe sections, this was not optimal, but allowed us to examine more specimens and prompted the use of an immersion bath for coupling purposes.

One goal was to achieve optimal efficiency of the transmitted pulse. In order to achieve this, our focus was directed to the pulser/receiver configuration as well. By programming an arbitrary waveform generator to custom design the filter used to drive the transmitter, we were able to increase the temporal response of the transmitter and more efficiently drive the crystal. On the

receive end, we used four Panametrics low frequency amplifiers in series to amplify the signal and limit the amount of electronic noise induced by the instruments. Laboratory tests looked promising so it was decided that an objective test should be performed to quantify the effectiveness of this technique.

EVALUATION OF SAFT-LOW FREQUENCY INSPECTION OF CCSS (EPRI ROUND ROBIN)

In order to fully evaluate the effectiveness of the specially designed low-frequency transducer combined with the SAFT technique, it was decided to participate in a blind test. The opportunity arose to participate in a round robin test being coordinated by the Electric Power Research Institute (EPRI) NDE Center and sponsored by Northeast Utilities and Yankee Atomic. The PNL SAFT-UT system was located at Oak Ridge National Laboratory (ORNL) where it was being used to inspect a reactor pressure vessel that was located there. PNL's participation in the CSS round robin occurred at ORNL, and was co-funded with the NRC covering PNL staff labor and Northeast Utilities covering the travel expenses for PNL staff to travel to ORNL, staying at Oak Ridge for one week, and returning to PNL.

The PNL team was provided with two sets of CCSS specimens; a practice (training) set consisting of one CCSS calibration block and three fitting-to-pipe sections, and a test set consisting of eight CCSS fitting-to-pipe and pipe-to-pipe sections. All but three specimens originated from the Westinghouse Owners' Group (WOG), with the remaining three specimens originating from PNL. The anisotropic and coarse-grained structure of the specimens presented could possibly cause the problem of not only detecting existing cracks, but also of misclassifying the uncracked specimens as cracked. The procedures employed by the PNL team have demonstrated a potential for discriminating between cracked and uncracked material. The PNL inspection team utilized a low frequency, long wavelength acoustic technique combined with the synthetic aperture focusing technique (SAFT).

A Compaq 486 computer containing an A/D converter was used to digitize incoming data and initialize a trigger output signal. The arbitrary waveform generator was used for programming and implementing custom-designed waveforms for driving the transmitter. The driving pulse was amplified by a low frequency, 200 watt RF power amplifier and sent to the transmitter. The pitch-catch received signal (echo) was then sent to a group of four Panametrics low-noise, wide-band amplifiers in series. High pass filtering at 100 kHz was implemented at each stage of amplification in order to allow suitable amplification while minimizing low frequency amplifier noise components. A linear averaging scheme was implemented, where the received A-scans were averaged 128 times per repetition for purposes of increasing signal-to-noise and minimizing the effects of motor noise from the robot.

The automated scanning mechanism consists of a fully automated PUMA 500 robotic arm, with transducer attachments. The robot has maneuverability over a wide range of motions utilizing six joints that allows freedom of movement in the X-, Y-, and Z- planes for automated data acquisition.

SAFT-UT technology has the potential to provide significant enhancements to the inspection of coarse-grained materials used in U.S. nuclear power plants. The resolution of all imaging systems is limited by the effective aperture area; that is, the area over which data can be detected, collected, and processed. SAFT is an imaging method which was developed to overcome some of the limitations imposed by large physical apertures, and has been successfully applied in the field of ultrasonic testing. Relying on the physics of ultrasonic wave propagation, SAFT is a very robust technique.

All SAFT processing software was contained in and invoked on a SUN Sparc 2 workstation. Images presented for analysis consisted of original photographs of the Sparc 2 monitor after post processing raw data. The objective was to acquire low frequency ultrasonic data on four CSS practice specimens and eight round robin CSS test specimens. This data was post-processed using the three-dimensional SAFT algorithm. The following two modes were employed for these inspections:

1. 45° L-wave at 350 kHz
2. 0° (normal) L-wave at 1 MHz

Given the SAFT presentation of ultrasonic data (in the B-scan format), the PNL team was looking for amplitude anomalies that occur appropriately in time, with a characteristic shape and at a characteristic angle of orientation to the angle of inspection; the following criteria were used:

1. Amplitude peaks (anomalies) that occur in a concentrated area that spans across the back surface line.
2. These areas must have a specific shape to them, not be just a random blotchy, scattered grouping of amplitude blips. Typically we look for a circular or elliptical shape with smooth contouring around the edges.
3. With a given shape, it is easy to see if the insonified area is appropriately oriented with respect to the incident beams angle. This angle is slanted such that the image appears nearly perpendicular to the angle of incidence of the insonifying beam.
4. Extent (length) across the back surface line.
5. Areas not complying with all four of these criteria may in part be due to, or constitute material geometry, noise, surface roughness effects, or a combination thereof.

Figure 1[2] shows the performance of the teams that participated in this round robin exercise. The vertical axis is the (cracked length that was called cracked)/(the total cracked weld length) and the horizontal axis is the (uncracked weld length that was called cracked)/(total uncracked weld length). The diagonal line represents performance that could be obtained by pure guessing where an equal number of right and wrong calls are made. The best

---

[2]This figure was provided by the EPRI NDE Center. The NDE Center report on this study is in preparation and we appreciate the permission from the EPRI NDE Center to publish this figure.

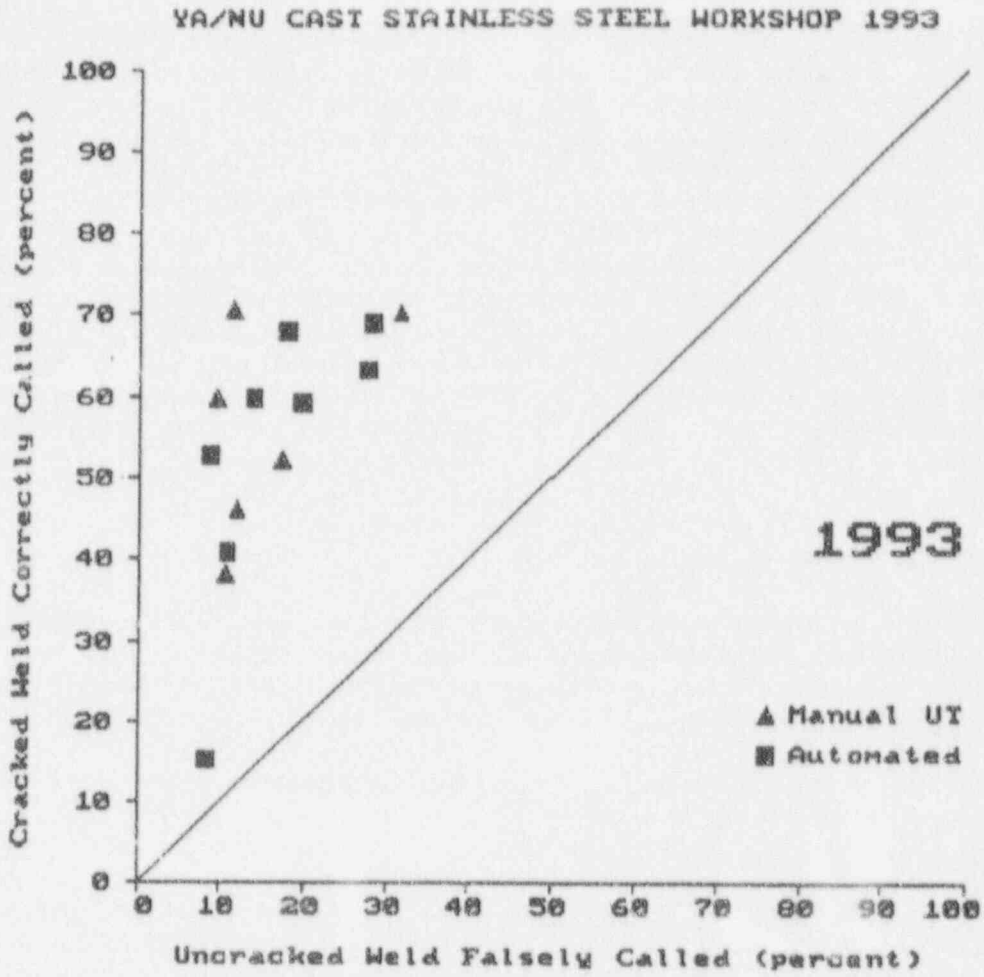


Figure 1. Detection Performance of Participants in EPRI NDE Center Coordinate Cast Stainless Steel Round Robin Workshop

performance is that which is further from this line. It should be noted that as is almost always found, there are a few manual inspectors that out-perform automated systems. It is clear that false calls are not negligible, but they are also not high either.

In the final analysis of the combined low frequency-SAFT inspection technique, results of the blind test proved to be among the top performers of the techniques evaluated. The PNL crack detection probability was 70%, while the false call probability was 30%. This indicates that the low-frequency SAFT-UT approach looks promising and further evaluation is planned for next fiscal year.

FRACTURE MECHANICS CALCULATIONS AND ANALYSIS

Work with fracture mechanics evaluations of CCSS was initiated using an approach utilizing work performed at Battelle-Columbus and Argonne National Laboratory (ANL) with regard to performing calculations to estimate dimensions of critical cracks in CCSS. The objective of the fracture mechanics study is to assemble and interpret information on the fracture of cast stainless steel components in order to make recommendations regarding the sizes of flaws that need to be detected for an effective inspection of cast materials. It was realized that current and even existing advanced UT methods will not detect flaws of the smaller sizes that can be readily detected in other materials. The detection of small flaws in cast materials remains a long-range goal for NDE development. Nevertheless, it is also important to establish what sizes of larger flaws are still below critical sizes for typical cast components, since significant benefits can be achieved if the NDE methods can detect these flaws of large sizes.

An in-depth literature search and review of current work on CCSS fracture mechanics evaluations was completed, and industry contacts resulted in providing little information useful to this study due to proprietary reasons. The bulk of this work contained summaries and descriptions of work performed at ANL on definitive lower bound J-R fracture curves for thermally aged CCSS. Estimates of critical flaw sizes for primary coolant piping using Argonne's toughness data, published data on piping loads, and one of Battelle-Columbus's methodologies have been completed. Service loads on PWR primary coolant piping are relatively low, and thus even severely aged CCSS can tolerate 50% through-wall circumferential flaws. Work has continued with a review of material characterization data used in the calculation and complete comparison of critical flaw sizes for aged versus unaged material. Both centrifugal cast and static cast materials have been addressed for properties at ambient and operating temperatures. The failure assessment curve of ASME Code Case N-494 was reviewed and revised to more accurately predict tearing instability failures of flawed piping with the tearing resistance and stress strain curves of cast stainless steel. All calculations have been updated using the improved failure assessment curve. The results of this work when completed will be used to support a basis for the design of performance demonstration CSS test sets for an ASME Code Section XI, Appendix VIII Supplement.

FUTURE WORK

Pursue further evaluation of low-frequency techniques, advanced signal processing methods such as adaptive ultrasonics, and complete the fracture mechanics evaluation for supporting a basis for the design of performance demonstration CSS test sets - Appendix VIII Supplement.

2. SAFT-UT PERFORMANCE

This work was part of a program which had the objective to develop and validate a real-time synthetic aperture focusing technique for ultrasonic testing (SAFT-UT) for the inservice inspection of light water reactor compo-

nents (Hall, Reid, and Doctor 1988). The SAFT-UT technology was developed through an extensive laboratory program and was deployed in the field. The technology has been validated through a series of blind tests. This section describes the most recent work in this validation activity.

BACKGROUND

One of the tests selected for validating the SAFT-UT technology was the PISC-III Full-Scale Vessel (FSV) Test conducted at the Materialpruefungsanstalt (MPA) Laboratory located in Stuttgart, Germany that involved the characterization of 12 indications in a full-scale reactor pressure vessel.

During December 1990, three PNL staff traveled to Stuttgart and spent 11 days performing inspections on the FSV. Eight of the inspection zones were examined from both the inside and the outside surfaces of the reactor vessel. In these examinations, there were over 650 Mbytes of data collected. The inspections included 0°, ±45°, ±60°, ±70°, and tandem SAFT. The data was not analyzed in Germany, but was shipped back to PNL for this evaluation.

Field trip notes were developed during the course of the testing at the MPA site. These notes were recorded on a PC to document the activities that occurred during the testing. This turned out to be very useful because there were a number of confusing points that these detailed notes clarified.

There were a number of things that were learned in this exercise. The SAFT system, in general, performed very well; but there were several areas that were found where improvements were needed. The most important of which was that the header for the files needed to be changed to accommodate the sizes of numbers to cover the dimensions of a full-sized reactor pressure vessel.

During January the SAFT equipment was returned to the United States. Upon arrival the equipment was set up and checked out to determine its condition. Several minor problems were encountered and some maintenance was performed on the scanner.

All 650 Mbytes of data were methodically analyzed. The analysis was performed by first evaluating the data from the clad surface, followed by the data from the unclad surface, and then evaluating the data combined. This approach allowed us to learn more from the data evaluation and gave us the opportunity to determine optimum inspection combinations.

During the analysis, it became apparent that the amount of data to be analyzed was substantially more than had been analyzed previously for any other inspection. In other examinations, most of the scanned material is blank; but in this case every area scanned had a substantial number of indications. One conclusion from this exercise is that improvements to the system are needed to facilitate handling of large data sets, and this to a large extent was accomplished when the system was upgraded to a Sun computer.

Another result from the data analysis was that the UT responses obtained from the various directions and inspection conditions lead to different conclusions

about how to interpret the indication. Consequently, a decision was needed as to which signals and interpretation to believe. Every attempt was made to follow the rules that had been established from previous work, but there were many instances of ambiguity associated with the interpretation. In these cases, a decision was reached by looking at the strength of the signals (top tip signal amplitude versus bottom tip amplitude), or recognizing that volumetric indications should be detected during a normal beam scan, etc. The tandem scans were very useful in determining if an indication was surface connected or if two signal tips were from a single indication or two different indications.

At the completion of the analysis, the results were reviewed by several knowledgeable PNL staff to ensure that nothing was overlooked in the evaluation and to confirm the flaw size estimates. The SAFT inspection results were provided to the JRC at Ispra, Italy. Overall the results were felt to be good, but there were difficulties in interpreting the data. This was due, in part, to the number of indications in each of the zones examined, and the fact that defects have a large range of scattering properties. Some indications were easy to interpret, but others were quite complex and did not fit simple models.

FSV SAFT-UT RESULTS

The data was analyzed by examining all files of a particular zone. The data was reduced by the PNL staff, and those indications that were felt to be of importance were reported; this sometimes included several indications in a particular zone. In several other cases, the indications were all plotted and then they were felt to all be part of a single larger indication and, thus, were reported as a single large indication. However, we did provide images showing the detailed images that were evaluated to arrive at that conclusion.

The full details of the study have not been released, but the true state data is known and the values submitted by PNL are shown in Table 1. What is listed in this table is the True State data obtained by destructive analysis and the results obtained using SAFT-UT. There was good general agreement for all the defects inspected except for Defect Numbers 5 and 6. In reviewing the data, the indications reported for defect zone 5 correlate with the intended defect but this is not true for defect zone 6. This latter zone might best be classified as not detected. Since the analysis is still in progress, the actual outcome and overall assessment will need to await further details.

Table 1. PISC III Action No. 2 Full-Scale Vessel Test - Phase 1

Defect Number	1			2			3			4		
	ΔX	ΔY	ΔZ	ΔX	ΔY	ΔZ	ΔX	ΔY	ΔZ	ΔX	ΔY	ΔZ
True-State	9	80	18	2	24	6	L = 24, Δ = 6			L = 83, Δ = 25		
SAFT Results	9	82	17	28 5.1 -	58 30.7 11.8	9* 5 5	not inspected			not inspected		

Defect Number	5			6			7			8		
	ΔX	ΔY	ΔZ	ΔX	ΔY	ΔZ	ΔX	ΔY	ΔZ	ΔX	ΔY	ΔZ
True-State	13	33	33	15	32	22	2	31	12	28	1089	110
SAFT Results	43 17.8 43.1	42 20.5 112	23 10.1 7.6	38	168	20	not inspected			23 18 5.1	1	110 58 33

Defect Number	9			10			11			12		
	ΔX	ΔY	ΔZ	ΔX	ΔY	ΔZ	ΔX	ΔY	ΔZ	ΔX	ΔY	ΔZ
True-State	20	1089	82	800	4	20	116	16	27	4	77	22
SAFT Results	20 8 8	- - -	71 58 64	not inspected			109	3	25	9	81	21

*This first one is formed by adding the reported zones together and forming a super large region containing all reported indications.

However, if one takes a simplistic approach to the assessment of the SAFT-UT performance and computes the mean, standard deviation and variance for the data as a function of the three orthogonal coordinates X, Y and Z, then one finds as shown in Table 2 that the SAFT-UT technology performed very well. It needs to be noted that most of the error for the Y dimension of the defects was associated defect 6. If this defect is eliminated, the greatest effect will be on the Y measurements as is shown in Table 3. This is more like what is expected since the operating parameters were selected so that the resolution of the system would be similar in both the depth and lateral directions. Because of the degraded performance due to surface roughness and the cladding, it was expected that the resolution would be 2 wavelengths which would be 2.44 mm to 3.0 mm for the transducer frequencies and modes used versus the theoretical limit of 1 wavelength.

Table 2. Statistical Values of SAFT-UT Performance on All FSV Flaws

	ΔX	ΔY	ΔZ
Mean	6.1 mm	19.5 mm	-3.5 mm
Standard Deviation	13.3 mm	47.2 mm	4.4 mm
Variance	12.4 mm^2	44.1 mm^2	4.1 mm^2

CONCLUSIONS BASED ON FSV TEST

The SAFT-UT system performed extremely well and pretty much as expected in these tests. This provided good validation data for thick section materials. We believe the SAFT technology performed very well in comparison with other techniques used in this test, but a full comparison will have to await the detailed analysis that is in progress by the PISC III Action 2 Data Analysis Group.

Table 3. Statistical Values of SAFT-UT Performance on All FSV Flaws Except No. 6

	ΔX	ΔY	ΔZ
Mean	3.7mm	3.0 mm	-3.7 mm
Standard Deviation	12.3 mm	3.8 mm	4.7 mm
Variance	11.4 mm^2	3.5 mm^2	4.3 mm^2

CONCLUSIONS

The validation test conducted and reported in this section provides a very good and strong case for the effectiveness of the SAFT technology. This coupled with the improvements in computer processing speed, RAM memory capacity, and laser disks makes for very compact and high performance systems that can process data as it is acquired and provide a high performance platform for conducting the image analysis. This work provides a strong case for use of this technology for characterizing ultrasonic indications in reactor pressure vessels.

3. PISC III PROGRAM STATUS

The Programme for the Inspection of Steel Components Phase 3 (PISC III) began with the objective to measure the inspection effectiveness of NDE for many different light water reactor components (Crutzen 1991). This included real components, real geometries, and real flaws in conjunction with conventional and advanced NDE techniques. The PISC III program will be completed in

calendar year 1993. A final symposium of the program work will be held in March of 1994 in Petten, Holland. There are many things that are coming to closure at the same time, and it will be an extremely tight schedule for the remainder of the program. The following is a very brief overview of the status of each action. Specific programmatic results cannot be released until the PISC III Management Board grants approval to do this. Therefore, the following defines the objectives and provides a status of the work being conducted on each Action but does not contain specific results since these are not publicly available at this time.

ACTION NO. 1 - REAL CONTAMINATED STRUCTURES

Action No. 1 seeks to collect results from specific investigations and limited round robin tests (RRTs) on real service-induced defects in materials and structures of the primary circuit of light water reactors. Very little work was performed on the action because this action was given low priority because of the broad spectrum of actions started and the high cost of transporting contaminated components, performing tests, conducting destructive examinations, and then disposing of the residual materials.

ACTION NO. 2 - FULL SCALE VESSEL (FSV) TESTS

Action No. 2 validates the results obtained by procedures in the PISC II exercise but using more realistic inspection conditions. The installation offered by Staatliche Materialprufungsanstalt (MPA), Universitat Stuttgart, Germany is being used. There are two phases to this action with the first phase being the assessment of the capability of techniques to size a series of zones which contain known defects. The NDT examinations have been completed, destructive evaluation of all defects has been made, draft reports have been sent out for review and comment, with the final report to be completed in the near future.

The second phase involves the use of a central mast manipulator to simulate the actual inspection that occurs during ISI. The results from these tests will be compared to the capability studies that were performed in other aspects of the PISC program. All data has been collected and analysis of this data has started. Destructive testing will use the results of the data analysis to aid in guiding the destructive testing process.

ACTION NO. 3 - NOZZLES AND DISSIMILAR METAL WELDS

The Action No. 3 round robin tests of four safe-ends represent some of the most difficult technical aspects of inservice inspection. In this work, a Japanese-Italian BWR assembly of nozzle plus safe-end, an American BWR assembly with two nozzles and safe-ends, and a Spanish PWR safe-end were inspected in 13 countries. All of the round robins have been completed and the destructive evaluation (DE) has been completed for the dissimilar metal welds. DE of the nozzle-to-shell welds is the one area that is uncertain as to whether it will be performed. Draft reports have been prepared and presented to the PISC III Management Board on all of the welds that have been analyzed and for those which have undergone DE.

ACTION NO. 4 - AUSTENITIC STEEL TESTS (AST)

Action No. 4 applies the PISC II methodology to the primary circuit piping of LWRs. Round robin tests for the capability assessment and parametric studies started in 1990; some reliability evaluation of the testing procedures will be considered. The two parametric studies on effects of counterbore and microstructure have been completed and draft reports have been circulated to the data analysis group for Action 4 (DAG 4) for review and comment. The study on counterbore designs is a very interesting one and will have an impact on counterbore designs for new construction and for component replacements.

The wrought stainless steel capability study is nearing completion. Circulation of the specimens was completed, the DE was performed by JAPEIC (Japan Power Engineering and Inspection Corporation), and data analysis is nearing completion. Initial data analysis has been performed using the relative operating curve (ROC) method.

The circulation of the wrought-to-cast and the cast-to-cast assemblies was completed in August of 1993. The DE began in the fall of 1993 and so has the data analysis. It is hoped that the analysis will be completed by late fall.

The wrought stainless steel reliability study is underway. Three teams from the USA have examined these specimens. The specimens are being prepared for shipment to Petten, Holland for the Europeans to inspect these assemblies. The significance of the current work is that full pipe cylinders are being used that contain flaws removed from operating nuclear power plants. Furthermore, the inspection and analysis time is not constrained such that for the 13 assemblies the teams have 12 days to perform both detection and sizing. All the teams finished in 11 days and were given the option to spend more time if they wanted, but in all three cases the teams declined this offer. This exercise will expand our knowledge of the inspection process and provide some insight into the influence of some of the inspection variables. The present plans indicate that it will be impossible to have DE performed as part of the PISC III program. This work will have to be conducted during the 1994 calendar year under the auspices of another European program that is interested in the results of this study.

ACTION NO. 5 - STEAM GENERATOR TUBES TESTING

Action No. 5 involves in its present phase round robin tests of individual tubes of steam generators containing realistic and artificial defects. Emphasis has been put on corrosion defects (IGA, SWSCC, PWSCC) at three key locations: tube sheet (above the rolling zone), tube support plates, and U-bend transition. This action has had a very large turnout of teams from all over the world. It has been a significant challenge just trying to adjust the schedule to allow all the teams that wanted to participate to have the opportunity to participate. All three of the round robins are completed and DE has been started. It will be a major challenge to get the DE completed and the data analyzed during the next year. This action will probably carry over into the 1995 calendar year.

ACTION NO. 6 - MATHEMATICAL MODELLING ON NDE

Action No. 6 has the objective to validate experimentally mathematical models and perform parametric studies in order to assess the importance of defect characteristics. An important objective is to promote the practical application of models as an aid to more effective and efficient inspection procedures and interpretation of results. This action has completed the validation of three models (two U.K. and one German) with a published report of the results of this validation effort. There are currently two models developed by French laboratories and one U.K.-developed model that are in the process of being validated. Following the completion of the validation effort, the models will be used to try to understand the performance of procedures to inspect some of the weldments in Action 3.

ACTION NO. 7 - HUMAN RELIABILITY STUDIES

Action No. 7 seeks to evaluate the influence of human interpretation of inspection results, equipment malfunctions, and human interaction on the overall inspection procedure. The majority of this work has been conducted at the Risley Nuclear Laboratory to study some of the human factors aspects of ISI. This has involved tests in a laboratory setting, the use of an UT simulator that was developed at Risley, and the use of the TEL (a controlled environment in a C-van that has welded specimens in which conditions like temperature, lighting, humidity, noise level, etc. can be controlled) to study the inspector during the inspection process to understand the significance of these variables on the inspection performance and, hopefully, to give some insight to how these variables can be controlled to limit their adverse impact on the inspection process. All of the studies have been completed and detailed analysis is underway. A draft report for review and comment was sent out during the fall of 1993.

ACTION NO. 8 - CODES AND STANDARDS

There are a number of activities in progress on this action. Its goal is to be the vehicle for identifying things from the other Actions that will impact codes and standards and then to facilitate the movement of these to the bodies that need to be aware of the results so that changes can be initiated. One activity is to prepare a glossary of terms for the PISC program because of all the acronyms that are used. A second activity is a computer compilation of available specimens that might be used for training or performance demonstration testing. A third activity is the development of the methodology that needs to be followed to develop a performance demonstration (PD) program. This includes defining the goals of the PD program to assess whether those goals have been met including all of the steps in between. This does not include any recommendations but defines the steps that must be followed. Furthermore, the approach is being written in a general sense to be applicable to a wide variety of industries and applications. This activity will carry on beyond the completion of the PISC III program to facilitate the movement of PISC III results to the various codes and standards. It is anticipated that this process will take several years at a minimum to move the results and recommendations into national and international codes and standards.

FUTURE WORK

The future work will involve support to bring the PISC-III program to closure, assess and review the program technical results to determine adequacy of the data bases, conduct any needed additional analysis and testing, and assemble the technical bases and proceed with support to making recommendations to Codes and/or regulatory organizations.

4. EVALUATION OF COMPUTER-BASED UT/ISI SYSTEMS

This paper reviews progress in fiscal years 1991-1993 on a task to evaluate the reliability and accuracy of interpretation of results from computer-based ultrasonic inservice inspection (UT/ISI) systems, part of the NRC program entitled "Evaluation of Computer-Based NDE Techniques and Regional Support of Inspection Activities," FIN No. L1100. The products of this task are to be published as an Introduction and a series of Supplements in NUREG/CR-5985, *Evaluation of Computer-Based Ultrasonic Inservice Inspection Systems*, in a loose-leaf format to facilitate periodic updates. The Introduction, scheduled for publication in late 1993, contains an exposition of computer-based UT, a list of systems to be evaluated, and a methodology for the evaluation. The Supplements each treat a specific computer-based UT/ISI system. Two systems have been characterized; the associated Supplements are scheduled for publication in early 1994. Previous work on this task was described in Taylor et al. (1991).

A seminar entitled "An Introduction to Computer-Based Inservice Inspection," given at Pacific Northwest Laboratory (PNL) in April 1991, was attended by 13 NRC Regional and Headquarters personnel. The seminar addressed benefits of computerization; imaging; computerized imaging; data display; image quality; component geometry and metallurgy; image classification; flaw sizing; and performance characteristics of selected systems. The seminar lecture notes have not been published, but many of the topics are dealt with in the Introduction to NUREG/CR-5985.

The Introduction to NUREG/CR-5985 provides expositions of topics in conventional and computer-based ultrasonics. Through text, diagrams, images, and a glossary, it lays the groundwork and establishes terminology for the understanding and evaluation of computer-based UT/ISI systems. Topics addressed include: scanning, arrays, data acquisition, image processing and display, and data analysis and interpretation. Appendix A provides a methodology in the form of a detailed, step-by-step procedure for evaluation of a system. It is in outline format, emphasizing multiple-choice answers, but encouraging the evaluator to consider special features of each system. The major headings are System Description, Training, Set-Up, Documentation, Image Interpretation, Scanner/Mechanical Measurements, Ultrasonic Measurements, Data Acquisition/Processing, Image Presentation, Digitization, Data Acquisition Limitations, Data Types, Processing Options, Data Storage And Portability/Third Party Review, Problems/Special Features, and Checklist Identification where potential improper system operation could occur. The procedure was sent out

for review to 23 organizations, two of whom responded, providing welcome and valuable suggestions that helped clarify it and broaden its scope.

Three test blocks were designed and fabricated as part of the evaluation effort. Their purpose is to characterize the image presentation of UT/ISI systems, and provide a basis for comparing the images from various systems. Two of them are described in the American Society for Mechanical Engineers (ASME) Boiler and Pressure Vessel Code, Section V, paragraph T-435 and Appendix E, figures E-10 and E-20. The first is a depth and lateral resolution block for normal-beam inspection. It contains two sets of holes: one at equal depth and varied spacing, and the other at equal spacing and varied depths (Figure 2). The second block contains four sets of holes: two sets for 45° inspections and two for 60°. The purpose and layout of each set is similar to the normal-beam block. The third block is designed to permit analysis of the small-scale motion of the scanner, and contains two grooves at right angles and a spherical-tipped hole. Imaging the grooves gives a more or less jagged line that reveals the degree of repeatability of the scanner, while imaging the hole in a depth mode produces a set of rings whose shape and regularity indicate the accuracy of scale of the system. All three blocks are described in detail, with drawings, in Appendix A of NUREG/CR-5985. They have been valuable in the system analysis, but could benefit from wider use and possible modification.

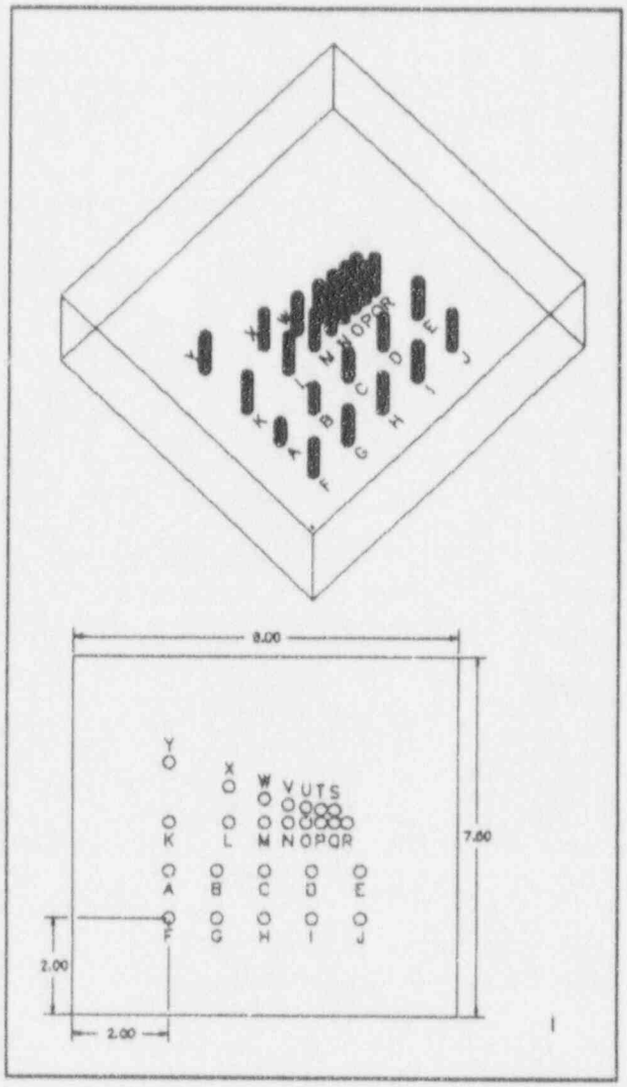


Figure 2. Normal-Beam Resolution Block

The remainder of this section presents the results of the two system evaluations performed so far. The material on P-Scan is extracted from the draft version of the Supplement. The material on IntraSpect is a preliminary summary.

An interesting general observation is that the two systems have different objectives, and consequently differ in their gathering, analysis, and presentation of data. P-Scan is a dedicated scanning and imaging system for pipes.

The images produced are specialized to the evaluation of weld defects and corrosion. IntraSpect is a general-purpose system, provided in many customized variants depending on the application. It provides more sophisticated visualization of volumetric positions of reflectors. P-Scan normally acquires only imaging data, and by exception, a limited amount of RF data. IntraSpect normally acquires full RF data, which is then analyzed for image presentation; IntraSpect therefore produces much larger data files than P-Scan. Image color choices for the P-Scan are restricted, but the print color automatically matches the screen display color. IntraSpect provides complete freedom in the choice of both screen and print colors, but no easy way to correlate the two. The ability to evaluate these two systems by using the same procedure is an early indication of the methodology's value.

Another observation of interest, noted in soliciting proposals for the use of various systems in the characterization process, is the varying degree of different manufacturers' concern with proprietary system functions. Some manufacturers freely provide information about their products' functioning, while others consider the methods, the operating manuals, and even the procedures used to operate the systems, as proprietary information. There is no obvious correlation between the secrecy imposed and the degree of sophistication of the system.

The first system characterized was the P-Scan system, manufactured by FORCE Institutes, Brondby, Denmark. P-Scan (short for Projection Scanning) is a computerized ultrasonic pipe-scanning system consisting of 3 modules: a PC-compatible system control module, an electronic scanner control module, and an electro-mechanical scanner module. The operating system and programs reside in read-only memory chips in the system control module. The operator sets up ultrasonic inspection parameters through the system control module, and physical inspection parameters through the scanner control module. Data is stored on 3-1/2 inch floppy disks. Noteworthy results of the P-Scan evaluation are presented under four categories: unusual features, positive features, negative features, and improper operating considerations.

Unusual features include P-Scan's three loosely coupled functions: motion control, position sensing, and data recording. These three are not tightly interdependent as in many systems. There is no minimum threshold set for signal recording: the maximum signal amplitude within each gate is recorded, no matter how low that amplitude is. In P-Scan images, the terms "side" and "end" refer to the weld, not the pipe: for a circumferential weld, "SIDE VIEW" refers to a view from the end of the pipe, and "END VIEW" refers to a view from the side of the pipe.

Positive features relate largely to the ease of use of P-Scan. Advantages of loose coupling among motion, position, and data are simplicity of system; ease of repeating or filling in part of scan; possibility to cover irregularly shaped areas by manual intervention. All data within gated zones (i.e., position and value of maximum amplitude within each gate) are always available. Data-taking functions are straightforward. System is easy to set up. All modules are compact. Scanner controller settings are clearly visible on the front panel. System always records all data in gates within its dynamic

range (over 100 dB). Gating levels are set during interpretation, rather than during scanning.

Negative features are primarily limitations, and in some measure are corollaries of simplicity. There are several disadvantages of loose coupling among motion, position, and data: the operator must assure proper coverage; the scan appearance may be unesthetic; the computer record may contain step sizes and axis speeds different from those actually used; the operator can possibly set the scan speed too high; the step value between scans can be set large enough to produce plots with blank lines, even when coverage is adequate. There are no HOME or GOTO positioning functions: only a JOG control. In normal imaging mode, there is no provision for changing the scale of the image. Screen image does not generally have a 1:1 aspect ratio, i.e., length, width, and height are to different scales. The X,Y,Z coordinates of a given datum cannot be determined, if there are other indications along both the same X and Y lines. The menu structure is difficult for the novice or occasional user. Raw data cannot be recovered; specifically, incorrect beam angle leads to a distorted image, that cannot be corrected in post-processing. There is no option for unidirectional scanning (taking data only during positive scan-axis motion).

Improper operating considerations focus mainly on potential problems in use of the P-Scan. Like many systems, P-Scan produces data in a proprietary format, with no provision for export to another format, so post-inspection review of data depends on printouts; detailed examination of the data requires access to a P-Scan program. The scanner head can slip out of adjustment if not well tightened, leading to undetected loss of coverage. Since the scanner parameters are set manually, independent of computer control or verification, full coverage must be assured by operator inspection of the scan results. Since there is no provision for changing the scale of the image, assuring sufficient data for evaluation may require rescanning to take A-scan data in areas of multiple overlapping indications. Because image aspect ratios are not generally 1:1, the shape of an indication on the display does not generally indicate its true shape (this may also be advantageous in highlighting one aspect of an indication). Skewed and mirrored images amy be obtained by improper angle specification. The "image processing" (smoothing) option should never be used before the inspection data has been stored, as it irretrievably alters the original data. A very helpful feature is the presence of baseline noise: because the system records data at every point inspected, it is easy to verify full coverage by review of the image at the highest gain.

The second system characterized was the IntraSpect I/MC system, manufactured by ABB AMDATA, Windsor, Connecticut. IntraSpect is a computerized ultrasonic inspection system consisting of a computer workstation, a remote data acquisition system, a remote pulser preamplifier, a scan controller, a scanner, and miscellaneous auxiliary equipment. The operating system and programs are kept on hard disk and are read into memory when the system is powered up. The operator sets up the system through the computer workstation. Data is stored on hard disk and archived to rewritable optical disks.

Unusual features of IntraSpect are the option to give a file a name starting with "%" to allow modification of key parameters after data-taking (useful for development), and the definition of two classes of users: the super-user, who can modify all parameters, and the ordinary user, who is restricted to minor modifications.

Positive features of IntraSpect include computer control over most inspection parameters; presentation of live A-scan during setup; ability to "teach" scan limits interactively; intuitive jog control, laid out like the motions; "go to" function, allowing repositioning over indications for ease of evaluation; ability to view C-Scan, B-Scan, B-scan end, and A-scan displays for all points; ability to move through B-scans automatically (although slowly); zoom capability for B- and C-scans; ability to move cursor to a highest-amplitude point; an on-line user's manual accessible during inspection and evaluation; unidirectional data presentation to avoid displaying the backlash; and the ease with which AMDATA can modify programs for special user needs.

Negative features of IntraSpect, as our test system was configured, included the bulkiness of the system (a corollary of its flexibility), some system down-time due to electronic problems; a problem with an encoder; cursor control is restricted to one dimension at a time (awkward for moving around on drawings); no unidirectional scanning or other real-time backlash compensation; lack of a half-wave rectification option for thickness measurements; inability to display original pixels in the condensed image of a large scan; inability to combine files (except adjacent ones of the same part); absence of a "stop" button on the scanner unit, for emergency use by the field operator.

IntraSpect aids to ensure proper operation include the following: most inspection parameters are controlled by computer, helping to assure correct recording of inspection parameters; full RF data is recorded, with scanner positions of each waveform; position feedback is used to prevent errors in positioning; the system stops if data is lost (from scan speed exceeding acquisition speed); image aspect ratio is normally 1:1; repetition rate is controlled by scanner motion, assuring intended scan density; x, y, and z positional information are provided on printouts, as well as metal path, depth, TOF, thickness, vee position, surface distance; in B-scan images, the relevant A-scan is shown; parameter files can be viewed with any HP word processor.

Difficulties in proper operation may include: lack of computer control over angulation and skew; possibility that operator neglects to reset position encoders after a position error; absence of a label indicating whether a B-scan view is from side or end; absence of scales on B-scan presentations; filter banks are manually changed, so the filter bank may not match the documentation; the C-scan shows transducer position, which for angle-beam inspection is not the indication position; and, like most systems, lack of export capability for data files.

Both the P-Scan and the IntraSpect performed all functions correctly, within the limitations of the characterization procedures and the system architectures. Analysis of additional systems may lead to a classification of system

types according to scanning, acquisition, and analysis capabilities, and to the proposal of a generic data export format. Additional systems planned for future evaluation are Accusonex, ARIS, GE-Smart UT, GERIS, Phased Array, SwRI/PAR EDAS, and UDRPS.

REFERENCES

Crutzen, S. 1991. *Summary of the Three Phases of the PISC Programme*, PISCDOC(91)47. Commission of the European Communities, Joint Research Centre. Ispra, Italy.

Hall, T. E., L. D. Reid, and S. R. Doctor. 1988. *The SAFT-UT Real-Time Inspection System - Operational Principles and Implementation.* NUREG/CR-5075. U.S. Nuclear Regulatory Commission, Washington, D.C.

Jeong, Y. (Peter) H. 1987. "An Ultrasonic Material State Classifier for Elastically Anisotropic Materials," p. 167; Ph.D. Thesis, Department of Mechanical Engineering and Applied Mechanics, Drexel University, Philadelphia, Pennsylvania.

Taylor, T. T., R. J. Kurtz, P. G. Heasler, and S. R. Doctor. 1991. "Evaluation of Computer-Based NDE Techniques and Regional Support of Inspection Activities," in *Proceedings of the U.S. Nuclear Regulatory Commission Eighteenth Water Reactor Safety Information Meeting*, NUREG/CP-0114, Vol. 3, pp. 123-136.

PROGRESS ON RISK-BASED INSPECTION GUIDELINES: APPLICATION OF SURRY-1 PILOT STUDY TO IMPROVED INSERVICE INSPECTION PLANS[1]

by
F.A. Simonen, T.V. Vo, H.K. Phan, M.A. Khaleel and B.F. Gore
Pacific Northwest Laboratory,
Operated for the U.S. Department of Energy
by Battelle Memorial Institute
Richland, WA 99352

ABSTRACT

This paper reports on risk-based studies being performed at Pacific Northwest Laboratory (PNL) for NRC as part of a research program entitled "Evaluation and Improvement in Nondestructive Examination Reliability for Inservice Inspection of Light Water Reactors (LWRs). The studies at PNL have been carried on in cooperation with efforts by the ASME Research Task Force on Risk-Based Inspection Guidelines, and with a newly formed Section XI Working Group on Implementation of Risk-Based Inspection. The objective of the work described in this paper is to explicitly quantify the factors (including inservice inspection) that govern the risks (core damage frequency) due to structural failures of pressure boundary components. Having identified the most risk significant components by using the risk-based methods, the results are being applied to develop improved inspection strategies (what, when and by what method). Following a discussion of on-going efforts in the area of risk-based inspection, this paper describes structural reliability models developed at PNL to evaluate the benefits of alternative inspection strategies.

INTRODUCTION

The Evaluation and Improvement of NDE Reliability for Inservice Inspection of Light Water Reactors (NDE Reliability) Program at PNL was established to determine the reliability of current inservice inspection (ISI) techniques and to develop recommendations that would ensure a suitably high inspection reliability if fully implemented. Much of this program has been directed to determining the reliability of ultrasonic ISI performed on commercial light-water reactor (LWR) primary systems (and other safety significant components), and to evaluating the degree of improvement that could be achieved using improved and advanced NDE techniques.

Once that NDE performance has been suitably enhanced, the next step has been to ensure that these methods are used to inspect those components which

---

[1]Work supported by the U.S. Nuclear Regulatory Commission under DOE Contract DE-AC06-76RLO 1830: A. Hiser, NRC Program Manager, FIN B2289.

contribute the greatest risks due to structural failures. The long-range goal is to propose changes in the inspection plans mandated by ASME Section XI. These improved criteria will help to establish priorities for selecting systems, components and structural elements for inspection, and will help to determine the extent, frequency, and method of examination. The improved ISI programs should detect degradation in a timely manner, ensure a suitably low failure probability, and thus contribute to safe nuclear power plant operation.

Past work on this task has reviewed and evaluated various concepts for probabilistic inspection criteria, and has included interactions with other industry efforts, notably through the ASME Research Task Force on Risk-Based Inspection Guidelines (NRC 1993). Starting in FY90 risk-based calculations have addressed inspection priorities at a detailed component level, and have focused on a plant-specific pilot study for the Surry Unit 1 Nuclear Power Station. This pilot study began with the reactor pressure vessel, reactor coolant system, low pressure injection system and auxiliary feedwater system. More recent work has begun to rank components in the five remaining Surry-1 systems of interest (high pressure injection system, residual heat removal system, service water system, component cooling water system and power conversion system). The initial effort for these final five systems was an expert elicitation workshop held during February 1992 to estimate the component rupture probabilities.

A second part of the risk-based inspection work is to identify the most effective inspection strategies for the high ranked components, where an effective strategy is one that ensures component failure probabilities which meet target risk goals. Probabilistic fracture mechanics calculations using the pc-PRAISE computer code (Harris, Dedhia, and Lu, 1992) are being performed to predict the relative benefits of alternative inspection strategies. Applications of this computer code to Surry-1 piping systems have estimated the reliability of the low pressure injection (LPI) system piping, and evaluated the effectiveness of alternative inspection strategies.

ASME RESEARCH TASK FORCE ON RISK-BASED INSPECTION GUIDELINES

During the past year PNL has continued to participate on a special ASME Research Task Force on Risk-Based Inspection Guidelines, with Dr. F. A. Simonen, Dr. B. F. Gore and Dr. T. V. Vo serving as members of the Task Force. The ASME group has been identified by PNL as an effective route to achieve long-range goals for improved inspection criteria. PNL's activities on the Research Task Force are now focused on a Working Group that is addressing Nuclear Power Plant Components. The goal of this working group is to make recommendations to ASME Section XI on the use of risk-based methods.

During the past year, the Research Task Force published a document specifically directed to light water reactor nuclear power plants titled "Risk-Based Inspection - Development of Guidelines - Volume 2 - Part 1 - Light Water Reactor (LWR) Nuclear Power Plant Components" (ASME 1992). This document recommends and describes specific methods to be used in developing risk-based

inspection plans for nuclear power facilities. Future efforts will apply the risk-based methodologies as recommended in the Volume 2 -Part 1 document to develop improved inspection programs for nuclear power plant components. The calculations now being performed on the new criteria task will become part of a companion Volume 2 - Part 2 Document (scheduled for publication during 1994) which will make specific recommendations for consideration by ASME Section XI.

There were five meetings of the LWR Nuclear Power Plant Components Working Group during the past year. Discussions were in two main areas. The first area was a review of PNL's risk-based rankings of Surry-1 components, and of PNL's probabilistic fracture mechanics calculations that predict the reliability of low pressure injection system components and the impact of inservice inspection on the reliability of these components. The second area of discussion was on the topic of decision risk analyses led by Dr. Robert Perdue of Westinghouse Electric Corporation. Decision analysis methods will address cost-benefit considerations which are beyond the scope of PNL's work. Members of the Working Group (including PNL) will be providing inputs that will permit the formulation of a decision risk model for the inspection of components of the LPI and other LWR systems. Dr. Perdue expects to begin his work for the ASME Center for Research and Technology Development. This work will address the relative safety and economic benefits of alternative inspection strategies.

Progress towards impacting ASME Section XI continued during the past year through interactions with a new Section XI Working Group on Implementation of Risk-Based Inspection. This Section XI Group began to meet regularly starting in August 1992. During the first meetings members of the Research Task Force made extended presentations on the concepts of risk-based inspection, and initiated discussions of how best to introduce the findings of risk-based studies into future editions of Section XI. Options considered have ranged from plant specific calculations for each plant that address all risk-related aspects of each plant to alternative approaches that generalize the major findings from a few plant specific studies. Recent efforts have been to develop "strawman" tables for inspection plans with these plans being based on PNL's Surry-1 results. These tables will specify an improved selection of ISI locations and frequencies for code inspections, and more importantly will serve to demonstrate to the Section XI membership how future editions of Section XI can codify the findings of risk-based studies.

PLANT SPECIFIC PRA APPLICATIONS TO SURRY-1

A major effort has involved the application of existing probabilistic risk assessments (PRA) to establish inspection priorities for pressure boundary systems and components. During the past year pilot applications of PRA methods to the Surry-1 plant continued.

The Surry-1 work has applied a methodology (Vo et al. 1989) that uses the results of PRA's in combination with the techniques of failure modes and effects analysis (FMEA) to identify and prioritize the most risk-important systems and components. The specific systems initially selected for analysis

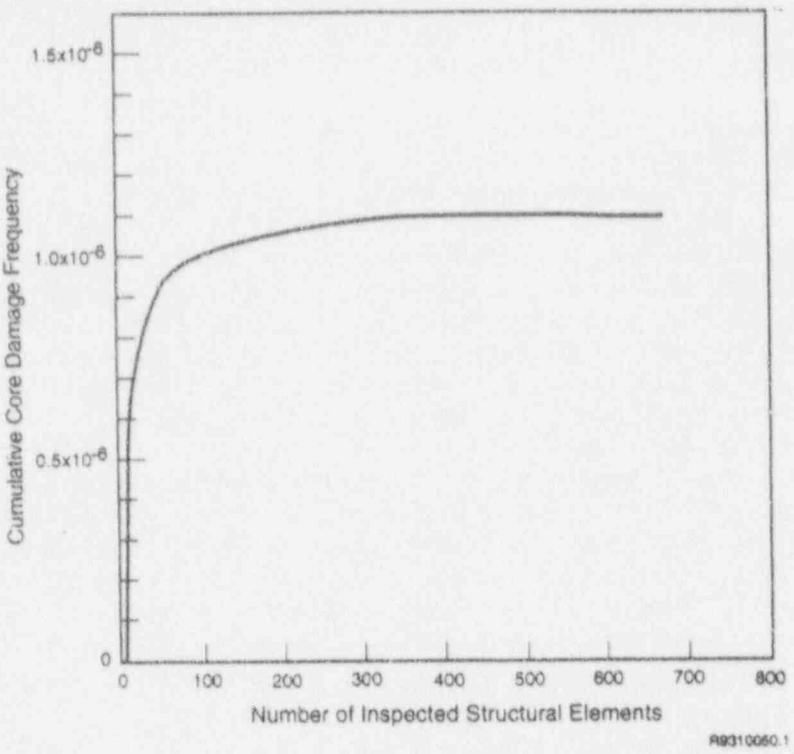


Figure 1. Rankings of Individual Structural Elements of Surry-1 Low Pressure Injection System

were the reactor pressure vessel, the reactor coolant, the low pressure injection (including the accumulators) and the auxiliary feedwater. The risk-based ranking of components within these four systems was completed during FY91, and results were summarized in a previous publication (Vo et al. 1992).

In the past year, detailed rankings have been developed for the 644 structural elements (and potential locations for ISI) in the Surry-1 low pressure injection system. These structural elements consisted of 426 welds, 130 elbows, 59 tee/branch connections, 25 valves, and 4 pumps. Figure 1 shows the cumulative core damage frequencies associated with these individual elements when ordered in decreasing importance as assigned by the risk-based ranking. This plot indicates that 55% of the overall core damage risk from pipe ruptures is associated with about 1% of the structural elements. These specific locations correspond to the six check valves at the interface between the high pressures of the primary coolant system and the low pressures of the standby LPI system. The failure mechanism which elevates the ranking of these six locations is the potential for thermal fatigue arising from back leakage past the check valves.

The calculations that developed the rankings shown by Figure 1 addressed both the consequences and probabilities of failure. The consequences were taken from the previous PRA-based evaluations that had calculated conditional core damage probabilities (given a pipe rupture) for each pipe segment making up

the LPI system. Probabilities of pipe rupture were assigned by allocating this overall rupture probability for each pipe segment (as obtained from the expert judgement elicitation) to the individual welds and fittings that make up the segment. This allocation was performed, again using expert judgement, with the assistance of Dr. Spencer Bush, a retired PNL staff member with extensive knowledge of operating experience of nuclear piping systems.

Future work will result in a comprehensive ranking of the most important components within all the Surry-1 plant systems. These risk-based priorities will permit evaluation of current inservice inspection requirements of Section XI of the American Society of Mechanical Engineers Code. The objective is to identify needed improvements to current ISI plans.

EXPERT JUDGEMENT ELICITATION FOR RUPTURE PROBABILITIES

The risk-based studies of the Surry-1 plant have required estimates of rupture probabilities on a detailed component-by-component level. Because neither sufficient data from operating experience nor detailed fracture mechanics analyses are available, the expert judgment elicitation process has been selected as a method to estimate needed rupture probabilities. PNL has conducted two expert judgment elicitation meetings on May 8-10, 1990 at Rockville, Maryland and more recently on February 3-6, 1992 in Washington DC.

During the past year, the data from the 1992 expert's meeting were entered into a computer data base for statistical analyses of the high pressure injection system, the residual heat removal system, the component cooling water system, the service water system and the power conversion system. The statistical analyses produced "bar and whisker plots" that display the median values of the estimates along with the range of values provided by the nine individual experts. In certain cases, all nine experts did not provide an estimate for a given pipe segment. Figure 2 shows an example of the rupture probability data, in this case for the residual heat removal (RHR) system. Table 1 shows the numerical failure probability estimates for components within the residual heat removal system. Complete sets of plots for all Surry-1 systems have been published elsewhere (Vo et al. 1991 and 1993).

An individual plot graphically displays the following features of the estimated failure probability distribution.

- The "whiskers" identify the extreme upper and lower values of the distribution.
- The box itself locates the 25% and 75% quantiles (i.e., quartiles) of the distribution. In other words, 50% of the data points are within the box. The 25% and 75% quartiles were chosen for uncertainty estimates to eliminate the two most extreme values of the distribution.
- The line within the box intersecting with the circle or dot is the median of the distribution.

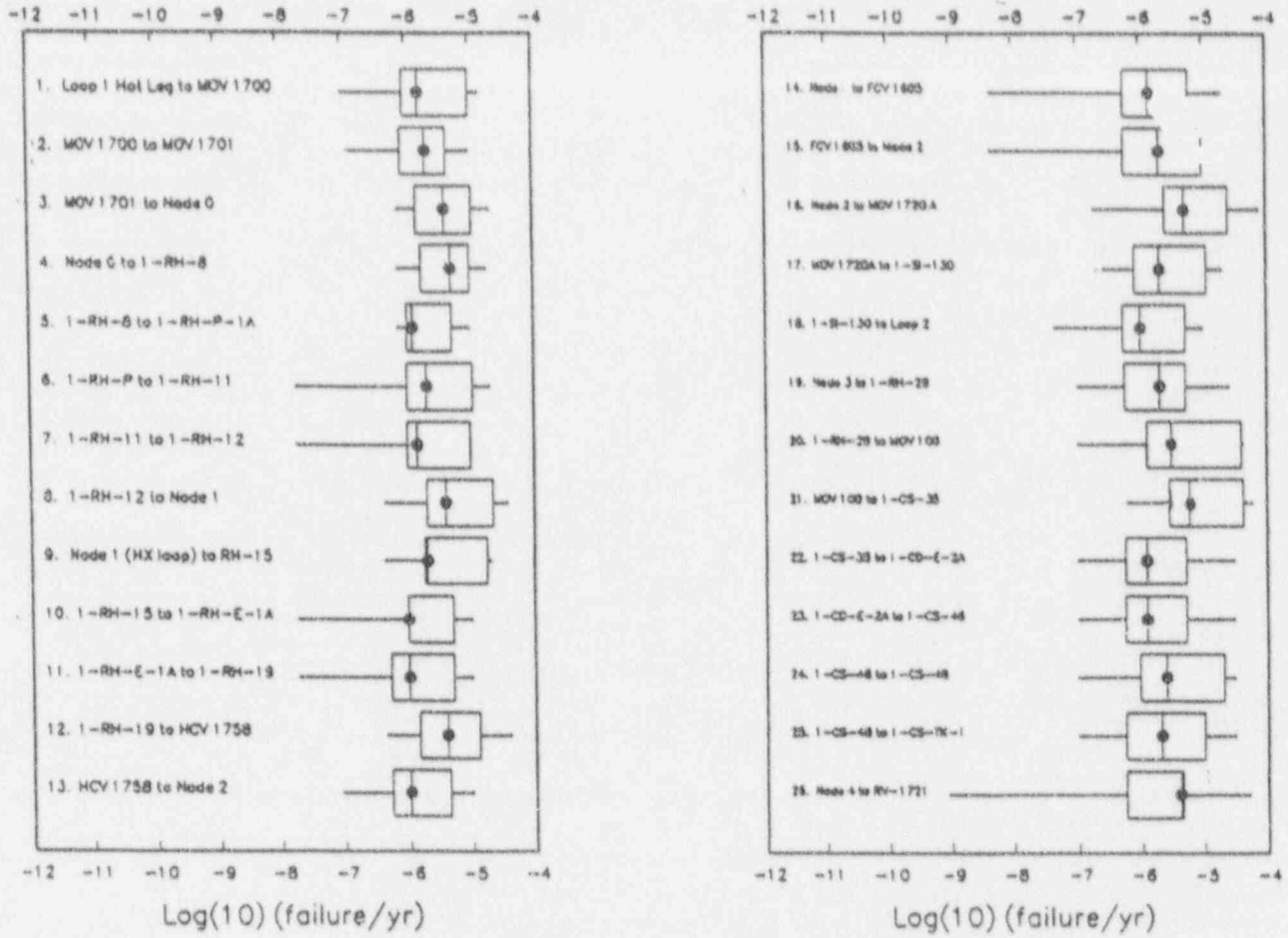


Figure 2. Failure Probability Estimates for the Residual Heat Removal System Components

A boxplot is a popular univariate data display which is used for exploratory data analysis. It aims to summarize a batch of data by displaying several important features such as the central value, spread and the extreme values. The quartiles take on particular importance because they are the basis for the fences in the rule for flagging potential outliers. In the literature a number of definitions of the quartiles exist. In this project the lower quartile Q_1 in terms of the ordered observations $x_{(1)} \leq x_{(2)} \leq \ldots \leq x_{(n)}$ is defined as (Hoaglin and Iglewicz, 1987):

$$Q_1 = (1 - g)\, x_{(j)} + g x_{(j+1)} \qquad (1)$$

where $j+g = n/4 + 5/12$, j is an integer part of $n/4 + 5/12$ and $0 \leq g < 1$. The upper quartile Q_2 is defined using the above equation with $j+g = 3n/4 + 5/12$.

Table 1. Median and Quartile Estimates for the RHR System Components

		Failure Probability		
			Percentile	
	Component	Median	25	75
1	Loop 1 HL to MOV 1700	1.60E-06	9.47E-07	.00E-05
2	MOV 1700 to MOV 1701	2.00E-06	8.91E-07	4.45E-06
3	MOV 1701 to Node 0	4.00E-06	1.48E-06	1.12E-05
4	Node 0 to Valve 1-RH-8	5.00E-06	1.78E-06	1.00E-05
5	Valve 1-RH-8 to Pump 1A	1.20E-06	1.00E-06	5.61E-06
6	Pump 1A to Valve 1-RH-11	2.00E-06	1.00E-06	1.12E-05
7	Valve 1-RH-11 to 1-RH-12	1.40E-06	1.00E-06	9.87E-06
8	Valve 1-RH-12 to Node 1	4.00E-06	2.00E-06	2.29E-05
9	Node 1 to Valve 1-RH-15	2.00E-06	1.88E-06	1.79E-05
10	Valve 1-RH-15 to RHR Hx	1.00E-06	9.93E-07	5.61E-06
11	RHR Hx to Valve 1-RH-19	1.00E-06	6.59E-07	5.61E-06
12	Valve 1-RH-19 to HCV 1758	4.00E-06	1.59E-06	1.41E-05
13	Valve HCV 1758 to Node 2	1.00E-06	6.59E-07	4.45E-06
14	Node 1 to Valve FCV 1605	1.40E-06	6.81E-07	8.30E-06
15	Valve FCV 1605 to Node 2	2.00E-06	6.81E-07	9.87E-06
16	Node 2 to MOV 1720A	5.00E-06	2.83E-06	2.71E-05
17	MOV 1720A to Valve 1-SI-130	2.00E-06	8.75E-07	1.19E-05
18	Valve 1-SI-130 to Loop 2 CL	.00E-06	6.59E-07	5.61E-06
19	Node 3 to Valve 1-RH-29	2.00E-06	6.81E-07	5.61E-06
20	Valve 1-RH-29 to MOV 100	3.00E-06	1.46E-06	4.00E-05
21	MOV 100 to Valve 1-CS-35	6.00E-06	3.12E-06	4.31E-05
22	Valve 1-CS-35 to 1-CD-E2A	1.20E-06	6.81E-07	5.61E-06
23	1-CD-E2A to Valve 1-CS-46	1.20E-06	6.81E-07	5.61E-06
24	Valve 1-CS-46 to 1-CS-48	2.40E-06	1.21E-06	2.03E-05
25	Valve 1-CS-48 to RWST	2.00E-06	6.81E-07	9.87E-06
26	Node 4 to Valve RV-1721	4.00E-06	6.81E-07	4.45E-06

Strictly speaking the adopted definition yields the fourths. The fraction of the data distributed inside of the box includes 50 percent of all observations. The upper and lower fences are usually defined in terms of Q_1 and Q_3 and they lie at

$$Q_1 - k\,(Q_3 - Q_1)$$

and

$$Q_3 + k\,(Q_3 - Q_1)$$

The length of the line (whisker) on each end of the box(es) is determined based on the multiplier k. The value specified here is multiplied by the length of the box to determine the length of the step. The line extends up to the highest value in the data within the step and extends to the lowest value in the data within the step.

In the literature a number of values of k have been recommended for use as a rule of thumb for flagging observations as outliers. Because the sample size is small and because of the high reliability of the experts' judgments, the rate of outliers (i.e., observations with values above the upper fence or below the lower fence) per sample approaches 0. This implies that the probability of a random sample of n observations to contain one or more outside observations is 0. Therefore, the upper fence, in this study, identically equals the maximum observation and the lower fence is the minimum observation (a k multiplier of the value 10 was used).

In summary an enormous amount of technical information was gathered from the elicitation process. Knowledge and understanding of the issues were significantly enhanced by the exchanges of information between experts and observers at the meeting. Information gained from the expert judgment elicitation greatly enhanced the credibility of the Surry-1 plant analyses. The data provided by the expert panel appeared to be reasonable, and generally agreed with and reflected Surry-1 plant operating experience. The estimates will be used in combination with plant specific PRA results in future calculations to develop a complete risk-based picture of the most significant components within the Surry-1 plant.

IMPORTANCE RANKINGS FOR HPI SYSTEM

Calculations during the past year addressed pipe segment inspection priorities for the high pressure injection system (HPI). This system performs an important safety function in providing coolant to the reactor during normal and emergency conditions. The FMEA methodology was used for these calculations (Vo et al. 1989) to determine the importance index, or relative importance, for each pipe segment within the system. This importance index is based on both the expected consequence of failure of the pipe segment and the estimated probability of core damage resulting from the pipe failure (rupture) of the pipe segment. The probability of core damage resulting from pipe ruptures is calculated from:

$$P_{cd} = P_{f_i} * \sum_i [P_{cd}|_{s_i} * P_{s_i}|_{P_f} * R_i] \qquad (2)$$

where P_{cd} = probability of core damage resulting from pipe failure (rupture)

P_{f_i} = rupture probability of the pipe segment i

$P_{cd|s_i}$ = conditional probability of core damage, given a system i failure

$P_{s_i|P_f}$ = conditional probability of system i failure, given a pipe-segment rupture

R_i = probability that the operator fails to recover, given a system i failure

This equation is summed over the system failures by direct effects (loss of system function), and the indirect effects of pipe ruptures on other systems in the zone of interest (e.g., damage to other systems due to pipe whip, jet impingement, flooding, etc.). The results of an expert judgement elicitation were used to assign values for component rupture probabilities.

The first step of the evaluation was to identify the component locations and the number of subcomponents within each pipe segment. The major structural components of interest within the HPI system are pipe segments, including straight lengths of pipe, elbows, elbows, tee fittings, reducers, pump and valve bodies, and all the welds joining the individual components. Additionally, tanks and heat exchangers were included in the evaluation. The FMEAs were initially formulated using plant system drawings and other information for the Surry-1 plant.

The HPI system fault tree obtained from the Surry-1 PRA was used to determine the conditional probability of system failure given a pipe segment rupture ($P_{s|p_s}$), Bertucio et al. 1986 and Bertucio and Julius, 1990. The Birnbaum importance (Vesely et al. 1983) for the HPI system provided the conditional probability of core damage given the system failure ($P_{cd|p}$). The Standard Review Plan 3.6.2 was used to determine the potential effects of component failures on other system components of interest (NRC 1981). To ensure that plant models were as realistic as possible and reflected operational practices, visits were conducted for system walkdowns, and discussions were held with operational and technical staff at Surry-1. By considering the failure location and/or accident scenario, the recovery action was assigned an estimated probability (R_i), based on discussions with the Surry-1 staff and on information obtained from the PRA. The relative importance of each pipe segment was then calculated to rank the various pipe segments of the HPI system.

There are approximately 150 major pipe segments within the HPI system. By assuming that identical pipe segments in identical trains within the same system have the same failure probabilities and consequences, these 150 pipe segments are reduced to approximately 66 segments. For ranking purposes, pipe segments within the same train can be further grouped, based on major discontinuities (e.g., between pumps and major valves). This resulted in 10 major pipe segment groups.

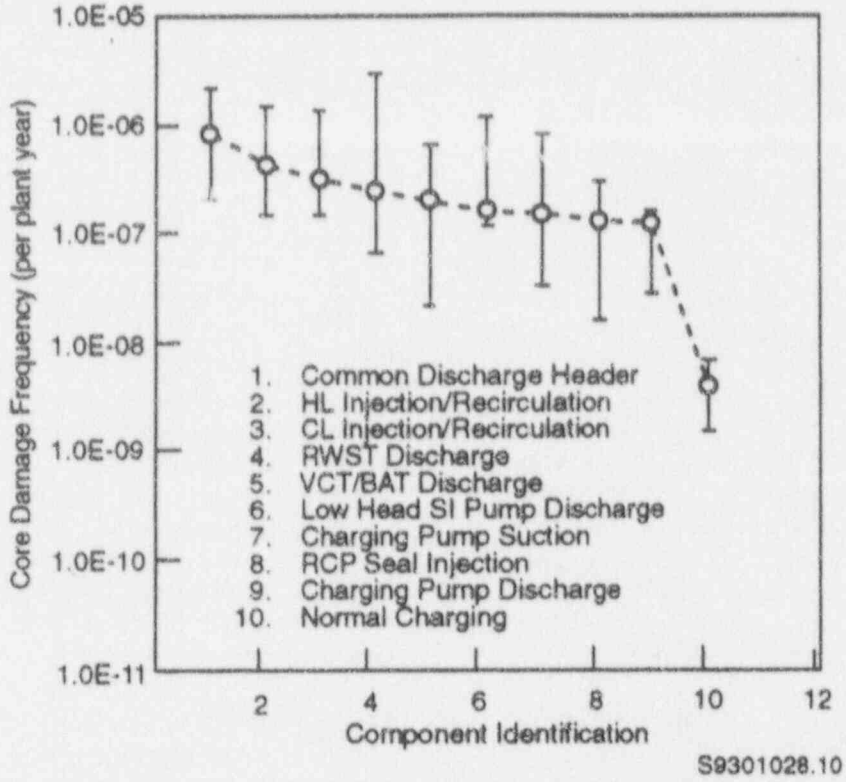


Figure 3. High-Pressure Injection System Component Importance Rankings

Figure 3 shows the risk importances of the 10 major segment groups. Contributions of individual component ruptures to core-damage frequency, based on the median values, ranged widely from approximately 1.0×10^{-6} to 5.0×10^{-9} per plant year. The most risk-important component is the common discharge header, extending from the charging pump discharge lines to the normal charging line. Numerous key pipe segments (e.g., portions of the hot- and cold-leg injection and recirculation line, reactor coolant pump [RCP] seal cooling line) are connected to this common header. Rupture of any pipe segment within the common discharge header results in a complete loss of the high-pressure functions.

Of about equal importance are the components located within the hot-leg (HL) and cold-leg (CL) injection/recirculation lines extending from the containment-isolation valves to the reactor coolant loops. The refueling water storage tank (RWST) discharge line, the volume control tank and boric acid tank (VCT/BAT) discharge line, the low-head safety injection (SI) pump discharge lines, and the RCP seal-injection cooling were also identified as having relatively high risk importance. Although the RWST lines have relatively low pressure, their failure would disable the entire HPI system and thus contribute significantly to core damage. Depending on rupture locations, failure of the VCT/BAT discharge lines could also disable or degrade the required operations of the HPI system. The charging-pump suction and discharge lines were also identified as having moderate-risk importance rankings. Ruptures of these lines at some key locations may disable the entire HPI

system. The normal charging lines were identified as being of relatively lower in risk rankings.

PROBABILISTIC MODELS OF PIPING RELIABILITY

Probabilistic fracture mechanics models of piping reliability that have been developed to predict the probabilities of leaks and breaks in stainless steel reactor piping, and to predict the effects of alternative inservice inspection strategies on reducing these probabilities. The particular calculations described in this paper focus on the low pressure injection system at the Surry-1 plant, and address the propagation of fatigue cracks (both mechanical and thermal fatigue). The approach has been to perform calculations in a structured parametric format, with the parameters selected to cover the ranges of pipe sizes and operating stresses relevant to the LPI system. This permitted estimates to be made of piping reliability at the potential ISI locations without the prohibitive costs of individual calculations for the hundreds of welds and fittings that make up the LPI system. Furthermore, the results of these parametric calculations were intended to be generally applicable to fatigue of stainless piping in other systems with similar sizes of piping. Future work will address fatigue of ferritic steel piping, and stainless steel piping subject to stress corrosion cracking.

Probabilistic fracture mechanics (PFM) combines the methods of reliability theory and fracture mechanics to assess the reliability of components which contain defects. The PFM computer code pc-PRAISE (Piping Reliability Analysis Including Seismic Events) has been used for the evaluations of this paper. The pc-PRAISE code (Harris, Dedhia, and Lu, 1992) was developed for the Lawrence Livermore National Laboratory for probabilistic analysis of piping containing surface cracks. This code calculates the failure probability caused by the growth of pre-existing cracks due to cyclic load, by the initiation and growth of stress corrosion cracks. The model considers two-dimensional cracks with both crack length and depth described by statistical distributions. The initial crack size distributions are modified as a result of preservice or inservice inspections, with a defined probability of detection (POD) as a function of the crack size. Because of the low probability of failure and large number of input parameters, a Monte Carlo simulation with variance reduction by stratified sampling is applied to calculate probabilities.

Flaw Size Distributions

The distribution of initial flaws is perhaps the most uncertain aspect of the fracture mechanics model. After a review of available data, the results presented in this paper were based largely on information on defects in piping welds that was provided to the ASME Research Task Force on Risk-Based Inspection Guidelines by Mr. O.J.V Chapman. These data were developed by an application of an expert system model (Chapman 1993). Inputs to the expert system were provided by PNL to describe the pipe sizes and welding practices relevant to Surry-1 LPI system piping.

Chapman's model makes use of expert knowledge of the types and number of defects found in welds, and considers the likelihood that such defects will go undetected. The model then predicts histograms of the sizes and locations of the defects remaining in the completed weld. Larger flaws are associated with defects in adjacent weld beads that combine to act as one larger defect. Figure 4 shows a histogram of defects as predicted for a circumferential weld in a 6-inch Schedule 120 stainless steel pipe. For calculations with the pc-PRAISE code this histogram was approximated by standard statistical distributions of the exponential and lognormal types.

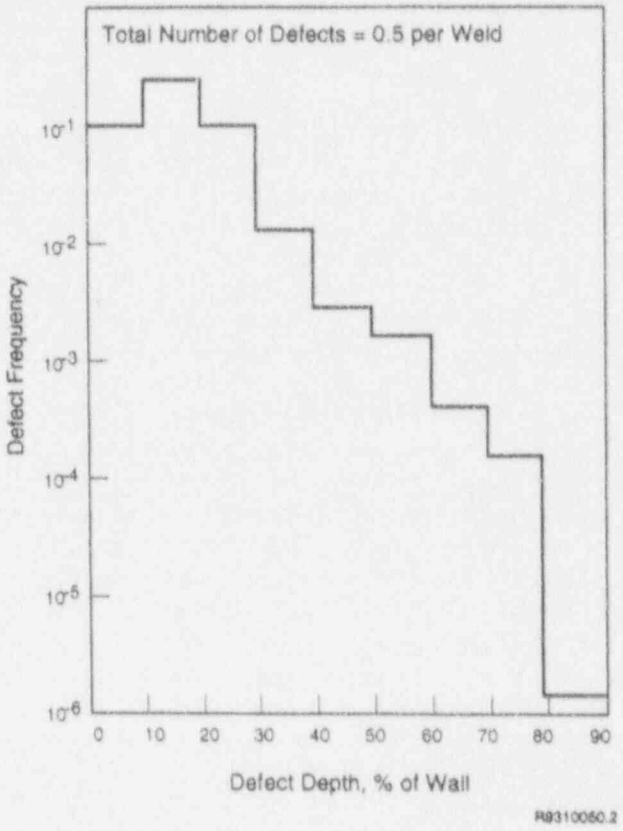


Figure 4. Total Defect Distribution for 6-inch Schedule 120 Pipe as Estimated by Method of Chapman (1992)

In this study all initial flaws were circumferential and were conservatively assumed to be located at the inside pipe surface. The semi-elliptical surface cracks had depths between zero and the full wall thickness. Surface lengths were between a semi-circular shape and the full pipe circumference. Several alternative distributions of crack depth were assumed as follows.

1. Exponential distribution: Phillips et al. (1991) assumed that the crack depth is distributed exponentially with a mean depth of 0.06 inches.

2. Uniform distribution: A uniform distribution of depths ranging from 0.002 to 0.010 inches represented the small fabrication flaws of acceptable size that would be undetectable or that would be detected and sized to be considered acceptable. These flaws also represented cracks that could initiate under service conditions.

3. Lognormal distribution: Chapman's model generated a data base for defect depths. The data when plotted on logarithmic probability paper yielded a lognormal distribution for the defect depth with a median = 0.051 inch and a shape parameter = 0.657.

The distribution of the aspect ratio β was given by

$$f_0(\beta) = \begin{cases} 0 & \beta < 1 \\ \dfrac{C_\beta}{\lambda\beta(2\pi)^{1/2}} e^{-\frac{1}{2\lambda^2}(\ln\beta/\beta_m)^2} & \beta \geq 1 \end{cases} \quad (3)$$

where $\lambda = 0.5382$, $C_\beta = 1.419$, and $\beta_m = 1.136$. The number of cracks in a material volume V was assumed to be Poisson distributed with a mean density $\rho_V^* = 0.38$ defects/in^3 (i.e., 0.5 defect/weld for 6-inch Schedule 120 pipes). Assuming no interactions between adjacent cracks, the probability of failure of a weld given one defect or more is exactly equal to the probability of failure given only one defect. Since the probability of having 4 or more cracks is very small, the total failure probability is P_f = P(failure/one crack) / 2.55, where 2.55 accounts for the number of cracks per weld as estimated by Chapman's model assuming a Poisson distribution for the number of cracks per weld. Results are presented in terms of the conditional failure probability given a flaw rather than the total failure probability.

Crack Growth Rates

Fatigue crack growth rates were calculated for stainless steels using the existing crack growth laws of the pc-PRAISE code. The crack growth rate was given by

$$\frac{da}{dN} = C\left[\frac{\Delta K}{(1-R)^{1/2}}\right]^n \quad (4)$$

where $\Delta K = K_{max} - K_{min}$
$R = K_{min}/K_{max}$
C = lognormally distributed constant
K_{max} = maximum stress intensity factor during transient
K_{min} = minimum stress intensity factor during transient.

This equation approximates the ASME Section XI stainless steel for air environment (R=0). The literature shows crack growth rates in water (for low

rates of cycling) to be up to 10 times greater than the air curve. A zero threshold ΔK for the fatigue crack growth threshold was assumed. The median value of the C and the 90th percentile were 9.14×10^{-12} in/cycle and 3.5×10^{-11} in/cycle, respectively. For piping systems the exponent m used by Harris and Lim (1983) was 4.0.

To address the factors most important to fatigue crack growth (level of cyclic stress and number of cycles), the parameter Q was defined as:

$$Q = \alpha N (\Delta\sigma)^4 \tag{5}$$

where N is number of fatigue cycles and $\Delta\sigma$ is the stress range. The constant α is determined by setting Q=1 for N = number of cycles accumulated at five cycles per year over 40 years, and $\Delta\sigma$ = 15 ksi. Five cycles per year is representative of operating heatup/cooldown cycles and $\Delta\sigma$ = 15 ksi is a typical level of cyclic stress. Table 2 gives values for the fatigue crack growth parameter Q. These values correspond to spectrum of cyclic stress levels and cyclic frequencies of potential interest to reactor piping.

Probability of Detection Curves

Evaluations of alternative inspection strategies required probability of detection (POD) curves for ultrasonic examination of welds in stainless steel piping of the sizes relevant to the Surry-1 LPI system. The approach taken for the calculations was to establish three POD curves that represented widely differing levels of NDE performance. These curves were intended to bound performance expected from inspection teams operating in the field. To establish POD curves, an informal expert judgment elicitation was made using NDE experts at Pacific Northwest Laboratory (PNL).

It was recognized that a population of inspection teams operating under field conditions can exhibit a considerable range of POD performance, even though all such teams have successfully completed a performance demonstration. The basic premise was that all teams had passed the ASME Section XI Appendix VIII performance demonstration. ASME Section XI requires a minimum of 10 flaws and 20 blanks to be examined, and requires a failing grade for more than two false calls or if the team fails to detect 8 of the 10 flaws. The informal expert judgment also considered information and trends observed in the PNL mini round robin on UT inspection of wrought stainless steel piping with wall thicknesses of 0.60 to 1.0 inches (Bates et al. 1987, Heasler et al. 1990).

The NDE experts at PNL were asked to define POD curves by estimating parameters for the following form of a POD function used in the pc-PRAISE code:

$$P_{ND}(A) = \varepsilon + \frac{1}{2}(1-\varepsilon)\,\mathrm{erfc}\left[\nu \ln\left(\frac{A}{A^*}\right)\right] \tag{6}$$

Table 2. Fatigue Crack Growth Parameter (Q) Used for Correlation of Leak Probability

Cyclic Frequncy	Cyclic Stress Range, ksi									
	5	10	15	20	30	40	60	80	100	120
1 cycle per year	2.5E-03	3.9E-02	2.0E-01	6.3E-01	3.2E+00	1.0E+01	5.1E+01	1.6E+02	3.9E+02	8.2E+02
5 cycles per year	1.2E-02	2.0E-01	1.0E+00	3.2E+00	1.6E+01	5.1E+01	2.6E+02	8.1E+02	2.0E+03	4.1E+03
1 cycle per month	3.0E-02	4.7E-01	2.4E+00	7.6E+00	3.8E+01	1.2E+02	6.1E+02	1.9E+03	4.7E+03	9.8E+03
1 cycle per week	1.3E-01	2.0E+00	1.0E+01	3.3E+01	1.7E+02	5.3E+02	2.7E+03	8.4E+03	2.0E+04	4.3E+04
1 cycle per day	9.0E-01	1.4E+01	7.3E+01	2.3E+02	1.2E+03	3.7E+03	1.9E+04	5.9E+04	1.4E+05	3.0E+05
5 cycles per day	4.5E+00	7.2E+01	3.6E+02	1.1E+03	5.8E+03	1.8E+04	9.3E+04	2.9E+05	7.2E+05	1.5E+06
1 cycle per hour	2.2E+01	3.5E+02	1.7E+03	5.5E+03	2.8E+04	8.9E+04	4.5E+05	1.4E+06	3.5E+06	7.2E+06
5 cycles per hour	1.1E+02	1.7E+03	8.8E+03	2.8E+04	1.4E+05	4.4E+05	2.2E+06	7.1E+06	1.7E+07	3.6E+07
1 cycle per minute	1.3E+03	2.1E+04	1.0E+05	3.3E+05	1.7E+06	5.3E+06	2.7E+07	8.5E+07	2.1E+08	4.3E+08
5 cycles per minute	6.5E+03	1.0E+05	5.3E+05	1.7E+06	8.4E+06	2.7E+07	1.3E+08	4.2E+08	1.0E+09	2.1E+09
1 cycle per second	7.8E+04	1.2E+06	6.3E+06	2.0E+07	1.0E+08	3.2E+08	1.6E+09	5.1E+09	1.2E+10	2.6E+10
10 cycles per second	7.8E+05	1.2E+07	6.3E+07	2.0E+08	1.0E+09	3.2E+09	1.6E+10	5.1E+10	1.2E+11	2.6E+11
100 cycles per second	7.8E+06	1.2E+08	6.3E+08	2.0E+09	1.0E+10	3.2E+10	1.6E+11	5.1E+11	1.2E+12	2.6E+12

where P_{ND} is the probability of nondetection, A is the area of the crack, A* is the area of crack for 50% P_{ND}, ϵ is the smallest possible P_{ND} for very large cracks, and ν is the "slope" of P_{ND} curve. Based on measured performance for PNL's mini round robin teams, a range of estimates for A^* (crack area for 50% POD) was provided by the NDE experts. Harris, Dedhia, and Lu (1992) assumed that the "slope" parameter ν is 1.6. Several POD curves from PNL studies were reviewed, and it was determined that a value of $\nu = 1.6$ was consistent with published curves. While the assigned value of the slope parameter ν was held constant, the actual slope of the plotted curves becomes more steep for better POD curves. Thus, the slope is correlated to the detection threshold parameter A^*. The value of ϵ was assigned such that a smaller value of A^* also implies a smaller value of ϵ. Three POD curves were selected:

- Marginal Performance: If a team has a true POD performance that is described by this curve, then this team has a small chance of passing an Appendix VIII performance demonstration.

- Very Good Performance: This curve corresponds to the very best teams. Such teams significantly exceed the level of performance needed to pass an Appendix VIII performance demonstration test.

- Advanced Performance: This curve corresponds to a team that has a level of performance significantly better than expected from any teams that have to date passed an Appendix VIII-type of performance demonstration. Such a team would need to apply advanced technologies and/or improved procedures that could be developed in the future.

Table 3 summarizes the input data for the above three POD curves.

Table 3. Parameters of POD Curves for Three Performance Levels

Inspection Performance	a^*(% a/t)	ϵ	ν
Marginal	40	0.10	1.6
Very Good	15	0.02	1.6
Outstanding	05	.005	1.6

Results of Parametric Calculations

Figures 5 through 7 provide results of parametric calculations, and show the sensitivity of calculated leak and break probabilities to the cyclic stresses and to the assumed flaw depth distributions. In these calculations it was assumed there was exactly one flaw in the weld of interest. All cases were

Table 4. PRAISE Model of LPI System: Baseline Case

Flaw Depth Distribution	Exponential (Mean Depth = .06")
Flaw Aspect Ratio	Lognormal (Parameter = .689)
Stress Through Wall Thickness	Uniform Tension
Cyclic Stress Amplitude	15 Ksi / 5 cycles per year
da/dN Curves	As given in Eq. (4)
Threshold ΔK for da/dN	0.00
Flow Stress	Normal (Mean = 43 ksi, C.O.V.* = .0977)
Pipe Inner Radius	2.75 inches
Pipe Wall Thickness	0.562 inch
Pressure	2.250 ksi
Dead Weight Stress	3 ksi
Thermal Expansion Stress	10 ksi
Inspection	No PSI and No ISI

*C.O.V. = Coefficient of variation = standard deviation / mean

based on the dimensions of a 6-inch Schedule 120 stainless steel pipe and other baseline parameters listed in Table 4.

Two flaw depth distributions were considered, the first being the exponential distribution of Phillips et al. (1991) with a mean flaw depth of 0.06 inch. The second distribution represented much smaller and more likely flaws as described by a uniform distribution of depths ranging from 0.002 to 0.010 inch. All defects were assumed to be surface defects at the inside diameter of the pipe.

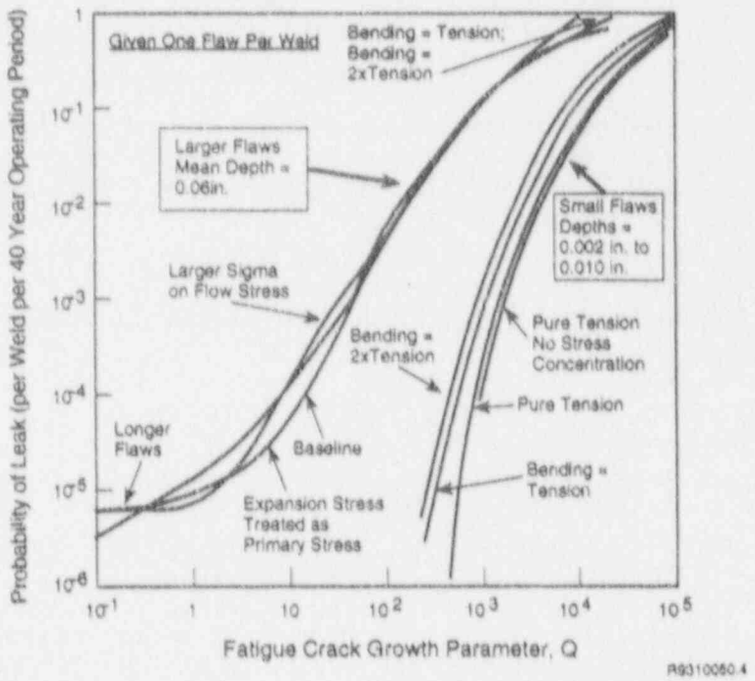


Figure 5. Probability of Leak as Function of Fatigue Crack Growth Parameter Q

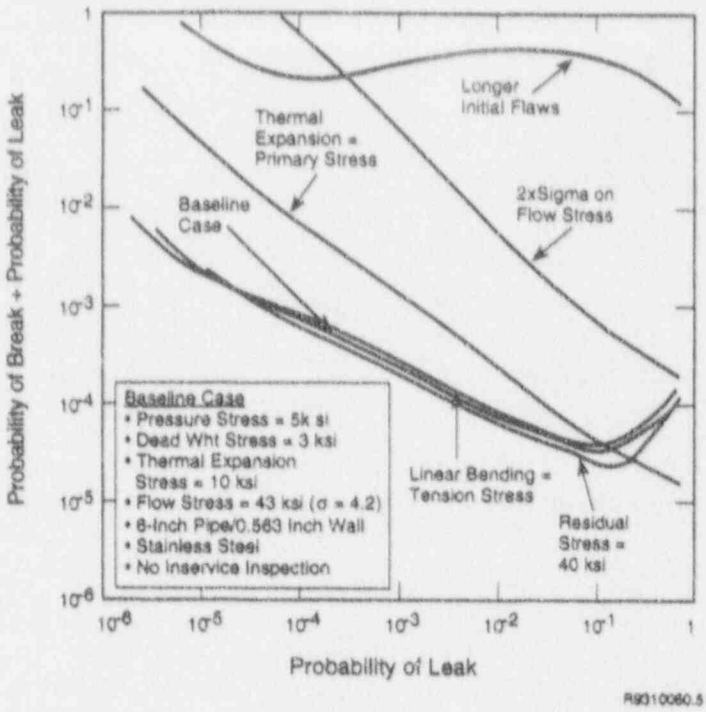


Figure 6. Probability of Break as Function of the Leak Probability

The flaw length was sampled from an aspect ratio distribution, which predicted most flaws to have aspect ratios of 6:1 or less. In sensitivity calculations, the length distribution was modified to simulate much longer flaws whereby there was about an equal probability of given length up to a length equal to the full circumference of the pipe.

In all cases the fatigue crack growth parameter Q was calculated using an average value of cyclic stress (i.e., as averaged through the thickness of the pipe wall). Various cases of nonuniform through-wall stress distributions are indicated in Figures 5 and 6. In each of these cases, the average stress had a superimposed component of cyclic stress which represented bending stresses (tension on the inner surface and compression on the outer surface) and/or local stress concentrations (factor of 3.0 at the ID of the pipe) due to geometric irregularities such as a weld root.

Figure 5 shows that the calculated leak probabilities differ significantly for the two categories of flaws. Note also that the initial flaw length has little effect on leak probabilities, whereas longer flaws markedly increase break probabilities (Figure 6). Both categories of flaw depth distributions result in leak probabilities that approach 100 percent for sufficiently high values of the fatigue crack growth parameter Q (e.g., for $Q = 10^5$). Leak probabilities are relatively insensitive to the different types of superimposed bending and local stress concentration. Therefore, later calculations were focused only on a uniform through-wall distribution of tension stress.

Predicted rupture probabilities are presented in Figure 6 as a ratio of the calculated rupture probability to the corresponding leak probability. Low values of this ratio imply that conditions for leak-before-break are achieved. As indicated, pipe failures are more likely to be in the form of breaks when the corresponding leak probabilities are relatively small. These ruptures correspond to initial flaws that are both very deep and very long. Cases with higher leak probabilities correspond to flaws of much smaller initial depths. It should be noted that the fatigue crack growth process gives more significant increases in flaw depth as opposed to flaw length.

The calculations of critical crack sizes of unstable crack propagation were based on a net section collapse criteria of fracture. Increasing the standard deviation of the flow stress (by a factor of two) in Figure 6 significantly increases the probability of pipe break.

Figure 7 was derived by considering the actual number of flaws that might be present in the weld rather than assuming exactly one flaw as in Figure 5. The estimated probability of having a flaw of the larger size category was 10^{-2} and the corresponding probability for a flaw of the small size category was 1.0. The probability of leak for the combined population of flaws corresponds

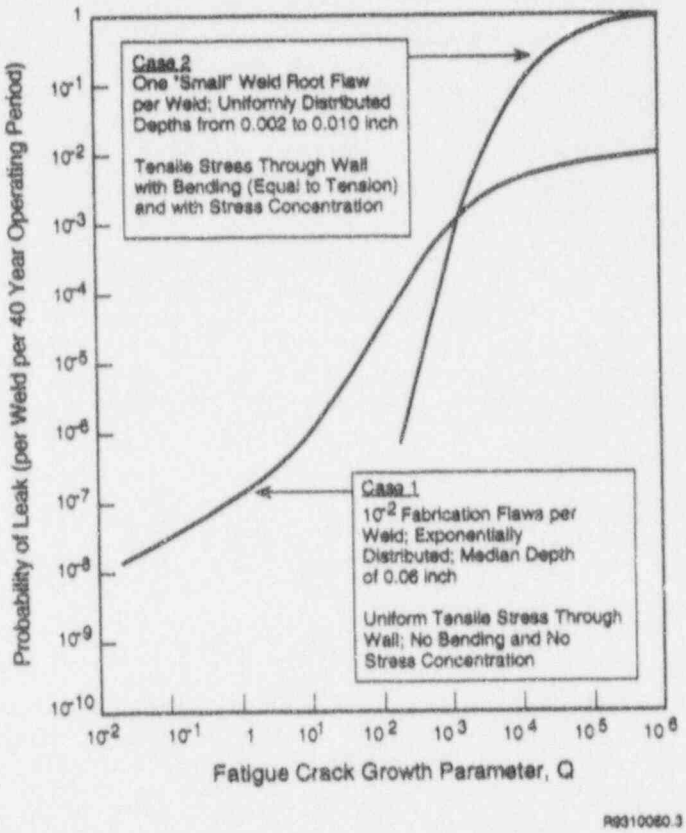


Figure 7. Probability of Leak as a Function of Fatigue Crack Growth Parameter Q for Two Categories of Defect Populations

to the sum of the probabilities for the two individual curves of Figure 7. It should be noted that the flaw frequency and size distribution of Chapman's plot of Figure 4 is approximately the same as the combined population of flaws addressed by Figure 7. Subsequent calculations (reported below) were therefore based on a lognormal fit of Chapman's defect histogram.

Pipe Sizes and Duty Cycles for LPI System

The parametric calculations of leak and rupture probabilities were performed to evaluate the reliability of piping in the Surry-1 LPI system. Table 5 provides information on the pipe sizes and cyclic stress levels for this system, along with values of the fatigue crack growth parameter Q as determined from Table 2.

Table 5. LPI Pipe Sizes and Fatigue Crack Growth Parameter for Pressure Cycles due to Testing

Pipe Size	Cyclic Axial Stress, ksi	Cyclic Frequency, Cycles per Year	Fatigue Crack Growth Parameter, Q
6" Sch. 120 6.625" OD x 0.562" Wall	4.995 ksi Pressure = 2.25 ksi	5	1.3×10^{-2}
6" Sch. 120 6.625" OD x 0.562" Wall	0.435 ksi Pressure = 0.178 ksi	52	7.3×10^{-6}
10" Sch. 40 10.750" OD x 0.365" Wall	1.178 ksi Pressure = 0.178 ksi	52	3.9×10^{-4}
10" Sch. 10 10.750" OD x 0.165" Wall	2.766 ksi Pressure = 0.178 ksi	52	1.2×10^{-2}
10" Sch. 140 10.750" OD x 1.000" Wall	0.348 ksi Pressure = 0.178 ksi	52	3.0×10^{-6}
8" Sch. 40 8.625" OD x 0.322" Wall	1.059 ksi Pressure = 0.178 ksi	52	2.6×10^{-4}

Discussions with staff at the Surry-1 plant and at the Westinghouse Electric Corporation indicated that the operating cycles for the LPI system are relatively benign, particularly since Surry-1 does not utilize LPI piping for

any residual heat removal functions as is the case at many other Westinghouse plants. The maximum thermal expansion bending stress in the system is reported to be about 15 ksi at the design temperature of 300°F. However, the piping will attain such temperatures only during the late stages of a severe loss of coolant accident, when the LPI system is pumping heated water drawn from the sump of the containment building. Therefore, the 15 ksi bending stress level is not relevant to fatigue evaluations of the LPI system.

The Surry-1 staff indicated that the main source of stress cycling are from testing of the LPI pumps, which is currently performed quarterly. During this testing, operation of the plant continues and the LPI pump discharge pressure increases to 178 psi. Pumps are run for 15-20 minutes to stabilize flow, and the system is given a walkdown to look for leakage. Both LPI pumps are run and this gives two pressure cycles for each quarterly system test.

Tests are also performed at each refueling outage (at 2 year intervals). Pressures range from 90 to 178 psi depending on flow conditions. Flow through check valves into RCS piping is achieved in these tests. There is an accumulation of 6 to 8 pressure cycles before testing is completed.

Leak Probabilities for Mechanical and Thermal Fatigue

Leak and rupture probabilities for Surry-1 LPI piping were estimated using the results of the above parametric calculations. The procedure was to first establish values for the fatigue crack growth parameter Q based on the mechanical or thermal fatigue cycles. Using this value of Q, a leak or rupture probability was then estimated from the parametric plots of Figures 5 through 7.

Mechanical fatigue is addressed by Table 5, which lists values of Q for the various piping sizes of the LPI system. These values of Q are all less than 10^{-1} and as such are less than the Q values of the parametric plots. Therefore, the estimated leak and rupture probabilities over the 40 year life of the plant are less than 10^{-5}. These estimates are even lower than the values provided for the LPI piping by the expert judgement elicitation (Vo et al. 1991). Therefore, the pc-PRAISE calculations support the very low estimates of failure probability from the elicitation.

Pipe cracking due to thermal fatigue cracking was identified by the expert judgement elicitation as the most likely rupture scenario for LPI piping. Table 6 addresses such failures which would be associated with back leakage of hot primary system (RCS) water through the check valves into the colder fluid in the standby LPI system. Such leakage has occurred in many systems at operating plants. The estimated thermal stratification stresses would be less than a calculated bounding value of 120 ksi, and most likely would be in the range of 15 to 30 ksi.

Thermal fatigue requires that the thermal stresses be cyclic in nature. An evaluation by Phillips et. al. (1991) was based on plant operating data that showed intermittent leakage that has occurred at frequencies of 1 cycle each 2 to 20 minutes. Detailed characterization of the potential thermal fatigue

Table 6. Fatigue Crack Growth Parameter (Q) and Estimated Leak and Break Probabilities for Thermal Fatigue at the LPI Crack Valve Locations

Cyclic Frequency	Cyclic Stress Range, ksi			
	15	30	60	120
5 cycles per year (plant cycles)	$Q = 1.0$ $P_L = 6.0\times10^{-8}$ $P_B = 6.0\times10^{-10}$	$Q = 1.6\times10^{1}$ $P_L = 1.0\times10^{-6}$ $P_B = 1.0\times10^{-8}$	$Q = 2.6\times10^{2}$ $P_L = 2.0\times10^{-3}$ $P_B = 2.0\times10^{-5}$	$Q = 4.1\times10^{3}$ $P_L = 5.0\times10^{-2}$ $<P_B = 6.0\times10^{-4}>$
1 cycle per week (LPI testing)	$Q = 1.0\times10^{1}$ $P_L = 6.0\times10^{-7}$ $P_B = 6.0\times10^{-9}$	$Q = 1.7\times10^{2}$ $P_L = 5.0\times10^{-4}$ $P_B = 5.0\times10^{-6}$	$Q = 2.7\times10^{3}$ $P_L = 4.0\times10^{-2}$ $<P_B = 4.0\times10^{-4}>$	$Q = 4.2\times10^{4}$ $P_L = 3.0\times10^{-1}$ $P_B = 3.0\times10^{-3}$
1 cycle per day	$Q = 7.3\times10^{1}$ $P_L = 4.0\times10^{-5}$ $P_B = 4.0\times10^{-7}$	$Q = 1.2\times10^{3}$ $P_L = 1.1\times10^{-2}$ $<P_B = 1.1\times10^{-4}>$	$Q = 1.9\times10^{4}$ $P_L = 3.0\times10^{-1}$ $P_B = 3.0\times10^{-3}$	$Q = 3.0\times10^{5}$ $P_L = 6.0\times10^{-1}$ $P_B = 6.0\times10^{-3}$
1 cycle per 20 minutes (INEL estimate)	$Q = 5.2\times10^{3}$ $P_L = 1.0\times10^{-1}$ $<P_B = 1.0\times10^{-3}>$	$Q = 8.4\times10^{4}$ $P_L = 5.0\times10^{-1}$ $P_B = 5.0\times10^{-3}$	$Q = 1.3\times10^{6}$ $P_L = 8.0\times10^{-1}$ $P_B = 8.0\times10^{-3}$	$Q = 2.2\times10^{7}$ $P_L = 8.0\times10^{-1}$ $P_B = 8.0\times10^{-3}$
1 cycle per 2 minutes (INEL estimate)	$Q = 5.2\times10^{4}$ $P_L = 5.0\times10^{-1}$ $P_B = 5.0\times10^{-3}$	$Q = 8.4\times10^{5}$ $P_L = 8.0\times10^{-1}$ $P_B = 8.0\times10^{-3}$	$Q = 1.3\times10^{7}$ $P_L = 8.0\times10^{-1}$ $P_B = 8.0\times10^{-3}$	$Q = 2.1\times10^{8}$ $P_L = 8.0\times10^{-1}$ $P_B = 8.0\times10^{-3}$

Notes:

1) P_L = Probability of Leak Over 40 years
   P_B = Probability of Break Over 40 years

2) It has been assumed that the leak probability is a factor of 100 greater than the break probability.

3) The prior estimates of rupture frequency (per year) for thermal fatigue at the LPI check valve location is 1.0×10^{-5}. This value is based on the expert judgement elicitation from the 1991 workshop and independent discussions with Dr. S. H. Bush. The corresponding probability of failure over 40 years is 4.0×10^{-4}.

stresses for the Surry-1 LPI system was beyond the scope of the current evaluation. Nevertheless, Table 6 indicates that plausible thermal fatigue scenarios are consistent with leak probabilities as great as 10^{-1}.

Study of Inspection Strategies

A pc-PRAISE computer model was applied to simulate inservice inspections of piping with pre-existing defects in circumferential welds. These cracks were assumed to grow by fatigue due to plant transients. The input data for the baseline case is shown in Table 4. Figures 8 and 9 show results of evaluations of inspection strategies.

Inspections were simulated in the Monte Carlo calculation by checking crack sizes at the prescribed times of inspections to determine if potential pipe leaks or breaks were detected for the specified POD curve. Typical results are presented here to illustrate the trends of ongoing calculations. In future work these evaluations will be used to quantify the benefits of alternative inspection strategies, and will generate inputs to the decision risk analyses that will be performed as part of the activities of the ASME Research Task Force on Risk-Based Inspection Guidelines.

It is useful to define a parameter to serve as a measure of effectiveness of an inspection strategy (inspection method and inspection interval). We have selected a commonly used parameter from the structural reliability literature, "Factor of Improvement," which is defined as the ratio of the probability of failure given that no inspection is performed to the probability of failure for a given inspection strategy. A Factor of Improvement of 1.0 corresponds to no inspection or to a totally ineffective inspection strategy. An effective inspection strategy would (for example) have a Factor of Improvement ≥ 10 meaning that the inspections will detect all but 10 percent of the flaws that have a potential to cause a failure.

To investigate the effect of the arrival time of the first inspection on the leak probability, several arrival times were considered. Typical results are shown in Figure 8 for four different arrival times. In each case, an inspection is performed every 10 years thereafter. Until arrival of the first inspection, the calculated probabilities of failure for all POD curves are identical, as they must be. After the first inspection, the probabilities of failure diverge as a consequence of detecting and eliminating defects before they grow to critical values. Figure 8 shows that the cumulative leak probability for an arrival of t=2 years is 3 times lower than that of an otherwise identical strategy but with an arrival time at t=10 years.

The relative benefits of preservice and inservice inspections were compared. As shown in Figure 8, a good preservice inspection is the best strategy in those cases where cyclic loadings are modest (i.e., low Q values). A single preservice inspection can eliminate those larger flaws that can grow significantly over the service life of the plant. However, inservice inspection becomes the preferred strategy for high levels of cyclic stresses (large values of Q). In this case, the associated crack growth rates are sufficient to cause even relatively small fabrication flaws to grow to through-wall

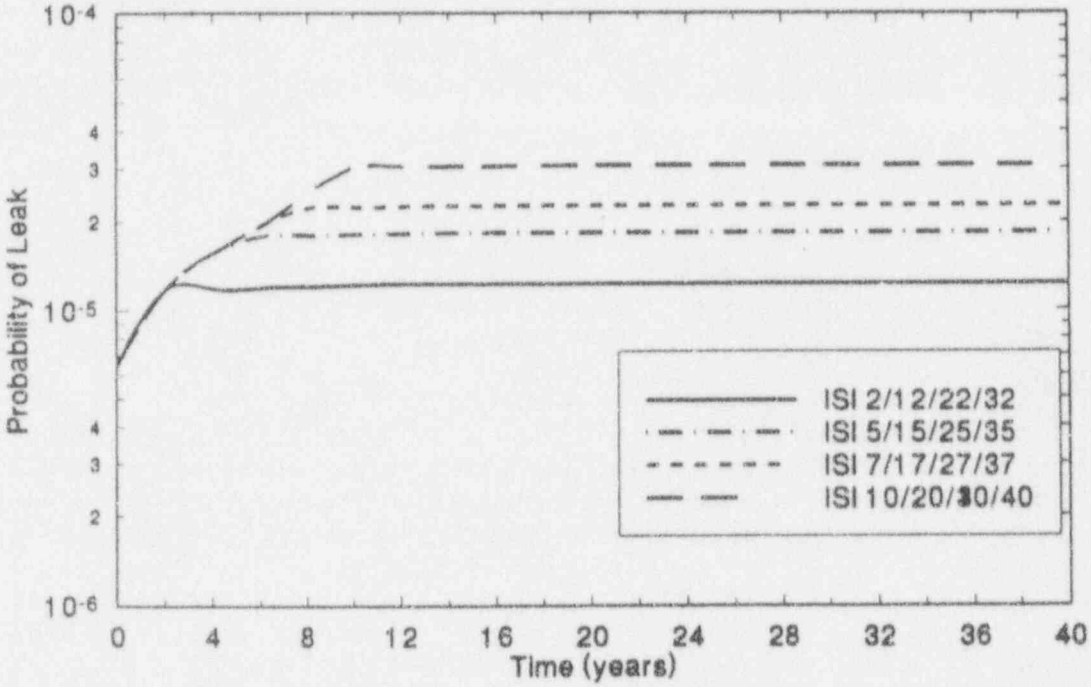


Figure 8. Effect of Arrival Time of Inservice Inspection on the Leak Probability of Failure

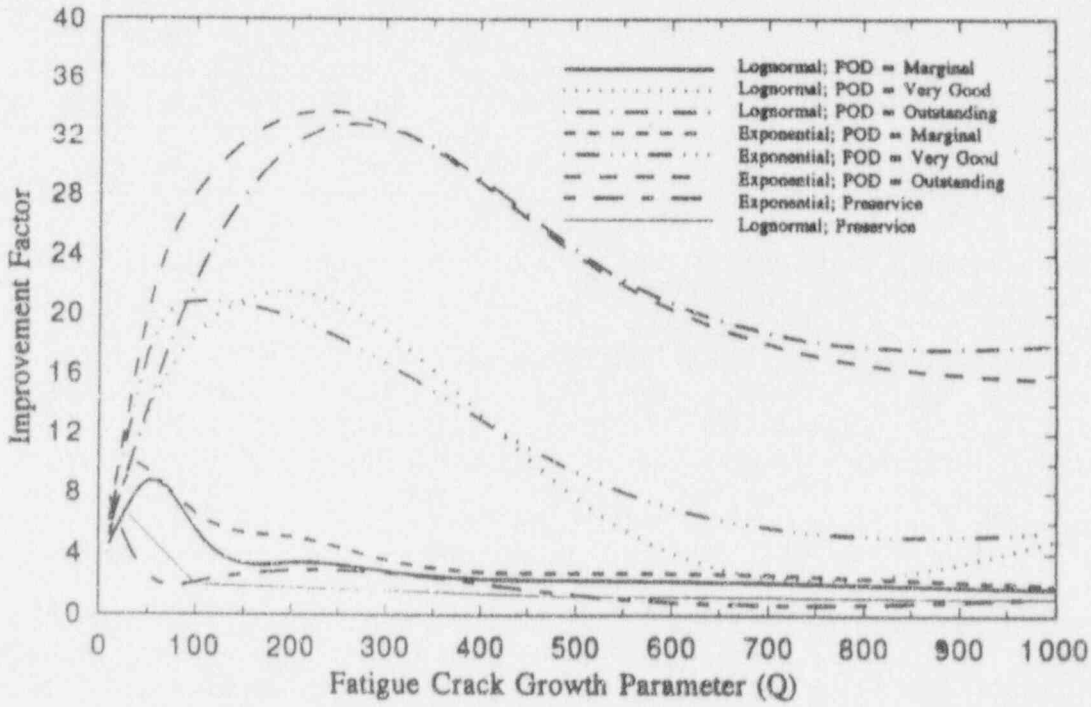


Figure 9. Effect of Initial Crack Distribution on the Improvement Factors

depths. On the other hand, Figure 9 shows that the assumed initial crack depth distribution (lognormal versus exponential) used to fit Chapman's histogram of flaw sizes had very little influence on the value of the improvement factor.

In summary, a piping reliability model for predicting leak and break probabilities of piping due to fatigue has been developed. An initial defect size distribution is combined with a crack growth law in order to estimate the influence of inservice inspection on failure probabilities. The inspection programs have considered different numbers of inspections over the 40-year design life and three different levels of NDE reliability. The time at which the first inspection is performed was found to be a significant factor, which supports a strategy of performing a high quality preservice inspection to ensure detection and repair of fabrication defects. In other cases the most fabrication flaws will be small and therefore undetectable at the time of a preservice inspection. For these cases, an optimum strategy is that of an ongoing program of inservice inspections.

FUTURE WORK

Future activities in the area of risk-based inspection will include:

- Continuing support of the ASME Research Task Force on Risk-Based Inspection Guidelines and of the ASME Section Task Group on Implementation of Risk-Based Inspection.
- Probabilistic fracture mechanics calculations to evaluate the effects of inservice inspection on the reliability of vessel and piping components.
- Continuing with the risk-based ranking of components for the final five systems at the Surry-1 nuclear power station.
- A pilot application of the risk-based methodology to a nuclear power plant of the boiling water reactor type, through cooperative arrangements with the utility owner of the plant.

REFERENCES

ASME. 1992. "Risk-Based Inspection - Development of Guidelines, Volume 2 - Part 1, Light Water Reactor (LWR) Nuclear Power Plant Components." CRTD-Vol. 20-2, prepared by the ASME Research Task Force on Risk-Based Inspection Guidelines for the ASME Center for Research and Technology Development.

Bates, D. J., S. R. Doctor, P. G. Heasler, and E. Burck. 1987. *Stainless Steel Round Robin Test: Centrifugally Cast Stainless Steel Screening Phase.* NUREG/CR-4970, PNL-6266, PISC III Report No. 3. Prepared by Pacific Northwest Laboratory for the U.S. Nuclear Regulatory Commission, Washington, D.C.

Bertucio, R. C., et al. 1986. *Analysis of Core Damage Frequency for Surry Unit One Nuclear Power Station.* NUREG/CR-4550, Sandia National Laboratories, Albuquerque, New Mexico.

Bertucio, R. C. and J. A. Julius. 1990. *Analysis of Core Damage Frequency: Surry Unit 1 Internal Events.* NUREG/CR-4550, prepared by Sandia National Laboratories for the U.S. NRC, Washington, D.C.

Chapman, V. 1993. "Simulation of Defects in Weld Construction." Pressure Vessel and Piping Conference. American Society of Mechanical Engineers, New York.

Harris, D. O. and E. Y. Lim. 1983. *Application of a Probabilistic Fracture Mechanics Model to the Influence of In-Service Inspection on Structure Reliability. Probabilistic Fracture Mechanics and Fatigue Methods: Applications for Structural Design and Maintenance.* ASTM STP 798, J. M. Bloom and J. C. Ekrall, Eds. American Society for Testing and Materials. pp. 19-41.

Harris, D. O., D. D. Dedhia, and S. C. Lu. 1992. *Theoretical and User's Manual for pc-PRAISE, A Probabilistic Fracture Mechanics Computer Code for Pipe Reliability Analysis.* NUREG/CR-5864, UCRL-ID-109798. U.S. Nuclear Regulatory Commission, Washington, D.C.

Heasler, P. G., T. T. Taylor, J. C. Spanner, S. R. Doctor, and J. D. Deffenbaugh. 1990. *Ultrasonic Inspection Reliability for Intergranular Stress Corrosion Cracks, A Round Robin Study of the Effects of Personnel, Procedures, Equipment, and Crack Characteristics.* NUREG/CR-4098. Prepared by Pacific Northwest Laboratory for the U.S. Nuclear Regulatory Commission, Washington, D.C.

Hoaglin, D. C. and B. Iglewicz. 1987. "Fine-Tuning Some Resistant Rules for Outlier Labeling," *Journal of American Statistical Association*, Vol. 82, No. 400, pp. 1147-1149.

Phillips, J. H., W. S. Roesener, H. L. Magleby, W. Reuter, and V. Geidel. 1991. *Development and Demonstration of Methods to Include Aging of Passive Components in PRAs.* NUREG/CR-5730.

U.S. Nuclear Regulatory Commission (NRC). 1981. *Standard Review Plan 3.6.2 Determination of Rupture Locations and Dynamic Effects Associated with the Postulated Rupture of Piping.* NUREG-0800, Rev. 1, Washington, D.C.

U.S. Nuclear Regulatory Commission (NRC). 1993. "Risk-Based Inspection - Development of Guidelines, Volume 2 - Part 1, Light Water Reactor (LWR) Nuclear Power Plant Components." NUREG/GR-0005 prepared by the ASME Research Task Force on Risk-Based Inspection Guidelines for U.S. Nuclear Commission Office of Nuclear Regulatory Research.

Vesely, W. E., T. C. Davis, R. S. Denning, and N. Saltos. 1983. *Measures of Risk Importance and Their Applications.* Battelle Columbus Laboratories, Columbus, Ohio.

Vo, T. V., B. F. Gore, F. A. Simonen, and S. R. Doctor. 1992. "Development of Generic In-Service Inspection for Light Water Reactors," *Fatigue Fracture and Risk - 1992*, PVP-Vol. 241, pp. 109-117, American Society of Mechanical Engineers, New York, New York.

Vo, T. V., B. F. Gore, E. Eshbach, and F. A. Simonen. 1989. "Probabilistic Risk Assessment Based Guidance for Piping In-Service Inspection." *Nuclear Technology* 88(3). American Nuclear Society, La Grange Park, Illinois.

Vo. T. V., P. G. Heasler, S. R. Doctor, F. A. Simonen, and B. F. Gore. 1991. "Estimates of Rupture Probabilities for Nuclear Power Plant Components: Expert Judgement Elicitation." *Nuclear Technology* 96(3). American Nuclear Society, La Grange Park, Illinois.

Vo, T. V., F. A. Simonen, B. F. Gore, and J. V. Livingston. 1993. "Expert Judgement Elicitation on Component Rupture Probabilities for Five PWR Systems." *Reliability and Risk in Pressure Vessels and Piping*, PVP-Vol. 251, pp. 127-140, American Society of Mechanical Engineers, New York, New York.

Detection and Effects of Pump Low-Flow Operation*

D. A. Casada and R. H. Greene

Oak Ridge National Laboratory
Oak Ridge, TN 37831-8038

ABSTRACT

Operating experience and previous studies performed for the Nuclear Plant Aging Research Program have shown that a significant cause of pump problems and failures can result from low-flow operation. Operation at low-flow rates can create unstable flows within the pump impeller and casing. This condition can result in an increased radial and axial thrust on the rotor, which in turn causes higher shaft stresses, increased shaft deflection, and potential bearing and mechanical seal problems.

Two of the more serious results of low-flow pump operation are cavitation and recirculation. Both of these conditions can be characterized by crackling sounds that accompany a substantial increase in vibration and noise level, and a reduction in total head and output capacity. Cavitation is the formation and subsequent collapse of vapor bubbles in any flow that is at an ambient pressure less than the vapor pressure of the liquid medium. It is the collapse of these vapor bubbles against the metal surfaces of the impeller or casing that causes surface pitting, erosion, and deterioration. Pump recirculation, reversal of a portion of the flow back through the impeller, can be potentially more damaging than cavitation. If located at the impeller eye, recirculation damages the inlet areas of the casing. At the impeller tips, recirculation alters the outside diameter of the impeller. If recirculation occurs around impeller shrouds, it damages thrust bearings. Recirculation also erodes impellers, diffusers, and volutes and causes failure of mechanical seals and bearings. This paper reports on a utility pump failure caused by low-flow induced phenomena.

ORNL has continued to investigate the results of low-flow pump operations by evaluating the types of measurements and diagnostic techniques that are currently used by licensees to detect pump degradation. A new, enhanced application of motor current and power data analysis has been developed that uses a signal comparison methodology to produce an instability ratio indicative of normal or unstable flow conditions. Examples of this type of low-flow detection technique are presented in this paper along with a brief discussion of the various types of technologies currently being used by licensees to evaluate pump operation and determine possible degradation.

---

*Research sponsored by the Office of Nuclear Regulatory Research, U.S. Nuclear Regulatory Commission under Interagency Agreement DOE 1886-8082-8B with the U.S. Department of Energy under contract No. DE-AC05-84OR21400 with the Martin Marietta Energy Systems, Inc.

INTRODUCTION

The Nuclear Plant Aging Research (NPAR) Program has sponsored several studies to study the effects of low-flow operations on nuclear plant pumps. The Oak Ridge National Laboratory (ORNL) has just completed the latest NRC-funded study that is documented in the draft report, "Detection of Pump Degradation," NUREG/CR-6089. This research focuses on testing and surveillance methods currently implemented at domestic and overseas nuclear plants to detect pump degradation and assure the operability of safety-related pumps. The primary conclusions of this study reveal that:

1. The routine collection, trending, and analysis of pump vibration spectra is the single most powerful diagnostic tool for the detection of numerous types of pump degradation, such as misalignment, unbalance, looseness, and various bearing anomalies. If vibration spectral analysis was included into required ASME code testing of nuclear plant pumps, it may merit the reduction of the frequency of testing.

2. New advances in thermographic measurement equipment have enabled machinery analysts to detect anomalies not readily identified through other conventional diagnostic techniques.

3. The historical trending of lubricant analysis data can verify normal and abnormal machinery wear and degradation. The recent development of the on-site analysis device could allow maintenance organizations to increase the population of pumps benefiting from lubricant analysis and alleviate administrative burdens associated with off-site transfer and analysis of contaminated samples.

4. Numerous operational problems thought to be caused by pump degradation were found to actually be the result of motor degradation. Recent advances in non-intrusive motor monitoring techniques can be used to detect rotor bar degradation and also provide in-situ information on hydraulically unstable ranges of operation for a pump system.

5. The required monthly-to-quarterly technical specification/ASME testing using minimum flow loops may have created unstable flow configurations that contributed to pump degradation at some nuclear plants. A new analysis technique has been developed using motor current and power data that can assist in revealing a reliable range of pump operation under varying load conditions. The concept of an instability ratio, based on motor power data analysis, is presented to enable the determination of unstable system operational regimes.

This report discusses the possible consequences of low-flow operation and testing of pumps, and how nuclear plants may be able to ascertain if their current testing or operational procedures are inadvertently placing systems in unstable flow regimes that could cause pump degradation.

MINIMUM FLOW TESTING HISTORY

Many of the installed minimum flow lines in nuclear plants were originally intended by manufacturers to be used solely for pump starting and stopping. However, the required ASME code testing as well as the necessity of using specific pumps for plant startup and shutdown support has resulted in a considerable amount of operation at low-flow conditions. Historically, minimum flow capacity for centrifugal pumps was based on ensuring that the temperature rise through the pump would be less than 15°F. The thermodynamic problem that arises when a centrifugal pump is operated at extremely reduced flows is caused by the heating up of the liquid handled. The difference between the brake horsepower (BHP) consumed and the water horsepower developed represents the majority of the power losses in the pump; these power losses are converted to heat and transferred to the liquid passing through the pump. Although temperature rise is important to determining a pump's allowable minimum flow, the flow rate required to achieve hydraulically stable flow conditions may be a more limiting factor, particularly for the high-energy, high-suction specific speed pumps.

Experience has often demonstrated that destructive hydraulic forces, not temperature rise, limit safe minimum flow. Degradation can occur as the result of unstable flow conditions within the pump, which result in substantial radial and axial forces (static as well as dynamic) on both the stationary and rotating parts. Damage can be manifested in a number of ways, including impeller or diffuser breakage, thrust bearing and/or balance device failure due to excessive loading, cavitation damage on suction stage impellers, increased seal leakage or failure, seal injection piping failure, shaft or coupling breakage, and rotating element seizure.[1] In addition to the internal forces generated by unstable flow within the pump itself, interaction between the pump and the system at low-flow conditions can result in substantial surging and vibration that can affect not only the pump, but also other system components and supports.

In a previous research sponsored by the NRC,[2] ORNL and consultant personnel met with representatives of four of the major original equipment manufacturers (OEMs) of pumps who have furnished about 75% of the pumps used in safety-related systems in U.S. nuclear plants. There was consistent agreement among these OEMs that testing pumps under minimum flow conditions was of little value to demonstrating actual hydraulic performance. Two changes they recommended to existing in-service testing practices were:

1. Periodically conduct testing as close as possible to the pump's best efficiency point (BEP) and trend the results to verify that pump performance has not substantially degraded.

2. Minimize or discontinue the practice of routinely testing pumps at minimum flow conditions in order to demonstrate pump operability.

Proposed changes to the ASME O&M Code Subsection ISTB (OM-6) reflect the concerns emanating from minimum flow testing. In the proposed revised standard, testing on minimum flow loops would not be permitted except in rare cases.

LOW-FLOW DEGRADATION CASE HISTORY

In September 1991, Ingersoll-Rand issued a 10 CFR 21 report[3] on broken cast iron diffusers in multistage pumps used in auxiliary feedwater (AFW) applications at an eastern U.S. nuclear plant. Following a reactor trip, low flow to one steam generator was noted. Inspections found that pump diffuser vane pieces had lodged in a venturi, thereby restricting flow.

Subsequent inspections found that cavitation damage to the AFW cast iron diffusers was evident, particularly at the leading edge of the diffuser vanes. Damage was most evident at the first stage diffuser, although deterioration was also seen in other stages. There was also damage found at some areas of diffuser vane to shroud junctions, which was also believed to be the result of low-flow induced cavitation erosion. The utility reported that the pumps had historically been used only for testing and occasionally for hydrotests (and in response to automatic starts following reactor trips and other transients), but were not used in support of normal startup and shutdown activities. This finding prompted the utility to make inspections of all AFW pumps at all its nuclear plants. Additional cavitation-related damage was discovered in other AFW pumps.

Following extensive examination and metallurgical testing of the affected diffuser, Ingersoll-Rand reported that the primary cause of the breakage was cavitation damage at the leading edge of the diffuser vanes which resulted from accumulated operation of the pump at minimum flow. The NRC was notified that this type of degradation could affect AFW pumps at sixteen different nuclear sites.

After finding indications of similar damage in other pumps, Ingersoll-Rand issued the 10 CFR 21 report. It should be noted that in several of the instances in which damage was found, the pumps were "satisfactory," according to technical specifications and ASME Section XI required testing results. This could be anticipated in light of the fact that the pumps are tested at minimum flow conditions using Section XI measurement techniques that cannot detect internal degradation of this nature. Furthermore, utility personnel noted that they had acquired vibration spectral data at both minimum flow and full-flow conditions prior to the failure (as well as measuring hydraulic performance at both conditions), and their analysis of this data did not suggest pump degradation.

The following photographs depict some of the results of the metallurgical analyses. Figure 1 shows the "as received" damaged AFW pump first-stage diffuser vane plate assembly. Figure 2 is a photomicrograph of a section of a different first-stage AFW diffuser plate with two years of service. Shown are a cavitation-related cavity and a microcrack originating from the cavity along a graphite flake. Figure 3 is a photomicrograph of a fatigue crack in the vane transition region of a AFW pump diffuser plate taken from a different plant. The pump was in service for 10 years. Figure 4 is a photomicrograph of a fatigue crack in the vane transition region of an AFW pump diffuser that had been in service for 15 years.

Ingersoll-Rand recommended periodic inspection of the pumps for damage of the diffusers, and replacement of the cast iron parts with stainless steel, if necessary. They further recommended conducting periodic testing at higher flow rates, if possible.

In the aftermath of this 10 CFR 21 report, at least one plant has elected to modify the AFW pumps by changing the impeller/diffuser gap clearances. This type of design change has been successfully employed on a large number of high energy fossil power plant pumps. The potential benefit offered by this change, in lieu of or in addition to the material replacement change, is the fact that the root cause of the diffuser vane damage is being more directly addressed. This action has the benefit of not only mitigating cavitation damage, but also of reducing overall loading on the pump rotating and stationary parts, thereby minimizing other vibration-related problems that have resulted from low-flow operation.

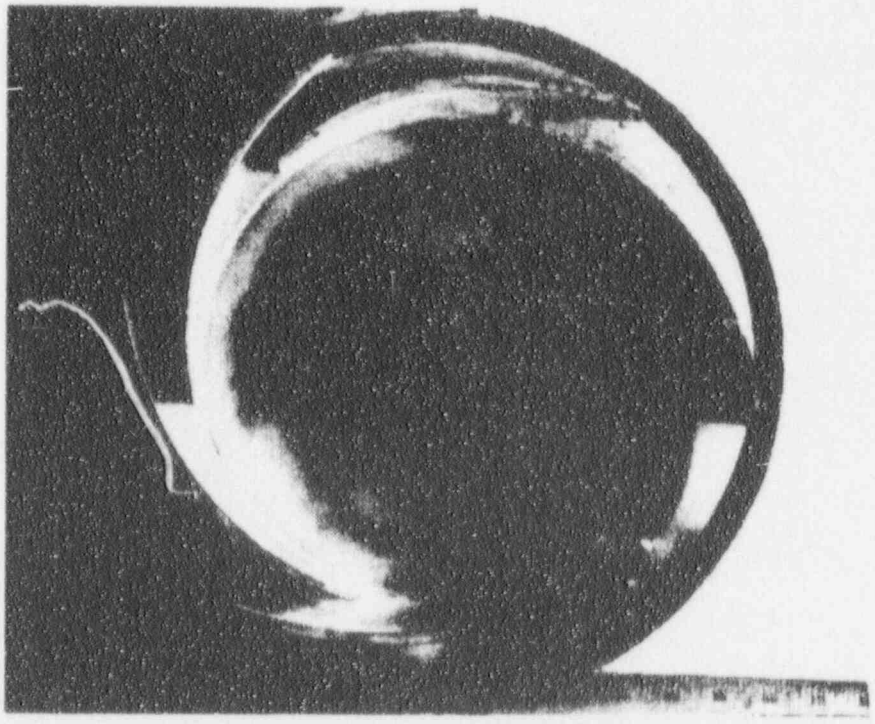


Figure 1. "As received" photograph of damaged AFW pump first-stage diffuser plate assembly.

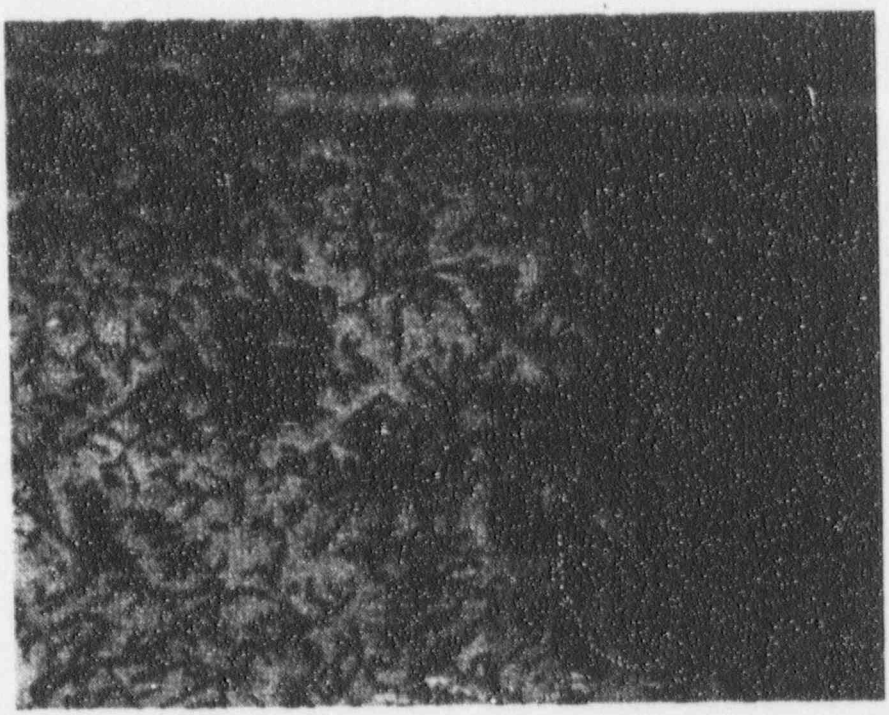


Figure 2. Photomicrograph of a cavitation induced fatigue crack at an AFW pump first-stage diffuser plate after two years of service. Unetched; magnification 50X.

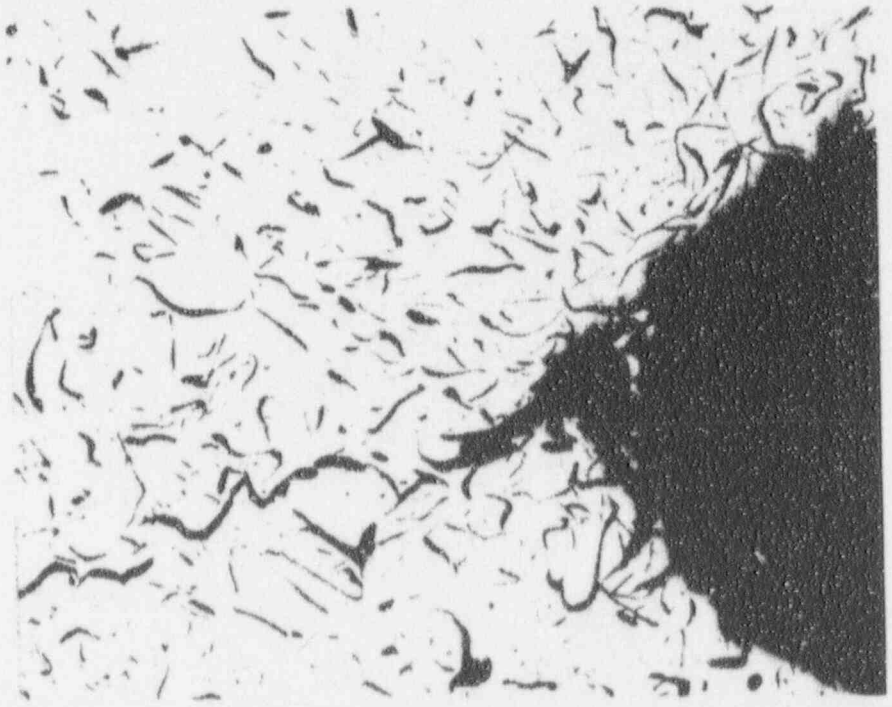


Figure 3. Photomicrograph of a fatigue crack in the vane transition region of an AFW pump diffuser plate from another plant that had been in service 10 years. Unetched; magnification 50X.

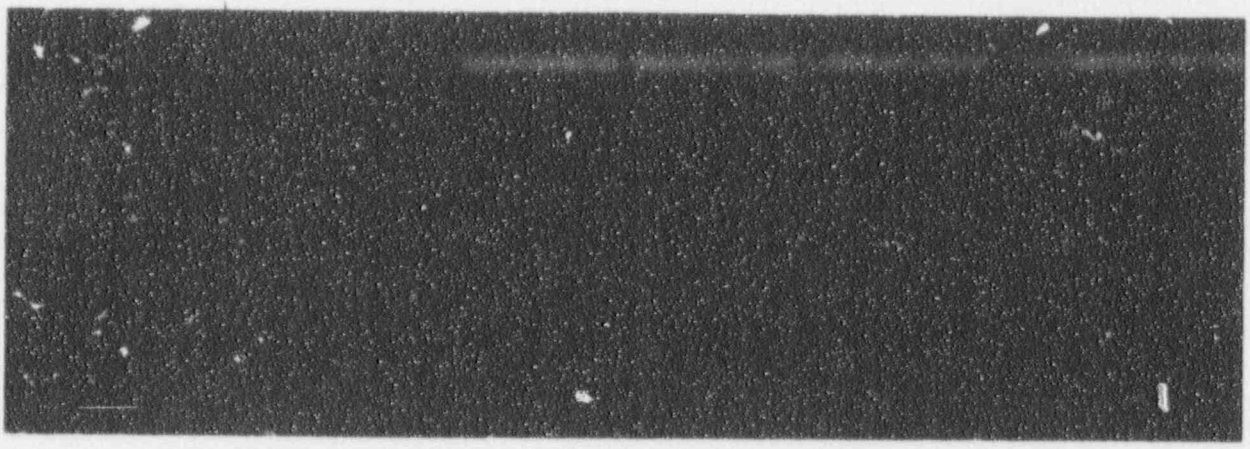


Figure 4. Photomicrograph of a fatigue crack in the vane transition region of an AFW pump that had been in service 15 years. Unetched; magnification 50X.

The phenomenon that caused these cracks is cavitation. Since it is doubtful that the resulting microscopic diffuser vane cracks would have manifested a suspect deviation that could have been discernible through conventional vibration spectral analysis, then to detect this type of degradation, analysis techniques must focus on ascertaining the onset of cavitation itself, or, at least, determining the ranges of unstable flow regimes that can produce such damaging phenomena. The following discussion presents two different methodologies pursued by ORNL researchers to identify unstable hydraulic conditions that could result in pump degradation.

USING POWER DATA ANALYSIS TO DETECT HYDRAULIC INSTABILITY

One objective of the pump degradation research has been to further study conditioned motor current and power data in hopes of developing and/or enhancing analysis techniques that might provide information and insight on abnormal or unstable pump operations. Previous laboratory pump and motor testing have yielded the observation that pump load changes produce power fluctuations in the motor. ORNL researchers have endeavored to determine the relationship between the changing, unstable hydraulic conditions that produce measurable power oscillations in the motor power.

Because motor input power compares almost linearly with motor load (particularly within a small load range), the motor can be used as an effective load transducer. When a pump's hydraulic load changes, the torque load on the motor shaft also changes, and as a result, the motor encounters a variation in its load. These permutations in motor load produce corresponding fluctuations in motor input power that can be quantified.

The instantaneous motor input power for each phase is:

(1) $P_\phi(t) = V_\phi(t) * I_\phi(t)$

where:

$P_\phi(t)$ = Instantaneous power for phase ϕ
$V_\phi(t)$ = Instantaneous voltage for phase ϕ
$I_\phi(t)$ = Instantaneous current for phase ϕ

The total instantaneous input power is the sum of all three phases:

(2) $P_{tot}(t)^* = P_{\phi a}(t) + P_{\phi b}(t) + P_{\phi c}(t)$

The product of the 60-Hz voltage and current ac waveforms results in a 120 Hz waveform with a dc offset; the calculated average of these values for all three phases defines the average input power. By continuously averaging the power over an adequate period (e.g., 1/60th of a second), a running average can be tabulated that realistically characterizes the entire data sample. This running average fluctuates as motor power changes. As noted above, the motor input power varies in response to the input motor load. Therefore, the level of fluctuation of motor input power is a measure of the stability of the motor's load.

Figure 5 shows four illustrations of this concept as it is applied to a pump and motor set operating in a test loop at ORNL. The figures represent normalized power, i.e., the calculated running average power divided by the long-term average for four flow conditions. All of the data was collected at the pump's motor control center by using current and voltage sensors. For simplicity, only one phase of the motor power was analyzed, and power was assumed to be symmetrical for the three phases. At 0 gpm ("shutoff"), relatively significant power fluctuations are experienced by the motor. At the shutoff condition, the pump is essentially stirring the water within or adjacent to the pump casing; there actually is flow within the pump, but no net flow within the system. Clearly, the flow profiles are skewed and unstable at this condition, and produce the observed power fluctuations. At 40 gpm, which is 20% of the manufacturer's best efficiency point (BEP), the normalized fluctuations have reduced slightly; this indicates there are still significant variations in power due to the unstable flow conditions. At 100% of the BEP (200 gpm), the normalized power signal is well defined and has the least overall variation in amplitude; the relatively low level of variation of the power signal indicates that the pump is operating in a relatively stable mode, as expected. At 340 gpm, which is 170% of the BEP, the power fluctuations become erratic again; the flow conditions are becoming increasingly unstable (approaching pump runout), and the instability is reflected in increased normalized motor power variation.

---

* If the three motor phases are symmetrical, total power can be assumed to be three times an individual phase's power without incurring significant error.

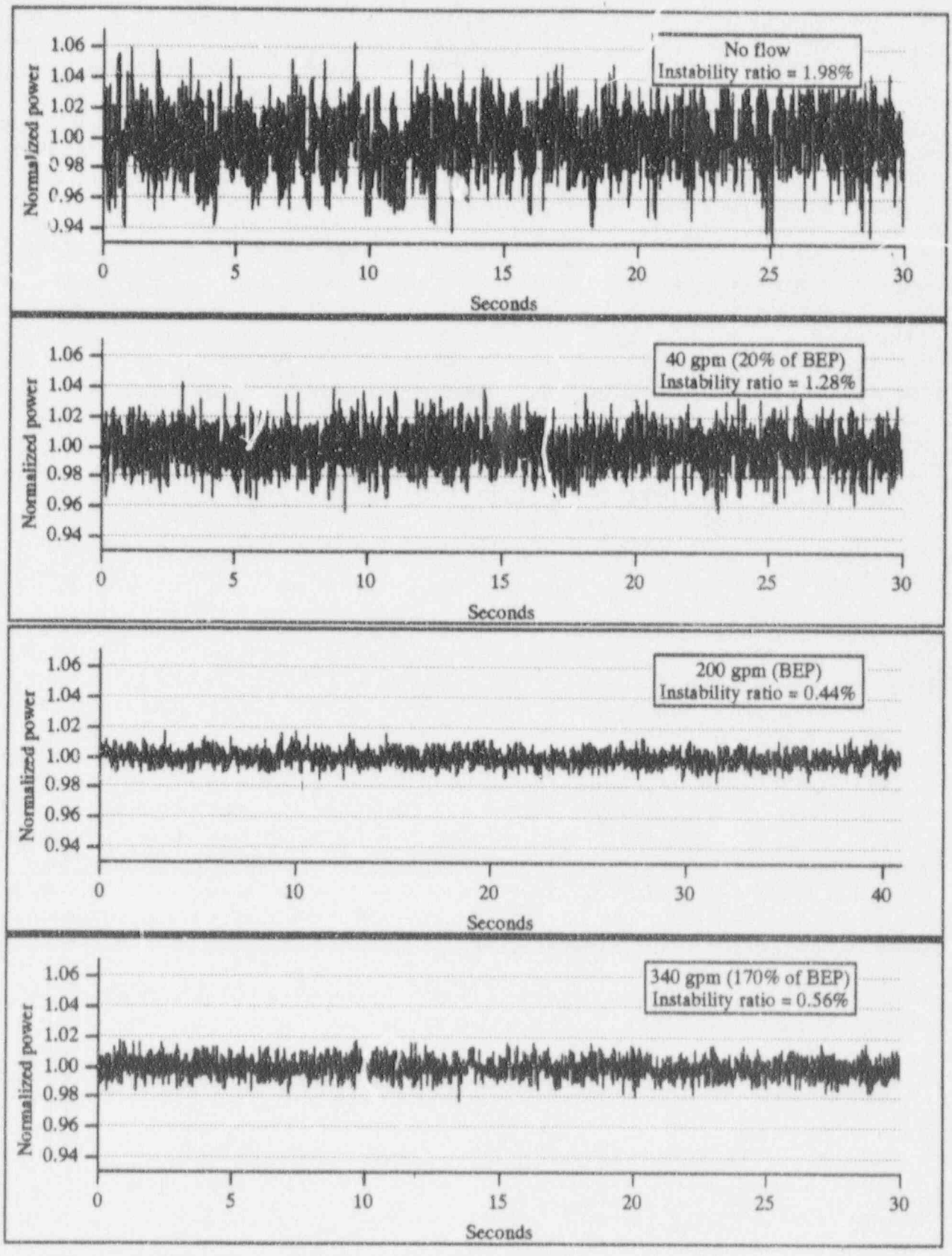


Figure 5. Normalized power at four flow conditions for test loop pump.

A single figure of merit that can be obtained from the normalized power is its standard deviation. ORNL researchers have named the standard deviation of the normalized power the "instability ratio." To further evaluate this quantity, additional testing was conducted on two different hydraulic systems: the test loop pump at ORNL which uses a 7.5 hp motor and a 50 hp motor-driven fire pump owned by a domestic utility. Data was acquired from the motor control center at each pump using current and voltage probes. Measurements were recorded at steady-state conditions that were achieved at various flow rates over the complete range of operation for both pumps.

As displayed in Figure 6, both pumps exhibit their most stable operating characteristics where the instability ratio is at its minimum. For these particular pumps, this occurs over an operating range of approximately 50% to 110% of the BEP. In these flow ranges, the instability ratio is less than 0.5% of the total power being input to the motor; therefore, this interval of flow rates represents the operation range where both pumps are operating stable. Also noteworthy is the shape of the instability ratio curve; it is generally flat from 50% to 110% of the BEP. This indicates a pump system that is relatively unaffected by a wide range of flow rates. For hydraulic applications that must handle a variety of flow rates and loads, the system dynamics would desirably be characterized by a flat instability ratio curve over a wide range of flow rates in order to achieve the maximum efficiency. In addition, the instability ratio may be useful in verifying the design performance specifications (such as BEP) of a particular "as installed" pump.

A final observation of the instability ratio curve is that it provides fairly clear indication of the approach to a range of unstable flow conditions as well as their comparative magnitude. There has been variation in industry practices with regard to acceptable minimum flow rate specifications for pumps. With reference to the data presented in Figure 6, the increasing gradient of the instability ratio curve is more pronounced at flow rates less than 40% of the BEP for the test loop pump and at flow rates less than 20% of BEP for the fire loop pump. This demarcation in slope is where unstable flow conditions are thought to begin for each pump. Extended operation of a pump at these lesser flow rates would possibly cause damage to its components. If these observations made for the tested pumps are found to the applicable to a broader pump population, it may be possible to relatively easily characterize the level of hydraulic load instability for various pumps and flow conditions. Such a characterization could provide a moderately clear indication of the flow regimes to avoid.

To summarize, preliminary studies on pump and motor set power data using instability ratio analysis have yielded the following insights:

1. Enable a measurement of the stable flow range for a specific pump and motor configuration.

2. Establish a stability figure of merit for comparison with other pumps.

3. Provide an alternative indication of relative pump efficiency.

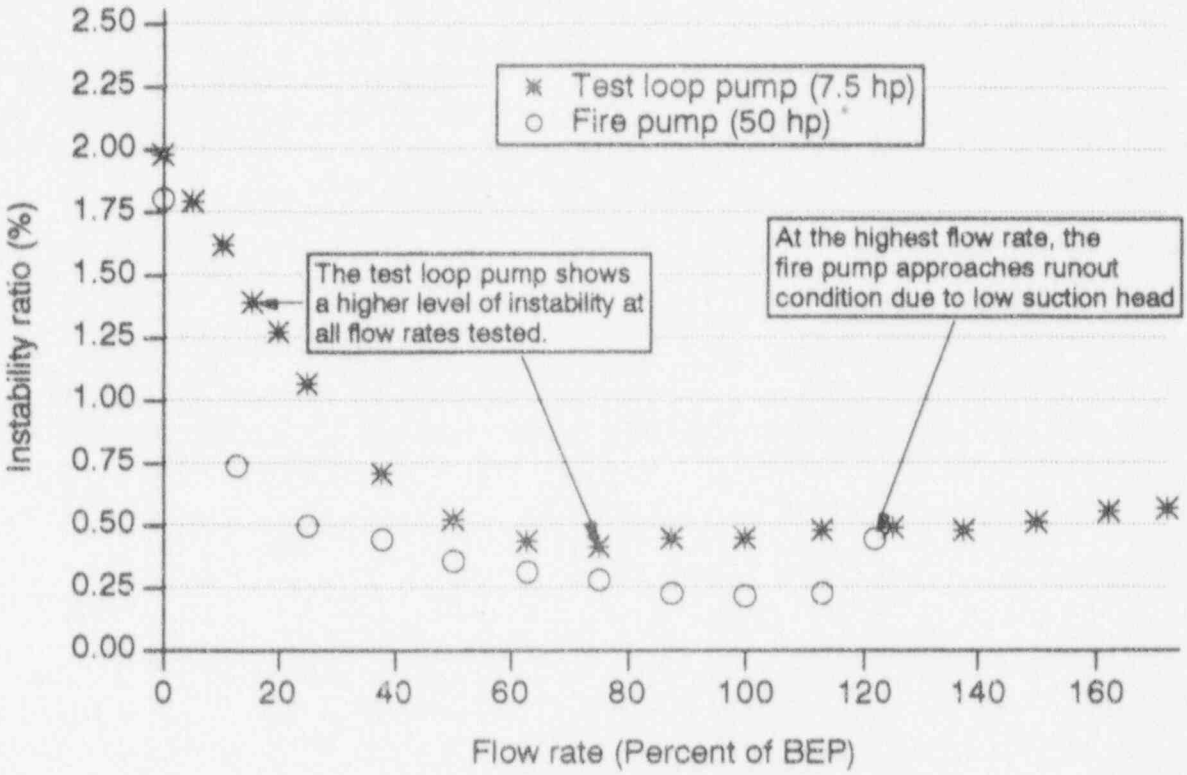


Figure 6. Instability ratio versus flow rate for two pumps

In addition, if preliminary tests are conducted on a particular system prior to planned modifications, such as additional valving or flow restricting devices, it may be possible to quantify the effects of these changes on the overall system's performance. Because the instability ratio is affected by changes in the system load, it is considered to be a sensitive indicator of hydraulic system changes.

CONCLUSIONS

Research into determining the causes and effects of pump degradation has yielded insight regarding damaging phenomena which are characteristic of low-flow pump operation that may be occurring during required ASME code testing on nuclear plant pumps. Testing pumps under low-flow or in minimum flow loops not only fails to provide an assessment of pump operability under off-design emergency conditions but also may prematurely age and degrade pump components. Recently proposed revisions to the ASME pump testing code recognize the deleterious effects of minimum flow testing and have recommended the elimination of this practice. Cavitation, a low-flow phenomenon, has been attributed for the damage of several auxiliary feedwater pumps at two different nuclear sites that have only been operated during required in-service testing via minimum flow loops.

Numerous types of pump degradation can be detected by the routine collection, trending, and analysis of pump vibration spectra. Recent revisions to the ASME testing code allow the use of velocity measurements instead of displacement measurements but make no mention of the benefits of vibration spectral analysis. Because there is a wealth of diagnostic information contained in spectral analysis, its incorporation into the ASME code could merit the reduction of the required testing schedule.

Operational problems once thought to be caused by pump degradation have been determined to be the result of motor degradation. Recent advances in non-intrusive motor monitoring techniques can be used to detect certain types of motor degradation as well as provide in-situ verification of unstable flow regimes. The concept of an instability ratio could provide a measurable assessment of actual minimum flow conditions as well as establish acceptable operational ranges to achieve optimum pump and motor efficiency.

REFERENCES

1. "Aging and Low-Flow Degradation of Auxiliary Feedwater Pumps," M. L. Adams, Proceedings of the Aging Research Information Conference, NUREG/CP-0122, Vol. 1, pp. 365-388, September 1992.

2. "Potential Safety-Related Pump Loss: An Assessment of Industry Data," D. A. Casada, NUREG/CR-5706 (ORNL-6671), NRC Bulletin 88-04, June 1991.

3. Letter to R. Fuhrmeister (USNRC) from G. Young (Ingersoll-Rand), *10 CFR 21 Reportability of A Potential Safety Hazard from Broken Cast Iron Diffuser Pieces in Auxiliary Feed Water Pumps*, September 19, 1991.

Understanding Aging in Containment Cooling Systems*

Robert J. Lofaro
Brookhaven National Laboratory
Department of Advanced Technology
Building 130
Upton, New York 11973

ABSTRACT

A study has been performed to assess the effects of aging in nuclear power plant containment cooling systems. Failure records from national databases, as well as plant specific data were reviewed and analyzed to identify aging characteristics for this system. The predominant aging mechanisms were determined, along with the most frequently failed components and their associated failure modes. This paper discusses the aging mechanisms present in the containment spray system and the containment fan cooler system, which are two systems used to provide the containment cooling function. The failure modes, along with the relative frequency of each is also discussed.

INTRODUCTION

The effects of aging degradation on safety-related systems in nuclear power plants has been a continuing concern of the U.S. Nuclear Regulatory Commission (NRC). If not properly managed, aging degradation can adversely affect equipment performance and, hence, the safe operation of the plant. In light of this, the NRC Nuclear Plant Aging Research (NPAR) program strives to provide a better understanding of how to properly manage aging. The NPAR program is described in detail in NUREG-1144[1].

One of the systems studied under the NPAR program is the containment cooling system[2] since it is one of many plant systems that ensure public safety in the event of an accident. Containment cooling is actually provided by several different plant systems, depending on the type and design of the plant. The containment spray system (PWRs and BWRs) and the containment fan cooler system (PWRs), which are the subject of this paper, were selected for study since they are the primary means of removing containment heat during accident conditions. While the suppression pool cooling system is also an important means of containment heat removal in BWR plants, it is an operating mode of the residual heat removal system, which is the subject of a separate NPAR study[3].

---

*Work performed under the auspices of the U.S. Nuclear Regulatory Commission

SYSTEM DESIGN AND OPERATION

Containment Spray System

A primary function of the containment spray system is to reduce the temperature and pressure inside the containment structure by condensing steam in the event of an unintentional release of coolant from the reactor or its related piping. This adverse environment could occur through either a loss of coolant accident (LOCA) or a main steam line break (MSLB). Reducing the containment pressure and temperature reduces the chances that any radioactive release to the environment would occur by 1) lowering the probability of containment failure due to high pressure and/or temperature, 2) mitigating the pressure differential, and thus the driving force between the containment and the atmosphere. Some designs use chemical sprays to assist in fission product cleanup inside containment.

The containment spray function is a standby function which is only initiated during accident conditions. The system providing this function can have several different designs, depending on the type and design of the plant, and may or may not be a standby system. In pressurized water reactors (PWRs), there is typically an independent containment spray system, with dedicated pumps and associated equipment, which is maintained in standby status during normal plant operation. In boiling water reactors (BWRs), the residual heat removal (RHR) system is typically used to perform the containment spray function. The RHR system also operates in several other modes, and, therefore, is not always in standby status.

The containment spray system functions by pumping water through spray nozzles located inside containment to cool the containment atmosphere. In a typical PWR design, the water is initially taken from the refueling water storage tank (RWST) and then, when the RWST is depleted, from the containment sump. In BWRs the water is taken from the suppression pool, and the RHR pumps are used to provide the spray motive force. The spray system typically includes two or more independent trains, each with dedicated pumps, spray rings, spray nozzles, and numerous valves and piping. Chemicals can also be injected into the spray from a chemical injection system to help remove fission products from the air. A common PWR containment spray system schematic is shown in Figure 1.

Containment Fan Cooler System

Unlike the containment spray system, fan coolers are used in PWRs and BWRs during normal plant operation to maintain a suitable atmosphere for the equipment located within the containment. In most PWR plants, and several BWR plants, fan coolers are also used as an engineered safety feature to reduce the containment temperature and pressure following a LOCA or MSLB. In most BWRs, fan coolers are not used under accident conditions.

The basic design of the fan cooler units includes cooling coils, through which cooling water circulates; a fan, which blows the containment air over the cooling coils; and various duct work and dampers to direct the air flow (Figure 2). Older plants typically use a centrifugal fan design, while newer plants use a vane-axial fan design. Some units also have filters to help remove particula-

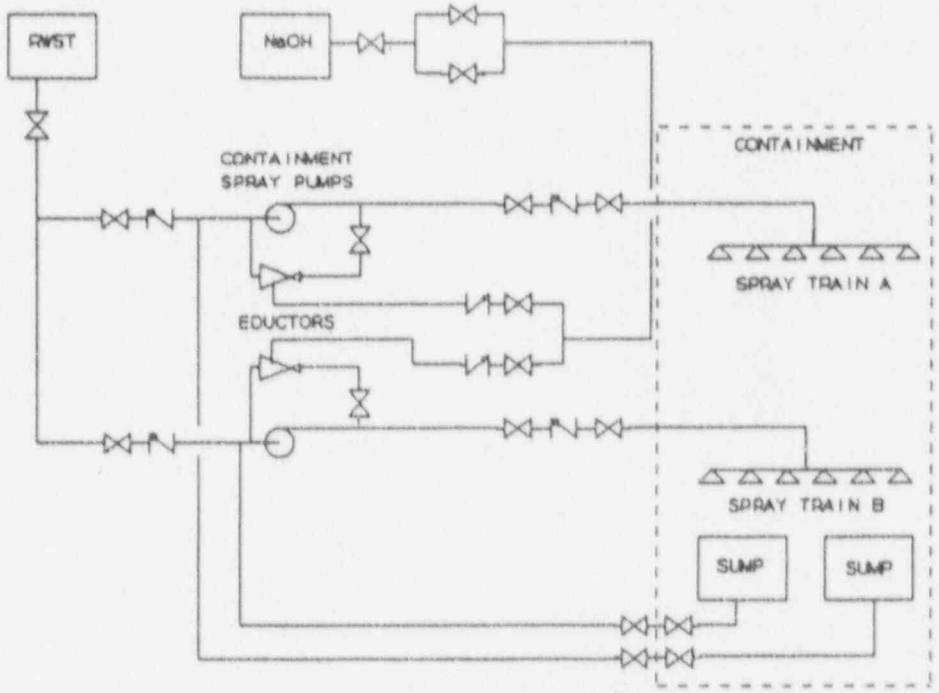


Figure 1 Common PWR containment spray system design

tes from the air. There are typically three or more fan cooler units located within containment, depending on the plant, each with one or two fans per unit.

AGING ASSESSMENT

In order to characterize the effects of aging in containment spray and fan cooler systems, the Nuclear Plant Reliability Data System (NPRDS) was searched to obtain failure information. The search of the NPRDS database covered the five and one-half year period from January 1986 to June 1991, and produced approximately 1400 records related to failures of the containment spray system, and approximately 800 records related to failures of fan cooler systems. These records were reviewed and analyzed to determine system and component aging characteristics. In addition to the NPRDS review, licensee event reports (LERs), and actual plant data were obtained and analyzed to corroborate the NPRDS findings[2]. This paper focuses on the results of the NPRDS analysis.

Aging Characteristics for Containment Spray Systems

As part of the data analysis, a determination was made as to whether each failure was aging related. To make this determination, the NPAR definition of aging, as described in Reference 1, was applied. By this definition, a failure is considered aging related if it is the result of cumulative changes with the passage of time which, if unchecked, may result in loss of function or impairment of safety. Factors causing aging include natural internal chemical or physical processes during operation, external stresses caused by storage or operating

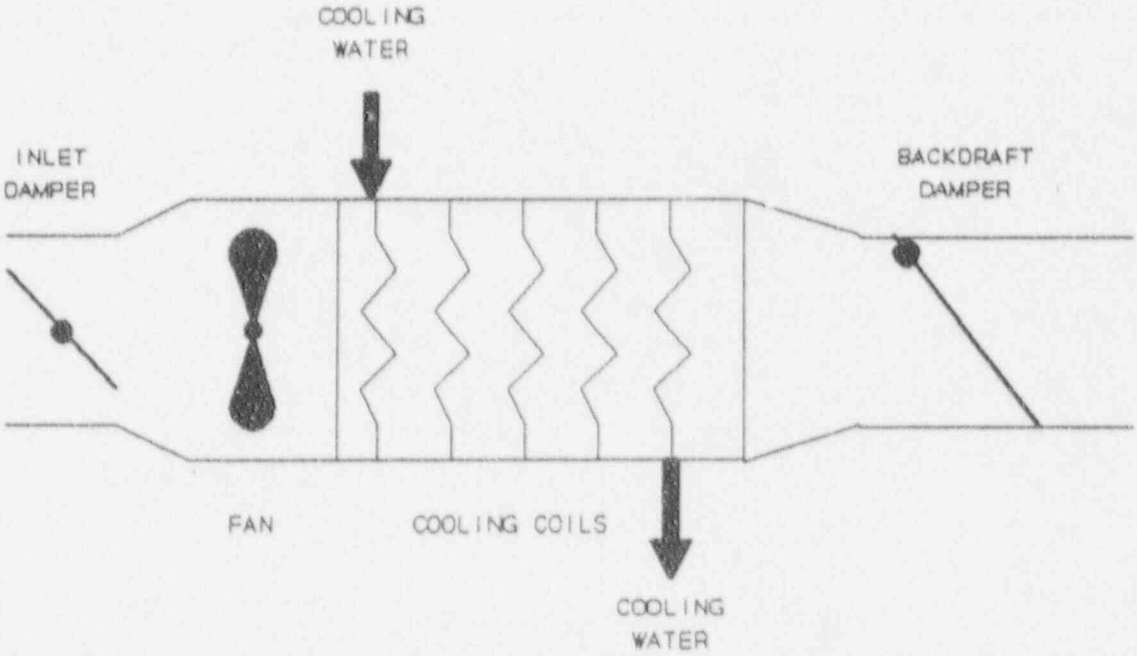
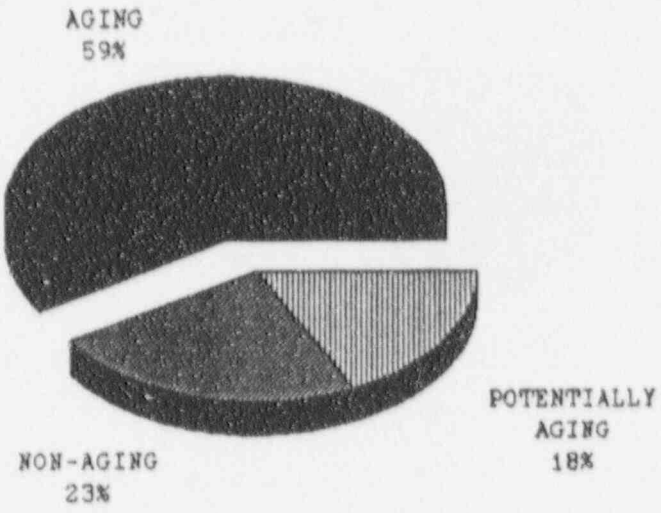


Figure 2 Common fan cooler unit schematic

environment, service wear, and excessive testing. Improper installation, application, or maintenance can also lead to aging degradation under certain conditions, if the degradation occurs over a period of time. In addition, components must have been in service for a minimum of six months to eliminate burn-in or infant mortality type failures.

The NPRDS data indicate that aging degradation plays a major role in containment spray system failures, with 59% of the failures being aging related (Figure 3). Typical examples of aging related failures are leakage of containment spray pump shaft seals due to normal wear, or incorrect instrumentation readings due to calibration drift over a period of time. In some cases, insufficient information was available to determine whether or not the failure was related to aging. These were classified as "potentially aging related" since they could have resulted from aging degradation.

The data were also examined to identify the cause of failure. To do this, the data were sorted into three broad categories; namely, normal service, human error, and other. Normal service includes exposure to any stresses the component would normally be expected to see during the course of daily operation and testing. This could include, for example, wear of pump shaft seals due to pump operation, or corrosion of valve internals due to exposure to poor quality water. Failures caused by normal service are typically aging related. Failures caused by human error include improper or lack of maintenance, installation errors, and operational errors. Failures classified as "other" include those caused by failures of other components or systems, manufacturing and design errors, or failures for which the cause could not be determined.



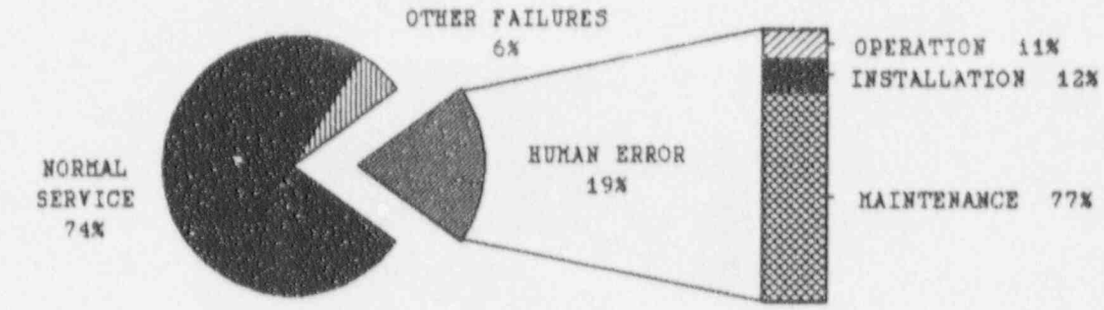
SOURCE: NPRDS 1/86 TO 8/91

Figure 3 Fraction of containment spray system failures related to aging

Normal service is the predominant failure cause for the containment spray system, accounting for 74% of the failures (Figure 4). This supports the high aging fraction discussed previously. Human error contributes to approximately 19% of the failures. The breakdown of human error failures presented in Figure 4 shows that most human errors are in the area of maintenance. This includes maintenance which was not performed properly and subsequently resulted in component failure, or maintenance which was not performed when required. These findings indicate that failures due to human error can be reduced by focusing on improvements in current maintenance practices.

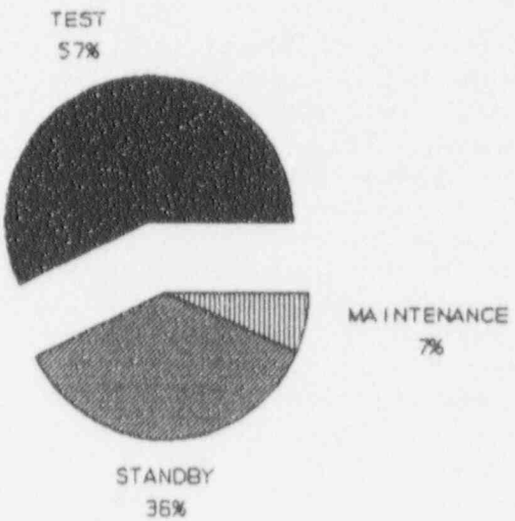
During normal plant operation the containment spray system is maintained in a standby condition, which is the condition this system spends most of its time in. Surveillance tests and maintenance, which are performed periodically, account for the remaining time. Most failures are detected while the system is being tested (Figure 5). Approximately one-third of the failures are detected while the system is in standby, and less than 10% are detected during maintenance. This shows the importance of performing surveillance tests for this predominantly standby system. Failures which may be present while the system is in standby awaiting an accident initiation signal may not be detected until the system is called into operation and it fails to perform its function.

Since the predominant number of failures are detected while the system is being tested, it is expected that the test results are the most common means of detecting failures for the containment spray system. This is confirmed by the data, which show a correspondingly high percentage of failures detected by test results (Figure 6). The data also show that the failure detection method most useful while the system is in standby is inspections, which includes system



SOURCE: NPRDS 1/86 TO 6/91

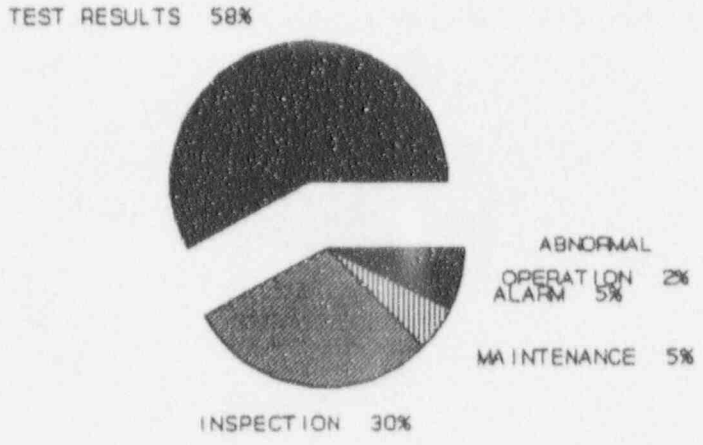
Figure 4 Causes of containment spray system failures



SOURCE: NPRDS 1/86 TO 6/91

Figure 5 Status of the containment spray system during failure detection

walkdowns. This includes planned inspections, which are performed on a routine basis, as well as unplanned inspections or casual observations. Detection methods used to a lesser degree are maintenance actions, alarms, and operational abnormalities.



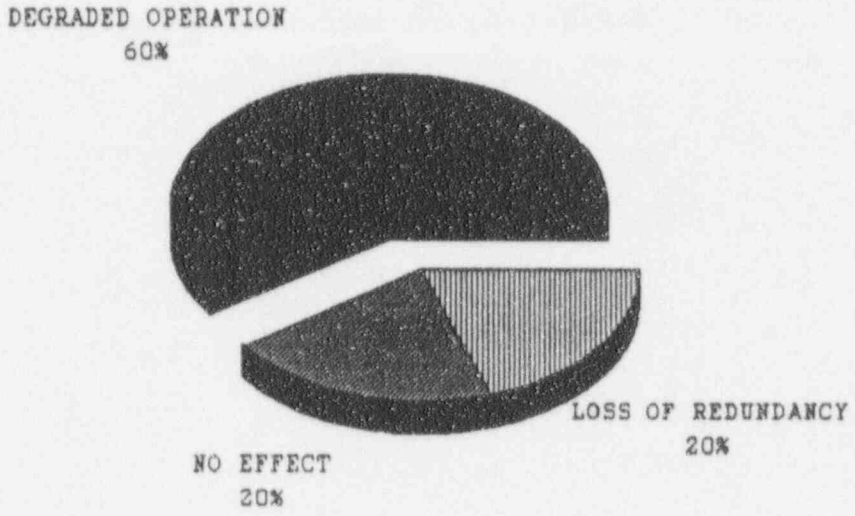
SOURCE: NPRDS 1/86 TO 6/91

Figure 6 Detection methods for containment spray system failures

The predominant number of failures result in degraded operation of the system (Figure 7). The remaining failures either have no effect on system performance (20%), or result in a loss of redundancy (20%). These findings indicate that the failures occurring in the containment spray system typically are not severe enough to cause a complete loss of system function. However, they can affect the availability and reliability of the system. In particular, failures resulting in a loss of redundancy have a direct effect on system reliability since a single failure can result in loss of system function if one of two trains is already failed.

To provide a better understanding of how aging degradation affects the containment spray system components, the data were analyzed to identify the components most frequently failed. No failures were found for those containment spray system components that are predominantly in standby status, such as the containment spray rings and spray nozzles. Of those components that are operated periodically, valves account for the predominant number of failures in the system (Figure 8). These data were not normalized to account for population effects since the intent of this analysis was to identify areas where additional effort is needed to control aging degradation, and not to calculate failure rates. Instrumentation and controls are the second most frequently failed components, followed by circuit breakers, pumps, and heat exchangers, respectively.

The aging mechanisms and failure modes for the most frequently failed components were identified from the data to help form a basis for determining how well current inspection, testing, and maintenance practices are able to detect aging degradation and incipient failures. In general it was found that each



SOURCE: NPRDS 1/86 TO 6/91

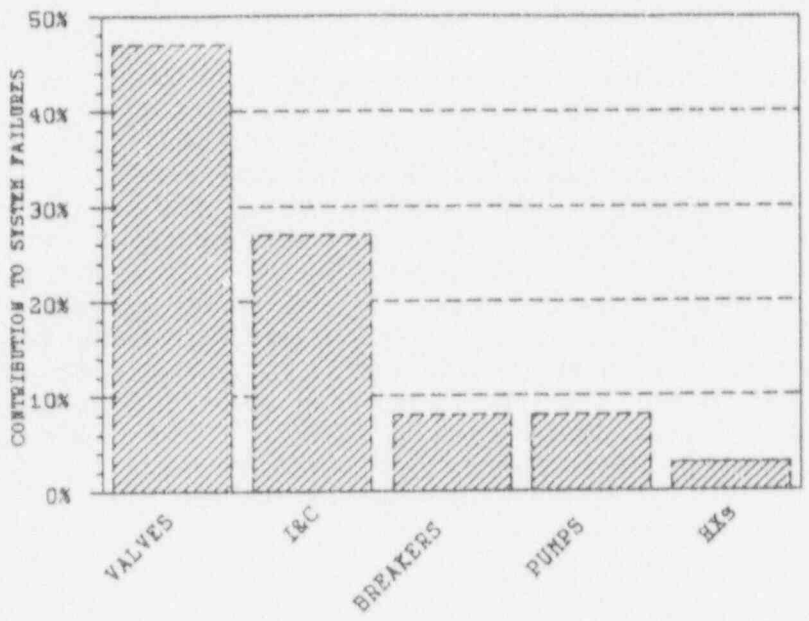
Figure 7 Effect of containment spray system failures

component has one predominant aging mechanism and failure mode. However, there are typically several others which also need to be addressed to completely control the aging process. The results are summarized in Table 1. In addition to identifying the aging mechanisms and failure modes, the percentage of failures attributed to each was also determined based on the data reviewed.

One of the primary reasons for understanding and managing aging of nuclear power plants is that as components and systems age there may be an increase in failure rate due to unchecked aging degradation. If this occurs, one of the results could be a decrease in system availability. To determine the significance of this, a system unavailability analysis was performed to simulate the effects of increasing component failure rates due to uncontrolled aging.

As the basis of this analysis, an existing PRA was obtained which included a common design for a containment spray system, with sodium hydroxide injection. A system fault tree model was developed, and several system components that could be affected by aging were identified. A base case unavailability was calculated using the failure rates specified in the utility PRA or generic databases. A parametric study was then performed in which the failure rate for selected components was artificially increased to simulate the effect of increasing failure rates due to aging. The system unavailability was recalculated for each case.

The containment spray system design analyzed consists of two trains; each with one normally closed motor operated valve, one check valve, and one motor driven pump. Also included in each train are several manual valves, which are used for test and maintenance purposes, along with piping, instrumentation, and spray nozzles. The success criterion for the containment spray system is for one



SOURCE: NPRDS 1/86 TO 6/91

Figure 8 Most frequently failed containment spray system components

out of two trains to inject into the containment when signaled. For this simplified analysis, only the injection phase of containment spray was modeled.

The base case unavailability for the containment spray system was calculated to be 4.1×10^{-3} per demand. The combination of events that lead to a failure (cutsets) show that the failure to correctly reposition manual valves after surveillance testing are the dominant events leading to system unavailability. These human errors appear in 11 of the top 15 cutsets, which, when combined, contribute to 85% of the system unavailability.

For the components that can be affected by aging, failure of the pumps to start, including common cause failures, contributes to 21% of the system unavailability. Motor Operated Valve (MOV) failure to open is the next largest, contributing to 15% of the system unavailability. Maintenance unavailability, test unavailability, and nozzle plugging are much smaller contributors at 1.4%, 1.0%, and 0.4%, respectively.

Using the base case model of the containment spray system, a parametric study was performed to determine the potential influence of aging on the system unavailability. Basic events that could be affected by aging were identified and analyzed. The failure rates for these events were multiplied by factors of two, five, and ten, and a new system unavailability was calculated. The events analyzed for the containment spray system are pump failure to start, MOV failure to open, check valve failure to open, nozzle plugging, and maintenance unavailability. Maintenance unavailability was included since aging degradation can lead to an increase in downtime for maintenance.

An increase in pump and motor operated valve (MOV) failure rate has the greatest influence on total system unavailability (Figure 9). If the pump failure rate were to increase by a factor of five, its contribution to system unavailability becomes approximately equal to that of the human error related to repositioning the manual valves. At ten times the base case failure rate, the total system unavailability increases by a factor of three, and the top cutset contributing to system unavailability involves pump failures instead of the human errors. Similar results are seen for MOVs. These results show that, for the particular design analyzed, if pump or MOV aging degradation is not properly controlled and failure rates increase over time, failures of these components can become an important contributor, and lead to an increase in containment spray system unavailability. If all component failure rates were to increase due to uncontrolled aging, a dramatic increase in system unavailability would result, as shown in Figure 9. It should be noted that for other system configurations, other components may be more important than those chosen for this illustrative example.

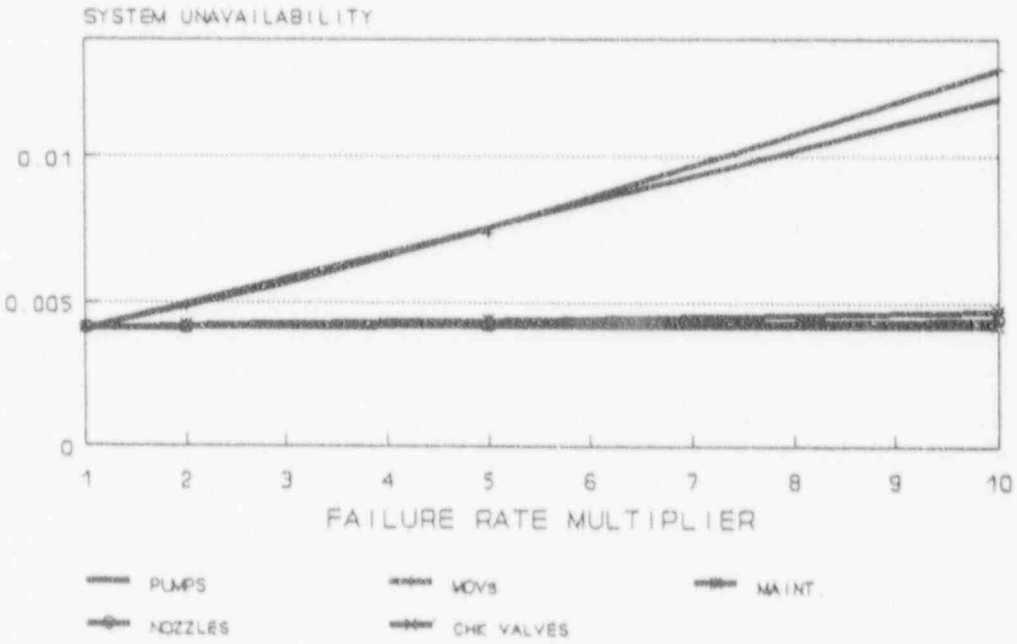
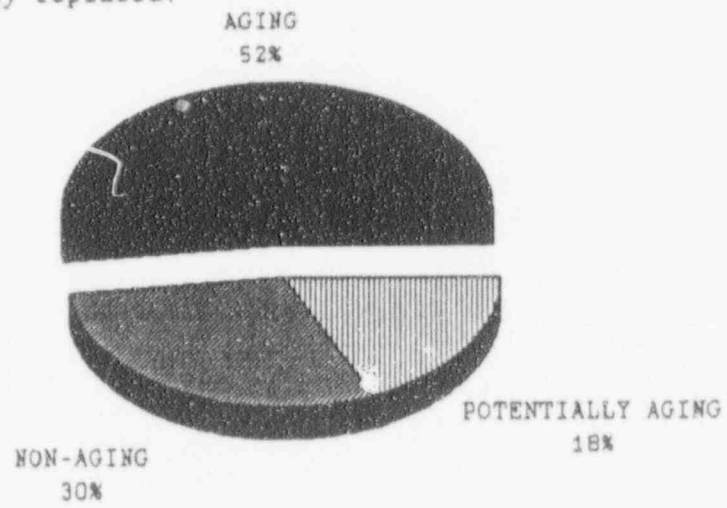


Figure 9 Containment spray system unavailability versus component failure rate

Aging Characteristics for Fan Cooler Systems

As was done for the containment spray system, the fan cooler data were sorted to identify the fraction of failures related to aging. The results indicate that aging degradation is also an important contributor to failures of the fan cooler units with over 50% of the failures related to aging (Figure 10). As an example of an age related fan cooler unit failure, one plant reported that low flow and high temperature alarms were received for one of the containment cooling units. Investigation found that the alarms were caused by reduced air flow through the cooling coils due to the accumulation of dirt and dust on the coils. This was corrected by cleaning the coils. In another case a plant reported that a fan motor circuit breaker failed its functional test. The breaker failed to recharge and could not close. Investigation found that the drive pawl, ratchet assembly, and pawl pivot were worn due to normal wear. These parts were subsequently replaced.

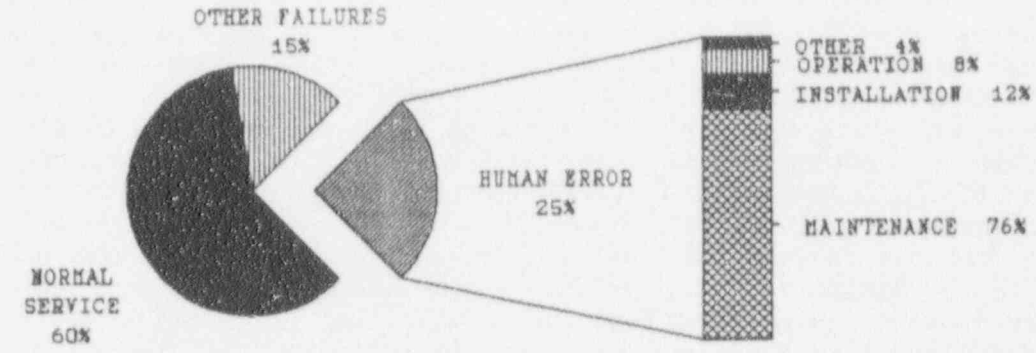


SOURCE: NPRDS 1/86 TO 6/91

Figure 10 Fraction of fan cooler unit failures related to aging

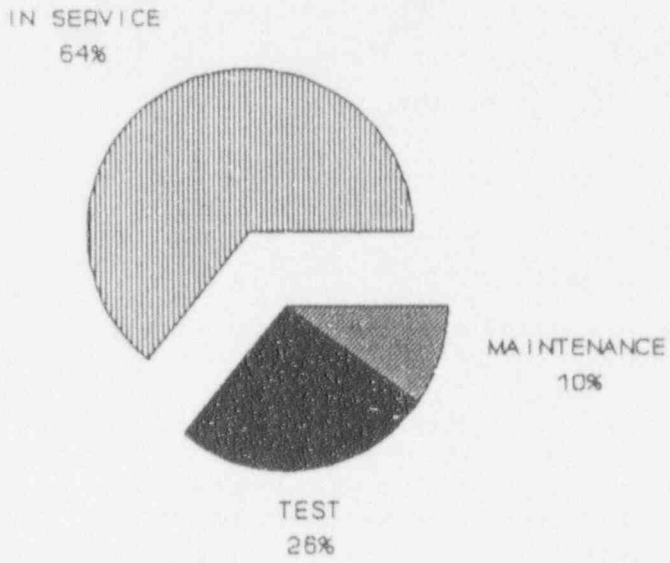
Normal service is the predominant failure cause for fan coolers (Figure 11). This is consistent with the high percentage of failures related to aging, and indicates that aging management is important for fan coolers. Human errors account for approximately 23% of the failures, and these are dominated by maintenance related errors.

Most fan cooler failures are detected while the units are in service (Figure 12). The category "in service" includes the time when the unit is actually operating, as well as the time the unit is in standby waiting for a start signal. The remainder of the failures are detected while the unit is being tested or is out for maintenance.



SOURCE: NPRDS 1/86 TO 6/91

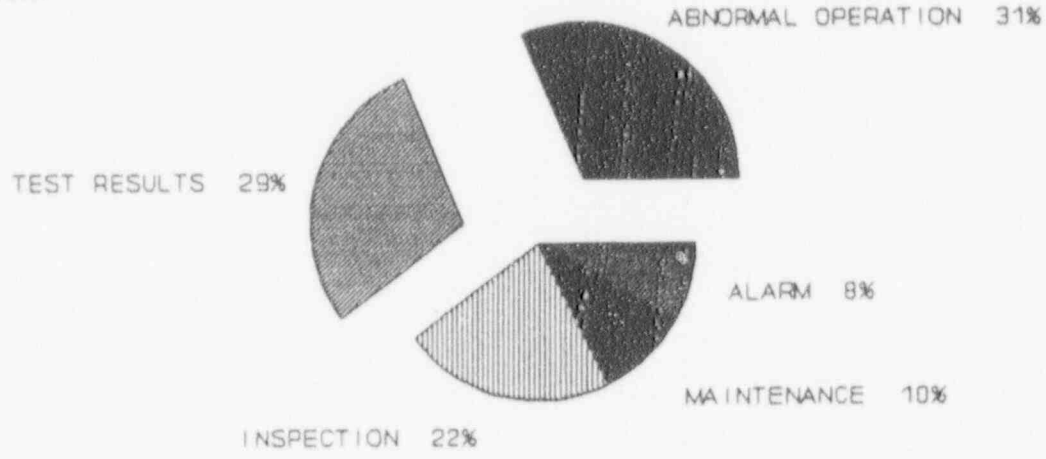
gure 11 Causes of fan cooler failures reported to NPRDS



SOURCE: NPRDS 1/86 TO 6/91

Figure 12 Status of fan coolers during failure detection

While the units are in service, operating abnormalities and inspections are the predominant methods used to detect failures (Figure 13). Alarms account for approximately 8% of the failures detected. While this percentage is low, it does not indicate that the system is inadequately instrumented since many of the more common failures (e.g., leaks) do not require instruments to detect them. The remaining failures are detected by test results and maintenance, which is consistent with the findings for the status of the units during failure detection.

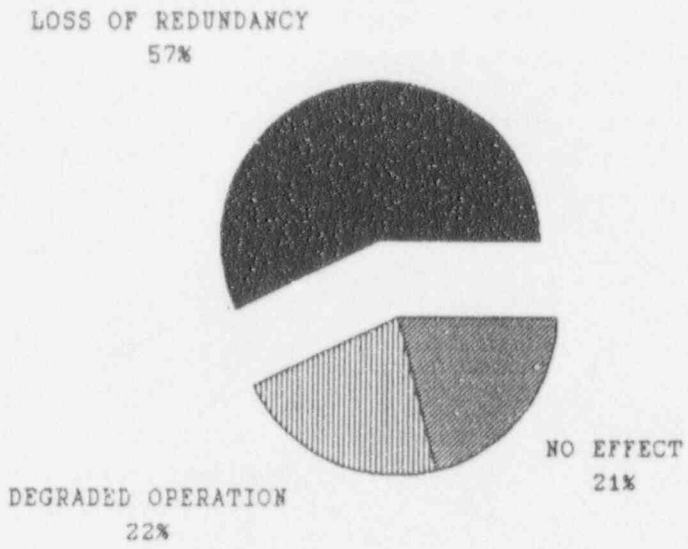


SOURCE: NPRDS 1/86 TO 6/91

Figure 13 Detection methods for fan cooler failures

As previously discussed, plants typically have three or more fan coolers inside containment to provide redundancy. In the event one unit fails, another available unit can be put into operation to make up for the failed unit. In cases such as this, the effect of the failure would be classified as a loss of redundancy. The containment cooling function would not be affected. In other cases, the failure may not be severe enough to cause the fan cooler unit to be inoperable. However, some corrective action is required or the condition would worsen and eventually lead to a complete failure of the unit. In these cases the failure would be classified as degraded component operation.

The data were sorted based on the aforementioned classifications to identify the effect of the failures on fan cooler performance. The predominant failure effect was found to be a loss of redundancy (Figure 14). This indicates that most failures are severe enough to cause a loss of function of the fan cooler unit. From this finding the importance of redundancy becomes apparent. The remainder of the failures are equally divided between causing degraded component operation and having no effect on fan cooler performance.



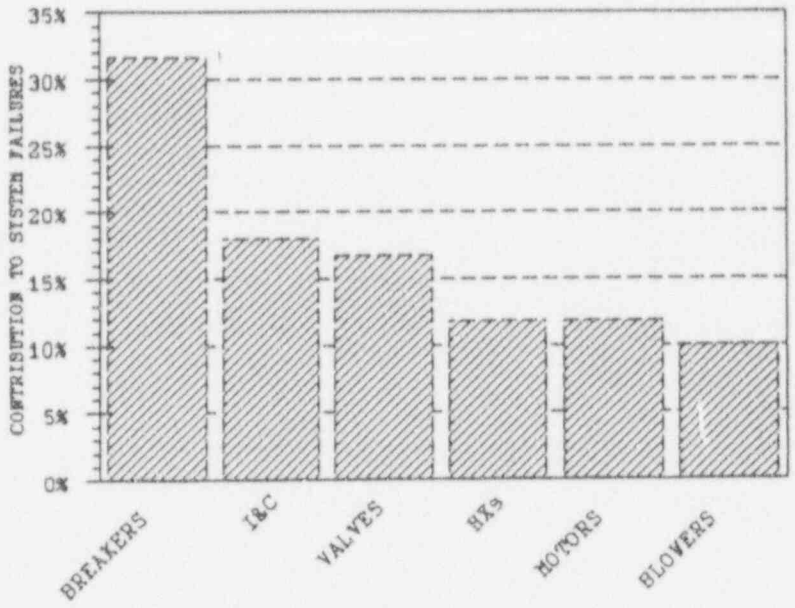
SOURCE: NPRDS 1/86 TO 6/91

Figure 14 Effect of fan cooler failures reported to NPRDS

There are a number of different components which must function properly in order for a fan cooler unit to operate. Each component can be affected by aging to a different degree. Circuit breakers supplying power to the fan cooler units are the most frequently failed component, accounting for approximately one-third of all fan cooler failures (Figure 15). Typical circuit breaker problems include blown fuses, worn trip units, burned contacts, worn springs, defective overload relays, and trip settings out of calibration. In addition to circuit breakers, other commonly failed components are instrumentation and controls, valves, heat exchangers (i.e., cooling coils), fan motors, and blowers. The aging mechanisms and failure modes for the fan cooler system components were identified, and the results are summarized in Table 2.

An unavailability analysis was also performed for a typical fan cooler system. To perform this analysis, fault trees were developed that modeled the individual fan cooler subcomponents that could be subject to aging degradation. The subcomponents modeled are the fan motors, cooling coils, circuit breakers, and dampers. As for the containment spray system, maintenance unavailability was also included in the model.

The plant design chosen as the basis for this analysis is a PWR with five fan cooler units inside containment. The units are normally operating, as required, to maintain the containment temperature within specified limits. On an accident signal, the operating fan coolers switch to a slower speed and the standby units start. Three units are sufficient to maintain the containment pressure within design limits for the design basis accident.



SOURCE: NPRDS 1/86 TO 6/91

Figure 15 Most frequently failed fan cooler components reported to NPRDS

The base case containment fan cooler system unavailability was calculated to be 5.3×10^{-5} per demand. This is based on a success criteria of three of five fan cooler units operating, thus the system fails when three fan cooler units fail. As a result, most cutsets have three elements. Unlike the containment spray system, there are no dominant failure contributors. The top cutset is the common mode failure of the fan motors, which itself contributes 11% to the system unavailability. The remaining 807 cutsets generated from the analysis contribute less than 1% each.

The unavailability analysis of one common PWR fan cooler system design showed no dominant, single contributor to system unavailability. The largest single contributor was a common mode failure of the fan motors. Based on a cumulative contribution from all cutsets in which it appears, the unavailability analysis results show maintenance unavailability to be the leading contributor to system unavailability at 79%. This is followed by dampers failing to open, which contributes 65%, circuit breaker malfunction, which contributes 50%, and the common cause failure of the fan motors, which contributes 11%. Cooling coil failures do not significantly contribute to system unavailability.

A parametric study similar to that done for the containment spray system was performed for the fan cooler system. For each event analyzed, the base case failure rate was multiplied by factors of two, five, and ten to simulate the effects of aging degradation where no provisions are made to properly manage it.

For the system design modeled, an increase in fan damper failure rate due to uncontrolled aging would have the greatest influence on system unavailability (Figure 16). When the failure rate is doubled, the system unavailability increases by a factor of approximately two. For a ten fold increase in failure rate, system unavailability increases by a factor of approximately 66. The exponential increase in unavailability is due to the redundancy of the components in the system design. When circuit breaker failure rate increases by a factor of 10, system unavailability increases by a factor of approximately 13. These results indicate that, for this particular design, aging of dampers and circuit breakers should be properly controlled since an increase in failure rate could result in a significant increase in system unavailability.

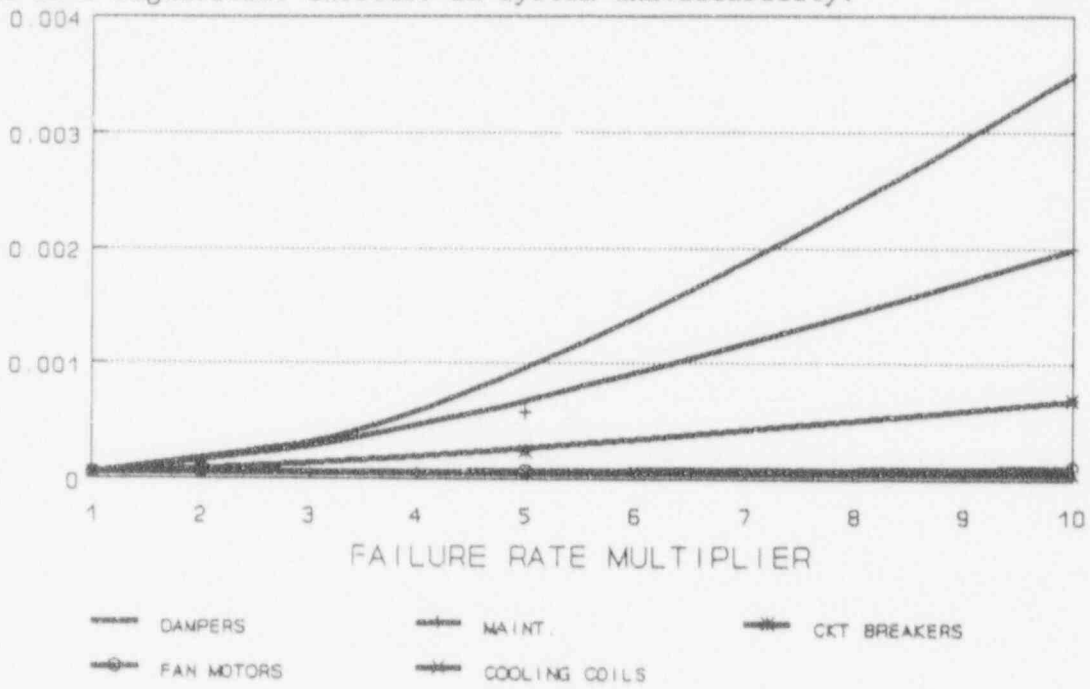


Figure 16 Fan cooler system unavailability versus component failure rates

CONCLUSIONS

This phase I aging analysis has provided a basis for understanding the effects of aging in containment cooling systems. For the containment spray and fan cooler systems, aging characteristics, such as aging mechanisms, failure modes, detection methods, and components most frequently failed were identified. Conclusions and recommendations resulting from this study are summarized below:

- Aging degradation exists in containment cooling systems and is a significant contributor to failures. Since these systems play an important role in accident mitigation, plant programs should specifically address the proper management of aging in containment cooling systems. Each of the aging mechanisms identified

in this study[2], and summarized in Tables 1 and 2 should be addressed by at least one monitoring technique.

- Most containment spray system failures are detected by surveillance tests and inspections. This is significant since it shows the importance of performing tests and inspections on standby systems to detect degradation before it results in an operational failure. It should also be noted that for standby systems, testing can be a significant contributor to aging degradation.

- Approximately 30% of fan cooler system failures are detected by abnormal operation. This indicates that approximately one third of the failures are not detected by current testing or inspections. Therefore, the need for improved IS&M practices should be evaluated.

- The review of industry and plant specific data has shown that the failures occurring in the containment cooling systems are usually not severe enough to result in a complete loss of system function. Typically, the most severe failure result in a loss of redundancy, however, the system is still able to perform its design function.

- If aging is not properly controlled and component failure rates increase with age, this will result in a corresponding increase in system unavailability. Therefore, plant programs should include measures to identify any time-dependent trends in component failures so they can be properly managed.

REFERENCES

1. Vora, J., "Nuclear Plant Aging Research (NPAR) Program Plan," NUREG-1144, U. S. Nuclear Regulatory Commission, Revision 2, June 1991.

2. Lofaro, R. and Subudhi, M., "The Effects of Age on Nuclear Power Plant Containment Cooling Systems," NUREG/CR-5939, Brookhaven National Laboratory, to be published 1993.

3. Lofaro, R., et al., "Aging Study of Boiling Water Reactor Residual Heat Removal System," NUREG/CR-5268, Brookhaven National Laboratory, June 1989.

Table 1 Summary of aging mechanisms and failure modes for containment spray system components

Component	Major Aging Mechanisms	Percentage	Major Failure Modes	Percentage
Valves	- Wear	49%	- Leakage	58%
	- Adjustment Drift	17%	- Does Not Open	18%
	- Galling/Binding	14%	- Does Not Close	11%
	- Dirt/Dust Intrusion	7%	- Does Not Operate	8%
	- Short/Burnout	4%	- Exceeds Limit	3%
	- Loss of Lubrication	3%		
Instruments & Controls	- Calibration Drift	39%	- Incorrect Reading/ Loss of Function	100%
	- Wear	27%		
	- Internal Defects	22%		
	- Contamination	5%		
	- Degradation of Power Supply	4%		
	- Binding	3%		
Circuit Breakers	- Adjustment Drift	22%	- Does Not Close	59%
	- Galling/Binding	17%	- Does Not Open	18%
	- Short/Burnout	17%	- Does Not Operate	17%
	- Wear	16%		
	- Dirt/Dust Intrusion	9%		
	- Loss of Lubrication	7%		
	- Fatigue	4%		
	- Corrosion	3%		
Pumps	- Wear	62%	- Leakage	48%
	- Galling/Binding	14%	- Does Not Run	24%
	- Adjustment Drift	10%	- Does Not Start	14%
	- Short/Burnout	3%		
	- Service Outside Limits	3%		
	- Dirt/Dust Intrusion	2%		
	- Fatigue	2%		
Heat Exchangers	- Plugging/fouling	62%	- Plugged	66%
	- Corrosion	21%	- Leakage	15%
	- Wear	6%	- Fouled	15%
	- Vibration	4%		

Table 2 Summary of Aging Mechanisms and Failure Modes for Fan Cooler System Components

Component	Major Aging Mechanisms	Percentage	Major Failure Modes	Percentage
Circuit Breakers	- Short/Burnout/Pitting	30%	- Does Not Close	67%
	- Wear	15%	- Does Not Open	17%
	- Adjustment Drift	14%	- Does Not Operate	6%
	- Fatigue/Cracking	13%		
	- Galling Binding	10%		
	- Dirt/Dust Intrusion	6%		
	- Loss of Lubrication	2%		
	- Corrosion	1%		
Instruments & Controls	- Calibration Drift	22%	- Incorrect Reading/ Loss of Function	100%
	- Wear	22%		
	- Short/Burnout	20%		
	- Contamination	17%		
	- Binding	4%		
Dampers	- Wear	23%	- Does Not Close	40%
	- Galling/Binding	22%	- Does Not Operate	21%
	- Adjustment Drift	17%	- Does Not Open	20%
	- Fatigue/Cracking	11%	- Leakage	15%
	- Short/Burnout/Pitting	6%		
	- Loss of Lubrication	6%		
	- Dirt/Dust Intrusion	5%		

PHASE I AGING ASSESSMENT OF NUCLEAR AIR-TREATMENT SYSTEM HEPA FILTERS AND ADSORBERS

W. Kevin Winegardner
Pacific Northwest Laboratory

ABSTRACT

A Phase I aging assessment of high-efficiency particulate air filters and activated carbon gas adsorption units was performed by the Pacific Northwest Laboratory as part of the U.S. Nuclear Regulatory Commission's Nuclear Plant Aging Research Program. Information was compiled concerning design features; failure experience; aging mechanisms, effects, and stressors; and monitoring methods. Over 1100 failures, or 12 percent of the filter installations, were reported as part of a U.S. Department of Energy survey. Investigators from other laboratories have suggested that aging could have contributed to over 80 percent of these failures. Several instances of impaired performance as the result of the premature aging of carbon were reported. Filter aging mechanisms range from those associated with particle loading to reactions that alter properties of gaskets. Mechanisms that can lead to impaired adsorber performance include the loss of potentially available active sites as a result of the adsorption of moisture or pollutants. Stressors include heat, moisture, radiation and airborne particles and contaminants.

INTRODUCTION AND BACKGROUND

This paper describes the Phase I interim aging assessment of the high-efficiency particulate air (HEPA) filters and gas adsorption units (adsorbers) of nuclear air-treatment or cleaning and ventilation systems. The Phase I aging assessment of HEPA filters and adsorbers is part of an evaluation of the effects of aging on Engineered Safety Feature (ESF) systems, one of the groups of systems of current interest in the Nuclear Plant Aging Research (NPAR) Program (USNRC 1991). The study was performed for the U.S. Nuclear Regulatory Commission (USNRC) by Pacific Northwest Laboratory (PNL)[a]. Information concerning the design and construction of the two air-treatment system components is summarized. References to the documents that combine to provide basic physical, chemical, test, and performance standards for filter media and impregnated activated carbon as well as for assembled components are also included.

Aging mechanisms and effects are discussed in conjunction with stressors, the agents or stimuli that can result in degradation. Failure experience, based on analyses of Licensee Event Reports (LERs) and a survey of

---

(a) Operated for the U.S. Department of Energy by Battelle Memorial Institute under Contract DE-AC06-76RLO 1830.

U.S. Department of Energy (USDOE) sites, is summarized and, where possible, related to aging. The discussion of failure experience also includes exhaust-air treatment experience associated with the Three Mile Island (TMI) accident.

Inspection, surveillance, and monitoring methods (ISMM) are reviewed. These methods are used to establish the condition of the filters and adsorbers once the components have been placed in operation. Surveillance tests, which are a series of tests periodically performed to monitor component condition and demonstrate the current ability to remove fine particles and iodine and iodine compounds, are described.

The identification of potential safety related aging issues, coupled with the need to avoid duplication, were the key considerations in identifying candidate ESF systems for initial study. Air-treatment or cleaning and ventilation systems were ultimately selected because failure of these systems can impact both plant and public safety. Predominately system components filters and adsorbers can be the last barrier in preventing the release of radioactivity to the public following an accident, including that associated with the airborne iodine and cesium radionuclides that can provide a substantial contribution to total dose. Further, air-treatment systems are needed to ensure safe shutdown of the plant or to allow equipment to be serviced. Satisfactory performance of certain air-treatment systems is essential to ensure control room habitability. Air-treatment systems and components are also used to provide a safe and/or controlled environment for personnel and equipment during normal operations. Operability of some safety-related equipment depends on particular systems to remove heat from the rooms where these components are installed.

Air-treatment systems consist of some or all of the following components: moisture separators or demisters, electrical heaters, prefilters, HEPA filters, adsorbers, postfilters, fans or blowers, ductwork, dampers, and valves. The first step in the Phase I study was to identify a boundary to isolate the components that would be assessed. The fundamental components in terms of providing plant and public safety are those designed to capture radioactive gaseous and particulate contaminants; namely, the adsorbers and HEPA filters, respectively. One or both are installed in nuclear air-treatment systems. The particles could be radioactive chemical compounds or otherwise inert airborne material contaminated by radioactive species. Gasses of primary interest include the elemental and organic forms of radioiodine. Activated carbon is used to remove the gaseous or volatile forms of iodine and is usually impregnated with other chemicals to enhance the removal of the organic species. HEPA filters and activated carbon adsorption units were selected as the focus for initial Phase I assessment not only because they are essential for safety, but in the case of the adsorbers, it has long been established, and was evidenced again during the TMI accident, that aging mechanisms associated with this component can lead to impaired performance (Burchsted et. al. 1976; Wilhelm and Deuber 1991).

COMPONENT DESIGN AND CONSTRUCTION

The particle filtration and gas (vapor) adsorption units (adsorbers) included in nuclear air-treatment systems are designed to remove radioactive materials. The materials, airborne particles or volatile species, may be suspended in or exist as gas phase constituents of recirculating aerosols, gaseous effluents, or accidental releases. The adsorbers, activated carbon beds, can effectively remove elemental radioiodine and are often impregnated with other chemicals to enhance the retention of organic species. The fine particle filters, HEPA filters, may also be significantly involved in radioiodine removal because iodine can be in the form of solid cesium iodide (CsI).

HEPA filters clean or treat aerosols by separating suspended particles from an essentially atmospheric pressure gas stream. The filter media is made from a mixture of glass fibers and is in the form of filter "paper." Particles are collected by interception, impaction, and Brownian diffusion. The continuous gas phase passes through virtually unchanged. A HEPA filter is defined as a "high-efficiency particulate air filter having a fibrous medium with a particle removal efficiency of at least 99.97% for 0.3 μm particles of dioctyl phthalate [DOP]" (ASME 1989). An excellent review of the construction and service characteristics of HEPA filters has been prepared by First (1991). As indicated by First, "Filters constructed with paper pleated the full depth of the rigid outer frame and with adjacent pleats held apart by full-depth corrugated separators are the most widely used." In other words, the glass fiber filter paper is in the form of a continuous sheet pleated vertically over the separators.

As indicated above, adsorbers are used to remove gaseous radioiodine species from effluents. Various standards and specifications permit the use of any adsorbent medium that has been demonstrated to be equal to or better than activated carbon in terms of radioiodine retention. However, only activated carbon is discussed because it is essentially the only material used and supporting testing procedures and acceptance criteria are specific to its use. Gasses are directed through tightly packed beds of activated carbon granules. The carbon or charcoal is prepared by controlled heating in a steam environment to remove volatile organic material. The heating generates a material with a large surface-to-mass ratio and internal surfaces or sites where adsorption of iodine molecules can take place. The active media is usually "...activated charcoal that is derived from either coal or coconut shells. Although elemental radioiodine is retained efficiently by activated carbon alone..., the charcoal is often impregnated with additional chemicals to improve its retention of organic species (e.g., methyl iodide)." (Wilhelm and Deuber 1991).

Basic qualifications for the filter media and assembled HEPA particulate filters are contained in two military specifications (U.S. Department of Defense 1985, 1986). Primary standards for adsorbent media, assembled adsorbers, and related testing methods are presented in Sections FD, FE, and FF of ASME/ANSI code AG-1 and two ASTM specifications (ASME/ANSI 1988; ASTM 1989, 1990). Numerous documents supplement and/or support the preceding five

references, including USNRC and other ASME and ASTM publications. One of the most closely related USNRC publications is Regulatory Guide 1.52, *Design, Testing, and Maintenance Criteria for Post Accident Engineered-Safety-Feature Atmosphere Cleanup System Air Filtration and Adsorption Units of Light-Water-Cooled Nuclear Power Plants* (USNRC 1978).

AGING MECHANISMS, EFFECTS, AND STRESSORS

The obvious effect of service associated with HEPA filter use is the increased pressure drop (resistance to air flow) through the filter media arising from particle retention (loading). In a relatively clean environment, filters may be used for several years before replacement is required. Dust loading, along with heat and radiation, also have the potential to reduce the effectiveness of the organic materials used to strengthen the filter medium and provide water repellency. High moisture content is another potential normal stressor, an agent or stimuli that stems from normal conditions and that can produce aging mechanisms and effects, which can lead to increased pressure drop as well as reduced filter medium strength.

Filter media may embrittle from prolonged exposure to air containing normal concentrations of oxygen and oxides of nitrogen and sulfur. Aging mechanisms or processes that can gradually change the physical characteristics of HEPA filter components other than the media include corrosion of metal members and physicochemical reactions that alter the properties of sealants, gaskets, and water repellents. Metal components that could be affected include the frames and corrugated separators. Heat and radiation are stressors associated with physicochemical reactions potentially affecting face gaskets and the adhesives and sealants that are used to splice the medium, fasten the gaskets to the filter face, and seal the filter pack to the frame.

Exposure to air containing stressors (namely, moisture and contaminants or pollutants) can slowly and continuously degrade the performance of gas adsorbers. This aging, also termed weathering, is inherent because of the nature of the material used, in that it has been "activated" to dramatically increase surface to mass ratio and provide countless reaction sites, and because of the essentially ubiquitous nature of the contaminants. Many airborne constituents, including moisture, can readily react or be adsorbed by carbon beds, reducing the number of active "sites" that otherwise would be available for radioiodine adsorption. During normal operation, charcoal may be exposed to air flows containing such contaminants as volatile organic solvents, sulfur dioxide, nitrogen oxides, and carbon monoxide. Because of system flow rates, even traces of pollutants can have a significant, cumulative effect. Oxidation as well as competitive loading can impair bed performance, including decreasing the efficiency of the impregnant. Because airborne constituents can vary dramatically with time and among sites, it is essentially impossible to provide criteria for the useful life of impregnated activated carbon.

It should be emphasized that the possibility of impaired performance in terms of radioiodine retention as a result of the aging or weathering of impregnated activated carbon has been a concern almost from the start of the

nuclear industry's existence. In fact, concern about the useful life of carbon could be considered one of the first, if not the first, aging issues.

FAILURE EXPERIENCE

An unusually large amount of potentially useful failure data were found in the literature. Analyses of LERs submitted by commercial nuclear power plant operators, covering the periods from January 1, 1975 through June 30, 1978, 1978-1981, 1985-1987, and 1988-1991, to identify those pertaining to air-monitoring, air-treatment, and ventilation systems, have been prepared by Moeller (1979), Moeller and Sun (1983), Jacox (1989), and Sommer and Otermat (1992). In summary, 15% of 43,500 reports were associated with the subject systems while an estimated roughly 100, or about 2%, of the system reports appeared to be associated with HEPA filters and carbon adsorbers. No relationship to aging was reported. Moeller and Kotra (1985) and Moeller and Sun (1987) reviewed LERs for the periods 1981 through 1983 and 1984 through 1986, respectively, to isolate those pertaining to control room habitability. Of the approximately 20,800 reports, 4% were related to this subject. About 60 of the LERs were associated with impaired filter or adsorber efficiency. Several instances of the premature aging of carbon from error-induced conditions were reported.

Using a survey, Carbaugh (1983) collected data on the numbers of and reasons for HEPA filter changeouts and failures at USDOE sites for the years 1977 through 1979. A total of 1,105 filter failures, or 12% of the 9,154 filter applications, were reported. A majority of the failures occurred for unknown or unreported reasons. Johnson et al. (1989) explained the results of the above survey: "If one examines the categories reported for filter failure, it is evident that the effects of aging could contribute to 81% of these failures, except for the 19% resulting from handling or installation damage." These same investigators reported results of an experimental evaluation of the tensile breaking strength of aged filter media specimens that revealed that 42% of the samples did not meet the specifications for new material. A significant loss in water repellency from values specified for new media was also measured (Johnson et al. 1989).

Selection of adsorbers for Phase I study was reinforced by literature references revealing that the low radioiodine decontamination factors associated with the TMI accident were attributed to the premature aging of charcoal. Before presenting details related to aging issues, it should be emphasized that building ventilation systems played an important role in decreasing the radionuclide release associated with this incident and in fact, prevented the release of most of the radioiodine. However, the terms "somewhat dismal results" and "rather unsatisfactory" have been used to describe exhaust air filtering experience during the TMI accident (OECD 1984; Wilhelm and Deuber 1991). In summary, it was determined that the filtering systems installed at the time of the accident provided a decontamination factor (DF) of 9.5 for all species of radioiodine (corresponds to a retention efficiency of 89.5%) and the radioiodine releases were higher by about a factor of five than they would have been if there had been no system deterioration. The preceding values and reasons for the degradation are

detailed by Rogovin and Frampton (1980) and discussed by Bellamy (1981) in a paper that was prepared to summarize pertinent (related to air-cleaning technology) efforts and recommendations of various investigative groups. Briefly, system degradation and the fact that the radioiodine retention efficiency was only 89.5% were ultimately attributed to pre-accident aging of the impregnated activated carbon. For a number of reasons, ventilation air was passed through exhaust systems from the time of carbon installation to just shortly after the accident. This approximately one-year time frame included periods of exposure of the carbon beds to fumes from painting and cleanup efforts. Furthermore, exemptions to technical specifications postponed surveillance tests that could have revealed the extent of aging.

Review indicated that releases of radioactive material in particulate form during the TMI accident were negligible. Postaccident efforts included changeout of HEPA filters as well as carbon. As indicated by Rogovin and Frampton (1980), "These HEPAs were visually examined before changeout and were intact and in satisfactory condition, but were damaged during changeout...". Unfortunately, no used HEPA filters or sections of filter media were retained for analysis."

INSPECTION, SURVEILLANCE, AND MONITORING METHODS

The use of surveillance tests, a series of tests periodically performed to monitor component condition and demonstrate the current ability to remove fine particles and iodine and iodine compounds, is emphasized. Surveillance tests include in-place leak tests and visual inspections to evaluate filter banks and adsorbers in terms of component damage and bypass. Also included, and specifically related to aging concerns, are laboratory tests of used or aged carbon samples to determine remaining radioiodine adsorption capacity. In addition to the surveillance tests, HEPA filter pressure drop is continuously monitored (alarmed and indicated).

Surveillance leak testing of installed HEPA filters and adsorbers is specified because gradual deterioration and leaks could develop under standby as well as service conditions. These tests are based on a DOP or halide challenge aerosol or gas introduced upstream of the filters or the adsorbers, respectively. Concentrations upstream and downstream are then measured. It should be emphasized that these are leak rather than efficiency tests. For adsorbers, however, the leak test is supplemented with laboratory tests of aged or used carbon samples to determine system efficiency and remaining capacity for methyl iodide. It is stated in ASME N509 that "Sufficient test canisters or other means of obtaining samples... of used adsorbent shall be installed in the adsorber system to provide a representative determination of the response of the adsorbent to the service environment over the predicted life of the adsorbent. Test canisters shall be installed in a location where they will be exposed to the same air flow conditions as the adsorbent in the system, shall have the same adsorbent bed-depth as the adsorbent in the system, and shall be filled with representative adsorbent from the same batch of adsorbent as that of the system" (ASME 1989).

CONCLUSIONS

There appear to be adequate inspection, surveillance, and monitoring methods (ISMM) for normal conditions. It is recognized that, excluding local ruptures and tears, neither pressure drop monitoring nor surveillance leak testing of installed HEPA filters will provide indications of aging in terms of reduced filter media strength. However, even aged, intact filters can still effectively remove particles under normal conditions. On the other hand, this lack of indication may be important when considering reactor accident conditions. Regulations require atmospheric cleanup systems to mitigate the consequences of postulated accidents and, as indicated earlier, system components can be the last barrier against the release of radioactivity to the public.

The Phase I study found that the HEPA filters and adsorbers are considered to have a long service life, especially the filters. Thus, if a severe accident happens it is likely to occur at a time when these two final confinement barriers have been in use for an extended period, even years. Even with existing ISMM methods, aged and possibly degraded components could fail to provide the radiation protection needed for safe shutdown or be the weak link that allows the release of radionuclides to the environment. Furthermore, the assessment has revealed the need for an improved definition of accident conditions and the possible need for additional information to evaluate the performance of aged components under such conditions. Past design basis evaluations based on the assumption that iodine is primarily in the volatile form may be neither correct nor conservative when evaluating air-cleaning system performance. It is recognized that improving the definition of accident conditions is outside the scope of the NPAR program. It is also recognized that comprehensive assessments limited solely to the development of information for performance evaluation could be made. However, for such studies to be definitive, knowledge concerning challenges must ultimately be obtained, as will be discussed below.

Limited information concerning the range of challenges expected for filters and adsorbers during accidents is already available as a result of source term reassessment and reactor risk studies (Silberberg et al. 1986; USNRC 1990). Subsequent work has revealed further insights into iodine chemical form. Although this follow-on effort did not address ultimate disposition, using calculated data from seven severe accident sequences, it was found that "in most of the calculations for the seven sequences, iodine entering containment from the reactor cooling system was almost entirely in the form of CsI with very small contributions of I or HI" (Beahm, Weber, and Kress 1991). Additional insights concerning accident conditions should also become available as a result of recent regulatory efforts to provide improved source term definitions. As part of several regulatory activities to incorporate severe accident insights into the safety assessment of future plants, the NRC has issued a proposed revision of the reactor accident source terms. The proposed revision is in terms of fission product composition, magnitude, timing, and iodine chemical form, for release into containment (Soffer 1992). Utilization of these revised source terms should provide improved estimates of accident conditions and the associated challenges to

filters and adsorbers. For example, evaluation of iodine chemistry during the portion of the transient that follows release into containment will be needed, resulting in better estimates of whether iodine remains primarily in the particulate form or is converted to a volatile species before it reaches filters and adsorbers.

Even if details concerning accident conditions were available, there might be insufficient information to develop reliable predictions concerning the performance of aged components. Quantification of the structural limits and failure mechanism of aged filters in moist airflows and of the particle loadings that would cause failure of reduced strength and/or particle-laden filter media are examples of potential information needs. Statistically designed engineering-scale experiments, involving aged components and utilizing the improved estimates of the ranges and combinations of challenges, may ultimately be justified. It is also possible that improved estimates of conditions could negate the need for further work, because either moderate or extremely severe stressors were predicted. In the case of moderate stressors, additional study would be unwarranted if near-normal operating conditions were identified. In the case of severe conditions, HEPA filters are simply not sized to handle the massive loading of nonradioactive particles that conceivably could result from molten core-concrete interactions.

An improved definition of accident conditions may also reveal that aging concerns associated with the filters and adsorbers of "normal" treatment systems may equal those of ESF systems and that the designations of primary and secondary used in RG 1.52 (USNRC 1978) for ESF systems may be trivial in terms of accident considerations. One of the findings resulting from investigations into the TMI accident was the fact that "...a nonengineered safety feature filter system designed for normal operation only, i.e., the auxiliary building exhaust ventilation filtration system, greatly reduced the quantity of radioiodine release to the environment...the safety grade versus nonsafety grade designation [for the two air treatment systems operating at the time of the accident] was meaningless..." (Rogovin and Frampton 1980). An improved understanding of severe accident conditions could also further emphasize the importance of other air-treatment system components. For example, along with HEPA filters, greater emphasis would be placed on coarse or roughing pre-filters and even demisters if it were determined that high particle concentrations were involved.

Finally, it should be emphasized that information used to estimate the performance of aged air-treatment system components can have a significant impact on the calculated consequences of postulated accidents. This is illustrated by the analysis of a postulated loss-of-decay-heat-removal accident at Browns Ferry. The standby gas treatment system (SGTS) failure model used, listed as the area of greatest uncertainty with respect to informal sensitivity analyses, includes best estimates concerning the filter loading that will cause failure, the type of failure, and the functioning of the adsorber under the projected accident environment. It is noted that "the SGTS failure model assumes prime importance because the SGTS is the last barrier to the atmosphere in this accident sequence" (Wichner et al. 1984).

REFERENCES

ASME. 1989. *Nuclear Power Plant Air-Cleaning Units and Components.* ASME Standard N509-1989, The American Society of Mechanical Engineers, New York.

ASME/ANSI. 1988. *Code on Nuclear Air and Gas Treatment.* ASME Code ASME/ANSI AG-1-1988, The American Society of Mechanical Engineers, New York.

ASTM. 1989. *Standard Test Method for Nuclear-Grade Activated Carbon.* ASTM Standard D3803-89, American Society for Testing and Materials, Philadelphia, Pennsylvania.

ASTM. 1990. *Standard Specification for Impregnated Activated Carbon Used to Remove Gaseous Radio-Iodines from Gas Streams.* ASTM Standard D4069-90, American Society for Testing and Materials, Philadelphia, Pennsylvania.

Beahm, E. C., C. F. Weber, and T. S. Kress. 1991. *Iodine Chemical Forms in LWR Severe Accidents.* NUREG/CR-5732, U.S. Nuclear Regulatory Commission, Washington, D.C.

Bellamy, R. R. 1981. "Investigations into the Air Cleaning Aspects of the Three Mile Island Accident." In *16th DOE Nuclear Air Cleaning Conference: Proceedings*, Vol. 1, ed. M. W. First, pp. 1427-1441. CONF-801038, Harvard University, Boston, Massachusetts.

Burchsted, C. A., J. E. Kahn, and A. B. Fuller. 1976. *Nuclear Air Cleaning Handbook.* ERDA 76-32, Oak Ridge National Laboratory, Oak Ridge, Tennessee.

Carbaugh, E. H. 1983. "Nuclear Air Cleaning: The Need for a Change in Emphasis." In *Proceedings of the Fourth DOE Environmental Protection Information Meeting.* CONF-821215, U.S. Department of Energy, Washington, D.C.

First, M. W. 1991. "Removal of Airborne Particles from Radioactive Aerosols." Chapter 2 in *Treatment of Gaseous Effluents at Nuclear Facilities*, eds. W.R.A. Goossens, G. G. Eichholz, and D. W. Tedder, pp. 13-66. Harwood Academic Publishers, New York.

Jacox, J. W. 1989. "Review of Nuclear Air Treatment System Related License Event Reports for Period 1985-1987." In *Proceedings of the 20th DOE/NRC Nuclear Air Cleaning Conference*, Vol. 1, ed. M. W. First, pp. 386-407. NUREG/CP-0098, U.S. Nuclear Regulatory Commission, Washington, D.C.

Johnson, J. S., D. G. Beason, P. R. Smith, and W. S. Gregory. 1989. "The Effect of Age on the Structural Integrity of HEPA Filters." In *Proceedings of the 20th DOE/NRC Nuclear Air Cleaning Conference*, Vol. 1, ed. M. W. First, pp. 366-380. NUREG/CP-0098, U.S. Nuclear Regulatory Commission, Washington, D.C.

Moeller, D. W. 1979. "Failures in Air-Monitoring, Air-Cleaning, and Ventilation Systems in Commercial Nuclear Power Plants (Jan. 1, 1975 - June 30, 1978)." *Nuclear Safety*, Vol. 20, No. 2.

Moeller, D. W., and J. P. Kotra. 1985. "Commentary on Nuclear Power Plant Control Room Habitability Including a Review of Related LERs (1981-1983)." In *18th DOE Nuclear Airborne Waste Management and Air Cleaning Conference: Proceedings*, Vol.1, ed. M. W. First, pp. 145-161. CONF-840806, U.S. Department of Energy, Washington, D.C.

Moeller, D. W., and L-S. C. Sun. 1983. "Failures in Air-Cleaning, Air Monitoring, and Ventilation Systems in Commercial Nuclear Power Plants, 1978-1981." *Nuclear Safety*, Vol. 24, No. 3.

Moeller, D. W., and L-S. C. Sun. 1987. "Review of LERs Pertaining to Control Room Habitability." *Nuclear Plant Journal*, November-December.

OECD. 1984. *Air Cleaning in Accident Situations, Report to CSNI by an NEA Group of Experts*. Organization for Economic Co-operation and Development, Paris, France.

Rogovin, M., and G. T. Frampton, Jr. 1980. *Volume II, Part 2, Three Mile Island, A Report to the Commissioners and to the Public, Nuclear Regulatory Commission Special Inquiry Group*. U.S. Nuclear Regulatory Commission, Washington D.C.

Silberberg, M., J. A. Mitchell, R. C. Meyer, and C. P. Ryder. 1986. *Reassessment of the Technical Bases for Estimating Source Terms*. NUREG-0956, U.S. Nuclear Regulatory Commission, Washington, D.C.

Soffer, L. 1992. "Revision of Reactor Accident Source Terms and Implications for Nuclear Air Cleaning Requirements." In *Proceedings of the 22nd DOE/NRC Nuclear Air Cleaning Conference*, Vol. 1, ed. M. W. First, pp. 362-373. NUREG/CP-0130, CONF-9020823, U.S. Nuclear Regulatory Commission, Washington, D.C.

Sommer, R. R. and J. E. Otermat. 1992. "A Review of Licensee Event Reports Relating to Nuclear Air Treatment Systems and Heating, Ventilating, Air Conditioning Systems Filed During the Period 1988-1991." In *Proceedings of the 22nd DOE/NRC Nuclear Air Cleaning Conference*, Vol. 2, ed. M. W. First, pp. 899-905. NUREG/CP-0130, CONF-9020823, U.S. Nuclear Regulatory Commission, Washington, D.C.

U.S. Department of Defense. 1985. *Filter Medium, Fire-Resistant, High-Efficiency*. Military Specification MIL-F-51079D, Washington, D.C.

U.S. Department of Defense. 1986. *Filters, Particulate (High-Efficiency Fire Resistant)*. Military Specification Mil-F-51068F, Washington, D.C.

USNRC. 1978. *Design, Testing, and Maintenance Criteria for Post Accident Engineered-Safety-Feature Atmosphere Cleanup System Air Filtration and Adsorption Units of Light-Water-Cooled Nuclear Power*. Regulatory Guide 1.52, U.S. Nuclear Regulatory Commission, Washington, D.C.

USNRC. 1990. *Severe Accident Risks: An Assessment for Five U.S. Nuclear Power Plants*. NUREG-1150, U.S. Nuclear Regulatory Commission, Washington, D.C.

USNRC. 1991. *Nuclear Plant Aging Research*. NUREG 1144, Rev. 2, U.S. Nuclear Regulatory Commission, Washington, D.C.

Wichner, R. P., C. F. Weber, S. A. Hodge, E. C. Beahm, and A. L. Wright. 1984. *Noble Gas, Iodine, and Cesium Transport in a Postulated Loss of Decay Heat Removal Accident at Browns Ferry*. NUREG/CR-3617, U.S. Nuclear Regulatory Commission, Washington, D.C.

Wilhelm, J. G., and H. Deuber. 1991. "The Removal of Short-Lived Iodine Isotopes." Chapter 3 in *Treatment of Gaseous Effluents at Nuclear Facilities*, eds. W.R.A. Goossens, G. G. Eichholz, and D. W. Tedder, pp. 67-101. Harwood Academic Publishers, New York.

PRIORITIZATION OF MOTOR OPERATED VALVES BASED ON RISK IMPORTANCES

W. E. Vesely (SAIC)
G. H. Weidenhamer (NRC)

In response to Generic Letter 89-10 which recommends testing of motor operated valves (MOVs), the use of probabilistic risk assessments is evaluated as a tool for prioritizing MOV tests and for determining test schedules. A PRA-based prioritization of MOVs can potentially identify those MOVs which are important to risk and which optimize testing resources. In previous research carried out under the Nuclear Plant Aging Research (NPAR) Program, PRA-based approaches have been developed to prioritize components when multiple degradations and common cause failures could exist. These degradation and failure scenarios are similar to those described in Generic Letter 89-10. Using the NPAR work as a basis, criteria are defined for validly applying a PRA to assist in developing a response to Generic Letter 89-10. Considerations for satisfying the criteria are described, and a validation approach is presented. Examples of PRA applications are also illustrated.

PRIORITIZATION OF MOTOR OPERATED VALVES BASED ON RISK IMPORTANCES

W. E. Vesely (SAIC)
G. H. Weidenhamer (NRC)

Introduction

Generic Letter 89-10[1] (hereafter identified as GL 89-10) identifies operational problems that may exist in specific, affected safety related motor operated valves (MOVs) that may impede their proper functioning in mitigating accidents. Consequently, GL 89-10 recommends that each utility review and assure the technical basis for the operability of each affected safety-related MOV in the plant. The correct settings for each MOV are to be determined to assure that the MOV properly functions, i.e. opens or closes as required, against the differential pressures which occur during accident conditions. GL 89-10 recommends that the capability of each MOV to function should be demonstrated by dynamically testing the MOV under appropriate pressures and flow conditions. In addition to the dynamic tests, GL 89-10 recommends that tests be performed throughout the life of the plant to assure that the proper MOV switch settings are maintained.

Since the conduct of a dynamic test is relatively expensive and since from 50 to 300 MOVs may need to be tested depending on the plant, compliance with GL 89-10 involves significant resources. However, if the MOVs are not able to properly function then the risk of an accident at a plant can be significantly increased. Thus, even though the tests are expensive, it is important to carry out the dynamic tests to assure their functionability and to minimize the risk. Also, it is important to carry out surveillance tests during the lifetime of the plant to assure that the valves remain functional.

A Probabilistic Risk Assessment (PRA) for a plant has the potential of being an important tool in responding to GL 89-10. The plant PRA can potentially be used in two important ways. First of all, the PRA can be used to prioritize the dynamic tests of the MOVs in terms of their risk importance. The tests could then be carried out in a phased manner in which the most risk important MOVs are tested first, then the second highest group of MOVs are tested, etc. Secondly, the PRA can be used to identify surveillance test schedules for the MOVs to assure that their risk contributions are controlled throughout the life of the plant. The test schedules could also be optimized according to the risk importance of the MOVs.

The plant PRA thus has the potential for helping to define a response to GL 89-10 which both minimizes the risk impacts and minimizes the resource requirements. By identifying and focusing on the most risk important MOVs first, the risk impacts associated with the potential MOV problems are minimized. By developing a graded, prioritized response, the associated resource requirements are furthermore optimized. However, in order for the PRA to be validly

used, specific issues and validation requirements need to be addressed. These are discussed in the following sections and recommendations, as well as demonstrations of results, are given.

Issues

To support a response to GL 89-10, a plant PRA can be used to prioritize the MOVs for the dynamic tests and can be used to determine schedules for the surveillance tests. In developing a PRA-supported approach to respond to GL 89-10, various issues need to be addressed. A checklist of these issues is given in Table 1. These issues, along with response considerations, are:

1. *The MOVs included in the PRA are only a subset of those addressed by GL 89-10.*

   All the safety related MOVs in the plant which are addressed by GL 89-10 need to be first of all identified. Those particular MOVs included in the plant PRA then need to be marked. These marked MOVs represent the subset of MOVs addressable by the PRA.

2. *The particular failure modes addressed by GL 89-10 need to be those covered by the PRA.*

   GL 89-10 identifies the critical failure modes of concern, i.e. failure to open and failure to close. The failure modes covered in the PRA need to be consistent with these critical failure modes. If they are not then this further reduces the subset of MOVs addressable by the PRA.

3. *The failure rates used for the MOVs in the PRA may be too low for GL 89-10 response.*

   PRAs standardly utilize MOV failure rates which are based on test data and experience data which do not necessarily include the hydraulic binding failures addressed in GL 89-10. These failures as well as other relevant accident-condition failures occur under pressures and pressure differentials which are not generally covered in test and experience data. Thus, even when the MOVs have their correct settings, their failure rates for accident response can be higher than those used in the PRA. A failure rate as high as 8.7×10^{-2} per demand can exist under accident conditions as indicated in the supporting documents to GL 89-10. These higher failure rates thus need to be considered, at least for sensitivity studies, in responding to GL 89-10.

TABLE 1. CHECKLIST OF ISSUES TO BE ADDRESSED IF THE PRA IS USED TO RESPOND TO GL 89-10

1. The MOVs included in the PRA are only a subset of those addressed by GL 89-10.
2. The particular failure modes addressed by GL 89-10 need to be those covered by the PRA.
3. The failure rates used for the MOVs in the PRA may be too low for GL 89-10 response.
4. Common cause failures among MOVs as treated in the PRA may be inadequate for GL 89-10 response.
5. PRA importance prioritizations of MOVs need to consider joint MOV importances.
6. MOVs may be unimportant for core damage frequency prevention but may be important for consequence mitigation, shutdown risk control, or when external events are considered.
7. The cascading effects of MOV failures may not be adequately addressed in the PRA.
8. Truncations in the PRA may cause MOV importances to be underestimated.
9. The MOV prioritization criteria and test scheduling criteria need to account for the associated risk impacts.
10. The prioritized groupings of MOV dynamic tests and MOV test schedules need to be validated for their risk control.
11. To develop a complete response to GL 89-10, the PRA evaluations need to be integrated with deterministic evaluations.

4. *Common cause failures among MOVs as treated in the PRA may be inadequate for GL 89-10 response.*

   If an MOV has the operational problem identified in GL 89-10 then because of the systematic nature of the problem it is likely that other MOVs of similar design and function will also have the problem. Thus, common cause failures (CCFs) among the affected MOVs can be relatively likely. PRAs generally don't treat this type of CCF, but instead utilize general historical information. To respond to GL 89-10, the CCF models in the PRA thus need to be extended to cover the groups of potentially affected MOVs identified in GL 89-10.

5. *PRA importance prioritizations of MOVs need to consider joint MOV importances.*

   Standard PRA importance measures, such as risk achievement worth and the Fussell-Vesely importance, evaluate importances of failures which occur one at a time. An MOV may be singly unimportant if it alone fails or is degraded. However, the MOV may be a member of a set of MOVs which if the set all fails or is degraded causes large risk impacts. Thus, the MOV is singly unimportant but jointly important. It is consequently necessary to consider these joint importances in prioritizing the MOVs for GL 89-10 because of the systematic nature of the problems and because sets of MOVs will be prioritized for testing.

6. *MOVs may be unimportant for core damage frequency prevention but may be important for consequence mitigation, shutdown risk control, or when external events are considered.*

   If an MOV is assessed to be in an unimportant category based on the risk result evaluated in the PRA, it still may be important when other risks or other initiating events are considered. These other risks or initiating events need thus to be evaluated in responding to GL 89-10. Bounding or qualitative assessments can be adequate if they are based on valid engineering assessments.

7. *The cascading effects of MOV failures may not be adequately addressed in the PRA.*

   GL 89-10 addresses MOV failures which can occur under higher pressures and pressure differentials. When one or more MOVs fail under these conditions then the MOVs may subsequently rupture, spewing water or steam which may fail other nearby components. These potential cascading effects and interactions thus need to be considered since they can cause unimportant MOVs to become important. PRAs do not often consider these effects because of their assessed small likelihood. However, under the conditions addressed by GL 89-10 this likelihood can be increased. The increase in likelihood needs to be assessed and, if significant, then the cascading effects need to be evaluated or be bounded using the PRA.

8. *Truncations in the PRA may cause MOV importances to be underestimated.*

   A PRA standardly truncates contributors because of assessed low failure probabilities. In particular, the minimal cutsets used to quantify importances and risk values are truncated based on a probability cutoff. Under the conditions defined in GL 89-10 the failure rates of MOVs and their common cause failure likelihoods can be significantly increased. Thus, the validity of the PRA truncations will need to be reassessed. In particular the minimal cutsets need to be regenerated to properly include the MOV contributions under increased failure rate and increased common cause failure probability conditions. The regenerated minimal cutsets can be used to prioritize the MOVs.

9. *The MOV prioritization criteria and test scheduling criteria need to account for the associated risk impacts.*

   The criteria which are used to partition the MOVs into different priority groups need to account for the risk impacts of dynamically testing the different groups at different times. Similarly, criteria which are used to determine test intervals need to account for the risk impacts which are incurred from using the test intervals. Risk-based allowed outage time (AOT) approaches and risk-based surveillance test interval (STI) approaches can be used for these evaluations provided the GL 89-10 conditions are incorporated into the evaluations. NUREG/CR-5425[2] and NUREG/CR-5775[3] describe these approaches.

10. *The prioritized groupings of MOV dynamic tests and MOV test schedules need to be validated for their risk control.*

    Once the prioritized groupings of MOV tests are identified, a validation check needs to be carried out to assure the risk is controlled. To carry out this check, the conditions described in GL 89-10 can be incorporated into the PRA. With the highest priority group of MOVs assumed to be tested, the PRA can then be run to determine the resulting risk level until the next group of MOVs are tested. In this PRA run, only the tested MOVs are modified, i.e. the failure rates and CCF probabilities are modified to after-test conditions. The next group of MOVs can be assumed to be tested and the PRA rerun, and so forth. If the prioritized groupings validly address GL 89-10, the resulting risks incurred should not be significant. The validation runs can demonstrate this. Similar PRA validation runs can be carried out for proposed MOV test schedules.

11. *To develop a complete response to GL 89-10, the PRA evaluations need to be integrated with deterministic evaluations.*

    The PRA results only provide a partial response to GL 89-10. The MOVs covered by GL 89-10 but not included in the PRA need to be separately evaluated for their importance ranking and test scheduling. Engineering assessments need to be carried out with the bases for the proposals clearly documented. Also, those MOVs assessed to be unimportant using

the PRA should be rechecked from an engineering standpoint to assure they are not important from a plant operations standpoint. The complete response to GL 89-10 can then be prepared, integrating the PRA results and the deterministic, engineering evaluations.

The following sections highlight and further discuss certain of the above issues because of their special considerations. These highlighted issues are Issue 5 involving joint importances, Issue 8 involving PRA truncations, and Issue 10 involving validation.

Joint Risk Importances

One of the important issues that is identified above is Issue 5 which is the need to consider MOV joint importances. In general, the joint risk importance of a set of components is the risk impact from the set of components jointly failing or being jointly degraded. The joint importance of a set of MOVs is the risk impact from all the MOVs being jointly affected by the operational problems identified in GL 89-10.

In using the PRA to prioritize the MOV dynamic tests, the objective is to identify sets of MOVs addressed by GL 89-10 which have high joint risk importance. The set of priority MOVs to be tested should reduce the high joint importances caused by GL 89-10 to low acceptable values.

Prioritizing the MOVs by their individual risk importances which are standardly computed in PRAs will not necessarily identify the set of MOVs of highest joint importance. This is because the joint risk importance is not directly related to the individual risk importance. An MOV may have small individual risk importance but may belong to a set of high joint risk importance. Table 2 illustrates examples of individual importances and joint importances of two MOVs being failed for a particular PRA. The importances here are risk achievement worths with regard to core damage frequency (CDF). As observed, the individual importances of MOVs are relatively small to moderate while the joint importances of specific doublets of MOVs are extremely high. Larger combinations of MOVs have even higher importances.

The set of MOVs which is identified as highest priority using a proposed prioritization may not focus on the highest joint importances if single importance prioritization techniques are used. This is one reason why the separate validation step identified in Issue 10 is needed to assure that the risk is indeed controlled by the identified set. Various algorithms can be used to calculate the joint importances and to identify the sets of highest joint importance to carry out the most efficient testing. Joint importance approaches were developed in NRC's Nuclear Plant Aging Research (NPAR) Program to evaluate joint aging effects of components. These joint importance approaches are described in NUREG/CR-5510.[4]

TABLE 2. INDIVIDUAL MOV IMPORTANCES VERSUS JOINT MOV IMPORTANCES

CDF IMPORTANCES OF INDIVIDUAL MOVS	
VALVE IDENTIFIER	CDF RELATIVE IMPORTANCE
LPR-MOV-FT-1862A	5
LPR-MOV-FT-1860A	3
LPR-MOV-FT-1890A	3
PPS-MOV-FC-1535	3
PPS-MOV-FC-1536	3
HPI-MOV-FT-1350	3
LPR-MOV-FT-1862B	1
LPR-MOV-FT-1860B	1
HPI-MOV-FT-1115C	1
HPI-MOV-FT-1115E	1
LPR-MOV-FT-1890B	1
HPI-MOV-FT-1115B	1
HPI-MOV-FT-1115D	1

CDF IMPORTANCES OF PAIRS OF MOVS		
VALVE PAIR		CDF RELATIVE IMPORTANCE
PPS-MOV-FC-1535	PPS-MOV-FC-1536	700
LPR-MOV-FT-1862A	LPR-MOV-FT-1862B	80
LPR-MOV-FT-1860A	LPR-MOV-FT-1862B	50
LPR-MOV-FT-1860B	LPR-MOV-FT-1862A	50
HPI-MOV-FT-1115C	HPI-MOV-FT-1115E	30
LPR-MOV-FT-1890A	LPR-MOV-FT-1890B	30
LPR-MOV-FT-1860A	LPR-MOV-FT-1860B	30
HPI-MOV-FT-1115B	HPI-MOV-FT-1115D	30

Truncation in the PRA

To determine risk importances of MOVs for dynamic testing or to determine surveillance testing schedules for the MOVs, it is important that truncations are addressed as Issue 8 identifies. These truncations generally cause specific MOV importances to be underestimated. Truncation of the PRA minimal cutsets is a major contributor for this potential underestimation. If the importances of MOVs are determined using the PRA's original cutsets, then the importances can be significantly underestimated because of the truncation of MOV contributions to the minimal cutsets. The potential for higher MOV failure rates and higher likelihoods of common cause failures identified in GL 89-10, as well as the need to determine joint importances, can cause the original minimal cutsets to be invalid, or at least to be highly suspect.

Table 3 illustrates the additional MOVs that were identified as being important from the regenerated minimal cutsets for a PRA. Minimal cutsets containing MOVs were particularly regenerated. Risk important events were defined to be important for this exercise if their failure caused an increase in the core damage frequency of at least a factor of 3. The MOVs identified in Table 3 which were truncated in the original PRA are important particularly from the standpoint of GL 89-10 since failures of combinations of these MOVs will cause the entire emergency core cooling (ECC) function to be lost. Since the cutoff criteria of a factor of 3 does not directly indicate the final core damage frequency that will be achieved, a separate validation run is needed to check that even the larger set of MOVs if tested does indeed control the core damage frequency. This need for a validation run is identified in Issue 10. In carrying out the validation run, the original truncated minimal cutsets again cannot be used, but regenerated minimal cutsets should be used.

Validation

Issue 10 identifies the need to carry out a validation run to demonstrate that the risk is indeed controlled by the prioritization approach or testing scheduled which is proposed. This validation check is needed because the prioritization criteria or testing schedule criteria do not, in general, directly indicate the risk level, e.g. the core damage frequency, which is actually achieved if the proposal is followed. The validation is carried out by rerunning the PRA with the proposed MOVs tested or the proposed testing schedules utilized.

If the hydraulic binding problems exist as identified in Generic Letter 89-10, then specific groups of MOVs can be nonoperational. The MOVs in a given group are likely to be those of the same design and function. Consequently, a prioritization approach should be able to address this problem and provide acceptable risk levels when the given proposed priority valves are tested.

TABLE 3. ADDITIONAL IMPORTANT MOVS FROM REGENERATING THE MINIMAL CUTSETS OF A PRA

LCI-MOV-HW-MV13A
LCI-MOV-HW-MV13B
LCI-MOV-HW-MV13C
LCI-MOV-HW-MV13D
LCI-MOV-CC-MV25A
LCI-MOV-CC-MV25B
LCS-MOV-HW-MV7A
LCS-MOV-HW-MV7B
LCS-MOV-HW-MV7C
LCS-MOV-HW-MV7D
LCS-MOV-CC-MV12A
LCS-MOV-CC-MV12B
HSW-MOV-CC-MV174
HSW-MOV-CC-MV176
RCI-MOV-CC-MV20
RCI-MOV-CC-MV21
RCI-MOV-CC-MV131
RCI-MOV-CC-MV132

As input to a validation procedure, the proposed prioritization approach is first of all carried out and the priority classes of MOVs are determined along with their testing schedules, if testing schedules are also determined. A validation procedure then consists of the following steps:

1. Identify all groups of MOVs which have the same design and same function. For each MOV group, set the individual MOV failure rates to 8.7×10^{-2}. Set the common cause failure (CCF) probabilities of the MOVs in each similarity group to be equal to 1 to reflect a high likelihood of all the MOVs in the group being affected if one is.

2. Identify the highest priority set of MOVs to be tested. Remove the high CCF probabilities from these MOVs and set the CCF probabilities to their nominal PRA values. Also, set the failure rates of the first priority class of MOVs to be tested to their nominal PRA values. Do not modify any of the other MOV failure rates or probabilities.

3. Calculate the risk using the PRA under the state defined in Step 2. Regenerate the minimal cutsets as part of the PRA run. The calculated risk level represents the risk level which is achieved after having tested those MOVs identified as being priority by the prioritization approach.

4. If several priority classes are identified then repeat Steps 2 and 3 except that the CCF probabilities and failure rates of the next lower priority class of MOVs are modified. All other failure rates and failure probabilities are kept at their values in the previous step. The results represent the risk level when the MOVs have also been tested in the next priority class which has been identified. Repeat this step until all priority classes are evaluated which are to be tested.

If the groups of MOVs which have common cause failures are uncertain, then several PRA runs can be carried out to evaluate the sensitivity to these groupings. Also, as a sensitivity study, after testing, instead of setting the MOV failure rates to their nominal PRA values they can be set to 8.7×10^{-2} to reflect the situation where the individual MOV failure rates remain at these higher values after testing.

Conclusions

The plant PRA can be a potentially useful and powerful tool for helping to define an effective response to GL 89-10. The plant PRA can be used to prioritize the MOV dynamic tests. The plant PRA can also be used to determine test schedules for the MOVs. In order for the PRA to be validly used to respond to GL 89-10, various issues need to be validly addressed. Eleven issues are specifically identified and responses to these issues are outlined. The issues of joint MOV importance, PRA truncation, and validation of the proposed approach are specifically highlighted and more detailed response considerations are described. As in all PRA applications, sensitivity studies and uncertainty considerations should be incorporated in the

PRA evaluations. If these issues are addressed, then a risk-minimized and burden-optimized response to GL 89-10 can be developed.

References

1. U. S. Nuclear Regulatory Commission, "Safety-related Motor-Operated Valve Testing and Surveillance", Generic Letter 89-10, June 28, 1989.

2. W. E. Vesely, "Evaluation of Allowed Outage Times (AOTs) From a Risk and Reliability Standpoint", NUREG/CR-5425, August 1989.

3. I. S. Kim, S. Martorell, W. E. Vesely, and P. K. Samanta, "Quantitative Evaluation of Surveillance Test Intervals Including Test-Caused Risks", NUREG/CR-5775, February 1992.

4. W. E. Vesely, R. E. Kurth, and S. M. Scalzo, "Evaluations of Core Melt Frequency Effects Due to Component Aging and Maintenance", NUREG/CR-5510, June 1990.

Aging Management of Light Water Reactor Concrete Containments

V. N. Shah
Idaho National Engineering Laboratory
EG&G Idaho, Inc.
Idaho Falls, Idaho 83415

C. J. Hookham
Consultant, Formerly with Multiple Dynamics Corporation

Abstract

This paper evaluates aging of light water reactor concrete containments and identifies three degradation mechanisms that have potential to cause widespread aging damage after years of satisfactory experience: alkali-silica reactions, corrosion of reinforcing steel, and sulfate attack. The evaluation is based on a comprehensive review of the relevant technical literature. Low-alkali cement and slow-reacting aggregates selected according to ASTM requirements cause deleterious alkali-silica reactions. Low concentrations of chloride ions can initiate corrosion of the reinforcing steel if the hydroxyl ions are sufficiently reduced by carbonation, leaching, or magnesium sulfate attack. Magnesium sulfate attack on concrete can cause loss of strength and cementitious properties after long exposure. Techniques to detect and mitigate these long-term aging effects are discussed.

Introduction

This paper evaluates the long-term aging concerns related to light water reactor (LWR) reinforced and prestressed concrete containments and foundation elements. The paper also presents insights for effective management, which will maintain the required containment structural integrity. The paper is based on a comprehensive review of the technical literature related to containment design and construction, material degradation, field experience, and insights gained form inspection, testing, monitoring, and mitigation activities. The paper was prepared for the USNRC Nuclear Plant Aging Research Program. No new basic research or development has been carried out in its preparation.

Review of the documented performance of the seventy concrete containments in the United States, 29 of which are reinforced concrete and 41 are prestressed concrete, has revealed no widespread aging damage except for a few instances of age-related degradation. However, the operating experience with LWR concrete containments is less than 25 years, and the main question is whether there are any degradation mechanisms that could cause widespread aging damage to the concrete containments after years of satisfactory performance.

Review of the operating experience with nonnuclear concrete structures in Europe has revealed that many structures built during the 1950–70s have experienced widespread aging

damage after 10 to 15 years of satisfactory experience. Three examples of such damage include use of high-alumina cement that resulted in the concrete slowly loosing its strength, use of calcium chloride as an admixture that caused corrosion of reinforcing steel, and use of new cement that resulted in concrete with high permeability, which caused rapid carbonation of the concrete. These examples are described in the Appendix. These specific concrete aging concerns have been addressed by the LWR containment design in the United States and, therefore, are not relevant. However, the experience with nonnuclear concrete structures suggests the question raised in the preceding paragraph.

The paper first discusses the containment design and materials. Then, it evaluates three degradation mechanisms that do have a potential for causing long-term widespread aging damage to concrete containments: Alkali-silica reaction, corrosion of reinforcing steel, and sulfate attack. Different nondestructive testing techniques are also discussed and various mitigation techniques are identified.

Concrete Containment Design

Reinforced concrete containments were constructed using concrete and deformed, reinforcing steel bars (mild carbon steel) exclusively in all elements, including the foundation (basemat). Prestressed concrete containments were constructed using both conventional reinforcing steel and prestressed steel elements to provide the strength and ductility necessary for required functions. Several different designs are used for pressurized water reactor (PWR) and boiling water reactor (BWR) concrete containments. Figure 1 shows a PWR containment, which consists of a cylindrical wall, dome, and basemat. A portion of the containment is belowgrade and exposed to soil

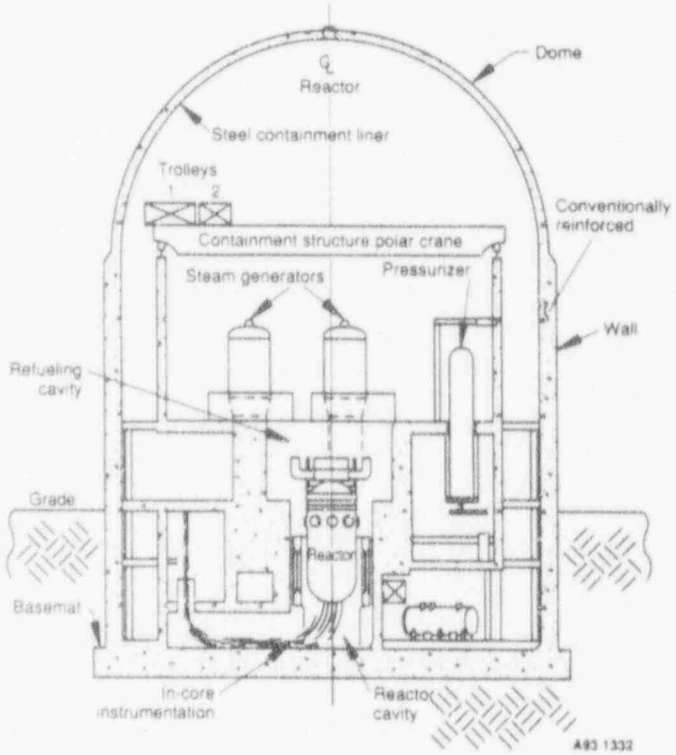


Figure 1. PWR reinforced concrete subatmospheric containment.

and ground water. The upper portions of the walls and dome are abovegrade and exposed to the external environment. (The internal concrete structures are not within the scope of the paper.)

Figure 2 shows a typical cross section through a reinforced concrete containment wall. The figure also identifies the typical constituents of containment construction. The most important design and construction feature of these containments is the cover concrete on the exterior. The minimum cover thickness has been specified by structural design codes—ACI 1989, ASME 1992, and earlier versions—based on anticipated exposure conditions and type of structure; the minimum design cover thickness varies from 19 to 76 mm. Cover concrete generally has the same properties, consistency, and performance as internal structural concrete, but it is not used for structural resistance to loads. Rather, the cover is designed to protect the reinforcing steel and prestressing steel from corrosion and protects the interior structural concrete of the containment from aggressive chemical attack, provided the cover is constructed properly and crack formation is controlled. The walls and domes of the reinforced concrete vessels are more prone to concrete cracking than their prestressed counterparts, in which the concrete is subject to a steady-state compressive loading from the tendons.

The inside surface of a containment is typically lined with welded carbon steel plates, as shown in Figure 2, which are generally coated with a zinc-rich primer and a polyamide epoxy or modified phenolic as intermediate and top coatings to protect against corrosion. In some BWR plants, the inside surface of the suppression pool is lined with stainless steel plates.

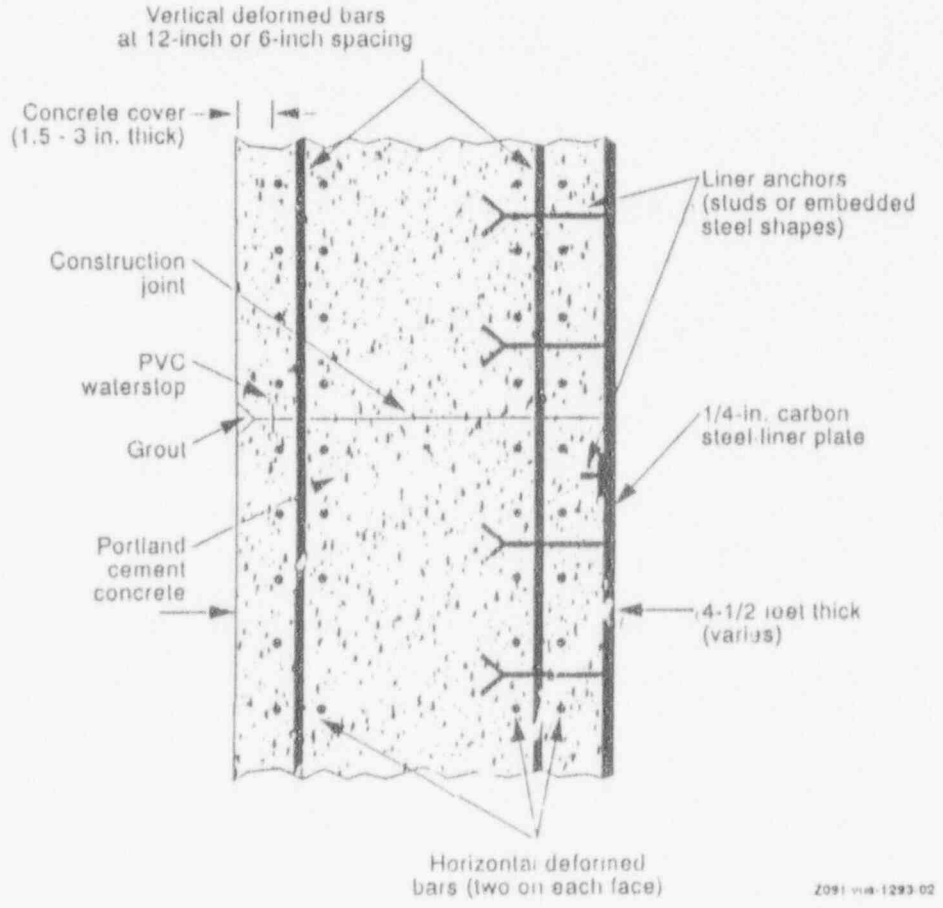


Figure 2. Typical PWR reinforced concrete containment wall section.

The design and construction of concrete containments and basemats generally employed a number of other nonstructural components and systems to protect the containment vessel and structural materials from environmental exposure: waterstops, joint sealant, dewatering systems at sites where groundwater levels are high or flooding is possible, and cathodic protection systems at a few plants to reduce corrosion of the piles. Waterstops and joint sealants are used in belowgrade and certain abovegrade construction joints in the concrete, as shown in Figure 2. Construction joints are parallel planes of concrete at which the installation of concrete was discontinued and fresh concrete was later poured against the previous concrete pour. The term construction joint may also refer to locations where building components intersect (e.g., dome to wall). Waterstops restrict fluid or gas intrusion and passage along the joint. They are typically made from polyvinyl chloride and are orthogonal to the construction joint. There are many other types of stop and sealant materials, and performance criteria exist and are identified in ACI Report 504R-77 (ACI 1977). Should a waterstop fail to perform its function, water may intrude because the construction joint would act like a crack. Recent testing has shown that the performance of water stop material may be influenced by temperatures similar to those experienced by the concrete containment wall (Deans, Sato, and Bhat 1989). The magnitude of these temperatures is determined by the thermal gradients present in the wall, which result from the difference between internal (operating) and external (natural) temperatures and from startup/shutdown cycles.

The exterior surface of the belowgrade portion of the containment is coated with material such as coal tar epoxies and water proofing compounds, and the basemat is covered with waterproof rubber membranes that protect embedded steel from corrosion. The waterproofing compounds traditionally included bituminous saturated felt or fabric layered and cemented with coal tar pitch or asphalt. The outside surface of the abovegrade portion of some containments is coated with alkyds or urethane topcoat over various primers.

Containment Concrete Materials

The concrete that was typically used in LWR containment structures consists of Type II portland cement, coarse and fine aggregates, water, admixtures, and curing agents for improved performance of the concrete. Desired strength and performance properties typically determined the proportion of these constituents in the concrete mix. Type II portland cement, which conforms to ASTM C 150 (ASTM 1992a), has been used in the containments built in the United States because it is more resistant to sulfate attack than the more common Type I cement. Another important feature of Type II portland cement is that it has a lower heat of hydration than Type I cement. As the sections of concrete containments are relatively thick, this lower heat of hydration reduces the potential for thermal shrinkage cracks. Coarse aggregates (sizes larger than 4.75 mm) include gravels and crushed stones; fine aggregates (sizes smaller than 4.75 mm) include sand. Only fine aggregates are used in the grout used for sealing construction joints, bonded tendon systems, and other applications. Approximate values of the initial water-to-cement ratios (weight basis) for the reinforced and prestressed concretes were about 0.5 and 0.35, respectively.

The concrete mixes used in the containment construction typically contain fewer admixtures and curing agents than are used in current industry practice. Therefore, the potential of concrete degradation from incompatibilities of multiple admixtures is low. The principal admixtures were those to improve air entrainment and workability. Air-entraining admixtures improve the

durability of concrete exposed to freeze-thaw cycling. Mineral admixtures such as pozzolans, which have been used in containment construction at newer vintage plants, reduce thermal shrinkage and cracking. Experience with these admixtures, though not extensive, show that they are essentially inert following curing.

The main solid constituents of well-hydrated cement paste are calcium silicate hydrate, calcium hydroxide, and calcium sulfoaluminates. The calcium silicate hydrate phase is the principal solid constituent of the hydrated paste, having a large surface area, which may range between 200 to 300 m^2/g (Brown and Clifton 1988), and making up 50 to 60% of the volume of the solids. The principal source of strength in the hydrated cement paste results from van der Waals' forces of attraction between solid surfaces; these forces are the main cause of adhesion between different solid constituents of the hydrated paste and also between the hydrated paste and the aggregates (Mehta 1986). Because of its large surface area, the calcium silicate hydrate phase is the major contributor to the strength of the hydrated cement paste. The strength-contributing potential of the other two constituents is limited because of their smaller volume and surface area; calcium hydroxide crystals make up to 20 to 25% of the volume of the solids, whereas calcium sulfoaluminate compounds (tricalcium aluminate phase) occupy 15 to 20%. The presence of calcium hydroxide is essential for stability of the calcium silicate hydrate phase and corrosion protection of the reinforcing steel. Therefore, any substantial loss of these solid constituents would lead to reduction in concrete strength and corrosion of reinforcing steel; such losses can be caused by carbonation, magnesium sulfate attack, or leaching.

The compressive strength of concrete increases as the water-to-cement ratio decreases. The minimum compressive strength in reinforced concrete containments was typically 27.6 MPa (4 ksi) after 28 days of curing, whereas that in a prestressed concrete containment was typically in the range of 41 to 48 MPa. The tensile strength of concrete for a water-to-cement ratio of 0.5 is about 10 times lower than the compressive strength (Neville 1981).

Concrete Permeability

Permeability is an important property of concrete that affects both initiation and propagation of its aging degradation. It is a measure of the ease with which a fluid flows into the concrete. Three materials-related factors determine the permeability of concrete: permeability of the hydrated cement paste, permeability of large aggregates, and microcracks at the cement paste-aggregate interface. The size and continuity of capillary voids in the hardened cement paste determine the permeability of the paste. The coefficient of permeability for freshly mixed cement paste is on the order of 10^{-4} to 10^{-5}cm/s. As hydration of cement progresses, the pores are reduced in size and lose their interconnections; the permeability of the paste is thereby reduced, unless the hydration process is interrupted, for example, by a reduction in surrounding temperature or by application of a sealant on the exposed surface. The coefficient of permeability for hardened paste is lower for a lower initial water-to-cement ratio; the coefficient of permeability is on the order of 10^{-11} cm/s for an initial water-to-cement ratio of about 0.4 and of 10^{-8} cm/s for a ratio of 0.7 (Mehta 1986). The permeability of aggregates generally increases as aggregate size increases (Mehta 1986). The coefficients of permeability of large aggregates varies between 10^{-8} cm/s for sandstone and 10^{-11} cm/s for quartz diorite. The resulting permeability of concrete that has aggregate particles of low permeability is expected to be low.

However, the permeability of concrete can be higher than that of the hydrated cement paste or of the aggregates because of microcracking at the aggregate-paste interface.

Two additional factors related to construction and design also affect the overall permeability of a concrete component: good surface-finishing practices, which include thorough consolidation and curing, and component thickness. Concrete permeability is lower when good surface finishing practices are followed because the pore structure is more compact and local discontinuities are not present. The fluid flow path in concrete, which connects capillary pores and microcracks, also becomes more tortuous as concrete thickness increases; therefore, resistance to the fluid flow through the thickness increases.

Concrete Containment Degradation Mechanisms

There are several degradation mechanisms associated with LWR concrete containments. Those that have potential to cause significant aging damage to the containment structure are referred to as primary degradation mechanisms, which include aggressive chemical attack, alkali-aggregate reactions, leaching, corrosion of reinforcing and prestressing steels, and stress relaxation of prestressed steel. Aggressive chemical attack includes attack by groundwater, acidic precipitation, and chemical spills in the plant. Sulfates found in groundwater (and also in various soils) can chemically interact with the constituents of the hydrated cement paste and can cause two types of damage; such attack is called sulfate attack. Sulfate interaction with calcium sulfoaluminate forms an expansive product that can cause concrete cracking after short exposure. Use of Type II Portland cement has made the containment concrete resistant to this cracking. The sulfates, especially magnesium sulfates, can also chemically interact with calcium hydroxide and calcium silicate hydrate and, after prolonged exposure, cause loss of concrete strength and then concrete cracking. This type of sulfate attack is also called magnesium attack.

Alkali-aggregate reactions are internal reactions between alkalis in the cement or from other sources and certain reactive components of the aggregates. These reactions can form hygroscopic products, which swell in the presence of moisture and eventually cause concrete cracking. The alkali-aggregate reactions include alkali-silica, alkali-silicate, and alkali-carbonate reactions. Leaching includes dissolution and hydrolysis of several constituents present in the hydrated cement paste by flowing soft or pure water. Leaching reduces the pH of the pore solution and concrete strength, and makes concrete more porous. Corrosion of reinforcing steel is initiated by chlorides, carbonation, or stray current and eventually causes the concrete cover to crack, disbonding between the concrete and the steel, and loss of reinforcing bar cross section.

The prestressing steel (tendons) is susceptible to pitting, general corrosion, stress corrosion cracking, and hydrogen embrittlement. A small reduction in load bearing area can ultimately lead to reduced structural capacity. Relaxation of the prestressed steel, along with creep and shrinkage of the concrete, produces a loss of prestress, which in turn produces a reduced level of compressive stress in the containment concrete. Excessive relaxation can have significant consequences during an accident because the concrete and steel liner could enter into a tensile state, resulting in cracking. Industry results to date suggest that relaxation of both the tendons and concrete is generally within the design range. Because of concern over excessive loss of prestress, inservice monitoring of the prestress in tendons is required.

Mechanisms not likely to cause significant aging damage are referred to as secondary degradation mechanisms; these include freeze/thaw cycling, settlement and shrinkage, creep, thermal exposure damage, fatigue, and radiation damage. These mechanisms have been properly addressed in the design and construction of the U. S. containments. Concrete used in the construction of containments typically contains an air-entraining admixture, water-cement ratios below 0.5, and appropriate natural aggregates. Therefore, widespread damage caused by freeze/thaw cycling is not likely. Initial settlement and shrinkage effects generally manifest themselves during the construction phase and early years of operation and are not long-term aging concerns. Design requirements and use of quality control measures during the containment construction have prevented significant settlement and shrinkage. Creep deformation of the concrete containments has generally been within predicted design values, as witnessed by the relative absence of documented volume changes. Therefore, creep is not likely to be a primary degradation factor within the concrete containment vessels. However, reliable estimates of creep deformation for prestressed concrete containments are important because concrete creep is a contributor to loss of the prestressing.

Concrete containments are generally exposed to temperatures less than 65°C (150°F) under normal operating conditions, except the concrete around the feedwater and main steam line penetrations in a few older plants where the penetrations are not cooled. Therefore, widespread degradation of containment concrete caused by thermal exposure is not expected. Fatigue of the concrete containments is not a major concern because the normal plant operation produces stresses of relatively small amplitudes. Fatigue-related damage has not been reported in the Nuclear Plant Experience Database nor in the Nuclear Plant Reliability Data System. Radiation does not have a detrimental effect on the concrete containments because the radiation levels to which LWR containment structures are exposed are below the threshold value. The reasons for low radiation levels are the large distances between the containment and the nuclear steam supply system (NSSS) equipment and the attenuation provided by the structures and equipment that surround the NSSS equipment.

Long-Term Aging Concerns

As discussed above, there are three primary degradation mechanisms that could cause widespread aging damage to the concrete containments in the United States after a long term of satisfactory operation: alkali-silica reactions, corrosion of reinforcing steel (also prestressing steel), and sulfate attack, particularly magnesium sulfate attack that causes loss of concrete strength. Hookham (1991) has also identified these three mechanisms as having the greatest potential for producing aging damage. The presence of these mechanisms is not easily detectable and they have potential to cause widespread concrete cracking and strength loss.

Damage caused by leaching and sulfate attack, which produces expansive products, occurs after a relatively short exposure and is detectable at the concrete surface; no widespread damage caused by these two mechanisms has been reported. The relaxation of prestressed steel was monitored and found to be within design limits. Therefore, these mechanisms do not pose a long-term aging concern.

Alkali-Silica Reaction

The most common alkali-aggregate reaction is the alkali-silica reaction, in which hydroxyl ions react with certain forms of silica to form an alkali-silica gel. Concrete deterioration caused by an alkali-silica reaction has been reported in several countries. For example, this reaction has caused widespread deterioration of concrete structures in the United Kingdom over the past 10 to 15 years and has seriously affected hospitals and car parks, requiring major repairs or demolition. The most extensive damage has been reported in highway bridges, and some damage has been reported in dams (Bungey 1991). In the United States, aggregates containing active silica are generally found to occur in the western states. No damage to the concrete containments resulting from alkali-silica reaction has been reported in the United States because such aggregates had been identified prior to construction using the ASTM tests and excluded from the containment concrete. However, recent research results and field data show that the ASTM tests are not fully effective in avoiding the alkali-silica reactions. Therefore, there is a potential long-term aging concern associated with alkali-silica reactions. We first describe the alkali-silica reactions, then discuss the deficiencies of the ASTM tests, and then discuss the detection and mitigation techniques.

Damage Caused by Alkali-Silica Reaction. The actual chemical reactions and mechanisms that produce the expansion and cracking are complex and not well-understood. It appears that the presence of both hydroxyl ions and alkali metal ions (sodium and potassium) is necessary for the reaction. In as much as large amounts of calcium hydroxide are present in hydrated cement paste, this reaction is limited by the supply of the alkali-metal ions. The alkali-metal ions are present in the cement and may also be available from other sources, such as alkali-containing admixtures and sea water that had penetrated into the concrete. Active silica from the aggregate dissolves in the pore solution and forms alkali-silica gel. This dissolution is a function of the pH of the pore solution. Only small amounts of silica dissolve at a pH of 12.5, but significantly larger amounts dissolve at a pH of 13 (Clifton and Knab 1989).

Note that the presence of alkali-silica gel by itself is not harmful, and not all types of alkali-silica gel are hygroscopic. Only hygroscopic gel, which swells in the presence of water, is harmful. As the amount of water imbibed increases, swelling increases. The resulting internal pressure, if large enough, can cause macrocracking on the concrete surface. The crack pattern in unreinforced concrete is irregular and is, therefore, referred to as map cracking. The cracks in reinforced concrete are often parallel to the main reinforcement (Clark 1991). Reactive coarse aggregate may lead to pop-out. Gel slowly leaking out through the cracks may indicate the presence of a reaction. The strength and stiffness of the concrete is reduced by concrete cracking. Critical locations include the portions of the containment exposed to moisture.

Factors Affecting the Damage Rate. Several factors influence the rate and amount of swelling and disruption: size and amount of reactive aggregates, aggregate porosity, amount of alkali in the concrete, mix proportions of the concrete, and the availability of water. When a large amount of reactive silica is present in a finely divided form (under 75 μm), there can be considerable evidence of reaction, but the reaction product is innocuous (nonexpanding) alkali-silica gel. On the other hand, if the size of reactive silica is in the range of 1 to 5 mm, the resulting reaction product is expansive alkali-silica gel (Mehta 1986, Neville 1981). The reactive mineral

may be present in a small amount and its distribution may vary from aggregate to aggregate. The magnitude of swelling decreases with the increase in aggregate porosity because expanding gel can be accommodated by porous aggregates without causing concrete expansion.

The relative amounts of the sodium and potassium oxides in the cement affects the extent and rate of the swelling. Potassium oxide causes expansion to start earlier, but the rate of expansion is lower than that caused by sodium oxide. Hence, the final expansion is greater with sodium oxide. The potassium oxide content is greater in the cements used in the United Kingdom and Germany, whereas the sodium oxide content is greater in some cements used in North America and Australia (Clark 1991).

ASTM Tests for Identifying Reactive Aggregates. Much of the research to date relates to identifying during construction the cause of and methods to prevent alkali-silica reactions. Three test methods were developed in the 1960s for identifying reactive aggregates: ASTM Practice for Petrographic Examination of Aggregates for Concrete (C 295); ASTM Test for Potential Reactivity of Aggregates (C 289), which is a rapid chemical test; and ASTM Test for Potential Alkali Reactivity of Cement-Aggregate Combinations (C 227), which consists of a mortar bar expansion test (Smith and Raba 1986, Stark 1979). If an aggregate is found to be suspect in the petrographic examination, the chemical test is performed to further determine the magnitude of the reactive aggregates. If the chemical test indicates that the aggregate is potentially dangerous, then a mortar bar expansion test is performed. The specimens in a mortar bar expansion test are kept over, but not in contact with, water in a storage container, which is then sealed and kept at about 38°C (100°F). The changes in specimen length are measured after certain time intervals as specified in the standard.

In normal practice, the mortar bar expansion test (ASTM C 227) has been performed only with high-alkali cement (alkali content greater than 0.6% of equivalent Na^2O) because earlier laboratory tests with certain reactive aggregates showed that excessive expansion can be avoided if the cement alkali level does not exceed 0.6%. Subsequently, the 0.6% cement alkali level was interpreted as an exact cutoff point (below which excessive expansion can be avoided) and applied to other reactive aggregates without further testing. For high-alkali cement, the test requires that the expansion of a mortar bar held above the water surface in a sealed container should not exceed 0.05% after three months and 0.1% after six months.

The expansion caused by the alkali-silica reaction was not supposed to be a concern for the concrete containments because the above mentioned ASTM tests were used to avoid certain reactive aggregates. However, recent field and laboratory results show that use of low-alkali cement (<0.6% equivalent Na2O) or slow-reacting aggregates which pass the ASTM test (C 227), may still result in excessive expansion and cracking. Deleterious alkali-silica reaction involving low-alkali cement has been identified in pavements, bridge structures, sidewalks, and curb concrete. Figure 3 shows an example of severe cracking in a bridge deck caused by the use of low-alkali cement. Some concrete with slow-reacting siliceous aggregates in the eastern states that passed the ASTM test (C 227) has shown the deleterious effects of an alkali-silica reaction. Figure 4 shows an example of severe cracking in a bridge deck caused by the use of slow-reacting aggregates. Because of these deficiencies of the ASTM tests, there exists a potential concern for a deleterious alkali-silica reaction in concrete containments with low-alkali cement or slow-reacting aggregates.

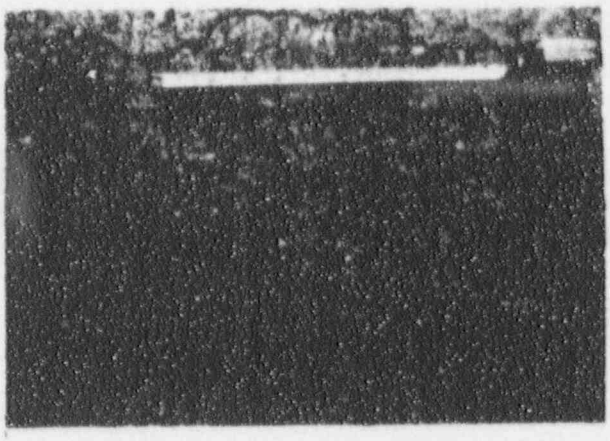


Figure 3. Severe cracking in bridge deck caused by reactions between low-alkali cement and aggregates containing active silica. Courtesy of D. Stark, Portland Cement Association, Skokie, IL.

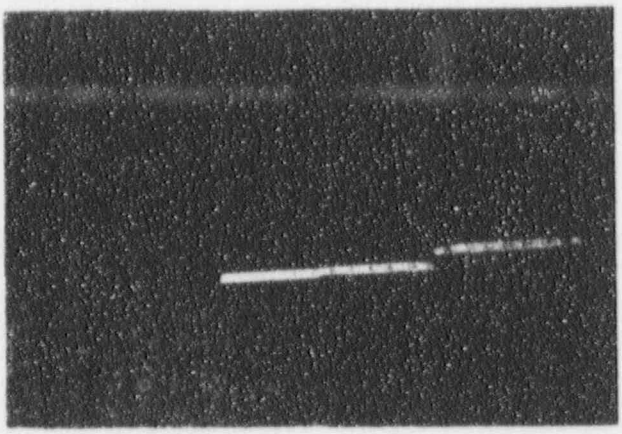


Figure 4. Severe cracking in bridge deck caused by reactions between slow-reacting aggregates and cement. Courtesy of D. Stark, Portland Cement Association, Skokie, IL.

The ASTM test can be improved by making two changes. First, a separate cutoff point for the cement alkali level can be determined for each of the reactive aggregates under consideration. Second, the test period can be extended to nine months, for example, and the acceptable expansion limit can be lowered to below 0.1%.

Detection and Mitigation. An in situ test was recently developed for identifying alkali-silica reaction products in concrete. The reaction products are identified by staining them with uranyl ions, which have a characteristic greenish yellow fluorescence under short wave ultraviolet light. This staining technique appears to uniquely identify the products of alkali-silica reaction (Natesaiyer, Stark, and Hover 1991). Thus, this technique can detect the alkali-silica reaction taking place before any concrete expansion and cracking occur. Ultrasonic pulse velocity and attenuation measurements have been found sensitive to concrete expansion and cracking caused by alkali-silica reaction.

Excessive expansion of alkali-silicate gel can be averted if the relative humidity of the concrete is maintained below 80% and a coating is maintained on the surface to prevent any ingress of moisture into the concrete.

Corrosion of Reinforcing Steel

Properly installed portland cement concrete protects reinforcing steel, liner anchorages, and other metallic embedments against corrosion because portland cement concrete generally has high alkalinity (pH between 12 and 14) and, therefore, has a passivating effect on embedded steel.

In addition, the concrete provides a protective barrier against corrosive agents. The concrete has high alkalinity because its pore solution is saturated with calcium hydroxide and, in addition, it contains potassium and sodium hydroxides (Locke 1983). A protective oxide layer is formed on the steel surface in the presence of an alkaline environment. This is termed passivation of steel. Therefore, corrosion of the reinforcing steel is unlikely unless the steel is depassivated as a result of the presence of aggressive chemicals such as chloride ions in the pore solution or reduced alkalinity of the solution, which could be caused by carbonation. However, corrosion initiation is likely to take a long time because low permeability concrete and a 50-mm-average concrete cover are used in LWR concrete containments. For example, corrosion initiation by carbonation could take about 100 years.[a] (As discussed in the Appendix, such corrosion has taken place in much shorter periods in certain nonnuclear concrete structures because of high concrete permeability.) Once corrosion is initiated, concrete cracking and spalling can occur within 5 to 20 years. Corrosion would also cause loss of bond between the reinforcing steel and the surrounding concrete, and eventually would lead to reduced tensile capacity of the structure. The presence of stray electric current can also cause corrosion of reinforcing steel, but it does not pose a long-term aging concern. We first discuss the passivation of the reinforcing steel, the factors affecting initiation and growth of chloride-induced corrosion and carbonation-induced corrosion, then then discuss the detection and mitigation of reinforcing steel corrosion.

Passivation of Reinforcing Steel. Figure 5 is a simplified Pourbaix diagram for pure iron in contact with a chloride-free aqueous solution at 25°C. Reinforcing steel embedded in concrete is highly related to iron in an aqueous solution. The diagram describes the corrosion behav-

a. Personal communications with J. R. Clifton, National Institute of Standards and Technology, July 1993.

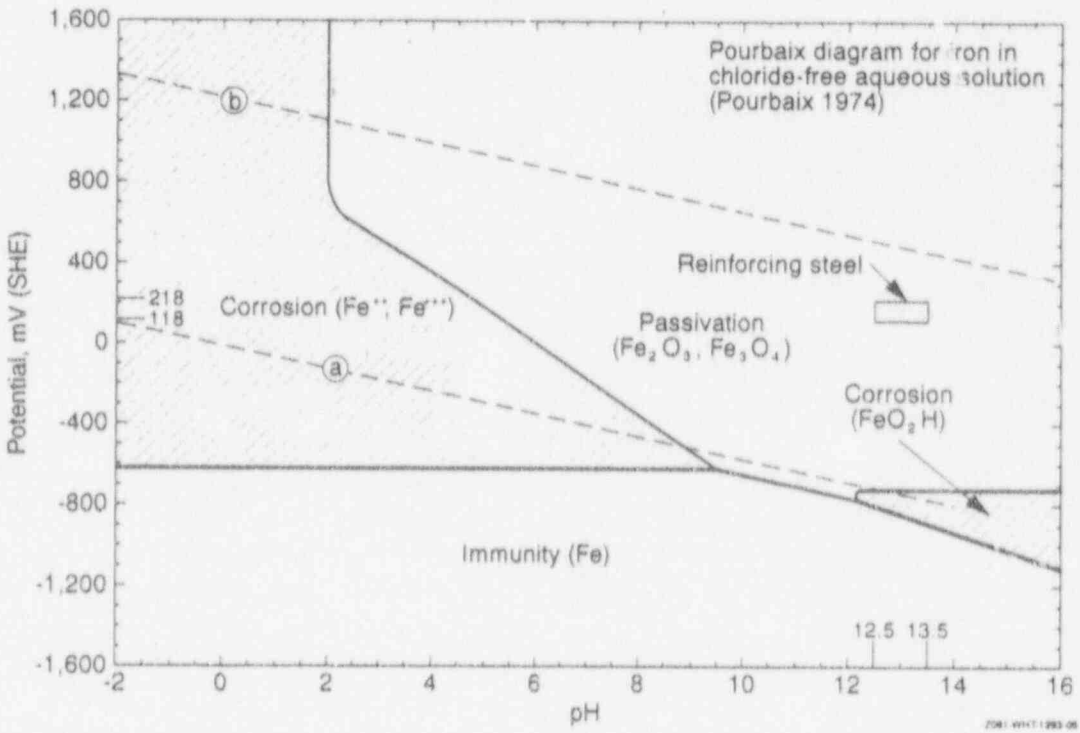


Figure 5. Pourbaix diagram for iron in a chloride-free aqueous solution (Pourbaix 1974). The shaded box shows typical values of potentials and Ph levels for reinforcing steel.

carbon steel. Penetration of chlorides to the steel surface destroys the passivity and makes the steel susceptible to pitting or general corrosion, depending on the electrochemical potential and pH. However, the passivity is not completely destroyed at pH levels above about 6. The diagram indicates that, even with a very high chloride concentration, a region of perfect passivity remains. This suggests that the corrosion of steel exposed to a high-chloride environment can be prevented by polarizing it to a potential in this region of perfect passivity.

Chloride-Induced Corrosion of Steel. Figure 7 illustrates the electrochemical process of corrosion of reinforcing bar embedded in concrete. The process consists of anodic and cathodic reactions. As discussed above, the anodic reaction cannot occur until the passive iron oxide film is made permeable by the action of Cl^- ions. The cathodic reaction cannot occur until a sufficient supply of oxygen and moisture are available at the steel surface. The anodic and cathodic reactions must balance each other; if either is limited, the corrosion process as a whole is limited. As shown, the electrons flow in the steel from anode to cathode, and the hydroxyl ions (OH^-) flow in the electrolyte (pore solution) from cathode to anode. The electric current flows in the opposite direction. The current flowing in the electrolyte is called anodic current.

Corrosion of reinforcing steel by chloride ions depends on several factors, including chloride concentration, cement type, chloride penetration rate, oxygen level, concrete resistivity, and temperature. The first three factors affect the passivity of reinforcing steel and, thus, determine the time required to initiate corrosion. The last three factors dictate the corrosion rate once the passivity is destroyed.

Factors Affecting Corrosion Initiation — There are two sources of chlorides: internal chlorides present in the concrete mix and external chlorides from the sources such as sea water, brackish ground water, and soils—that diffuse through the cured concrete section. However, not all of these chlorides are responsible for corrosion. Only the water soluble chlorides present in the pore solution are responsible. The water soluble chlorides are not uniformly distributed along reinforcing steel; this nonuniform distribution may lead to the development of a corrosion cell.

The threshold value of chloride ions necessary to initiate corrosion of reinforcing steel depends on the level of hydroxyl ions in the pore solution, which is reduced by leaching or car-

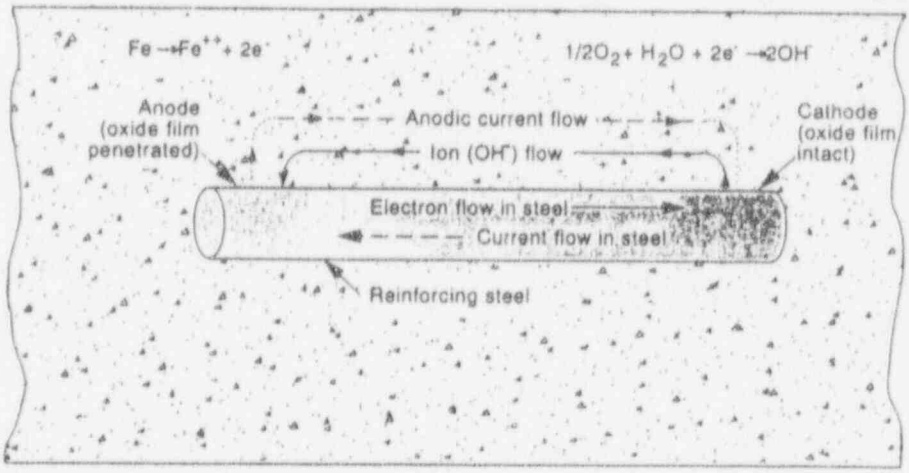


Figure 7. Electrochemical process of corrosion of reinforcing steel.

ior of the iron under equilibrium conditions as a function of electrode potential and the alkalinity or acidity of the surrounding solution, specifically the concrete pore solution. This diagram is also called a potential-pH diagram; the vertical axis represents the potential of the iron measured with reference to a standard hydrogen electrode (SHE), and the horizontal axis represents the pH level of the solution in immediate contact with the metal surface. The typical range for the potential of the reinforcing steel embedded in concrete is 118 to 218 mV (standard hydrogen electrode), which is equivalent to -100 to -200 mV (standard Cu/CuSO4 electrode). The potential increases as the oxygen content in the solution increases. Figure 5 can be divided into three regions in which the metal or its different chemical compounds are stable. In the region marked passivation, the product of the anodic reaction between the iron and the solution is an oxide (either Fe_2O_3 or Fe_3O_4), which protects the steel. The presence of oxygen is necessary for the steel to reach a passive state. In the region marked immunity, the reaction rate is sufficiently low that the absence of corrosion can be expected. In the region marked corrosion, the corrosion products are ferrous or ferric ions when the pH values are below about 9; the corrosion products are complex iron ions when the pH values are above about 12. This is the region of general corrosion for iron. The basis for the passivity of the steel in an alkaline concrete environment is apparent from the diagram. There are three potential cathodic reactions that may take place. In the region between the sloping lines a and b water is stable (no evolution of oxygen or hydrogen takes place), and oxygen reduction takes place. Above line b oxygen evolution takes place, and below line a both oxygen reduction and hydrogen evolution take place. Oxygen reduction is the main cathodic reaction in most cases of reinforcing steel corrosion.

Figure 6 is a modified Pourbaix diagram for iron in contact with an aqueous solution containing 355 ppm Cl^- (Pourbaix 1974). The diagram shows the effect of chlorides on the passivation of iron and can be used to describe the effect of chlorine in the surrounding concrete on the

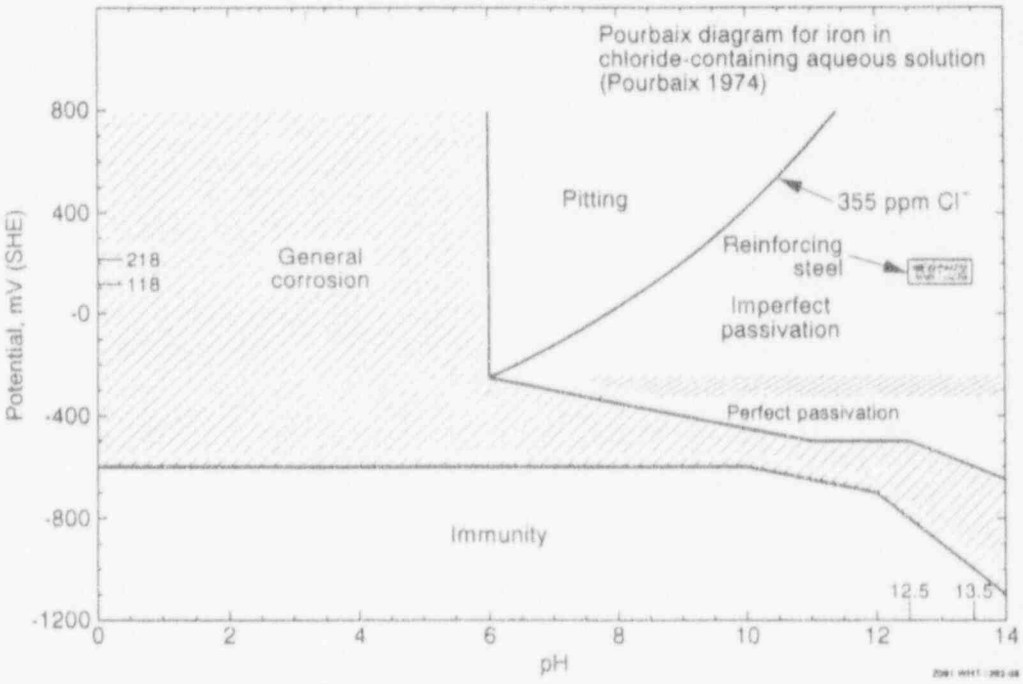


Figure 6. Modified Pourbaix diagram for iron in a solution containing 355 ppm Cl^- (Pourbaix 1974). Shaded box shows typical values of potentials and pH levels for reinforcing steel.

In addition, the concrete provides a protective barrier against corrosive agents. The concrete has high alkalinity because its pore solution is saturated with calcium hydroxide and, in addition, it contains potassium and sodium hydroxides (Locke 1983). A protective oxide layer is formed on the steel surface in the presence of an alkaline environment. This is termed passivation of steel. Therefore, corrosion of the reinforcing steel is unlikely unless the steel is depassivated as a result of the presence of aggressive chemicals such as chloride ions in the pore solution or reduced alkalinity of the solution, which could be caused by carbonation. However, corrosion initiation is likely to take a long time because low permeability concrete and a 50-mm-average concrete cover are used in LWR concrete containments. For example, corrosion initiation by carbonation could take about 100 years.[a] (As discussed in the Appendix, such corrosion has taken place in much shorter periods in certain nonnuclear concrete structures because of high concrete permeability.) Once corrosion is initiated, concrete cracking and spalling can occur within 5 to 20 years. Corrosion would also cause loss of bond between the reinforcing steel and the surrounding concrete, and eventually would lead to reduced tensile capacity of the structure. The presence of stray electric current can also cause corrosion of reinforcing steel, but it does not pose a long-term aging concern. We first discuss the passivation of the reinforcing steel, the factors affecting initiation and growth of chloride-induced corrosion and carbonation-induced corrosion, then then discuss the detection and mitigation of reinforcing steel corrosion.

Passivation of Reinforcing Steel. Figure 5 is a simplified Pourbaix diagram for pure iron in contact with a chloride-free aqueous solution at 25°C. Reinforcing steel embedded in concrete is highly related to iron in an aqueous solution. The diagram describes the corrosion behav-

a. Personal communications with J. R. Clifton, National Institute of Standards and Technology, July 1993.

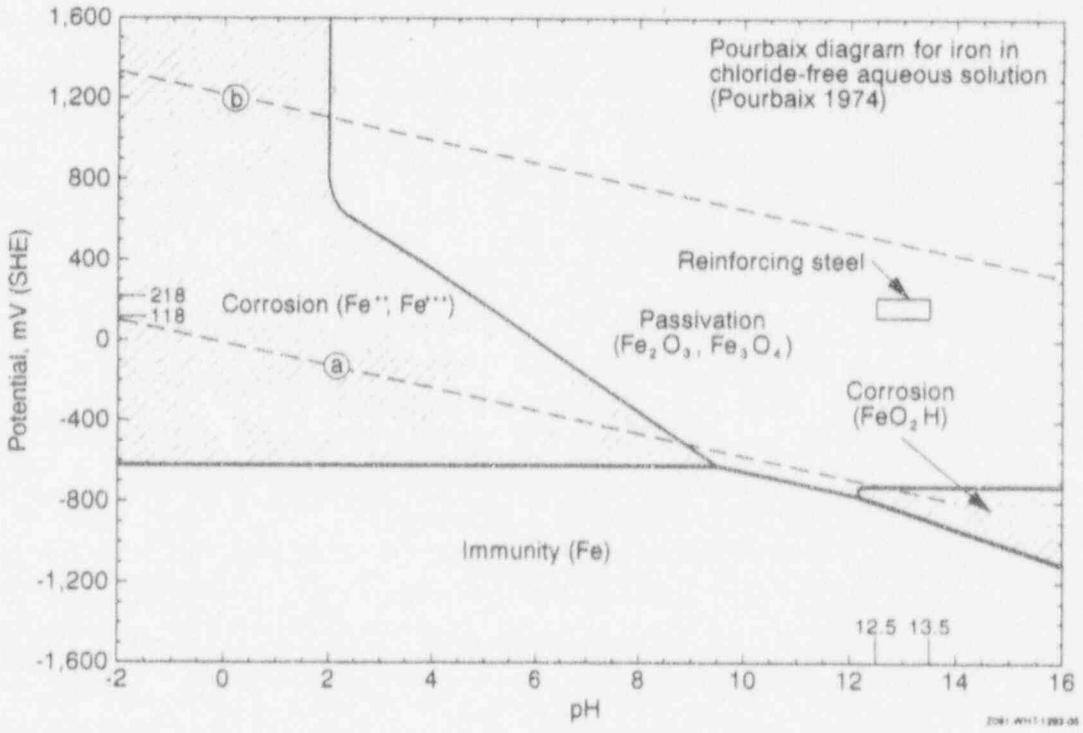


Figure 5. Pourbaix diagram for iron in a chloride-free aqueous solution (Pourbaix 1974). The shaded box shows typical values of potentials and Ph levels for reinforcing steel.

bonation. As the hydroxyl ion level, and, therefore, the pH level, reduces, the threshold value of chloride ions necessary to initiate corrosion also reduces. Research results show that the depassivation of reinforcing steel is a function of the Cl^-/OH^- ratio in the pore solution rather than of chloride content alone (Hausmann 1967, Locke 1986, Rasheeduzzafar 1992). A Cl^-/OH^- ratio of 0.3 has been recommended as a critical ratio below which reinforcing steel is not susceptible to chloride-induced corrosion.

Chloride ion penetration in concrete is by a diffusion process, which is driven by differences in concentration of chloride ions, and by a convection process (also known as bulk flow), which is driven by pressure differences including hydrostatic pressure differences (Pommersheim and Clifton 1990). As the pore size in the containment concrete is in the range of 1.5 to 100 nm, the diffusion process generally controls the penetration. [Chloride ions can easily pass through these pores because their diameters are less than 0.2 nm (Burge 1983).] However, if cracks, even of microscopic size, are present in the concrete, the convection process will control the penetration of chloride ions and other deleterious species. The convection process will also control the penetration if large pressure gradients are present across the concrete section.

Factors Affecting the Corrosion Rate — Dissolved oxygen must be available for corrosion of the reinforcing steel to take place, because oxygen reduction is the main cathodic reaction in a high-pH environment, as shown in Figure 7. [This reaction takes place between lines (a) and (b) in Figures 5 and 6.] The rate of oxygen diffusion is higher for a concrete with a higher initial water-to-cement ratio (ACI 1989). Gaseous oxygen diffuses at a much faster rate in dry concrete than in wet concrete. If the concrete is continuously water-saturated (100% relative humidity), the solubility and diffusivity of oxygen are severely reduced and the oxygen needed to sustain corrosion is not available. As a result, the corrosion rate of reinforcing steel in water-saturated concrete is very small, even in the presence of chlorides. However, as discussed in the following paragraph, a relatively humid environment (less than 100% relative humidity) will support electrochemical reactions. Some test results show that the corrosion rate is maximum at about 95% relative humidity and is about two orders of magnitude higher than the rate at 100% relative humidity (Clifton 1991).

The electrical resistivity of the concrete determines the flow of ions in the pore solution from the cathodic to the anodic areas on the reinforcing steel. The resistivity of the concrete depends mainly on the moisture content of the concrete. The resistivities of very dry concrete (<1 wt% H_2O) and water-saturated concrete (13 to 15 wt% H_2O) are about 10^9 Ohm-cm and 10^3 Ohm-cm, respectively (Locke 1983). A low electrical resistivity of the concrete is conducive to pit formation because it facilitates the migration of ions between small anode and large cathode regions. Significant corrosion is not observed in concrete with a resistivity above 5 to 7×10^4 Ohm-cm (Mehta 1986). If the reinforced concrete is expected to remain dry or protected from moisture during service, then a higher percentage of water-soluble internal chloride ions in the hardened cement (1.0 wt% of cement) is permitted for protection against corrosion of the concrete (ACI 1992). If moisture is present, the limits on the internal chlorides are lower.

Several other factors may influence the initiation and propagation of corrosion within the reinforcing steel and embedment system. These include temperature, stray electrical currents from external sources, possible electrical connection of different reinforcing steel layers, previous con-

carbon steel. Penetration of chlorides to the steel surface destroys the passivity and makes the steel susceptible to pitting or general corrosion, depending on the electrochemical potential and pH. However, the passivity is not completely destroyed at pH levels above about 6. The diagram indicates that, even with a very high chloride concentration, a region of perfect passivity remains. This suggests that the corrosion of steel exposed to a high-chloride environment can be prevented by polarizing it to a potential in this region of perfect passivity.

Chloride-Induced Corrosion of Steel. Figure 7 illustrates the electrochemical process of corrosion of reinforcing bar embedded in concrete. The process consists of anodic and cathodic reactions. As discussed above, the anodic reaction cannot occur until the passive iron oxide film is made permeable by the action of Cl^- ions. The cathodic reaction cannot occur until a sufficient supply of oxygen and moisture are available at the steel surface. The anodic and cathodic reactions must balance each other; if either is limited, the corrosion process as a whole is limited. As shown, the electrons flow in the steel from anode to cathode, and the hydroxyl ions (OH^-) flow in the electrolyte (pore solution) from cathode to anode. The electric current flows in the opposite direction. The current flowing in the electrolyte is called anodic current.

Corrosion of reinforcing steel by chloride ions depends on several factors, including chloride concentration, cement type, chloride penetration rate, oxygen level, concrete resistivity, and temperature. The first three factors affect the passivity of reinforcing steel and, thus, determine the time required to initiate corrosion. The last three factors dictate the corrosion rate once the passivity is destroyed.

Factors Affecting Corrosion Initiation — There are two sources of chlorides: internal chlorides present in the concrete mix and external chlorides from the sources such as sea water, brackish ground water, and soils—that diffuse through the cured concrete section. However, not all of these chlorides are responsible for corrosion. Only the water soluble chlorides present in the pore solution are responsible. The water soluble chlorides are not uniformly distributed along reinforcing steel; this nonuniform distribution may lead to the development of a corrosion cell.

The threshold value of chloride ions necessary to initiate corrosion of reinforcing steel depends on the level of hydroxyl ions in the pore solution, which is reduced by leaching or car-

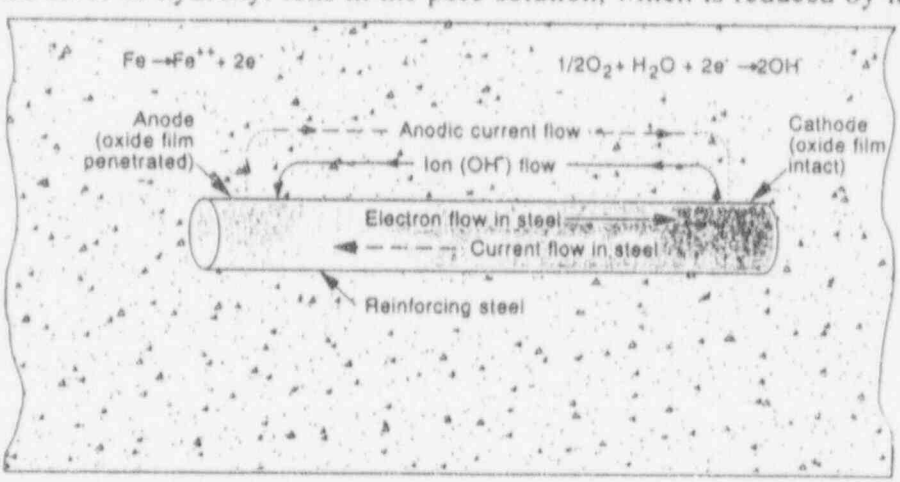


Figure 7. Electrochemical process of corrosion of reinforcing steel.

crete repairs, and poor construction practices. The corrosion rate increases with an increase in the surrounding temperature. Some test results show that the rate is doubled by a 10°C increase in the temperature (Clifton 1991).

Stray electrical currents and electrical connection of bar layers are, typically, local events and may produce intensified cathode/anode cell formation and eventual corrosion. Cathodic protection of underground piping located near the containment vessel may also contribute stray currents. Previous concrete repair areas might have greater permeability than the surrounding sound concrete or might have introduced additional chlorides into the concrete. These are not considered critical long-term aging concerns but could lead to local damage if not properly managed.

In concrete with cracks, chloride-initiated corrosion takes place almost immediately in the crack zone, and then it continues uninterrupted, as shown in Figure 8, until the concrete cover is cracked. The corrosion process is then accelerated.

It appears that the determining parameter for the corrosion rate is the ambient environment, not the crack width, as shown in Figure 9 (Tuutti 1982). The crack width only affects the timing of corrosion initiation. According to Figure 9, the depth of corrosion at the end of four years is linearly related to crack width: depth of about zero for a 0.1-mm-wide crack and 0.13 mm for a 0.5-mm-wide crack. At the end of ten years, the depth of corrosion associated with different crack widths is somewhat more uniform: a depth of 0.17 mm for a 0.1-mm-wide crack and a 0.22 mm for a 0.4-mm-wide crack.

Carbonation of Concrete. Carbonation refers to a reaction between the calcium hydroxide in the cement paste and carbon dioxide, in the presence of moisture, which results in a reduction of the concrete pH. The reaction produces calcium carbonate, which is neutral (pH=7). Carbonated concrete has a pH of about 8.3, which is low enough to cause a general

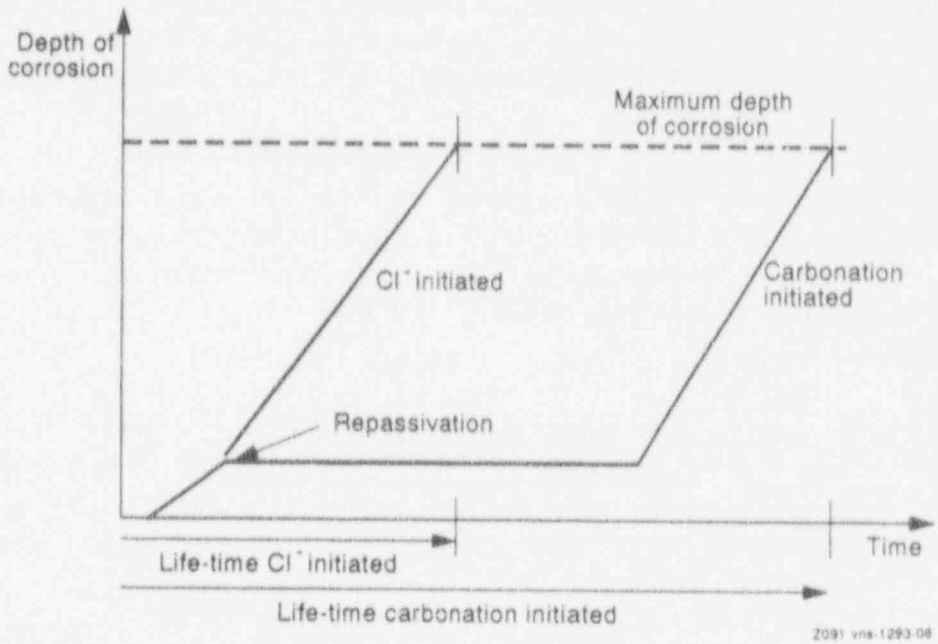


Figure 8. Comparison of chloride initiated and carbonation initiated corrosion of reinforcing steel as a function of time (Tuutti 1982).

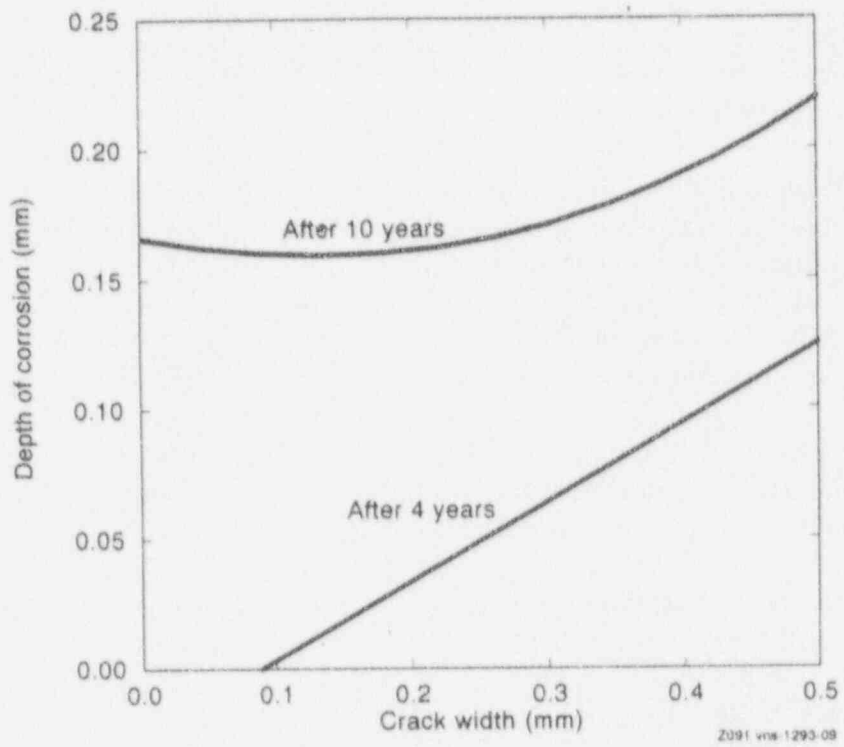


Figure 9. Depth of corrosion of reinforcing steel as a function of concrete crack width (Tuutti 1982).

loss of passivity of the reinforcing steel provided by the surrounding concrete (Vesikari 1988, Tomosawa et al. 1984). As a result, the steel is likely to experience general corrosion (Arup 1983). However, carbonation is normally an extremely slow process (except at the high temperatures that occur, for example, in the Middle Eastern countries) that begins at the surface of the cover concrete and propagates inward. The depth of carbonation may be determined by phenolphthalein testing of removed core sample. The corrosion problems strictly caused by carbonation are not as widespread as those caused by chloride intrusion. However, as carbonation reduces the pH level of the pore solution, the threshold level of chloride ions necessary to initiate corrosion will also be reduced.

Carbonation does not cause general disruption of concrete. Carbonation of hydrated cement paste results in reduced concrete permeability and increased hardness (Walton et al. 1990). The strength of concrete generally increases during carbonation. However, concrete does experience shrinkage under carbonation, which could cause microcracks on the surface; but these cracks are unlikely to be continuous.

Empirical formulas have been developed to predict the depth of carbonated concrete with time, assuming a constant flow of carbon dioxide (Tomosawa et al. 1984, Vesikari 1988, Clifton 1991). The resulting relationships show that an environment with a relative humidity in the range of 50 to 70% is most conducive to carbonation; the depth of carbonation is proportional to the square root of the exposure time. The carbonation rate is lower for dry concrete (for example, the concrete sheltered under a roof) because this concrete has insufficient moisture to promote an acid/base reaction (Lewis 1985). For surfaces of aboveground containment walls and domes sheltered from rain (assuming average values for a water-to-cement ratio of 0.55 and a cover of 5 cen-

timeters), full carbonation of the cover concrete would not occur until after 100 years of service life. The carbonation rate is also lower if the concrete is saturated with water that impedes diffusion of any carbon dioxide. The accuracy of the empirical formulas to predict the depth of carbonation is still in doubt, and many influencing factors exist. For example, the empirical formulas do not account for the reduced concrete permeability caused by carbonation. As a result, the depth of carbonation is likely to be less than that predicted by these formulas.

For outdoor concrete structures not sheltered from rain, carbonation has a sharp front; the concrete pH level at the carbonation front abruptly drops to about 8.3 (Tuutti 1982). For the sheltered structures, carbonation does not have a sharp front; the concrete pH level gradually drops from its normal value at the front to 8.3 at a certain distance from the front.

In concrete with cracks, carbonation-initiated corrosion takes place almost immediately in a crack zone, but the corrosion products seal the crack and repassivation of the reinforcing steel then takes place. As a result, the corrosion process is interrupted, as shown in Figure 8. The process starts again after a long period of time when the entire concrete cover is destroyed by carbonation and, then, the corrosion process continues uninterrupted (Tuutti 1982). As discussed, such interruption does not take place in the chloride-initiated corrosion process.

Detection and Mitigation. Corrosion of the reinforcing steel in a concrete containment may be detected by visual examination, and its rate can be estimated by electrochemical techniques. The outer reinforcing steel layers in the containment structure have the greatest potential for corrosion, and cracking and spalling caused by the expansive corrosion products and the presence of rust staining can indicate the presence of corrosion. The cracks in the concrete are generally parallel to the corroding reinforcing bars. Visual examination may be used to estimate the length, width, and depth of these cracks. Acceptance criteria relating to cracking and spalling may then be used for dispositions such as further evaluation, no action, or repair.

Electrochemical techniques include a standard technique for measuring the corrosion potential (also called half-cell potential) and advanced techniques for estimating the rate of corrosion. The standard technique includes estimating the reinforcing steel potential against a surface reference electrode and plotting potential maps. This technique is based on ASTM C876-91 (ASTM 1991) and is used worldwide. It can help in identifying zones of corrosion before appreciable damage occurs. Plotting of isopotential contours may allow identification of high versus low corrosion rate areas. However, this technique cannot estimate the absolute corrosion rate.

Advanced techniques that can be used to estimate corrosion rates in the identified regions include the linear polarization resistance technique, electrochemical impedance technique, and guard ring method (Burdekin et al. 1986). In the linear polarization resistance technique, the corroding metal is polarized a few millivolts (~10 mV) away from its corrosion potential and the change in applied current density is measured to estimate polarization resistance. The estimated corrosion rate is inversely proportional to the polarization resistance (Fontana 1986). However, the estimation of corrosion rate requires the area of the reinforcing steel being polarized, which is generally unknown and polarization of large structure is not feasible. Therefore, this technique cannot be used to estimate the corrosion rate of reinforcing steel. Use of the guard ring method, discussed later, along with this technique could overcome this limitation.

The electrochemical impedance technique monitors the variation of current in response to a series of applied variable frequency sine wave potentials of a small known amplitude (typically ±10 mV). Then, the value of the complex impedance for each applied frequency is calculated. Based on the analysis of these results, it is possible to determine the type of corrosion occurring and the corrosion rate. However, the exact area of the reinforcing steel being polarized must be known. Again, using the guard ring method along with this technique could overcome this limitation.

The guard ring method used with either linear polarization measurement or electrochemical impedance technique is a potential method for estimating the reinforcing steel corrosion rate in the field. This method makes it possible to polarize a small area of known size (~10 cm^2) of the reinforcing steel by means of a central reference electrode and, therefore, it is likely that an estimate of corrosion rate can be made. The guard ring arrangement comprises a central electrode and an outer ring, which is operated simultaneously with the central electrode such that actual measurement is made on the central electrode. Thus, this method can be used to measure the corrosion rate at the zones of corrosion identified by the potential measurement technique.

Cathodic Protection — Cathodic protection has been successfully used for corrosion protection of steel in reinforced concrete pipelines and in highway bridge structures (Hartt and Brown 1983), but it has not been used on U.S. concrete containments. The technique consists of a direct current provided from an external source applied to the metal so that the net anodic current (see Figure 7) is reduced or eliminated. This direct current is called a cathodic current and the protection system is called an impressed current system. The system employs a rectifier (a source of low-voltage d.c. power), connecting cables, auxiliary anodes such as graphite or platinum wire, and a reference electrode to monitor the potential of the steel to be protected. Both the auxiliary anodes and the reference electrode are embedded in the concrete.

Two design features of the reinforced concrete containments make the application of cathodic protection more difficult than for bare steel. First, the concrete electrolyte, i.e., the pore solution, has a high resistivity, which makes uniform distribution of the cathodic current difficult. Reinforcing steel in close proximity to an external source may be overprotected, and steel at a great distance may be unprotected. Overprotection of steel may result in hydrogen evolution at the steel-concrete interface and possibly result in a reduction of the bond strength. In the case of prestressed steel, hydrogen embrittlement may be a concern. The problem of overprotection is generally addressed by applying a low resistivity coating on the concrete surface in which several of the auxiliary anodes are embedded. Consequently, the cathodic current spreads uniformly along the coating and then travels the short distance to the reinforcing steel. Thus, a relatively uniform current density results. The second design feature of reinforced concrete containments is the possible lack of electrical continuity between reinforcing steel members or the presence of an electrical connection having a high resistance. In either of these two cases, corrosion damage will result because the cathodic current will return from the reinforcing steel to the ground.

Sulfate Attack

Sulfates found in groundwater (and also in soil and sea water) can chemically interact with the constituents of hydrated cement paste and cause degradation of the concrete. This is known as sulfate attack. Sulfate attack is known to cause two distinctly different types of concrete degra-

dation: concrete cracking by expansive chemical products and progressive loss of concrete strength after prolonged exposure (Mehta 1983). The first type of degradation does not pose a long-term concern, whereas the second type does.

Concrete Cracking by Expansive Chemical Products. Sulfates in the groundwater chemically react with calcium sulfoaluminate, also called the tricalcium aluminate phase, which is a constituent of hydrated cement paste. This reaction produces an expansive high-sulfate chemical product called ettringite, which causes concrete cracking after short-term exposure. The extent of damage to the exposed concrete depends on the sulfate content of the groundwater and on permeability and composition of the concrete. Such cracking has been one of the major causes of concrete degradation in nonnuclear structures in the western United States and Canada. However, nuclear power plant containment concrete is not likely to experience severe cracking caused by expansive chemical products because it has low permeability and is made of Type II cement with a low tricalcium aluminate content, which is more resistant to such cracking. Therefore, concrete cracking caused by expansive product formation is probably not a long-term concern. One possible exception is as follows. Groundwater with a low concentration of sulfate ions can produce solutions of high concentration if it wets the concrete surface, evaporates, and builds up a quantity of precipitated salts that then dissolve to form a nearly saturated solution that could cause concrete cracking in long term (Cohen and Mather 1991, Clifton 1991). If the expansive products are formed, the concrete cover over the belowgrade portion of the containment structure will crack first, which can be visually detected, provided the sites are made accessible by excavating the surrounding soil.

Loss of Concrete Strength Caused by Sulfate Attack. The sulfates in the groundwater also chemically combine with the calcium hydroxide and start crystalizing gypsum. A continuous supply of sulfates will consume most of the calcium hydroxide in the process of forming gypsum. This leads to a reduced stiffness and strength of the concrete, followed by its expansion and cracking. In addition, gypsum may react with other constituents of the hydrated cement paste, causing further expansion and deterioration of concrete (Brown and Clifton 1988). After prolonged exposure, significant loss of strength takes place, even in concrete made with low tricalcium aluminate cements.

Depending on the type of sulfate present in the groundwater, the chemical reaction with the calcium hydroxide can also affect the alkalinity of the cement. If alkali sulfates such as sodium sulfate are present, the resulting products include soluble sodium hydroxide, and the high alkalinity of the cement paste is maintained. High alkalinity is essential for the stability of the calcium silicate hydrate, which is the principal cementitious constituent of the hydrated cement paste. However, if magnesium sulfate is present in the groundwater, the resulting products include insoluble and poorly alkaline magnesium hydroxide; this reduces the stability of the calcium silicate hydrate in the cement paste, which will cause further reduction in strength. In addition, the reduced alkalinity of the cement paste increases the susceptibility of the steel components to corrosion, as discussed in the preceding section. Therefore, the presence of magnesium sulfate in groundwater is more harmful than that of alkali sulfates.

Magnesium sulfate and the other magnesium salts (magnesium chlorides and bicarbonates) present in groundwater also chemically attack the calcium silicate hydrate. After prolonged expo-

sures to groundwater, calcium ions in the calcium silicate hydrate are replaced by magnesium ions. The ultimate product of this chemical reaction is a nonexpansive magnesium silicate hydrate, which is associated with the loss of cementitious characteristics of the hydrated cement paste. Little research has been performed to evaluate and quantify the long-term effects of magnesium sulfate attack on concrete strength.

Detection and Mitigation. Visual inspection is the primary method that can be used for detecting the damage caused by sulfate attack. Degradation typically takes the form of cracking, disintegration of the hydrated cement paste, popout causing a loss of coarse aggregate, and general surface erosion and staining. Inspection of belowgrade wall surfaces may require excavating the surrounding soil.

Mitigative actions for the damage from aggressive chemical attack may include adding protective coatings, installing fluid barriers, constructing a drainage/diversion path for the aggressive chemical, removing groundwater via pumping, or combinations thereof. Mitigative actions may also require the installation of structural repair materials or partial reconstruction if the state of degradation is severe.

Conclusions

The main conclusions related to long-term aging concerns for the concrete containments are as follows:

1. Alkali-silica reactions, corrosion of the reinforcing steel, and magnesium sulfate attack all have potential to cause widespread aging damage after years of satisfactory experience.

2. Excessive concrete expansion caused by alkali-silica reactions resulting from the use of low-alkali cement or slow-reacting aggregates can occur in material that meets the current ASTM requirements.

3. The threshold value of chloride ions needed for corrosion initiation will be lower if the hydroxyl ions are reduced by carbonation, leaching, or magnesium sulfate attack.

4. Some research results show that corrosion of reinforcing steel starts almost immediately in the crack zone. Once started, chloride-initiated corrosion continues without pause, whereas carbonation-initiated process stops until the entire concrete cover is carbonated.

5. The ambient environment, not the crack width, appears to be the determining parameter for reinforcing steel corrosion.

6. Magnesium sulfate attack on concrete causes a loss of strength and cementitious properties after long exposure. Further research is needed to fully understand this phenomena.

7. Alkali-silica reaction products can be uniquely identified by staining them with uranyl ions, which have a characteristic greenish yellow fluorescence under short-wave ultraviolet light.

8. The potential measurement method can be used to identify reinforcing steel sites susceptible to corrosion prior to any concrete expansion and cracking take place. The guard ring method is a potential method to estimate the reinforcing steel corrosion rate in the field.

9. Maintenance of a surface coating and crack repair are effective to mitigate aging damage.

References

ACI 1992. "Building Code Requirements for Reinforced Concrete," *Manual of concrete Practice*, ACI 318, American Concrete Institute, Detroit, MI.

ACI 1989. "Corrosion of Metals in Concrete," ACI 222R.85, *Manual of Concrete Practice*, American Concrete Institute, Detroit, MI.

ACI 1977. "Guide to Joint Sealants for Concrete Structures," *Manual of Concrete Practice, ACI 504R-77*, American Concrete Institute, Detroit, MI.

Arup, H. 1983. "The Mechanisms of the Protection of Steel by Concrete," *Corrosion of Reinforcement in Concrete Construction*, A. P. Crane (editor), Society of Chemical Industry/Ellis Horwood Limited (Publishers), Chichester, United Kingdom, pp. 151-157.

ASME 1992. *ASME Boiler and Pressure Vessel Code*, Section III, Division 2, "Code for Concrete Reactor Vessels and Containments," 1992, American Society of Mechanical Engineers, New York, NY.

ASME 1989. "Specification for Carbon Steel Plates for Pressure Vessels for Moderate and Lower Temperature Service," ASME-SA-516, *Material Specifications*, Part A, American Society of Mechanical Engineers, New York, NY.

ASTM 1992a. "Standard Specification for Portland Cement," ASTM C 150, American Society for Testing and Materials, Philadelphia, PA.

Brown, P. W. and J. R. Clifton 1988. "Mechanisms of Deteriorations in Cement-Based Materials and Lime Mortar," *Durability of Building Materials*, 5, pp. 409-420.

Bungey, J. H., 1991. "Ultrasonic Testing to Identify Alkali-Silica Reaction in Concrete," *British Journal of NDT, 33*, 5, May.

Burdekin, F. M., et al. 1986. "Non-Destructive Methods for Field Inspection of Embedded or encased High Strength Steel Rods and Cables," Phase 1, Corrosion and Protection Centre Industrial Service, University of Manchester Institute of Science and Technology, *National Cooperative Highway Research Program Transportation Research Board National Research Council, UMIST/CAPCIS* 851214, October.

Burge, T. A. 1983. "Densified Silica-Cement Coating as Effective Corrosion Protection, *Corrosion of Reinforcement in Concrete Construction*, A. P. Crane (editor), Society of Chemical Industry/Ellis Horwood Limited, Chichester, United Kingdom, pp. 333-342.

Clark, L. A. 1991. "Modeling the Structural Effects of Alkali-Aggregate Reactions on the Reinforced Concre[illegible] *CI Materials Journal*, American Concrete Institute, May–June, pp. 271–277.

Clifton, J. R. 1991. *Predicting the Remaining Service Life of Concrete*, NISTIR4712, U.S. Department of Commerce, USNRC Structural Aging Program, November 1991.

Clifton, J. R. and L. I. Knab 1989. *Service Life of Concrete*, NUREG/CR-5466, NISTIR 89-4086, National Institute of Standards and Technology, Gaithersburg, MD.

Cohen, M. D. and B. Mather 1991. "Sulfate Attack on Concrete—Research Needs," *ACI Materials Journal*, January-February, pp. 62-69.

Deans, J. J., J. A. Sato, and P. D. Bhat 1989. "The Effect of High Temperature on the In-Situ Condition of PVC Waterstop," *Transactions of the 10th International Conference on Structural Mechanics in Reactor Technology*, Atomic Energy Society of Japan, p. 213.

Fontana, M. G., 1986. *Corrosion Engineering*, 3rd edition, New York: McGraw-Hill, pp. 502–503.

Hartt, W. H. and R. P. Brown 1983. "Cathodic Protection of Steel in Concrete," *Seminar Solving Rebar Corrosion Problems in Concrete*, Paper No. 6, NACE Seminar, Sept. 27-29, Chicago, IL

Hausmann, D. A. 1967. "Steel Corrosion in Concrete—How does it occur?" *Materials Protection*, November, pp. 19–23.

Hookham, C., 1991. Structural Aging Assessment Methodology for Concrete Structures in Nuclear Power Plants, ORNL/NRC LTR-90/17, Oak Ridge National Laboratory, Oak Ridge, Tennessee.

Lewis, G. 1985. "Degradation of Building Materials Over a Life Span of 30-100 Years," *Nuclear Science and Technology*, Commission of European Communities, CEB.

Locke, C. E. 1986. "Corrosion of Steel in Portland Cement Concrete: Fundamental Studies," *Corrosion Effects of Stray Currents and the Techniques for Evaluating Corrosion of Rebars in Concrete*, V. Chaker (ed.), ASTM STP 906, American Society for Testing and Materials, Philadelphia, PA, pp. 5-14.

Locke, C. E. 1983. "Mechanism of Corrosion of Steel in Concrete," *Solving Rebar Corrosion Problems in Concrete*, National Association of Corrosion Engineers, Preprint No. 2.

Mehta, P. K. 1986. *Concrete Structure, Properties, and Materials*, 1986, Prentice-Hall, Inc., Englewood Cliffs, NJ.

Mehta, P. K. 1983. "Mechanisms of Sulfate Attack on Portland Cement — Another look," *Cement and Concrete Research, 13*, pp. 401 –406.

Natesaiyer, K., Stark, D., and Hover, K. C. 1991. "Gel Fluorescence Reveals Reaction Product Traces," *Concrete International*, January, pp. 25–28.

Neville, A. M. 1981. *Properties of Concrete*, 3rd edition, The Pitman Press, Bath, England.

Neville, A. M. 1963. "A Study of Deterioration of Structural Concrete Made with High-Alumina Cement," *Proceedings of the Institution of Civil Engineers, 25*, pp. 287-324.

Pommersheim, J. M. and Clifton, J. R. 1990. *Models of Transport Processes in Concrete*, NIS-TIR 4405, National Institute of Standards and Technology, September.

Pourbaix, M. 1974. "Applications of Electrochemistry in Corrosion Science and Practice," *Corrosion Science*, January, pp. 25-82.

Rasheeduzzafar 1992. "Influence of Cement Composition on Concrete Durability," *ACI Materials Journal*, November-December, pp. 574-586.

Scannell, W. T. and W. H. Hart 1987. "Cathodic Polarization and Fracture Property Evaluation of a Prestressed Steel Tendon in Concrete," *Corrosion of Metals in Concrete*, Paper No. 127, Proceedings of the CORROSION/87, NACE (National Association of Corrosion Engineers), Houston, TX.

Smith, R. and C. F. Daba, Jr. 1986. "Recent Developments in the Use of Fly Ash to Reduce Alkali-Aggregate Reaction," *Alkalis in Concrete*, V. H. Dodson (ed.), ASTM STP-930, 1986, American Society for Testing and Materials, Philadelphia, PA.

Stark, D. C., 1979. "Alkali-Silica Reactivity: Some Reconsiderations," Research and Development Bulletin RD076.OIT, Portland Cement Association, based on a paper presented at the Symposium on Nonstandard Test Methods Useful in Determining Physical-Chemical Characteristics of Cements, San Diego, California, December 12, 1979, ASTM Committee C-1 on Cement, American Society for Testing and Materials, Philadelphia, PA.

Tuuti, K., 1982. *Corrosion of Steel in Concrete*, Swedish Cement and Concrete Institute, Stockholm.

Vesikari, E. 1988. *Service Life of Concrete Structures with Regard to Corrosion of Reinforcement*, 1988, Technical Research Center of Finland.

Walton, J. C., L. E. Plansky, and R. W. Smith 1990. *Models for Estimation of Service Life of Concrete Barriers in Low-Level Radioactive Waste Barriers*, NUREG/CR-5542, EGG-2597, 1990, U.S. Nuclear Regulatory Commission, Washington, D.C.

Appendix

Widespread Aging of Nonnuclear Concrete Structures

Review of the literature related to aging of nonnuclear concrete structures reveals that many structures in Europe built in the 1950s have experienced widespread aging damage after 10 to 15 years of satisfactory experience (Neville 1985). Three examples are presented here. They are related to degradation of concrete materials and include use of high-alumina cement, use of calcium chloride as an admixture in structural concrete, and carbonation. High alumina cement was developed for use in concrete resistant to sulfate attack. The hydrated cement paste contains calcium aluminate as the main cementitious compound, which is chemically unstable. Concrete slowly looses its strength, possibly because of increased permeability, which eventually leads to structural failure (Neville 1963). The use of high alumina cement in the United Kingdom was discontinued in the 1970s after several reported failures.

Calcium chloride was used for a long time as an admixture for rapid hardening of cement, but its deleterious role in corrosion of reinforcing steel was only recognized in 1970s after several reported corrosion cases, and then its use was stopped. But it was too late. At present, chloride ions are at work in numerous existing structures, which may require expensive repair in the future. It is interesting to note that the use of calcium chloride in prestressed concrete was banned in the 1950s after failure of a prestressed concrete pipeline in Canada; however, its role in corrosion of reinforcing steel was not recognized for 20 more years.

Concrete structures built in the 1970s are susceptible to rapid corrosion of reinforcing steel because of carbonation. The concrete used a new British cement whose modified chemical composition facilitated development of more rapid strength. Use of new cement permitted a high water-to-cement ratio, which resulted in concrete with lower density and higher permeability. Such concrete undergoes carbonation more rapidly than the old concrete having a low permeability. Eventually, this results in concrete cracking and spalling.

In all three above cases, it is the materials that have caused the significant aging damage. However, these materials were not tested for their deleterious effects. These effects were manifested after 10 to 15 years of satisfactory performance, and then the degradation was rapid. Periodic inspection and testing of the concrete structures can detect deleterious effects earlier, which then could be mitigated.

References

Neville, A. M. 1981. *Properties of Concrete*, 3rd edition, The Pitman Press, Bath, England.

Neville, A. M. 1985. "Recent Problems with Concrete," *Karlhans Wesche Gewidmet*, Baustoffe, Wiesbaden, Germany, pp. 148–150.

Probabilistic-Based Evaluation of Design Rules for Components Affected by Intersystem LOCAs[1]

A. G. Ware
Idaho National Engineering Laboratory
EG&G Idaho, Inc.
Idaho Falls, Idaho

ABSTRACT

The methodology outlined in NUREG/CR-5603 was used to evaluate (on a probabilistic basis) design rules for systems in advanced light water reactors (ALWRs) that could be subjected to intersystem loss-of-coolant accidents (ISLOCAs). The methodology is intended for piping elements, flange connections, on-line pumps and valves, and heat exchangers. The NRC has directed that design rules be evaluated at 350°F for BWR and PWR pressures of 1025 and 2235 psig, respectively, and has established a goal of 90% probability that system rupture will not occur during an ISLOCA event. The results of the calculations show that components designed for a pressure of 0.4 of the reactor coolant system operating pressure will satisfy the NRC survival goal in most cases. Specific recommendations for BWR and PWR applications are made.

INTRODUCTION

Low-pressure piping systems that branch to the reactor coolant systems (RCSs) of light water reactors (LWRs) are normally protected by multiple valves from the reactor coolant. Failure or misalignment of these isolation valves leads to an intersystem (sometimes called interfacing system) loss-of-coolant accident (ISLOCA), and to the potential leak or rupture of low-pressure systems.

SECY-90-016 (NRC, 1990) and the associated Staff Requirements Memorandum from the Nuclear Regulatory Commission (NRC) Commissioners require evolutionary advanced LWR (ALWR) plant designers to include ISLOCA in the design basis; this requirement has been extended to passive plant designers as well. However, the NRC did not initially provide design stress allowables or uniform criteria for ISLOCA design. Subsequently, it was decided to use ASME Service Level A design stresses and a fraction of the actual design pressure to achieve an acceptable overall system failure probability.

Four ALWRs are presently under review by the NRC staff: ABWR, SBWR, AP600, and System 80+. The piping systems of these plants that may be affected

---

[1] Work supported by the U.S. Nuclear Regulatory Commission, Office of Nuclear Regulatory Research, under DOE Contract No. DE-AC07-76ID01570.

by ISLOCAs include, for example, the residual heat removal system, the safety injection system, the makeup and purification system, and other low pressure lines which branch to the RCS. While the chief safety concern deals with low pressure lines which bypass containment, piping which remains entirely within the containment is of concern as well.

To date no full ISLOCAs have occurred in U.S. nuclear plants, although there have been several instances of leakage past valves from the RCS to connecting systems. These instances have been benign and correctable by the plant staff. The total ISLOCA core damage frequency for existing LWRs was estimated to be in the range of 2×10^{-6} events per reactor per year (Galyean et al., 1993). Thus it is a low probability event. Since the maintenance procedures and operator training[2] on ALWRs are expected to be similar to that at present LWRs, the ISLOCA probability for ALWRs is expected to be in the same range as for current LWRs.

The NRC has established an objective that evolutionary ALWRs (and by extension, passive ALWRs) provide some protection against ISLOCA sequences. The NRC position is that ISLOCA, for purposes of design, can be treated as a severe accident with very low frequency of occurrence, thereby allowing relatively high conditional failure probabilities given an ISLOCA. The present NRC goal (but not a requirement) is to ensure that each connecting system (including piping, flanges, valves, etc.) has at least a 90% chance of surviving an ISLOCA event.

It appears that European nuclear safety authorities are considering similar actions. The French and Germans released their safety goals in "Common Safety Approach for Future Pressurized Water Reactors", in which it was stated that "containment bypass is to be practically eliminated by such measures as adequate piping design pressure" (*Inside N.R.C.*, 1993).

A comprehensive research program to investigate ISLOCAs was carried out in a previous research program at the Idaho National Engineering Laboratory (INEL). The results are summarized in Galyean et al. (1993). A part of that overall program concentrated on the failure probabilities of mechanical components in currently operating LWRs. That portion of the program is documented in NUREG/CR-5603 (Wesley et al., 1990) and NUREG/CR-5862 (Wesley, 1992). The purpose of the present program was to use the methodology outlined in NUREG/CR-5603 to evaluate design rules for ISLOCA systems in ALWRs on a probabilistic basis. More details of the program may be found in Ware (1993). The Design of systems for ISLOCA pressures of 40% of the primary system operating pressure was the base case evaluated. The methodology is intended to include piping elements, flange connections, on-line pumps and valves, heat exchangers, and tanks. The NRC has directed that the design rules be evaluated for BWR pressures of 1025 psig, and PWR pressures of 2235 psig, at 350°F.

---

[2] Plant personnel actions are the leading cause of ISLOCAs.

METHODOLOGY DEVELOPMENT

A methodology for evaluating probabilistic pressure capacities for selected components in systems potentially susceptible to ISLOCA events was developed and reported in NUREG/CR-5603 (Wesley et al., 1990). For some components (e.g., pipes, tanks) the methodology for evaluating design rules is based on an allowable stress concept. The basic methodology is to compute failure stresses which can be used with an ISLOCA survival curve to calculate the probability of component survival at a given system pressure. For other components (e.g., flanges), the methodology is based on limiting the leak rate for gasketed connections below the makeup capability of the plant (a 200 gpm leak rate will be assumed). The original NUREG/CR-5603 methodology has been slightly modified in a few places, but remains basically the same as described in NUREG/CR-5603.

Methodology outline for allowable stresses

The major steps and assumptions associated with the allowable stress methodology are:

Step 1. Determine the stress induced in the pipe during ISLOCA conditions

- the ISLOCA failure mode is assumed to be from a statically-applied pressure alone
- the stress in the pipe wall can be calculated using the equation for hoop stress (pr/t)

Step 2. Estimate the median failure stress

- the median ultimate tensile strength (UTS) of the piping materials can be obtained using material property data
- the median value can be reduced to account for triaxial stresses and the differences in the gage length of the tensile specimens and the actual piping
- a further reduction can be applied to account for the increase in pipe diameter caused by the plastic strain in the pipe wall

Step 3. Estimate the uncertainty of the failure stress

- the failure stress curve is assumed to have a lognormal distribution
- the uncertainty of the failure stress curve can be estimated by assuming that the failure probability at the yield stress (YS) is 10^{-3} (or some smaller value) to account for cracking (original or induced)

Attention can be given to the manufacturer's tolerance and the corrosion allowance

Discussion of failure mode assumption

To establish design rules based on the failure probability of piping during an ISLOCA event, it is desirable to have a simple general methodology that will apply to all ALWR piping systems rather than factor in the specific operating stresses for each individual design. However, the magnitudes of piping stresses (other than the ISLOCA pressure stress which can be assumed to be the full primary system pressure) are design-specific, small compared to the ISLOCA pressure stresses, and depend on the plant conditions at the time of the ISLOCA event. Thermal and deadweight stresses will be present to some degree, while there is a very low probability that seismic or water hammer stresses will exist during the ISLOCA event. These stresses represent only a portion of the overall design stresses (they do not include the pressure stress), which have already been limited according to ASME Code rules for A through D Service Levels, and these stresses would not increase significantly during the ISLOCA event as does the pressure stress.

The methodology simply assumes that the only cause of failure is over-pressure, and includes the effect of the other stresses in the determination of the failure stresses and the uncertainty, as follows. The hoop stress caused by the pressure loading is set equal to a failure stress. However, this failure stress will be reduced from the median UTS. Moreover, a wide uncertainty has been assigned by selecting the 99.9% survival confidence as the median YS. This accounts for the probability of a large crack existing in the material, and also provides margin for the additional stresses such as thermal and deadweight stresses present in the pipe. Thus, the design stresses based on high confidences of survival are much closer to the YS than to the median UTS.

Failure probability determination

In NUREG/CR-5603 the median[3] UTSs for carbon and stainless steels were obtained from the open literature and were reduced by factors of 0.85 for stainless steel and 0.9 for carbon steel to account for the following differences between the specimens from which the strength data were generated and nuclear piping:

1. the material property data were based on testing uniaxial tensile specimens, whereas a state of triaxial stress will exist in the actual piping (however, only two of the three stress components are significant)

2. the uniaxial tensile specimen gage length was very small when compared to that of the actual piping, which is assumed to be the pipe circumference.

---

[3] The median is the stress at which the failure probability is 50%.

These reduction factors were based on Manjoine's (1975) work. Chu et al. (1989) reported that General Electric conducted burst tests on seamless A106 carbon steel pipes and found that "the average burst hoop stress of unflawed pipe specimens was found to be at approximately 90% of the UTS independent of the pipe size". Unfortunately, there were no corresponding data for stainless steel.

After stress reduction factors are applied, the resulting stress is called the median failure stress (σ_t). The lognormal curve results in the following equation for the failure stress (σ_c) at a given percent confidence of survival c:

$$\sigma_c = \sigma_t \, e^{-\beta x} \tag{1}$$

The logarithmic uncertainty of the failure stress (β) is determined by using the following values of σ_c and x:

σ_c = σ_y
x = the value from the normal probability tables for a survival probability of 10^{-3} (that is, 3.09)

and solving Equation 1 for β. A sensitivity study also was conducted for a survival probability of 10^{-4} at σ_y.

Once the failure probability curves are determined, the survival probability (which is 1 minus the failure probability) for any stress is calculated and corrected for the expansion caused by plastic stress. This correction is applied because the hoop stress in the piping is computed based on the original surface area that the pressure acts upon on the inside wall of the pipe. However, the pipe radius expands as the pressure causes plastic deformation in the wall; consequently, the surface area on which the pressure acts increases with strain [the increased radius is $r(1 + \epsilon)$]. To apply such a correction for the plastic strain, we assume that the stress-strain relation is bilinear with the break point at the YS (σ_y).[4] Then the strain ϵ_t corresponding to the median (50% confidence) failure stress (σ_t) can be adjusted by the following ratio to estimate the corresponding strain at the failure stress (σ_c):

$$R = \frac{\sigma_c - \sigma_y}{\sigma_t - \sigma_y} \tag{2}$$

---

[4] Actually, the stress-strain curve is not linear between the yield strength and the ultimate tensile strength. A straight line between the two points results in a higher strain and therefore a lower allowable stress that would the actual curve; thus the assumption is slightly conservative.

The corrected value[5] of σ_c is calculated by dividing σ_c by $(1 + R\epsilon_f)$.

$$\sigma_{sc} = \frac{\sigma_f \, e^{-\beta x}}{(1 + R\epsilon_f)} \tag{3}$$

where:

σ_{sc} = σ_c corrected for plastic strain
$R\epsilon_f$ = strain at σ_c

Hoop stress (pr/t) versus temperature curves for several survival probabilities are plotted in Figures 1 through 3. The ASME Section III Class 2/3 Level D stress limits (for an ABWR pressure of 1025 psig and no corrosion allowance) also are included, with the hoop stress computed as follows:

$$\frac{pr}{t} = S - 0.6\,p \tag{4}$$

where:

p = primary system design pressure
r = inside radius
t = wall thickness
S = ASME Code design stress limit

The Level D limit allows a factor of 2 increase in pressure over the normal primary system operating pressure, so piping designed for 50% of the expected ISLOCA pressure would meet the Level D stress limit. The Level D limit provides about a 98% confidence of survival at 350°F for Type 304 stainless steel with an assumed 10^{-3} failure probability at the YS (Figure 1). Piping designed for 40% of the primary system operating pressure would meet a 2.5 Level A stress limit. The 2.5 Level A confidence level is about 90%. The Level D confidence level at 350°F would increase to greater than 99% for an assumed 10^{-4} failure probability at YS (Figure 2), while the 2.5 Level A confidence level is about 93%. Both the Level D and 2.5 Level A limits provide greater than 99% confidence of survival at 350°F for carbon steel with an assumed 10^{-3} failure probability at YS (Figure 3).

---

[5] It would be more logical to apply the correction for plastic strain as a multiplier to r in the pr/t stress calculations, but in practice when performing sensitivity studies using several pr/t values, it is easier to apply the correction only once to the allowable stress, and thereby not have to perform the correction for each pr/t that is calculated.

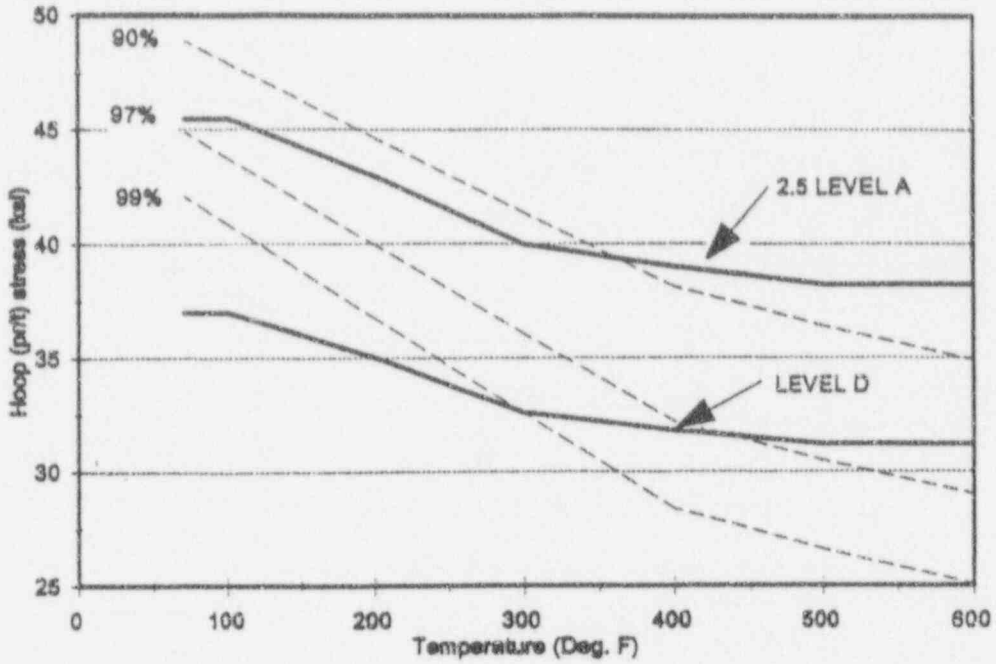


Figure 1. Comparisons of allowable stress limits for Type 304 stainless steel pipe: ASME Code Level D and probability-based confidence limits (10^{-3} probability of failure at YS)

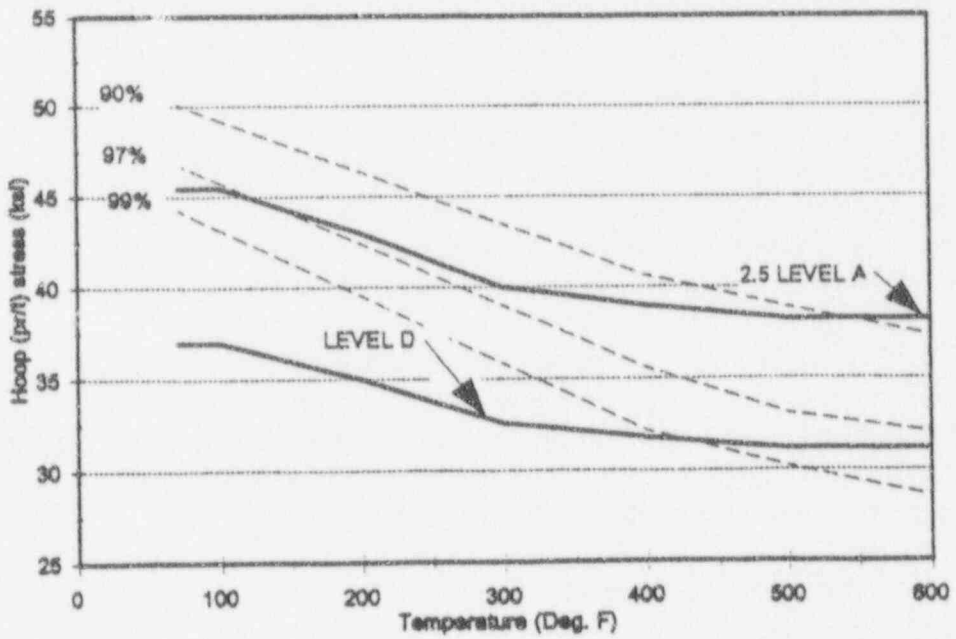


Figure 2. Cornparisons of allowable stress limits for Type 304 stainless steel pipe: ASME Code Level D and probability-based confidence limits (10^{-4} probability of failure at YS)

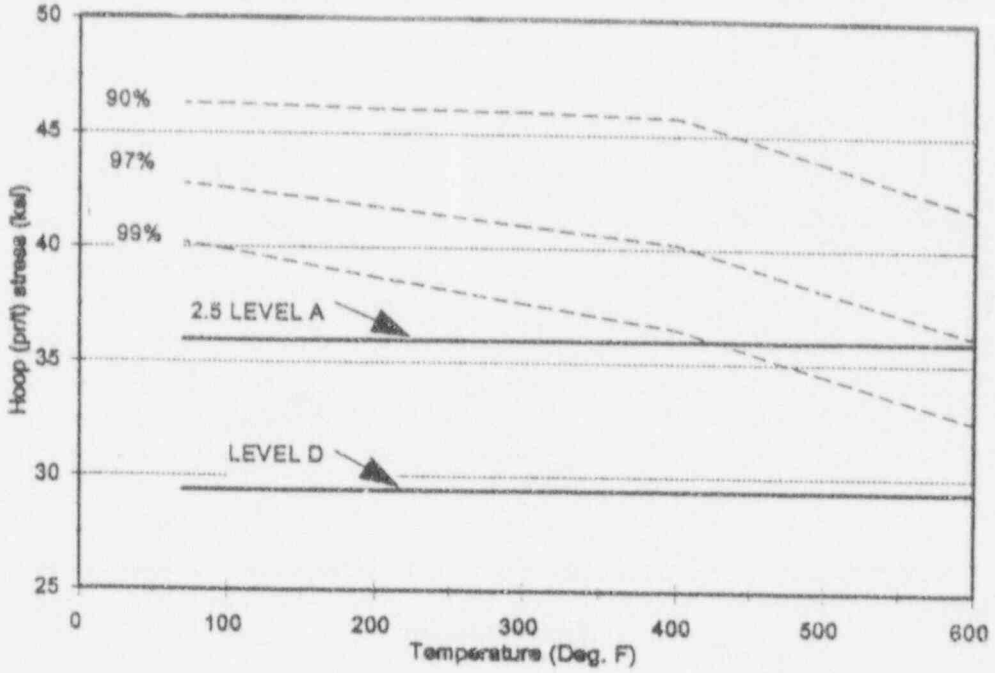


Figure 3. Comparisons of allowable stress limits for SA-106 Grade B carbon steel pipe: ASME Code Level D and probability-based confidence limits (10^{-3} probability of failure at YS)

Methodology for leak rate assumptions

For nonmetallic components such as gaskets and seals (where leakage will occur before rupture) and in the case of metallic components such as piping and vessels, the basic assumption will be to limit the leakage to a small amount that is within the capability of the plant's coolant makeup system.

A related question that is not within the scope of the present study, but which is planned to be addressed later, is whether small lines under a certain diameter (as yet to be determined) that branch from the main system, may be excluded from consideration because the leakage from a ruptured line in the system will be within the capacity of the plant's coolant makeup system.

Investigations of other possible assumptions

A number of assumptions were made in the previous section to obtain pipe survival probability curves. In some cases alternative assumptions were investigated to determine how different assumptions would affect the results. For example, the lognormal distribution represents a distribution that is appropriate when

the variable is the product of a number of factors. Other probability distributions (such as Weibull or beta distributions) also could be used. Consequently, the lognormal distribution and the Weibull distribution, a distribution that was conceived for failure data, were compared. The Weibull distribution results in about a 3 to 4 ksi increase in allowable stress levels over the lognormal curve. Thus the lognormal curve provides more conservative stress values than does the Weibull curve.

Figures 1 and 3 show that using the previous failure assumptions, carbon steel has a higher probability of survival than does stainless steel. This does not mean, however, that carbon steel is a preferred material; the higher failure probability for carbon steel is a result of the ratios of the YS and UTS of carbon and stainless steels, and the basis that is used in the ASME Boiler and Pressure Vessel Code for selecting allowable stresses. The ASME Code uses the lesser of 1/4 of the UTS or 2/3 of the YS as the allowable stress for Class 2 piping.

The allowable stress is based on 1/4 of the UTS for SA-106 Grade B carbon steel, but on 2/3 of the YS for Type 304 stainless steel at 400°F.[6] For carbon steel the ratio of the YS to the design stress is 2, while the ratio is only 1.5 for stainless steel. Thus the 99% survival confidence stress (YS) is twice the design stress (the Level D limit) for carbon steel, but twice the design stress for stainless steel is greater than the YS so the survival confidence at the Level D limit is less than 99%.

Brookhaven National Laboratory has attempted to define the failure uncertainty by assigning the average UTS as the 99% failure limit to the failure curve, and 90% of the average UTS as the median of the curve (Chu, 1989). The basis for the 90% value as the median of the curve was from the GE pipe burst test results previously mentioned in which the hoop stress at burst was 90% of the UTS. The resulting failure probability at the YS ranged from 2×10^{-3} to 8×10^{-3}, which is about the same order of magnitude as the failure probability of 1×10^{-3} assumed in NUREG/CR-5603. While the Brookhaven study has a defensible basis for the median and upper confidence level, the lower confidence level was not based on anything physical and did not take into account the possibility of cracking, but was decided by the parameters of the upper portion of the curve. Yet it is in the lower region of the curve that we are interested since we need to determine stress limits for high probabilities of survival.

The difficulties in establishing the lower survival confidence limit in the Brookhaven and NUREG/CR-5603 studies show that there is no straightforward way to define the lower limit. We have no data for overpressure failures of nuclear piping that has been designed to ASME Code stress limits. However, we do know that for piping designed to ASME Code requirements, there have been no

---

[6] S is used throughout the text to indicate ASME Code stresses (e.g., S_y is the Code yield stress and S_u is the Code ultimate tensile strength), whereas σ is used in the text to denote computed stresses.

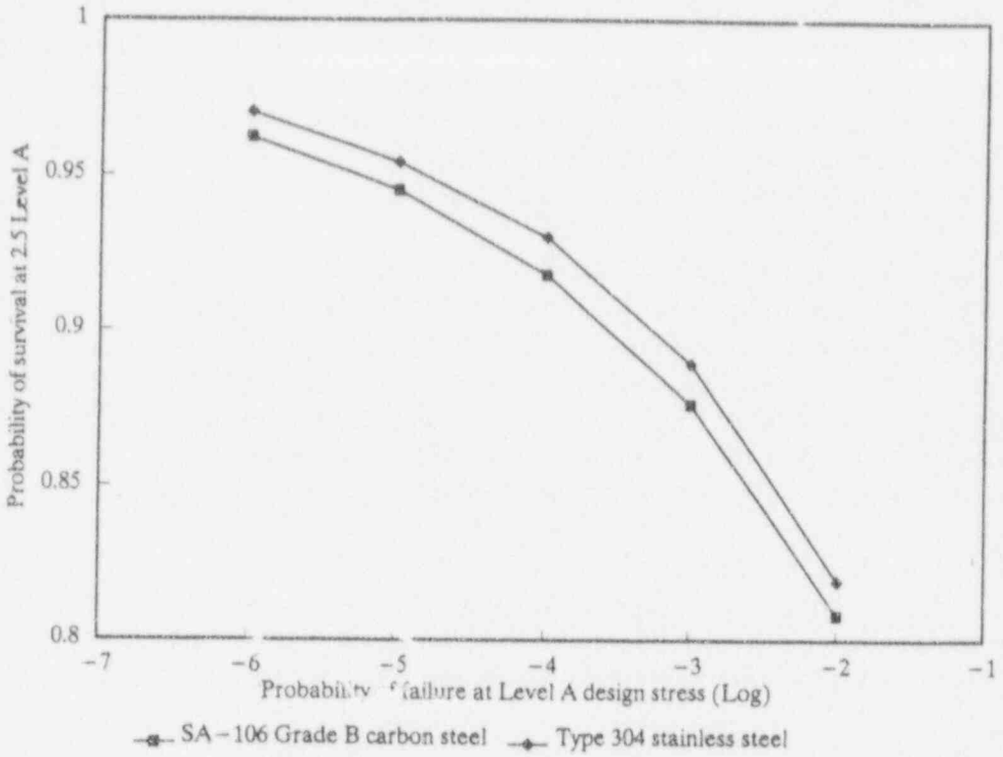


Figure 4. Survival confidences at 2.5 times the Level A stress for various probabilities of failure at the Level A stress

overpressure failures (excluding piping thinned by erosion/corrosion), so the failure probability must be "low". If we assign various failure probabilities to represent this "low" number at the Level A design stress and the failure stress in Table 1 as the median stress, the survival probabilities at 2.5 times the Level A stress for 350°F are as shown in Figure 4. Using this argument, the lower confidence limit is now based on something physical for which we have data, namely the design stress value for which we have experience at operating pressures. However, we have no operating data at higher pressures, nor do we have any precise knowledge of the magnitude of the failure probability at the design stress.

Based on operating experience of LWRs worldwide, the failure probability at the design stress is estimated to be less than 10^{-4} events per reactor per year, so the survival confidence from Figure 4 at 2.5 times the Level A stress is about 92% or greater. The survival confidences in Figure 4 are approximately the same for carbon and stainless steels, whereas using the assumption of 10^{-3} failure probability of failure at the YS, the survival confidence is substantially greater for carbon than for stainless steels.

The alternate method of developing an uncertainty for the failure curves leads to basically the same conclusion as does the method in NUREG/CR-5603, that is, the minimum survival confidence at 2.5 times the Level A design stress is greater than 90%. This argument is based on actual operating data, and shows a better balance between the carbon and stainless steel survival probabilities than does the NUREG/CR-5603 method.

MATERIAL PROPERTIES

In NUREG/CR-5603 the median UTSs for carbon and stainless steels were obtained from Harvey (1985) and Weiss and Sessler (1963). In a September 1992 presentation by the author to the ASME Subgroup on Design in New York, a question was asked whether the NUREG/CR-5603 data had been compared to the data used in generating the ASME Code material property values. In response, material property data were obtained from alternate sources and compared to the NUREG/CR-5603 data. The ASME staff stated that the original data are found in some old ASTM publications, designated DS5 (stainless steel) and DS11 (carbon steel) and their supplements (Simmons and Van Echo, 1965; Simmons and Cross, 1952 and 1955; Smith, 1969 and 1972). The data in the five ASTM publications are carefully referenced (in almost all cases) as to the source, the product form (bar, plate, pipe/tube, etc.), and the test temperature. Individual data points (as opposed to averages) are tabulated. Therefore, these publications make excellent sources to which the NUREG/CR-5603 median values can be compared. Data from several other sources also were used to supplement the ASME/ASTM data, where applicable. Dr. Gery Wilkowski of Battelle Columbus Laboratories was particularly helpful in identifying material property data sources.

From discussions with ALWR vendors and a review of the materials in operating plants, the following materials are believed to be those that will likely be used in systems subject to ISLOCA in ALWRs:

- Type 304 stainless steel pipe (wrought and cast) and plate
- Type 316 stainless steel pipe (wrought and cast)
- SA-106 Grade B carbon steel pipe
- SA-516 Grade 70 carbon steel plate

A comparison of the NUREG/CR-5603 values to the material property data obtained from alternate sources indicates that the NUREG/CR-5603 values are conservative and/or representative for most types of materials. However, there are two cases where the NUREG/CR-5603 values appear to be nonconservative. These are for Type 316 stainless steel and SA-516 Grade 70 carbon steel. Alternate material property data were used in this study for all materials except SA-106 Grade B carbon steel, for which the NUREG/CR-5603 values were used.

COMPONENT EVALUATIONS

To achieve the goal of 90% system survival confidence for the ISLOCA event, each of the components in the system (piping, flanges, pumps, valves, heat exchangers) must have a survival confidence such that the product of the confidences equals 90%. If the survival confidence goal for each of these five components is set for 98%, then the overall system survival confidence will be about 90%.

The methodology of NUREG/CR-5603 defined the uncertainty in the failure stress by assigning a failure probability at the YS. Since the probability of failure at the YS is essentially zero for unflawed material, this methodology assumes that a large flaw exists in the material in a small percentage of cases. The probability of a large flaw existing increases with the amount of material, such as the length of piping or the number of welds in a component. However, this was not taken into account in NUREG/CR-5603. Although it is not based on failure probabilities, the ASME Code follows this same logic in that the design allowable stresses are applied regardless of the size of a component or the number of welds.

The NUREG/CR-5603 methodology was applied to the components that make up the systems that will be designed for ISLOCA. Specifically, the survival confidences for components designed to 40% of the operating pressure at 350°F are calculated. Corrosion allowances were included, where applicable, but manufacturing tolerances were not included.

Piping

Calculations were performed to estimate the percent survival probability of various sizes (2 to 20 in. nominal diameter) of carbon and stainless steel pipes. A design temperature of 350°F and design pressures of 410 (BWRs) and 894 (PWRs) psig (40% of the operating pressures of 1025 and 2235 psig for current plants) were used. The minimum wall thickness for each pipe size was calculated using Equation (3) of ASME Code Section III NC-3641.1 and corrosion allowance values of 0.120 and 0.004 in. (BWRs) and 0.060 and 0.003 in. (PWRs) for carbon and stainless steel pipe, respectively. Based on the value of the calculated minimum wall thickness, the next higher standard pipe schedule was identified.

Three survival confidences were calculated:

(1) The confidence based on the wall thickness from the ASME Code minimum wall thickness calculations.

(2) The confidence based on the wall thickness of the lowest standard pipe schedule with a wall thickness greater than the calculated thickness in (1).

(3) If the survival confidence in (2) was less than 99.0%, the calculations were repeated for the next larger (higher) pipe schedule.

In the design of actual piping systems, piping with *minimum* wall thicknesses will not generally be used, but rather *standard* pipe schedules. Therefore, standard pipe schedules were selected from B36 [ASME (1985a, 1985b)] using the following approach. B36.10 lists a number of thicknesses for each nominal size pipe. However, only those designed by a Schedule number (for example, 20, 30, 40, etc.) or by standard (STD), extra-strong (XS), or double extra-strong (XXS) designations have been chosen for the tables. For carbon steel, the approach uses the minimum thickness standard schedule from B36.10 that is greater than the minimum calculated thickness. B36.19 lists pipe schedules for stainless steels where the schedule designation is followed by an "S". For stainless steel, the approach uses standard schedules from B36.19. However, B36.19 lists no 40S or 80S schedules above 12-in. nominal diameter, so B36.10 schedules are used for these larger sizes.

The calculations are summarized in Tables 1 though 6 for Types 304 and 316 stainless and SA-106 Grade B carbon steel pipes. No manufacturing tolerances are included in these calculations. Otherwise, they represent conservative survival confidences in that no pressure resistance is allowed for the material within the corrosion allowance.

Tables 1 through 3 show that for BWRs, STD pipe schedules will give greater than 99% survival confidence for all three materials. Using 40% of the operating pressure as the design pressure would result in 5S piping being chosen for piping up to 12 in. for Type 316 stainless steel, and up to 6 in. piping being chosen for Type 304 stainless steel. STD piping would be chosen for all carbon steel piping except for sizes 8 to 12 in., for which less than STD schedules would give 99.9% survival confidences.

Tables 4 through 6 show that for PWRs, XS pipe schedules will give greater than 98% survival confidence for all three materials, with the exception of the larger sizes. Schedule 60 is needed for all sizes greater than 18 in. for carbon and Type 316 stainless steel, and for sizes greater than 16 in. for Type 304 stainless steel.

Pipe fittings purchased to the requirements of ANSI B16.9 and analyzed to the requirements of the ASME Code are assumed to be of equal strength to the same schedule of straight pipe.

Flanges

Although NUREG/CR-5603 includes a methodology for leak rate calculations where gross leakage is taking place (since this is needed to evaluate operating plants), the best approach at the design stage is to size the flange and prescribe bolt preloads so that no gross leakage is allowed. In flange terminology, this means that the gross leak pressure (GLP), where the internal fluid pressure equals the gasket stress, is not exceeded for the desired confidence level. To assure that gross leakage does not take place during an ISLOCA event, it is recommended that high strength bolts be used in flanges, so that the bolt YS is not exceeded.

Table 1. Survival confidences for Type 304 stainless steel BWR pipe

Nominal Diameter (in)	Actual Diameter (in)	Corrosion Allowance (in)	Design Pressure (psi)	Calculated Thickness (in)	Hoop stress (ksi)	Survival Confidence (%)	Standard Pipe Schedule	Wall Thickness (in)	Hoop stress (ksi)	Survival Confidence (%)	Next Larger Schedule	Wall Thickness (in)	Hoop stress (ksi)	Survival Confidence (%)
20	20.000	0.004	410	0.2515	40.39	80.1	STD	0.375	26.80	99.9				
18	18.000	0.004	410	0.2268	40.39	80.1	10	0.250	36.48	81.6	20	0.312	28.93	99.9
16	16.000	0.004	410	0.2020	40.39	80.1	10	0.250	32.31	97.7	20	0.312	26.60	99.9
14	14.000	0.004	410	0.1773	40.39	80.1	10	0.250	28.14	99.6				
12	12.750	0.004	410	0.1618	40.39	80.1	10S	0.180	36.10	82.4	STD	0.375	18.59	99.9
10	10.750	0.004	410	0.1370	40.39	80.1	10S	0.165	33.19	96.9	STD	0.365	14.24	99.9
8	8.625	0.004	410	0.1107	40.39	80.1	10S	0.148	29.87	99.2				
6	6.625	0.004	410	0.0880	40.39	80.1	5S	0.109	31.31	98.4				
4	4.500	0.004	410	0.0897	40.39	80.1	5S	0.083	29.17	99.6				
3	3.500	0.004	410	0.0473	40.39	80.1	5S	0.083	21.68	99.9				
2	2.375	0.004	410	0.0334	40.39	80.1	5S	0.065	18.93	99.9				
20	20.000	0.004					STD	0.375	26.80	99.9				
18	18.000	0.004					STD	0.375	23.84	99.9				
16	16.000	0.004					STD	0.375	21.08	99.9				
14	14.000	0.004					STD	0.375	18.31	99.9				
12	12.750	0.004					STD	0.375	18.59	99.9				
10	10.750	0.004					STD	0.365	14.24	99.9				
8	8.625	0.004					STD	0.322	12.88	99.9				
6	6.625	0.004					STD	0.280	11.28	99.9				
4	4.500	0.004					STD	0.237	8.87	99.9				
3	3.500	0.004					STD	0.216	7.44	99.9				
2	2.375	0.004					STD	0.154	7.08	99.9				

Table 2. Survival confidences for Type 316 stainless steel BWR pipe

Nominal Diameter (in)	Actual Diameter (in)	Corrosion Allowance (in)	Design Pressure (psi)	Calculated Thickness (in)	Hoop stress (ksi)	Survival Confidence (%)	Standard Pipe Schedule	Wall Thickness (in)	Hoop stress (ksi)	Survival Confidence (%)	Next Larger Schedule	Wall Thickness (in)	Hoop stress (ksi)	Survival Confidence (%)
20	20.000	0.004	410	0.2287	45.01	<77.5	10	0.250	40.84	84.9	STD	0.375	26.80	99.9
18	18.000	0.004	410	0.2044	45.01	<77.5	10	0.250	36.48	94.2	20	0.312	28.93	99.9
16	16.000	0.004	410	0.1821	45.01	<77.5	10	0.250	32.31	98.5				
14	14.000	0.004	410	0.1598	45.01	<77.5	10	0.250	28.14	99.7				
12	12.750	0.004	410	0.1459	45.01	<77.5	5S	0.165	38.58	87.9	10S	0.180	36.10	84.7
10	10.750	0.004	410	0.1237	45.01	<77.5	5S	0.134	41.36	92.6	10S	0.165	33.19	97.9
8	8.625	0.004	410	0.1000	45.01	<77.5	5S	0.109	41.07	93.7	10S	0.148	29.87	99.5
6	6.625	0.004	410	0.0778	45.01	<77.5	5S	0.109	31.31	99.0				
4	4.500	0.004	410	0.0641	45.01	<77.5	5S	0.083	29.17	99.7				
3	3.500	0.004	410	0.0430	45.01	<77.5	5S	0.083	21.68	99.9				
2	2.375	0.004	410	0.0304	45.01	<77.5	5S	0.065	18.93	99.9				

Nominal Diameter (in)	Actual Diameter (in)	Corrosion Allowance (in)
20	20.000	0.004
18	18.000	0.004
16	16.000	0.004
14	14.000	0.004
12	12.750	0.004
10	10.750	0.004
8	8.625	0.004
6	6.625	0.004
4	4.500	0.004
3	3.500	0.004
2	2.375	0.004

Standard Pipe Schedule	Wall Thickness (in)	Hoop stress (ksi)	Survival Confidence (%)
STD	0.375	26.80	99.9
STD	0.375	23.84	99.9
STD	0.375	21.08	99.9
STD	0.375	18.31	99.9
STD	0.375	18.59	99.9
STD	0.365	14.24	99.9
STD	0.322	12.88	99.9
STD	0.280	11.28	99.9
STD	0.237	8.87	99.9
STD	0.216	7.44	99.9
STD	0.154	7.08	99.9

Table 3. Survival confidences for SA-106 Grade B carbon steel BWR pipe

Nominal Diameter (in)	Actual Diameter (in)	Corrosion Allowance (in)	Design Pressure (psi)	Calculated Thickness (in)	Hoop stress (ksi)	Survival Confidence (%)	Standard Pipe Schedule	Wall Thickness (in)	Hoop stress (ksi)	Survival Confidence (%)	Next Larger Schedule	Wall Thickness (in)	Hoop stress (ksi)	Survival Confidence (%)
20	20.000	0.12	410	0.3804	36.88	94.1	30	0.500	25.95	99.8				
18	18.000	0.12	410	0.3833	36.89	94.1	STD	0.375	35.15	99.6				
16	16.000	0.12	410	0.3383	36.89	94.1	STD	0.375	31.13	99.9				
14	14.000	0.12	410	0.3093	36.89	94.1	20	0.312	36.34	99.9				
12	12.750	0.12	410	0.2924	36.88	94.1	30	0.330	30.09	99.0				
10	10.750	0.12	410	0.2663	36.89	94.1	30	0.307	28.44	99.9				
8	8.625	0.12	410	0.2366	36.88	94.1	20	0.250	32.98	99.8				
6	6.625	0.12	410	0.2096	36.88	94.1	STD	0.280	20.20	99.9				
4	4.500	0.12	410	0.1806	36.88	94.1	STD	0.237	18.89	99.9				
3	3.500	0.12	410	0.1673	36.89	94.1	STD	0.216	17.86	99.9				
2	2.375	0.12	410	0.1621	36.89	94.1	STD	0.154	34.77	99.8				
20	20.000	0.12					STD	0.375	19.17	98.1				
18	18.000	0.12					STD	0.375	36.15	99.6				
16	16.000	0.12					STD	0.375	31.13	99.9				
14	14.000	0.12					STD	0.375	27.11	99.8				
12	12.750	0.12					STD	0.375	24.80	99.9				
10	10.750	0.12					STD	0.365	21.48	99.9				
8	8.625	0.12					STD	0.322	20.86	99.9				
6	6.625	0.12					STD	0.280	20.20	99.9				
4	4.500	0.12					STD	0.237	18.89	99.8				
3	3.500	0.12					STD	0.216	17.86	99.9				
2	2.375	0.12					STD	0.154	34.77	99.8				

Table 4. Survival confidences for Type 304 stainless steel PWR pipe

Nominal Diameter (in)	Actual Diameter (in)	Corrosion Allowance (in)	Design Pressure (psi)	Calculated Thickness (in)	Hoop stress (ksi)	Survival Confidence (%)	Standard Pipe Schedule	Wall Thickness (in)	Hoop stress (ksi)	Survival Confidence (%)	Next Larger Schedule	Wall Thickness (in)	Hoop stress (ksi)	Survival Confidence (%)
20	20.000	0.003	894	0.5368	39.86	82.7	40	0.594	36.58	93.4	60	0.812	25.39	99.9
18	18.000	0.003	894	0.4831	39.86	82.7	XS	0.500	36.24	87.1	40	0.562	33.75	98.2
16	16.000	0.003	894	0.4298	39.86	82.7	XS	0.500	33.74	96.2	60	0.656	25.15	99.8
14	14.000	0.003	894	0.3784	39.86	82.7	40	0.438	33.73	96.2	XS	0.500	29.24	99.4
12	12.750	0.003	894	0.3431	39.86	82.7	STD	0.375	36.07	92.4	40	0.406	33.12	99.8
10	10.750	0.003	894	0.2896	39.86	82.7	30	0.307	37.28	89.7	STD	0.365	30.96	96.7
8	8.625	0.003	894	0.2331	39.86	82.7	20	0.250	36.79	90.8	30	0.277	33.94	97.1
6	6.625	0.003	894	0.1797	39.86	82.7	STD	0.280	24.49	99.9				
4	4.500	0.003	894	0.1230	39.86	82.7	STD	0.237	19.26	99.9				
3	3.500	0.003	894	0.0964	39.86	82.7	10S	0.120	31.19	98.5	STD	0.216	18.13	99.9
2	2.375	0.003	894	0.0664	39.86	82.7	10S	0.109	22.80	99.9				
20	20.000	0.003					XS	0.500	42.73	<77.5				
18	18.000	0.003					XS	0.500	38.24	87.1				
16	16.000	0.003					XS	0.500	33.74	96.2				
14	14.000	0.003					XS	0.500	29.24	99.4				
12	12.750	0.003					XS	0.500	28.43	99.9				
10	10.750	0.003					XS	0.500	21.94	99.9				
8	8.625	0.003					XS	0.500	17.18	99.9				
6	6.625	0.003					XS	0.432	15.02	99.9				
4	4.500	0.003					XS	0.337	12.82	99.9				
3	3.500	0.003					XS	0.300	10.93	99.9				
2	2.375	0.003					XS	0.218	10.11	99.9				
20	20.000	0.003					80	0.812	25.39	99.9				
18	18.000	0.003					80	0.750	24.89	99.9				
16	16.000	0.003					80	0.562	29.75	99.2				
14	14.000	0.003					XS	0.500	29.24	99.4				
12	12.750	0.003					XS	0.500	28.43	99.9				
10	10.750	0.003					STD	0.365	30.96	99.7				
8	8.625	0.003					STD	0.322	27.99	99.7				
6	6.625	0.003					STD	0.280	24.49	99.9				
4	4.500	0.003					STD	0.237	19.26	99.9				
3	3.500	0.003					STD	0.216	18.13	99.9				
2	2.375	0.003					STD	0.154	16.34	99.9				

Table 5. Survival confidences for Type 316 stainless steel PWR pipe

Nominal Diameter (in)	Actual Diameter (in)	Corrosion Allowance (in)	Design Pressure (psi)	Calculated Thickness (in)	Hoop stress (ksi)	Survival Confidence (%)	Standard Pipe Schedule	Wall Thickness (in)	Hoop stress (ksi)	Survival Confidence (%)	Larger Schedule	Wall Thickness (in)	Hoop stress (ksi)	Survival Confidence (%)
20	20.000	0.003	894	0.4834	44.28	<77.5	XS	0.500	42.73	78.3	40	0.593	36.85	96.4
18	18.000	0.003	894	0.4384	44.28	<77.5	30	0.437	44.11	<77.5	XS	0.500	38.24	90.9
16	16.000	0.003	894	0.3874	44.28	<77.5	XS	0.500	33.74	97.4	80	0.656	25.15	99.9
14	14.000	0.003	894	0.3393	44.28	<77.5	STD	0.375	39.62	87.2	40	0.438	33.73	97.5
12	12.750	0.003	894	0.3093	44.28	<77.5	STD	0.375	38.07	94.9	40	0.406	33.12	97.9
10	10.750	0.003	894	0.2612	44.28	<77.5	30	0.307	37.28	92.8	40S	0.365	30.95	99.1
8	8.625	0.003	894	0.2102	44.28	<77.5	20	0.250	36.79	93.7	40S	0.322	27.98	99.9
6	6.625	0.003	894	0.1621	44.28	<77.5	STD	0.280	24.49	99.9				
4	4.500	0.003	894	0.1111	44.28	<77.5	10S	0.120	40.75	54.8	40S	0.237	19.26	99.9
3	3.500	0.003	894	0.0871	44.28	<77.5	10S	0.120	31.19	99.0				
2	2.375	0.003	894	0.0601	44.28	<77.5	5S	0.065	40.57	55.1	10S	0.109	22.60	99.9
20	20.000	0.003					XS	0.500	42.73	78.3				
18	18.000	0.003					XS	0.500	38.24	90.9				
16	16.000	0.003					XS	0.500	33.74	97.4				
14	14.000	0.003					XS	0.500	29.24	99.5				
12	12.750	0.003					XS	0.500	26.43	99.9				
10	10.750	0.003					XS	0.500	21.94	99.9				
8	8.625	0.003					XS	0.500	17.16	99.9				
6	6.625	0.003					XS	0.432	15.02	99.9				
4	4.500	0.003					XS	0.337	12.82	99.9				
3	3.500	0.003					XS	0.300	10.93	99.9				
2	2.375	0.003					XS	0.218	10.11	99.9				
20	20.000	0.003					60	0.812	25.39	99.9				
18	18.000	0.003					40	0.562	33.75	97.4				
16	16.000	0.003					XS (40)	0.500	33.74	97.4				
14	14.000	0.003					40	0.438	33.73	97.4				
12	12.750	0.003					40	0.406	33.12	97.9				
10	10.750	0.003					STD	0.365	30.95	99.1				
8	8.625	0.003					STD	0.322	27.98	99.9				
6	6.625	0.003					STD	0.280	24.49	99.9				
4	4.500	0.003					STD	0.237	19.26	99.9				
3	3.500	0.003					STD	0.216	16.13	99.9				
2	2.375	0.003					STD	0.154	15.34	99.9				

Table 6. Survival confidences for SA-106 Grade B carbon steel PWR pipe

Nominal Diameter (in)	Actual Diameter (in)	Corrosion Allowance (in)	Design Pressure (psi)	Calculated Thickness (in)	Hoop stress (ksi)	Survival Confidence (%)	Standard Pipe Schedule	Wall Thickness (in)	Hoop stress (ksi)	Survival Confidence (%)	Standard Pipe Schedule	Wall Thickness (in)	Hoop stress (ksi)	Survival Confidence (%)
20	20.000	0.06	894	0.8421	38.18	99.4	80	0.812	27.49	99.9				
18	18.000	0.06	894	0.5839	38.18	99.4	80	0.750	28.92	99.9				
16	16.000	0.06	894	0.5257	38.18	99.4	80	0.656	27.77	99.9				
14	14.000	0.06	894	0.4675	38.18	99.4	XS	0.500	33.32	99.9				
12	12.750	0.06	894	0.4311	38.18	99.4	XS	0.500	30.15	99.9				
10	10.750	0.06	894	0.3729	38.18	99.4	XS	0.500	26.07	99.9				
8	8.625	0.06	894	0.3110	38.18	99.4	STD	0.322	34.55	99.8				
6	6.625	0.06	894	0.2529	38.18	99.4	STD	0.280	31.42	99.9				
4	4.500	0.06	894	0.1910	38.18	99.4	STD	0.237	28.18	99.9				
3	3.500	0.06	894	0.1619	38.18	99.4	STD	0.216	22.84	99.9				
2	2.375	0.06	894	0.1291	38.18	99.4	STD	0.154	28.00	99.9				
20	20.000	0.06					XS	0.500	48.58	91.8				
18	18.000	0.06					XS	0.500	43.48	97.7				
16	16.000	0.06					XS	0.500	38.40	99.9				
14	14.000	0.06					XS	0.500	33.32	99.9				
12	12.750	0.06					XS	0.500	30.15	99.9				
10	10.750	0.06					XS	0.500	26.07	99.9				
8	8.625	0.06					XS	0.500	19.67	99.9				
6	6.625	0.06					XS	0.432	17.87	99.9				
4	4.500	0.06					XS	0.337	15.92	99.9				
3	3.500	0.06					XS	0.300	14.08	99.9				
2	2.375	0.06					XS	0.218	14.58	99.9				
20	20.000	0.06					40	0.593	39.70	99.7				
18	18.000	0.06					XS	0.500	43.48	97.7				
16	16.000	0.06					XS (40)	0.500	38.40	99.5				
14	14.000	0.06					40	0.438	39.15	99.8				
12	12.750	0.06					STD	0.375	43.00	98.7				
10	10.750	0.06					STD	0.365	37.15	99.9				
8	8.625	0.06					STD	0.322	34.55	99.9				
6	6.625	0.06					STD	0.280	31.42	99.9				
4	4.500	0.06					STD	0.237	28.18	99.9				
3	3.500	0.06					STD	0.216	22.84	99.9				
2	2.375	0.06					STD	0.154	28.00	99.9				

The study showed that for initial bolt preload stresses of 40 ksi, all sizes of Class 300 flanges can be pressurized to the ABWR pressure of 1025 psig without exceeding the 99% confidence GLP. Section 3.2.1 of NUREG/CR-5603 states that a bolt preload of 30 ksi is a representative -3β lower bound for Class 300 and 600 flanges. A calculation using a 30 ksi bolt preload showed that the lowest 99% confidence GLP was 1440 psi. For initial bolt preload stresses of 40 ksi, all sizes of Class 600 flanges can be pressurized to the PWR pressure of 2235 psig without exceeding the 99% confidence GLP. A calculation using a 30 ksi bolt preload showed the lowest 99% confidence GLP to be 2446 psi.

Valves

Unlike piping and flanges, which more or less have standard designs, there are many different styles of valves, each of which has unique features based on the valve's functional purpose. Since for ISLOCA design we are only interested in the valve's pressure-retaining capabilities, the internals of valves were not considered.

As discussed in NUREG/CR-5603, there are three areas of the valve where leakage may take place: the valve body (and bonnet), bolted connections, and packing. The pressure ratings for valves from ASME B16.34 (1981) are identical to those for flanges. Section III (NC-3521) of the ASME Code states that the valve section modulus and metal area shall not be less that 110% of the comparable piping parameters. Table NC-3521-1 of ASME Code Section III allows a 1.1 factor on design pressure for Service Level B. From this we can conclude that the walls of the valve will be at least as thick as the walls of the attached piping, so the survival confidences for the valve body will be at least as great as that of the attached piping. Valves will be hydrostatically pressure tested to (or very nearly to) the ISLOCA pressure.

The recommendations for Class sizes and bolt preloads made for flanges also were considered to be applicable for valve bolted connections. The packing leakage is expected to be minimal since the leak area through any degraded areas of the packing material is expected to be small.

Pumps

In contrast to piping and flanges, which more or less have standard designs, there are many different types of pumps, each of which has unique features. Since for ISLOCA design we are only interested in the pump's pressure-retaining capabilities, the pump internals will not be examined in this report.

There are three general areas of the pump where the loss of the pressure-retaining boundary may take place: the casing, bolted connections, and seals. Piping connected to pumps is designed to a minimum wall thickness proportional to the pipe radius. The pressure stresses in the pump casing should be less than in the adjoining piping, and the survival confidence of the pump casing will be greater

the adjoining piping, and the survival confidence of the pump casing will be greater than that of the adjacent piping. The recommended Class sizes and bolt preloads made for flanges also are considered applicable for pump bolted connections.

Seals are judged to be have the highest potential for leakage of the pump subcomponents. NUREG/CR-5603 recommends that a nominal leak rate of 100 to 200 mg/sec be assumed as the pump seal leakage rate under ISLOCA conditions. Since 200 mg/s is much less than 1 gpm, a leak rate of this magnitude would have a negligible affect on the total RCS fluid inventory. Westinghouse Electric Corporation (1993) has stated that the RHR pump seal is the only AP600 component connected to the RCS that is not designed to have an ultimate rupture strength equal to the normal RCS operating pressure. They report that the rupture pressure of the seals with the RHR pumps operating is 670 to 700 psig, and that a seal designed to withstand full RCS pressure will likely experience abnormally fast wear during normal operation. Based on the minimal leakage expected through the pump mechanical seals during an ISLOCA event, it appears that the Westinghouse proposal of allowing the mechanical seals to fail, but to minimize and control the leakage, is a satisfactory approach.

Heat Exchangers

Heat exchangers can be designed using either the shell or the tube side as the boundary for the hotter coolant. The tubes and tubesheet separate the hotter and cooler fluids. The tubesheet is located between two bolted flanges and sealed from the flanges by gaskets on the tubesheet top and bottom; however, there are several varieties of flange and tubesheet design [TEMA (1982)].

Although the ASME Code has design rules for component stress allowables, it is not detailed enough to deal with all the special features of heat exchanger design. A universally accepted code that provides minimum standards for heat exchanger design is the TEMA Standards (1982). This standard was originally designed to supplement Section VIII, Division 1, of the ASME Code.

Shells. Hoop stresses for cylindrical shells were calculated the same as for piping for BWR and PWR conditions. Survival probabilities at a pressure ratio of 0.4 (410 psi for BWRs, 894 psi for PWRs) were calculated to be about 85 to 90%. A pressure ratio of about 0.48 to 0.49 is needed to achieve a survival confidence of 98% (10^{-3} failure probability at YS), and about 0.45 at 10^{-4} failure probability at YS. Since there is less metal in heat exchangers than in pipes, a 10^{-4} failure probability at YS would seem appropriate for the shells. However, like pipes, the shells would be made of plate that would probably be chosen to the nearest 1/8 inch. For cylindrical shells designed for BWR conditions and constructed of plates where the thickness is divisible by 1/8 inch, six of the ten example thickness survival confidences were calculated to be greater than 98%. Similar calculations for SA-516 Grade 70 carbon steel shells showed that the survival confidences were greater than 99% for both BWR and PWR conditions.

Hemispherical heads. The thickness for hemispherical heads needs to be only about half of that of the cylindrical shell. Therefore for cylindrical shells and heads of nearly equal thickness, failure is controlled by burst of the cylindrical shell.

Torispherical and ellipsoidal heads. NUREG/CR-5603 discusses two failure modes for dished heads - plastic collapse and knuckle buckling. For dished heads with low r/t ratios, Galletly and Aylward (1979) determined that head failure will occur because of plastic collapse rather than knuckle buckling. Galletly defines plastic collapse as the pressure where the deflection of the crown is twice the deflection that occurs at a pressure when the material yields. However, plastic collapse by itself does not represent a failure of the head, only that a certain strain level has been reached, or a lower-bound plastic hinge will form. Bennett (1987) has tested torispherical heads modeling nuclear reactor containments, and found that failure occurs first by the occurrence of knuckling buckling, and later at a higher pressure 2.4 to 3.7 times the buckling pressure. No mention is made of plastic collapse. Therefore, for design considerations for ISLOCA, plastic collapse will not be considered as a credible failure mode.

NUREG/CR-5603 recommends increasing the analytically computed pressures by a factor of 1.78 (based on limited experimental data) to determine the expected mean capacities. Bennett (1987) reports a rupture pressure of 2.7 to 3.4 times the buckling pressure calculated using the BOSOR-5 Code. The NUREG/CR-5603 approach was followed in this ISLOCA study. Bennett (1987) states that based on his experiments, "no truly conservative, and accurate equation has been found to predict the results of these fabricated shell experiments at this time. ... For margin-to-buckling studies, where actual containment geometry is known, a BOSOR-5 analysis or the Galletly formula using the 'worst meridian' will provide a good estimate of the buckling pressure". Consequently, the calculations in the study used the Galletly equations.

To provide an example for torispherical heads with representative numbers, we can use the dimensions in Figure NC-3324.2-1 of Section III, where L/D = 1.5 + 1.75/2 + 2 = 0.857, and a knuckle radius of 0.06 of the crown radius. The results (using β = 0.224 for stainless steel and 0.245 for carbon steel) showed that using the equation from Radhamoham and Galletly (1979), the 99% buckling pressures are all above the ISLOCA pressure, even without applying the 1.78 factor to compute the failure pressure.

The Galletly and Aylward (1979) equation for ellipsoidal head knuckle bucking was used to calculate the buckling pressures, which were multiplied by 1.78 to obtain the estimated failure pressure, and from these the 99% survival confidence pressures were calculated. These all were above the ISLOCA pressures. However, it is assumed in NUREG/CR-5603 that in 20% of buckling cases, a crack will develop at the critical buckling pressure. For the case with the least margin, Type 304 stainless steel at BWR conditions, the survival confidence at 1025 psi is 73.6%. If failure occurs during 20% of the 26.4% of the cases where buckling occurs at

1025 psig, then failure (rupture) will occur only 5.3% of the time, and the overall survival confidence is 94.7%. Since there will be some margin based on fabricating the head from plate that is made in 1/8-inch increments, the confidence will no doubt be greater than 98% for actual heads.

Tubes and tubesheets. The survival confidences for heat exchanger tubes can be calculated the same as for pipes. Using the methodology for piping, the minimum survival confidences for heat exchanger tubes subject to internal pressure designed to 40% primary coolant pressure at 350°F are 90% for Type 304 stainless steel. However, if the minimum tube thicknesses specified in the TEMA standards are used, the minimum survival confidences for tubes up to 2 inches (under internal pressure) are higher. A corrosion allowance of 0.004 inches for BWRs and 0.003 inches for PWRs was used. Tubes with wall thicknesses made according to TEMA standards would have greater than 99.9% survival confidence at BWR pressures, and also for PWR pressures with the exception of 1 and 1 1/4 in. tubes. The 1-in. 20 gage tube has a survival confidence of 97.4%, but the 1 1/4-in. 20 gage tube has only an 88.2% survival confidence. A 1 1/4-in. 18 gage tube has a survival confidence of greater than 99%.

Since tubesheets are basically flat plates, their primary failure modes would be from shear or bending, not from bursting as in the case of piping. The bending and shear stresses are related to the tube hole pattern, and therefore are tubesheet dependent. Formulas (both bending and shear) for the minimum design thickness of tubesheets, based on the type of construction, are given in the TEMA standards. The major concern with tubesheets is leakage at flanged joints. The recommendations on Class sizes and bolt preloads made for flanges also are applicable for tubesheet flanges.

Tanks

In most if not all cases, it will probably prove impractical to design large tanks for ISLOCA pressures. Should there be cases in which tanks will be designed for ISLOCA conditions, the formulas and method for vessels in Section 4.5 can be used. These showed that for the cylindrical portion of the shell, a pressure ratio of between 0.45 and 0.50 is required to meet ISLOCA confidence limits for Type 304 stainless steel. A pressure ratio of 0.40 would provide 99% survival confidence for SA-516 Grade 70 carbon steel.

CONCLUSIONS AND RECOMMENDATIONS

The NUREG/CR-5603 methodology for system rupture survival during an ISLOCA event has been applied to ALWR plants. Conditions of 350°F and BWR pressures of 1025 psig and PWR pressures of 2235 psig were used. The goal of the study was to develop criteria such that each of the types of components in the system will achieve about a 98% survival confidence, so that the overall system survival confidence would be about 90%.

The confidence limits were determined by developing stress failure curves that used a failure stress, defined as 0.9 and 0.85 times the median UTS for carbon and stainless steel, respectively, as the median failure stress. The uncertainty was determined by selecting the 0.001 confidence failure stress as the median YS. This assumption in establishing the uncertainty is based on the probability of a large crack existing in the metal, either induced during manufacture or in operation. There does not appear to be a straightforward way to establish the uncertainty. An alternate approach considered the operating experience in nuclear components that have been designed and operated according to the ASME Code. The alternate method of developing an uncertainty for the failure curves leads to basically the same conclusion as does the method in NUREG/CR-5603, that is, the minimum system survival confidence at 2.5 times the Level A design stress is greater than 90%. This argument is based on actual operating data, and shows a better balance between the carbon and stainless steel survival probabilities than does the NUREG/CR-5603 method.

Available YS and UTS data were used to evaluate the YS and UTS values used in NUREG/CR-5603. It was concluded that the NUREG/CR-5603 values were representative for SA-106 Grade B carbon steel, but alternate curves were developed and used for stainless steels and SA-516 Grade 70 carbon steel.

A pressure ratio of 0.4 (the design pressure divided by the operating pressure) was investigated. The conclusions were that this pressure ratio was a suitable value for most cases. The recommended sizes for components are:

- Pipe and pipe fittings

  BWR - STD for all materials
  PWR - STD up to 10 in. for all materials
  SA-106 Grade B - 12 in., STD; 14 to 20 in., Sch. 40
  Type 316 - 12 to 18 in., Sch. 40.; 20 in., Sch. 60
  Type 304 - 12 to 14 in., XS; 16 to 20 in., Sch. 60

- Flanges

  BWR - Class 300
  PWR - Class 600
  Bolts - High strength with 40 ksi preload

- Valves

  BWR - Class 300
  PWR - Class 600

- Pumps

  Design for 0.4 pressure ratio
  Seals - Need not design for ISLOCA but allow minimal leakage

- Heat exchangers

  Cylindrical shell - Design for pressure ratio of 0.40 (SA-516 Grade 70 carbon steel), 0.45 (Type 304 stainless steel)[7]
  Heads - Design for 0.4 pressure ratio
  Tubes and tubesheets - Design to TEMA standards except 20 gage for 1-in and 18 gage for 1 1/4 in. tube for PWRs

These recommendations will satisfy the goal of 90% confidence that gross leakage will not occur to the system during an ISLOCA, but will not assure that component will remain operable during, or fit for service after, an ISLOCA event.

REFERENCES

American Society of Mechanical Engineers, 1992, ***Boiler and Pressure Vessel Code***, Section III, Division 1, Subsection NC and Appendix I.

American Society of Mechanical Engineers, 1988, ***Pipe Flanges and Flanged Fittings***, B16.5.

American Society of Mechanical Engineers, 1981, ***Valves--Flanged and Buttwelding End***, B16.34.

The American Society of Mechanical Engineers, 1985a, ***Welded and Seamless Wrought Steel Pipe***, ANSI B36.10M-1985.

The American Society of Mechanical Engineers, 1985b, ***Stainless Steel Pipe***, ANSI B36.19M-1985.

Bennett, J. G., 1987, ***An Assessment of Loss-of-Containment Potential Because of Knuckle Buckling for 4:1 Steel Containment Heads***, NUREG/CR-4926, LA-10972-MS.

Chu, T.-L., et al., 1989, ***Interfacing Systems LOCA: Boiling Water Reactors***, NUREG/CR-5124, BNL-NUREG-52141.

[7] Based on 10^{-4} survival confidence at yield stress.

Galletly, G. D., and R. W. Aylward, 1979, "Plastic Collapse and the Controlling Failure Pressures of Thin 2:1 Ellipsoidal Shells Subjected to Internal Pressure", ***Journal of Pressure Vessel Technology 101***, pp. 64-72.

Galyean, W. J., et al., 1993, ***ISLOCA Research Program Final Report***, NUREG/CR-5928, EGG-2685.

Harvey, P. D., Editor, 1985, ***Engineering Properties of Steel***, American Society for Metals, Metals Park, Ohio.

Inside N.R.C., 1993, "French, German Safety Officials Set Common Goals for Advanced PWR", Vol. 15, No. 15, July 26, 1993, pp. 1, 14-16.

Manjoine, M. H., 1975, "Ductility Indices at Elevated Temperature", ***Journal of Engineering Materials and Technology 97, Series H, Number 2***, pp. 156-161.

Nuclear Regulatory Commission, 1990, "Evolutionary Light Water Reactor (LWR) Certification Issues and Their Relationship to Current Regulatory Requirements", SECY-90-016.

Radhamoham, S. K., and G. D. Galletly, 1979, "Plastic Collapse of Thin Internally Pressurized Torispherical Shells", ***Journal of Pressure Vessel Technology 101***, pp. 311-320.

Simmons, W. F., and J. A. Van Echo, 1965, ***Report on the Elevated-Temperature Properties of Stainless Steels***, ASTM Data Series Publication DS 5 - S1 (Supplement to Publication DS 5, formerly STP 124).

Simmons, W. F., and H. C. Cross, 1952, ***Elevated-Temperature Properties of Stainless Steels***, ASTM Special Publication No. 124.

Simmons, W. F., and H. C. Cross, 1955, ***Elevated-Temperature Properties of Carbon Steels***, ASTM Special Publication No. 180.

Smith, G. V., 1969, ***An Evaluation of the Yield, Tensile, Creep, and Rupture Strengths of Wrought 304, 316, 321, and 347 Stainless Steels at Elevated Temperatures***, ASTM Data Series DS 5 - S2 (Supplement to Publication DS 5, formerly STP 124).

Smith, G. V., 1972, ***Elevated Temperature Static Properties of Wrought Carbon Steel***, ASME Special Technical Publication 503.

Tubular Exchanger Manufacturers Association, Inc., 1982, ***Standards of Tubular Exchanger Manufacturers Association***.

Ware, A. G., 1993, ***Component Evaluation for ISLOCA in ALWRs (Draft)***, NUREG/CR-6121, EGG-2717.

Weiss, V., and J. G. Sessler, Editors, 1963, ***Aerospace Structural Metals Handbook, Volume 1: Ferrous Alloys***, ASD-TDR-67-741, Air Force Materials Laboratory, Wright-Patterson Air Force Base, Ohio.

Wesley, D. A., et al., 1990, ***Pressure-Dependent Fragilities for Piping Components***, NUREG/CR-5603, EGG-2607.

Wesley, D. A., 1992, ***Screening Methods for Developing Internal Pressure Capacities for Components in Systems Interfacing with Nuclear Power Plant Reactor Coolant Systems***, NUREG/CR-5862, EGG-2673.

Westinghouse Electric Corporation, 1993, Response to Question 440.30, NRC Request for Additional Information, AP600.

NOTICE

This paper was prepared as an account of work sponsored by an agency of the United States Government. Neither the United States Government nor any agency thereof, or any of their employees, makes any warranty, expressed or implied, or assumes any legal liability or responsibility for any third party's use, or the results of such use, of any information, apparatus, product or process disclosed in this report, or represents that its use by such third party would not infringe privately owned rights. The views expressed in this paper are not necessarily those of the U.S. Nuclear Regulatory Commission.

STRUCTURAL AGING PROGRAM APPROACH TO PROVIDING AN IMPROVED BASIS FOR AGING MANAGEMENT OF SAFETY-RELATED CONCRETE STRUCTURES*

Dan J. Naus and C. Barry Oland
Oak Ridge National Laboratory (ORNL)
Oak Ridge, TN 37831-8056

Bruce Ellingwood
The Johns Hopkins University
2400 N. Charles Street
Baltimore, MD 21218

ABSTRACT

The Structural Aging (SAG) Program is being conducted at the Oak Ridge National Laboratory (ORNL) for the United States Nuclear Regulatory Commission (USNRC). The SAG Program is addressing the aging management of safety-related concrete structures in nuclear power plants for the purpose of providing improved technical bases for their continued service. The program is organized into four tasks: Program Management, Materials Property Data Base, Structural Component Assessment/Repair Technologies, and Quantitative Methodology for Continued Service Determinations. Objectives and a summary of recent accomplishments under each of these tasks are presented.

1. INTRODUCTION

Concrete structures play a vital role in the safe operation of all light-water reactor plants since they provide foundation, support, shielding, and containment functions. History tells us that concrete can be a very durable material. However, a number of factors can compromise its performance, singly or in combination: (1) faulty design, (2) use of unsuitable materials, (3) improper workmanship, (4) exposure to aggressive environments, (5) excessive structural loads, and (6) accident conditions. Furthermore, aging of nuclear power plant concrete structures occurs with the passage of time and has the potential, if its effects are not controlled, to increase the risk to public health and safety. Many factors complicate the affect of aging on the residual life of the concrete structures in a plant. Uncertainties arise due to: (1) differences in design codes and standards for components of different vintage; (2) lack of past measurements and

*Research sponsored by the Office of Nuclear Regulatory Research, U.S. Nuclear Regulatory Commission under Interagency Agreement 1886-8084-5B with the U.S. Department of Energy under Contract DE-AC05-84OR21400 with Martin Marietta Energy Systems, Inc.

The submitted manuscript has been authored by a contractor of the U.S. Government under Contract No. DE-AC05-84OR21400. Accordingly, the U.S. Government retains a nonexclusive, royalty-free license to publish or reproduce the published form of this contribution, or allow others to do so, for U.S. Government purposes.

records; (3) limitations in the applicability of time-dependent models for quantifying the contribution of aging to overall structure failure; and (4) inadequacy of detection, inspection, surveillance, and maintenance methods or programs [1].

2. BACKGROUND

In general, the performance of concrete materials and structures in nuclear power plants has been good. To a large degree, this can be attributed to the effectiveness of the quality control/quality assurance programs in detecting potential problems (and subsequent remedial measures) prior to plant operation [2]. However, there have been several instances in nuclear power plants where the capability of concrete structures to meet future functional and performance requirements has been challenged due to problems arising from either improper material selection, construction/design deficiencies, or environmental effects. Examples of some of the potentially more serious instances include anchorhead failures, voids under vertical tendon bearing plates, dome delaminations, and corrosion of steel tendons and rebars. Other problems such as the presence of voids or honeycomb in concrete, contaminated concrete, cold joints, cadweld (steel reinforcement connector) deficiencies, concrete cracking, higher than code-allowable concrete temperatures, materials out of specification, misplaced steel reinforcement, lower than predicted prestressing forces, post-tensioning system buttonhead deficiencies, water contaminated corrosion inhibitors, water intrusion through basemat cracks, low tensile strength of post-tensioning tendon wire material, leaching of concrete in tendon galleries, and leakage of corrosion inhibitor from tendon sheaths also have been identified [3-5].

3. STRUCTURAL AGING PROGRAM

Incidences of structural degradation related to the concrete components in nuclear power plants indicate that there is a need for improved surveillance, inspection/testing, and maintenance to enhance the technical bases for assurances of continued safe operation of nuclear power plants. The Structural Aging (SAG) Program has the overall objective of preparing documentation that will provide the USNRC license reviewers with the following: (1) identification and evaluation of the structural degradation processes; (2) issues to be addressed under nuclear power plant continued-service reviews, as well as criteria, and their bases, for resolution of these issues; (3) identification and evaluation of relevant in-service inspection or structural assessment programs; and (4) methodologies required to perform current assessments and reliability-based life predictions of safety-related concrete structures. To accomplish this objective, the SAG Program is addressing the sources of uncertainty identified earlier with respect to determination of the residual life of safety-related concrete structures. Structural Aging Program activities are conducted under four task areas: (1) program management, (2) materials property data base, (3) structural component assessment/repair technologies, and (4) quantitative methodology for continued service determinations.

3.1 Program Management

3.1.1 Objective and Scope

The overall objective of the program management task is to effectively manage the technical tasks undertaken to address priority structural safety issues related to nuclear power plant

continued service assessments. Management duties include planning, integrating, monitoring, reporting, and technology transfer. A key part of the management function is the integration of the technical objectives and the efforts of program participants. Figure 1 presents program participants listed by task under which their particular activity falls.

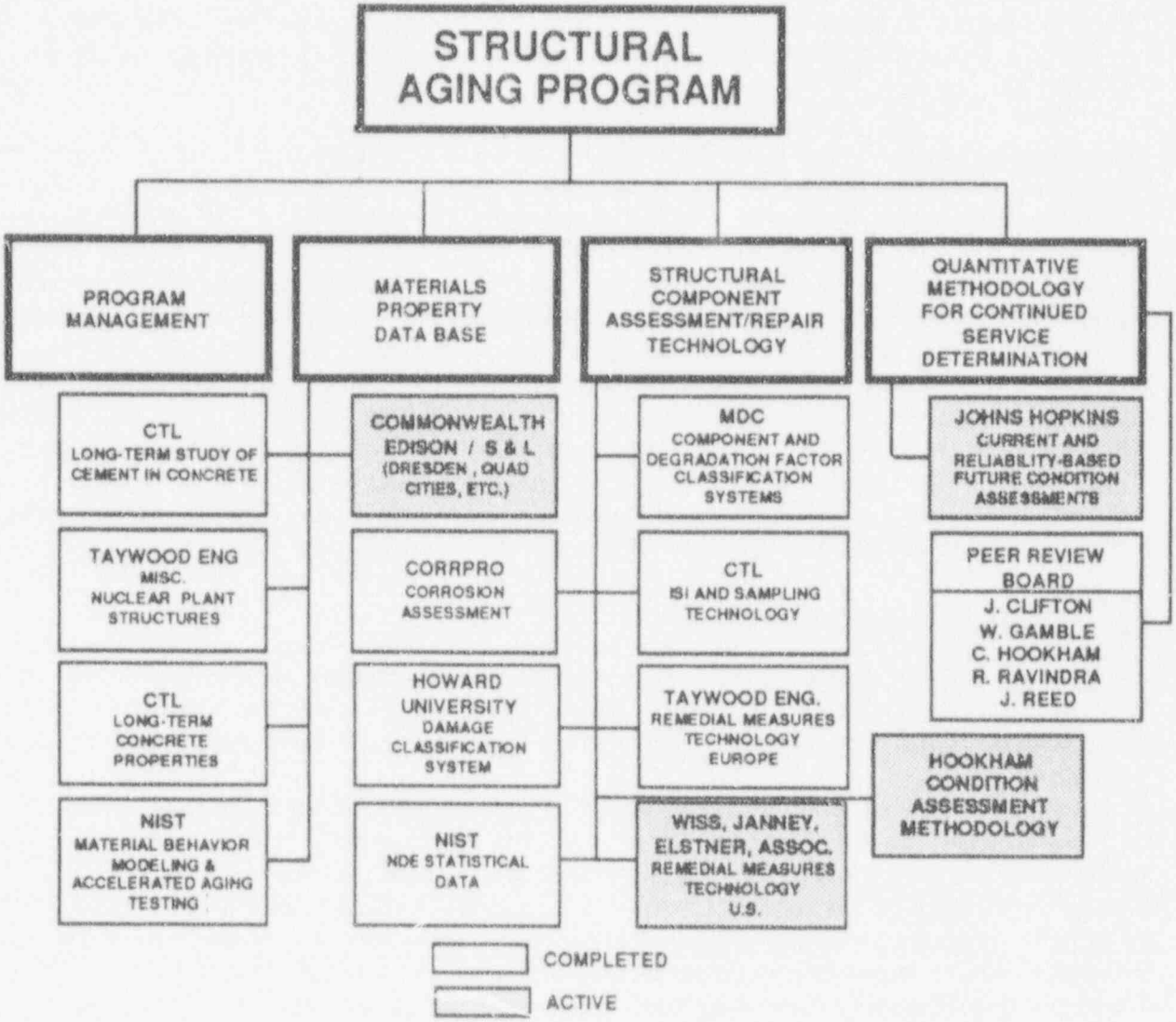


Figure 1. Organization of the Structural Aging Program.

3.1.2 Summary of Recent Accomplishments

Recent activities under this task have included administration of six subcontracts, and preparation of an annual technical progress report [6] and two foreign trip reports [7,8]. Program presentations have been made at the *NIST 1993 Building Technology Symposia Series* [9], *Electric Power Research Institute Life Cycle Management Subcommittee Meeting* [10], *International Conference on Failures of Concrete Structures* [11], *International Atomic Energy Agency Coordinated Research Program Meeting on Management of Ageing of Concrete Containment Buildings* [12], *American Society of Mechanical Engineers Pressure Vessel and Piping Conference* [13], *International Conference on Safety and Reliability* [14], *12th*

International Conference on Structural Mechanics in Reactor Technology [15-17], and *Post-SMiRT Conference Seminar - Containment of Nuclear Reactors* [18]. In addition, program personnel participated in technical committees of the American Concrete Institute (Service Life Prediction, Concrete Materials Property Database, and Radioactive and Hazardous Waste Management), American Society of Mechanical Engineers (Section XI Working Group on Concrete Pressure Components and Subgroup on Containments), and International Union of Testing and Research Laboratories for Materials and Structures (Damage Classification of Concrete Structures).

3.2 Materials Property Data Base

3.2.1 Objective and Scope

The objective of the materials property data base task is to develop a reference source which contains data and information on the time variation of material properties under the influence of pertinent environmental stressors and aging factors. This source will be used to assist in the prediction of potential long-term deterioration of critical structural components in nuclear power plants and to establish limits on hostile environmental exposure for these structures. Primary activities under this task have included continuing the development of the Structural Materials Information Center and assemblage of materials property data. In addition, survey data and a durability assessment review of several reinforced concrete structures contained as a part of several nuclear power stations located in England were assembled.

3.2.2 Summary of Recent Accomplishments

Structural Materials Information Center (SMIC). Formatting of the SMIC has been completed and results presented in a report [19]. Contained in the report are detailed descriptions of the *Structural Materials Handbook* and the *Structural Materials Electronic Data Base* which form the SMIC.

The *Structural Materials Handbook*, when issued, will be an expandable, hard-copy reference document containing complete sets of data and information for each material. The handbook includes four volumes that will be provided in loose-leaf binders for ease of revision and updating. Volume 1 will contain performance and analysis information useful for structural assessments and safety margins evaluations, e.g., performance values for mechanical, thermal, physical, and other properties presented as tables, graphs, and mathematical equations. Volume 2 will provide test results and data used to develop the performance values in Volume 1. Volume 3 will contain material data sheets providing general information, as well as material composition and constituent material properties, for each material system contained in the handbook. Volume 4 will contain appendices describing the handbook organization, and updating and revision procedures. Example pages contained in Volumes 1-3 which have been prepared for a long-term study of concrete properties [20] are presented in Figs 2-4, respectively.

The *Structural Materials Electronic Data Base* when issued will be an electronically accessible version of the *Structural Materials Handbook*. Due to software limitations, the electronic data base will not be as comprehensive as the handbook, but it will provide an efficient means for searching the various data base files to locate materials with similar characteristics or properties. The electronic data base is being developed on an IBM-compatible personal computer and employs two software programs: Mat.DB [21] and EnPlot [22]. Mat.DB is a menu-driven software program for data base management that employs window overlays to access data searching and editing features. It is capable of maintaining, searching, and

displaying textual, tabular, and graphical information and data contained in electronic data base files. EnPlot is a software program that incorporates pop-up menus for creating and editing

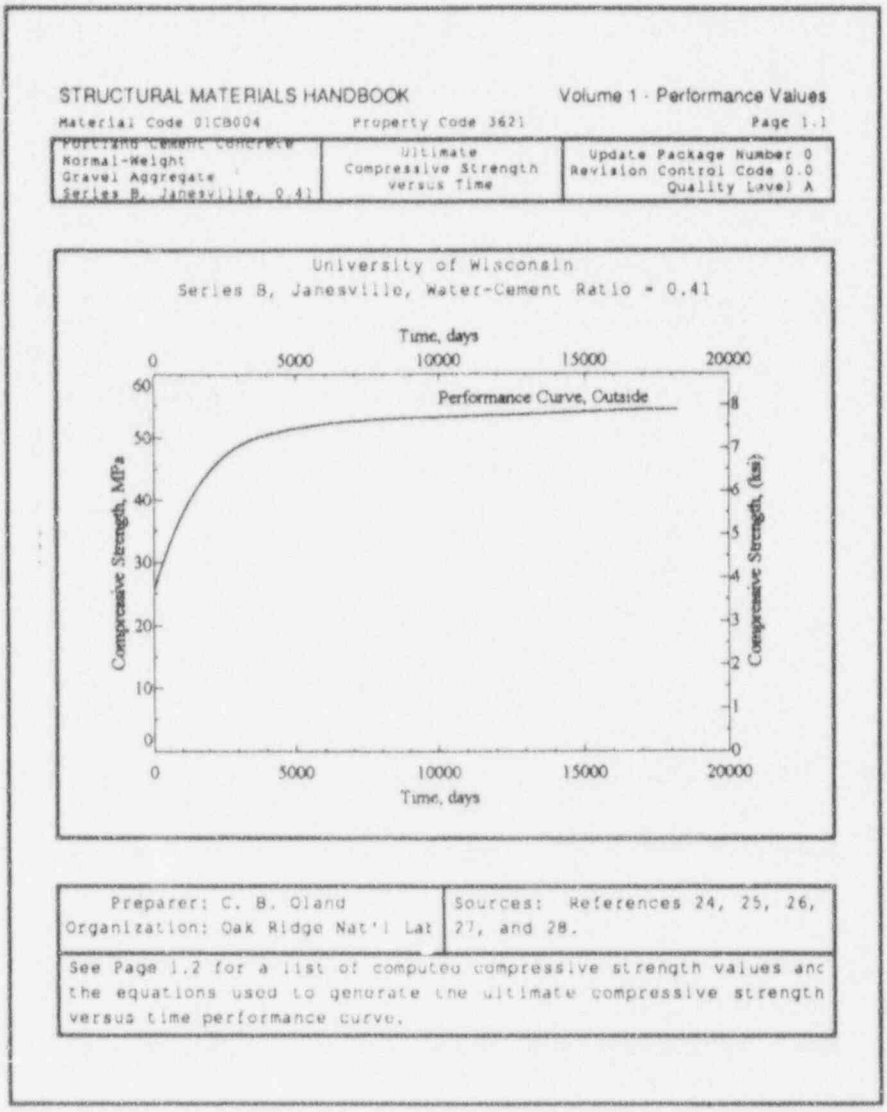


Figure 2. Example of page from Volume 1 (Performance Values) of Structural Materials Handbook.

engineering graphs. It includes curve-fitting and scale-conversion features for preparing engineering graphs and utility features for generating output files. The graphs generated with EnPlot can be entered directly into the Mat.DB data base files.

To date, 139 material data bases (123 concrete, 12 metallic reinforcement, 1 prestressing steel, 2 structural steel, and 1 rubber material) have been developed. Concrete material property data and information files currently contained in the SMIC include: ultimate compressive strength, dynamic modulus of elasticity, and flexural strength versus time for several different concrete materials which had been cured under a variety of conditions (air drying, moist curing, or outdoor exposure) for periods up to 50 years; ultimate compressive strength and modulus of elasticity versus temperature at exposures up to 600°C for durations up to four months; dynamic modulus of elasticity, ultimate compressive strength, flexural strength and weight change versus

STRUCTURAL MATERIALS HANDBOOK Volume 2 - Supporting Documentation

Material Code 01CB004 Property Code 3621 Page 1.3

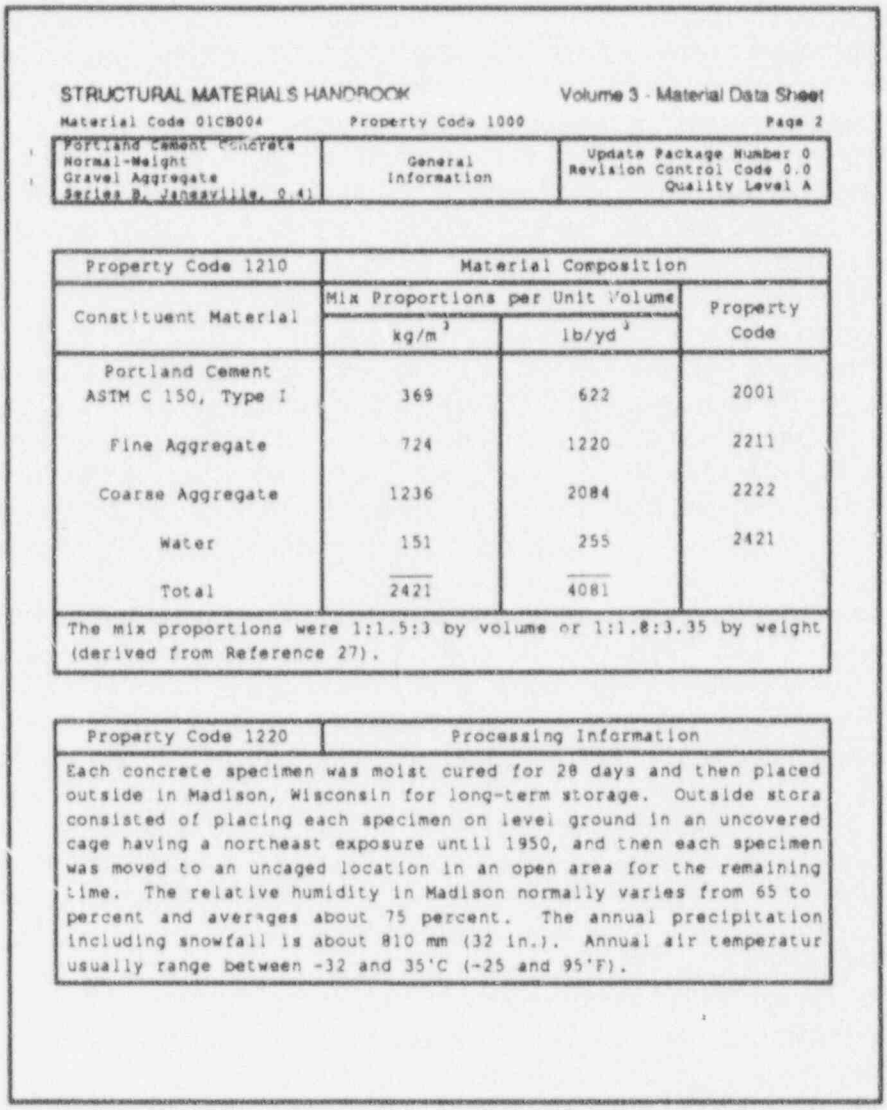
Portland Cement Concrete Normal-Weight Gravel Aggregate Series B, Janesville, 0.4)	Ultimate Compressive Strength versus Time	Update Package Number 0 Revision Control Code 0.0 Quality Level A

Cement Vendor	Compressive Strength Test Results for Specimens Stored Outside, MPa (psi) at: 7 Days	28 Days	1 Year	5 Years	10 Years	25 Years	50 Years
Medusa (3M)	16.0 (2325)	22.9 (3315)	31.6 (4580)	46.7 (6780)	50.1 (7260)	51.0 (7400)	49.0 (7110)
Lehigh (4M)	18.1 (2620)	23.8 (3455)	33.9 (4910)	47.8 (6930)	49.6 (7195)	52.1 (7555)	59.7 (8660)
Universal (5M)	17.4 (2530)	27.8 (4035)	34.8 (5050)	48.0 (6960)	47.6 (6900)	55.1 (7990)	48.7 (7070)
Marquette (7M)	19.3 (2805)	28.2 (4095)	35.8 (5190)	49.3 (7145)	52.5 (7615)	54.1 (7850)	60.1 (8715)
Average	17.7 (2570)	25.7 (3725)	34.0 (4930)	48.0 (6955)	49.9 (7240)	53.1 (7700)	54.4 (7890)

Test specimens were cast with each of these four cements, moist cu for 28 days, and then placed outside in Madison, Wisconsin for long-term storage. Each value listed above is the average compressive strength (Property Code 3023) from five test specimens (Reference 27).

Figure 3. Example of page from Volume 2 (Supporting Documentation) of Structural Materials Handbook.

radiation exposure; ultimate compressive strength for stressed (maintained at 20 to 55% baseline compressive strength while heated) and unstressed specimens versus temperature for exposures up to 871°C; weight loss versus time for specimens subjected to sulfuric acid concentrations (by weight) of 0.0016 to 0.02%; length change versus time for specimens subjected to wet (2.1% Na_2SO_4 solution) - dry cycling; creep of sealed concrete exposed to temperatures of either 20°, 40°, or 70°C while loaded to ~0.2 the 28-day ultimate compressive strength; porosity versus time for thermal exposures to either 20°, 40°, or 70°C; Poisson's ratio versus time for thermal exposures to 232°C for periods up to 1198 days; and bond stress versus slip for reinforced concrete bond test specimens exposed for 14 days to either direct or alternating current (potential up to 20 volts). Metallic reinforcement data and information files include: ASTM A 615 uncoated, plain and uncoated, deformed carbon steel reinforcing bar material ambient and temperature-dependent engineering stress-strain performance curves (Grades 40, 60 and 75), and S - N (fatigue) performance curves (Grade 40 material); and ASTM A 15 uncoated, plain and



STRUCTURAL MATERIALS HANDBOOK Volume 3 - Material Data Sheet

Material Code 01CB004 Property Code 1000 Page 2

Portland Cement Concrete Normal-Weight Gravel Aggregate Series B, Jansaville, 0.41	General Information	Update Package Number 0 Revision Control Code 0.0 Quality Level A

Property Code 1210	Material Composition		
Constituent Material	Mix Proportions per Unit Volume		Property Code
	kg/m^3	lb/yd^3	
Portland Cement ASTM C 150, Type I	369	622	2001
Fine Aggregate	724	1220	2211
Coarse Aggregate	1236	2084	2222
Water	151	255	2421
Total	2421	4081	

The mix proportions were 1:1.5:3 by volume or 1:1.8:3.35 by weight (derived from Reference 27).

Property Code 1220	Processing Information

Each concrete specimen was moist cured for 28 days and then placed outside in Madison, Wisconsin for long-term storage. Outside stora consisted of placing each specimen on level ground in an uncovered cage having a northeast exposure until 1950, and then each specimen was moved to an uncaged location in an open area for the remaining time. The relative humidity in Madison normally varies from 65 to percent and averages about 75 percent. The annual precipitation including snowfall is about 810 mm (32 in.). Annual air temperatur usually range between -32 and 35°C (-25 and 95°F).

Figure 4. Example of page from Volume 3 (Material Data Sheet) of Structural Materials Handbook.

uncoated, deformed billet steel ambient engineering stress-strain performance curves (all grades), and S-N (fatigue) performance curves and temperature-dependent stress-strain performance curves (Intermediate Grade material). Prestressing tendon data and information files (ASTM A 421, Type BA material) include a temperature-dependent engineering stress-strain performance curve, a tensile yield strength vs temperature performance curve, an ultimate tensile strength vs temperature performance curve, and an ultimate tensile elongation vs temperature performance curve. Structural steel data and information files (ASTM A 36 material) include a temperature-dependent engineering stress-strain performance curve, a tensile yield strength vs temperature performance curve, an ultimate tensile strength vs temperature performance curve, and an ultimate tensile elongation vs temperature performance curve. Rubber data and information files [ethylene propylene diene (EPDM), ASTM D 1418] include a temperature-dependent hardness vs time performance curve.

Data Collection. In parallel with efforts to develop the SMIC, activities are being conducted to establish materials property data for input into the SMIC. Two approaches have been utilized: (1) obtaining and testing of prototypical concrete materials, and (2) pursuing technology transfer with U.S. and foreign research establishments.

Several U.S. organizations have been contacted to pursue the possibility of removing and testing concrete core samples from prototypical structures. These contacts have resulted in procurement of samples from the Shippingport Power Station; EBR-II site; Palisades, Midland, Dresden, Braidwood, Quad Cities, Zion, and LaSalle Power Stations; and Vallecitos Nuclear Center. Specimens have been tested and material property data bases developed for heavyweight and normal-weight concrete materials obtained from the EBR-II site, and for normal-weight concrete materials obtained from the Vallecitos Nuclear Center and Midland Power Station. The relation between compressive strength, 28-day reference compressive strength, and age at testing for specimens prepared from these samples is shown in Figure 5. Specimens obtained from the Palisades, Midland, Dresden, Braidwood, Quad Cities, Zion, and LaSalle Power Stations have been tested, but material property data bases have not been completed because baseline data and information have not been completely assembled. Reference [6] presents additional information on these materials.

In a related activity, prototypical nuclear power plant concrete materials have been tested under a subcontract with Taywood Engineering Ltd. (London, England) [23]. Twenty-nine specimens cast in conjunction with the nuclear power stations at Wylfa, Heysham, Hartlepool Torness, and Sizewell "B" were tested. The specimens had ages from 4 to 24 years and had been stored in a sealed condition at temperatures ranging from 10° to 95°C while either loaded to 13.8 MPa or unloaded. Variables investigated included age of specimen, concrete mix design, loaded or unloaded while curing, and storage temperature. Prior to compression testing each specimen was submitted to a series of nondestructive tests (density, ultrasonic pulse velocity, Schmidt hammer, surface hardness, and dynamic modulus of elasticity). Results indicate that, with only one or two exceptions, there was a consistent trend for the concrete moduli of elasticity and compressive strength to increase with age for each of the mixes. From the limited results which were available for specimens continuously stored at 10° to 20°C, increases in modulus of elasticity ranged from 3% for the Sizewell "B" concrete (test age of 4.8 years) to 112% for the Wylfa concrete (test age of 21 years). Figure 5 summarizes the compressive strength test results.

Associated with the Taywood Engineering Ltd. subcontract was an activity to collate surveillance data for several prestressed concrete reactor vessels (PCRVs) in England. Prestressing tendon lift-off load measurement data, results of corrosion examinations, and visual examination results were compiled from surveillance records for the vessels at Wylfa, Hartlepool, and Heysham I stations. Two PCRVs are located at each of these stations. Results obtained covered time periods since prestressing of 23, 14.5, and 13.4 years for the Wylfa, Hartlepool, and Heysham I stations, respectively. As expected, the tendon lift-off load measurements showed a general trend for the loads to decrease with time due to the combination of prestressing steel relaxation and concrete creep. Examination of prestressing strands removed for inspection and testing revealed only a few minor, structurally insignificant pits indicating that the combination of waxes and greases used to inhibit corrosion of the ungrouted prestressing systems has been effective. Tensile test results for the prestressing strands exceeded design requirements. Visual examination of the concrete surfaces revealed a few surface cracks, with the cracks < 0.30-mm wide, and when active their rate of growth was <20 microns per year. The cracks were associated with drying shrinkage. More detailed surveillance results for each of the three power stations is contained in Ref. [24].

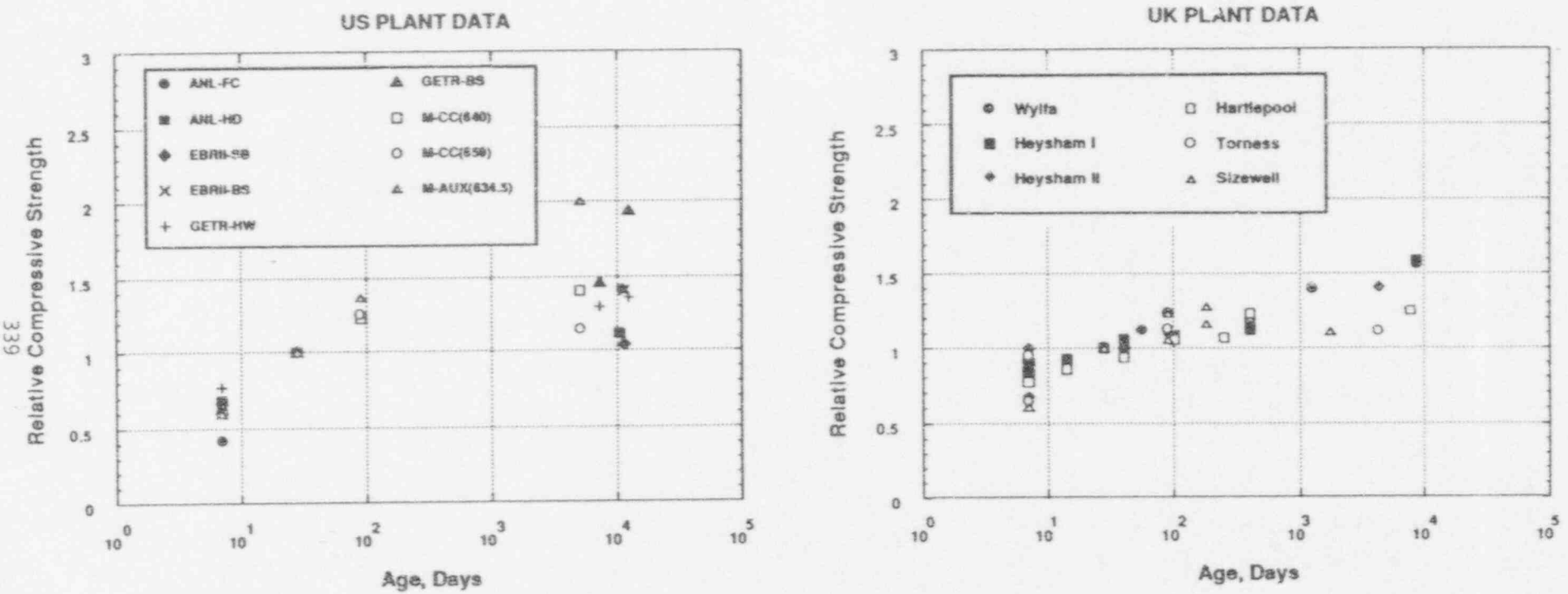


Figure 5. Relative concrete compressive strength versus age for nuclear power plant concretes.

Material Behavior Modeling. Modeling studies under this subtask are designed to complement, as closely as possible, related activities conducted under other NRC programs such as "Performance Criteria for Concrete-Based Barriers for Low-Level Waste Disposal Facilities." During the previous reporting period, a review and evaluation was conducted to identify and evaluate models and accelerated aging techniques and methodologies which can be used in making predictions of the remaining service life of concrete in nuclear power plants [25]. Recent activities have focused on development of prototypical data for input into the service life prediction models that have been identified for corrosion of reinforced concrete.

A collation of survey data and a durability assessment review of reinforced concrete structures contained as a part of several nuclear power stations located in England has been completed [26]. The nuclear power station surveys were aimed primarily at providing data which can be used to predict the onset of corrosion of steel reinforcement due to carbonation or chloride ingress. Corrosion of steel reinforcement was recognized to be a two-stage process: activation and propagation. The present state-of-the-art for modeling carbonation and chloride migration into concrete was reviewed along with factors which affect the time to corrosion activation, e.g., concentration level, environmental conditions, and diffusion coefficient. Survey data obtained at selected locations in the Windscale Advanced Gas-Cooled Reactor, and Hinkley Point "A," Bradwell and Wylfa Nuclear Power Stations included chloride content, carbonation depth, compressive strength, resistivity, moisture content, sorptivity, oxygen diffusivity, and petrography. Environmental conditions (temperature, relative humidity, and rainfall) and survey results were used to predict the onset of steel reinforcement corrosion due to either carbonation or chloride ingress at selected locations in these stations. Predicted maximum age for steel reinforcement corrosion activation due to carbonation or chloride ingress ranged from 31 to >140 years and 43 to >140 years, respectively. Visual surveys at the stations indicated that for interior structures the steel reinforcement and concrete were sound with no corrosion, whereas the external concrete in most instances exhibited only a few localized areas of cracking and spalling. The exception to this was at Wylfa where the cooling plant exhibited severe rust staining and spalling due to chloride ion penetration. Other survey results were that the depths of carbonation reached up to 50 mm for uncoated internal concrete, chloride ingress was generally low (<0.05% in surface 10 mm) except for Wylfa, and the concretes were free of alkali-silica reactivity and sulfate attack.

3.3 Structural Component Assessment/Repair Technology

3.3.1 Objective and Scope

The objectives of this task are to: (1) develop a systematic methodology which can be used to make quantitative assessments of the presence, magnitude, and significance of any environmental stressors or aging factors which adversely impact the durability of safety-related concrete structures in nuclear power plants; and (2) provide recommended in-service inspection or sampling procedures which can be utilized to develop the data required both for evaluating the current condition of concrete structures and for trending the performance of these components. Associated activities include an assessment of techniques for repair of concrete components which have experienced an unacceptable degree of deterioration, and the identification and evaluation of techniques for mitigation of any environmental stressors or aging factors which may act on critical concrete components.

3.3.2 Summary of Recent Accomplishments

LWR Critical Concrete Component Classification. Under this subtask a methodology has been developed which provides a logical basis for identifying the critical concrete structural elements in a nuclear plant and the degradation factors which can potentially impact the performance of these structures. The methodology was described previously [27].

NDE/Sampling Inspection Technology. Nondestructive and sampling/analysis procedures which are available for performing in-service inspections of the critical concrete components in nuclear power plants are evaluated under this subtask. Also, recommended criteria are being developed for use in inspection of these components to assess their current condition as well as to develop trending information for use in continued service assessments. Primary activities under this subtask have included a review and assessment of in-service inspection techniques and methodologies for application to concrete structures in nuclear power plants, and development of statistical data for selected techniques used to determine the in-place compressive strength of concrete.

A review of direct and indirect techniques that can be used to detect degradation of concrete materials and structures was conducted [28]. Capabilities, accuracies and limitations of available nondestructive evaluation testing techniques were assessed. Also included in the review was a discussion of methodologies used to indicate the condition of concrete structures and emerging methods under development which potentially have application to detection of concrete degradation, i.e., leakage flux, polarization resistance, ultraviolet radiation, etc.

Correlation curves and statistical data were developed for selected nondestructive testing techniques [29]. This information is required where destructive and nondestructive tests can not be conducted in tandem at noncritical locations to develop a regression relation between the two tests. Monovariant linear regression analyses were applied to data obtained from publications on selected nondestructive testing techniques that are commonly used to indicate concrete compressive strength, e.g., break-off, pullout, rebound hammer, ultrasonic pulse velocity, and probe penetration. Figure 6 presents an example of the relationship between concrete cylinder compressive strength and rebound number that was obtained from data for gravel-aggregate concretes having water-cement ratios from 0.37 to 0.56 by weight, and coarse aggregate contents from 0.45 to 0.49, by mass.

Remedial/Preventative Measures. Basic activities under this subtask are related to an assessment of repair procedures for concrete material/structural systems and establishment of criteria for their utilization. Techniques which can be used to mitigate the effects of environmental stressors or aging factors are being identified. Recommended preventative measure procedures which can be used to effectively offset, counteract, or minimize any minor deterioration effects to prevent them from becoming significant are being established. Current work is directed at reviews of European and North American practices for the repair of reinforced concrete structures, preparation of a state-of-the-art report on corrosion of reinforced concrete, and development of damage assessment and repair prioritization criteria.

A report [30] has been prepared providing an overview of the European perspective on concrete repair, e.g., methods of damage assessment and repair strategies. Specific topics covered include: (1) criteria used in selection of a particular repair procedure, (2) descriptions of various repair materials and procedures currently utilized, (3) an assessment of the effectiveness of the various repair techniques as determined by both in-situ evaluation (testing) or performance history, and (4) an assessment of the future direction of concrete repairs within Europe. Although there are no European standards governing repair of concrete, there are several documents that

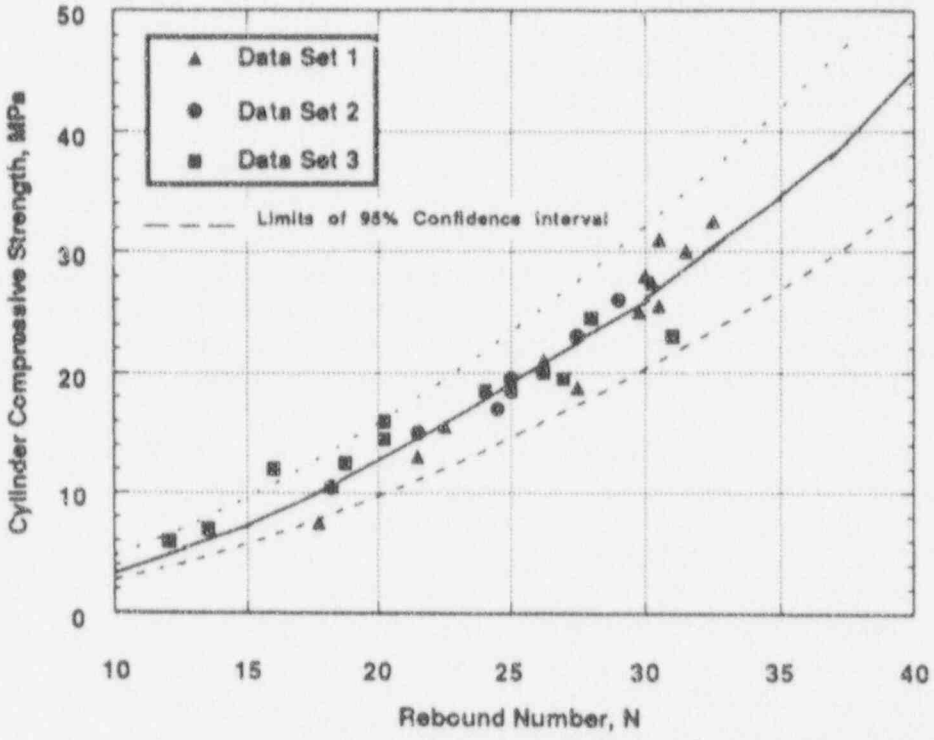


Figure 6. Relationship between cylinder compressive strength and rebound number for selected gravel concretes.

provide guidelines, with the most widely developed regulations having been prepared by the German Committee on Reinforced Concrete [31]. Steel reinforcement corrosion occurring as a result of concrete carbonation or chloride presence are the most important sources of reinforced concrete distress in Europe. For carbonation, the emphasis has been placed on anti-carbonation surface treatments, protective properties of patch materials, and the durability/compatibility of these materials. For chloride attack, efforts are underway to provide an improved understanding of the corrosion mechanisms, the mechanism of incipient anode development, and the use of cathodic protection to overcome the problem.

A complementary activity to the one described above is reviewing North American practices for concrete repair. The distinction between the two efforts is that European repair activities have primarily (but not exclusively) addressed those for corrosion damaged reinforced concrete in building and general civil engineering structures, while in North America, repair activities have concentrated on roads and bridge structures. A draft of a state-of-the-art repair manual [32] has been prepared which identifies methodologies and materials for repair. Basic components of the manual include discussions of: when a specific repair technique is applicable, e.g. specific crack sizes; how the techniques or materials are used, e.g., injection, grouting; how to evaluate and test a repair; how to maintain the repair after it has been installed; the expected life of the repair technique; methods for determining when a repair has failed; and methods for re-repair. Information specifically addressing repair of reinforced concrete structures in light-water reactor plants was assembled through responses to a questionnaire which was sent to the utilities. In addition to a general description of the particular plant, the questionnaire requested

each utility to provide information on inspection procedures utilized, types of deterioration that have occurred, the deterioration mechanism(s), repair actions that have been undertaken, research investigations on repair materials, and performance history of repair procedures utilized. Responses to the questionnaire were provided by 29 sites representing 41 units. Preliminary analyses of the survey responses indicate that the majority of the plants perform inspections of the concrete structures only in compliance with the integrated leak-rate test requirements and surveillances of the prestressed concrete containment post-tensioning systems. The 12 plants which do conduct regular inspections specifically addressing the concrete structures do so at intervals ranging from one to five years and rely mainly on visual techniques. The performance of the concrete structures, in general, has been good with the primary forms of degradation that have occurred being concrete cracking, spalling, and staining, and steel reinforcement corrosion. The most common causes of deterioration were drying shrinkage, acid/chemical attack, thermal movement, freeze/thaw cycles and sea water exposure. The most common locations of deterioration for the pressurized-water reactor plants were the containment dome and in the walls and slabs of auxiliary structures. For the boiling-water reactors, the locations of deterioration were primarily in the walls, slabs, and equipment supports or pedestals of the reactor buildings and auxiliary structures. Most of the repair activities were associated with problems during initial construction (cracks, spalls, and delaminations), with the repairs performed on an as-needed basis. Little information was available on the materials used for repair, the repair procedure, or the durability of the repair. Where the performance of a repair was evaluated, visual inspection was used.

A review of corrosion of reinforced concrete structures, with an emphasis on stray electrical current-induced corrosion and use of cathodic protection to control the occurrence of corrosion in these structures has been completed. Four components are required for corrosion to occur: anode, cathode, electrolyte, and metallic path. Types of corrosion that can occur on metals embedded in concrete include uniform, bimetallic, fretting, crevice, pitting, selective leaching, intergranular, stress corrosion cracking, corrosion fatigue, and hydrogen embrittlement. Conditions that affect the corrosion rate include oxygen level, conductivity of electrolyte, concentration of ions, anode/cathode area, temperature, corrosion resistance of metals, electrical relationship between metals, radiation (affects crystal structure of metal potentially making it more susceptible to localized corrosion), and bacteria. Methods which are available to detect corrosion include visual observations, half-cell potential measurements, delamination detection, electrolyte chemistry, corrosion monitors, acoustic emission, radiography, ultrasonics, magnetic perturbation, metallurgical properties, and electrical resistance. Advantages and disadvantages of each of these methods have been identified. Remedial methods to control corrosion include damage repair, cathodic protection, inhibitors, chloride removal, membrane sealers, stray current shielding, dielectric isolation, coatings, structural modifications to prevent water accumulation, material selection, and environmental modification. Stray electrical current is any current flowing in a path other than its intended circuit. Stray current will take all available conductive parallel paths back to its source and has a magnitude inversely proportional to the resistance of the path(s). With the exception of prestressing tendons, the portion of the structure picking up stray current will not experience corrosion damage. However, the area of discharge will result in metal dissolution. The amount of metal lost will be directly proportional to the current density and duration of exposure. In the case of prestressing tendons, hydrogen embrittlement corrosion may result where the structure is picking up the stray current. For the nuclear power industry, stray current can be anticipated from a variety of sources with the most significant being cathodic protection systems, high voltage direct current systems, and direct current welding operations. Half-cell potential versus time study, half-cell potential versus distance study, and cooperative (interference) testing are techniques commonly used to detect stray current. Mitigation measures

for stray current include prevention or elimination of the current source, installation of cathodic protection, draining the current from the affected source, and shielding the structure from the source. Cathodic protection is not only a rehabilitation technique for corroding structures but is also a corrosion prevention technique for steel that may lose its inherent passivity by contamination of the concrete at a later time or even due to occurrence of stray currents. It mitigates the corrosion reaction by imposing direct current flow between an anode placed on the concrete surface and the metal to be protected. Cathodic protection systems are of the impressed current or sacrificial anode type. Impressed current systems use a DC power supply (rectifier) to force current flow from a relatively inert electrode (anode) through the concrete to the steel surface to be protected. In sacrificial systems a metal that is more anodic (higher tendency to corrode) than the steel embedded in the concrete is used as the source of energy. The theory of cathodic protection is basically that all galvanic corrosion of steel is halted when the potential difference between the anodic and cathodic areas on the steel can be made equal to zero. Criteria commonly used for atmospherically exposed bridge structures to indicate when this condition is sufficiently met include 100 mV polarization decay, E log I analysis, macrocell current reversal, fixed current density, voltage probe measurement, half-cell potential measurement and rebar probe polarization decay. To be most effective, cathodic protection requires electrical continuity of all metallic components within a concrete structure. Since cathodic protection systems are DC, they have the potential to cause stray current corrosion in other structures, and application of cathodic protection to high-strength steel used in prestressing wires or strands may result in embrittlement due to generation of hydrogen at the cathode. More detailed information on corrosion of steel embedded in concrete, stray current-induced corrosion of reinforced concrete structures, and cathodic protection systems is contained in Ref. [33].

A systematic rating system for application in the repair of degraded reinforced concrete structures in nuclear power plants is being developed. Similar computerized rating systems have been developed for evaluating general civil works concrete structures, e.g., BRAIN (Building Rating Analysis and Investigation System). The first phase of this work reviewed existing damage assessment and repair prioritization systems for bridge and building structures to determine their applicability to nuclear power plant concrete structures and an approach was identified for development of a rating system for nuclear power plant concrete structures [34]. Input developed under the first phase was used in the second phase to develop a computer program [35] which simplified use of the aging assessment methodology (see Ref. [27]). The program was validated through its application to the three examples presented in Ref. [27]. The approach used in development of the damage rating system is similar to that for the aging assessment methodology, except that instead of using four factors to develop a rating (repair prioritization number) two factors are considered, i.e. the environmental exposure and the damage significance. The resulting repair rating system is of the form:

$$RPN = w_1(EE) + w_2(DS), \qquad (1)$$

where,

RPN = repair priority number,
EE = environmental exposure, and
DS = damage significance.

A qualitative presentation of the repair rating system for reinforced concrete structures subjected to chloride environments is shown in Figure 7. Criteria are being developed so that a quantitative assessment of the damage to a structure can be made, i.e., environmental exposure

and damage values are being developed so that scales can be applied to Figure 7 and regions indicating testing and evaluation or repair actions delineated. When completed, results developed under this phase will provide a logical connection between the structural aging assessment methodology and the repair activities noted above.

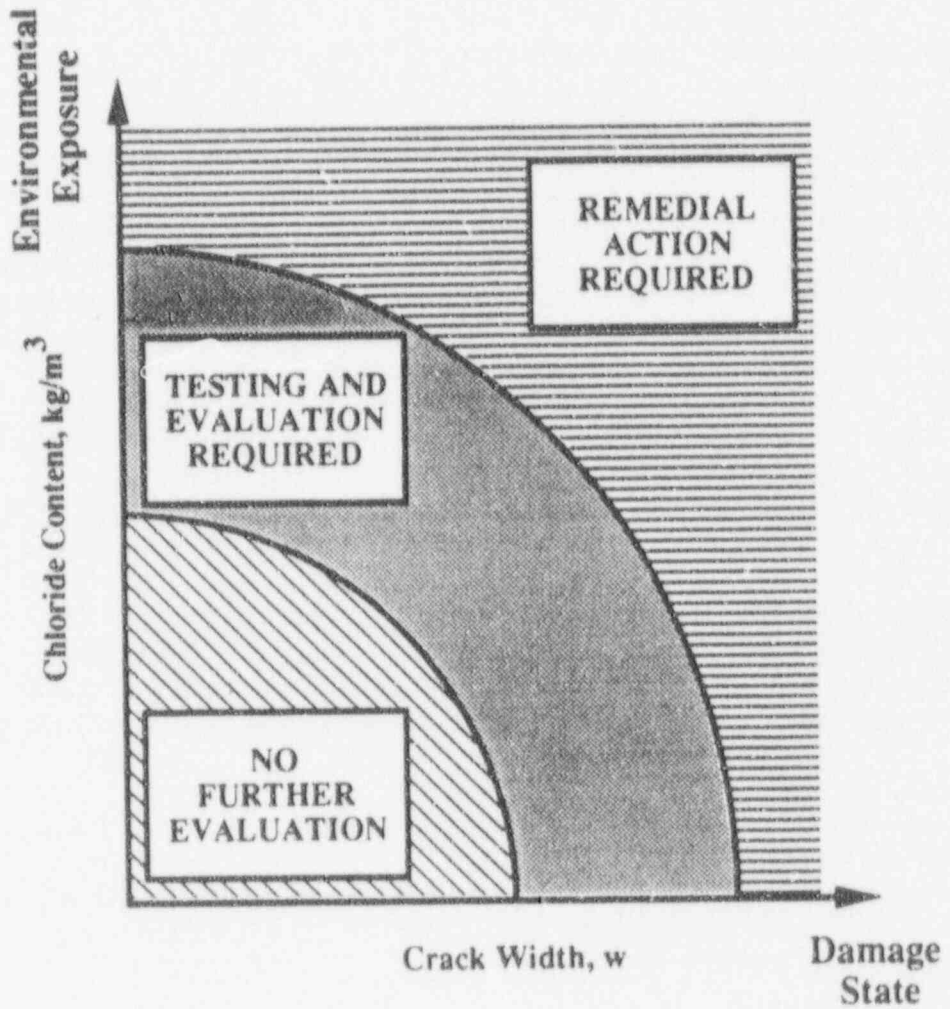


Figure 7. Model for development of repair prioritization methodology.

3.4 Quantitative Methodology for Continued Service Determinations

3.4.1 Objective and Scope

The objective of this task is to develop a methodology to facilitate quantitative assessments of current and future structural reliability and performance of concrete structures in nuclear power plants, taking into account those effects that might diminish the ability of these structures to withstand future operating, extreme environmental or accident conditions. Specific objectives associated with accomplishing this goal are to: (1) identify models to evaluate changes in strength of concrete structures over time in terms of initial conditions, service load history, and

aggressive environmental factors; and (2) formulate a methodology to predict structural reliability of existing concrete structures during future operating periods from a knowledge of initial conditions of the structure, service history, aging, nondestructive condition assessment techniques, and inspection/maintenance strategies. This task will implement results obtained under other program tasks to develop a reliability-based evaluation methodology for concrete structures which will enable the factors that affect structural durability to be taken into account.

3.4.2 Summary of Recent Accomplishments

Since the last Water Reactor Safety Information Meeting status report [36], three journal articles [37,38,39] and a report [40] have been completed which describe the methodology for condition assessment and reliability-based life prediction of concrete structures in nuclear power plants. The methodology includes models to predict structural deterioration due to environmental stressors, a data base to support the use of these models, and methods for analyzing time-dependent reliability of concrete structural components subjected to stochastic loads. The methodology can be used to provide a basis for selecting appropriate periods for continued service and/or determining optimum intervals of inspection and maintenance. Inspection/maintenance strategies have been identified to minimize the expected future cost of keeping the failure probability of a structure at or below an established target failure probability during its anticipated service period. Results of this evaluation are provided in a report which has been prepared [40]. A summary is provided below.

The failure probability of a structural component under stationary random loading can be evaluated as a function of time if the degradation function defining the fraction of initial strength remaining at time, t, and the probabilistic characteristics of the initial strength and loads modeled as stochastic processes are known [41]. In order to evaluate the effect of periodic inspection and maintenance on the failure probability of a structure, it is necessary to relate the strength degradation to the damage intensities and to determine the impact of various repair strategies on strength.

Degradation Function Based On Individual Damage Intensities. The damage intensity is modeled in the abstract as a state variable taking a value within the interval [0, 1]; the values 0 and 1 indicate no damage and no residual strength, respectively. An example of this state variable would be the ratio of area of reinforcement lost due to corrosion to the original area. The following assumptions are made:

(a) Initiation of damages in a component is described by a Poisson process in which the expected number of damages in time interval $(t, t + \Delta t]$ is $\int_t^{t+\Delta t} \nu(\tau)d\tau$ for $t > 0$. $\nu(\tau)$ is dependent on the surface area or volume of the component.

(b) Damages initiate homogeneously over the surface area or volume of the component.

(c) Once damage initiates at location j, it grows according to,

$$X_j(t) = \begin{cases} 0 & ;0 \le t < T_{I_j} \\ C_j\left(t - T_{I_j}\right)^{\alpha} & ;t \ge T_{I_j} \end{cases} \qquad (2)$$

in which $X_j(t)$'s are the intensity of damage at time t, T_{Ij}'s are the random times at which damage initiates, C_j's are damage growth rates which are assumed to be identically

distributed and statistically independent random variables described by a cumulative distribution function (cdf) $F_C(c)$, and α is a deterministic parameter. Parameters C and α depend on the degradation mechanism (e.g., [42]).

(d) The degradation function, $G(t)$, for a component, defining the fraction of initial strength remaining at time t, can be given in terms of damage intensities as,

$$G(t) = 1 - \max_{all\ j}\left\{X_j(t)\right\}. \tag{3}$$

Consider damages which initiate within interval $(t_1, t]$. Given that the number of these damages equals n, the rank-ordered initiation times, $T_{I_1}, ..., T_{I_n}$ are n order statistics of random variables $W_{I_1}, ..., W_{I_n}$ which are statistically independent and identically distributed with probability density function (pdf) expressed as [40],

$$f_{W_I}(w) = \begin{cases} \dfrac{\nu(w)}{\int_{t_1}^{t} \nu(\tau)d\tau} & ;t_1 \le w \le t \\ 0 & ;\text{Otherwise} \end{cases} \tag{4}$$

From assumption (c), the cdf of $X_j(t)$, $F_X(x;\, t_1, t)$,

$$F_X(x;\, t_1, t) = \int_{t_1}^{t} F_C\left(\frac{x}{(t-\tau)^{\alpha}}\right) f_{W_I}(\tau)d\tau. \tag{5}$$

The cdf of X_{max} $(t_1;t)$ = $\max_j\left\{X_j(t) \text{ initiating within } (\ t_1, t\ )\right\}$ [40],

$$F_{X_{max}}(x;\, t_1, t) = \exp\left[-\int_{t_1}^{t} \nu(\tau)d\tau\left\{1 - F_X(x;\, t_1, t)\right\}\right]. \tag{6}$$

From assumption (d), the mean of the degradation function is evaluated by,

$$\mathrm{E}[G(t)] = 1 - \int_0^1 \left[1 - F_{X_{max}}(x;\, 0, t)\right]dx. \tag{7}$$

In the course of the analysis, it was found that the variability in $G(t)$ has a secondary effect on the time-dependent reliability of a component, and thus the reliability can be evaluated considering only the mean of $G(t)$, defined as $g(t)$ [40].

Degradation Function After Repair. No nondestructive evaluation (NDE) method can detect a given defect with certainty. The imperfect nature of NDE methods must be described in statistical terms. Figure 8 illustrates conceptually the probability, $d(x)$, of detecting a defect of size x. Such a relation exists, at least conceptually, for each in-service inspection technology.

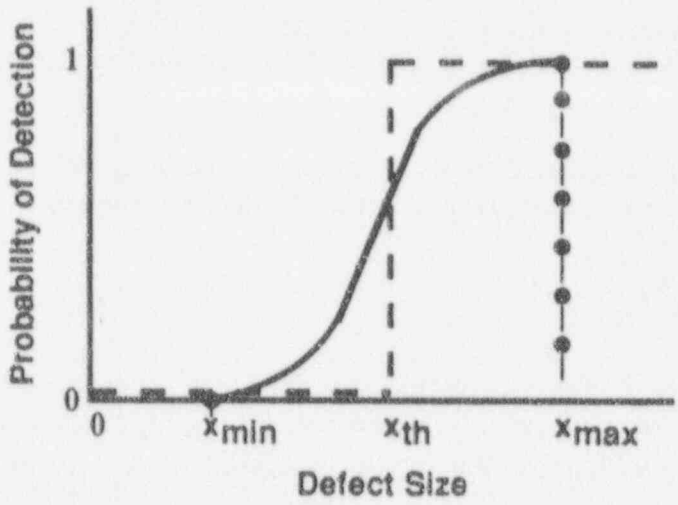


Figure 8. Probability of detection of a defect of size x.

Assume that during inspection/maintenance the entire component is inspected, that all detected damages are repaired immediately and completely, and that the repaired parts of the component are restored to their initial strength levels. Then the effect of inspection/maintenance on $g(t)$ depends on the detectability function, $d(x)$, associated with the NDE method. The inspection with higher $d(x)$ makes repair more likely and, accordingly, leads to higher values of the degradation function, $g(t)$. In the limit, if an inspection is perfect, i.e., $d(x) = 1$ for $x > 0$, then the component is restored to its original condition by the repair.

First assume that the detectability function, $d(x)$, is defined as,

$$d(x) = \begin{cases} 0 & ; \quad 0 \le x < x_{th} \\ 1 & ; \quad x_{th} \le x \le 1 \end{cases} \tag{8}$$

where x_{th} is the minimum detectable value of damage (see Fig. 8). The same detection threshold values are assumed for all inspections. Following m inspections at $t_R = \{t_{R_1}, \ldots, t_{R_m}\}$, some of the damages are repaired and the cdf describing $X(t)$ and the number of damages existing at time $t > t_{R_m}$, $N(t)$, changes. The intensities of damages that initiate after t_{R_m} are independent of repair, and only the pdf of the intensities of damages initiating before t_{R_m} is updated. Let us consider damages which exist at time t and initiate with (A) $(0, t_{R_m}]$ and (B) $(t_{R_m}, t]$. The number of damages left unrepaired after t_{R_m}, $N_{(A)}$, can be described by a filtered Poisson process with a parameter $p \cdot \nu(w)$ where,

$$p = P\left[\text{A damage is not repaired by } t_{R_m}\right] = F_X\left(x_{th}, 0, t_{R_m}\right) \tag{9}$$

while the number of damages initiating within $(t_{R_m}, t]$, $N_{(B)}$, is described by a Poisson process with a parameter $\nu(w)$. In other words, the number of defects existing at time t can be described by a nonstationary Poisson process within a parameter $\nu''(w)$ given by,

$$\nu''(w)=\begin{cases} p\cdot\nu(w) & ;0<w\le t_{R_m} \\ \nu(w) & ;t_{R_m}<w\le t \end{cases} \tag{10}$$

Therefore, the procedure to estimate the degradation function for a component before an inspection/repair can be used to estimate the function after multiple inspection/repair, replacing $\nu(w)$ by $\nu''(w)$, and $F_X(x;\,0,\,t)$ by the updated cdf $F''_X(x;\,t_{R_m},\,t)$.

By the theorem of total probability, $F''_X(x;\,t_{R_m},\,t)$ can be expressed as,

$$F''_X\left(x;\,t_{R_m},\,t\right)=F_{X_{(A)}}\left(x;\,t_{R_m},\,t\right)\cdot P(A)+F_{X_{(B)}}\left(x;\,t_{R_m},\,t\right)\cdot P(B) \tag{11}$$

in which $F_{X_{(A)}}\left(x;\,t_{R_m},\,t\right)$ and $F_{X_{(B)}}\left(x;\,t_{R_m},\,t\right)$ are the cdf of intensity of damages in group (A), $X_{(A)}(t)$, and intensity of damages in group (B), $X_{(B)}(t)$, respectively, and $P(A)$ and $P(B)$ are the probabilities that a defect belongs to group (A) or (B),

$$P(A) = P\left[W_I\le t_{R_m}\right]=\int_0^{t_{R_m}} f_{W_I}(w)dw \tag{12}$$

$$P(B) = 1-P(A) \tag{13}$$

in which $f_{W_I}(w)$ is evaluated by Eqn. (4) replacing $\nu(w)$ with $\nu''(w)$. $F_{X_{(A)}}\left(x;\,t_{R_m},\,t\right)$ is expressed as,

$$F_{X_{(A)}}\left(x;\,t_{R_m},\,t\right)=P\left[X(t)<x\,\middle|\,X\left(t_{R_m}\right)<x_{th}\right]$$

$$=\frac{\int_0^{t_{R_m}} F_C\left(\min\left\{\frac{x}{(t-\tau)^{\alpha}},\frac{x_{th}}{\left(t_{R_m}-\tau\right)^{\alpha}}\right\}\right)f_{W_I}(\tau)d\tau}{\int_0^{t_{R_m}} F_C\left(\frac{x_{th}}{\left(t_{R_m}-\tau\right)^{\alpha}}\right)f_{W_I}(\tau)d\tau}. \tag{14}$$

The cdf $F_{X_{max(B)}}(x;\,t)$ is given by,

$$F_{X_{max(B)}}(x;\,t)=F_X\left(x;\,t_{R_m},\,t\right). \tag{15}$$

In general, the detectability function, $d(x)$, is not a step function but rather a non-decreasing function of damage intensity (see Fig. 8). Procedures for dealing with this more general detectability function and for partial inspections have been developed and described elsewhere [17,40].

Effect of Inspection/Repair Operations on Reliability. In order to study a simple case, assume that:

(a) The initiation of damages is described by a stationary Poisson process with $\nu = 5$/yr.

(b) Damage grows linearly as a function of time as described by Eqn. (2) with $\alpha = 1$; moderate reinforcement corrosion is typified by such growth [40].

(c) The degradation rate, C, is lognormally distributed with mean value, $\mu_C = 0.00125$, which corresponds to $E[X(40)|T_I = 0] = 0.05$, and with coefficient of variation, $V_C = 0.5$.

The effect on the mean degradation function of inspection/repair described by several detectability functions is illustrated in Figure 9. The first detectability function considered is a step detectability function in which $x_{th} = 0.03$; in the second, X_{th} is uniformly distributed (i.e., $d(x)$ is linear between x_{min} and x_{max}, where $d(x_{min}) = 0$ and $d(x_{max}) = 1$); in the third and fourth, X_{th} is lognormally distributed with mean, $\mu_{X_{th}}$, equal to 0.03, and coefficient of variation, $V_{X_{th}}$, equal to 0.3 or 0.5. It is assumed that inspection/repair is carried out at $t_{R_m} = 20$ years. The mean degradation function decreases as $V_{X_{th}}$ increases (which would result in lower reliability); however, the effect of the general shape of $d(x)$ (Fig. 8) is not significant and decreases with time elapsed since inspection. This insensitivity of the mean degradation to the choice of detectability function suggests that a general detectability function might be approximated for practical purposes by a step function with $x_{th} = \mu_{X_{th}}$. This would be advantageous for NDE technologies currently used for reinforced concrete structures because information on $\mu_{X_{th}}$ may be more readily available than information on $d(x)$.

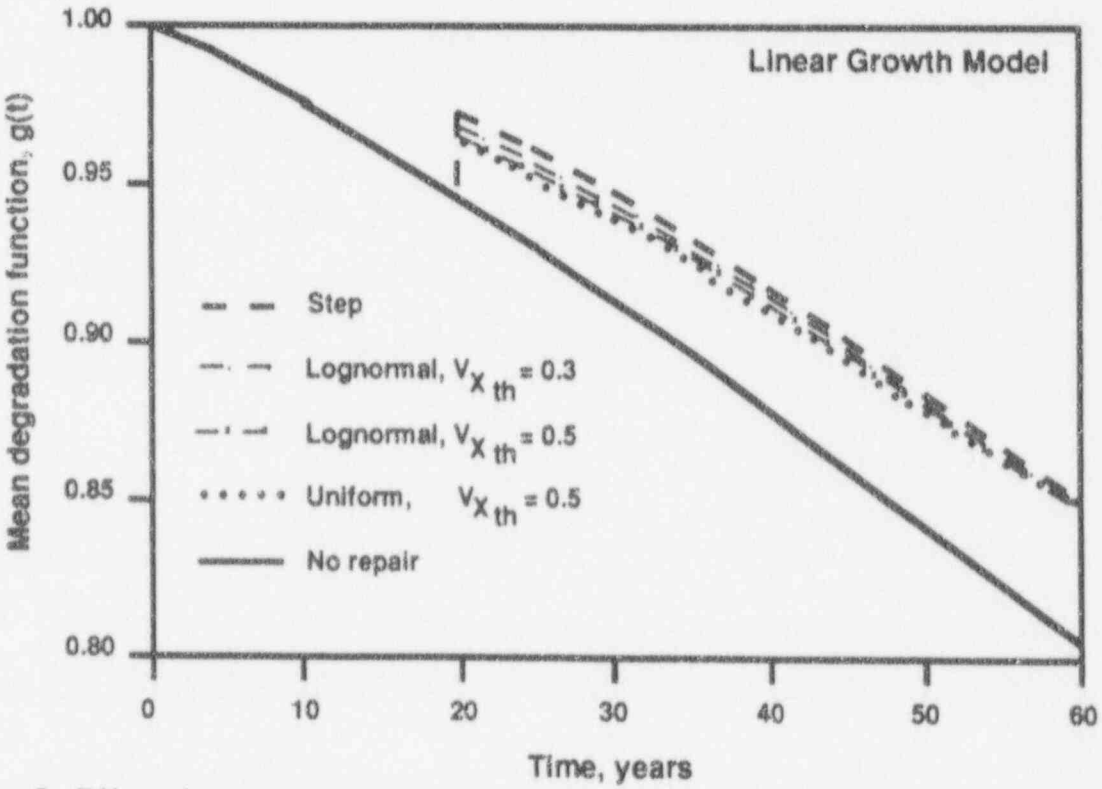


Figure 9. Effect of several detectability functions on mean degradation function of inspection.

The effect of multiple inspections/repairs on the mean degradation function is illustrated in Figure 10, considering the step detectability function. Inspections/repairs are carried out at 20, 30, 40 and 50 years with $x_{th_j} = x_{th} = 0.05$, or at 30 years with $x_{th} = 0.01$. With multiple

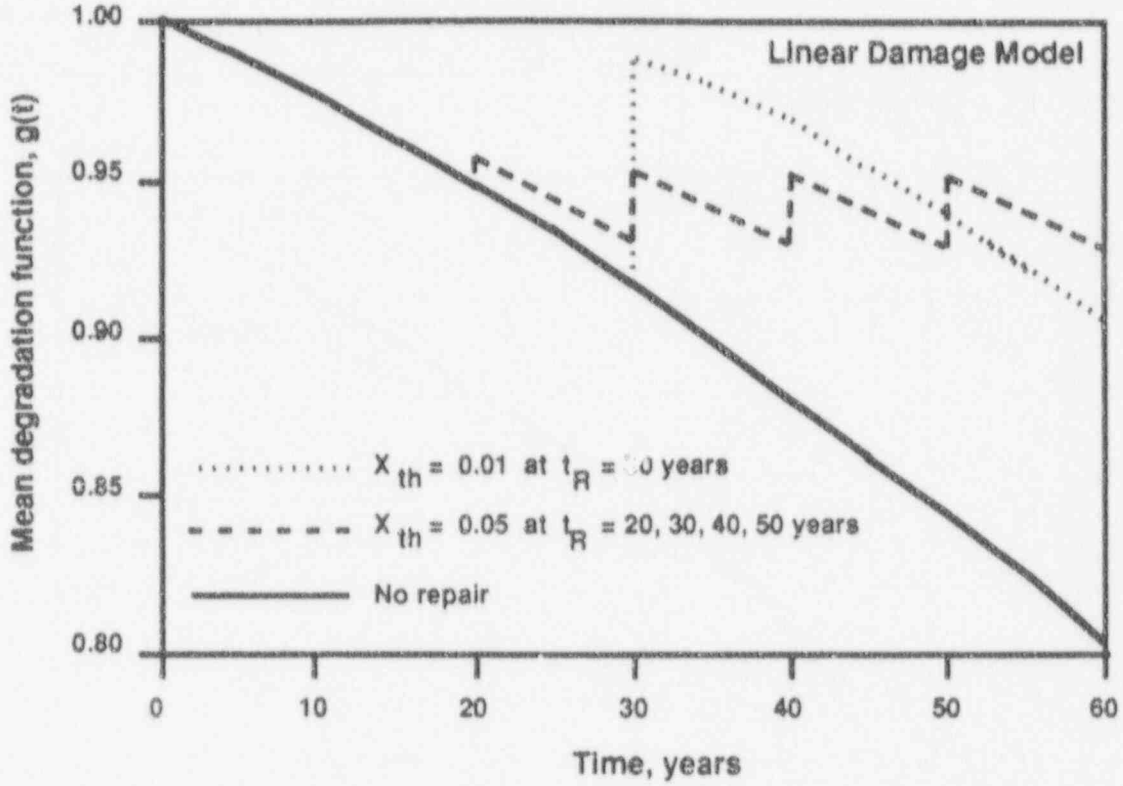


Figure 10. Effect of multiple inspection/repairs on mean degradation function.

inspection/repair, the mean degradation function can be kept within a narrow range during the service life of a structure; the width and the location of the range can be controlled by the frequency and the threshold value of the inspections.

Failure probabilities for a service life of 60 years evaluated with the degradation functions illustrated in Figure 10 are presented in Figure 11 for a reinforced concrete component designed for flexure using the design load combination for dead plus live load in ACI Standard 318 [43],

$$0.9R_n = 1.4D_n + 1.7L_n \tag{19}$$

in which R_n is the nominal strength, and D_n and L_n are the nominal dead and live loads, respectively The probabilistic models of load intensity used in this illustration are summarized in Table 1 [40, 41]. It is assumed that the initial strength has a lognormal distribution with $\mu_R = 1.15R_n$ and coefficient of variation (c.o.v.) $V_R = 0.15$, and that $D_n = L_n$. The slope of $F(t)$ changes at the time of repair. The combined effect of multiple repairs with $x_{th} = 0.05$ leads to a failure probability during 60 years that is comparable to that of the single more intensive repair.

Conclusions. Results such as shown in Figure 11 suggest the existence of an optimum inspection/maintenance strategy in which the failure probability of a component is kept below an established target probability during its service life and the total expected cost, defined as the

Table 1. Load process parameters.

	Mean*	C.O.V.	pdf	λ (yr^{-1})	t
Dead Load	1.00 D_n	0.07	Normal	---	40 years
Live Load	0.40 L_n	0.50	Type I	0.5	3 months

*D_n and L_n are nominal loads.

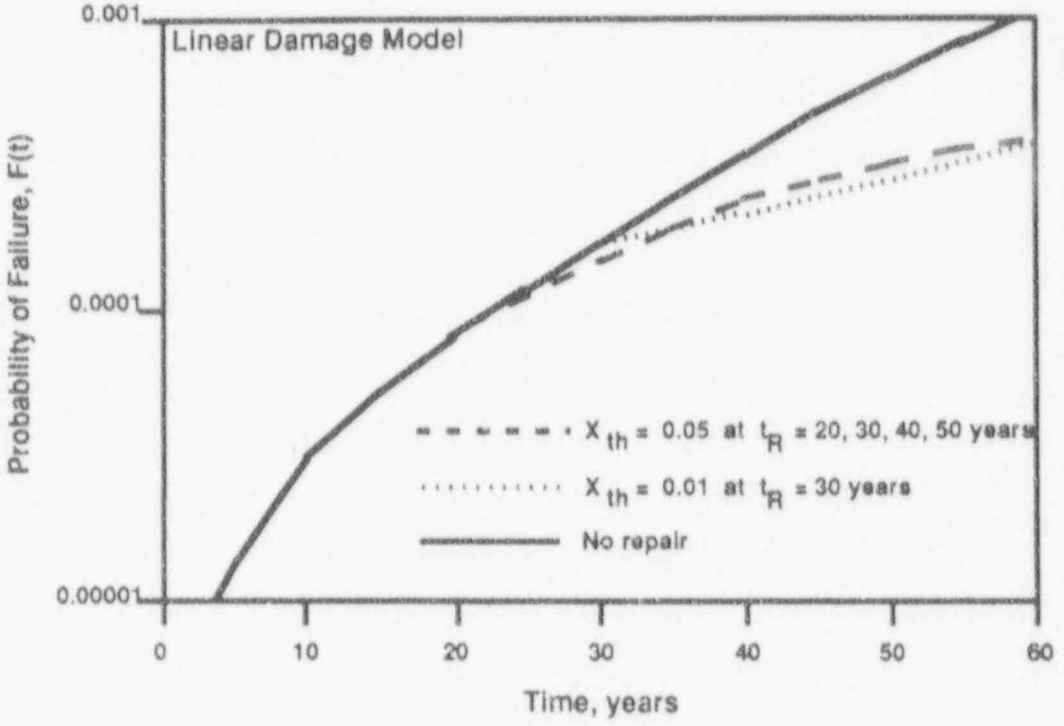


Figure 11. Failure probability with multiple inspections/repairs.

sum of the cost of inspections/repairs and the expected loss due to failure, is minimized [40]. In situations where the cost of failure dominates the expected total cost, the optimum policy involves inspection/repair at nearly uniform intervals during the service life of the structure.

4. APPLICATION OF PROGRAM RESULTS

Potential regulatory applications of this research include: (1) improved predictions of long-term material and structural performance and available safety margins at future times, (2) establishment of limits on exposure to environmental stressors, (3) reduction in total reliance by licensing on inspection and surveillance through development of a methodology which will enable the integrity of structures to be assessed (either pre- or post-accident), and (4) improvements in damage inspection methodology through potential incorporation of results into national standards which could be referenced by standard review plans.

5. REFERENCES

1. "Regulatory Options for Nuclear Power Plant License Renewal," NUREG-1317, Division of Reactor and Plant Systems, Office of Nuclear Regulatory Research, U.S. Nuclear Regulatory Commission, Washington, D.C., June 1988.

2. J. H. Willenbrock, H. R. Thomas, Jr. and J. L. Burati, Jr., "Final Summary Report: A Comparative Analysis of Structural Concrete Quality Assurance Practices of Nine Nuclear and Three Fossil Fuel Power Plant Construction Projects," COO/4120-3, Dept. Civil Eng., The Pennsylvania State Univ., University Park, December 1978.

3. D. J. Naus, "Concrete Component Aging and Its Significance Relative to Life Extension of Nuclear Power Plants," NUREG/CR-4652 (ORNL/TM-10059), Martin Marietta Energy Systems, Inc., Oak Ridge Natl. Lab., Oak Ridge, TN, September 1986.

4. C. J. Hookham, "Life Assessment Procedures for Major LWR Components – Concrete Containments," NUREG/CR-5314, Idaho National Engineering Research Laboratory, Idaho Falls, ID, April 1990 (draft).

5. H. Ashar and D. Jeng, "Effectiveness of In-service Inspection Requirements of Prestressed Concrete Containments - U.S. Experience," Second International Conference on Containment Design and Operation, Canadian Nuclear Society, Toronto, October 14-17, 1990.

6. D. J. Naus and C. B. Oland, "Structural Aging Program Technical Progress for Period January - December 1992," NUREG/CR-6015 (ORNL/TM-12342), Martin Marietta Energy Systems, Inc., Oak Ridge Natl. Lab., Oak Ridge, TN, July 1993.

7. C. B. Oland, "Report of Foreign travel of C. B. Oland, Engineer, Structural Aging Program, Engineering Technology Division, September 24 - October 2, 1992," ORNL/FTR-4416, Martin Marietta Energy Systems, Inc., Oak Ridge Natl. Lab., Oak Ridge, TN, October 16, 1992.

8. D. J. Naus, "Report of Foreign travel of D. J. Naus, Manager, Structural Aging Program, Engineering Technology Division," Letter DJN/93-53 from D. J Naus, Martin Marietta Energy Systems, Inc., Oak Ridge Nat'l Lab., Oak Ridge, TN, to E. G. Arndt, U.S. Nuclear Regulatory Commission, Washington, D.C., July 22 1993.

9. C. B. Oland, "Issues and Ideas About Concretes in Computerized Material Property Data Bases," *1993 Building Technology Symposia Series*, National Institute of Standards and Technology, Gaithersburg, MD, May 11, 1993.

10. D. J. Naus, "A Status Report on the Structural Aging Program," *Electric Power Research Institute Life Cycle Management Subcommittee Meeting*, Pittsburgh, PA, May 17, 1993.

11. D. J. Naus, C. B. Oland, B. R. Ellingwood, Y. Mori, and E. G. Arndt, "Continuing the Service of Safety-Related Concrete Structures in Nuclear Power Plants," *Proceedings of the RILEM International Conference on Failures of Concrete Structures*, EXPERTCENTRUM-BRATISLAVA, Strbske Pleso, Slovakia, June 14-18, 1993.

12. D. J. Naus, "SAG Program Research in Support of Continuing the Service of NPP Safety-Related Concrete Structures," *International Atomic Energy Agency Coordinated Research Program Meeting on Management of the Aging of Concrete Containment Buildings*, Vienna, Austria, June 30, 1993.

13. D. J. Naus, C. B. Oland, B. R. Ellingwood, Y. Mori, and E. G. Arndt, "Towards Assuring the Continued Performance of Safety-Related Concrete Structures in Nuclear Power Plants," PVP-Vol. 252, *Technical Sessions on Nuclear Plant Systems/Components Aging Management and Life Extension*, ASME Pressure Vessel and Piping Conference, July 25-29, 1993, Denver, CO, 1993.

14. Y. Mori and B. Ellingwood, "Reliability-Based Condition Assessment of Concrete Structures," *Proceedings of the 6th International Conference on Structural Safety and Reliability*, International Association for Structural Safety and Reliability, Innsbruck, Austria, August 9 -13, 1993.

15. D. J. Naus, C. B Oland and E. G. Arndt, "Continuing the Service of Aging Concrete Structures in Nuclear Power Plants," *Transactions of the 12th International Conference on Structural Mechanics in Reactor Technology*, Session DH06 - Concrete and Containment Structures, Vol. D, pp. 473-478, Stuttgart, Germany, August 15-20, 1993.

16. C. B. Oland, D. J. Naus and S. Jerath, "A Data Base for Aging of Structural Materials," *Transactions of the 12th International Conference on Structural Mechanics in Reactor Technology*, Session DH06 - Concrete and Containment Structures, Vol. D, pp. 461-466, Stuttgart, Germany, August 15-20, 1993.

17. B. R. Ellingwood and Y. Mori, "Role of InService Inspection and Maintenance in Reliability Assurance of Concrete Structures in Nuclear Plants," *Transactions of the 12th International Conference on Structural Mechanics in Reactor Technology*, Session M - Structural Reliability and Probabilistic Safety, Vol. M, pp. 87-92, Stuttgart, Germany, August 15-20, 1993.

18. A. Marchertas, "Management of Aging of Concrete Containment Structures," *Post-SMiRT Conference Seminar - Containment of Nuclear Reactors*, Karlsruhe, Germany, August 23, 1993.

19. C. B. Oland, and D. J. Naus, "Structural Materials Information Center for Presentation of Time Variation of Material Properties," ORNL/NRC/LTR-90/22, Martin Marietta Energy Systems, Inc., Oak Ridge Natl. Lab., Oak Ridge, TN, September 1990.

20. G. W. Washa, J. C. Seamann and S. M. Cramer, "Fifty Year Properties of Concrete," *Materials Journal* **86**(4), 367-371, American Concrete Institute, Detroit, MI, July-August 1989.

21. *Mat.DB*, Version 1.0, ASM International, ASM/Center for Materials Data, Materials Park, OH, 1990.

22. *EnPlot*, Version 2.0, ASM International, ASM/Center for Materials Data, Materials Park, OH, 1989.

23. S. J. Widdows, "Testing of Aged Concretes from UK Nuclear Power Stations," Report No. 1303/92/6037 (Subcontract No. 31X-SH469V), Taywood Engineering Ltd., London, England, April 1993.

24. P. Dawson and M. J. M. Wilson, "Surveillance Data for PCPVs at Wylfa, Hartlepool and Heysham I Power Stations," Report No. 1302/92/5957 (Subcontract No. 31X-SH469V), Taywood Engineering Ltd., London, England, January 1993.

25. J. R. Clifton, "Predicting the Remaining Life of In-Service Concrete," NISTIR 4712, National Institute of Standards and Technology, U.S. Department of Commerce, Gaithersburg, MD, November 1991.

26. J. Hartley and P. B. Bamforth, "Collation of Survey Data and Review of the Durability Assessment of Reinforced Concrete Structures at Nuclear Power Stations in the UK," Report No. 1303/92/6163 (Subcontract No. 31X-SH469V), Taywood Engineering Ltd., London, England, April 1993.

27. C. J. Hookham, "Structural Aging Assessment Methodology for Concrete Structures in Nuclear Power Plants," ORNL/NRC/LTR-90/17 (Subcontract report from Multiple Dynamics Corp., Southfield, MI), Martin Marietta Energy Systems, Inc., Oak Ridge Natl. Lab., Oak Ridge, TN, September 1990.

28. T. M. Refai and M. K. Lim, "In-service Inspection and Structural Integrity Assessment Methods for Nuclear Power Plant Concrete Structures," ORNL/NRC/LTR-90/29 (Subcontract Report from Construction Technology Laboratories, Inc., Skokie, Ill.), Martin Marietta Energy Systems, Inc., Oak Ridge Natl. Lab., Oak Ridge, TN, September 1991.

29. K. A. Snyder, J. R. Clifton and N. J. Carino, "Nondestructive Evaluation of the In-Place Compressive Strength of Concrete Based Upon Limited Destructive Testing," NISTIR 4874, National Institute of Standards and Technology, Gaithersburg, MD, July 1992.

30. W. F. Price,. P. B. Bamforth, and G. K. Glass, "Review of European Repair Practice for Corrosion Damaged Reinforced Concrete," Report No. 1303/91/5823 (Subcontract No. 31X-SH469V), Taywood Engineering Ltd., London, England, April 1993.

31. German Committee on Reinforced Concrete, "Richtlinie für Schutz und Instandesetzung von Betonbauteilen," Part 2: Bauplanung und Bauausführung, Deutscher Ausschuss für Stahlbeton, Berlin, Germany, August 1990.

32. P. Krauss, "Repair Materials and Techniques for Concrete Structures in Nuclear Power Plants," ORNL/NRC/LTR-93/28 (Subcontract Report 90X-SJ024C from Wiss, Janney, Elstner Associates, Inc., Northbrook, Illinois), Martin Marietta Energy Systems, Inc., Oak Ridge Nat'l Lab., Oak Ridge, TN, May 1993 (draft).

33. W. J. Swiat, W. Young, J. Pajak, M. Funahashi, D. Burke and J. Wagner, "State-of-the-Art Report - Corrosion of Steel in Concrete," ORNL/NRC/LTR-93/2 (Subcontract Report 1BX-SK529V from Corrpro Companies, Inc., Medina, Ohio), Martin Marietta Energy Systems, Inc., Oak Ridge Nat'l Lab., Oak Ridge, TN, May 1993.

34. G. M. Sabnis and A. T. Kemngang, "Development of a Damage Rating and Repair Prioritization Methodology for Reinforced Concrete Components in Nuclear Power Plants," Phase I Report Subcontract No. 11X-SD343V, Howard University, Washington, D. C., June 10, 1992.

35. G. M. Sabnis and A. T. Kemngang, "Damage Rating and Repair Prioritization of Concrete Structural Components in Nuclear Power Plants," Subcontract Report 19X-SJ685V from Howard University, Washington, D.C., to Martin Marietta Energy Systems, Inc., Oak Ridge Nat'l Lab., Oak Ridge, TN, July 1993.

36. D. J. Naus, C. B. Oland, B. R. Ellingwood, Y. Mori and E. G. Arndt, "An Update on the Structural Aging Program," *Proceedings of United States Nuclear Regulatory Commission Twentieth Water Reactor Safety Information Meeting* held at Marriott Hotel, Bethesda, MD, October 28-30, 1992.

37. Y. Mori and B. Ellingwood, "Time-Dependent System Reliability Analysis by Adaptive Importance Sampling," *Journal of Structural Safety* 12, 59-73, 1993.

38. Y. Mori and B. Ellingwood, "Reliability-Based Service Life Assessment of Aging Concrete Structures," *Journal of Structural Engineering*, American Society of Civil Engineers 119(5), pp. 1600 - 1621, 1993.

39. B. Ellingwood and Y. Mori, "Probabilistic Methods for Condition Assessment and Life Prediction of Concrete Structures in Nuclear Power Plants," Nuclear Engineering and Design 142, pp. 155-166, North-Holland, 1993.

40. Y. Mori and B. Ellingwood, "Methodology for Reliability Based Condition Assessment - Application to Concrete Structures," NUREG/CR-6052 (ORNL/Sub/93/SD684), Department of Civil Engineering, The Johns Hopkins University, Baltimore, MD, August 1993.

41. B. R. Ellingwood and Y. Mori, "Probabilistic Methods for Life Prediction of Concrete Structures in Nuclear Power Plants, "Transactions of the 11th International Conference on Structural Mechanics in Reactor Technology, Vol. D, pp. 291 - 296, Tokyo, Japan, August 1991.

42. J. R. Clifton and L. I. Knab, "Service Life of Concrete," NUREG/CR-5466, U.S. Nuclear Regulatory Commission, Washington, D. C., November 1989.

43. American Concrete Institute Committee 318, "Building Code Requirements for Reinforced Concrete," ACI Standard 318-89, American Concrete Institute, Detroit, MI, 1989.

SAND93-1606C

EXPERIMENTS TO EVALUATE BEHAVIOR OF CONTAINMENT PIPING BELLOWS UNDER SEVERE ACCIDENT CONDITIONS[1]

L. D. Lambert, M. B. Parks
Sandia National Laboratories
Albuquerque, NM 87185

Abstract

Bellows are an integral part of the containment pressure boundary in nuclear power plants. They are used at piping penetrations to allow relative movement between piping and the containment wall. In a severe accident they may be subjected to high pressure and temperature, and a combination of axial and lateral deflections. A test program to determine the leak-tight capacity of containment penetration bellows is being conducted at Sandia National Laboratories, Albuquerque, New Mexico. Several different bellows geometries, representative of actual containment bellows, are being subjected to extreme deflections along with pressure and temperature loads. The bellows geometries and loading conditions are described along with the testing apparatus and procedures. A total of thirteen tests have been conducted. The tests showed that bellows are capable of withstanding relatively large deformations, up to, or near, the point of full compression before developing leakage. The test data is presented and discussed.

INTRODUCTION

The bellows tests are part of the Containment Integrity Programs [1], which are being conducted at Sandia under the sponsorship of the Nuclear Regulatory Commission (NRC). The final goal of the Containment Integrity Programs is to generate a complete set of validated methods that can be used to predict containment behavior when subjected to severe accident conditions. In pursuit of this goal, a series of scale model containment buildings have been tested to failure. The models were subjected to static internal overpressurization at ambient temperatures, with the response being monitored by a large number of sensors. The measured response was then compared

[1]This work was supported by the U.S.Nuclear Regulatory Commission and performed at Sandia National Laboratories, which is operated by the U. S. Department of Energy under contract number DE-AC04-94AL85000.

with analytical results that were compiled both before and after the test, in order to verify the analytical methods.

Because of the limited number and scale of the containment models, separate programs have been conducted to further investigate the severe accident behavior of containment penetrations. Electrical penetration assemblies, compression seals and gaskets, inflatable seals, personnel airlocks, and equipment hatches have been tested. These programs are summarized in Reference 1. The ongoing bellows experiments are a part of the containment penetration test series.

BACKGROUND

The bellows test program was initiated as a result of concerns that bellows could be a possible source of containment leakage during a severe accident. Bellows are used at the piping penetrations of steel containments to minimize the loadings imposed on the containment shell by differential movement between the pipe and the containment wall. Since these bellows are an integral part of the containment pressure boundary, they are subjected to the same conditions as the containment building. During a severe accident, those conditions would involve combinations of axial and lateral displacements, internal pressure, and elevated temperatures. Analytical methods were unable to model the bellows at the large deformations required for bellows failure [2], therefore, an experimental program was initiated. The objective of this program is to determine if bellows are a possible source of containment leakage during a severe accident, and if so, to develop methods to estimate the conditions that would likely cause such a failure.

Bellows are used primarily in steel containments, and are of two main types [3]. One type, used in both Boiling Water Reactor (BWR) and Pressurized Water Reactor (PWR) containments, is process piping bellows, which vary in size from 6 to 60 inches in diameter. The other type is vent line bellows that are used in BWR Mk-I containments. They range in size from 65 to 125 inches in diameter. Process piping bellows are normally constructed of two plies of SA240, type 304, stainless steel which are separated by a thin wire mesh (~0.010-inch wire diameter). The redundant outer ply provides a check for leakage of the bellows by pressurizing the space between plies and noting any drop in pressure. Vent line bellows are typically one-ply; approximately 10% are two-ply. Figures 1, 2 and 3 illustrate the relative location and construction details of some typical containment bellows.

Bellows are designed to accommodate differential movements that occur between the containment shell and the pipe to which they are attached. The design basis for these movements are obtained by summing the maximum deformations associated with normal operation, safe shutdown earthquake (SSE), and loss of coolant accident (LOCA). The design standards are provided by the Expansion Joint Manufacturers Association (EJMA) [4]. Normally, bellows are conservatively designed to withstand about 5000 cycles of design-basis loading, although they typically experience only a few minimal cycles due to startup and shutdown of the reactor. Design capabilities of

two-ply bellows to resist pressure is also very conservative, as each ply is sized to resist the full containment design pressure.

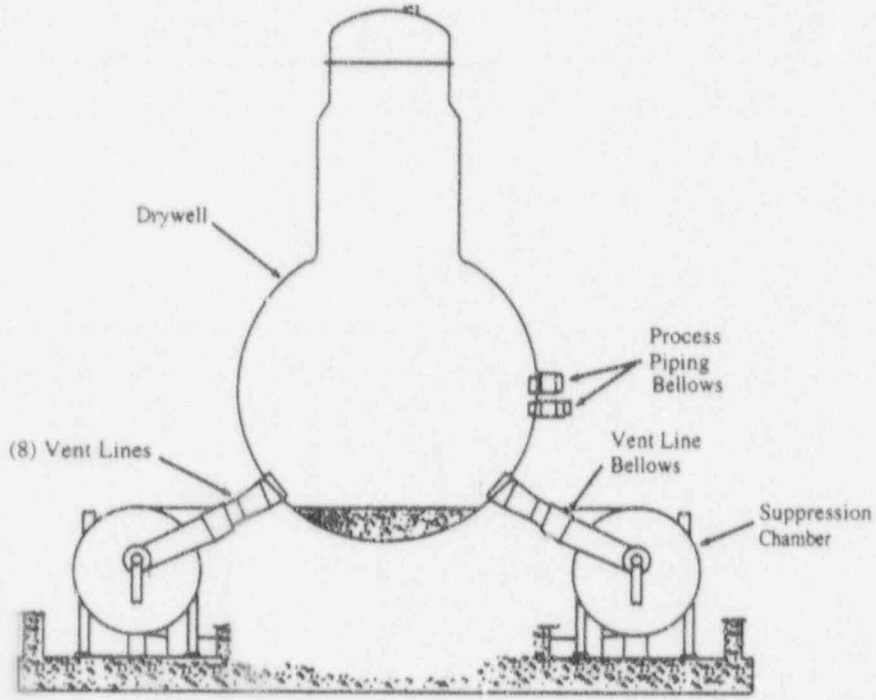


Figure 1. BWR Mark-I Containment

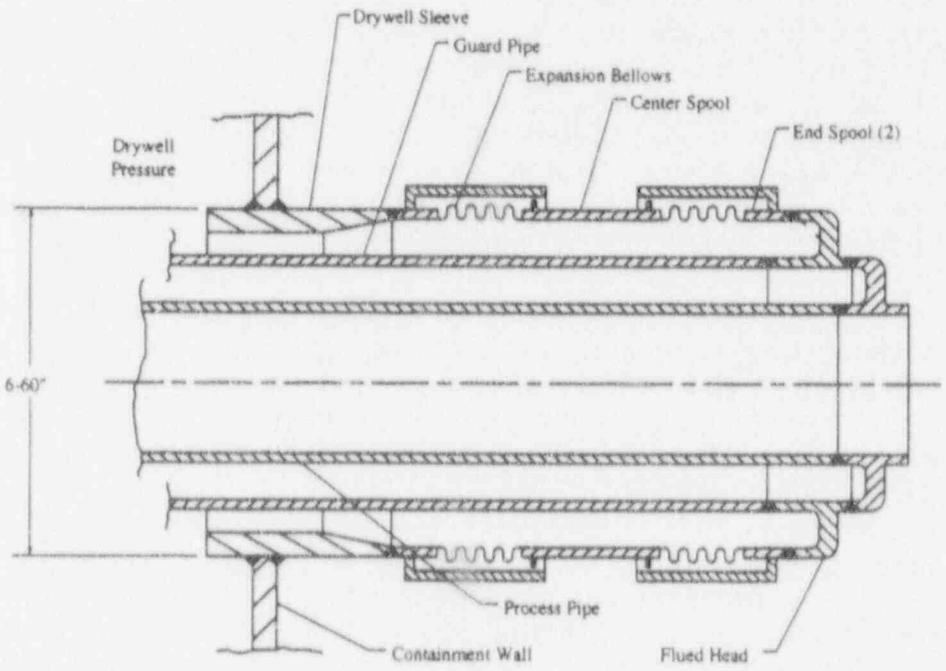


Figure 2: Typical Process Piping Bellows Configuration

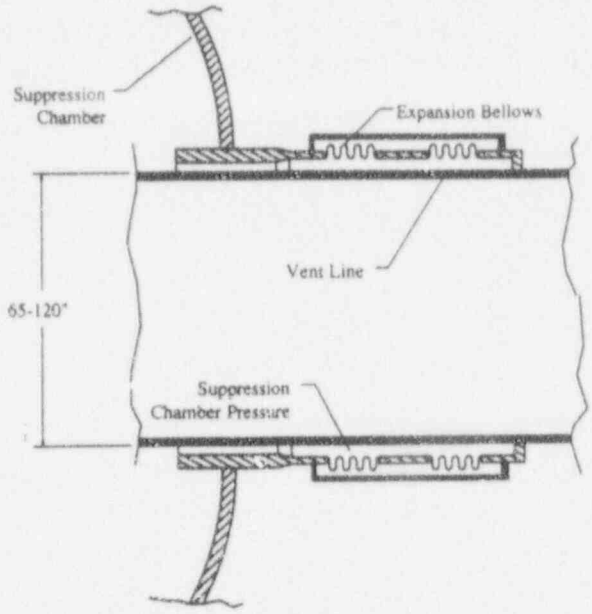


Figure 3: Typical Vent Line Bellows Configuration

In the event of a severe accident, the bellows would be subjected to pressure, temperature, and deflections well beyond the design basis. In most cases, radial growth of the containment due to internal pressure would impose axial compression on the bellows. In a few cases, the bellows would be elongated due to the bellows being installed on the inside of containment. The bellows would also be deflected transversely, due to the upward movement of the containment caused by pressure acting on the dome, and/or thermal growth of the containment shell. It is likely that the bellows would fail if the convolutions become fully compressed. Failure would occur as the end spools (see Figure 2) cut through the thin bellows material or as a result of failure of the connection of the end spools to the piping, since these connections were not designed for transferring the movement (loading) of the containment shell directly to the piping.

After determining that no data on the performance of bellows subjected to severe accident conditions existed, a test series was formulated to examine the behavior of various bellows geometries under severe accident loadings. The test series contained thirteen tests of nine different bellows geometries that are representative of those found in actual containments.

The test series subjected representative bellows to severe accident loadings. During the tests, various levels and combinations of internal pressure, temperature, axial compression or elongation, and lateral deformation were applied. The goal of this research program is to develop methods to predict the pressure and deformation conditions that would likely cause a tear in the bellows, which would produce a leak path through the containment boundary.

Because of the insignificant number and magnitude of loading cycles during normal operating conditions, it was decided to test the bellows in like-new condition without considering fatigue issues. Corrosion was also not considered in these experiments. Additional testing of bellows in a degraded condition is planned.

The material properties of type 304 stainless steel, which is used in the bellows construction, degrades with increasing temperature. The elongation (or 'ductility') at failure is reduced by about 35% from ambient to 400°F (see Figure 4). Since ductility is important in determining bellows tearing, some of the bellows tests were conducted at temperatures of 425° ± 25°F.

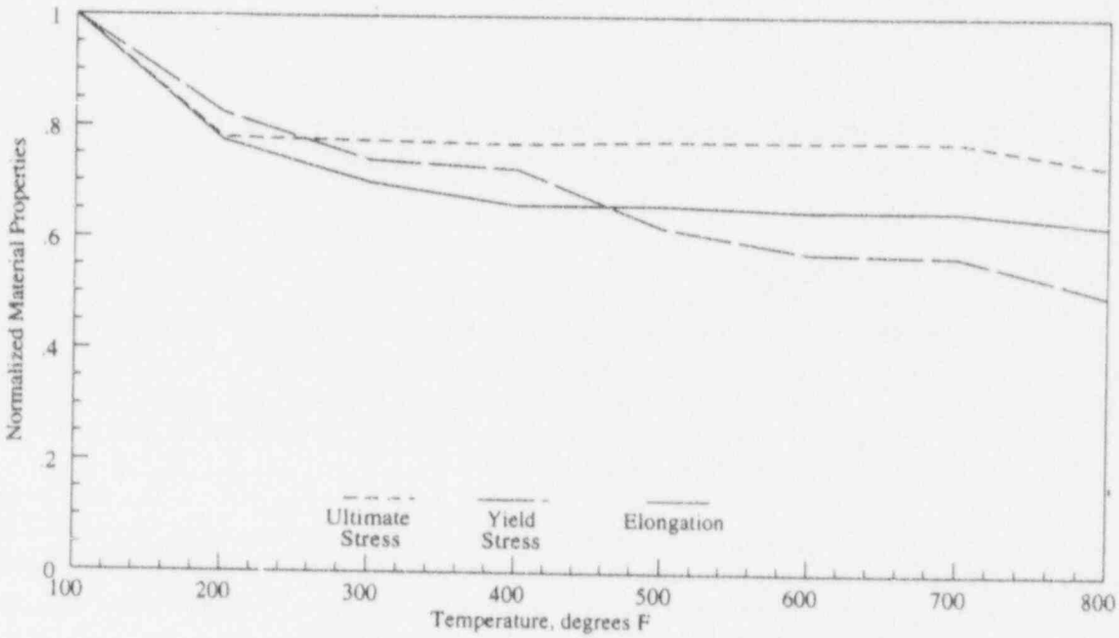


Figure 4. Effect of Elevated Temperature on Fu, Fy, and e of Type 304 Stainless Steel

TEST SPECIMENS

The specimen geometries were selected after a lengthy search to determine the types most frequently used by the nuclear power industry, and to derive a representative cross-section of those types. An effort to include extremes in numbers of convolutions, depth of convolutions and universal versus single element bellows (see Figure 5) was made.

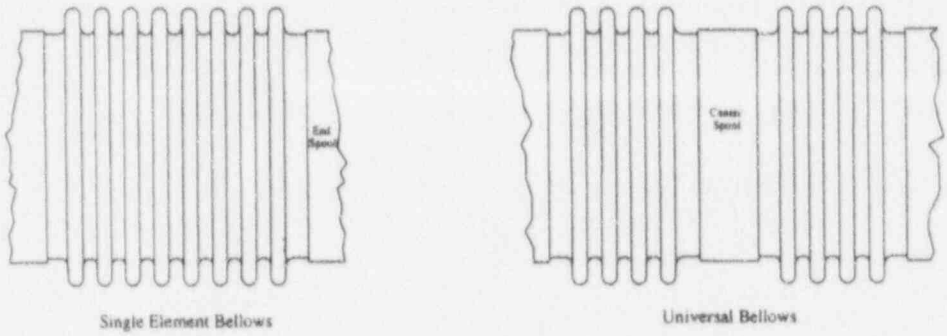


Figure 5. Bellows Configurations

The geometry of the tested bellows specimens is provided in Table 1. Figures 6 and 7 define the bellows convolution parameters listed in Table 1.

DESCRIPTION OF TESTS

The Bellows Test Series is divided into two test types. There are 11 tests of Phase I specimens and 2 tests of Phase II specimens. Phase I tests are intended to determine which, if any, of nine different geometries are more likely to leak when subjected to severe accident conditions, and to determine the capacity of bellows in general. Table 2 provides a description of the Phase I tests.

Phase II specimens are representative of specific bellows geometries, with one of the specimens representing approximately 1:4 - scale vent line bellows (VL specimens) in a BWR Mark - I and the other one being representative of a full size process piping bellows (PP specimens) in a PWR containment.

As shown in Table 1, a total of two tests were performed in Phase II. The displacements and pressures specified for this sequence are derived from analyses of the response of a containment to severe accident conditions. The first test of Phase II was of specimen PP-2. Table 2 provides a list of the combinations of internal pressure, lateral deformation and axial compression that were applied. The bellows specimens were held at 425° ± 25°F at all times during the test. As shown in Table 2, the internal pressure, axial compression, and lateral deformation were increased until the bellows was fully compressed at an internal pressure of approximately 75 psig. Per the test plan, if the bellows is still intact when fully compressed, the applied test conditions are reversed by removing axial and lateral deformation as well as internal pressure at the same rate at which each was originally applied. This process continues until either a crack develops or until all originally applied deformation and pressure has been removed.

Table 1: Bellows Test Specimen Data

Specimen I.D.	Number Required	Pressure (psig)	Inner Diameter d_i (in.)	Number of Convolutions N	Number of Plies, n	Ply Thickness t (in.)	Convolution Depth w (in.)	Convolution Pitch q (in.)	End Tangent l_t (in.)	Center Spool L_c (in.)
Phase I:										
A-8-2	3	75	12.00	8	2	0.020	0.50	0.50	1.00	Single*
A-8-2-e**	1	75	12.00	8	2	0.020	0.50	0.50	1.00	Single
A-8-1-e	1	75	12.00	8	1	0.020	0.50	0.50	1.00	Single
B-8-2	2	45	12.00	8	2	0.020	1.25	0.75	1.00	Single
B-8-2-e	1	45	12.00	8	2	0.020	1.25	0.75	1.00	Single
B-8-1-e	1	45	12.00	8	1	0.020	1.25	0.75	1.00	Single
B-12-2	2	45	12.00	12	2	0.020	1.25	0.75	1.00	Single
Subtotal	11									
Phase II:										
PP-2	1	25	19.25	6	2	0.031	1.50	1.00	2.00	9.50
VL-2	1	75	19.25	4	2	0.020	0.50	0.50	1.00	3.00
Subtotal	2									
Total	13									

Specimen I.D. numbers in Phase I tests denote the bellows construction. The first letter (A or B) indicates convolution depth. The first number indicates the number of convolutions (8 or 12), and the second number indicates one or two plies.

*Specimens A and B are single bellows. PP (process piping) and VL (vent line) are universal (2 convoluted sections with a center spool) bellows.

**"e" indicates that the end tangent shall be attached to the outer diameter of the end spool for these specimens (total 4). All other details of the connection are the same as shown in Figures 6 and 7. The end tangents of the remaining specimens shall be attached to the inner diameter as shown in Figure 7.

Table 2
Load Combinations for PP-2
Phase II Test

Internal Pressure (psig)	Lateral Deformation (in.)	Axial Compression (in.)
0.2	0.24	0.13
0.6	0.73	0.39
1.0	1.21	0.64
5.0	1.34	0.73
10	1.48	0.85
20	1.71	1.08
30	1.90	1.26
40	2.14	1.47
45	2.06	1.59
50	2.22	1.77
52	2.25	1.89
54	2.28	2.08
56	2.31	2.35
58	2.33	2.80
60	2.34	3.61
62	2.37	4.45
64	2.39	5.37
66	2.40	6.37
68	2.42	7.43
70	2.44	8.55
72	2.46	9.85
74	2.48	11.25

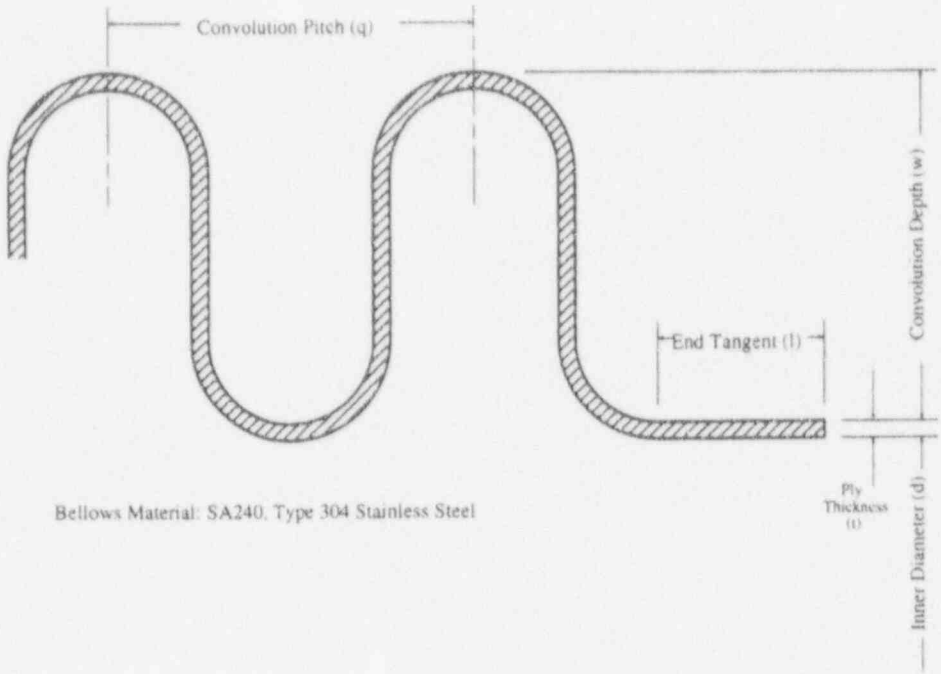


Figure 6. Bellows Convolution Detail

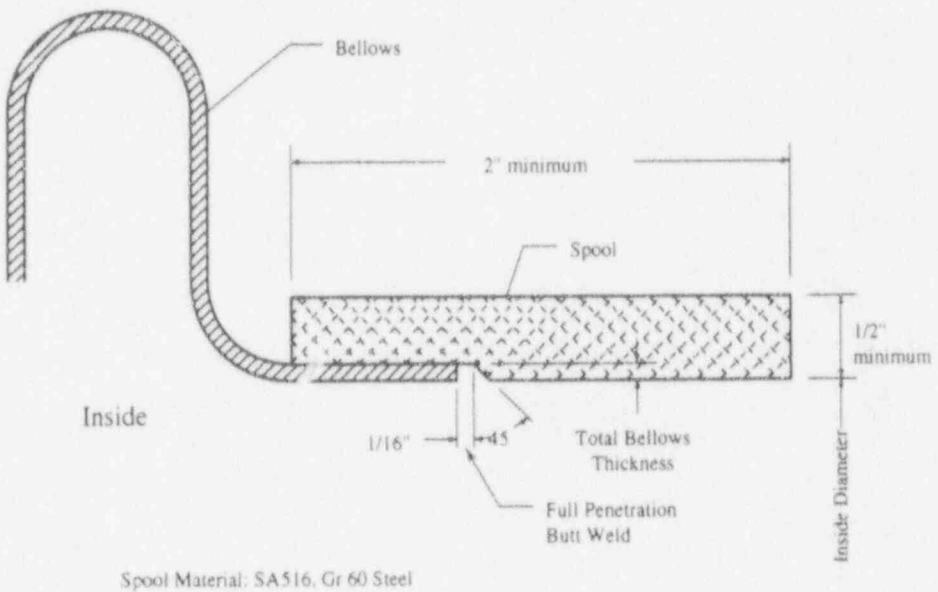


Figure 7. Internal Bellows to End (or Center) Spool Connection Detail

The other Phase II test was of specimen VL-2. For this test, the VL-2 specimen was simultaneously subjected to axial compression, internal pressure, and lateral deformation. These loadings were linearly increased from ambient conditions such that the internal pressure was 150 psig and the lateral deformation was 1inch when the bellows were fully compressed axially. All points on the bellows specimen were held at 425° ±25°F throughout the test. Per the test plan, if the bellows is still intact when fully compressed, the applied test conditions are reversed by removing axial and lateral deformation as well as internal pressure at the same rate at which each was originally applied. This process continues until either a crack develops or until all originally applied deformation and pressure has been removed.

TEST APPARATUS

All of the bellows specimens were tested on a hydraulically actuated load frame (Figure 8). The cylinders that load the bellows in the axial and lateral directions have force capabilities of 350,000 pounds and 250,000 pounds, respectively. The hydraulic power unit contains a variable flow pump for each cylinder. The flow rate is adjusted before the start of the test. The load frame is displacement-controlled by a computer that operates solenoid valves controlling the hydraulic system, based on operator commands and input from displacement transducers. That computer also controls the pressure and oil circulating system and records test data.

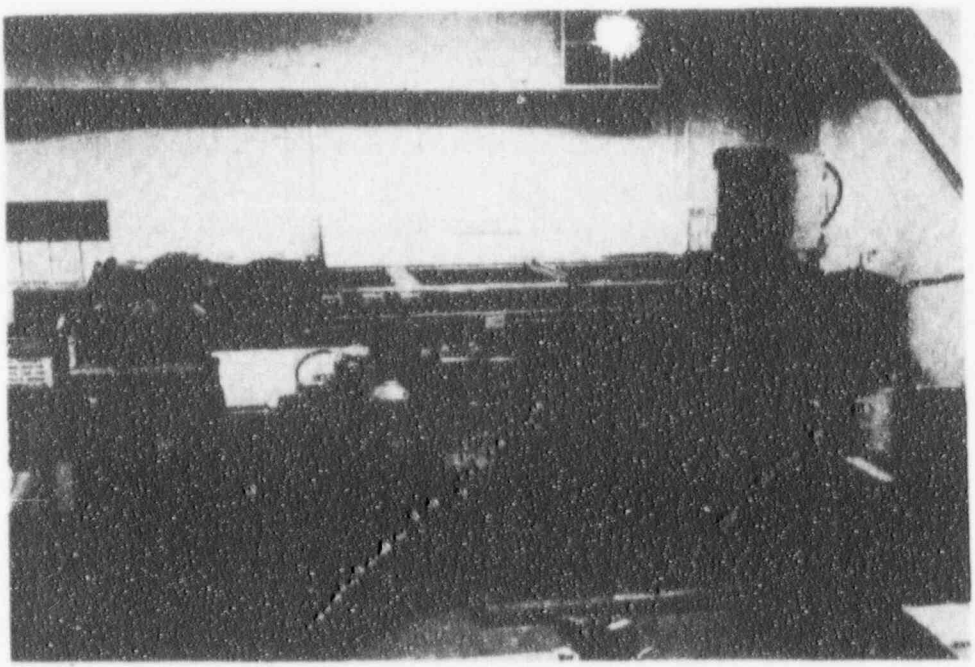


Figure 8. Bellows Load Frame

A second computer receives load, displacement, internal pressure, and temperature data from the first and displays it in a window over a video image of the specimen during the test for recording on video tape.

A still camera also captures images of the bellows specimen during the test. A grid is superimposed over the image of the bellows by means of a partially reflective glass plate located in front of the camera, where the image of the grid is reflected.

The test specimen is bolted into the load frame by means of flanges that are welded to the end spools of the bellows. The bellows is positioned so that the axial dimension is equal to the free length of the bellows measured outside of the load frame. The bellows is then incrementally displaced as the test progresses. In the case of a test that includes internal pressure, or internal pressure and temperature, as test parameters, the bellows is filled with oil prior to being mounted in the load frame.

The pressurizing system is nitrogen gas over oil, which minimizes the stored energy in the test specimen and facilitates the input of heat to the specimen for the elevated temperature tests.

Instrumentation used during testing consists of strain gages (ambient temperature only; Figure 9), displacement transducers, load cells, thermocouples, pressure transducers, and flowmeters. Strain gages were not used on the elevated temperature tests due to difficulties in measuring large strains at elevated temperatures.

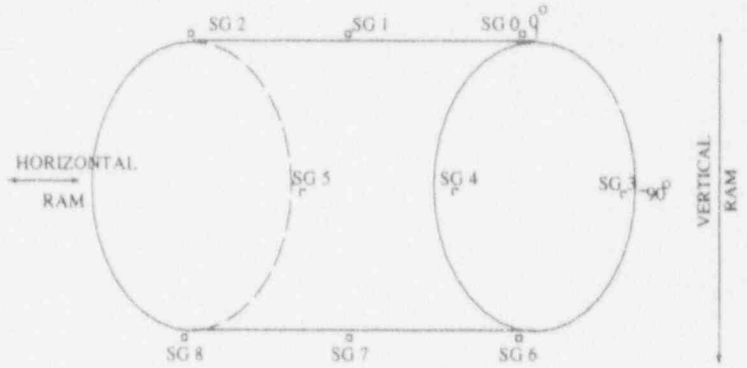


Figure 9. Strain Gage Locations

SUMMARY OF TEST RESULTS

Thirteen tests have been conducted. These tests subjected bellows to extreme axial and lateral deformations such as those that could be experienced during a severe accident. The bellows have demonstrated the ability to withstand large deformations before developing leakage. Most of the test specimens were able to endure one complete cycle of full compression, or full extension, with 2 inches of lateral displacement and remain leak tight.

The test identification number is coded to indicate the test phase (I or II), the test number (1 through 20) and the test type (e.g. CL, SE, etc.-see Table 4).

Table 3
Description of Phase I Tests

Test no.	Specimen I.D.	Test Designation	Maximum Test Pressure (psig)
Compression Tests:			
2	A-8-2	SC	150
3	B-8-2	SC	75
4	B-8-2	SCT	75
9	B-12-2	SC	75
10	B-12-2	SCT	75
11	A-8-2	CL	0
12	A-8-2	LC	0
Elongation Tests:			
13	A-8-1-e	SE	0
14	A-8-2-e	SE	0
15	B-8-1-e	SE	0
16	B-8-2-e	SE	0

Test Designation	Procedure
CL	Axially compress the bellows until all convolution roots are fully compressed. If the bellows are still leak-tight, apply lateral deformation until a tear in the bellows occurs. No internal pressure will be applied during this test.
LC	Apply lateral offset until the bellows become unstable (i.e., very small increase in lateral load produces relatively large lateral deformation). If the bellows are still intact, apply axial compression until all convolutions are fully compressed. If the bellows are still intact after being fully compressed, apply additional lateral deformation until a tear develops in the bellows. No internal pressure will be applied during this test.
SC	Simultaneously apply internal pressure, axial compression and lateral deformation. Internal pressure, axial compression and lateral deformation shall be increased linearly such that the internal pressure pressure level in Table 2 is reached when the total applied lateral deformation is 2" and the bellows are fully compressed.

Table 3 (cont.)

	If the bellows are still intact after being fully compressed, reverse the applied test conditions by removing axial and lateral deformation as well as internal pressure at the same rate at which each was originally applied. Continue unloading until either a crack develops or until all originally applied displacement and pressure has been removed.
SCT	Same as SC except test temperature is 425° ± 25°F throughout the specimen for the entire test.
SE	Simultaneously apply axial elongation and lateral deformation. Axial elongation and lateral deformation shall be increased linearly such that the total applied lateral deformation is 2" when the bellows are fully elongated. If the bellows are still leak-tight after being fully elongated, reverse the applied test conditions by removing elongation and lateral deformation at the same rate at which each was originally applied. Continue this process until either a crack develops or until all originally applied deflection has been removed. No internal pressure will be applied during this test.

Most containment bellows are installed outside containment, where they would be subjected to internal pressure and compressive displacements in the event of a severe accident. In a few cases, however, bellows are installed inside containment, and would be subjected to external pressure and elongation during a severe accident.

Because of the relatively small number of bellows located inside containment, and the added cost and complexity of subjecting test specimens to external pressure during the tests, it was decided that external pressure would not be included in the 'SE' elongation type tests.

The test results of all the tests are summarized in Table 4.

Phase I Elongation Tests

Those tests that subjected bellows to elongation were tests I-13 through I-16[2] (Figure 10). In all cases, the bellows exhibited remarkable capabilities to remain leak-tight after severe deformation. Two of the four specimens (A-8-1-e, A-8-2-e) remained leak-tight after being displaced to their maximum extension, where all the convolutions were flattened out and the bellows was essentially a cylinder again (Figure 11). The other two specimens (B-8-1-e, B-8-2-e) were almost fully extended before developing a leak. The bellows with the deeper convolutions were more than twice their original length at full extension.

---

[2]These tests followed the SE loading condition that is described in Table 3.

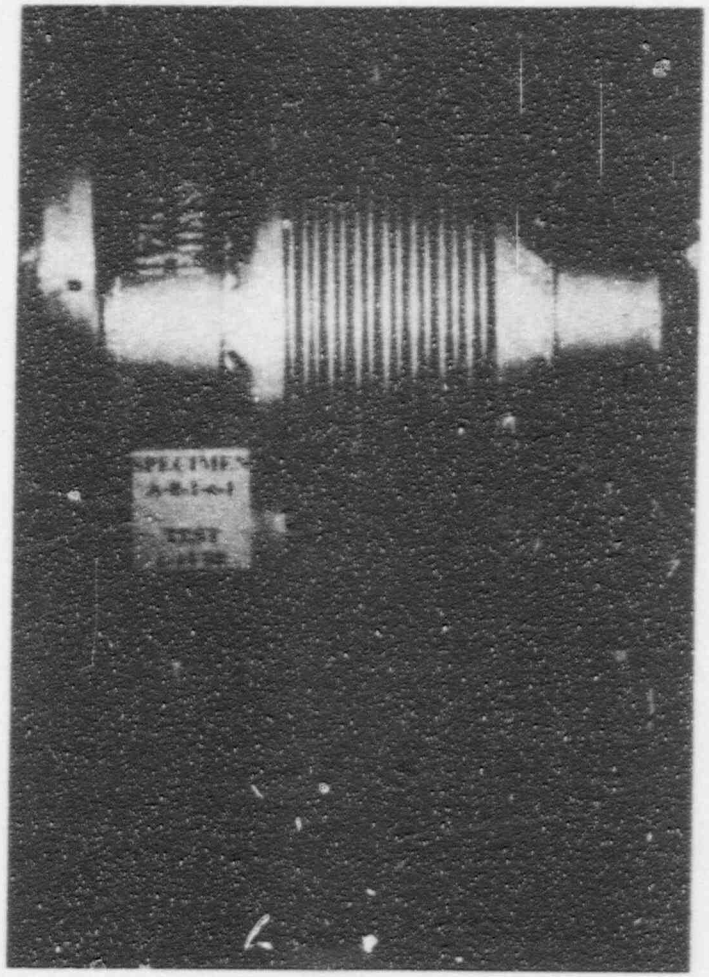


Figure 10. Bellows Specimen A-8-1e-1
(Test I-13-SE)

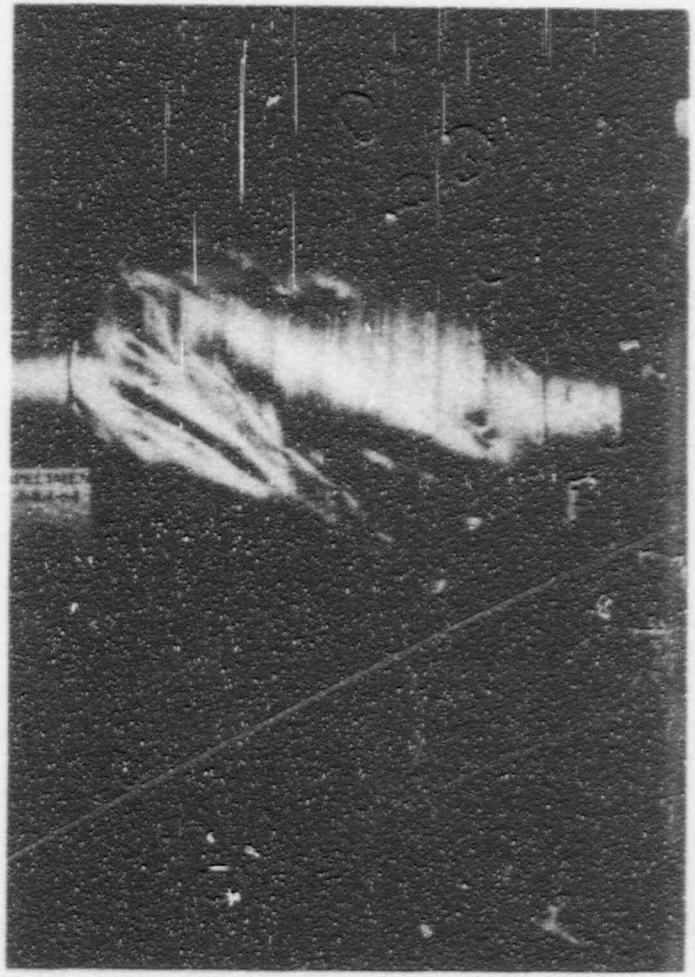


Figure 11. Bellows Specimen A-8-1e-1
At begining of Leakage
(Test I-13-SE)

Table 4
Bellows Failure Conditions

Test	Specimen	Pressure (psig)	Temperature (°F)	Axial Compression (in.)	Lateral Offset (in.)
I-11-CL	A-8-2-1	NA	NA	3-1/4[3]	2-5/8
I-12-LC	A-8-2-2	NA	NA	3-3/8[3]	2-3/8
I-13-SE	A-8-1-e	NA	NA	-5-3/4[4]	1-1/4
I-14-SE	A-8-2-e	NA	NA	-6[4]	2
I-15-SE	B-8-1-e	NA	NA	-17[4]	2
I-16-SE	B-8-2-e	NA	NA	-18[4]	2
I-3-SC	B-8-2-1	75	NA	4-3/4[3]	2-1/4
I-4-SCT	B-8-2-2	65	415	4-5/8	1-7/8
I-2-SCT	A-8-2-3	150	420	3-3/4[3]	2
I-10-SCT	B-12-2-1	68	410	7-3/8	1-7/8
I-9-SC	B-12-2-2	72	NA	8-3/8	2
II-19-SCT	VL-2	150	415	3[3]	2-7/8
II-17-SCT	PP-2	74	400	10-1/2[3]	5

Phase I Axial Compression Tests

A total of seven Phase I tests were conducted in which the bellows were compressed axially. Two tests were done to determine the most severe loading sequence for the bellows. In one test (I-12-LC) the specimen was subjected to a 2 inch lateral displacement followed by compressing the bellows until all the convolutions and the end spools were in metal-to-metal contact (Figure 12)[5]. The lateral displacement was limited to 2 inches based on conservative estimates of the amount of vertical displacement that the containment building could experience during a severe accident[6]. The other test (I-11-CL) reversed the loading sequence with the bellows being fully compressed at the start of lateral displacement (Figure 13). In both cases, the bellows remained leak-tight up to the point of full compression and further displacement in the lateral direction was required to cause a leak. In test I-12-LC, the loading sequence was reversed and the specimen was returned to the starting point and loaded again, before being displaced laterally to approximately 2-3/8 inches where a leak developed.

Five other tests examined bellows performance when subjected to additional loads in the form of elevated temperature and pressure. All of these tests were simultaneous compressive tests, with the displacement being incremented both axially and laterally at each load step.

---

[3]Reached full compression without leakage.

[4]Elongation shown as negative value.

[5]At this point, the bellows condition is defined as 'fully compressed'.

[6]Two inches seems to be an upper bound on the gap between the outside of the piping and the containment opening.

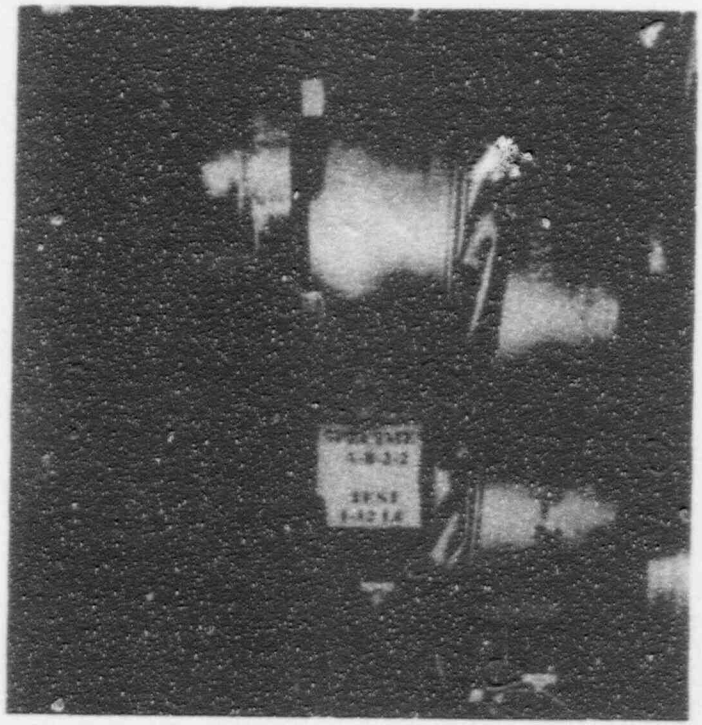


Figure 12. Bellows Specimen A-8-2-2
Fully Compressed
(Test I-12-LC)

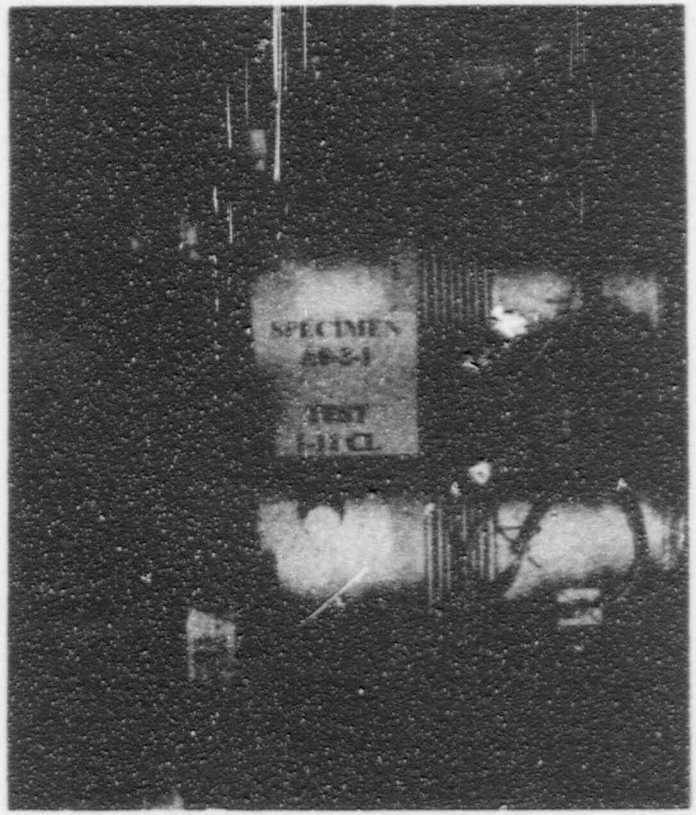


Figure 13. Bellows Specimen A-8-2-1
Fully Compressed
(Test I-11-CL)

The pressure was also incremented so that the maximum pressure was reached concurrent with maximum displacement. The temperature of the bellows was increased to 425°F ± 25°F before the start of an elevated temperature test. The temperature was maintained throughout the test.

One test was completed using a bellows with 1/2 inch deep convolutions (Test I-2-SCT) and two-ply construction. The bellows temperature was 425°F throughout the test. The specimen was subjected to full axial compression and 2 inch lateral displacement without leaking. The internal pressure was 150 psig at the maximum displacements. Upon reversing the displacement direction so that the bellows was being extended toward its original dimensions, a leak developed through one ply. Only after being fully compressed and extended for a second time, did the bellows develop a leak through both plies.

Tests I-3-SC and I-4-SCT were conducted on identical specimens with 1-1/4 inch convolution depth. Both specimens were subjected to internal pressure, but only the specimen tested in I-4-SCT was heated to 425°F. Both specimens remained leak-tight during large displacements. The heated specimen failed just before reaching the fully compressed state, at axial and lateral displacements of 4-5/8 inches and 1-7/8 inches, respectively, at an internal pressure of 65 psig (full compression would have occurred at axial displacement of 5 inches), however, the room temperature bellows remained leak-tight up to the point of full axial compression. The room temperature bellows eventually failed during the reversal of displacement direction (displacements of 4-1/4 inches and 2 inches axially and laterally, respectively) after maximum axial and lateral displacements of 4-3/4 inches and 2-1/4 inches, respectively (Figures 14 & 15).

The fact that the bellows in the elevated test failed earlier than identical bellows at room temperature is consistent with the loss of ductility that occurs in the bellows material with increasing temperature, as shown in Figure 4.

The bellows constructed with deeper convolutions develop sharp creases in the crest of the convolutions relatively early in the displacement cycle compared to the bellows with shallower convolutions. Development of these sharp creases appeared to be soon followed by tears in the bellows material. Thus, the bellows with relatively shallow convolutions seem to be more resistant to extreme deformations than those with deeper convolutions. An example of the sharp creases developed in specimen B-8-2-1 during Test I-3-SC is shown in Figure 16. These sharp creases eventually tear and leak.

Two identical bellows with 12 of the deeper convolutions were examined in tests I-9-SC and I-10-SCT. The convolutions are 1-1/4 inch deep and are very flexible (Figure 17). A relatively large axial displacement was required to close the gap between all the convolutions and the end spools. The bellows were subjected to more than 8 inches of axial compression along with 2 inches of lateral deflection. Again, the heated bellows failed slightly earlier than the room temperature specimen.

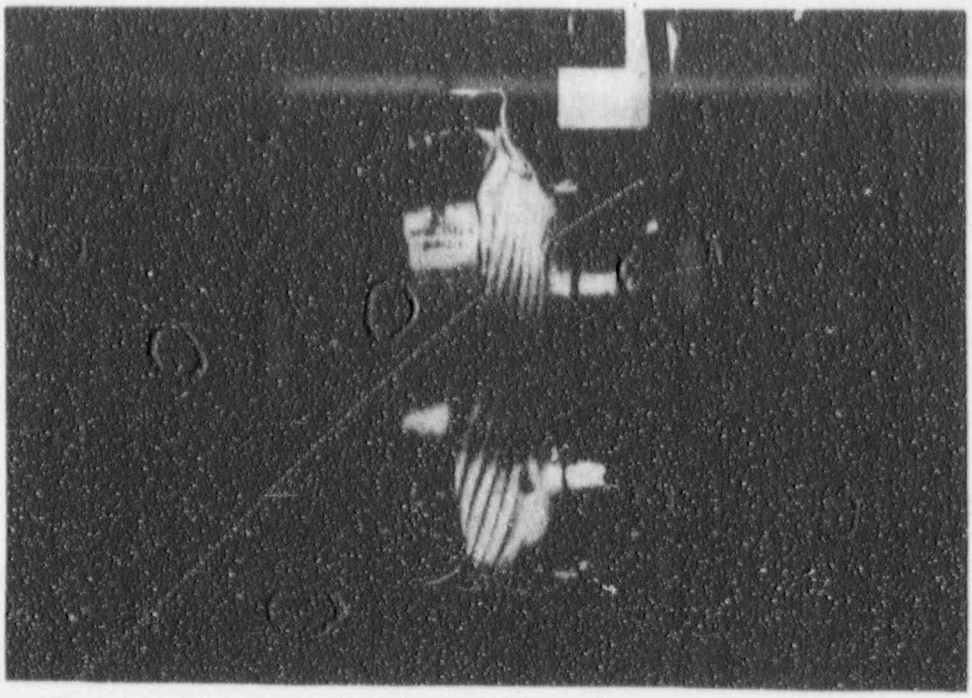


Figure 14. Bellows Specimen B-8-2-1
Fully Compressed
(Test I-3-SC)

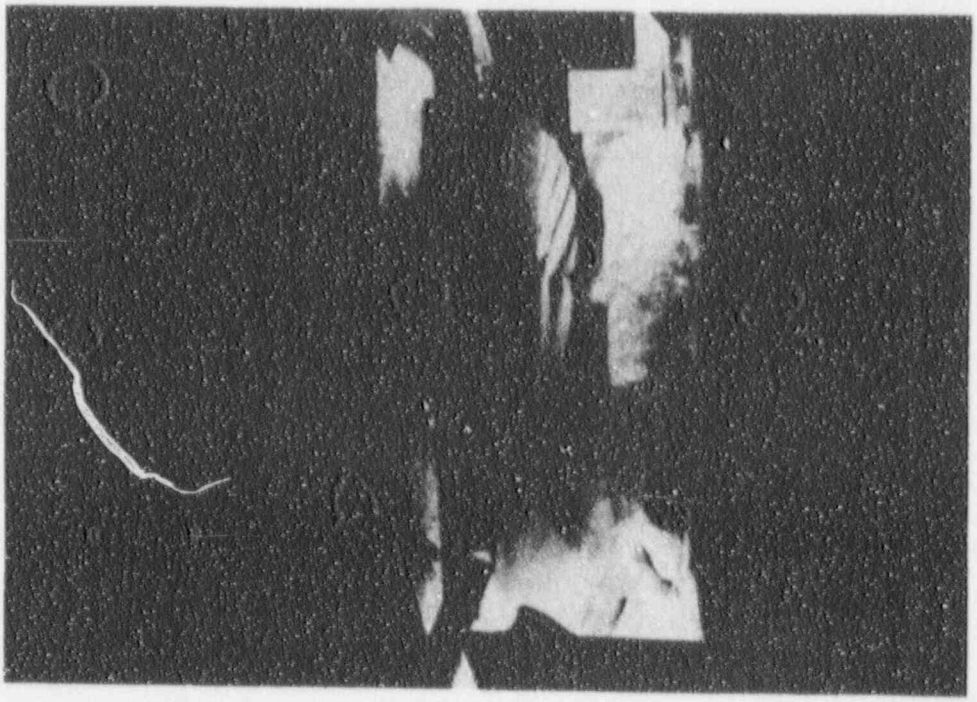


Figure 15. Bellows Specimen B-8-2-2
Fully Compressed
(Test I-4-SCT)



Figure 16. Bellows Specimen B-8-2-1
Tear at Sharp Crease
(Test I-3-SC)

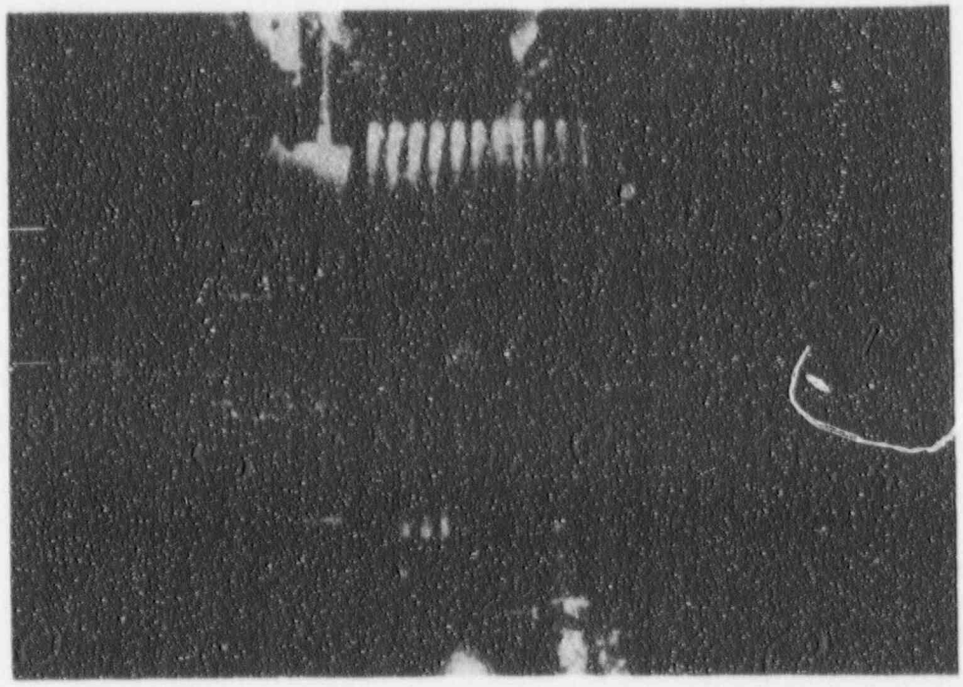


Figure 17. Bellows Specimen B-12-2-2
(Test I-9-SC)

The axial and lateral displacements at the time of leakage for the elevated temperature test was 7-3/8 inches and 1-7/8 inches, respectively, (Figure 18) versus 8-3/8 inches and 2 inches, respectively, for the room temperature test (Figure 19). Neither of the bellows reached the point of full axial compression before leakage began, but even the specimen tested at elevated temperature was over 85% compressed. For both specimens, full compression would have been reached at an axial displacement of approximately 8-1/2 inches. Internal pressure for the two tests were 72 psig for Test I-9-SC and 68 psig for Test I-10-SCT. In these tests the failure mode was different than most of the previous tests. Immediately prior to leakage, the bellows convolutions were observed to roll over the end spool. The specimens have not been dissected to see exactly where the leak occurred, but it appeared to be a case of the spool cutting into the thin bellows material.

Phase II Tests

Two tests were completed on the larger piping penetration and vent-line bellows specimens. The vent line bellows specimen that was tested was a universal bellows of two ply construction. The test was II-19-SCT, utilizing specimen VL-2. Figure 20 shows the bellows at the start of the test. Insulation covers the end spools and lower part of the bellows to aid in maintaining the test temperature. The test was conducted at 425°F, with a maximum internal pressure of 150 psig. The specimen proved to be very durable, and was subjected to two complete cycles of compression and extension without developing a leak. The lateral displacement was limited to 1 inch during the compression cycle because the specimen is approximately 1:4 scale, and that displacement is a conservative value for lateral shear that could be imposed by a containment building. After enduring two complete compression cycles, the bellows was sheared an additional amount laterally, while fully compressed at an internal pressure of 150 psig. The specimen developed a leak through the outside ply at a lateral displacement of approximately 2-1/2 inches and leaked through both plies at approximately 2-7/8 inches lateral displacement (Figure 21).

The last test that was completed in this series was a full size piping penetration bellows identified as PP-2 (Figure 22). The specimen was a universal bellows of two-ply construction. The test identification number was II-17-SCT. The test followed the parameters tabulated in Table 2, which represent a severe accident scenario for this type of bellows. The specimen was maintained at 425°F during the test, with a maximum internal pressure of 74 psig at full axial compression. The specimen developed a leak through the inner ply after being fully compressed. The outer ply did not develop a leak after two complete loading cycles. At this point, the bellows was displaced laterally an additional distance for a total lateral displacement of approximately 5 inches (Figure 23), which was the limit of the test apparatus. The direction of displacement was then reversed so that the bellows was being returned to lateral zero while maintaining full axial compression and maximum internal pressure. The outer ply began leaking as the lateral displacement approached 1-3/4 inches.

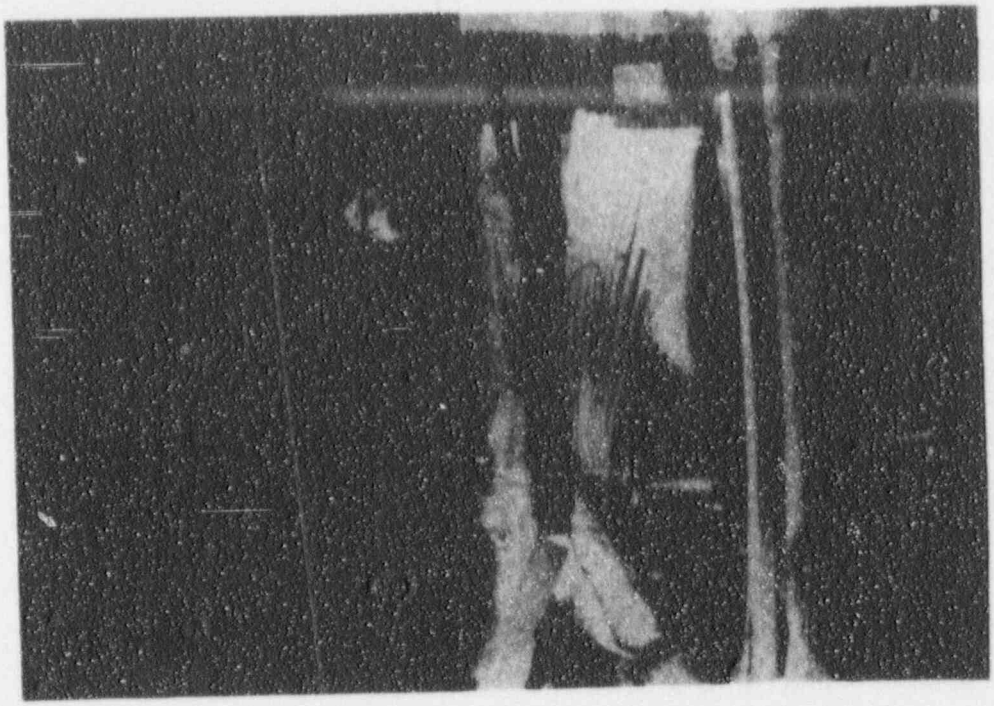


Figure 18. Bellows Specimen B-12-2-1
Begining of Leakage
(Test I-10-SCT)



Figure 19. Bellows Specimen B-12-2-2
Begining of Leakage
(Test I-9-SC)

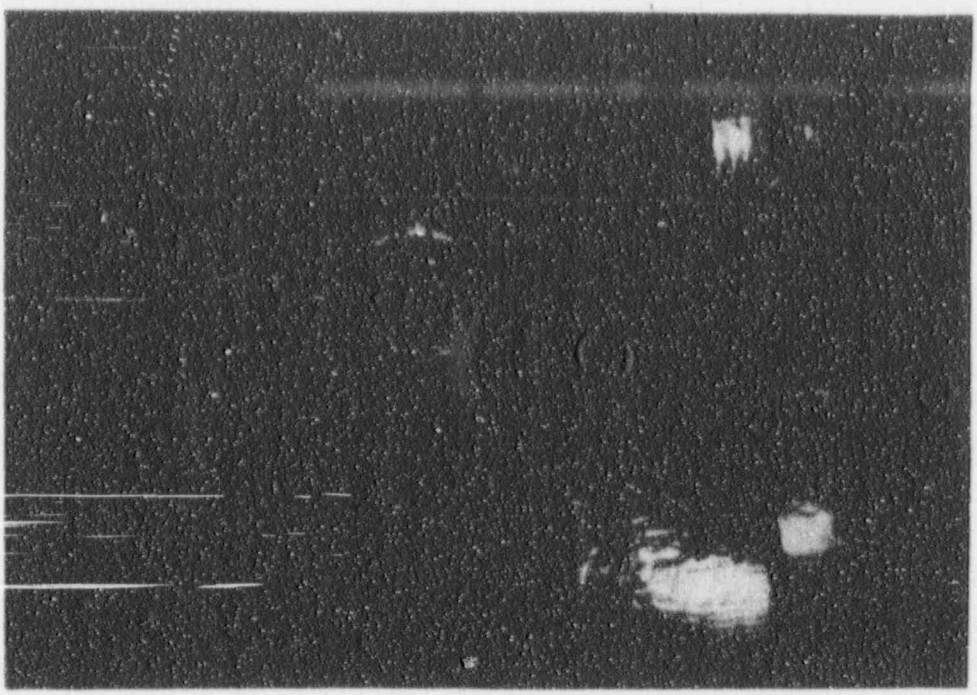


Figure 20. Bellows Specimen VL-2
(Test II-19-SCT)

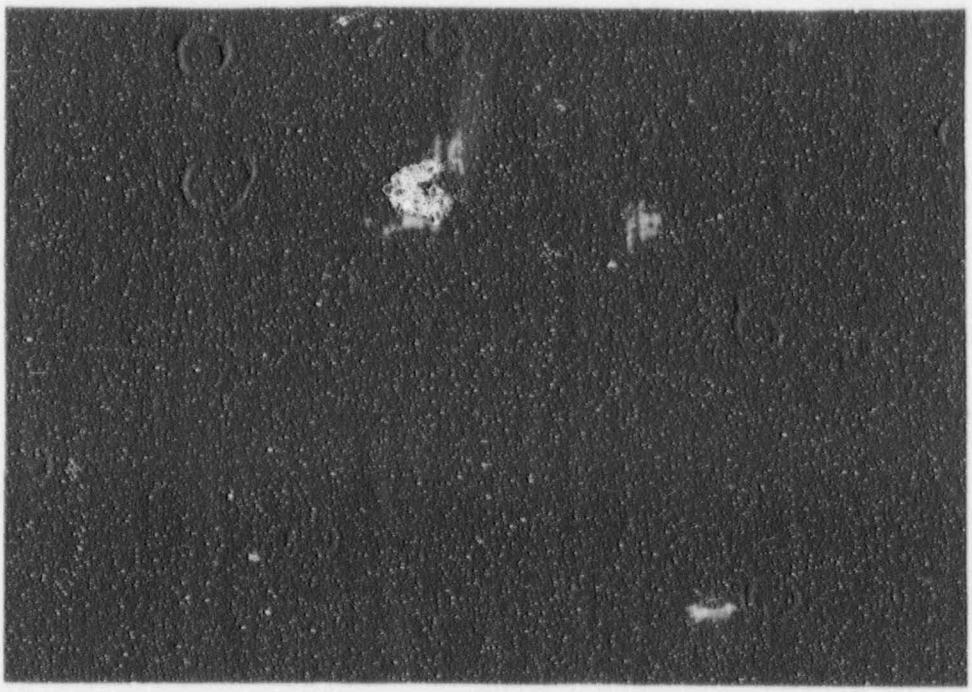


Figure 21. Bellows Specimen VL-2
Begining of Leakage
(Test II-19-SCT)

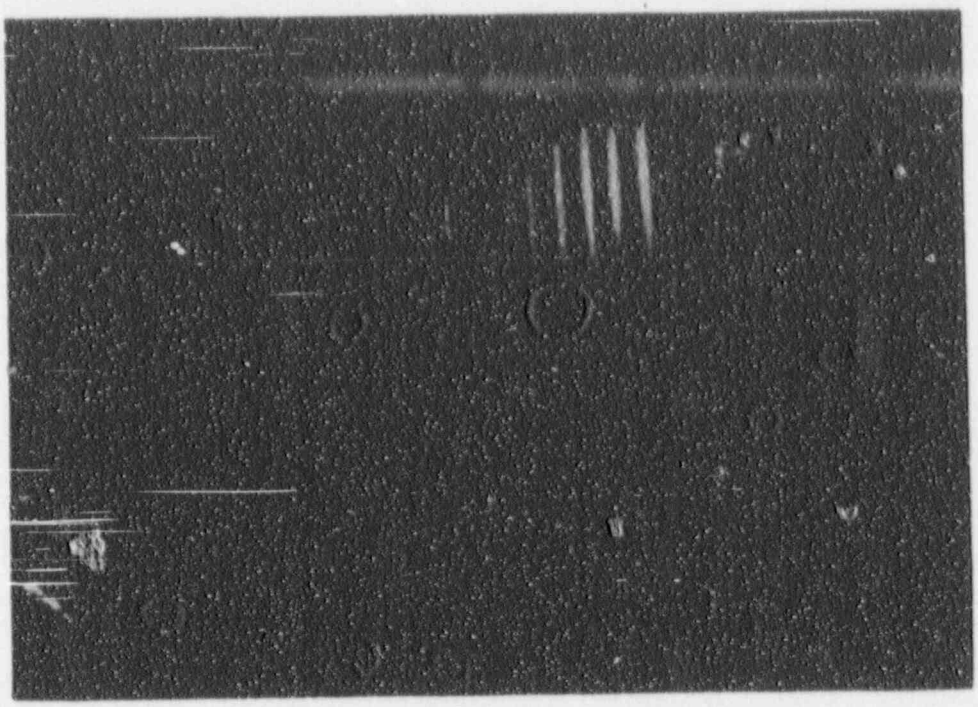


Figure 22. Bellows Specimen PP-2
(Test II-17-SCT)

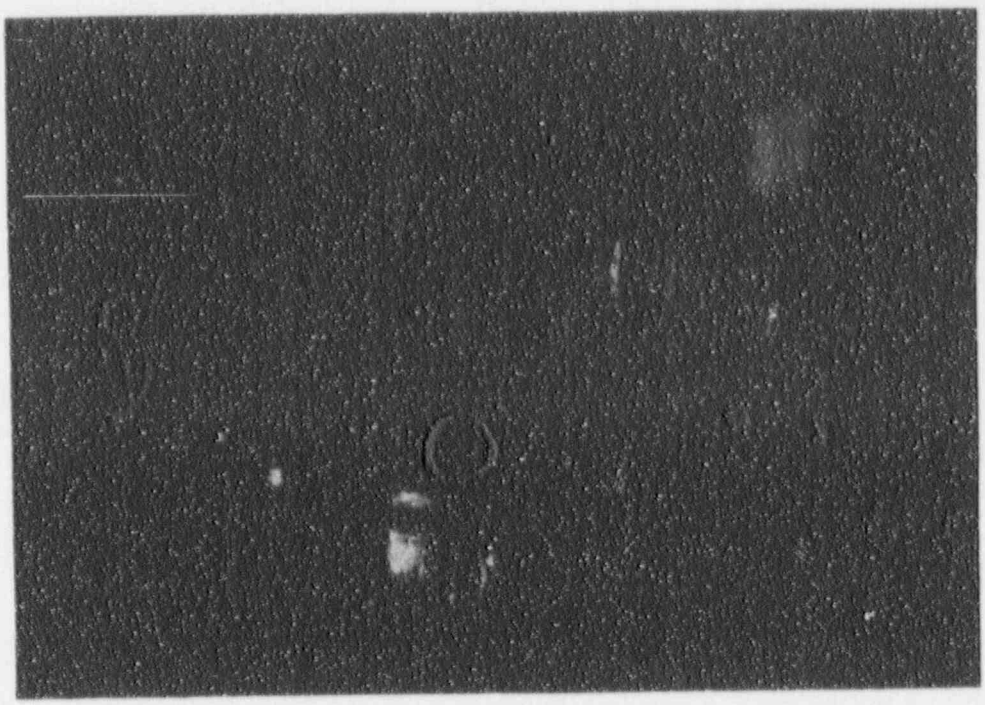


Figure 23. Bellows Specimen PP-2
Fully Compressed
(Test II-17-SCT)

DISCUSSION

The tests that have been conducted thus far indicate that bellows are capable of enduring extreme loads in the form of relatively large displacements, and elevated internal pressure and temperature while remaining leak tight. Bellows capacity is somewhat degraded by temperature, but they still are capable of remaining leak-tight during extreme conditions.

As expected, the universal type of bellows can withstand more extreme lateral displacements due to its design. Sharp creases do not develop until the lateral displacement is very large. Another geometric factor that affects performance is the depth of convolutions. The deeper convolutions develop sharp creases with less lateral displacement than those with shallow convolutions. Tears usually developed at one of these creases. The deeper convolutions also seem more prone to roll over the end spools and possibly be sheared by them.

These tests show that a wide range of containment bellows, if in 'good' condition, will remain leak-tight up to, or near, the point of full axial compression, while subjected to extreme conditions of internal pressure, elevated temperature, and lateral deformation. After being fully compressed, additional outward movement of the containment will likely cause large leakage as the bellows are either cut by the end spools or the connection of the bellows to the end spools will fail, since it was not designed to withstand this type of loading.

Since all the bellows in this series were tested in 'like-new' condition, the question of degraded capacity as a result of corrosion has not been answered. The specimens that were not tested during this series of tests will be subjected to accelerated corrosion and tested at a later date.

REFERENCES

[1] M. B. Parks, D. S. Horschel, W. A. vonRiesemann, Summary of NRC-Sponsored Research on Containment Integrity, Transactions of the Eleventh Conference on Structural Mechanics in Reactor Technology, Tokyo, Japan, 1991.

[2] L. Greimann, et al., Analysis of Bellows Expansion Joints in the Sequoyah Containment, NUREG/CR-5561, SAND90-7020, Sandia National Laboratories, Albuquerque, New Mexico (December 1991).

[3] M. H. Shackleford, et al., Characterization of Nuclear Reactor Containment Penetrations, NUREG/CR-3855, SAND84-7180, Sandia National Laboratories, Albuquerque, New Mexico (1985)

[4] Standards of the Expansion Joint Manufactures Association, Inc., 5th Edition, (1985 addenda), EJMA, Inc., 25 North Broadway, Tarrytown, NY.

GUIDELINES FOR SEISMIC QUALIFICATION BY EXPERIENCE IN ALWRs

Kamal K. Bandyopadhyay
Brookhaven National Laboratory
Upton, N.Y. 11973

ABSTRACT

The methodologies and acceptance criteria for seismic qualification of equipment are provided in IEEE Std. 344 endorsed by the Nuclear Regulatory Commission (NRC) in the Standard Review Plan. The IEEE Standard allows seismic qualification by use of the similarity analysis method. Data available from past earthquake events or vibration tests can be used in this regard. The nuclear industry has collected a vast amount of earthquake experience and test data in the last decade, and is planning to use it for seismic qualification of equipment in advanced light water reactor (ALWR) plants. This paper discusses the existing data bases including their limitations and describes the ways these data bases can be used for equipment qualification in ALWR plants.

1.0 INTRODUCTION

Seismic qualification of a component demonstrates its ability to perform an intended function in a given vibratory environment. The science of seismic qualification provides reliable as well as cost-effective methods for implementation. The aim is to simulate the desired vibratory environment and operate the component to verify its functionality. The seismic qualification methods can be broadly divided into three groups: testing; dynamic and static analysis; and similarity analysis. In a test program, the component is tested under static or dynamic loads, and its performance is monitored. In a structural analysis, static or dynamic, a mathematical model is created to represent the component and the responses under the appropriate loads are analytically computed. In a similarity analysis, a component that has been already qualified (e.g., either by testing, or by dynamic or static analysis) is used as a reference and the target component is compared with the reference component to demonstrate similarity. The selection of one or more of the above methods depends on the qualification attributes such as functionality and structural integrity. The ultimate objective is to demonstrate that the component functions. For some components, a demonstration of structural integrity ensures their functionality. On the other hand, a component may be severely damaged but still performs its intended function. In order to avoid such occurrences, one may choose to demonstrate both functionality and structural integrity, especially since the damaged state of a component is extremely nonlinear and the functionality may not be repeatable. Thus, the selection and successful implementation of an appropriate qualification method depends on adequate knowledge of the use and function of the component.

So far in the above discussion, the term "component" has been used in a general sense such that either a structural member or an equipment item can be called a component. In a broader sense, the above discussion is equally applicable for a system which consists of a number of sub-systems or smaller items. An experimental program provides more reliable results but is typically more expensive than other means. Moreover, it may have limited use unless the results can be extended to other components. Thus, in an initial phase, an experimental approach is used, and when sufficient knowledge has been

gained, the mathematical or similarity analysis method is employed. This has been the case with qualification of structural components. Basic parameters and validation of the analysis models are demonstrated by testing. Areas requiring further knowledge are still being addressed by testing (recent examples: validation of stiffness of shear walls, failure analysis of block walls, response in soil-structure interaction).

For the remaining discussions in this paper, the term "component" is used in a narrower sense to mean "equipment." Seismic qualification of equipment has been extensively performed in the last 25 years for nuclear power plants. A large number of dynamic test programs have been carried out using laboratory shake tables. On the other hand, several strong earthquakes occurred during this period and their consequences on equipment in industrial applications have been studied by the industry. This data base can also be used to verify seismic capability of equipment.

Recently, there have been several efforts to collect the existing test and earthquake experience data for nuclear power plant equipment [1,2]. Some of this information is currently being used for addressing seismic adequacy of equipment in existing older nuclear power plants under the scope of the NRC Unresolved Safety Issue A-46. An important conclusion of the above efforts is that certain equipment classes perform much better than others in a vibratory environment.

Currently, the industry is designing a new generation of reactors (Advanced Light Water Reactors or ALWRs) and attempting to use the experience data base for qualification of equipment in these plants. This paper discusses the strengths and weaknesses of these data bases, and describes the ways these data bases can be used for seismic qualification of equipment in ALWR plants. The approach that is employed to make use of an experience data base for qualification is the similarity analysis. Therefore, the method of qualification by similarity analysis is described first.

2.0 SIMILARITY ANALYSIS

An equipment item that is *similar* to one in the experience data base is expected to perform in a *similar* manner in a *similar* vibratory environment. In other words, if the equipment item can be shown to be similar to one that has successfully withstood a specified vibratory motion, it will be qualified up to that vibration level, typically measured in terms of a response spectrum. Thus, a similarity of both the equipment items and vibratory motions should be demonstrated.

For equipment similarity, a knowledge of the equipment design, its functional mechanisms, weak links and dynamic responses is required. The equipment mass, mass distribution, size, stiffness, model numbers, etc. are frequently used for comparison.

On the other hand, a demonstration of similarity of the vibratory environment requires knowledge of the damage potential of the vibratory motions. This is accomplished by comparison of the response spectra, power spectral densities, frequency contents, peak-to-RMS ratios, etc.

If both the above similarity comparisons are established, the "similar" equipment item is qualified for the "similar" vibratory environment. Any extrapolation of "similarity" beyond the above definition will require further justifications.

3.0 EXPERIENCE DATA BASES

The experience data bases can be grouped into three major categories according to their sources: past qualification, earthquake events, and equipment development. The relative strengths and weaknesses of each data base are further discussed as follows:

Past Qualification - This type of data base is available with EPRI, NRC, vendors and testing laboratories. The strength of this data base is that the vibration data have been controlled and monitored, and therefore are reliable. The weakness is that often not enough details of equipment are available in the qualification documents. This is especially true for data bases with EPRI, NRC and testing laboratories.

Earthquake Experience - EPRI and its consultants maintain a vast amount of earthquake experience data. The strength of this data base is that the information of equipment can be obtained to the desired details. Another attractive feature is that the data represent real earthquake events. But, the actual motion experienced by equipment in almost all cases is estimated and expected to be narrow-banded.

Equipment Development - As part of development of their products, the vendors most often performed testing that provides an in-depth knowledge about equipment performance including weak links. The vibratory motion is also well characterized. But, typically such information is proprietary to the respective manufacturers or vendors.

Regardless of the data bases, the following general observations can be made as a result of general discussions of these data bases available in the public domain:

- Certain equipment classes are by design simple *and* can sustain high seismic motions.
- For certain equipment classes, the weak links are well understood *and* the qualification levels are adequately known.
- Certain equipment classes are by design complex *and* sensitive to vibratory motions.

These observations provide the necessary inspiration for development of an approach for qualification by use of the experience data.

4.0 QUALIFICATION OF EQUIPMENT IN ALWR PLANTS

For ALWR plants, the experience data bases are given as described above but the equipment types to be qualified are unknown since they have not yet been designed and the design details are not known. Currently, the basic requirements for seismic qualification of equipment are documented in the IEEE Std 344 [3] and NRC Standard Review Plan [4]. In order to verify whether the experience data bases can be used for qualification of equipment in ALWR plants, the NRC has appointed an Expert Panel[1]. Using the following parameters, the Panel recommended categorization of equipment into three general groups and a graded approach for qualification of each group:

---

[1]The Expert Panel consists of the author and Drs. Daniel Kana, Robert Kennedy and Anshel Schiff. The views expressed in this paper are not necessarily supported by other Panel members and the NRC.

- Excitation-related damage severity potential
- Degree of equipment malfunction sensitivity
- Uncertainty associated with identification of malfunction mechanisms.

4.1 Group 1 Equipment

The Group 1 equipment classes are those (a) that by design demonstrate sufficient resistance to seismic motion; (b) that are designed for special considerations, e.g., operating loads, mechanical vibration; and (c) whose function is insensitive to seismic motion. For this group of equipment, less rigors are required to demonstrate similarity of equipment and motion.

4.2 Group 2 Equipment

The Group 2 equipment classes are not fit for Group 1 categorization but their malfunction mechanisms are sufficiently known from past experience. A rigorous similarity analysis is required for this group with a particular emphasis on the malfunction mechanism.

4.3 Group 3 Equipment

The Group 3 equipment classes are not fit for Groups 1 and 2, and are typically complex equipment whose malfunction mechanisms are not well identified. Shake table testing or a combination of testing and analysis is the recommended qualification approach for this group.

5.0 RECOMMENDATIONS

The following are some general recommendations for the ALWR equipment design and qualification:

- Learn from past practices, e.g., design weaknesses and failure occurrences.
- Use broader data bases.
- Increase vendor participation.
- Eliminate past weak links with sound procurement specifications.
- Encourage known sound design practices through procurement specifications.

The single-most important point is that the industry should strive for improvement of products rather than expending resources on qualification of poorly designed equipment since unlike in the past the ALWR equipment can be procured as desired by writing appropriate specifications.

6.0 ACKNOWLEDGEMENTS

The author is grateful to the NRC program managers and staff John O'Brien, Roger Kenneally, Nilesh Chokshi, Pei-Yen Chen and Shou Hou for their support and guidance. The author also sincerely acknowledges the contributions of the other Panel members.

REFERENCES

1. EPRI Report NP-5223, Rev. 1, "Generic Seismic Ruggedness of Power Plant Equipment in Nuclear Power Plants," February 1991.

2. Bandyopadhyay, K.K., et al., "Seismic Fragility of Nuclear Power Plant Components," NUREG/CR-4659, Vols. 1, 2, 3 and 4, 1986-1991.

3. IEEE Standard 344-1987, "Recommended Practice for Seismic Qualification of Class 1E Equipment for Nuclear Power Generating Stations."

4. U.S. Nuclear Regulatory Commission Standard Review Plan NUREG 800, Section 3.10.

Large-Scale Seismic Test Program at Hualien, Taiwan

H. T. Tang
B. E. Fong
Electric Power Research Institute

H. L. Graves
U. S. Nuclear Regulatory Commission

Y. C. Liao
Taiwan Power Company

ABSTRACT

The large-scale seismic test (LSST) program at Hualien, Taiwan is a follow-on to the soil-structure interaction (SSI) experiments at Lotung, Taiwan. The Electric Power Research Institute (EPRI) and the Taiwan Power Company (Taipower) organized a consortium to conduct the program and took the lead in planning and managing the program. Other organizations participating in the consortium that are providing cofunding, cost-sharing and technical as well as management input to the LSST program are: the U.S. Nuclear Regulatory Commission (NRC), the Central Research Institute of Electric Power Industry (CRIEPI), the Tokyo Electric Power Company (TEPCO), the Commissariat A L'Energie Atomique (CEA), the Electricite de France (EdF), Framatome, the Korea Electric Power Corporation (KEPCO), the Korea Institute of Nuclear Safety (KINS) and the Korea Power Engineering Company (KOPEC).

The LSST was initiated in January 1990 and is envisioned to monitor and collect earthquake data for five years following the completion of the test facility in 1993. The goal of this program is to collect real earthquake induced soil structure data in order to evaluate computer codes used in SSI analysis of nuclear power plant structures. A major task completed in 1993 was the construction of a 1/4 scale model of a reinforced concrete containment with instrumentation located on the structure and in the field along a three dimensional strong ground motion array. Also to date two forced vibration tests (FVT) have been conducted, one without backfill and one with backfill. The design of a vertical flat bottom tank has been completed and construction is ongoing. This paper describes progress of the Hualien project with emphasis on the FVT without backfill (FVT-1) and the blind prediction results.

1.0 INTRODUCTION

Optimal seismic designs of massive structures typically seen in nuclear power plants require a detailed understanding of dynamic soil-structure interaction (SSI) effects. Numerous analytical and experimental studies on the SSI problems have been performed for various research projects. Methods of analytical approaches to the SSI problems have been investigated through experimental studies like forced vibration tests (FVT) and earthquake observations in both actual or model structures. However, most of the experimental studies have been conducted at low acceleration levels and do not have sufficient information on dynamic behavior of actual structures under strong earthquake motions.

The countries of France, Japan, Korea, Republic of China and the United States are collaborating to investigate the SSI effects during strong earthquakes. Electric Power Research Institute (EPRI) in cooperation with Taiwan Power Company (Taipower) and companies from the aforementioned countries - the U.S. Nuclear Regulatory Commission (NRC), the Central Research Institute of Electric Power Industry (CRIEPI), the Tokyo Electric Power Company (TEPCO), the Commissariat A L'Energie Atomique (CEA), the Electricite de France (EdF), Framatome, the Korea Electric Power Corporation (KEPCO), the Korea Institute of Nuclear Safety (KINS) and the Korea Power Engineering Company (KOPEC) - is conducting a large scale seismic test (LSST) in Hualien, Taiwan, which is located in an area of high seismic activity. TEPCO is the sponsor of the FVT series, and CRIEPI has conducted the geotechnical and soil tests. To evaluate the reliability of the SSI methodologies, an extensively instrumented, one-quarter scale containment model of a nuclear power plant has been constructed at Hualien and has been subjected to forced vibration tests.

The experiment is being performed in three phases:

- FVT-1 - Forced vibration tests prior to backfill of the soil surrounding the model (discussed in this report).
- FVT-2 - Forced vibration tests after backfill.
- Actual earthquake events.

Each phase is comprised of a blind prediction and subsequent investigation of the measured and predicted responses.

All organizations of the Hualien consortium participated in the blind prediction phase of FVT-1. The data provided for the prediction included geometric and mechanical properties of the containment model, soil data, force exciter locations and the vibration measurement sensor locations.

Analytical results consist of normalized deflections and deflected shapes, transfer functions and associated phase relationships. The results of these prediction analyses will be systematically compared with the measured response

data. The validities, conservatisms and sensitivities of the SSI analysis methodologies and input parameters used in these analyses will be evaluated and assessed through comparison and correlation of the analytically predicted results with the measured responses. Differences between measured and predicted responses will be shared as part of the lessons learned, and model improvements will be incorporated from the results.

2.0 TEST MODEL

The 1/4-scale containment model test structure is a cylindrical shell of reinforced concrete having a height of 16.13 meters, an outer diameter of 10.52 meters and a shell thickness of 0.30 meters. The roof slab and the footing slab have thicknesses of 1.5 and 3.0 meters, respectively. The test structure has been constructed after excavating to a depth of 5.0 meters below the ground surface, and it rests on a gravelly layer .

The FVT-1 analyses were performed using soil profiles described in Reference 1. Figures 2-1 and 2-2 provide the unified soil model of the ground just beneath the model foundation and in the free field, respectively.

As can be seen in Figure 2-1, the differences in the soil profiles beneath the foundation are in the 5-12 meter depth below ground level as indicated by lines A and B. Line A presents the distribution of shear wave velocities measured after the excavation. Line B describes shear wave velocities directly beneath the foundation after construction of the containment model. The shear wave velocities have been determined on the basis of the cross-hole test results and/or the down-hole test results. To establish the deeper soil model, the shear wave velocity distribution down to a depth of 200 meter has been given, as shown in Figure 2-3.

Also, the soil densities have been obtained from dry densities of frozen samples, and the soil material damping ratios have been decided on the basis of the laboratory cyclic triaxial test data. The Poisson's ratios of the soils have been calculated by using P and S wave velocities.

For the concrete structures, Taiwan Power Company has recommended using material properties summarized in Table 2-1 [2]. The damping factor of 2% for the concrete has been specified to perform the blind analyses.

For the forced vibration tests, steady-state forcing functions are applied by using a ten ton exciter with sinusoidal harmonic motions. The horizontal north-south (NS), the horizontal east-west (EW) and the vertical excitation cases have been performed for the exciter set on the roof floor (elevation +11.13 meters) and on the first floor (elevation -2.00 meters). The selected test cases used in the FVT-1 blind analysis are as follows:

- The horizontal NS excitation at the roof floor.
- The horizontal NS excitation at the first floor.
- The vertical excitation at the first floor.

The general layout of the measuring points and selected components used for the FVT-1 blind analysis are listed in Table 2-2.

3.0 ANALYTICAL RESULTS

Various impedance-method (substructuring) and direct-method SSI approaches have been utilized by the participants for the FVT-1 phase. The containment structure and surrounding soil have been represented in the various analysis with models ranging from simple lumped mass systems to complete 3-dimensional (full, half or axisymmetric) finite element systems.

All analyses have been carried out to a minimum frequency of 20 Hz. Normalized transfer functions and phase angle relationships have been calculated for specified load cases at selected locations. Maximum displacement responses at any location have been obtained from the peak of the normalized transfer function for that location.

The results found by the participating United States organizations are summarized in Tables 3-1 to 3-5.

4.0 TEST COMPARISON

As discussed in Section 2 of this report, forced vibration tests (FVTs) were performed on the 1/4-scale containment model by applying an exciting force generated by an exciter installed on the first floor and on the roof slab. Directions of excitation were in the horizontal north-south (NS), horizontal east-west (EW) and vertical directions. Displacement meters measured the responses of the test model and surrounding soil surface. In addition, earth pressure cells recorded soil pressure responses. All instruments for the FVTs (i.e., exciter, data processing system and displacement meters) were imported from Japan and prepared according to the execution program.

The FVT-1 test was conducted in October and November 1992, and the FVT-2 test was conducted in February 1993.

The fundamental frequencies, damping ratios and displacement ratios found for FVT-1 are summarized in the following table [3]. The FVT-2 results are not available since blind predictions have not been completed.

Excitation Position	Excitation Direction	Natural Frequency (Hz)	Damping Factor (%)	Displacement Ratio (%)		
				Translation	Rocking	Deformation
Roof	D1	4.1	3.6	12	67	21
	D2	4.6	3.7	12	65	23
Basemat	D1	4.2	3.6	14	61	25
	D2	4.6	3.7	12	66	22
Basemat	UD	11.0	29.4	(Soil) 83		17

Fundamental frequencies for FVT-1, before backfill, are about 4.1 Hz for D_1 and 4.6 Hz for D_2, (D_1 and D_2 are the principal axes at 34° clockwise from NS) and the damping factors are about 4% for both directions. The sway ratio in the displacement at the roof floor is about 13% and that of rocking is about 64% for basemat excitation. For roof excitation, the ratios are 12% and 66%, respectively.

Shown in the following table is a statistical summary of the critical frequencies reported by all of the participating organizations.

	Frequency (Hz)			
	Horizontal Direction (North-South)		Vertical Direction	
	Soil Type A	Soil Type B	Soil Type A	Soil Type B
Minimum	4.66	4.93	8.86	9.70
Maximum	5.44	6.00	12.80	13.40
Average	4.92	5.49	11.53	11.89
Std Dev.	0.22	0.32	0.95	1.22

In general, the SSI analytical predictions slightly overpredict the fundamental frequency of the test model in both the horizontal (4.92 vs 4.1 or 4.6 Hz) and vertical (11.53 vs 11.0 Hz) directions.

REFERENCES

1. T. Kokusho, et al., "Geotechnical Investigation in the Hualien Large Scale Seismic Test Project," 12-SMiRT, K03/4, Stuttgart, Germany, August 15-20, 1993.
2. "Concrete and Rebar Properties of Hualien Containment Model," Tjing Ling Industrial Research Institute, December 31, 1992.
3. H. Morishita, et al., "Forced Vibration Test of the Hualien Large Scale SSI Model," 12-SMiRT, K02/1, Stuttgart, Germany, August 15-20, 1993.

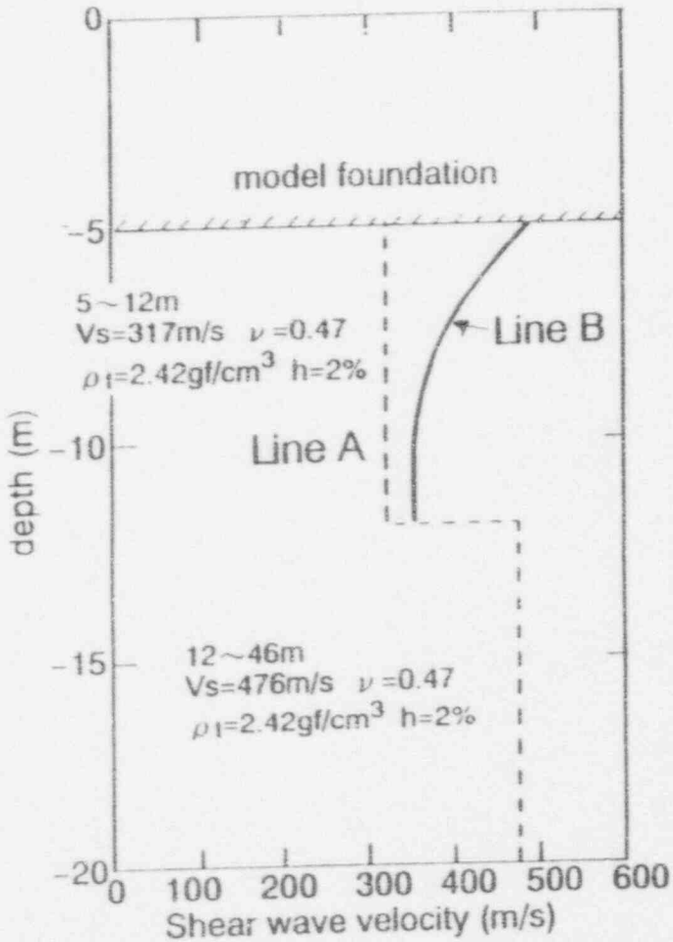


Figure 2-1 Unified model of the ground just beneath the model foundation for the FVT-1 analysis

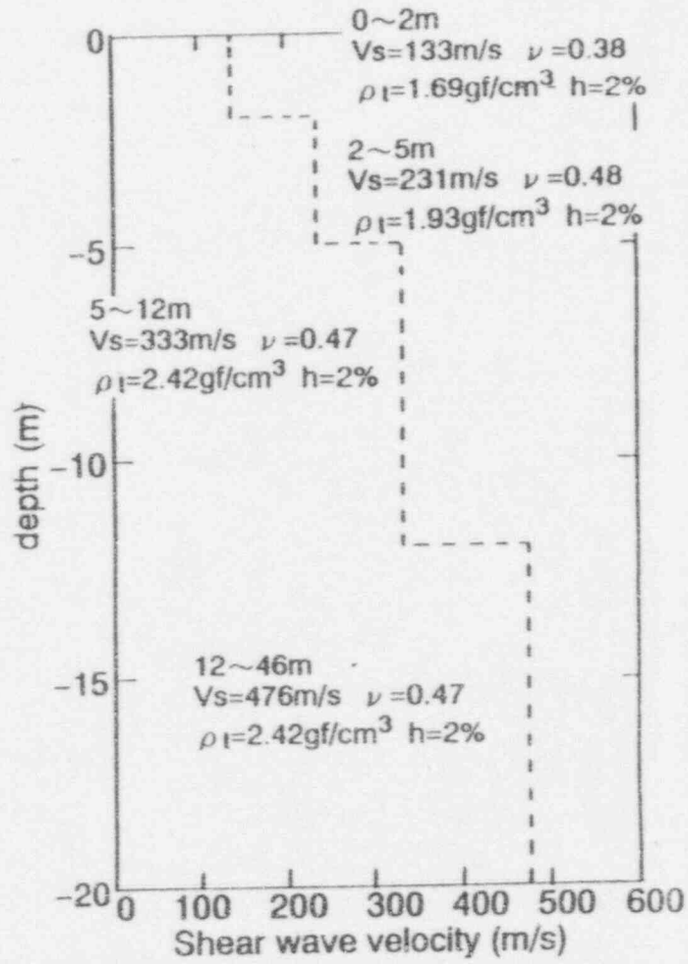


Figure 2-2 Model of the ground in the free-field

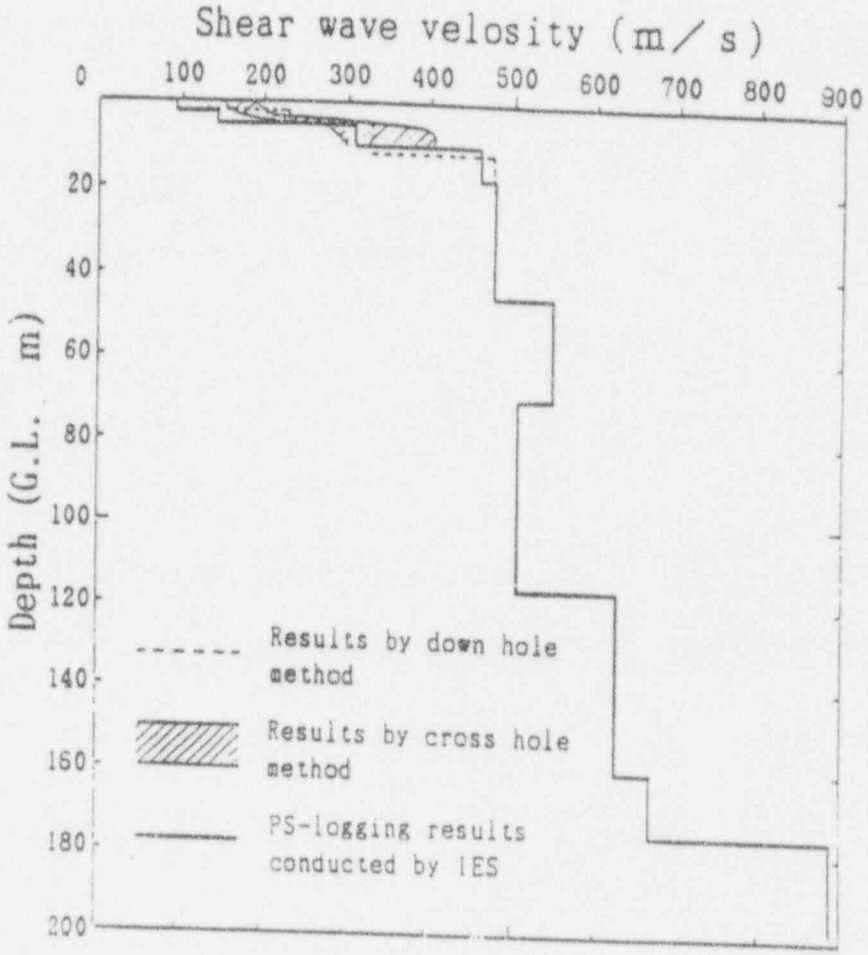


Figure 2-3 V_S distribution down to 200 m

Table 2-1 Material Properties

	Density (kg/m^3)	Strength (kgf/cm^2)	Young's Modulus (kgf/cm^2)	Poisson's Ratio
Concrete	2400	280 (Ultimate)	2.88E+05	0.16
Rebar	7850	2800 (Yield) 4200 (Yield)	2.05E+06	

Table 2-2 Observation Points and Response Components

Test	Response Component	Location	Observation Point Coordinates (m)		
			x	y	z
NS	H15 (y)	Roof	-4.82	0	11.13
	V9 (z)	Roof	-0.08	4.81	11.13
	H7 (y)	Floor	-4.74	0	0
	V3 (z)	Floor	-0.08	4.76	0
Vertical	V11 (z)	Roof	-1.42	0.08	11.13
	V10 (z)	Roof	4.82	0	11.13
	V4 (z)	Base	-0.80	0	0
	V5 (z)	Base	4.74	0	0

Table 3-1 ABB Impell FVT-1 Blind Predictions Using SASSI Computer Code

Soil Profile	Load Direction	Response Component	Frequency of Peak (Hz)	Amplitude at Peak (μm/ton)	Displacement Ratio (%)		
					Translation	Rocking	Deformation
A	H@B	H@B	4.74	3.80E+00			
A	H@B	H@R	4.79	2.10E+01	9.0	43.5	47.5
A	H@R	H@B	4.79	5.60E+01			
A	H@R	H@R	4.79	3.30E+02	6.2	55.7	38.1
A	V@B	V@B	11.96	1.16E+00			
A	V@B	V@R	12.65	1.64E+00			
B	H@B	H@B	5.18	2.30E+00			
B	H@B	H@R	5.22	1.42E+01	7.9	38.6	53.6
B	H@R	H@B	5.22	4.00E+01			
B	H@R	H@R	5.22	2.70E+02	5.3	48.5	46.3
B	V@B	V@B	12.40	7.70E-01			
B	V@B	V@R	14.01	1.16E+00			

H = Horizontal
V = Vertical
R = Roof
B = Basemat

Table 3-2 City University of New York FVT-1 Blind Predictions Using CARES Computer Code

Soil Profile	Load Direction	Response Component	Frequency of Peak (Hz)	Amplitude at Peak (μm/ton)	Displacement Ratio (%)		
					Translation	Rocking	Deformation
(Best Estimate)							
A	H@R	H@B	4.8	2.50E+01			
A	H@R	H@R	4.8	1.20E+02	8.0	73.0	19.0
A	H@R	V@R	4.8	4.20E+01			
A	V@B	V@B	12.0	9.00E-01			
A	V@B	V@R	12.0	1.10E+00			

H = Horizontal
V = Vertical
R = Roof
B = Basemat

Table 3-3a EPRI FVT-1 Blind Predictions Using FLUSH Computer Code

Plan	Soil Profile	Load Direction	Response Component	Frequency of Peak (Hz)
Rectangular	A	H	H @ R	5.44
Rectangular	A	V	V @ B - center	10.40
Rectangular	A	V	V @ B - wall	11.20
Rectangular	A	V	V @ R - wall	32.50
Rectangular	B	H	H @ R	5.59
Rectangular	B	V	V @ B - center	10.40
Rectangular	B	V	V @ B - wall	11.50
Rectangular	B	V	V @ R - wall	31.90
Square	A	H	H @ R	5.13
Square	A	V	V @ B - center	9.80
Square	A	V	V @ B - wall	11.20
Square	A	V	V @ R - wall	31.10
Square	B	H	H @ R	5.22
Square	B	V	V @ B - center	9.70
Square	B	V	V @ B - wall	11.90
Square	B	V	V @ R - wall	31.10

H = Horizontal

V = Vertical

R = Roof

B = Basemat

Table 3-3b EPRI FVT-1 Blind Predictions Using SASSI Computer Code

Soil Profile	Load Direction	Response Component	Frequency of Peak (Hz)	Amplitude at Peak (μm/ton)	Displacement Ratio (%)		
					Translation	Rocking	Deformation
A	H @ B	H @ B	4.98	1.12E+01			
A	H @ B	H @ R	4.98	5.07E+01	8.0	67.0	25.0
A	H @ B	V @ B	4.98	1.03E+01			
A	H @ B	V @ R	4.98	1.34E+01			
A	H @ R	H @ B	4.98	5.27E+01			
A	H @ R	H @ R	4.98	2.44E+02	8.0	66.0	26.0
A	H @ R	V @ B	4.98	4.97E+01			
A	H @ R	V @ R	4.98	6.48E+01			
A	V @ B	V @ B - center	11.80	1.21E+00			
A	V @ B	V @ B - wall	10.70	1.49E+00			
A	V @ B	V @ R - wall	12.10	1.42E+00			
B	H @ B	H @ B	5.76	5.93E+00			
B	H @ B	H @ R	5.76	3.02E+01	7.0	60.0	33.0
B	H @ B	V @ B	5.76	5.60E+00			
B	H @ B	V @ R	5.76	8.03E+00			
B	H @ R	H @ B	5.76	3.21E+01			
B	H @ R	H @ R	5.76	1.68E+02	7.0	59.0	34.0
B	H @ R	V @ B	5.76	3.12E+01			
B	H @ R	V @ R	5.76	4.48E+01			
B	V @ B	V @ B - center	12.20	7.30E-01			
B	V @ B	V @ B - wall	10.00	1.07E+00			
B	V @ B	V @ R - wall	13.10	8.70E-01			

H = Horizontal
V = Vertical
R = Roof
B = Basemat

Table 3-3c EPRI FVT-1 Blind Predictions Using Soil-Spring Method

Soil Profile	Load Direction	Response Component	Frequency of Peak (Hz)	Amplitude at Peak (μm/ton)	Displacement Ratio (%)		
					Translation	Rocking	Deformation
A	H@B	H@B	4.74	7.40E+00			
A	H@B	H@R	4.74	3.42E+01	8.0	70.0	22.0
A	H@B	V@B	4.74	6.99E+00			
A	H@B	V@R	4.74	7.08E+00			
A	H@R	H@B	4.74	8.55E+01			
A	H@R	H@R	4.74	3.94E+02	8.0	70.0	22.0
A	H@R	V@B	4.74	8.01E+01			
A	H@R	V@R	4.74	8.12E+01			
A	V@B	V@B	8.86	9.60E-01			
A	V@B	V@R	11.20	1.09E+00			
B	H@B	H@B	5.35	6.01E+00			
B	H@B	H@R	5.35	3.09E+01	6.0	65.0	29.0
B	H@B	V@B	5.35	5.82E+00			
B	H@B	V@R	5.35	5.90E+00			
B	H@R	H@B	5.35	6.94E+01			
B	H@R	H@R	5.35	3.55E+02	6.0	65.0	29.0
B	H@R	V@B	5.35	6.70E+01			
B	H@R	V@R	5.35	6.79E+01			
B	V@B	V@B	11.90	6.60E-01			
B	V@B	V@R	15.20	8.50E-01			

H = Horizontal
V = Vertical
R = Roof
B = Basemat

Table 3-4 EQE Engineering FVT-1 Blind Predictions Using CLASSI, SASSI and SUPELM Computer Codes

Method-Soil Profile	Load Direction	Response Component	Frequency of Peak (Hz)	Amplitude at Peak (μm/ton)	Displacement Ratio (%)		
					Translation	Rocking	Deformation
CLASSI-A	H@B	H@R	4.80	7.80E+00	21.9	57.7	20.5
CLASSI-A	H@B	V@R	4.80	2.09E+00			
CLASSI-A	H@R	H@R	4.77	3.37E+01	21.5	57.8	20.7
CLASSI-A	H@R	V@R	4.77	9.17E+00			
CLASSI-A	V@B	V@R	12.01	1.75E-01			
CLASSI-B	H@B	H@R	5.59	4.61E+00	19.5	52.3	28.2
CLASSI-B	H@B	V@R	5.59	1.22E+00			
CLASSI-B	H@R	H@R	5.59	2.32E+01	20.4	55.3	24.2
CLASSI-B	H@R	V@R	5.59	5.91E+00			
CLASSI-B	V@B	V@R	12.94	1.06E-01			
SASSI-A	H@B	H@R	5.39	6.02E+00	20.5	53.2	26.2
SASSI-A	H@R	H@R	5.39	2.78E+01	20.1	53.5	26.4
SASSI-A	H@B	V@R	5.39	1.59E+00			
SASSI-A	H@R	V@R	5.39	7.34E+00			
SASSI-A	V@B	V@R	12.06	1.37E-01			
SUPELM-A	H@B	H@R	5.20	5.10E+00	20.9	55.0	24.2
SUPELM-A	H@B	V@R	5.20	1.36E+00			
SUPELM-A	H@R	H@R	5.20	2.32E+01	20.4	55.3	24.2
SUPELM-A	H@R	V@R	5.20	6.12E+00			
SUPELM-A	V@B	V@R	10.01	1.12E-01			
SUPELM-B	H@B	H@R	5.94	3.19E+00	18.2	50.0	31.8
SUPELM-B	H@B	V@R	5.94	8.56E-01			
SUPELM-B	H@R	H@R	5.94	1.67E+01	17.7	50.5	31.8
SUPELM-B	H@R	V@R	5.94	4.49E+00			
SUPELM-B	V@B	V@R	10.01	7.65E-02			

H = Horizontal

V = Vertical

R = Roof

B = Basemat

Table 3-5 Sargent & Lundy FVT-1 Blind Predictions Using SASSI Computer Code

Soil Profile	Load Direction	Response Component	Frequency of Peak (Hz)	Amplitude at Peak (μm/ton)	Displacement Ratio (%)		
					Translation	Rocking	Deformation
B	H @ B	H @ B	5.80	5.50E+00			
B	H @ B	H @ R	5.80	2.95E+01	7.0	57.0	36.0
B	H @ B	V @ B	5.80	6.00E+00			
B	H @ B	V @ R	5.80	8.50E+00			
B	H @ R	H @ B	5.80	3.10E+01			
B	H @ R	H @ R	5.80	1.65E+02	7.0	57.0	36.0
B	H @ R	V @ B	5.80	3.40E+01			
B	H @ R	V @ R	5.80	4.90E+01			
B	V @ B	V @ B-center	10.40	1.04E+00			
B	V @ B	V @ R-center	13.40	1.00E+00			
B	V @ B	V @ R-wall	13.40	9.00E-01			

H = Horizontal
V = Vertical
R = Roof
B = Basemat

INTEGRAL TESTING OF RELAYS AND CIRCUIT BREAKERS

Kamal K. Bandyopadhyay
Brookhaven National Laboratory
Upton, N.Y. 11973

ABSTRACT

Among all equipment types considered for seismic qualification, relays have been most extensively studied through testing due to a wide variation of their designs and seismic capacities. A temporary electrical discontinuity or "chatter" is the common concern for relays. A chatter duration of 2 milliseconds is typically used as an acceptance criterion to determine the seismic capability of a relay. Many electrical devices, on the other hand, receiving input signals from relays can safely tolerate a chatter level much greater than 2 ms.

In Phase I of a test program, Brookhaven National Laboratory performed testing of many relay models using the 2-ms chatter criterion. In Phase II of the program, the factors influencing the relay chatter criterion, and impacts of relay chatter on medium and low voltage circuit breakers and lockout relays were investigated. This paper briefly describes the Phase II tests and presents the important observations.

1.0 INTRODUCTION

A large number of relays are used in a nuclear power plant. They perform various logic functions in integral electrical and electronic circuits. If the structure housing the relays is subjected to ground shaking due to an earthquake, the relay contacts vibrate causing the potential for opening or closing of the contacts. Most contacts experience repeated opening and closing in a vibrating environment, and this is commonly known as contact chatter. A single chatter may be as short as a fraction of a millisecond. Therefore, most circuits do not respond to many of the contact chatters in the event of an earthquake. The maximum duration of chatter that can be tolerated in a circuit varies depending on, for example, capacitance and inductance of the circuit. The current industry practice is to use 2 ms as the maximum acceptable chatter duration for seismic qualification of relays. In an effort to explore the chatter-tolerant capability of power circuits, BNL conducted an experimental program with relays and circuit breakers. The program was carried out in two parts: electrical and vibration. Both electrical and vibration experiments including a data analysis are discussed in this paper.

2.0 ELECTRICAL EXPERIMENTS

2.1 Test Procedures

Electrical experiments were performed in two phases. In the first phase, eleven low and medium voltage circuit breakers, and two lockout relays were tested at locations for determination of the time required for these devices to trip. The trip current vs. time plots were recorded with a portable oscilloscope.

In the second phase, three lockout relays, three circuit breakers and eight auxiliary self-reset relays were tested at a power testing laboratory. The trip current traces were recorded. In addition, electrical pulses of minimum durations required for tripping were determined.

2.2 Test Results

A sample oscilloscope trace is shown in Figure 1. The abscissa represents the time and the ordinate indicates the voltage or current as it builds up as a DC power source is applied to the trip solenoid. The total trip time for breakers and lockout relays varied between 20 and 60 ms except for the fast lockout relay. The total trip time consists of the time required for energization of the trip solenoid and the time required for the latching mechanism to complete its motion until trip occurs as pictorially presented in Figure 2. As expected, the trip time increased as the voltage was dropped. Laboratory tests with single and multiple pulses provided further understanding of the field test data. The required duration of a single pulse corresponds to the energization time (Figure 2). In summary, the minimum pulse duration required to trip a device is about a half of the total trip time. The minimum pulse durations for most breakers are comparable to those for lockout relays. The latter justifies the use of lockout relays as surrogates in integral testing.

3.0 VIBRATION EXPERIMENTS

3.1 Test Procedures

The vibration tests were performed with a group of source relays producing the chatter and a group of load devices responding to the chatter, all connected in integral circuits. Five protective and auxiliary relays were used as the source relays, and a medium voltage circuit breaker, two lockout relays and another auxiliary relay were used as the load devices. Initially, the source relays were placed on the shake table and the load devices were seated on a stationary stand. Testing was conducted with both single frequency and multifrequency input motions. Subsequently, both the source relays and load devices were mounted in a switchgear cabinet and vibrated on the shake table with multifrequency input motion. Electrical outputs were monitored for both sets of experiments to determine the chatter durations required for tripping of the load devices. The circuit configuration is shown in Figure 3. The connections between the source relays and load devices were interchanged and the tests were repeated four times so that each source relay was once connected to a device. Monitoring current and load device voltage were varied for determination of their effect on chatter and tripping characteristics.

3.2 Test Results

3.2.1 Chatter/Trip Data

The chatter of source relays caused tripping of lockout relays and the breaker. The most common type of time relationship between the source relay chatter and load device (i.e., breaker or lockout relay) trip is shown in Figure 4A. The source relay initiates chatter at t_1 (i.e., temporary change-of-state) as the vibration continues and the load device trips a few milliseconds later at t_2. But the source relay remains in the alternate state for a few more milliseconds before it returns to its original electrical state at t_3, and the load device remains tripped. Therefore, the duration required to cause the trip after initiation of the chatter (i.e., a) is less than the chatter duration (i.e., b). Thus, in comparison with the electrical test data discussed in Section 2.2, "a" is similar to the "total trip time" of the breakers and

lockout relays. A sample chatter/trip test result is shown in Figure 5. In an integral circuit with the output of the source relay CO9 controlling operation of the lockout relay LOR, the lockout relay trips 6.25 ms after initiation of the source relay chatter. The source relay returned to its original state after 149.5 ms.

3.2.2 Single Frequency Vibration Data

The source relays were vibrated at selected frequencies and the vibration levels were adjusted until a trip occurred in the target load device. The highest vibration level achieved without a trip in the target load device is considered the capacity of the source relay in terms of its function in that particular circuit. For example, the capacity levels of IAV measured in terms of sine dwell amplitudes are shown in Figure 6. As evident from the data, the capacity of this relay to trip a 5 HK breaker is lower than that based on the conventional 2-ms criterion.

3.2.3 Multifrequency Vibration Data

The capacity data for the same IAV relay when subjected to multifrequency excitation are presented in Figure 7. These results were obtained from shaking of the source relay while the load device was located on a stationary stand. Figure 8 shows capacity levels of a CO9 relay in terms of the shake table motion (i.e., the control accelerometer reading) when the devices were mounted in a switchgear cabinet.

4.0 SUMMARY AND CONCLUSIONS

The duration of an electrical signal required to cause a trip in a circuit breaker or lockout relay is much less than the actual trip time of these devices. The minimum pulse durations required to trip circuit breakers and most lockout relays are comparable. Testing in integral circuits with electrical conditions representing field applications is recommended since the 2-ms chatter criterion can be unconservative.

ACKNOWLEDGEMENTS

The author is grateful to Dr. John O'Brien, the NRC Program Manager, for his support and comments. Messrs. Carl Kunkel, Leonard Scharf and Semyon Shteyngart assisted in planning the experiments and interpreting the data. Their support is sincerely appreciated. The author also acknowledges the assistance of KEMA Powertest and Wyle Laboratories for conducting the tests.

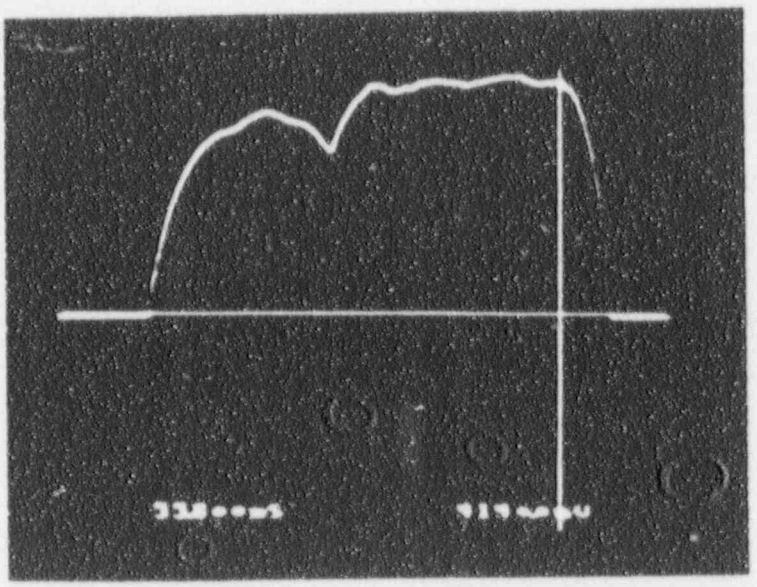


Figure 1 Oscilloscope Voltage (Current) Time Trace for Westinghouse Breaker DH3

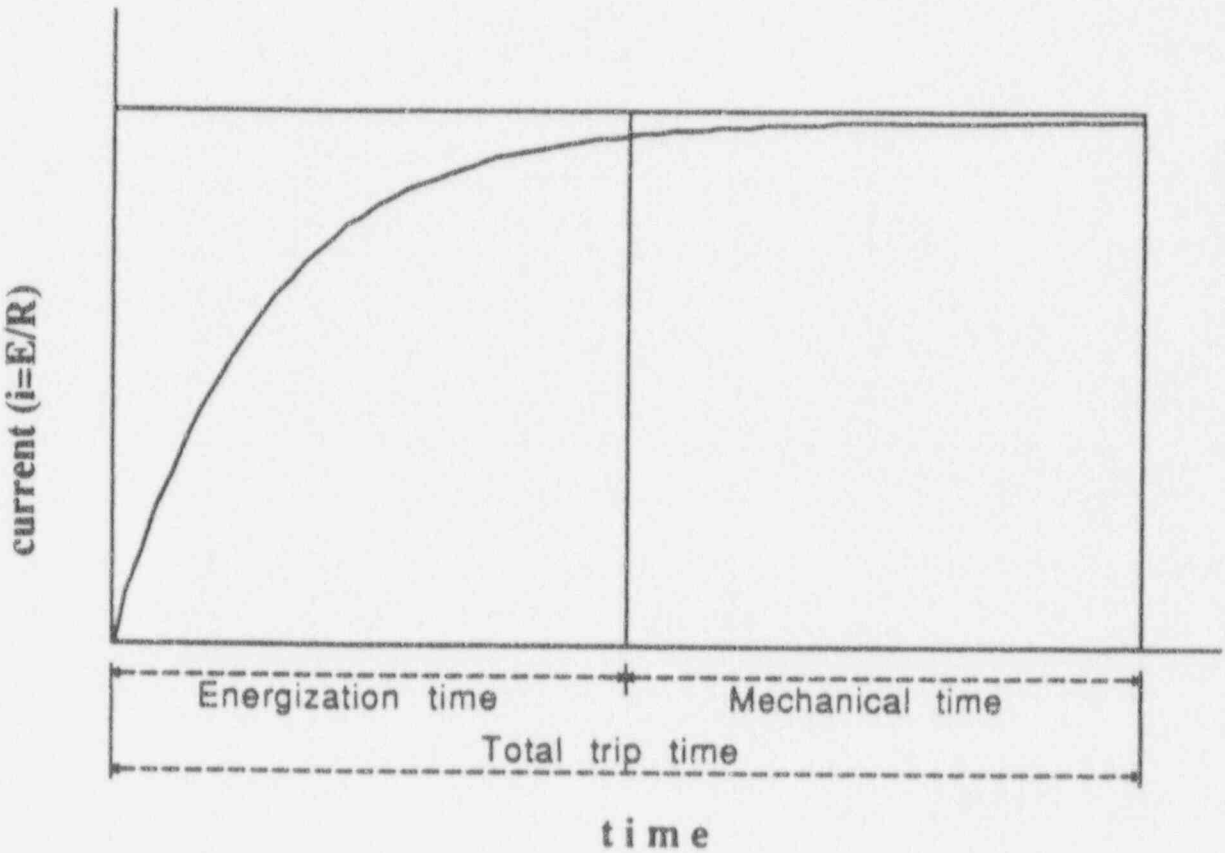
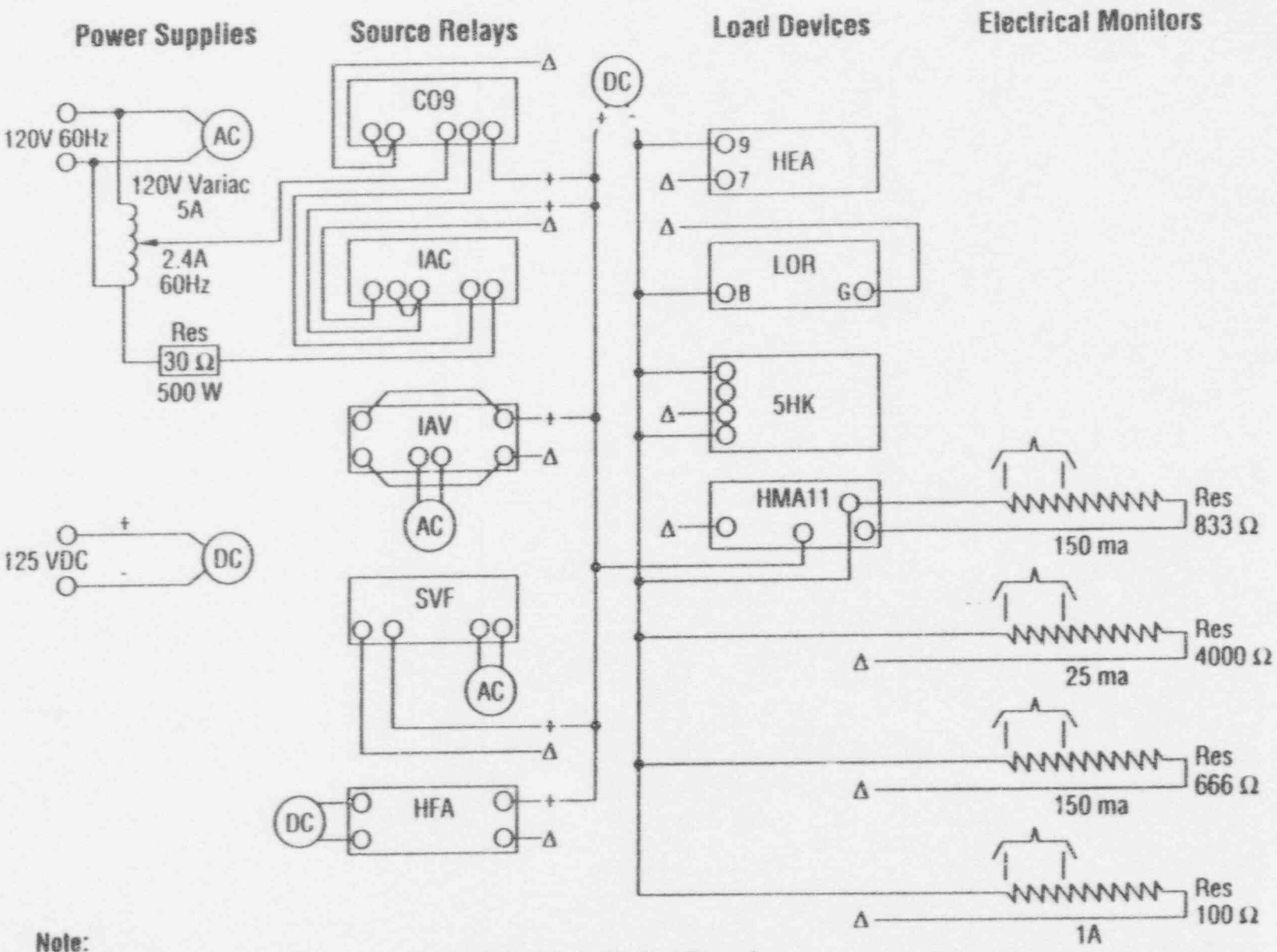


Figure 2 Current Build-Up vs. Trip Time



Note:
Source Δ's Were Connected to Load Δ's Per Schedule in the Test Procedure.

Figure 3 Electrical Connections for Vibration Tests

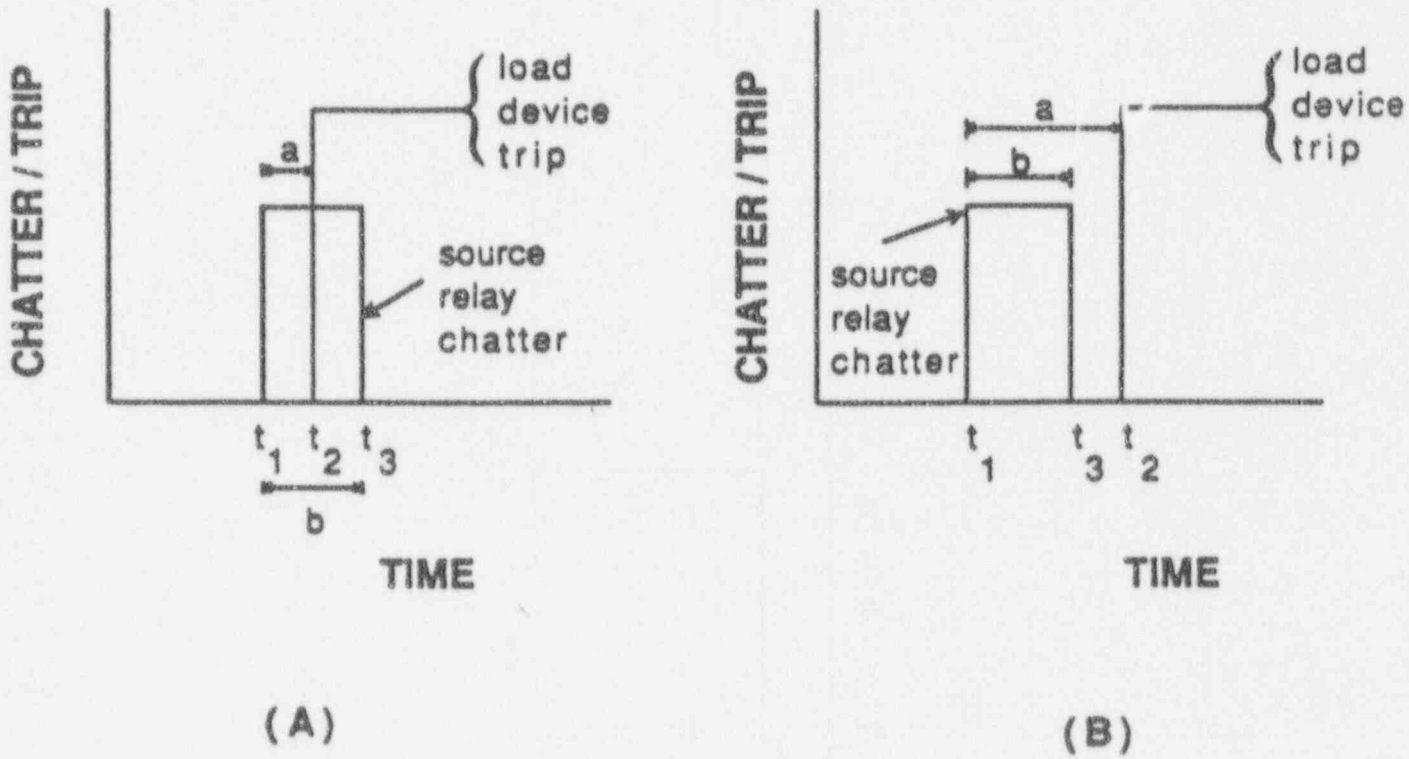


Figure 4 Effect of Source Relay Chatter on Load Device

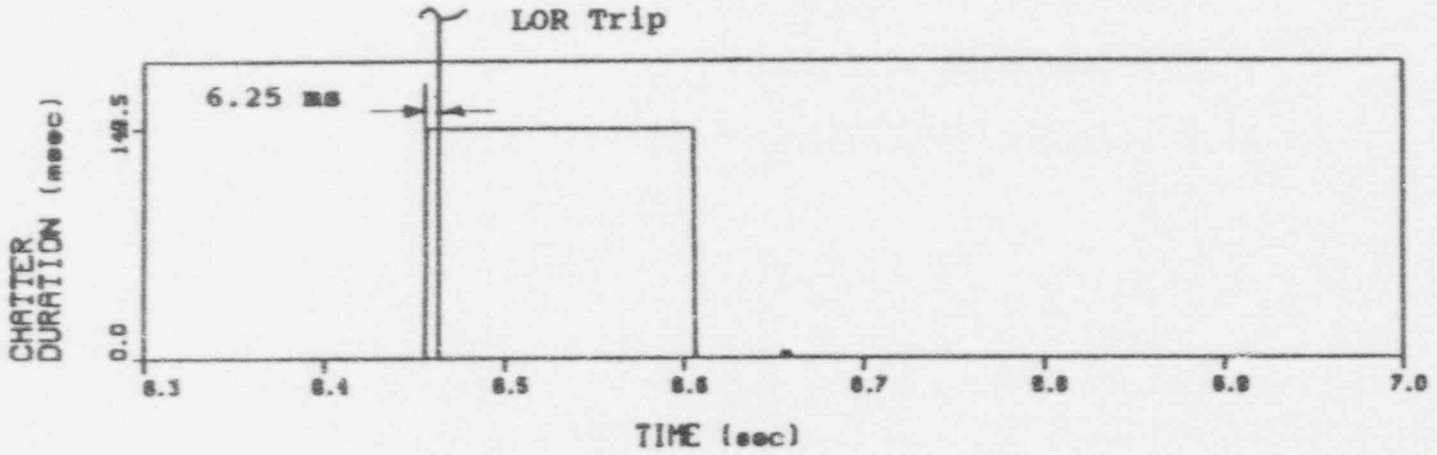


Figure 5 Effect of CO9 Chatter on LOR

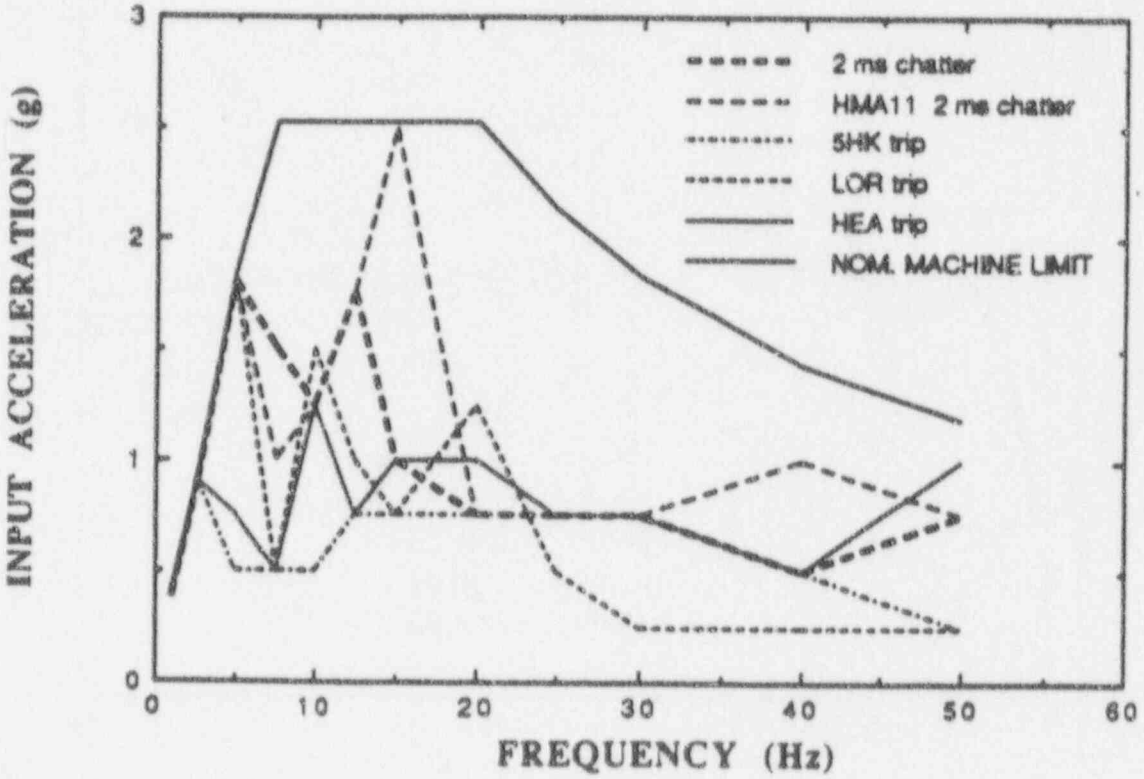


Figure 6 Sine Dwell Capacity Level, IAV, Vertical Direction

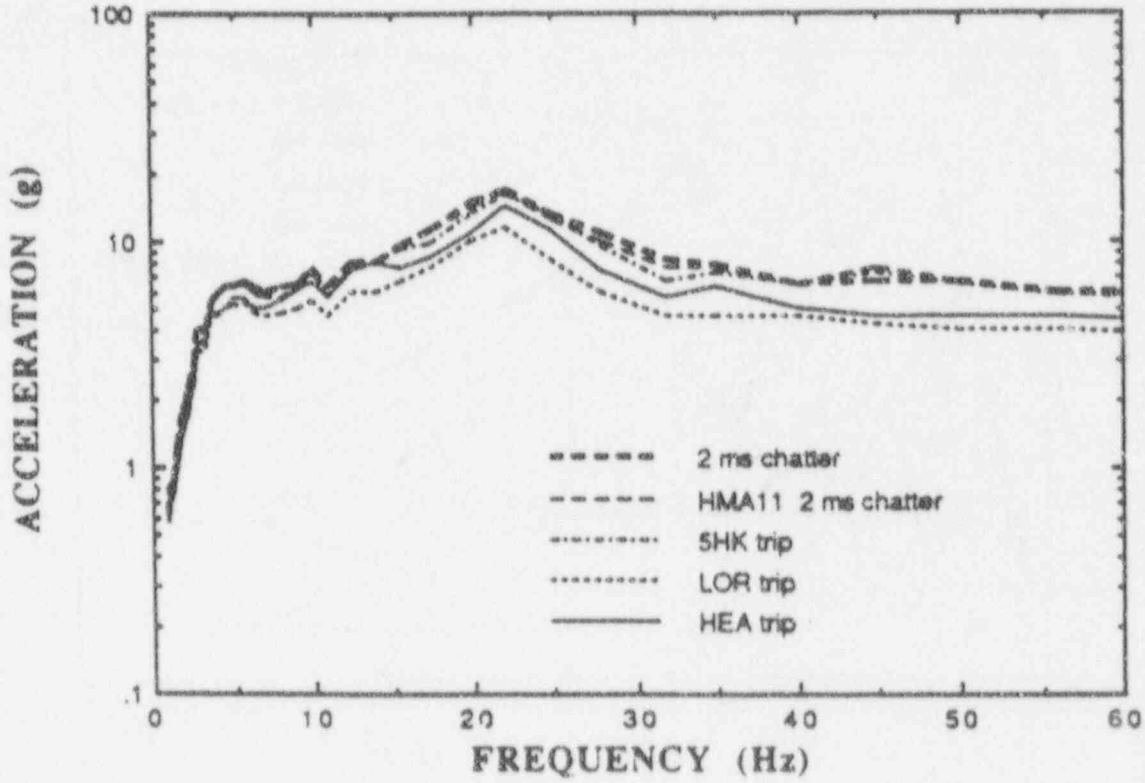


Figure 7 Multifrequency Capacity TRS @ 5% Damping, IAV, Vertical Direction

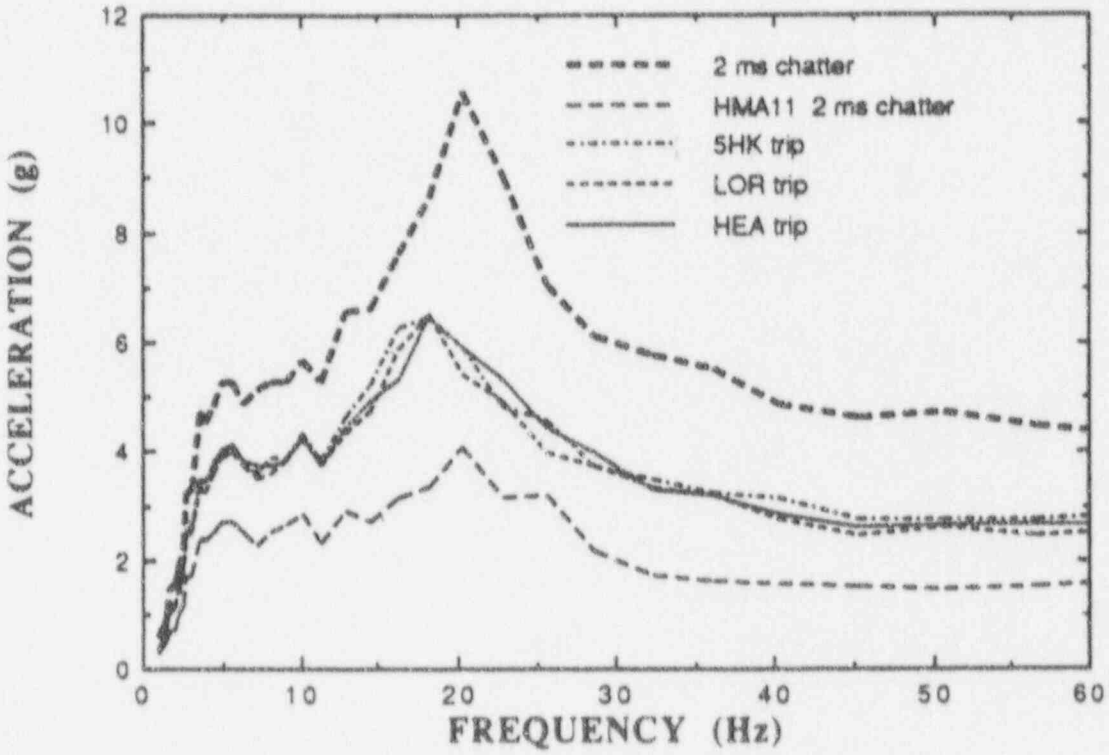


Figure 8 Multifrequency Capacity TRS @ 5% Damping, CO9 in Switchgear Cabinet, Vertical Direction (Shake Table Motion i.e., Control Accelerometer Reading)

Development of an Improved Methodology for Probabilistic Seismic Hazard Analysis

Robert J. Budnitz
Future Resources Associates, Inc.
2039 Shattuck Avenue, Suite 402, Berkeley, California 94704

In the late 1980s, the methodology for performing probabilistic seismic hazard analysis (PSHA) was exercised extensively for eastern-U.S. nuclear power plant sites by the Electric Power Research Institute (EPRI) and Lawrence Livermore National Laboratory (LLNL) under NRC sponsorship. Unfortunately, the seismic-hazard-curve results of these two studies differed substantially for many of the eastern reactor sites, which has motivated all concerned to revisit the approaches taken. This project is that revisitation.

The NRC, EPRI, and the U.S. Department of Energy (DOE) are jointly supporting an 18-month project that began in the spring of 1993, with the goal of developing a recommended methodology, including implementation guidelines, suitable for performing PSHA. The final product of the project will be a methodology that can be used in seismic regulation of nuclear power plants and other critical facilities.

To accomplish this objective, an independent committee of technical experts, the Senior Seismic Hazard Analysis Committee, has been established under joint NRC, DOE, and EPRI sponsorship.* This Committee is developing the desired implementation guidelines for PSHA. In the course of this work, it is expected that the Committee will evaluate the PSHA methodologies already developed by EFRI and under NRC sponsorship by LNLL.

Technical Support Panels sponsored by NRC, DOE, and EPRI will perform analyses and studies as defined by the Committee. A final Committee report will summarize the work performed in this project and provide the desired implementation guidelines, including a recommended methodology, suitable for the performance of PSHA.

This paper discusses the progress to date for this important project, including the approach being taken and some of the key technical issues that are being confronted. Among these are how to provide definitive guidance on seismic zonation, seismicity modeling, ground-motion modeling, and expert elicitation.

---

* The members of the Committee are Robert Budnitz (chair), George Apostolakis, David Boore, Lloyd Cluff, Kevin Coppersmith, Allin Cornell, and Peter Morris.

Geologically Recent Near-Surface Faulting and Folding in Giles County, Southwest Virginia: New Exposures of Extensional and Apparent Reverse Faults in Alluvial Sediments between Pembroke and Pearisburg

R.D. Law, M.C. Pope, R.H. Wirgart, , K.A. Eriksson,
E.S. Robinson, S. Sayer, E. J. Phinney & G.A. Bollinger

Department of Geologicial Sciences, Virginia Tech., Blacksburg, Virginia 24061

ABSTRACT: A series of faults have recently been identified which cut a folded succession of stratified alluvial deposits located along the north side of the New River Valley between Pembroke and Pearisburg in Giles County, Virginia. Although the age of neither the faults nor the sediments is currently known, the unlithified nature of the alluvial deposits suggests that both are, geologically, relatively recent (Tertiary or Quaternary). The faults are regarded by the authors as being of considerable potential importance to both the assessment of seismic hazard and to our understanding of fault development in this section of the Valley and Ridge Province as they would appear to indicate the, at least local occurence, of geologically recent near surface faulting.

The occurrence of faulting in these geologically recent sediments was first detected during excavation for land-fill material in early 1992 when two extensional faults were exposed on land owned by Mr Arnold Bostic of Pembroke, Virginia. The authors became aware of these newly exposed faults in late May 1992 and have since carried out a detailed analysis of the near surface folding and faulting of the sediments under Nuclear Regulatory Commission Contract No. NRC-04-85-121. This analysis has involved the excavation of five bench-type exposures (above road level) and one trench (below road level). Reconaissance geophysical surveys have also been undertaken in an attempt to trace to depth the structures revealed in these temporary exposures.

BACKGROUND INFORMATION

The excavation site is situated adjacent to Route 460 on the north side of the New River Valley between Pembroke and Pearisburg in Giles County, southwestern Virginia (Fig. 1). This area is covered by the Pearisburg Quadrangle 7.5 minute series topographic map. The site is located at an altitude of 1800' (549 m) above sea level and is 180' (55 m) above the local level of the New River. The geology of the Giles County area is shown on the 1:50,000 scale map prepared by Schultz et al. (1986) and has also been summarized by McDowell & Schultz (1990).

The deposits at the excavation site consists of a series of stratified, but unlithified, boulder beds, gravels and silts. According to the Giles County geological map of Schultz et al. (1986), the excavation site is situated on alluvial 'terrace' deposits of unspecified age. Mills & Wagner (1985) have divided the terrace deposits situated along the New River between Radford and Pembroke into three groups: lower terraces (including flood plains) at less than 25 m above the modern river level, intermediate terraces at 25-50 m above, and high terraces at greater than 50 m above the river. The excavation site deposits may therefore be tentatively correlated with either the intermediate or higher terraces of Mills & Wagner (1985).

Reconnaissance seismic refraction and gravity surveys indicate that this sequence of low density unconsolidated sediments reaches a thickness of more than 130' (40 m) at the excavation site and rests on an irregular basement surface. On the Schultz et al. (1986) map the terrace deposits are shown as resting on Lower Ordovician and Upper Cambrian rocks composed primarily of dolomite with some thin sandstone layers. Karst topography is locally developed.

AGE OF THE 'TERRACE' DEPOSITS

Age dating of the surficial deposits in this area is problematic (see Schultz et al. 1989). Mills (1988) has tentatively suggested a Pleistocene age for the colluvial deposits in the Mountain Lake area, to the east of Pembroke. Several authors (e.g. Hack 1980) have suggested that the age of river terrace deposits may be estimated by dividing their heights above the modern river level by the regional erosion rate. However, Houser (1980, 1981) has shown that such calculations must, in karst areas, also take into account increases in local erosion rate due to limestone solution.

The excavation site terrace deposits are situated 55.0 m above the current level of the New River. Using the curves of Houser (1980) this would indicate that these deposits are between 3.0 and 1.5 million years old (assuming regional erosion rates of between 20 and 40 meters per million years). Mills (1986) has suggested that the erosion rates used by Houser (1980) may be too low, and that erosion rates of up to 290 meters per million years may be appropriate (see also Bartholomew & Mills 1991). Based on this erosion rate, the excavation site deposits would be estimated at 190,000 years old.

It should also be born in mind that the unlithified deposits at the excavation site could be of a much older age. Lowry (1979, p. 4) has suggested that the present course of the New River was established as early as Mississipian times. Lignite found within high-level gravels near the divide between the New and Tennessee rivers at an elevation of 3150' (960 m) on Brushy Mountain in Smyth County has been assigned a late Cretaceous or early Tertiary age (Sears 1957). W.D. Lowry (pers. comm. 1992) has suggested to the authors that the excavation site deposits could also be of late Cretaceous or Miocene age. However, unless faulting has dropped down high-level gravels by some 350 m, it seems unlikely that the excavation site deposits can be correlated with the lignite-bearing gravels of Smyth county. To the best of the author's

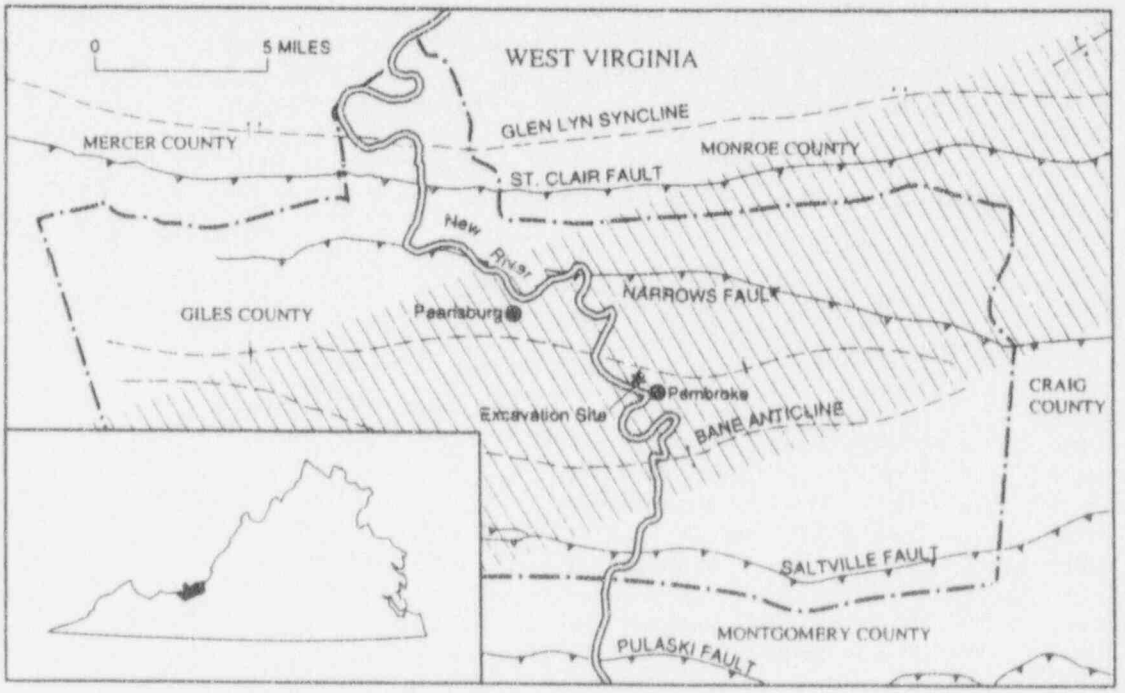


Figure 1. Location map showing position of the Pembroke excavation site in relation to the New River, Pearisburg, the Giles County seismic zone (approximate position indicated by ruled ornament), and the main Valley & Ridge thrust faults (Alleghenian age). Also shown are axial traces of the Alleghenian age Glen Lyn (or Hurricane Ridge) syncline and the Bane anticline (or dome). Inset shows position of Giles County in relation to Virgina state boundaries.

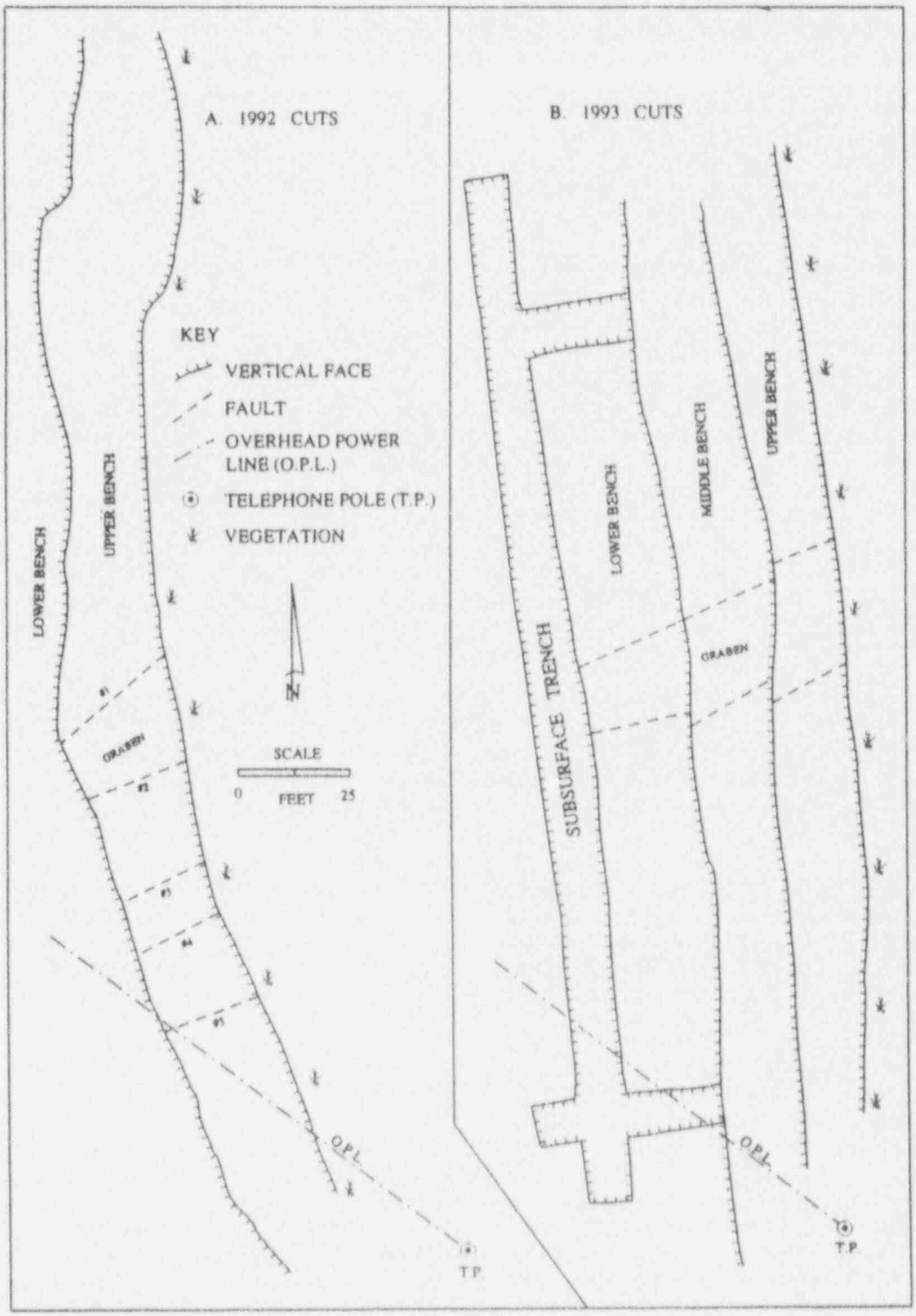


Figure 2. Site plans of excavations carried out at the Pembroke site in 1992 and 1993.

a) September 1992 - benching and two vertical cuts above road level made. Position of Faults 1-5 indicated.
b) April-May 1993 - benching and three vertical cuts above road level plus one trench (below road level) made. Position of the central graben (Faults 1 & 2) is indicated. Note position of telephone pole (TP) and overhead power line is the same in each site plan.

knowledge, no radiometric ages have been obtained for river terrace deposits in the Pembroke area of the New River valley. Detailed sampling and laboratory analysis at Virginia Tech, using standard sieving and chemical separation techniques, has so far failed to reveal any carbonaceous or fossil material which might facilitate the more precise dating of these highly oxidized sediments exposed at the excavation site.

SEISMICITY IN THE GILES COUNTY AREA

The Giles County area is located within the southern Appalachian seismic zone (Bollinger 1973). The Pearisburg earthquake which occurred within this zone on May 31, 1897 (Campbell 1898, Bollinger & Hopper 1971a,b) is the second largest known earthquake in the southeastern United States (modified Mercali intensity VIII; body wave magnitude = 5.8 according to Bollinger & Wheeler 1982). On the basis of seismic monitoring by the Virginia Tech. network, Bollinger (1981) has defined a planar seismic zone in Giles County that is about 40 km long, 10 km wide, and is oriented approximately northeast-southwest (Fig. 1). The earthquake hypoceneters define a tabular zone extending from a depth of 5 to 25 km and dipping almost vertically towards the northwest. These earthquakes are all situated within basement rocks beneath the detachment to the Appalachian overthrust belt (Bollinger 1981, Gresko 1985).

Bollinger & Wheeler (1983, 1988) have suggested that the Giles County seismic zone (Fig. 1) was the source of the 1897 earthquake and further proposed that the most likely fault mechanism was reactivation of an ancient basement fault produced by Iapetan rifting. Seismic reflection data across the Bane Dome in Giles County have been interpreted by Gresko (1985) as indicating that the contact between crystalline basement and late Precambrian-Cambrian sediments (located at a depth of between 6 and 8 km) is downthrown to the SE by 1-2 km on steeply dipping growth faults located beneath the Giles County seismic zone. Study of sediment thicknesses inferred from this seismic data suggests that these growth faults became inactive by Rome Formation (Lower Cambrian) times. Focal mechanism analysis of recent earthquake activity on the Giles County seismic zone indicate predominantly reverse or strike-slip motion (Munsey 1984, Munsey & Bollinger 1985). This sense of motion would uplift the Pearisburg area relative to the area located to the southeast of the seismic zone (Fig. 1), and is compatible with the greater elevation of the river terraces noted by Mills (1986) in the Pearisburg area.

EXCAVATION WORK

In order to investigate the geologic structures developed in the river terrace sediments at the excavation site, a series of benches (above road level) together with a trench (below road level) have been driven into the sediments (Fig. 2).

Two vertical cuts were made in September 1992:- the lower cut measuring 122.0 m in length and a maximum of 4.3 m in height, and the upper cut measuring 99.0 m in length and a maximum height of 4.0 m (Fig. 2a). Both these cuts trended N20°W (i.e. 340°-160°), the upper cut being set back some 6.0 m to the east from the lower cut. All geologic features exposed in the vertical cuts were surveyed at a scale of 1 inch = 2' and detailed photomontages were produced for both cuts. Detailed structural measurements were made of the following features exposed: a) bedding planes, b) fault planes, c) foliation within fault zones, d) lineations lying within the foliation planes of these fault zones.

A second series of vertical cuts trending N10°W (i.e. 350°-170°) were made in April - May 1993 (Fig. 2b). From west to east, four cuts were made: **a)** a trench measuring 70.0 m in length, with a maximum depth of 3.7 m below road level, **b)** a lower cut 76.0 m in length with a maximum height of 3.7 m, **c)** a middle cut 69.0 m in length with a maximum height of 2.1 m and, **d)** an upper cut 67.0 m in length with a maximum height of 2.7 m. Photomontages have been made for each of these cuts and surveying of the geologic features exposed is currently in progress at a scale of 1 inch = 2'.

GEOLOGICAL FEATURES EXPOSED

Fold structure

The stratified sediments are arched into a broad ENE-WSW trending antiform measuring a horizontal distance of at least 95 m from limb to limb, with dips of up to 30° on each fold limb (Fig. 3). A detailed analysis has been made of the geometry of this structure by measuring, in specially excavated 3D exposures, the strike and dip of bedding at a minimum of 30 sites in each cut. Stereographic analysis of poles to bedding planes exposed in the 1992 cuts indicates that the calculated fold axis plunges at 7° towards N64°E. Similarly, analysis of poles to bedding planes exposed in the 1993 trench indicates a calculated fold axis plunging at 14° towards N63°E (Fig. 4).

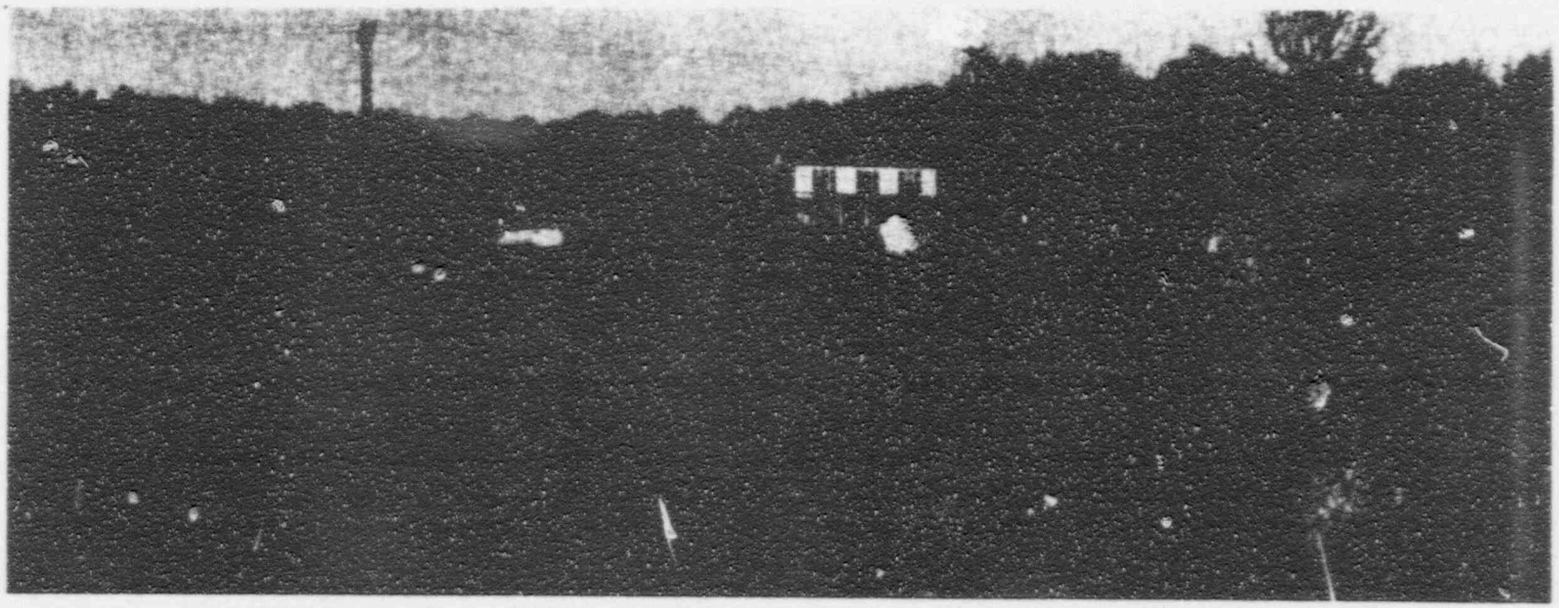
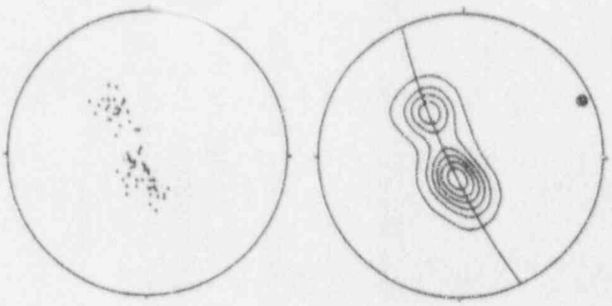


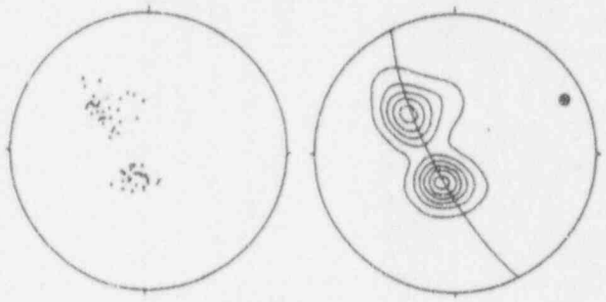
Figure 3. View towards the ENE of the September 1992 excavations showing the antiformal arch picked out by the boulder bed at the top of the exposed sequence of sediments.
The central graben (dark) is located in the hinge zone of the antiform. Faults 1 and 2 are located on the N (left) and S sides of the central graben respectively. A second smaller graben is exposed on the southern limb of the antiform (Faults 3 & 4 on the N and S sides of the graben respectively). Fault 5 is located to the S (right) of this smaller graben.

Poles to Bedding - 1992 benches



Fold axis plunges at 7° towards 064°

Poles to Bedding - 1993 trench



Fold axis plunges at 14° towards 063°

Figure 4. Poles to bedding measured in the September 1992 bench cuts and the 1993 trench excavation. Note that bedding poles define a highly cylindrical fold in these cuts and that the angle of fold plunge is steeper in the structurally lower 1993 excavation. 1992 benches - 68 poles to bedding measured, 1993 trench - 61 poles to bedding measured. Contour intervals: 1, 4, 7, 10 13 &16 times uniform distribution.

Faults

The sediments exposed at the excavation site are cut by a series of normal (extensional) faults (Figs. 2 & 3). Five of these faults display significant off-set (> 1.0 m) and are marked by 10-20 cm wide zones of green clay-rich fill. Within these zones, the basal planes of individual clay grains are oriented parallel to the planar fault zone margins and define a macroscopic foliation. In freshly excavated exposures, foliation is marked by polished and lineated cleavage surfaces. This lineation lying within the foliation surfaces appears to be constantly oriented within individual fault zones and is interpreted to be of tectonic origin, developing parallel to the individual fault's slip vector.

The average orientation of foliation and lineation within each of these fault zones was estimated by vector analysis, a minimum of 10-20 measurements for both foliation and lineation being recorded in each fault zone (Fig. 5). The local dip and strike of each fault (as exposed in the 1992 cuts) was estimated from this foliation data. Details for each of the five clay-rich faults are given below.

A central graben structure (Graben One), measuring 11.0 m in width at its highest currently exposed structural level, is present in the hinge zone of the antiform. Above road level, the graben is a downward -narrowing structure (Figs. 2 & 6) defined by two faults with orientations: strike N51°E, dip 71°SE (Fault 1) and N80°E, 56°N (Fault 2). A minimum apparent dip-slip off-set of 8.5 m is indicated by lithological correlation across these graben-defining faults. Traced downwards beneath road level, these faults steepen to become vertical, the graben measuring 4.6 m in width (Fig. 7).

A second, but much smaller scale, graben structure (Graben Two) is present on the SSE dipping limb of the antiform and is located 6.0 m to the ESE of Graben One. Graben Two is a downward-narrowing structure, measuring 5.0 m in width at its highest exposed structural level, and defined by two faults with orientations: strike N46°E, dip 71°SE (Fault 3) and N70°E, 57°N (Fault 4). Fault 3 defining the NW margin of Graben Two (Fig. 2) displays an apparent dip-slip off-sets of 1.37 m. Fault 4, defining the SE margin of Graben Two, displays an apparent dip-slip off-set of 1.0 m.

A further extensional fault (Fault 5) is located 6.0 m to the SSE of Fault 4 (Fig. 2). Fault 5 strikes N56°E, dips at 54° NW and displays an apparent dip-slip off-set of 2.8 m.

Faults 2, 4 and 5 dip away from the New River valley and, together with Faults 1 and 3, are marked by 10-20 cm wide zones of green clay-rich fill. Within these zones, the basal planes of individual clay grains are oriented parallel to the planar fault zone margins and define a macroscopic foliation. As exposed in the 1992 cuts, lineation on the foliation surfaces is constantly oriented within individual fault zones and, measured downward in the foliation from the SW-W



Figure 6. View towards the ENE of the central graben exposed in the upper 1992 cut. Graben is filled with homogeneous red sands (second highest stratigraphic unit exposed). Sediments on either side of the graben are stratigraphically older bedded and cross-bedded orange sands and gravels. Stratigraphic off-sets and lineation data indicate off-sets of 11.4 and 11.0 m on the N (Fault 1) and S (Fault 2) sides of the graben. Hammer for scale. Graben is 11.0 m wide at the top of the cut.



Figure 7. View towards the ENE of the central graben exposed in the April-May 1993 exposures. Surveying stakes are spaced at 4' intervals. Note the coarse boulder unit exposed in the trench (foreground); this boulder horizon is the stratigraphically lowest unit exposed in the 1992-3 excavations.

strike direction, pitches at 48°, 37°, 48°, 65° and 70° on Faults 1-5 respectively (Fig. 5). Assuming these lineations formed parallel to the fault slip vector, then total displacements of approximately 11.4 m, 11.14 m, 1.84 m, 1.1 m and 3.0 m are indicated for faults 1, 2, 3, 4 and 5 respectively. The close geometrical relationships between the observed fold and fault geometries (cf. Figs. 4 & 5) suggest that folding and faulting may be contemporaneous.

The green clay-rich fill marking the above faults are in strong contrast to the red oxidized mineral of the surrounding sediments. These green clays may indicate (D. Rimstidt, pers. comm 1993) that fluid flow along the fault zones occured under chemically reducing conditions, and that such conditions are indicative of upward (rather than downward) fluid flow.

In addition to the clay-rich extensional faults described above, three other fault-types are recognized at the Pembroke site.

i) Discrete extensional fault surfaces, without any clay fill, typically displaying off-sets of less than 30 cm. Many hundreds of these barren extensional faults have been recorded and, based on the observed thickening and thinning of individual stratigraphic units, at least some appear to be of syn-sedimentary origin.

ii) Barren faults on the limbs of the antiform with apparent reverse-sense off-sets of less than 30 cm. The orientation of these faults with respect to bedding indicates that, if they formed before folding, they could be extensional faults which have been tilted through the vertical during folding to produce apparent reverse-sense off-sets.

iii) Reverse faults with 5-10 cm of clay-rich fill located near the hinge-zone of the antiform, whose geometries indicate a reverse-sense of motion even if they formed before folding (Figs. 8 & 9). The clay-rich fill associated with these reverse faults is well foliated and displays a strongly developed down-dip lineation on the foliation planes. The lineation is oriented within the plane of the excavation face, indicating that true, rather than apparent, off-sets are being observed within the excavation face. These reverse faults, which are exposed in the middle bench of the 1993 excavations and dip towards the hinge zone of the antiform, display

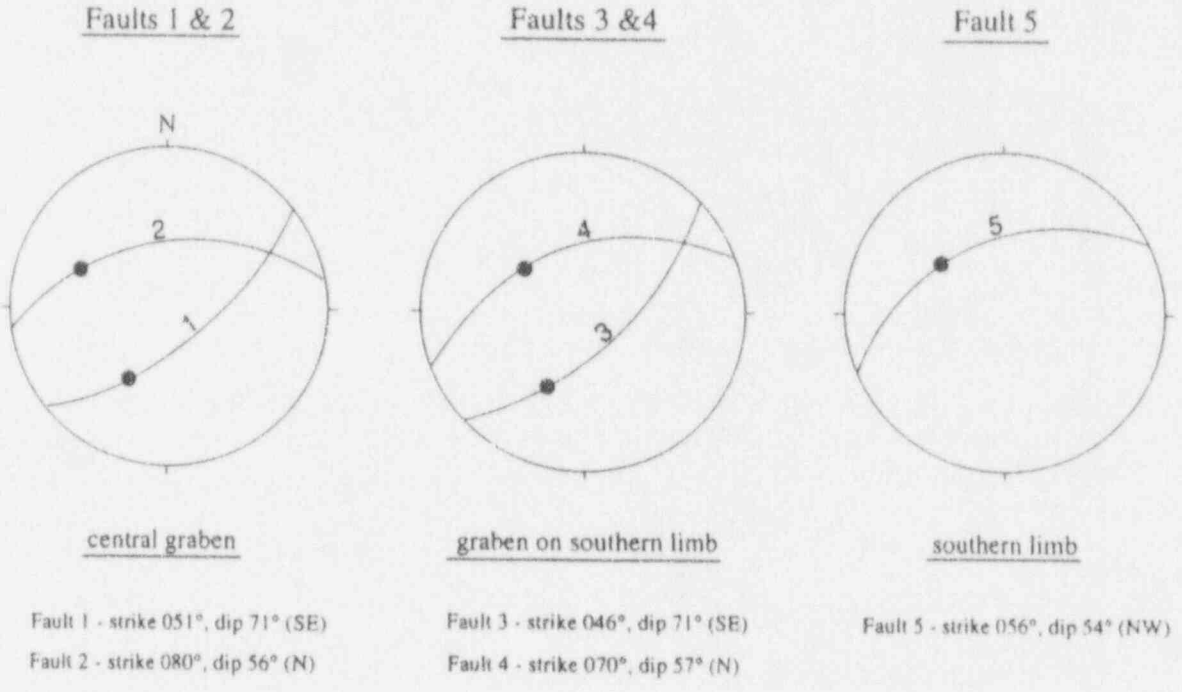


Figure 5. Structural data from the five major clay-rich faults exposed in the 1992 excavations. Great circles represent the vector mean orientation of foliation in each fault zone, circles represent vector mean orientation of lineation in each zone.

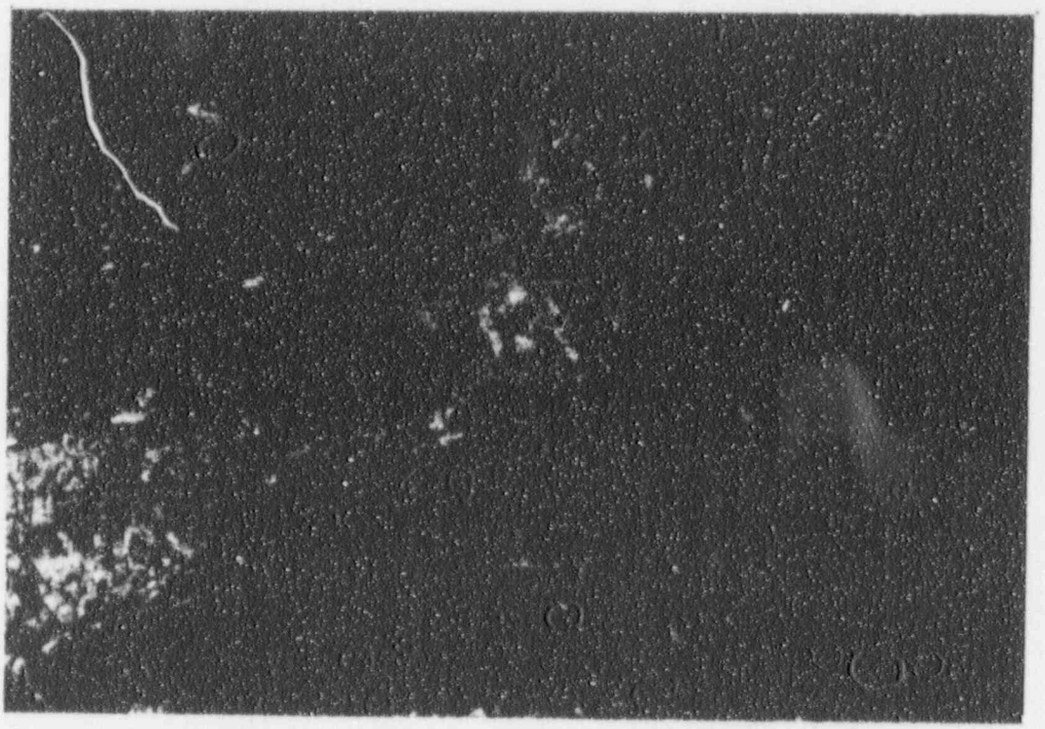


Figure 8. Clay-rich reverse fault viewed towards the ENE and exposed in the middle cut of the 1993 excavations. This south-dipping reverse fault is situated on the north side of the central graben (see Fig. 2) and displaces a paleosoil horizon (light colored) by 30 cm.

Note that even if faulting occured before tilting of the beds this fault would still show reverse sense geometry. Material at top of the cut is float. Hammer for scale. Vertical survey strings are spaced at 4' intervals.



Figure 9. Clay-rich reverse fault viewed towards the ENE and exposed in the middle cut of the 1993 excavations. This south-dipping reverse fault is situated on the south side of the central graben (see Fig. 2) and displaces a paleosoil horizon (light colored) by 60 cm.

Note that even if faulting occured before tilting of the beds this fault would still show reverse sense geometry. Material at top of the cut (above hammer) is float. Vertical survey strings are spaced at 4' intervals.

a top to-the N thrust sense on the northern limb of the antiform (with minimum off-sets of c. 30 cm) and a top to-the S thrust sense (off-sets of c. 60 cm) on the southern limb (Figs. 8 & 9 respectively).

Many of the above deformation features may post-date formation of the New River terrace gravels exposed at the excavation site. However, earlier syn-sedimentary deformation is also indicated by the presence of angular unconformities and small growth faults in the exposed sections. This suggests that tilting and faulting of the sediments may have occured over a considerable time interval and that the area was undergoing deformation during sedimentation.

GEOPHYSICAL SURVEYING

A geophysical survey of the Pembroke fault site was undertaken with the objectives of investigating the depth and character of the "basement" underlying the unconsolidated sediment in which faulting has been observed, and of investigating the horizontal extent and the depth of structures exposed by excavation. Results available at the present time include seismic refraction and electrical resistivity measurements along profiles whose locations are shown on Figure 10, and gravity and magnetic field intensity measurements at the grid of observation points shown in Figures 11 and 14 respectively.

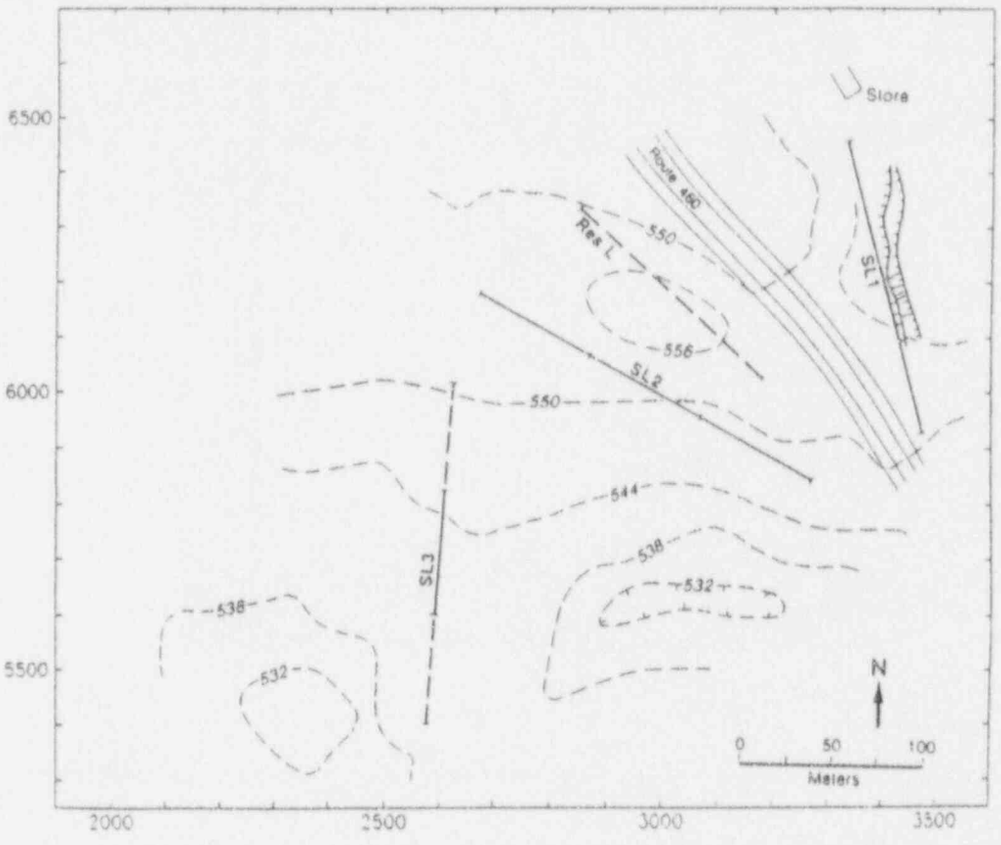


Figure 10. Geophysics study area showing locations of seismic refraction profiles (heavy solid lines) and electrical resistivity profiles (heavy solid lines and heavy dashed lines). Excavated embankment is shown close to line SL1. Topographic contours (light dashed lines) are shown at 6 m intervals. By adding 1,370,000 to the values along the south edge, and by adding 360,000 to values along the west edge of the map, Virginia state plane grid coordinates in units of feet are obtained.

Seismic refraction soundings were made along three separate lines using explosive charges ranging from 0.2 kg to 3 kg in shot holes of from 0.5 m to 1.5 m deep. Results for each line indicate a layer of unconsolidated sediment overlying a broken limestone terrane. Along line SL1 the average thickness of unconsolidated sediment is approximately 40 m. The thickness of this layer increases from 18 m at the southeast end to 40 m at the northwest end of line SL2, and is more than 24 m along line SL3. Variations in seismic wave speed along these lines indicate lateral inhomogeneity within the unconsolidated sediment, probably related to discontinuous lenses and wedges of sand, gravel, cobble and boulder deposits. Relatively low wave speeds in the underlying "basement" suggest a broken limestone terrane similar to that seen at the land surface bordering the deposits of unconsolidated sediment.

To obtain further information about possible relief on the basement surface, gravity accurate within + or - 0.02 mgal was measured with LaCoste & Romberg Meter G-311 at the locations shown in Figure 11. These observation points were placed approximately 15 m apart, and their relative positions and elevations were determined within + or - 2 cm using a Hewlett Packard Model 3810A infrared transit. Two sets of Bouguer gravity values were calculated assuming near

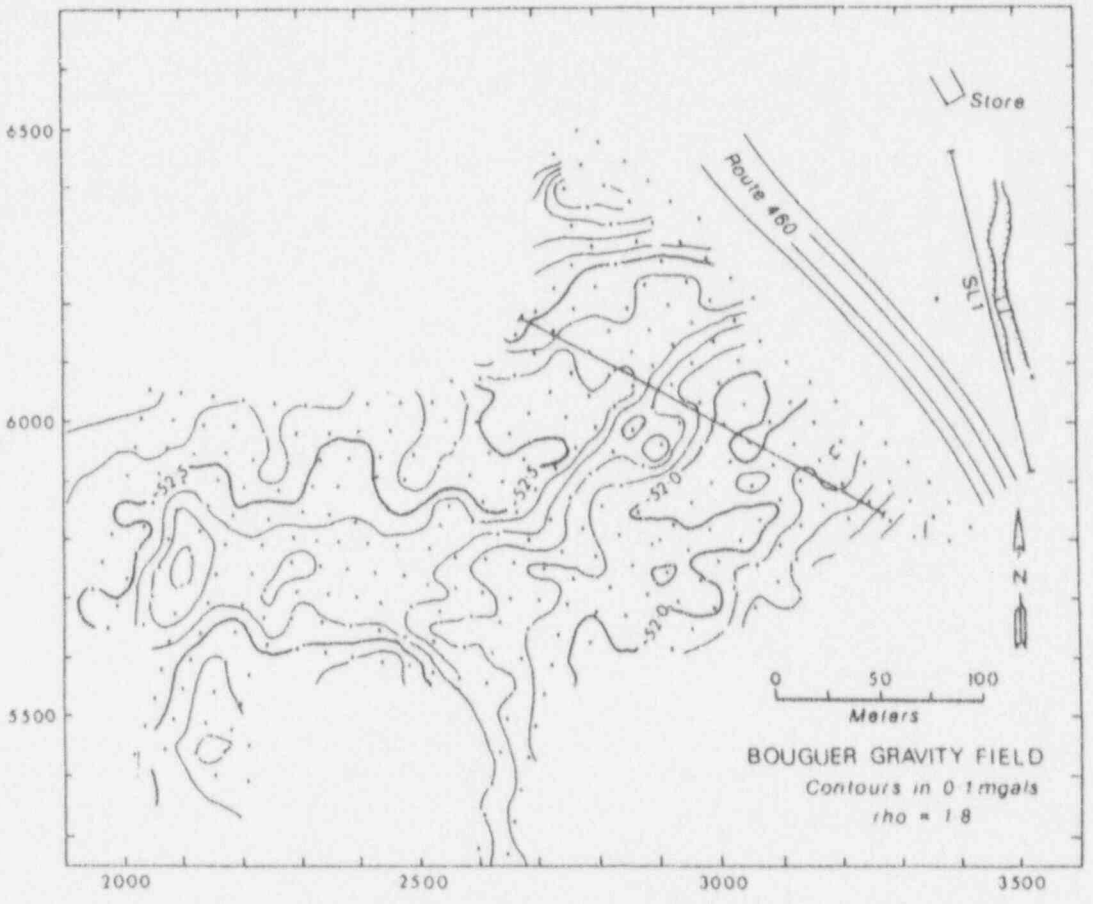


Figure 11. Contours at 0.1 milligal intervals of simple Bouguer gravity values calculated using a Bouguer plate density of 1.8 g/cc. Small solid dots indicate gravity observation sites.
The WNW trending line corresponds to SL2 in Figure 10. By adding 1,370,000 to the values along the south edge, and by adding 360,000 to values along the west edge of the map, Virginia state plane grid coordinates in units of feet are obtained. Position of the 1992 bench cuts located to the east of Route 460 is indicated (cf. Fig. 2). Large solid dots indicate position of telephone poles adjacent to bench cuts.

surface densities of 1.8 g/cc and 2.2 g/cc.

Results along line SL2 are presented in Figure 12 to illustrate how gravity data can be used to estimate the thickness of the layer of unconsolidated sediment. If Bouguer gravity variation along this profile is attributed solely to variation in thickness of sediment, then estimates of the contrast between sediment density and basement density can be calaulated using the values of sediment thickness determined at the end points of the profile from seismic refraction measurements and the Bouguer gravity values at those end points. For Bouguer gravity values computed with a sediment density of 2.2 g/cc, the estimated contrast is 0.81 g/cc, implying an unlikely basement density of 3.01 g/cc. For Bouguer gravity values computed with a sediment density of 1.8 g/cc the estimated contrast is 0.66 g/cc, which implies a basement density of 2.46 g/cc. These lat'er density values seem reasonable in view of the relatively low seismic wave speeds measured in the sediment and the basement. A conversion factor relating Bouguer gravity and sediment thickness was then determined. This conversion factor was used to calculate estimates of sediment thickness for each gravity station location.

Results seen in Figure 12 indicate the nature of the

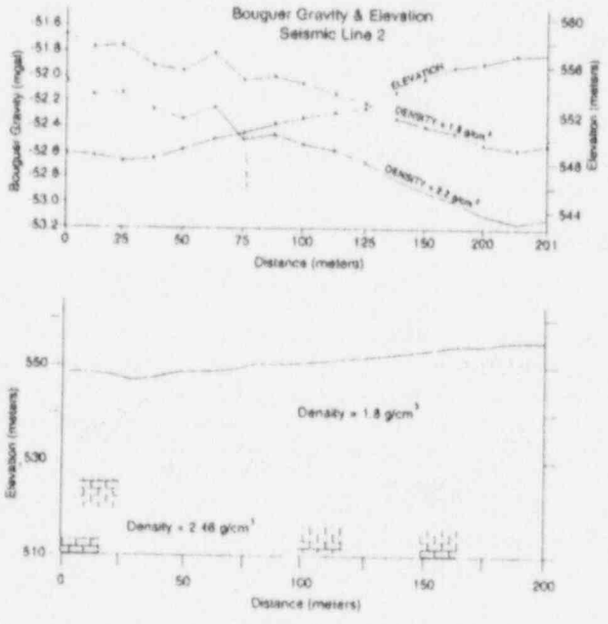


Figure 12. Bouguer gravity variation calculated using Bouguer plate densities of 1.8 g/cc and 2.2 g/cc, land surface elevation, and an interpretative cross section calculated using Bouguer gravity and seismic refraction soundings along profile SL2.

relief which may characterize the basement surface. Efforts are currently underway to calculate thickness estimates for all gravity observation sites using control points from other seismic lines and from measurements on the limestone terrane bordering the sediment. An interesting feature of the Bouguer gravity map is the trend of contour lines which extend NE from the grid location of (2700E, 5800N) approximately parallel but offset from the strike of faults exposed by excavation. Studies are now in progress to determine if the gradient indicated by these contours can be explained by an escarpment or by a more gradational slope on the underlying "basement" surface.

Electrical resistivity measurements were made along the three seismic lines and two additional lines by a roll-along offset sounding procedure using sixteen equally spaced electrodes connected to a switching unit by a segmented 16 conductor cable. The switching unit is used to select different 4-electrode combinations for connection to the resistivity bridge. Five expanding, but offset Wenner configurations were selected from the 16-electrode array. After measuring apparent resistivity from these five combinations the electrode and cable segment from one end is moved to the other end of the array, and another set of readings is obtained. As this procedure is repeated, the array "rolls along" in the same way that a seismic geophone spread advances in CDP reflection profiling. Apparent resistivity data are then displayed on a "pseudo-section" by plotting each value at the horizontal position of the center of its 4-electrode combination, and the vertical position equal to the spacing of those 4 electrodes. The array of values is then contoured to complete the pseudo-section.

Three pseudo-sections are displayed in Figure 13. The one labelled SL1-RES18 was prepared from measurements using 5.5 m electrode spacing along the part of SL1 passing directly over the central graben exposed by excavation. The other two were prepared from measurements using 3.0 m electrode spacing along profile ResL (Figure 10), and 4.5 m spacing along SL2. Along the latter two profiles the measurements crossed the estimated position of the central graben based upon projection of the strike direction determined from the excavated exposure. The dashed line in Figure 13 indicates the location of the graben on SL1, and the projected locations on ResL and SL2. Of importance are the steeply inclined contours which may indicate the existance of the graben and associated structure along the profiles offset from the excavation. Resistivity model analysis is planned to test this possibility.

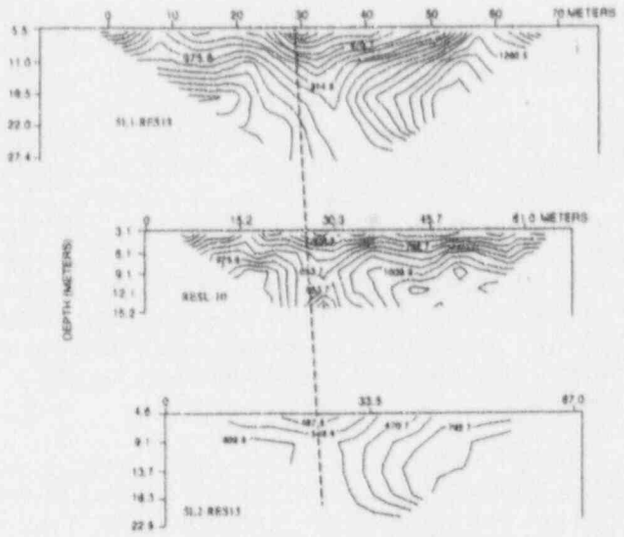


Figure 13. Electrical resistivity pseudo-sections prepared from measurements along profiles SL1, Res L, and SL2 shown in Figure 10. Contours are in units of ohm-meters. Distance and pseudo-depth are in units of meters. The dashed line indicates the position of the central graben exposed by excavation close to SL1, and its estimated position along Res L and SL2.

Neither the unconsolidated sediments nor the underlying limestone are likely to produce large magnetic anomalies. However, localized deposits of magnetite or ilmenite enriched sands, or iron oxides precipitated on the walls of ground water conducting channels might possibly produce weak magnetic anomalies. Insofar as magnetic sediment may have accumulated in structurally controlled depressions on a former land surface, or ground water channels may be related to fractures within the sediment, weak magnetic anomalies might reveal structurally controlled patterns.

To test this possibility total magnetic field intensity measurements were made at the same locations where gravity was measured using an EG & G Geometrics Model G856 proton precession magnetometer. Results of this survey are displayed in Figure 14. Comparison of this magnetic field with the Bouguer gravity field in Figure 11 reveals some interesting apparent correlations. Although dipolar magnetic anomalies have different form than gravity anomalies, similar anomaly locations suggest geologically related density and magnetization contrasts. In particular the local anomalies situated near grid coordinates (2900E, 5900N) and near (1900E, 5700N) and along the line connecting these end locations appear to indicate such geologically related anomaly sources.

In conclusion the seismic and gravity measurements indicate a layer of low density (1.8 g/cc) unconsolidated sediment reaching thicknesses of more than 40 meters, and resting upon an irregular basement surface. The basement appears to be characterized by a density slightly under 2.5 g/cc. This value is consistent with the broken limestone terrane that borders the deposits of unconsolidated sediment. The terrane consists mostly of angular fragments of limestone, with dimensions ranging from several centimeters to more than a meter, and is marked by karst features. Additional gravity analysis is now underway to ascertain if a NE trending linear escarpment or a more gradational slope extends along the basement surface approximately on strike with faults exposed by excavation. Electrical resistivity anomalies suggest structures within the unconsolidated sediment on strike and up to 200 m west of the structures exposed by excavation. Comparison of Bouguer gravity and total magnetic field intensity maps reveal an ENE alignment of anomalies which suggest the possibility of geologically related density and magnetization contrasts.

POSSIBLE DRIVING CAUSES FOR OBSERVED FAULTING AND FOLDING OF THE NEW RIVER TERRACE GRAVELS

In terms of seismic hazard assessment, it is clearly of critical importance to determine whether the faults and folds within the 'terrace' deposits have formed in response to surficial processes or to tectonic processes.

Within the Giles County area, spectacular examples of both modern landslides (Samford 1983) and large (km scale) ancient landslides (e.g Schultz 1986; Schultz & Southworth 1987, 1989; Gathright & Radar 1987; Schultz et al. 1989) have been documented. Relative dating of the slides based on weathering profiles and blocked streams places them in the Pleistoce to early Holocene (Schultz 1986). Radiocarbon dating of peat horizons within sag ponds located on top of one these large scale ancient landslides at White Gate, located 11 miles (18 km) to the southeast of the excavation site, has yielded ages ranging from 9860 +/- 250 to 7760 +/- 250 years before present (K.M. Farrell in Schultz et al. 1989, fig. 24). These earliest Holocene dates indicate the land slide and subsequent formation of a small sedimentary basin occured prior to Holocene times.

However, although numerous examples of landslides have been documented in the Giles County area, no examples of movement along foliated fault gouge surfaces similar to those observed at the excavation site appear to have been recorded. Deformation associated with these landslide structures

appears to have involved slip on fault surfaces dipping towards topographic valleys accompanied by locally intense brecciation (e.g. Schultz 1986). It will be recalled that the excavation site faults generally strike at a high angle to the trend of the New River valley in this area. One possible model explaning the folding and faulting of the Pembroke river terrace sediments in terms of a large-scale listric extensional fault underlying the excavation site, but detaching within the sediments, is illustrated in Figure 15.

The possibility must also be born in mind that the excavation site extension faults may have formed in response to solution collapse at depth. The terrace deposits at the excavation site have been mapped by Schultz et al. (1986) as resting on Lower Ordovician and Upper Cambrian rocks composed primarily of dolomite with some thin sandstone layers. No major sink hole surface features were reported by Miller & Hubbard (1986) in the immediate excavation site area on their map of karst features in Giles County. However, clear examples of sink hole formation can be seen. in the limestone bedrock immediately to the east of the excavation site. A schematic model of how solution collapse beneath the excavation site might have led to formation of the observed folding and faulting in the overlying sediments is illustrated in Figure 16.

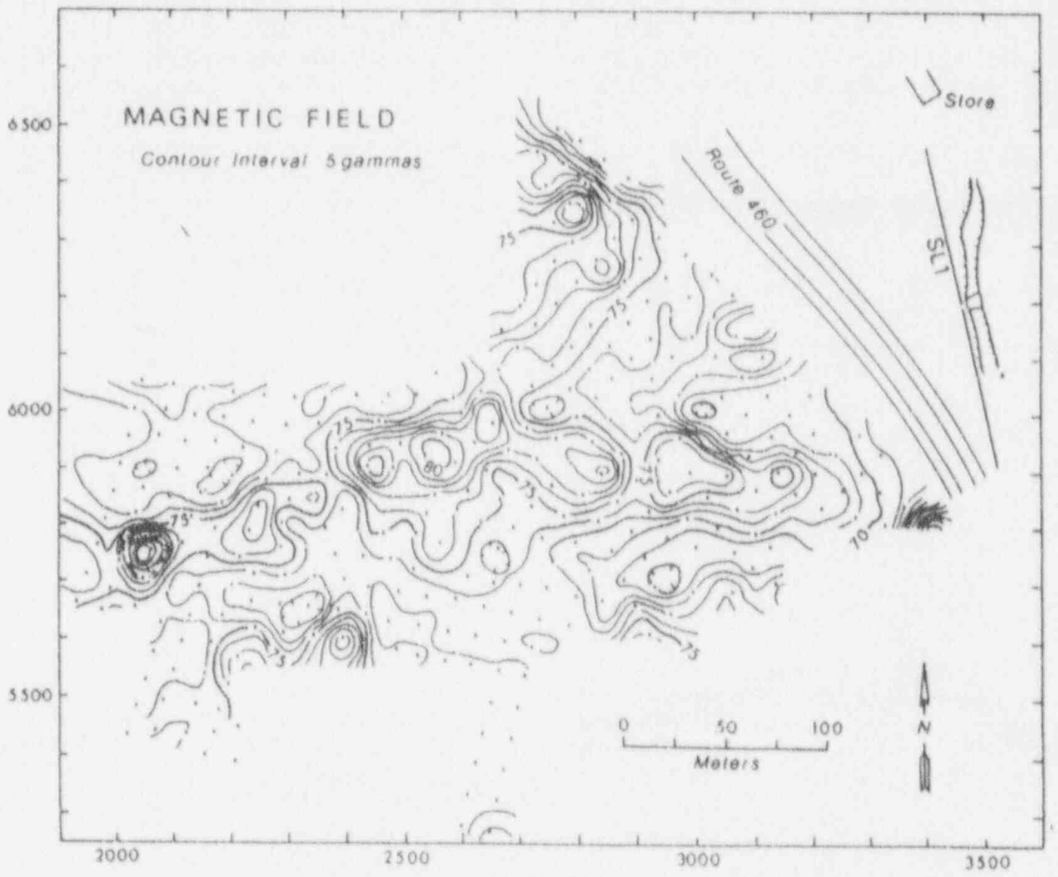


Figure 14. Variation of magnetic field intensity shown by contours at 5 gamma intervals. Total magnetic field intensity values are obtained by adding 53600 gammas to values indicated by the contours. By adding 1,370,000 to the values along the south edge, and by adding 360,000 to values along the west edge of the map, Virginia state plane grid coordinates in units of feet are obtained. Small solid dots indicate observation sites. Position of the 1992 bench cuts located to the east of Route 460 is indicated (cf. Fig. 2). Large solid dots indicate position of telephone poles adjacent to bench cuts.

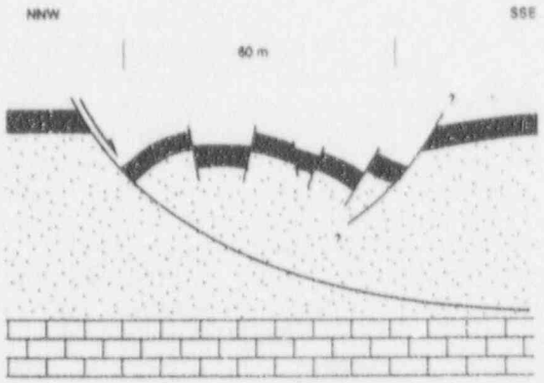


Figure 15. Schematic gravity sliding model for formation of observed folding and faulting in the 1992 excavations at the Pembroke site.
Folding and faulting developes in response to roll-over in the hangingwall of a listric extensional fault detaching within the river terrace sediments.

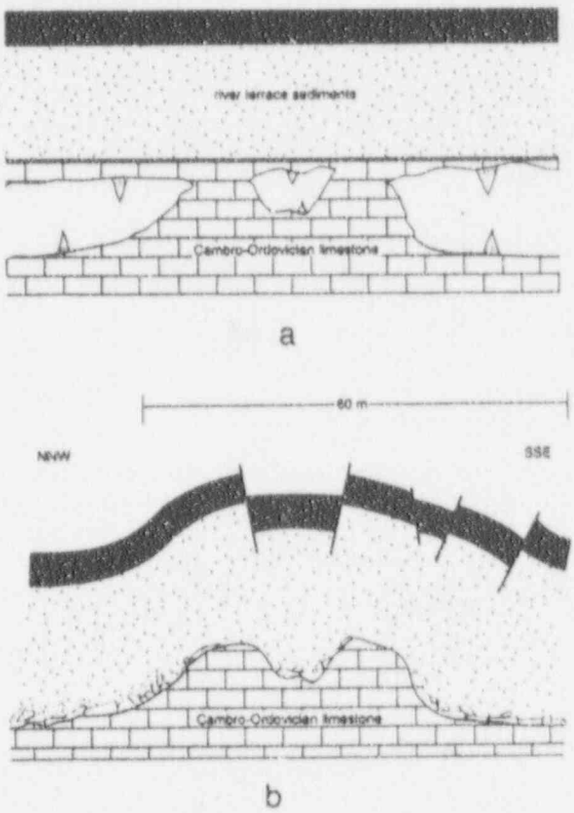


Figure 16 Schematic solution collapse model for formation of observed folding and faulting in the 1992 excavations at the Pembroke site.

a) Cavern configuration before collapse.
b) Collapse of cavern roofs leading to folding and faulting in the overlying river terrace sediments.

The authors have been unable to find any examples in the literature of solution collapse leading to the formation of foliated gouge-rich fault zones like those recorded in the excavation site. In addition, it seems unlikely that the unequivocal reverse faults exposed in the 1993 excavations (Figs. 8 & 9) can be easily explained in terms of solution collapse processes. Further, as previously mentioned, the presence of chemically reducing conditions associated with fluid flow along the clay-rich fault zones suggests upward directed fluid flow (D. Rimstidt, pers. comm 1993). If faulting had occured in response to solution collapse then one might intuitively expect downward rather than upward fluid flow along the fault zones.

The distinct possibility therefore remains that the excavation site faults may have formed in response to tectonic processes. Assuming that the 'terrace' deposits which are cut by these faults are geological recent, then the faults are of obvious importance to seismic hazard assessment. A schematic model illustrating how basement fracturing due to tectonic processes might lead to folding and faulting in the overlying sediments at the excavation site is illustrated in Figure 17. As indicated in an earlier section of this paper, the excavation site faults are situated within the currently active Giles County seismic zone (Fig. 1) as defined by Bollinger (1981). Mills (1986) has demonstrated on a statistical basis, that the terrace deposits along the New River in the Pearisburg area are at approximately a 27 m (90') higher structural level than their upstream equivilents in the Radford area located 25 km to the southeast. Mills (1986) has suggested that this relative

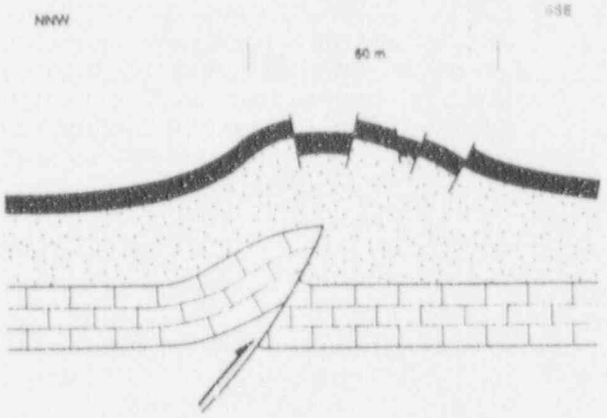


Figure 17. Schematic tectonic model for formation of observed folding and faulting in the 1992 excavations at the Pembroke site.
Folding and faulting developes within the sediments in response to reverse faulting of tectonic origin in the underlying basement rocks.

uplift of the Pearisburg area could be due to fault movement on the Giles County seismic zone and has estimated an averaged rate of differential uplift which could be as high as 200 mm per 1000 years.

Because of the presence of this active seismic zone, several extensive previous field searches have been made in the Giles County area for surface neotectonic features, in either bedrock or surficial deposits, that could be related to seismic activity (Mills 1988, McDowell & Schultz 1990). No such features were found.

SUMMARY

1. At the Pembroke excavation site the New River Terrace gravels are arched into a broad ENE-WSW trending antiform measuring a horizontal distance of at least 95 m from limb to limb, with dips of up to 30° on each fold limb. Stereographic analysis of poles to bedding planes exposed during the excavations indicates that the calculated fold axis plunges at between 7° and 14° towards N64°W, a shallower plunge being detected at the higher structural levels.

2. A graben structure, measuring 11.0 m in width at its highest currently exposed structural level, is present in the hinge zone of this antiform. Above road level, the graben is a downward -narrowing structure, defined by two fault zones with orientations: strike N51°E, dip 71°SE (Fault 1) and N80°E, 56°N (Fault 2). Traced downwards beneath road level, these faults steepen to become vertical, the graben measuring 4.6 m in width. Faults 1 and 2 are each marked by 10-20 cm wide zones of foliated and lineated green clay-rich fill. Assuming the lineations formed parallel to the fault's slip vector, then total extensional displacements of 11.4 m and 11.0 m are indicated by the stratigraphic off-sets on Faults 1 and 2 respectively.

3. A second graben structure is present on the southern limb of the antiform. The two clay-rich fault zones defining this smaller graben, have closely similar orientations to those defining the central graben, but displacements indicated by lineation and stratigraphic cut-off data are only on the order of 1.0 - 2.0 m. A fifth clay-rich extensional fault, dipping at 54° to the NW and displaying 3.0 m of displacement is present to the south of the smaller graben.

4. The close geometrical relationships between the observed fold and fault geometries suggests that these clay-rich faults may have formed during formation of the antiform.

5. In addition to the major clay-rich extensional faults, numerous barren faults, typically displaying off-sets of less than 30 cm, have also been observed. At least some of these faults appear to be of syn-sedimentary origin. Although most of these barren faults display extensional geometries, a small proportion display apparent reverse sense off-sets. Due to the geometrical relationships between these apparent reverse faults and the tilted bedding, these faults could be either true reverse faults or original extensional faults that were tilted through the vertical during formation of the antiform.

6. Unequivocal reverse faults are present near the hinge zone of the antiform. The 5-10 cm thick green clay-rich fill associated with these faults is strongly foliated and displays a down-dip lineation. These reverse faults, which strike approximately N70°E, dip towards the hinge zone of the antiform and display a top-to the N thrust sense on the northern limb of the antiform (with an off-set of c. 30 cm) and a top-to-the S thrust sense (off-set c. 60 cm) on the southern limb. The geometry of these faults with respect to bedding indicates a reverse sense of motion even if they formed before folding.

7. Although many of the fault structures may post-date sedimentation, earlier syn-sedimentary deformation is also indicated by the presence of angular unconformities and small-scale growth faults in the exposed section.

8. Reconnaissance geophysical surveys indicate that the river terrace sediments beneath the excavation site are at least 40 m thick and rest upon an irregular bedrock surface. Electrical resistivity surveying indicates that the central graben structure exposed in both the 1992 and 1993 excavations may extend for at least 200 m along strike to the west of the excavation site. Subsurface continuation towards the west of structures exposed in the excavation site is also indicated by an ENE alignment of anomalies in the Bouguer gravity and total magnetic intensity maps.

9. Age dating of these unlithified sediments remains problematic. Given their structural elevation above the present-day position of the New River, published erosion rates for the area would seem to indicate that the sediments are between 3.0 and 1.5

million years old. Extensive laboratory work has failed to reveal any carbonaceous or fossil material which might facilitate the more precise dating of these highly oxidized sediments.

10. Three models, involving landsliding, solution collapse and basement faulting of tectonic origin are proposed for formation of the fold and fault structures exposed at the excavation site, and the relative merits of each model discussed.

ACKNOWLEDGMENTS

Research reported in the paper was carried out under Nuclear Regulatory Commission Contract No. NRC-04-85-121. The authors wish to express their gratitude to Mr Arnold Bostic and Mr Mike Bostic of Pembroke, Virginia, for generously granting them permission to carry out long-term site excavations on their property during 1992 and 1993. The authors also wish to thank Cole Davisson for his help in drafting several of the figures included in this paper.

REFERENCES

Bartholomew, M.J. & Mills, H.H. 1991 Old courses of the New River: its late Cenozoic migration and bedrock control inferred from high-level stream gravels, southwestern Virginia. Bulletin Geological Society of America 103, 77-81.

Bollinger, G.A. 1973 Seismicity of the southeastern United States. Bulletin of the Seismological Society of America 63, 1785 - 1808.

Bollinger, G.A. 1981 The Giles County, Virginia, seismic zone: configuration and hazard assessment. In: Beavers, J.E. (editor) Earthquakes and earthquake Engineering, v. 1, The Eastern United States. Ann Arbor, Science Publishers, p. 277-308.

Bollinger, G.A. & Hopper, M.G. 1971a The earthquake history of Virginia, 1774 to 1900. Blacksburg, Department of Geological Sciences, Virginia Polytechnic Institute & State University, 87 p.

Bollinger, G.A. & Hopper, M.G. 1971b Virginia's two largest earthquakes: December 22, 1975 and May 31, 1897. Bulletin of the Seismological Society of America 61, 1033 - 1039.

Bollinger, G.A. & Wheeler, R.L. 1982 The Giles County, Virginia, seismogenic zone - Seismological results and geological interpretations. U.S. Geological Survey Open File Report 82-585, 136p.

Bollinger, G.A. & Wheeler, R.L. 1988 The Giles County, Virginia, seismic zone - seismological results and geological interpretations. U.S. Geological Survey Professional Paper 1355, 85 p.

Campbell, M.R. 1898 Earthquake shocks in Giles County, Virginia. Science 7, 233 - 235.

Gathright, T.M. & Radar, E.K. 1987 Recognition of disaggregated rock block slides in a structurally complex terrane in Virginia. In: Schultz, A.P. & Southworth, C.S.(editors) Landslides of eastern North America U.S. Geological Survey Circular 1008, 43 p.

Gresko, M.J. 1985 Analysis and interpretation of compressional (P wave) and shear (SH wave) reflection seismic and geologic data over the Bane Dome, Giles County, Virginia. Unpubl. PhD. thesis, Virginia Polytechnic Institute & State University, 74 p.

Hack, J.T. 1980 Rock control and tectonism - their importance in shaping the Appalachians. U.S. Geological Survey Professional Paper 1126-B, 17pp.

Hale, R.C. 1961 Geology of the Peters Mountain area, Giles County, Virginia. Unpubl. MS thesis, Virginia Polytechnic Institute & State University, 105 p.

Houser, B. 1980 Erosional history of the New River, southern Appalachians, Virginia. Unpubl. PhD. thesis, Virginia Polytechnic Institute & State University, 225 p.

Houser, B. 1981 Erosional history of the New River, southern Appalachians, Virginia. U.S. Geological Survey Open-File report 81-771, 225 p.

Lowry, W.D. 1979 Nature of thrusting along the Alleghany Front near Pearisburg and of overthrusting in the Blacksburg-Radford area of Virginia. Eleventh Annual Virginia Geological Field Conference, Virginia Polytechnic Institute & State University, Department of Geological Sciences, Guidebook 8, 66p.

McDowell, R.C. & Schultz, A.P. 1990 Structural and stratigraphic framework of the Giles County area, a part of the appalachian Basin of Virginia and West Virginia. U.S. Geological Survey Bulletin 1839, E1 - E24.

Miller, E.V. 1985 Graphical and digital slope stability analysis for Giles County, Virginia. Unpubl. MS thesis, Virginia Polytechnic Institute & State University, 193 p.

Miller, E.V. & Hubbard, D.A. 1986 Selected slope catagories and karst features map of Giles County, Virginia. Virginia Division of Mineral resources Publication 70, scale 1:50,000.

Mills, H.H. 1986 Possible differential uplift of New River terraces in southwestern Virginia. Neotectonics 1, 75 - 86.

Mills, H.H. 1988 Surficial geology and geomorphology of the Mountain Lake area, Giles County, Virginia, including sedimentological studies of colluvium and boulder streams. U.S. Geological Survey Professional Paper 1469.

Mills, H.H. & Wagner, J.R. 1985 Long-term change in regime of the New River indicated by vertical variation in extent and weathering intensity of alluvium. Journal of Geology 93, 131 - 142.

Munsey, J.W. 1984 Focal mechanism analysis for recent (1978 - 1984) Virginia Earthquakes. Unpubl. MS thesis, Virginia Polytechnic Institute & State University, 214 p.

Munsey, J.W. & Bollinger, G.A. 1985 Focal mechanism analyses for Virginia earthquakes. Bulletin of the Seismological Society of America 75, 1613-1636.

Samford, W.J. 1983 Narrows landslide, Giles County, Virginia. Virginia Minerals 29, 37 - 44.

Schultz, A.P. 1986 Ancient, giant rockslides, Sinking Creek Mountain, Southern appalachians, Virgina. Geology 14, 11 - 14.

Schultz, A.P., Mills, H., Farrell, K., Southworth, S., Thompson, R. & Rubin, M. 1989 Roadlog and site description for the 1989 Southeast friends of the pleistocene field exursion: surficial geology of the New River Valley, southwest Virginia. U.S. Geological Survey Open-File Report 89-635.

Schultz, A.P. & Southworth, C.S. 1987 Landslides of eastern North America U.S. Geological Survey Circular 1008, 43 p.

Schultz, A.P. & Southworth, C.S. 1989 Large bedrock landslides of the Appalachian Valley and ridge province of eastern North America. Geological Society of America Special Paper 236.

Schultz, A.P, Stanley, C.B., Gathright, T.M., Rader, E.K., Bartholomew, M.J., Lewis, S.E. & Evans, N.H. 1986 Geologic map of Giles County, Virginia. Virginia Division of Mineral Resources Publication 69, scale 1:50,000.

Sears, C.E. 1957 Late Cretaceous erosion surface in southwest Virginia (abstract). Geological Society of America Bulletin 68, 1883.

NRC FORM 335 (2-89) NRCM 1102, 3201, 3202

U.S. NUCLEAR REGULATORY COMMISSION

BIBLIOGRAPHIC DATA SHEET

(See instructions on the reverse)

1. REPORT NUMBER (Assigned by NRC, Add Vol., Supp., Rev., and Addendum Numbers, if any.)
NUREG/CP-0133
Vol. 3

2. TITLE AND SUBTITLE
Proceedings of the Twenty-First Water Reactor Safety Information Meeting

Primary System Integrity; Aging Research, Products & Applications; Structural & Seismic Engineering; Seismology & Geology

3. DATE REPORT PUBLISHED
MONTH: April
YEAR: 1994

4. FIN OR GRANT NUMBER
A3988

5. AUTHOR(S)
Compiled by Susan Monteleone, BNL

6. TYPE OF REPORT
Conference Proceedings

7. PERIOD COVERED (Inclusive Dates)
October 25-27, 1993

8. PERFORMING ORGANIZATION – NAME AND ADDRESS (If NRC, provide Division, Office or Region, U.S. Nuclear Regulatory Commission, and mailing address; if contractor, provide name and mailing address.)
Office of Nuclear Regulatory Research
U.S. Nuclear Regulatory Commission
Washington DC 20555-0001

9. SPONSORING ORGANIZATION – NAME AND ADDRESS (If NRC, type "Same as above"; if contractor, provide NRC Division, Office or Region, U.S. Nuclear Regulatory Commission, and mailing address.)
Same as Item 8 above

10. SUPPLEMENTARY NOTES
Proceedings prepared by Brookhaven National Laboratory

11. ABSTRACT (200 words or less)

This three-volume report contains 90 papers out of the 102 that were presented at the Twenty-First Water Reactor Safety Information Meeting held at the Bethesda Marriott Hotel, Bethesda, Maryland, during the week of October 25-27, 1993. The papers are printed in the order of their presentation in each session and describe progress and results of programs in nuclear safety research conducted in this country and abroad. Foreign participation in the meeting included papers presented by researchers from France, Germany, Japan, Russia, Switzerland, Taiwan, and United Kingdom. The titles of the papers and the names of the authors have been updated and may differ from those that appeared in the final program of the meeting.

12. KEY WORDS/DESCRIPTORS (List words or phrases that will assist researchers in locating the report.)
BWR type reactors - reactor safety, PWR type reactors - reactor safety, reactor safety - meetings, research programs - reviews, reactor accidents, reactor components, nuclear power plants - reliability, nuclear power plants - risk assessment, aging, probabilistic estimation, loss of coolant, reactor accidents -management, human factors, containment, systems analysis, leading abstract - proceedings, seismic effects, hydraulics - heat transfer, environmental engineering. International Organizations

13. AVAILABILITY STATEMENT
Unlimited

14. SECURITY CLASSIFICATION
(This Page)
Unclassified
(This Report)
Unclassified

15. NUMBER OF PAGES

16. PRICE



Federal Recycling Program

UNITED STATES
NUCLEAR REGULATORY COMMISSION
WASHINGTON, D.C. 20555-0001

OFFICIAL BUSINESS
PENALTY FOR PRIVATE USE, $300

SPECIAL FOURTH-CLASS RATE
POSTAGE AND FEES PAID
USNRC
PERMIT NO. G-67

120555139531 1 1AN1R11R21R31
US NRC-OADM
DIV FOIA & PUBLICATIONS SVCS
TPS-PDR-NUREG
2WFN-6E7
WASHINGTON DC 20555